N71-28330

NASA CR-72886

FINAL REPORT

PRESSURE MEASURING SYSTEMS FOR CLOSED CYCLE LIQUID METAL FACILITIES

by

Anthony J. Cassano

CONSOLIDATED CONTROLS CORPORATION
15 Durant Avenue
Bethel, Connecticut 06801

prepared for

NATIONAL AERONAUTICS AND SPACE ADMINISTRATION

April 30, 1971

CONTRACT NAS 3-4170

NASA Lewis Research Center
Cleveland, Ohio
James P. Couch, Project Manager
Space Power Systems Division

CASE FILE COPY

NOTICE

This report was prepared as an account of Government sponsored work. Neither the United States nor the National Aeronautics and Space Administration (NASA) nor any person acting on behalf of NASA:

A.) Makes any warranty or representation, expressed or implied, with respect to the accuracy, completeness, or usefulness of the information contained in this report, or that the use of any information, apparatus, method, or process disclosed in this report may not infringe privately-owned rights; or

B.) Assumes any liabilities with respect to the use of, or for damages resulting from the use of, any information, apparatus, method or process disclosed in this report.

As used above, "person acting on behalf of NASA" includes any employee or contractor of NASA, or employee of such contractor, to the extent that such employee or contractor of NASA or employee of such contractor prepares, disseminates, or provides access to any information pursuant to his employment or contract with NASA, or his employment with such contractor.

Requests for copies of this report should be referred to

National Aeronautics and Space Administration
Scientific and Technical Information Facility
P. O. Box 33
College Park, Md. 20740

TABLE OF CONTENTS

	Title	Page No.
	Table of Contents	i
	List of Illustrations	iv
	List of Tables	xiv
	Abstract	xv
1.0	Summary	1
2.0	Introduction	2
3.0	Transducer Design Concept	4
3.1	Thermionic Diode Sensor	5
3.1.1	Space Charge Operation	5
3.1.2	System Parameters	10
3.1.3	Emitter Considerations	11
3.1.4	Error Analysis	12
3.2	Transducer Mechanical Design	14
4.0	Pressure Deflection System	18
4.1	Initial Deflection Tests	19
4.1.1	Vacuum Test Facility	20
4.1.2	Diaphragm Deflection Measurement	22
4.1.3	Test Procedure	24
4.1.4	Test Results	26
4.2	Pressure Capsule Design	36
4.3	Pressure Capsule Fabrication	40

	Title	Page No.
5.0	Thermionic Diode Sensor	42
5.1	Cast Heater - Emitter Assembly	42
5.2	Lucalox Base Assembly	47
5.3	Sensor Assembly	50
6.0	Metal-Ceramic Seal	53
6.1	Seal Test Program	53
6.2	Metal-Ceramic Seal Evaluation	55
6.2.1	Metallographic Analysis	56
6.2.2	X-Ray Microprobe Analysis	61
6.3	Seal Thermal Cycling Tests	65
7.0	Liquid Metal Compatibility	67
7.1	Compatibility Testing	69
7.1.1	Examination of the Test Capsules	71
7.1.2	Potassium Analysis	75
8.0	Differential Pressure Transducer	80
9.0	Transducer Signal Conditioning	87
9.1	Heater Control	87
9.2	Constant Current Control	89
9.3	Pressure Computing Amplifiers	90
9.4	External Instrumentation	91
10.0	Vacuum Test Facility	92
11.0	Transducer Test Program	97
11.1	Experimental Test Devices	97

	Title	Page No.
11.2	Final Transducer Testing	121
11.2.1	Absolute Transducer 3	130
11.2.2	Absolute Transducer 4	137
	Summary of Results	144
	References	148
	Bibliography	149
	Appendix A - Variable Impedance Sensor	150
	Appendix B - Thermionic Diode Relations	160
	Appendix C - Pressure Transducer Test Program	166

LIST OF ILLUSTRATIONS

No.	Title
1.	Electron Potential Energy Diagram
2.	Current-Voltage Relation at Constant Temperature
3.	Thermionic Output Signal Curves
4.	Absolute Pressure Transducer
5.	Differential Pressure Transducer
6.	Differential Pressure Transducer
7.	Test Pressure Capsule Configuration
8.	Vacuum Test Facility Test Station
9.	Vacuum Test Chamber
10.	Vacuum Test Chamber Details
11.	Argon System for Testing
12.	Typical Metallographic Plate
13.	Deflection Test Chronology
14.	C-129Y Single Convolution, 0.0006 inch Test Pressure-Deflection, Room Temperature
15.	Pressure-Deflection, 500°F
16.	Pressure-Deflection, 1000°F
17.	Pressure Deflection, 1200°F
18.	Pressure-Deflection, 1400°F
19.	Pressure-Deflection, 1600°F
20.	Pressure-Deflection, 1800°F
21.	C-129Y Single Convolution, 0.001 inch Test Pressure-Deflection, Room Temperature
22.	Pressure-Deflection, 500°F
23.	Pressure-Deflection, 1000°F

No.	Title
24.	Pressure-Deflection, 1200°F
25.	Pressure-Deflection, 1400°F
26.	Pressure-Deflection, 1600°F
27.	Pressure-Deflection, 1800°F
28.	C-129Y Double Convolution, 0.002 inch Test Pressure-Deflection, Room Temperature
29.	Pressure-Deflection, 500°F
30.	Pressure-Deflection, 1000°F
31.	Pressure-Deflection, 1200°F
32.	Pressure-Deflection, 1400°F
33.	Pressure-Deflection, 1600°F
34.	Pressure-Deflection, 1800°F
35.	FS-85 Double Convolution, 0.001 inch Test Pressure-Deflection, Room Temperature
36.	Pressure-Deflection, 500°F
37.	Pressure-Deflection, 1000°F
38.	Pressure-Deflection, 1200°F
39.	Pressure-Deflection, 1400°F
40.	Pressure-Deflection, 1600°F
41.	Pressure-Deflection, 1800°F
42.	FS-85 Double Convolution, 0.002 inch Test Pressure-Deflection, Room Temperature
43.	Pressure-Deflection, 500°F.
44.	Pressure-Deflection, 1000°F
45.	Pressure-Deflection, 1200°F

No.	Title
46.	Pressure-Deflection, 1400°F.
47.	Pressure-Deflection, 1600°F
48.	Pressure-Deflection, 1800°F
49.	FS-85 Double Convolution, 0.004 inch Test Pressure-Deflection, Room Temperature
50.	Pressure-Deflection, 500°F
51.	Pressure-Deflection, 1000°F
52.	Pressure-Deflection, 1400°F
53.	Pressure-Deflection, 1800°F.
54.	T-222 Single Convolution, 0.0006 inch Test Pressure-Deflection, Room Temperature
55.	Pressure-Deflection, 500°F
56.	Pressure-Deflection, 1000°F
57.	Pressure-Deflection, 1200°F
58.	Pressure-Deflection, 1400°F
59.	Pressure-Deflection, 1600°F
60.	Pressure-Deflection, 1800°F
61.	T-222 Single Convolution, 0.001 inch Test Pressure-Deflection, Room Temperature
62.	Pressure-Deflection, 500°F
63.	Pressure-Deflection, 1000°F
64.	Pressure-Deflection, 1200°F
65.	Pressure-Deflection, 1400°F.
66.	Pressure-Deflection, 1600°F.
67.	Pressure-Deflection, 1800°F.

No.	Title
68.	W-25Re Double Convolution, 0.001 inch Test Pressure-Deflection, Room Temperature
69.	Pressure-Deflection, 500°F
70.	Pressure-Deflection, 1000°F
71.	Pressure-Deflection, 1200°F
72.	Pressure-Deflection, 1400°F
73.	Pressure-Deflection, 1600°F
74.	Pressure-Deflection, 1800°F
75.	W-25Re Double Convolution, 0.002 inch Test Pressure-Deflection, Room Temperature
76.	Pressure-Deflection, 500°F
77.	Pressure-Deflection, 1000°F
78.	Pressure-Deflection, 1200°F
79.	Pressure-Deflection, 1400°F
80.	Pressure-Deflection, 1600°F
81.	Pressure-Deflection, 1800°F
82.	W-25Re Double Convolution, 0.004 inch Test Pressure-Deflection, Room Temperature
83.	Pressure-Deflection, 500°F
84.	Pressure-Deflection, 1000°F
85.	Pressure-Deflection, 1200°F
86.	Pressure-Deflection, 1400°F
87.	Pressure-Deflection, 1600°F
88.	Pressure-Deflection, 1800°F
89.	C-129Y Final Time Test Procedure
90.	FS-85 Final Time Test Procedure
91.	C-129Y Full Scale Deflection-Temperature Curves

No.	Title
92.	FS-85 Full Scale Deflection-Temperature Curves
93.	T-222 Full Scale Deflection-Temperature Curves
94.	W-25Re Full Scale Deflection-Temperature Curves.
95.	Absolute Pressure Capsule
96.	Differential Pressure Capsule
97.	Electrical Discharge Machining Set-up
98.	5 psid Pressure Capsule Convolution
99.	Thermionic Diode Sensor
100.	Heater Assembly
101.	Emitters and Installation
102.	Emitter Surface Photomicrographs
103.	Lucalox Base Material
104.	Finished Lucalox Sensor Base
105.	Lucalox Braze Set-Up
106.	Thermionic Diode Sensor and Thermocouple
107.	Electrical Terminal
108.	Metal-Ceramic Test Unit
109.	Metal-Ceramic Test Unit After Test
110.	Ceramic to Metal Seal, Tube End, 100X
111.	Ceramic to Metal Seal, Tube End, 100X
112.	Tube End Interface, 500X
113.	Tube End Metal Member, 200X
114.	Ceramic to Metal Seal Tube End, 100X
115.	Tube End Metal Member, 200X

No.	Title
116.	Tube End Interface, 500X
117.	Bulged End Central Portion, 200X
118.	Ceramic to Metal Seal Bulged End, 100X
119.	Bulged End Metal Member, 200X
120.	Bulged End Metal Member, 200X
121.	Bulged End Interface, 500X
122.	Bulged End Interface, 500X
123.	Nb-Ti X-ray Microprobe Traces
124.	Ni-Al X-ray Microprobe Traces
125.	W-Y X-ray Microprobe Traces
126.	Metal-Ceramic Thermal Cycling Test Unit
127.	Compatibility Test Chamber - Internal Components
128.	Compatibility Test Chamber
129.	Compatibility Test Design for Columbium and Tantalum Capsules
130.	Compatibility Test Design for W-25Re Capsule
131.	Compatibility Test Design for Electrical Terminals
132.	Terminal Compatibility Capsule
133.	C-129Y Compatibility Capsule
134.	FS-85 Compatibility Capsule
135.	T-222 Compatibility Capsule
136.	W-25Re Compatibility Capsule
137.	Lower Portion of Terminal Compatibility Capsule
138.	Electrical Terminals
139.	C-129Y Compatibility Capsule Photograph
140.	FS-85 Compatibility Capsule Photograph

No.	Title
141.	T-222 Compatibility Capsule Photograph
142.	W-25Re Compatibility Capsule Photograph
143.	C-129Y Compatibility Capsule Micro-Photograph
144.	FS-85 Compatibility Capsule Micro-Photograph
145.	T-222 Compatibility Capsule Micro-Photograph
146.	W-25Re Compatibility Capsule Micro-Photograph
147.	Intergrannular Crack in T-222 Compatibility Capsule
148.	Differential Pressure Transducer Configurations
149.	Differential Pressure Transducer Deflection Characteristics
150.	Differential Mock-Up Force-Deflection Characteristics
151.	Transducer Electrical Signal Conditioning Schematic
152.	Electrical Signal Conditioner Panel
153.	Electrical Signal Conditioner Layout
154.	Early Vacuum Test Facility Configuration
155.	Vacuum Test Facility Schematic
156.	Basic Heater Assembly.
157.	Heater Assembly Before Casting
158.	Ceramic Base
159.	Encapsulated Heater-Ceramic Base-Support Plate Assembly.
160.	Space Charge Characteristics for T-4
161.	Pressure-Output Current Characteristics for T-4
162.	Emitter Heater Power Requirements for T-4
163.	T-4 Active and Reference Currents as Functions of Temperature

No.	Title
164.	Normalized Pressure-Output Characteristics for T-4
165.	Initial Space-Charge Data, T-6 (FS-85)
166.	Pressure-Output Data for Decreasing Temperatures, T-6 (FS-85)
167.	Pressure-Output Data for Increasing Temperature, T-6 (FS-85)
168.	Final Space-Charge Data, T-6 (FS-85)
169.	Initial Space-Charge Data, T-7 (C-129Y)
170.	Pressure-Output Data for Decreasing Temperatures, T-7 (C-129Y)
171.	Pressure-Output Data for Increasing Temperatures, T-7 (C-129Y)
172.	Final Space-Charge Data, T-7 (C-129Y)
173.	Initial Space-Charge Data, T-6 (FS-85)
174.	Pressure-Output Data for Decreasing Temperatures, T-6 (FS-85)
175.	Pressure-Output Data for Increasing Temperatures, T-6 (FS-85)
176.	Final Space-Charge Data, T-6 (FS-85)
177.	Initial Space-Charge Data, T-7 (C-129Y)
178.	Pressure-Output Data at 1800°F, T-7 (C-129Y)
179.	Pressure-Output Data at 1600°F, T-7 (C-129Y)
180.	Pressure-Output Data at 1400°F, T-7 (C-129Y)
181.	Pressure-Output Data at 1200°F, T-7 (C-129Y)
182.	Pressure-Output Data at 1000°F, T-7 (C-129Y)
183.	Pressure-Output Data at 1200°F, T-7 (C-129Y)
184.	Pressure-Output Data at 1400°F, T-7 (C-129Y)
185.	Pressure-Output Data at 1600°F, T-7 (C-129Y)

No.	Title
186.	Pressure-Output Data at 1800°F, T-7 (C-129Y)
187.	Final Space-Charge Data, T-7 (C-129Y)
188.	Emitter Braze Configuration
189.	Initial Space-Charge Characteristics, A-3
190.	Active and Reference Current Characteristics, A-3
191.	Zero-Shift Characteristics, A-3
192	Pressure-Output Characteristics, A-3
193.	Pressure-Output Characteristics, A-3
194.	Pressure-Output Characteristics, A-3
195.	Pressure-Output Characteristics, A-3
196.	Pressure-Output Characteristics, A-3
197.	Pressure-Output Characteristics, A-3
198.	Pressure-Output Characteristics, A-3
199.	Pressure-Output Characteristics, A-3
200.	Initial Pressure-Output Characteristics, A-4
201.	Initial Space-Charge Characteristics, A-4
202.	Active & Reference Current Characteristics, A-4
203.	Active & Reference Current Characteristics, A-4
204.	Active & Reference Current Characteristics, A-4
205.	Zero-Shift Characteristics, A-4
206.	Zero-Shift Characteristics, A-4
207.	Zero-Shift Characteristics, A-4
208	Pressure-Output Characteristics, A-4
209	Pressure-Output Characteristics, A-4

No.	Title
210	Pressure-Output Characteristics, A-4
211	Pressure-Output Characteristics, A-4
212	Pressure-Output Characteristics, A-4
213	Pancake Coil/Image Coil Geometry
214	Inductance-Distance Characteristics
215	Variable Impedance Test Fixture
216	Inductance-Distance Characteristics, Copper Diaphragm
217	Inductance-Distance Characteristics, Cupronickel Diaphragm
218	Inductance-Distance Characteristics, FS-85, Monel and K-Monel Diaphragms

LIST OF TABLES

No.	Title	Page No.
1	Signal Conditioning Parameters	10
2	Emitter Sheath Parameters	12
3	Thermionic Error Components	13
4	Pressure Capsule Linearity-Hysteresis Errors	27
5	C-129Y Pressure Capsule Deflection Variations (percent of full scale at 1800°F) with time at 1800°F	31
6	FS-85 Pressure Capsule Deflection Variations (percent of full scale at 1800°F) with time at 1800°F	32
7	T-222 Pressure Capsule Deflection Variations (percent of full scale at 1800°F) with time at 1800°F	33
8	W-25Re Pressure Capsule Deflection Variations (percent of full scale at 1800°F) with time at 1800°F	34
9	W-25Re Pressure Capsule Parameters	39
10	Metallographic Photo-Indexing System	57
11	Potassium Analysis Before and After Compatibility Test	76
12	Experimental Test Devices	98
13	Test Device T-4 Output Current Corrections	110
14	Zero Pressure Test Parameters, T-6 and T-7	115
15	Zero Pressure Test Parameters, T-6 and T-7	117
16	Emitter Etch Test Results	128
17	Test Chronology, Absolute Transducer 3	133
18	Test Chronology, Absolute Transducer 4	140

ABSTRACT

Development of a pressure transducer for use in liquid metal flow loops poses many design problems demanding the best from available materials. This report covers the development of a pressure transducer providing accurate measurements in the liquid, vapor, and two-phase streams of a potassium loop operating at temperatures up to 1800°F. In addition to potassium, the transducer may also find use in loops containing sodium, lithium, cesium or rubidium. The transducer uses a thermionic diode sensor to convert the motion of a pressure-actuated refractory alloy capsule into a suitable electrical output.

1.0 SUMMARY

The objective of this program was to develop pressure transducers which can be used in advanced Rankine cycle space systems using liquid metals as working and heat transfer media at elevated temperatures. The specific application involves measurements in a potassium loop operating at temperatures up to 1800°F. Both absolute and differential transducers were developed, for full scale ranges of 80 psia and ± 5 psid respectively.

The design approach uses the displacement of a refractory-alloy diaphragm member by the liquid metal pressure. The displacement is then monitored by a thermionic diode sensor whose output indicates the pressure. The main problem areas included the high-temperature diaphragm deflection characteristics, diaphragm compatibility with liquid metals, and the accuracy, sensitivity and lifetime of the thermionic diode sensor. The transducer was developed for use as either ground or flight hardware for measuring absolute and differential pressures. The absolute pressure instrument was developed for a full scale range of 80 psia and the differential instrument for ±5psid.

Extensive testing conducted on both the material requirements and the operating characteristics of the transducer indicate potassium - compatibility, mechanical integrity and transducer lifetime of more than 2000 hours. With some further work to minimize the effect of changes in operating temperature, a viable transducer design appears to be at hand.

2.0 INTRODUCTION

A great deal of present work on power generation and energy conversion involves closed cycle power systems using liquid metals as working and heat transfer media at elevated temperatures. Since small pressure changes could indicate the onset of instability, there exists a need for instrumentation that can follow and monitor both average and perturbed pressure conditions in the liquid, vapor and two-phase streams. Envisioned use of these power systems for space applications imposes the additional requirements of light weight and long-term unattended operation.

At present, pressure measurement techniques include the slack-diaphragm and the differential transformer transducers. The slack-diaphragm uses a room-temperature pressure pick-up that results in good accuracy but is severely limited in frequency response due to the long line between the test system and the pick-up. The differential transformer may be used with very short connecting tubing, resulting in reasonable frequency response, but is restricted to operation at temperatures under 900°F because of temperature limitations on the transformer. An obvious need exists for a pressure transducer capable of achieving combined requirements of accuracy, frequency response and ambient temperature.

This report covers the development of such a pressure transducer capable of providing accurate measurements in a potassium loop operating at temperatures up to 1800°F. In addition to potassium, the transducer may also find use in loops containing sodium,

lithium, cesium or rubidium. The transducer design is based on a refractory-alloy member which is displaced by the liquid metal pressure. The displacement is converted into an electrical signal by a thermionic diode sensor operating in the space-charge limited mode. This work was performed over the period from Frebruary 1964 to April 1969.

3.0 Transducer Design Concept

The objective of this program was to develop pressure transducers which could be used in advanced Rankine cycle space power systems using liquid metals as working and heat transfer media at elevated temperatures. The conceptual approach to the problem used the displacement of a diaphragm member by the liquid metal pressure and the subsequent transduction of this displacement into a suitable output signal. Two possible transducer systems were analyzed. One system is based upon the operation of a space-charge limited thermionic diode using the diaphragm as an electron collector. The other uses the diaphragm as a conducting surface whose distance from a pancake-type coil determines the inductance of the coil (variable impedance approach). The criteria used for evaluation of the two transduction systems involved signal level and deflection range. The deflection should be as small as possible, consistent with usable output, to minimize the stress levels in the diaphragm. Our initial tests indicated that under these conditions the variable impedance approach could not match the output performance of the thermionic diode sensor. In addition, the variable impedance device is a high frequency system with the attendant transmission line considerations as opposed to the relatively straight forward low-voltage dc thermionic system. For these reasons, the thermionic diode sensor was chosen for the transducer design. Our work on the variable impedance approach is outlined in Appendix A. The thermionic diode approach is expanded in the following sections of the report.

3.1 Thermionic Diode Sensor

The use of a high-vacuum thermionic diode as a pressure sensing element is based on device operation in the space-charge limited mode, where the current flowing between the emitter and collector is dependent upon the distance between the electrodes. If one of the electrodes (such as the collector) is moved as a function of pressure, the current is also a function of pressure. Now, if all other factors influencing the diode current can be controlled, an accurate high temperature pressure transducer can be constructed.

3.1.1 Space Charge Operation

The space charge effect denotes the repulsive force acting on emitted electrons due to an electron cloud in the interelectrode space. If an emitter is heated and a positive voltage is applied to the collector, the emitted electrons will move from emitter to collector with a finite increasing velocity. As the temperature of the emitter (and the associated electron emission) is increased, the number of electrons in the interelectrode space will increase. This increase will continue up to a point determined by the emitter-collector voltage. However, as the temperature is further increased, the repulsive force due to the interelectrode electrons will balance the attractive force of the collector voltage at the emitter surface. Any further temperature increase will result in the repulsive force becoming greater than the attractive force and the additional emitted electrons will return to the emitter surface. The emitter-

collector current therefore reaches a limit for a given collector voltage and will show very little further increase as emitter temperature exceeds this critical value. Figure 1 presents the electron potential energy diagrams related to the above statements. The symbols used in Figure 1 are:

FL_c: Collector Fermi level energy

FL_e: Emitter Fermi level energy

V: Voltage applied to the collector

V_c: Effective emitter-collector potential difference

V_e: Potential due to space charge effect

ϕ_c: Collector work function

ϕ_e: Emitter work function

d: Emitter-collector distance

x_c: Collector to maximum space charge distance

x_e: Emitter to maximum space charge distance

Curves A, B, C, depict situations for increasing temperature at constant voltage. Curve A is for low temperature (emission limited). The potential gradient is constant from emitter to collector. When the temperature is raised to the critical value mentioned above, Curve B is obtained. For this condition the potential gradient is zero at the emitter surface. A further increase in temperature results in Curve C, where the space charge creates a virtual emitter at distance x_e from the actual emitter surface. In distance x_e, there exist currents flowing in both directions between the emitter and the maximum space charge potential plane. In x_c, current flows only towards the collector.

Therefore, V_c becomes the effective diode potential difference. This assumes that there will be no electron reflection off the collector surface and that the collector-emitter electron current is negligible.

Thermal energy due to the emitter temperature will raise electrons over the potential barrier composed of the emitter work function ϕ_e and the space charge potential V_e. They are then attracted to the collector surface by potential V_c. Any kinetic energy gained by the electrons is dissipated as heat when the electrons reach the collector. Upon entering the collector, the electrons lose potential ϕ_c and fall to the collector Fermi level from which point they are raised, by the applied voltage V, to the emitter Fermi level. The cycle then repeats itself.

Theory and experiment have resulted in the formulation of two basic equations to determine the diode current density. These are the Langmuir-Child relation for operation in the space charge limited mode (see Curve C of Figure 1)

$$I = 2.34 \times 10^{-6} \frac{V_c^{3/2}}{X_c^2} \text{ amps/unit area} \qquad (1)$$

and the Richardson-Dushman relation for the emission capability of a surface (emission limited condition).

$$I_s = 120T^2 \exp \frac{(-e\phi_e)}{KT} \text{ amps/unit area} \qquad (2)$$

where T is the emitter temperature (°K), e is the electronic charge (1.60×10^{-19} coulomb) and K is the Boltzmann constant (1.38×10^{-23} joule/°K). Equation 2 represents the diode current

density for emitter temperature up to the critical temperature resulting in Curve B of Figure 1. Since this point is an important diode condition separating the emission limited and space charge limited regions, the critical current will be denoted as

$$I_c = 120T_c^2 \exp \frac{(-e\phi_e)}{KT_c} \text{ amps/unit area} \qquad (3)$$

As the temperature is increased above T_c. a space charge potential is developed and a virtual emitter is created at the position x_e from the emitter with an effective work function $(\phi_e + V_e)$. This condition is represented by Curve C of Figure 1. Therefore, the Richardson-Dushman relation can be written for the space charge limiting condition as

$$I = 120T^2 \exp\left[\frac{-e(\phi_e + V_e)}{KT}\right] \text{ amps/unit area} \qquad (4)$$

It should be stressed that Equations 1 and 4 are both valid representations for the space charge limited current density as shown in Figure 2. Equation 1 indicates the distance and voltage dependence while Equation 4 is useful in treating the emitter work function and temperature parameters.

From these relations, it can be seen that when the diode spacing is a function of pressure, and operation is confined to space charge limited conditions, the current flowing through the diode will be an indication of pressure. The device must not be allowed to become emission limited, since this condition would destroy the current-distance dependence.

The current-distance relation is a non-linear one. To achieve linearity, the system was developed which measures the difference between currents flowing through the pressure-actuated collector and the fixed reference collector. This signal conditioning system is treated in detail in Section 9.0. A power supply is programmed such that the voltage applied to the collectors maintains the sum of the two currents at the level determined by the parameters for zero pressure. This sum is from Equation 1 and substituting d for x_c

$$2\ (2.34\ X\ 10^{-6})\ \frac{V^{3/2}}{d^2}\ A_e = 0.144 \text{ ampere}$$

where V = 20 volts, d = 0.006 inch and A_e = 0.0123 $inch^2$ (emitter area). Table 1 presents data pertinent to the analysis. The subscripts "a" and "r" denote pressure-actuated collector and reference collector parameters respectively. The voltage values are obtained from the expression

$$i_a + i_r = 0.144 = 2.34\ X\ 10^{-6}\ V^{3/2}\ A_e \left(\frac{1}{d_a{}^2} + \frac{1}{d_r{}^2} \right)$$

where A_e = 0.0123 $inch^2$ and d_r = 0.006 inch.

Or

$$V^{3/2} = \frac{180\ d_a{}^2}{d_a{}^2 + 36}$$

where d_a is expressed in 10^{-3} inch. Decreasing values of d_a correspond to increasing pressure.

TABLE 1

SIGNAL CONDITIONING PARAMETERS

d_a Inch	d_r Inch	V Volts	i_a Amp.	ir Amp.	$(i_a + i_r)$ Amp.	$(i_a - i_r)$ Amp.
0.0060	0.0060	20.0	0.0720	0.0720	0.144	0.0000
0.0055	0.0060	19.0	0.0782	0.0660	0.144	0.0122
0.0050	0.0060	17.6	0.0850	0.0591	0.144	0.0259
0.0045	0.0060	16.1	0.0922	0.0520	0.144	0.0402
0.0040	0.0060	14.5	0.0998	0.0443	0.144	0.0555

Figure 3 graphically presents the results. Curve A plots values for i_a assuming a constant value of V = 20 volts. For this situation, i_r will remain constant at 72 ma. and a sum or difference measurement will contain the inherent non-linearity of Curve A. Curve B plots values for $(i_a - i_r)$ from Table 1. The maximum deviation, based on terminal type linearity, is seen to be about 3% of full scale.

3.1.2 System Parameters

The final design of the pressure sensor uses a common emitter, a pressure-actuated collector and a fixed reference collector. As will be treated later, the use of two collectors and a constant sum-of-the-currents power source eliminates almost all of the sources of error. The following design parameters have been assumed:

zero pressure:emitter - active collector spacing = 0.006 inch (0.01524 cm),

full pressure:emitter - active collector spacing = 0.004 inch (0.01016 cm),

emitter - reference collector spacing of 0.006 inch (constant),

emitter area of 0.0791 cm^2 (1/8 inch dia. disc).

In order to achieve high electron emission at low temperatures, a dispenser type emitter with a work function of about 2.1 ev is planned. The collectors are a refractory alloy with a work function of the order of 3 to 4 ev.

3.1.3 Emitter Considerations

From Figure 1 the relationship between the effective diode potential and the voltage applied to the collector is

$$V_c = V + (\phi_e + V_e - \phi_c) \qquad (5)$$

The reasonable assumption that $(\phi_e + V_e - \phi_c)$ is small compared to V results in $V_c \approx V$. The further assumption that V will be of the order of 20 volts and the use of the space charge relation (Equation 1) result in a current density of 2.04 amps/cm^2 at the minimum spacing of 0.004 inch. This represents the maximum expected diode current. An emitter operating at a temperature of 1420°K (2100°F) with a work function of 2.1 ev will provide a saturation current of 8 amps/cm^2. Thus, the maximum operating current density is 25 percent of the emitter capability which assures space charge regime for all conditions.

To evaluate the current-mechanical spacing relationship, the emitter-virtual emitter distance (x_e) must be determined. Nottingham (Reference 1) presents a nomograph from which the value of x_e may be determined as a function of emitter temperature and current density. Table 2 presents data calculated from Equation 1 and the nomograph.

TABLE 2

EMITTER SHEATH PARAMETERS

$V_c \approx V$	d = 0.006 in.			d = 0.004 in.		
	I	x_e		I	x_e	
Volts	amps/cm^2	cm	%d	amps/cm^2	cm	%d
1	10^{-2}	0.0065	42.6	0.0227	0.0045	44.4
5	0.113	0.0019	12.5	0.254	0.0013	12.8
10	0.319	0.0011	7.2	0.720	0.00075	7.4
15	0.584	0.00085	5.6	1.32	0.00057	5.6
20	0.905	0.0007	4.6	2.04	0.00047	4.6

If the system operates with applied voltages above 10 volts, it appears that the effect of x_e is minimal and may be neglected.

3.1.4 Error Analysis

An estimate may be made of the contributions of the various system parameters to the overall system error. Before the individual relations are developed, an expression for the space charge potential V_e will be obtained. The emission limit condition (Equation 2) applies for temperatures up to the critical temperature T_c at which point the potential gradient at the emitter is zero and the critical current is

$$I_c = 120\ T_c^2 \exp\left(\frac{-e\,\phi_e}{KT_c}\right) \qquad (3)$$

As the temperature increases above T_c, the space charge potential V_e develops and the current becomes

$$I = 120\ T^2 \exp\left[\frac{-e(\phi_e + V_e)}{KT}\right] \qquad (4)$$

Combining Equations 3 and 4 yields

$$V_e \cong \frac{\phi_e \Delta T}{T_c} - \frac{KT}{e}\frac{\Delta I}{I_c} \qquad (6)$$

where $\Delta T = T - T_c$ and $\Delta I = I - I_c$

The detailed development of Equation 6 and the error components are found in Appendix B. The diode parameters and their error terms are listed in Table 3.

TABLE 3

THERMIONIC ERROR COMPONENTS

(without sum-of-the-currents compensation)

System Parameter	Error in current ($\Delta I/I$)
Emitter Temperature, T	+ 2 ($\Delta T/T$)
Emitter Work Function, ϕ_e	0 for $T > T_c$
Distance, d	-2 ($\Delta d/d$)
Collector Work Function, ϕ_c	-1.5 ($\Delta \phi_c/V_c$)
Applied Voltage, V	+1.5 ($\Delta V/V_c$)

Some comment can be made about the various error terms. The use of the sum and difference current measuring system described previously minimizes, to a large extent, the effect of errors common to both collector circuits. A change in emitter

temperature demonstrates such a correction. An increase in emitter temperature increases the value of V_e. This (without correction) results in an increase in the sum-of-the-currents. However, since the power supply then decreases the supply voltage by a V_e increment the temperature influence is cancelled.

The above remarks apply equally to changes in the applied voltage. In addition, state-of-the-art technology in power supply design is sufficiently advanced to render this error negligible.

Proper design procedure will limit, if not completely eliminate, the effect of distance change during operation.

The rather surprising result that the current is independent of changes in emitter work function can be interpreted qualitatively. If ϕ_e decreases, more electrons will be emitted. This increase in electrons will raise the space charge potential V_e. If ϕ_e increases, fewer electrons will be emitted and the space charge potential will decrease. In both cases, there is a correction which preserves the current value. Effectively, the sum $(\phi_e + V_e)$ remains the same, thus keeping a constant current in accordance with Equation 4.

3.2 Transducer Mechanical Design

The mechanical designs for the pressure transducers were established around the use of a double housing concept; a main

housing of Nb-1Zr surrounded by an outer shell of L-605 cobalt-based alloy. The thermionic sensor is installed in the low vapor pressure Nb-1Zr and the outer shell of L-605 allows the transducer to operate in air. The space between the Nb-1Zr and the L-605 will be evacuated to prevent oxidation damage to the Nb-1Zr. Figure 4 presents a 2:1 scale sketch of the absolute pressure transducer design. Figures 5 and 6 are 2:1 scale sketches of the differential pressure transducer design.

Referring to Figures 4 and 5, all points exposed to the liquid metal environment will be electron-beam welded. The main welds in this category are:

1. the pressure capsule assembly welds,
2. the pressure capsule/main housing weld,
3. the welds connecting the Nb-1Zr/L-605 transition piece to the main housing and the outer shell,
4. the main housing/housing cover weld and
5. the differential beam assembly and installation welds.

The final closure welds will not be exposed to the liquid potassium environment and may be either electron-beam or heliarc type. The main welds in this category are:

1. the sensor vacuum shell assembly welds,
2. the thermal expansion diaphragm assembly weld,
3. the swaged cable assembly and installation welds and
4. the L-605 outer shall assembly welds.

A Nb-1Zr/Lucalox seal is used to seal the thermionic diode sensor chamber and preserve the high-vacuum environment. The sensor vacuum shell is made up of Nb-1Zr components, including a vacuum pinch-off tube. For the absolute pressure transducer, the pinch-off tube is inserted in the sensor vacuum shell (Figure 4). The differential pressure transducer has the pinch-off tube inserted into the main housing (not shown in Figure 5, but in Figure 6).

A Nb-1Zr thermal expansion diaphragm was incorporated into the design to absorb stresses set up by the difference in linear thermal expansion between the L-605 outer shell and the transducer Nb-1Zr inner structure.

The outer structure of the transducer, up to the swaged cable assembly, is L-605. All assembly welds will be heliarc type of similar metals, resulting in maximum reliability. The transition from the Nb-1Zr inner structure is made above the thermal expansion diaphragm with an L-605 tubular section. A Nb-1Zr/L-605 vacuum diffusion joint is used to accomplish the transition.

A design was developed for the electrical cable and connector set-up used to deliver power to the transducer and connect it to the electrical signal conditioning system. The cable is of a swaged design about 2 feet long. The internal insulation is a two-piece crushable magnesia ceramic. One piece is tubular and the other is shaped like a sprocket. The wires are placed in the sprocket grooves and the tubular section is slipped over the sprocket assembly. The outer cable shell is stainless steel

tubing to give the cable a certain amount of flexibility needed for loop installation. The cable is internally pressurized with argon and a metal-ceramic seal is used at both ends. A weld connection is made to the transducer while a minaturized multi-pin connector at the cold end of the cable allows the use of a standard design flexible cable to the signal conditioning equipment.

During the project, tests performed on assemblies configured according to the actual transducer parts demonstrated the feasibility of the various welds and metal-ceramic joints used in the design.

Transducer construction and tests used a W-25 Re pressure capsule, the thermionic diode sensor and their installation into the Nb-1Zr main housing. The transducers were evaluated in the Vacuum Test Facility (Section 10.0)

4.0 Pressure Deflection System

The typical pressure transducer depends upon the precision of a highly stressed spring member for its accuracy. In the present case, the spring member is a multi-convolution flat plate diaphragm which is displaced by liquid metal pressure. The maximum useful stress level is limited by the corrosion and creep characteristics of the diaphragm material in direct contact with the liquid metal; in this case potassium at 1800°F.

Corrosion by a liquid metal often takes place preferentially along grain boundaries. This attack is difficult to prevent completely, but its influence can be minimized by design. Selection of a diaphragm thickness that is large compared with the material grain size will lengthen the life of the diaphragm. Thus, material thicknesses of 0.02 to 0.06 inch are preferred over the conventional diaphragm thickness of 0.005 to 0.01 inch. Normally, to limit the attack by the alkali metals, unalloyed refractories (e.g., columbium or tantalum) must contain a low oxygen content. However, if the refractories are "gettered" by the addition of an element capable of forming a thermodynamically stable oxide (e.g., Zr, Ti, Y, Hf), the resistance to attack is considerably improved. In fact, materials containing such gettering elements are capable of tolerating oxygen contents approaching the stoichiometry of the gettering metal without adverse corrosion effects. If the oxygen content of the alloy exceeds the stoichiometric limit of the getter element, the alloy tends to act like ungettered material.

The alloys selected for investigation as possible diaphragm materials were:

C-129Y	(Cb-10W-10Hf-0,1Y)
FS-85	(Cb-28Ta-10W-1Zr)
T-222	(Ta-10W-2.5Hf)
W-25Re	

The test configuration used for evaluation of the above alloys consisted of a double convolution bellows arrangement made up of four flat plate diaphragms. The configuration is shown in Figure 7. The diaphragms were about 1 inch in diameter and 0.02 inch thick. The inner diameter was about 0.2 inch. The ring plate diaphragm design was used for the W-25Re alloy while the machined diaphragm design was used for the C-129Y, FS-85 and T-222 alloys. In view of the known harmful effects of oxygen in refractory metals exposed to liquid alkali metals, the test configurations were assembled by electron-beam welding techniques to avoid oxygen pick-up.

4.1 Initial Deflection Tests

The initial deflection tests were performed in the Vacuum Test Facility (10^{-8} torr or better) with high purity argon used for pressure cycling. The measured oxygen and water vapor content of the argon was held to maximum values of 0.5 and 1.2 parts per million respectively. The diaphragm deflection was measured to an accuracy of better than $\pm$ 20 microinches by combining a 40X magnification binocular microscope with a glass plate camera and using a shadowgraph instrument to read the resulting photos. Analysis of the data with limited pressure and temperature cycling yielded the following results.

1. Hysteresis effects at temperatures up to 1800°F were negligible for full scale deflections up to about 0.001 inch.
2. The increase in full scale deflection with temperature generally followed the predicted change based on literature values of Young's modulus.
3. Zero shift data generally showed that the W-25Re capsule was the most stable.
4. There is a definite need for extended pressure cycling to obtain stable pressure-deflection characteristics.

4.1.1 Vacuum Test Facility

The original function of the Vacuum Test Facility was to provide the means for pressure cycling the pressure capsule at 1800°F to determine its linearity, reproducibility, and creep parameters.

The objective of the facility design was to perform the evaluation of the pressure capsules under conditions that neither aggravate nor minimize the severity of the problems that the transducer must face. The major consideration was to avoid contaminating the metals with oxygen. The simplest way to accomplish this was to perform the tests in a high vacuum (10^{-8} Torr or better). To accomplish the pressure cycling, high purity argon was used.

A multiple station test facility was constructed for evaluating the pressure capsules. Later in the program, the facility would be used for conducting the potassium compatibility tests, and for tests

of the pressure transducer. Figure 8 depicts this arrangement for one of four identical test stations. The test part is enclosed in a heated, high vacuum chamber. The test part is heated radiantly with a set of Nb-1Zr resistance elements which surround the test zone. This zone is purposely large to assure uniform heating and to provide space for the reflectors used to control the end effects. The top plate contains the tubes used to apply the test pressure and also measure the operating temperatures. Since all support of the test assembly is from this upper plate, new assemblies can be quickly introduced to the facility. Figures 9 and 10 present the vacuum test chamber in greater detail.

For the pressure-deflection tests, the motion of the element was measured by detecting the change in position of two marks. One of the marks was on a fixed portion of the pressure capsule assembly and the other was on the moving element of the test diaphragm. The relative motion measurement was made by a combination microscope and camera mounted external to the vacuum chamber. The sighting took place through an optical window in the side of the test chamber.

The initial method for pressure calibrating and cycling the test element used a system as shown in Figure 11. High-purity high-pressure argon was supplied to the pressure capsule. During the initial start-up, the system was heated and evacuated several times to degas the surfaces and eliminate any absorbed moisture.

Then, the test argon was passed through oxygen and water analyzers to determine if the system was operating under high purity conditions. Pressure regulators in both the high purity and commercial lines were set at 15 psig to assure uninterrupted gas flow at constant pressure. Our initial tests showed that the commercial argon supply was sufficiently pure for our tests. The measured oxygen and water vapor content of the commercial argon was held to maximum values of 0.5 and 1.2 parts per million respectively.

4.1.2 Diaphragm Deflection Measurement

In performing the initial deflection tests, the motion of the diaphragm had to be measured to an accuracy of 1 percent of the total travel. A total travel of 0.002 inch required the motion to be measured to an accuracy of 20 microinches. Our work on deflection measurement was concentrated in two areas. One involved techniques for marking the capsule parts; the other concerned procedures for obtaining and processing the photos and extracting the data.

Two methods of marking the capsules were tried: the use of diamond indentors from hardness testing equipment and surface treating with a commercial abrasive unit (results in a cratered surface with high spots that reflect illumination). Both techniques provided distinct and recognizable characteristics. The lack of adequate space on the capsule dictated the use of the abrasive surface-treatment and this method was used exclusively.

Green light illumination was directed through one ocular of a binocular microscope (40X magnification) into the test chamber. The camera was attached to the other ocular system. Glass metallographic plates were used. The final readings were taken from the developed plates using a shadowgraph instrument capable of an accuracy of 0.0001 inch. Since the camera system operates at 40X magnification, this instrument accuracy corresponded to a marking distance of 2.5 microinches. A typical plate is shown in Figure 12. The plates were set in the shadowgraph so that readings of the reference marking distance were repeated from plate to plate. From this base, measurements were taken on the deflection marking distance.

Experience showed that the deflection data obtained between two capsule marking points could be read on the shadowgraph with a spread of less than 0.001 inch ($\pm$ 12.5 microinches actual distance) between the high and low readings in a set of ten. This was well below the original desired accuracy of $\pm$ 20 microinches. Statistical treatment of the data, which gives less weight to readings at the extremes, would result in better accuracy. Since data obtained from any five readings in the set could not be more inaccurate than that obtained from ten, the number of readings used to obtain an average was lowered from ten to five. This considerably speeded up the data gathering process.

4.1.3 Test Procedure

The deflection measurements using optical means gave the initial indications of pressure capsule behavior. The information included

1. capsule pressure-deflection characteristics as functions of temperature,
2. capsule creep characteristics when subjected to full-scale pressurization for periods up to 22 hours at 1800°F and
3. capsule overpressure characteristics for 2 hour periods at 1800°F.

The procedure developed to obtain this information involved the following steps:

1. Perform pressure-deflection calibration runs at room temperature, 500, 1000, 1200, 1400, 1600 and 1800°F.
2. Maintain full scale deflection and 1800°F for a period of 20 hours. Measure the full scale and zero pressure separations every 6 to 7 hours. Calculate the full scale deflections and zero shifts.
3. Perform pressure-deflection calibration runs at 500, 1400 and 1800°F.
4. Apply overpressure to 200 percent maximum deflection (or until the diaphragm is close to the mechanical stop) at 1800°F for a 2 hour period. Measure the full scale and zero pressure separations every hour. Calculate the full scale deflections and zero shifts.

5. Perform pressure-deflection calibration runs at 500, 1400 and 1800°F.

6. Maintain full scale deflection and 1800°F for a 6 hour period. Measure the full scale and zero pressure separations every 3 hours. Calculate the full scale deflections and zero shifts.

The term "zero pressure separation" refers to the distance between two markings, one on the capsule projection tip and the other on the capsule deflection yoke (see Figure 12) under conditions of zero psia capsule pressurization. When full-scale pressure is applied to the capsule, the distance between the same two markings is termed the "full scale separation". The "full scale deflection" is obtained by subtracting the full scale separation from the zero pressure separation. "Zero shift" refers to a change in value of the zero pressure separation.

A chronological representation of the test procedure is shown in Figure 13. Points at which full scale and zero pressure separations are measured along with total operation time and time at 1800°F are indicated. Variables in the procedure include the length of time of the sustained full scale pressure test (shown as 22 hours in Figure 13) and the overpressurization value used. The zero pressure separation reading after the first 6 to 7 hours of the sustained pressure test was not normally taken. Each pressure-deflection calibration test required about 2 hours; the pressure capsule experienced about 56 hours of total operation, 36 hours of which were at 1800°F. The capsule underwent a total of 13 full-scale pressure cycling tests at various ambient tempera-

tures. In addition, three 1800°F time tests were included in the test procedure; 22 hours at 100 percent pressure, 2 hours at 200 percent overpressure, and a final 6 hour test at 100 percent pressure.

The instrumentation has been discussed in a previous section and used a 40X magnification binocular microscope through which photographs were taken on glass metallographic plates. Separation readings were then taken from the developed plates using a shadowgraph instrument. This system exhibited accuracies better than ±20 microinches (±2 percent referred to a full scale deflection of 0.001 inch).

4.1.4 Test Results

A complete set of pressure-deflection-temperature tests were conducted on the four candidate pressure diaphragm materials (C-129Y, FS-85, T-222, W-25Re). To investigate fully the high temperature stress effects, full scale deflection values were selected which are realistic for transducer operation. In addition, both single and double convolution capsules were included in the test program.

A complete listing of the test capsules, the applicable full scale deflection parameters and the chronological order in which the deflection tests were performed is given in Table 4. The maximum deflection values of 0.0006 and 0.001 inch for single convolution capsules correspond to values of 0.001 and 0.0017 inch respectively for double convolution capsules.

TABLE 4

PRESSURE CAPSULE LINEARITY-HYSTERESIS ERRORS

Capsule Material	Number of Convolutions	Nominal Room Temp. Full Scale Deflection (inch)	Start of Test	Linearity-Hysteresis (a) Percent of Full Scale Deflection				Allowable Operating Temperature
				1000°F	1400°F	1600°F	1800°F	
C-129Y	1	0.0006	1/21/65	5.5(b)	5.5	4.8	4.7	1800°F
C-129Y	1	0.001	1/6/65	5.0	6.5	6.3	12	1600°F
C-129Y	2	0.002	11/30/64	6.4	4.7(b)	11	13	1400°F
FS-85	2	0.001	2/3/65	4.7	4.2	4.0	3.4	1800°F
FS-85	2	0.002	12/16/64	2.7	2.8	3.4	6.2	1600°F
FS-85	2	0.004	10/27/64	0.9	3.8	NM	10	1400°F
T-222	1	0.0006	2/5/65	8.7(b)	5.8	7.4	5.5(b)	1800°F
T-222	1	0.001	1/28/65	2.5	4.2	4.2	6.3	1600°F
W-25Re	2	0.001	1/12/65	8.3	9.3	8.3	9.0	1800°F
W-25Re	2	0.002	11/18/64	5.9	6.8	3.2	6.7	1800°F
W-25Re	2	0.004	12/10/64	2.6(b)	2.2	5.0	3.6(b)	1800°F

NM Not Measured

(a) The term linearity-hysteresis is used in this report to mean the error in percent of full scale deflection between the individual data points and the reference straight line.

(b) Identifies error values which have been calculated by omitting data points which appeared to be grossly different than the general data pattern. It is believed that this method provides the most representative description of actual capsule performance.

Figures 14 through 88 present the complete series of pressure-deflection-temperature data as scheduled in Figure 13 for time increments 0 to 14 (time scale a).

Information of interest which can be derived from these data as a function of operating temperature include linearity, hysteresis, zero shift and Young's modulus.

A straight line has been drawn close to the experimental points of each set of capsule data plots (Figures 14 to 88) to assist in the evaluation of the capsule linearity and hysteresis. Using the line as drawn on each figure, it will be noted that the linearity error is not apparent but as the operating temperature increases the hysteresis errors become more pronounced. The inability to discern the linearity error demonstrates that the capsule linearity error is smaller than the optical measurement system error. To simplify the problem of data evaluation, the linearity and hysteresis errors have been combined into a single term called "linearity-hysteresis error".

The linearity-hysteresis error is established by determining the deviation of the individual data points from the straight line and calculating the error in percent of full scale deflection at the operating temperature.

The maximum error value for each capsule test has been tabulated in Table 4. The test data contains some points which are grossly different from the general hysteresis pattern for a

particular test. In these instances, the maximum values representative of the data pattern were selected for use in Table 4. There are six values of this type identified in the table by note (b).

The purpose of Table 4 is to make possible the selection of the deflection limit for a particular candidate alloy when used as a pressure capsule. Table 4 also lists this deflection limit in terms of allowable operating temperature for each capsule tested. The selection is based on the last temperature test condition for which there is no noticeable increase in the linearity-hysteresis error. Using the C-129Y capsules as an example, it will be noted that for a single convolution capsule with 0.0006 inch full scale deflection there is no appreciable increase in the linearity-hysteresis error from 1000°F to 1800°F. When the full scale deflection is increased to 0.001 inch, the linearity-hysteresis error rises sharply between 1600°F and 1800°F.

For the C-129Y double convolution capsule with 0.002 inch full scale deflection, the change occurs between 1400°F and 1600°F. This information can be used to compute the maximum allowable operating stress for new capsule designs to assure that linearity-hysteresis will be small at the desired operating temperature. Each material has been operated at a stress level low enough to minimize the linearity-hysteresis error at 1800°F. The W-25Re capsule has shown the best range of useful operating conditions.

Tables 2, 3, 4, and 5 present the zero shift and full scale data scheduled by Figure 13 (see time scale b) at nominal times 2 to 24, 26 to 28, and 30 to 36. All data for this portion of the evaluation are at 1800°F. The purpose of the first time period (2 to 24 hours) was to provide a limited amount of pressure cycling and operating time at temperature to stabilize the performance of the pressure capsule before subjecting it to the 200 percent overpressure test (26 to 28) and the final time test for creep at full pressure and temperature (30 to 36).

The double convolution W-25Re capsule operated at 0.002 inch full scale deflection demonstrated repeatability close to that which can be obtained by the optical measuring system (see Table 8). These creep values of less than about 4 percent for a six hour period hold promise that a transducer can be built which will meet the desired long time stability requirements. The data for W-25Re at 0.001 inch full scale deflection seems to indicate that more pressure cycling at temperature is required to stabilize the capsule before the final creep data are taken. The 0.004 inch full scale deflection data show that this deflection generates higher stress than can be allowed for long term stability.

The T-222 pressure capsule data presented in Table 7 show the need for more capsule pressure cycling. This need is exemplified by the negative zero shifts typical for the T-222 capsule. After additional pressure cycling, T-222 may be a useful capsule material.

TABLE 5

FS-85 PRESSURE CAPSULE DEFLECTION VARIATIONS
(PERCENT OF FULL SCALE AT 1800°F) WITH TIME AT 1800°F

Number of Convolutions	2			2		
Nominal Room Temp. Full Scale Deflection (inch)	0.001			0.002		
	Test Hours (b)	Zero Press.	Full Scale	Test Hours (b)	Zero Press.	Full Scale
		±1.7%(a)			±0.7%(a)	
First Time Test	(2-9)	NM	24.2	(2-8)	64.9	59.9(c) 60.5(c)
	(2-18)	22.4	27.2(c) 17.9(c)	(2-14)	87.7	83.9(c) 77.4(c)
	(2-24)	22.2	25.8(c) 19.8(c)	(2-23)	110	90.1
200% Overpressure Test	(26-27)	3.4	0.4(c) 5.7(c)	(25-26)	14.3	9.0
	(26-28)	-3.2	12.3(c) 1.8(c)	(25-27)	NM	8.3
Final Time Test	(30-33)	12.0	21.1(c) 13.8(c)	(29-32)	NM	6.0
	(30-36)	12.8	21.4(c) 11.6(c)	(29-35)	24.8	7.1

(a) ±20 microinches measurement accuracy referred to max. full scale deflection at 1800°
(b) Refers to operating hours at 1800°F (scale b of Figure 3) between which variations took place
(c) Capsule brought to zero pressure between readings
NM Not measured

TABLE 6
C-129Y PRESSURE CAPSULE DEFLECTION VARIATIONS
(PERCENT OF FULL SCALE AT 1800°F) WITH TIME AT 1800°F

Number of Convolutions	1			1			2		
Nominal Room Temp. Full Scale Deflection (inch)	0.0006			0.001			0.002		
	Test Hours (b)	Zero Press.	Full Scale	Test Hours (b)	Zero Press.	Full Scale	Test Hours (b)	Zero Press.	Full Scale
		±3.3%(a)			±1.3%(a)			±0.8%(a)	
First Time Test	(2-9)	NM	29.0	(2-9)	135	133(c) 127(c)	(2-8)	142	147(c) 123(c)
	(2-17)	46.1	50.0	(2-15)	NM	NM	(2-16)	207	100(c) 196(c)
	(2-24)	NM	64.7(c) 63.3(c)	(2-24)	240	238(c) 228(c)	(2-21)	NM	231
200% Overpressure Test	(26-27)	15.2	23.2(c) 31.2(c)	(26-27)	-19.8	-13.3(c) -40.6(c)	(23-24)	NM	NM
	(26-28)	19.4	35.1	(26-28)	-79.0	-51.6	(23-25)	NM	NM
Final Time Test	(30-33)	26.4	54.6(c) 42.5(c)	(30-33)	NM	NM	(27-30)	NM	NM
	(30-36)	40.0	56.3(c) 56.8(c)	(30-36)	27.4	37.8	(27-33)	53.9	40.1

(a) ±20 microinches measurement accuracy referred to max. full scale deflection at 1800°F
(b) Refers to operating hours at 1800°F (scale b of Figure 13) between which variations took place
(c) Capsule brought to zero pressure between readings
NM Not measured

TABLE 7
T-222 PRESSURE CAPSULE DEFLECTION VARIATIONS
(PERCENT OF FULL SCALE AT 1800°F) WITH TIME AT 1800°F

Number of Convolutions	1			1		
Nominal Room Temp. Full Scale Deflection (inch)	0.0006			0.001		
	Test Hours (b)	Zero Press. ±3.1%(a)	Full Scale	Test Hours (b)	Zero Press. ±1.6%(a)	Full Scale
First Time Test	(2-9)	NM	-8.7	(2-8)	NM	30.2
	(2-18)	-1.3	6.7(c) -4.7(c)	(2-17)	26.2	25.1(c) 26.5(c)
	(2-24)	-22.3	-11.1(c) -24.0(c)	(2-22)	32.4	25.5(c) 26.3(c)
200% Overpressure Test	(26-27)	7.1	9.9(c) 8.1(c)	(24-25)	2.9	2.4(c) 4.9(c)
	(26-28)	-3.7	1.1(c) 0.5(c)	(24-26)	3.5	8.0(c) 2.3(c)
Final Time Test	(30-33)	-4.5	-8.5(c) 2.1(c)	(28-31)	-80.0	-71.8(c) -72.8(c)
	(30-36)	25.9	37.8(c) 30.4(c)	(28-34)	-18.5	-12.2

(a) ±20 microinches measurement accuracy referred to max. full scale deflection at 1800°F
(b) Refers to operating hours at 1800°F (scale b of Figure 13) between which variations took place
(c) Capsule brought to zero pressure between readings
NM Not measured

TABLE 8

W-25Re PRESSURE CAPSULE DEFLECTION VARIATIONS
(PERCENT OF FULL SCALE AT 1800°F) WITH TIME AT 1800°F

Number of Convolutions	2			2			2		
Nominal Room Temp. Full Scale Deflection (inch)	0.001			0.002			0.004		
	Test Hours (b)	Zero Press.	Full Scale	Test Hours (b)	Zero Press.	Full Scale	Test hours (b)	Zero Press.	Full Scale
		±1.9%(a)			±0.8%(a)			±0.5%(a)	
First Time Test	(2-9)	NM	-11.1	(2-6)	26.8	-2.2	(2-8)	6.4	18.3(c) 12.5(c)
	(2-18)	-11.4	-18.7(c) -22.3(c)	(2-14)	38.1	9.2(c) 7.2(c)	(2-15)	NM	21.9
	(2-24)	-34.8	-27.2	(2-20)	44.9	20.5(c) 15.1(c)	(2-22)	24.3	32.2(c) 28.7(c)
200% overpressure Test	(27-28)	0.3	7.0(c) 6.8(c)	(22-23)	NM	NM	(24-25)	NM	6.6
	(27-29)	5.3	8.0	(22-24)	NM	NM	(24-27)	5.2	5.9
Final Time Test	(31-34)	12.6	5.3(c) 5.3(c)	(26-29)	NM	NM	(29-32)	NM	NM
	(31-37)	-12.5	-12.1(c) -14.6(c)	(26-32)	2.3	3.9(c) 4.2(c)	(29-35)	14.2	7.7

(a) ±20 microinches measurement accuracy referred to max. full scale deflection at 1800°F
(b) Refers to operating hours at 1800°F (scale b of Figure 13) between which variations took place
(c) Capsule brought to zero pressure between readings
NM Not measured

Table 6 presents the data for the FS-85 capsule. This data and that of Table 5 for C-129Y also show the need for more pressure cycling at temperature. Figures 89 and 90 are presented to show the decrease in hysteresis with increased pressure cycling, which indicates that stabilization is taking place in both the C-129Y and FS-85 capsules during the pressure cycling of the final test (30 to 36 hours). Data taken at consecutive times are identified by letters A through H. The capsule achieves a considerably smaller hysteresis loop with each successive pressure cycle. Thus, after only one cycle the zero shift of the C-129Y capsule is reduced from 26.4 percent to 13.6 percent. Similarly, the full scale deflection creep is reduced from 54.6 percent to 13.8 percent. Comparable results have been measured for the FS-85 capsules. From Figure 90, the values are 21.1 percent full scale deflection creep in the first three hours and 7.6 percent in the second three hours. The zero shift in the first three hours is 12 percent of full scale as compared to only 0.8 percent in the second three hours. It is reasonable to expect that this trend will continue.

The influence of temperature on full scale deflection is presented in Figures 91 to 94. The measured deflection indicated in percent of full scale deflection is compared in each of the graphs with the predicted percent of full scale deflection based on the change in Young's modulus with temperature. These data seem to show similar trends to that shown by the hysteresis and

zero shift data previously discussed. In Figures 91 and 92, the measured values compare closely to the Young's modulus values up to about 1400°F. From Table 4, these same capsules showed a small change in hysteresis at a temperature of 1600°F and a large increase at 1800°F. Figure 93 for the T-222 material indicates that the material has not been fully stabilized as was also shown by the zero shift and full scale deflection-time data in Table 4. Figure 94 indicates a slightly larger change in Young's modulus for the capsule material than that used for the calculated curve.

4.2 Pressure Capsule Design

Experimental results presented in Section 4.1.4 indicated that the W-25 Re pressure capsule was the most stable of the four (C-129Y, FS-85, T-222 and W-25 Re) tested. Using W-25 Re as the final pressure capsule material, design calculations led to the absolute and differential pressure capsule configurations presented in Figures 95 and 96. The capsule is a double convolution assembly consisting of two ring members (1 and 2 in Figures 95 and 96) and a disc member (4 in Figures 95 and 96). Dimensions are shown for the 80 psia and ± 5 psid capsules. Three criteria were used to establish the pressure capsule design.

1. The maximum design stress in any capsule member was limited to 10,000 psi. This stress level was chosen to limit creep of the W-25 Re capsule.

2. The full-scale deflection of both the absolute and differential pressure capsules was chosen to be about 0.001 inch for the intended temperature range (1000-1800°F).

3. To insure liquid metal containment, the thickness of any capsule member was held to a minimum of 0.020 inch.

The capsule design was established using stress and deflection formulae such as found in Reference 2. The ring and disc members were treated separately.

For the ring member, the maximum stress and deflection are related to the capsule parameters by the following expressions:

$$s_r = 0.976 \beta w a^2/t_r^2$$

$$y_r = 0.976 \alpha w a^4/E t_r^3$$

where s_r = maximum stress in the ring member (psi); occurs in the radial direction at the outer edge.

β = function of a/b (tabulated on p.215, Reference 2).

a = radius to the outer edge (inch)

b = radius of the central boss (inch)

w = applied load (psi)

t_r = thickness of the ring member (inch)

y_r = deflection of the ring member (inch)

α = function of a/b (tabulated on p.215, Reference 2).

E = Young's modulus for W-25Re (psi)

The constant 0.976 includes the effect of the W-25 Re value of Poisson's ratio (0.336).

For the disc member, the maximum stress and deflection are related to the capsule parameters by the following expressions:

$$s_d = 3\ w\ a^2/4\ t_d^2$$

$$y_d = 3\ (m^2 - 1)\ w\ a^4/\ 16E\ m^2\ t_d^3$$

where s_d = maximum stress in the disc members (psi); occurs in the radial direction at the outer edge.

w = applied load (psi)

a = radius of the member (inch)

t_d = thickness of the disc member (inch)

y_d = deflection of the disc member (inch)

m = reciprocal of Poisson's ratio (1/0.336 = 2.98)

E = Young's modulus for W-25Re (psi)

Table 9 presents the pressure capsule parameters as determined from the above expressions. For the 80 psia capsule, the limiting value of stress (10,000 psi) was used to determine the thicknesses of the ring and disc members. For the ±5psid capsule, the member thickness was held to a minimum of 0.020 inch for liquid metal containment, leading to the decreased stress levels shown in Table 9.

TABLE 9

W-25Re PRESSURE CAPSULE PARAMETERS

	80 psia Capsule	±5psid Capsule
w (psi)	80	5
a (inch)	0.750	0.750
b (inch)	0.464	0.464
m	2.98	2.98
E (psi, 1800°F)	52.5×10^6	52.5×10^6
E (psi, 1000°F)	56.3×10^6	56.3×10^6
S_r (psi)	10,000	3,900
t_r (inch)	0.050	0.020
y_r (inch, 1800°F)	0.267×10^{-3}	0.261×10^{-3}
s_d (psi)	10,000	5,250
t_d (inch)	0.058	0.020
y_d (inch, 1800°F)	0.411×10^{-3}	0.627×10^{-3}
total deflection	$y = 3y_r + y_d$	
(inch, 1800°F)	1.21×10^{-3}	1.41×10^{-3}
(inch, 1000°F)	1.13×10^{-3}	1.31×10^{-3}

4.3 Pressure Capsule Fabrication

The individual members of the pressure capsule (1, 2 and 3 in Figures 95 and 96) are prepared in two operations; electrical discharge machining (EDM) to establish the correct diameter dimensions and the deep groove in piece 2, and machine grinding to establish the correct web contours. Using EDM, the outer diameter (1.70 inch) and the central hole (0.290 inch) are prepared with standard tungsten/copper electrodes.

The electrode wear is severe in EDM operations on refractories, and if the standard tungsten/copper electrodes are used to machine the deep groove in piece 2, continual shut-downs would be required to re-face the electrode. To machine the groove in the edge of the W-25Re disk, a technique using a travelling tantalum wire electrode was developed. The equipment used is shown in Figure 97. The entire assembly, consisting of a plate on which is mounted a number of adjustable pulleys and spools, together with a drive motor, is bolted onto the head of the EDM machine. The electrode, which is of 0.020 inch diameter tantalum wire several hundred feet long, is pulled over the pulleys with a drive motor. The pulleys are adjustable, so that up to four disks can be machined simultaneously.

Preliminary tests, in which the disk was rotated continuously, resulted in a groove that had two large bumps in the bottom, becoming progressively larger as machining proceeded.

When the disk was kept stationary, machining proceeded normally and no bumps were encountered. The groove is cut to the design root diameter and the disk is then rotated 90 degrees and a second cut is made, extending the groove around the disk. After four such cuts are made, the disk is indexed to the 45 degree points and cuts are made to eliminate the sharp corners at the base of the groove. A final dress pass is made to establish the root diameter. A photograph of a finished disc for the 5 psid pressure capsule is shown in Figure 98.

The final web dimensions of the pressure capsule members are established by surface and contour grinding. Standard mounting and grinding techniques do not apply because of heating effects generated during grinding.

The grinding is done in two steps. A magnetic-chuck surface grinder is used first to establish parallelism between the two sides of the piece. Then contour grinding is done by mounting in a lathe collet and using a tool-post grinder. During grinding, it is important that the piece be securely mounted and that adequate heat sinking be provided to prevent excessive temperature rise in the piece.

5.0 Thermionic Diode Sensor

The thermionic diode sensor consists of an emitter housing assembly, a cylindrical Lucalox ceramic base, and a mounting ring for installation of the sensor in the transducer main housing. A blow-up of the sensor is shown in Figure 99.

The following steps are performed in the fabrication of the sensor:

1. The heater structure is cast into the emitter housing.
2. The emitters are brazed into the emitter housing.
3. The Lucalox ceramic base is machined and metallized to provide the reference collector surface and a surface to which the sensor mounting ring is brazed.
4. The completed emitter housing assembly is mounted on the Lucalox base and a thermocouple is installed to measure the emitter temperature.

5.1 Cast Heater-Emitter Assembly

The electrically heated thermionic emitter assembly is designed to withstand shock and vibration loading and provide improved heat transfer between the electric heater and the thermionic emitters. Size and weight are kept to a minimum. The assembly incorporates two emitters.

The molybdenum emitter housing contains an internal cavity into which the electric heater is cast. The emitters are then brazed to opposite faces of the housing. A homogeneous cast structure assures shock and vibration resistance while providing maximum heat transfer.

After initial machining of the emitter housing, the internal cavity is formed by electric-discharge machining. To reduce embrittlement and thereby obtain longer heater life, a W-3Re heater is used. Figure 100 presents the pertinent information on the heater assembly.

The heater uses 0.003 inch diameter W-3 Re wire wound on a 0.004 inch diameter mandrel. Its undeveloped length is 2-5/16 inch. The developed dimensions are shown in Figure 100. The 0.5 inch pigtails are used for handling. Two external heater leads, 1.75 inch long, are prepared from 0.012 inch diameter rhenium wire. One end of each lead is ground to a diameter of 0.004 inch for a 0.040 inch length. The two pigtails are cut from the heater and the heater is trimmed to a finished length of 0.75 inch. The ground ends of the rhenium leads are inserted into the ends of the heater coil and spot-weld joints are made using tweezer electrodes. The joints are inspected under a microscope to check the quality of the welds.

The heater is then wound on a flat, grooved alumina ceramic coil form with the spot-weld joints about half-way down the alumina piece. The winding operation is performed under a microscope and each turn is cemented in place to prevent motion of the heater prior to installation in the emitter housing cavity. The winding arrangement is shown in Figure 100. When the heater is inserted into the cavity of the emitter housing, pieces of alumina are placed between the heater and the walls on all four sides and at the bottom of the cavity. These fillers prevent the heater shorting to the emitter housing during the casting operation. The dimensions and relative placement of these alumina fillers are shown in Figure 100.

The casting operation is performed using a 95 percent alumina/ 5 percent beryllia mixture. The powder mix is put into the cavity and carefully shaken down with a rubber-tipped vibrator tool. Enough powder is used to fill the cavity over the heater.

An induction-heating furnace is used for the cast. The following procedure is used for the first cast.

1. Purge in argon for 5 minutes.
2. Heat in argon for 10 minutes at 1500°F.
3. Heat in dry hydrogen for 4 minutes at 1500°F.
4. Heat in wet hydrogen for 10 minutes at 1750°F.
5. Heat in argon for 1 minute at 3200°F.
6. Let cool in argon for 10 minutes.
7. Evacuate work chamber with mechanical vacuum pump.
8. Backfill with helium and cool for 5 minutes.

During the cast, the powder mix will compact in the cavity. More than one cast will be needed to fill the cavity and result in a cast free of voids. For all additional casts, the cavity is refilled with the powder mix and the following procedure is used.

1. Purge in argon for 5 minutes.
2. Heat in dry hydrogen for 4 minutes at 1500°F.
3. Heat in wet hydrogen for 5 minutes at 1750°F.
4. Heat in argon for 1 minute at 3200°F.
5. Let cool in argon for 10 minutes.
6. Evacuate work chamber with mechanical vacuum pump.
7. Backfill with helium and cool for 5 minutes.

It is not necessary to evacuate the work chamber when changing gases. Continuous purging may be used. When the cast has filled the cavity sufficiently to completely cover the heater with no apparent voids, the assembly is checked electrically for heater continuity, resistance (about 2 ohms at room temperature) and electrical isolation between the heater and the emitter housing. The casting temperature prohibits the installation of the emitters until the casting is completed, at which time the emitters are brazed to the opposite faces of the housing using a nickel-oxide/ molybdenum alloy.

Philips Type B impregnated emitters are used. These emitters are of porous tungsten material (partial density 79 to 82 percent) impregnated with a BaO: CaO: Al_2O_3 mixture in a 5:3:2 mole ratio. The emitter dimensions are shown in Figure 101. When purchased, the emitters are subject to the following quality control checks.

1. All emitters of a given batch should be fabricated from one piece of porous tungsten.
2. The emitters are to be serialized and weighed before and after impregnation. The weight gain (in milligrams and percent) is to be tabulated along with the porous and impregnated weights. Quality control standards developed during the program indicate the porous and impregnated weights should range between 142-152 and 150-160 milligrams respectively. There should be an impregnant pickup of 4.5-5.5 percent.

3. All excess impregnant should be removed by ultrasonic water bath only. No machining of any kind should be done to the emitting surface.
4. A microscopic examination (at least 500X) of the emitting surface is made prior to brazing into the emitter housing. This examination verifies the existance of a uniform, open pore structure for the emitter. The microscopic examination is repeated after brazing to make certain that there was no braze coverage or contamination of the emitter surface.

Figure 102 presents photomicrographs showing typical emitter surfaces. The effect of any machining or grinding of the emitter is clearly shown, along with the results of braze coverage or contamination. In these instances, the uniform, open pore structure is completely destroyed. This prevents distribution of the impregnant over the emitter surface and results in the establishment of high work-function areas. If the work-function becomes sufficiently high, these areas may become emission-limited causing malfunction of the thermionic sensor.

The set-up used to braze the emitters into the emitter housing is shown in Figure 101. A powder alloy composed of 2/3 NiO and 1/3 Mo by weight is used for the braze. The alloy is put into each cavity to a depth of about 0.005 inch and the emitters are installed and clamped into place with a molybdenum clamping fixture. A separate piece of molybdenum is placed over the upper emitter (active emitter) to prevent it from being scratched by the spring member of the clamping fixture.

An induction-heating furnace is used for the braze. It is advisable to use molybdenum for any support structures and for the susceptor.

The assembly is fired in hydrogen at 2100°F for 4 minutes, and then heated to 2500°F, at which point, furnace power is shut off and the piece allowed to cool. As stated before, the emitting surfaces are microscopically examined after brazing to verify that no contamination has occurred and a uniform, open pore structure still exists.

5.2 Lucalox Base Assembly

The base of the thermionic diode sensor is configured from a piece of Lucalox ceramic. This ceramic is a high-alumina, silica-free material well suited for this application. It is compatible with liquid metals and has essentially-zero porosity, making it suitable for use in vacuum applications.

As purchased, the material is in rod form with eight 0.021 inch diameter axial holes (Figure 103). When machined for use as the sensor base, one end of the ceramic is castellated to provide a mounting for the emitter housing assembly and a surface for the reference collector (Figure 104). The grinding operation on the Lucalox is done with a diamond-impregnated grinding wheel. Care must be taken to square the corners at the bases of the three mounting posts. This will avoid any interference with the reference emitter surface. It is not advisable to attempt any machining on the mounting posts after they have been established. They are quite fragile and may crack.

After grinding, the ceramic is fired in an induction-heating furnace at 2300°F in wet hydrogen for 10 minutes, dry hydrogen for 5 minutes, and is cooled in dry hydrogen for 15 minutes. The firing operation prepares the ceramic for metallizing. Two surfaces are metallized: a band around the ceramic to which the sensor mounting ring will be brazed, and a paddle-shaped surface for the reference collector. Both of these surfaces are indicated in Figure 104.

The metallization is composed of 90-92 percent tungsten, 8-10 percent yttria alloy compounded and prepared in tape form. The tungsten/yttria compound is about 0.001 inch thick. The tape uses a Mylar backing and an organic binder to fix the metallizing.

The metallization is done in an induction - heating furnace using the following procedure.

1. Remove the Mylar backing from the tape, apply hexalon to the ceramic surface (to dissolve the tape binder) and apply the tape to the ceramic.
2. Fire in air at 700°F for 30 minutes.
3. Fire in wet hydrogen at 2200°F for 20 minutes.
4. Fire in dry hydrogen at 2200°F for 5 minutes.
5. Fire in argon at 3150°F for 40 minutes.
6. Slowly reduce the temperature, in argon, to below incandescence (about 1000°F).
7. Shut down furnace and allow to cool in argon.

Following metallization, the reference collector electrical lead and the sensor mounting ring are brazed. A 2 inch length of 0.020 inch diameter Nb-1Zr wire is used for the collector lead. The small 0.040 x 0.020 inch step in the Lucalox base is used to obtain maximum braze area around the lead and provide a braze reservoir for the joint. The sensor mounting ring is configured to eliminate cracking of the ceramic due to excessive stress build-up during brazing.

The braze alloy used is a 40/Ni/40Nb/20Ti powder alloy (+325 mesh). To prevent oxidation of the alloy, it is stored in an argon-environment glove box. Before use, the alloy is measured out, in sufficient quantity to perform the desired braze, into a bottle and methyl cellulose is added, just covering the alloy. The methyl cellulose serves as a vehicle for the alloy and affords oxidation protection when the alloy is removed from the glove box. The alloy is applied, in slurry form, to the braze areas using either a brush or stick applicator.

Both braze joints are made together in an induction-heating furnace using a molybdenum support structure and susceptor as shown in Figure 105. The braze is done in vacuum at 2100°F. If the braze does not flow at 2100°F, the temperature is raised slowly until visible flowing of the braze material takes place. The assembly is cooled for 30 minutes in vacuum, followed by 10 minutes in argon and 5 minutes in helium.

Both braze joints are examined under a microscope to assure good braze wetting and a continuous, homogeneous joint. Any excess braze material may be removed by careful abrasive-air blasting.

5.3 Sensor Assembly

The thermionic diode sensor is completed by mounting the emitter housing assembly on the Lucalox ceramic base. Initial assembly is made by mounting the emitter housing assembly on the three mounting posts of the Lucalox. The housing is held to the Lucalox by three small bolts through the mounting tabs of the emitter housing. These bolts pass through the holes in the Lucalox and are secured on the opposite end by matching nuts. Before installation, the bolts are rhenium plated to avoid any possible reaction between the Nb-1Zr material of the bolt and the high-alumina ceramic. Figure 106 shows the general assembly arrangement. When mounting the emitter housing assembly on the Lucalox base, the heater extension leads must be sharply and carefully bent so that they do not extend beyond the outer diameter of the Lucalox and do slide without tension through their respective holes. These two holes are on either side of the hole carrying the reference collector lead.

Once the emitter housing assembly is mounted on the Lucalox base, the reference emitter-collector spacing is established at 0.006 inch by using Nb-1Zr shims between the mounting tabs of the emitter housing assembly and the posts on the Lucalox base. A feeler gage is used to check this spacing and establish

parallelism between the emitter and collector surfaces. Before fastening the emitter housing assembly securely to the Lucalox base, a pre-activation is performed on the two emitters. The emitter housing assembly is set about 1/8 inch off the Lucalox base and a molybdenum shim is inserted between the reference emitter and collector. The pre-activation is performed in vacuum (about 10^{-6} torr) by heating the sensor to 2280°F for 25 minutes. The pre-activation is intended as a final cleaning of the emitter surface and allows the gross impurities expelled from the emitters during the first minutes of operation to be pumped away.

Following the pre-activation, the molybdenum shim is removed and the emitter housing assembly firmly fastened to the Lucalox base. One of the Nb-1Zr bolts serves as the electrical connection to the emitters. The 0.006 inch reference emitter-collector spacing should be rechecked.

The final step in assembly of the thermionic diode sensor is the installation of the thermocouple used to monitor the emitter temperature. This is a W-5Re/W-26Re thermocouple using 0.010 inch diameter wires and spot-welded to the emitter housing. The arrangement of the thermocouple leads are shown in Figure 106. Both leads are 4 inches long. When the sensor is held with the emitter housing assembly upward and the heater leads facing away, the W-5Re lead is inserted into the hole to the left of the center bolt, from the emitter mounting ring end of the sensor. The lead is pushed through and brought up alongside the emitter housing (see Figure 106). The W-26 Re lead is brought up through

the hole on the right side of the center bolt, bent across the emitter housing mounting tab, and over the end of the W-5Re lead. The thermocouple junction is spot-welded at this point to the emitter housing (See Figure 106).

The placement of the thermocouple leads is important, since the W-5Re lead is too brittle to be subjected to any bending. The thermionic diode sensor is now finished and ready to be installed in the transducer main housing. Prior to this installation, the sensor should be kept in a vacuum environment to prevent any possible contamination of the emitter surfaces.

6.0 Metal-Ceramic Seal

One of the program goals was to develop a suitable electrical terminal design. This design requires the use of metal-ceramic seal techniques capable of maintaining vacuum integrity under high-temperature conditions. In addition, the electrical terminal also must serve as a back-up seal. In the event of pressure capsule failure, the metal-ceramic seal must be able to withstand liquid metal attack and protect the integrity of the liquid metal loop in which the pressure transducer is installed.

Early in the program, investigations into the properties of several ceramic materials and tests performed on preliminary metal-ceramic configurations led to the choice of Lucalox ceramic, a high-purity (99.9 percent) alumina material. Its properties include compatibility with liquid metals and essentially zero porosity, making it suitable for high-vacuum rise.

6.1 Seal Test Program

During the program, two metal-ceramic seal approaches were evaluated. Both used Lucalox ceramic in conjunction with the refractory alloy Nb-1Zr.

1. The initial electrical terminal configuration obtained for evaluation is shown in Figure 107. This terminal was subjected to three consecutive test cycles with the following parameters.

   400 hours, 1800°F, 300 psia external argon pressure

   400 hours, 1800°F, 600 psia external argon pressure

   400 hours, 1800°F, 1000 psia external argon pressure

No electrical or mechanical failure was observed during the course of the test. Four of these terminals were also included in the potassium compatibility test program (see Section 7.0).

2. To extend the Lucalox/Nb-1Zr seal techniques to the point where they could be used with confidence in the transducer, a second, more general configuration was evaluated using metallization and brazing procedures developed in our laboratories. The test sample (Figure 108), as with the electrical terminals mentioned above, contained Nb-1Zr/Lucalox seals. The Lucalox was metallized with a tungsten-yttria compound and a nickel/niobium/titanium braze material was used. A life test was conducted on the test sample using the following schedule.

1000 hours, 1800°F, 500 psia internal argon pressure
100 hours, 1800°F, 600 psia internal argon pressure
100 hours, 1800°F, 700 psia internal argon pressure
100 hours, 1800°F, 800 psia internal argon pressure
100 hours, 1800°F, 900 psia internal argon pressure
1000 hours, 1800°F, 1000 psia internal argon pressure

This test represented a more stringent evaluation than that performed on the terminals described above. Internal pressurization was used, resulting in tensile stress on the seals.

The external pressurization applied to the terminal configuration produced compressive stress components which tended to maintain the seal integrity.

At the end of the life test, the seal was still intact and preparations were being made to raise the temperature above 1800°F when the test was terminated by a failure in the weld between the argon pressurization tubing (Nb-1Zr) and a Nb-1Zr disk, not involving the metal-ceramic joints under test. No electrical or mechanical failure was observed during the test. Metallographic and X-Ray microprobe analyses of the test sample are presented in the following section.

6.2 Metal-Ceramic Seal Evaluation

The metal-ceramic joining technique to be used in the transducer was tested to failure as described in Section 6.1. The test sample contained seals between Lucalox and Nb-1Zr. The Lucalox was metallized with a tungsten/yttria compound and brazed with a nickel/niobium/titanium alloy. A sketch of the test seal section after test is shown in Figure 109.

As seen in Figure 109 the failure occurred in the distended pressurizing tube which had been recrystallized by the heliarc welding. The seal was removed from the test fixture and microscopically examined. The location of the leak was determined by helium leak check and then pin-pointed by internal pressure and soap bubble technique.

The two bulged end plates and distended tube were measured to determine the amount of movement which had taken place. The center of the lower end plate had been displaced 0.010 inch. The upper end plate with welded tube had been displaced 0.022 inch. The pressure tube had distended in the recrystallized area from 0.090 inch OD to 0.107 inch OD. Its wall thickness was thinned in the area of failure from 0.007 to 0.003 inch.

6.2.1 Metallographic Analysis

The seal was sectioned and prepared for metallographic examination. Photomicrographs were taken of various areas of the section.

The areas of the seal that are shown in the photomicrographs are indicated in Figure 109. The photomicrographs are shown in Figures 110 to 122 inclusive. They have been arranged in 4 groups as indicated in Table 10.

The photomicrographs of the metal-ceramic interface of the upper end plate are shown in Figures 110 to 116 and represent areas I and II of Figure 109. The Nb-1Zr end plate is shown with a portion of the bonded Lucalox on each side. The Lucalox appears black in the photos.

In traversing from Lucalox to the Nb-1Zr member the following seal components are present:

TABLE 10

Metallographic Photo-Indexing System

(Areas Refer to Section Shown in Figure 109)

Figure No.	Position in Seal	Seal Area	Magnification	Remarks
110	Tube plate, right hand	I	100 X	Whole Cross Section
111	Tube plate, right hand	I	100 X	Whole Cross Section
112	Tube plate, right hand	I	500 X	Metal/Ceramic Interface
113	Tube plate, right hand	I	200 X	Whole Cross Section
114	Tube plate, left hand	II	100 X	Whole Cross Section
115	Tube plate, left hand	II	200 X	Whole Cross Section
116	Tube plate, left hand	II	500 X	Metal/Ceramic Interface
117	Blank end, center	III	200 X	Metal Only
118	Blank end, right hand	IV	100 X	Whole Cross Section
119	Blank end, right hand	IV	200 X	Whole Cross Section, Inside Edge of Ceramic
120	Blank end, right hand	IV	200 X	Whole Cross Section, Inside Edge of Ceramic
121	Blank end, right hand	IV	500 X	Metal/Ceramic Interface
122	Blank end, right hand	IV	500 X	Metal/Ceramic Interface, Enlargement "Dodged" to Show Ceramic Detail

1. Lucalox
2. Tungsten metallizing
3. Glass and crystal inclusions
4. Reaction zone between tungsten metallizing and Nb-1Zr
5. Nb-1Zr

Area III is represented in Figure 117 which shows the central portion of the lower end plate bulged 0.010 inch during test.

Figures 118 and 122 show photomicrographs of Area IV as indicated in Figure 109.

As in Area I, area IV shows the Nb-1Zr brazed between the two Lucalox members. Figures 119 and 120 in particular show the metal-ceramic joint at the inside surfaces of the two lower Lucalox rings. They are adjacent fields, and if placed together at reference marks, form a continuous photo.

Figures 120 and 122 show portions of Figure 118 at 200X and 500X magnification, respectively. Figure 122 was printed by "dodging" or shading the negative during printing so as to reveal the structure of the Lucalox as well as that of the metal. This particular section was selected for the X-ray microprobe traverse described in a later section of this report.

By comparing the relative grain sizes of the Nb-1Zr tube plate (Figures 113 and 115) and blank end plate (Figure 117) it is seen that there is a marked disparity between the two pieces. The grain size in the blank end plate (Figure 117) is non-uniform but falls in the range 0.001 to 0.008 inch diameter. On the

other hand, in the tube plate (Figures 113 and 115) the grains are so enlarged that the 0.018 inch thick Nb-1Zr sheet is essentially one grain thick. However, there are a few much smaller grains on one surface of the metal. The enlarged grain growth is considered to have occurred during the heliarc welding of the tube to the tube plate. The layer of small grains is due to the presence of surface contamination, probably oxygen, which exerted an inhibiting effect on grain growth. The smaller overall grain size in the blank end plate presumably occurred during annealing when brazing the assembly.

The structure of the actual metal-ceramic joints is rather complex. The layers adjacent to the Lucalox (the Lucalox appears black in all the Figures except Figure 122) originally consisted of a tungsten/yttria powder mixture, which was fired onto the Lucalox. The Nb-1Zr was then brazed with the Ni/Nb/Ti brazing alloy. Photomicrographs of the resultant joints show that nearly all the yttria has migrated out of the originally porous tungsten structure and that the brazing alloy , or certain elements contained in it, filled the resulting voids in the tungsten. There is some indication that the brazing alloy also penetrated the Nb-1Zr substrate for a short distance, in the order of 0.001 to 0.002 inch, primarily along the grain boundaries. At the same time or shortly afterwards, there appears to have been a reaction between the residual brazing alloy and the yttria which had migrated to the

surface of the tungsten to form a complex glass, or mixture of glasses. This glassy layer then appears to have penetrated the grain boundaries of the Nb-1Zr in the wake of the brazing alloy, in such a way as to form a nearly continuous layer between the metallizing and the Nb-1Zr. It also seems from the sinuous shape of the Lucalox/tungsten interface that the tungsten/yttria metallizing sinter conformed to the surface of the Lucalox, eroding it into a series of small depressions. These depressions do not appear to be associated with the grain boundaries of the Lucalox (See Figure 122). Therefore the metal-ceramic seal consists of a series of interlocking or dovetailing layers which form a seal of exceptional integrity and strength.

In addition there is evidence of diffusion, probably of oxygen, from the glass layer into the Nb-1Zr substrate. The diffusion of the brazing alloy and the constituents of the yttria into the tungsten metallizing caused delta-shaped "islands", grain boundary networks, and possibly a fine precipitate within the tungsten layer.

The layer of glass in some places appears to consist of several phases.

The structure of the seal shows an excessive amount of glass. Since this seal was only examined after 2400 test hours at 1800°F, it is not possible to determine the cause and extent of the diffusion of the different phases. Diffusion of some kind could have taken place during either the metallizing, the brazing operation, or the life test.

Explanation of the structure is rather difficult in view of the fact that much of the diffusion mechanism consisted of a liquid or viscous phase percolating through a porous structure, and infiltration in the opposite direction by a liquid alloy.

In all the sections of this seal examined, no evidence was observed of cracking, separation, peeling or exfoliation of any of the layers comprising the seal. Most noteworthy are the sections illustrated in Figures 119 and 120 which show the border of the metallizing at the inner face of the Lucalox rings. The metallizing at these borders was subjected to the most severe stress, so much so that the Nb-1Zr blank end disc bulged under the test pressure without causing the metallizing to peel or crack.

6.2.2 X-Ray Microprobe Analysis

An X-ray microprobe analysis was performed on a section selected to give optimum analysis of the phases observed in the photomicrographs. The trace traverse corresponds to the vertical line shown on Figure 122 running from Lucalox to Nb-1Zr. The traces given in Figures 123 to 125 have been displayed so that the right hand side of the trace corresponds to the top of the line indicated in Figure 122.

The elements analyzed for were W, Nb, Ni, Al, Y, and Ti. An accelerating potential of either 25 or 30 kilovolts was used. With a carbon-covered specimen, the current was 0.05 microampere. The variations in analysis across the section were recorded continuously, with marker pulses being recorded at 20 micron intervals.

The trace in Figure 123 was recorded using a lithium fluoride crystal at 25 kilovolts accelerating potential. The traces shown in Figures 124 and 125 were recorded using an ADP (ammonium di-hydrogen phosphate) crystal with a 4" radium at 30 kilovolts accelerating potential.

A negative print from a photomicrograph representing the same area traversed by the beam is shown in each figure, the photographs being lined up as closely as possible with the microprobe trace. The upper edge of the print represents the line actually traversed. An exact match was not feasible since the traces and photograph had to be enlarged or reduced for reproduction. The portions of the microprobe traces shown at the right hand side of each trace will be discussed in greater detail as they represent the start of the traverse which appears in Figure 122. The opposite ends of the traces are similar in form but not identical, and do not appear in Figure 122.

Each trace is indexed with a line marked "edge", which represents the interface between the Lucalox and the metallizing, also a "background level" for the element being analyzed. The height of the trace above the "background level" indicates the relative amount of the element present. The marker pulses were masked off during reproduction of the traces, but each major division of the trace represents 20 microns, or 5 major divisions represent approximately 0.004 inch.

In some places where the material is known to be of essentially constant composition, e.g., in the center of the Nb-1Zr

member, some peaks and valleys are observed. These are not peaks representing a change in composition, but are topographic features caused by discontinuities in the surface such as pits, grain boundaries, etc.

The traces of the different layers comprising the seal will be discussed separately in the following paragraphs:

a. Lucalox Layer

It is seen from all 6 traces that there is a sharp demarcation between the Lucalox and the metallizing. Except for a small Ti peak, which is probably topographic, there is no evidence of diffusion of any of the elements investigated into the Lucalox beyond the metal/Lucalox interface, although the photomicrograph shows irregular attack of the Lucalox by the metallizing.

b. Tungsten Metallizing Layer

The traces show the major elements present are W, Nb, and Ni. There is a remarkable similarity in the shapes of the W, Nb, and Ni traces which suggest an alloy of essentially uniform composition, i.e., a solid solution. Two sharp Al and Y peaks are present which presumably could represent the two rounded particles of glass observed in the photomicrograph of the tungsten layer (see Figure 122). Ti is present in small quantities.

c. Glass Layer

This layer, which is the major component of the reaction zone, appears to be composed of a high proportion of aluminum oxide, since the peaks are quite high in comparison to

the Lucalox peak, which represents essentially pure Al_2O_3. Steep peaks are also present for Nb, Ti, Ni, and Y indicating that these elements are localized in the glass area in a non-uniform manner.

d. Nb-1Zr Layer

Although a penetration zone can be seen between the glass layer and the Nb-1Zr in the photomicrographs, the microprobe traces do not indicate diffusion of any of the elements analyzed from the glass layer into the Nb-1Zr. The penetration zone might be caused by the penetration of oxygen into the Nb-1Zr.

A large number of test melts have been made where Ni/Nb/Ti alloys have been melted in small crucibles of Nb-1Zr alloy. In each case, metallographic examination showed that the molten alloys had attacked the Nb-1Zr crucible with little or no evidence of intergranular attack.

However, the photomicrographs presented in this report indicate that the Nb-1Zr substrate has been attacked primarily in an intercrystalline manner by the glass formed in the metallizing operation.

It would appear that the presence of the oxygen exerted a marked effect on the ability of the Ni/Nb/Ti alloy to attack the Nb-1Zr substrate. It is felt that the Nb-1Zr substrate was attacked by oxygen, primarily along the grain boundaries, and that the Ni/Nb/Ti alloy then attacked the substrate, following the oxygen-rich paths provided by the grain boundaries. The result was to produce intergranular penetration of the substrate for a short distance by the glassy phase. This penetration was not of such an extent to be harmful but served to bind the layers together.

6.3 Seal Thermal Cycling Tests

As a final step in certifying the Lucalox/Nb-1Zr seal techniques for use in the pressure transducer, a third seal configuration was prepared and subject to a thermal cycling test. The configuration, shown in Figure 126, used a Lucalox plug metallized with the tungsten/yttria compound and brazed to a Nb-1Zr tube with the Ni/Nb/Ti braze alloy. A seven degree taper was chosen for the Lucalox and Nb-1Zr braze areas.

The thermal cycling test was performed according to the following schedule:

10 cycles 1472°F (800°C) in flowing argon; leak tight
10 cycles 1832°F (1000°C) in flowing argon: leak tight
10 cycles 2192°F (1200°C) in flowing argon; leak tight
5 cycles 2552°F (1400°C) in flowing argon; leak tight
10 cycles 2552°F (1400°C) in flowing argon; leaked

Relatively short cycle times were used; six minutes to attain temperature, one minute at temperature, three to five minutes to cool to about 500°F. The seal was helium leak-tested after each of the sets of cycles outlined above.

The testing demonstrated the acceptibility of the seal for use in the pressure transducer temperature environment (1800°F). Test temperatures in excess of 1800°F were introduced to evaluate the upper limits of seal operation.

The fact that the seal was cycled between 35 and 44 times at temperatures up to 2552°F before failure indicated that 2552°F was not the upper operating temperature of this seal. While the initial melting point of the Ni/Nb/Ti braze alloy was 2300 to 2450°F, it appeared that its remelt temperature was about 2700 to 2900°F, since no remelting was observed during the testing.

7.0 Liquid Metal Compatibility

As part of the overall transducer effect, a program was developed to evaluate the potassium compatibility of the four candidate alloys (C-129Y, FS-85, T-222, W-25Re) and the metal-ceramic seals. The program included preparation of test samples, actual test procedures, and post-mortem testing. The program was defined as follows.

1. Preparation of Test Capsules
   a. Obtain a chemical analysis of the capsule materials.
   b. Obtain a chemical analysis of potassium batch.
   c. Fill the test capsules with potassium and identify the capsules.
   d. Weigh the completed test capsules.
2. Test Procedure
   a. Install the test capsules into the compatibility test chamber.
   b. Raise test chamber temperature to 1800°F. At no time shall the chamber pressure exceed 10^{-5} torr. For chamber temperatures above 700°F, the chamber pressure shall not exceed 5×10^{-7} torr.
   c. Maintain test chamber temperature at 1800°F for a period of 100 hours. This will establish a potassium vapor pressure inside the test capsules of about 80 psia. After 100 hours, bring the test chamber to room temperature.

d. Perform 2.c above five times to accumulate a total of 500 hours operation at 1800°F.

e. Remove the test capsules from the test chamber.

3. Post-Mortem Tests

a. Weigh the test capsules.

b. Visually inspect the test capsules for possible failures.

c. Extract the potassium from the test capsules and perform a chemical analysis on the potassium.

d. Test the capsules for leakage on a mass spectrometer.

e. Cut up, section and perform metallographic examination of diaphragms, weld joints, braze joints, ceramics, etc.

f. Perform chemical or microprobe analysis of any corroded layers indicated in 3.e above.

Performing individual compatibility tests on each capsule would occupy the Vacuum Test Facility a disproportionate amount of time; therefore, a compatibility test chamber was fabricated which held all capsules at the same time. The chamber had a separate pumping system. In design, the chamber was similar to the chambers on the Vacuum Test Facility. Cylindrical strip heaters, with shielding, were suspended in the chamber and cooling water coils were used around the outside. The capsules were tested at 1800°F, which established a potassium vapor pressure of about 80 psia. Thermocouples were used to monitor the temperature of the potassium liquid-vapor interface. The temperature of the test capsules was monitored by optical pyrometry through the chamber viewing window.

Figure 127 shows the internal components of the compatibility test chamber. Figure 128 shows the test chamber in operation with its vacuum system.

7.1 Compatibility Testing

Initial compatibility testing was performed on one sample of each of the candidate alloys and four representative metal-ceramic electrical terminals. Figure 129 through 131 show the designs.

To expedite fabrication of the test devices, only one convolution was used in the pressure capsules and there was no containment housing around the capsules. A yoke arrangement acted as a mechanical stop against excessive displacement and subsequent failure of the diaphragm disc.

Figure 129 shows the design for the columbium and tantalum alloy capsules (FS-85, C-129Y, T-222). The two-piece yoke and potassium containment tube are made of FS-85 alloy.

Figure 130 shows the design related to the W-25Re alloy capsule (electrical discharge machined discs) and used Mo-50Re tubing as a transition between the W-25Re capsule and the molybdenum yoke and TZM potassium containment tube. A Mo-50 Re ring was also used as a weld insert between the thermocouple well and the potassium containment tube.

Figure 131 shows the electrical terminal test configuration. The fixture accepted four terminals (see Figure 107) for test.

Since the electron-beam welding of the terminal cap was done in a vacuum of about 10^{-4} Torr, zirconium was inserted in the terminal assembly to act as an oxygen getter. Prior to the actual preparation of the compatibilitv devices, mock-ups were prepared for dummy runs to establish procedures for potassium charging and capsule closure (electron-beam welding the thermocouple well to the containment tube).

No potassium leakage was observed during the performance of the compatibility test schedule. Examination of the test capsules after completion of the test showed no visible signs of failure.

The potassium was removed from the test capsules inside a vacuum purged (10^{-5} torr) welding chamber back-filled with high-purity helium. The tops of the test capsules were cut off and the capsules were heated to 150-200°F. The potassium was drained from each test capsule into a platinum dish and, upon removal from the chamber, converted to KC.

To remove the residual potassium from the test capsules, the drained capsules were sealed inside a stainless steel distillation chamber. The distillation chamber was removed from the welding chamber and evacuated to 10^{-5} torr. The bottom half of the distillation chamber was heated to 800°F and the residual potassium was collected on an air-cooled finger at the top of the distillation chamber. The test capsules were heated in this manner for 72 hours, during which time the pressure remained at about 10^{-5} torr.

Upon removal from the distillation chamber, all five test capsules were found to be coated externally with a dark gray film. Much of this dark film appeared to be water-soluble and was probably caused by condensation of potassium vapor during the distillation process.

7.1.1 Examination of the Test Capsules

The test capsule containing the electrical terminals was opened first. This was done by machining off the weld bead around the rim, extracting the terminals, and then sectioning both the capsule and the upper tube by sawing them longitudinally.

The four pressure compatibility capsules were next sectioned by removing the capsules from the upper tube, and then sectioning the pressure capsules with a water-cooled cut-off wheel. The upper tubes were sectioned longitudinally by sawing with a band saw.

The longitudinal sections of the four pressure compatibility capsules appeared bright and clean, with little or no evidence of any attack by the potassium, whereas the inside of the capsule containing the terminals was blackened somewhat. When the vertical tubes of the pressure compatibility capsules were sectioned, they were also found to be slightly blackened. It appears likely that the black film existed inside the pressure capsules; but being water-soluble, the film was removed by the cooling water used with the cut-off wheel.

Figures 132 to 136 show photographs of the five test capsules in the "as sectioned" condition. Figure 132 shows the terminal capsule with one terminal in position, the other three terminals having been removed. It is seen that while the lower part of each terminal cavity was bright and clean, the housing showed traces of a white corrosion product where the Lucalox portion of the terminal was in contact with the housing. The upper tube showed a black corrosion product along its length.

Figures 133 to 136 show the pressure compatibility capsules after sectioning. It is seen that in each case the lower portions of the pressure capsules were clean and almost free of corrosion while the upper portions showed small amounts of a black corrosion product. As described above, this black coating could have been removed in some cases during sectioning the capsules with a water-cooled cut-off wheel. In the C-129Y capsule (Figure 133) and the FS-85 capsule (Figure 134), the boss in the center of the lower diaphragm was found to be pressure-welded to the limiting stop after the test at 1800°F.

The capsule containing the electrical terminals was examined immediately after sectioning longitudinally, and then photographed

(see Figure 132). The lower part of the capsule containing the electrical terminals was photographed at a higher magnification. (See Figure 137). Figure 137 shows that only the upper part of each cavity, which contained one terminal, was coated on the inside in varying degrees with a white incrustation of a salt-like material, probably a potassium oxide, hydrozide or carbonate.

Both the Lucalox and metal parts of the terminals showed a frosted or etched appearance compared with the "as received" terminals. Each one of the four terminals tested showed longitudinal and radial cracks in the outer band of Lucalox.

The four terminals were then opened by machining off the FS-85 caps on the lower ends of the terminals. Photographs of the terminals in this condition are shown in Figure 138. Two of the terminals when opened were found to contain the white potassium compound observed on the outside of the terminals. All four terminals were then helium leak tested; three were found to be leak-tight and one to have a leak. Of the three units that were found to be leak-tight, one was filled with the white potassium compound. Apparently, the electron-beam weld joining the small cap to the terminal leaked, because the potassium compound was only present in the

very bottom of the terminal. Thus, it appears that three out of the four terminals were leak-tight after the test, even though the outer band of Lucalox was cracked.

The pressure capsules were mounted in plastic, polished with emery strips and fine diamond paste. They were then polished by alternately etching in "mixed acids" (equal parts HF, H_2SO_4 and HNO_3, diluted 1:1 with water) and hand polishing on a wheel charged with fine alumina and moistened with 4% ammonium bi-fluoride solution. In each case the FS-85 housing around the capsules (or the molybdenum yoke around the W-25Re capsule) was removed by sawing prior to mounting. The yokes which had been welded across the bottom of the housings to limit the deflection of the capsules were found to be pressure welded to the small bosses projecting from the centers of the lower diaphragms in the case of the C-129Y and FS-85 capsules. This did not occur in the T-222 and W-25Re capsules.

Examination of the cross-sections of all the pressure capsules at up to 400X magnification showed no evidence of attack at the inside of the capsules by the potassium. The only abnormal feature found was that the capsule boss was pressure welded to the yokes as described above. In addition, an intergranular crack was observed in the outer surface of the T-222 capsule. This intergranular crack originated in the radius of the internal corner between the central boss of the lower diaphragm and the diaphragm proper, and extended inwards at a 45° angle approximately one-third of the way through the diaphragm. (See Figure 147). Apparently a machining fault provided a stress concentrating notch in the vicinity of the boss, causing the crack.

Photographs of the pressure capsules at 3X magnification are shown in Figures 139 to 142. These figures show the general arrangement of the parts in the pressure capsules and the welds.

The pressure capsules were next photographed at 25X magnification. In each case the area photographed comprised a section of the weld joining the diaphragm material to the tube, and also a portion of the lower diaphragm opposite the weld. It is seen that in each case (Figures 143 to 146) there is no evidence of attack of either the diaphragm material, the tube, or the weld nugget, which was composed of an alloy of the tube and diaphragm materials. In the case of the C-129Y, FS-85 and T-222 capsules the tube was FS-85, and in the case of the W-25Re capsule it was Mo-50Re.

Figure 147 shows the intergranular crack in the T-222 capsule diaphragm.

7.1.2 Potassium Analysis

The potassium was analyzed before and after the compatibility tests. The assay results are summarized in Table 11 where the left hand column shows the chemical analysis of the potassium at the start of the test, and the other columns show the chemical analysis of the potassium extracted from the test capsules after the test.

The Na assays of the potassium in each case showed some variation during the test, but this is not thought to be significant.

With the exception of the FS-85 capsule, in each case the V content of the potassium increased during the test. The spectrographic analysis of V is apparently not particularly sensitive,

TABLE NO. 11

Potassium Analysis Before and After Compatibility Test
(Test run for 500 hours at 1800°F and nominal 80 psia pressure)

Element	Before Test (ppm) (a)	After Test (ppm) C-129Y	FS-85	T-222	W-25Re	Terminal Capsule
Ag	<1	<1	<1	<1	<1	<1
Al	<1	1	<1	1	1	1
Be	-	<1	<1	<1	<1	<1
Ca	1	1	<1	10	1	10
Cb	<1	10	<1	<1	<1	<1
Co	<1	<1	<1	<1	<1	<1
Cr	<1	<1	<1	<1	1	1
Cu	<1	<1	<1	<1	<1	<1
Fe	<1	1	<1	1	5	5
Mg	<1	<1	<1	<1	<1	1
Mn	<1	<1	<1	<1	<1	<1
Mo	<1	<1	<1	<1	>25	<1
Na	5	10	5	<10	10	10
Ni	<1	1	<1	<1	<1	<1
Pb	<1	<5	<5	<5	<5	<5
Si	5	<10	<5	<10	<10	<15
Sn	<1	<5	<5	<5	<5	<5
Ti	<1	<1	<1	<1	1	<1
V	<5	<10	<5	<10	<10	<10
Zr	<1	<5	<5	<5	<5	<5
O (as K_2O)	3.4 - 7.6	-	-	-	-	-

(a) Samples of the potassium were cast in a stainless steel tube under a vacuum of 5 X 10^{-5} torr in an electron beam welding chamber, subsequent to filling the last capsule. The potassium samples were analyzed for oxygen by the mercury amalgamation method (helium cover gas) and for metallic impurities by spectrographic techniques.

so some doubt must be cast on the results, but the trend of the results suggests that V was leached out of these alloys during the test.

In all cases, the changes in potassium analysis are sufficiently small to indicate material compatibility.

Oxygen analysis was only performed on the potassium at the start of the test, and was reported as 3.4 to 7.6 ppm (as K_2O), the analysis being performed by the mercury amalgamation method under a helium cover. The most significant changes in the potassium analyses in each test capsule were as follows.

a. C-129Y Capsule. The most signficant change was an increase in Cb content of the potassium from <1 to 10 ppm. This Cb presumably was leached out of the C-129Y and not out of the FS-85 parts of the capsule, since no Cb was leached out of any of the other capsules containing FS-85 parts. This attack might have been a differential corrosion effect.

   Increases in Al, Fe, Ni, Pb, Si, Sn, V and Zr contents were also reported, but are not considered to be significant.

b. FS-85 Capsule. The potassium from this capsule showed the least change in composition during the test. The only increase in impurities observed were in the Sn and Zr contents of the potassium.

   The Si content showed a slight decrease. This exceptional stability may be due to the fact that the capsule was

fabricated entirely of FS-85 material, in contradistinction to all the other capsules which contained dissimilar materials.

c. T-222 Capsule. In this capsule a marked increase was observed in the Ca content of the potassium from <1 to 10 ppm. No explanation can be offered for this. Increases in Al, Fe, Pb, Si, Sn, V and Zr were also reported but are considered insignificant.

d. W-25Re Capsule. The most marked change was the relatively large increase in Mo content of the potassium from < 1 to >25 ppm. In view of the fact that Mo is normally considered to be quite resistant to potassium this attack, which is considered to be abnormally severe, is probably due to some preferential corrosion effect as a result of W-25Re, Mo-50Re and TZM molybdenum being in contact in the capsule.

Increases were found in the Al, Fe, Pb, Si, Sn, Ti, V and Zr contents of the potassium, but of these only the increase in Fe is considered to be significant.

e. Thermal Capsule. In this capsule the major changes in impurities in the potassium were increases in the Ca, Fe and Si contents, accompanied by minor increases in the Al, Cr, Mg and V contents.

The following analysis was obtained of the impurities in a sample of Lucalox.

MgO	1000 ppm
Fe_2O_3	100 ppm
SiO_2	300 ppm
CaO	100 ppm
CuO	Trace
NiO	Trace
MnO	Trace
Cr_2O_3	Trace

While not necessarily indicative of the average impurity level of the test terminals, it is seen that with the exception of V, all the impurities which increased during the test could have been present initially in the Lucalox, indicating that the Lucalox was the probable source of the additional potassium impurities.

8.0 Differential Pressure Transducer

The basic design problem of the differential pressure transducer (see Figure 5) was to transmit the motion of the pressure capsule operating in a liquid metal environment into a motion of an active collector surface in the vacuum environment of the thermionic diode sensor. The design configuration should provide for about 1:1 transmission of motion and should be capable of containing liquid potassium at 1800°F.

Preliminary analyses were performed on three mechanical configurations for the differential pressure transducer (±5 psid). Figure 148 shows the three configurations schematically. Each configuration utilizes the deflection of a composite beam assembly consisting of (1) an outer tubular beam member and (2) an internal beam member whose termination acts as the active collector surface for the thermionic diode sensor. The outer beam member is exposed to the liquid potassium environment. A wall thickness of 0.025 inch was assumed to be sufficient for liquid metal containment. The internal beam member is sealed from the liquid potassium and connected to the vacuum environment of the thermionic diode sensor.

For the differential pressure application, the thermionic diode sensor is removed from the interior of the pressure capsule, isolated from the pressurized volumes, and embedded in the capsule housing (see Figure 5). The pressures P_1 and P_2, whose differential (P_1-P_2) is to be monitored, are applied to the external and internal surfaces, respectively, of the pressure capsule. The main capsule housing inner diameter was assumed to be about 1.5 inches and the active collector surface extends 0.375 inch beyond the fixed support of the outer beam member.

For Case I (cantilever, end load), the displacement of the pressure capsule is transmitted directly to the cantilevered end of the outer beam member, establishing an end slope θ_1 relative to the horizontal position. The deflection of the active collector surface from equilibrium therefore becomes $(0.75 + 0.375)\theta_1$ inch less the deflection of the outer beam end. For Case II (end couple, one end fixed, one end supported), the pressure capsule displacement is transmitted by a yoke arrangement as a couple acting on a supported pivot point at one end of the outer beam member. If the end slope at the supported pivot point is θ_2, the active collector deflection from equilibrium becomes $(1.5 + 0.375)\theta_2$ inch. Case III (cantilever, combination end load and end couple) involves the removal of the supported pivot point of Case II, allowing free movement of the outer beam member subject to the superposition of two actions; i.e., the pressure capsule deflection transmitted by the yoke arrangement as (1) an end load and (2) an end couple.

The application relations are as follows (Reference 3).

Case I (cantilever, end load)

$$\theta_1 = \frac{-W\,t^2}{2EI}$$

$$y_1 = \frac{W\,t^3}{3\,EI}$$

Case II (end couple, one end fixed, one end supported)

$$\theta_2 = \frac{MT}{4EI} = \frac{Wt(2t)}{4EI} = \frac{Wt^2}{2EI}$$

Case III (cantilever, combination end load and end couple)

Due to end load:

$$\theta_{3L} = -\frac{WT^2}{2EI} = -\frac{2Wt^2}{EI}$$

$$y_{3L} = \frac{WT^3}{3EI} = \frac{8Wt^3}{3EI}$$

Due to end couple:

$$\theta_{3C} = \frac{MT}{EI} = \frac{Wt(2t)}{EI} = \frac{2Wt^2}{EI}$$

$$y_{3C} = -\frac{MT^2}{2EI} = -\frac{Wt(4t^2)}{2EI} = -\frac{2Wt^3}{EI}$$

Combining end load and end couple effects

$$\theta_3 = \theta_{3L} + \theta_{3C} = 0$$

$$y_3 = y_{3L} + y_{3C} = \frac{2Wt^3}{3EI}$$

In these equations, the sign convention employed is that end slopes and deflections are positive when in the upward direction (direction of force W in Figure 148) and

θ_1 = tubular outer beam end slope (Case I) (radians)

θ_2 = tubular outer beam end slope (Case II) (radians)

θ_3 = tubular outer beam end slope (Case III) (radians)

y_1 = tubular outer beam end deflection (Case I) (inch)

y_3 = tubular outer beam end deflection (Case III) (inch)

W = force exerted by pressure capsule on beam (assumed to be 1 pound)

t = tubular outer beam length (Case I) (0.75 inch)

T = tubular outer beam length (Cases II & III) (1.5 inch)

M = moment produced by pressure capsule (Cases II & III) (Wt pound-inches)

E = modulus of tubular outer beam material (assumed to be 30×10^6 psi)

I = moment of inertia of tubular outer beam section $= 0.049 (D^4 - d^4)$ inch^4

D = outer diameter of tubular outer beam (inch)

d = inner diameter of tubular outer beam (inch)

The results of the analysis are presented in Figure 149. The deflections for the Case I configuration are negative, using the sign convention outlined above.

The data show that Case II holds promise of providing an active collector deflection of 0.001 inch for reasonably sized tubular beams. The value of 0.001 inch full scale deflection would result in a feasible output for the thermionic diode sensor. However, the difficulties inherent in Case II, which requires that the supported pivot point be inside the main capsule housing, made it mandatory to concentrate further on Cases I and III, for which the fabrication requirements were far less stringent. Case III had the further advantages of providing (1) a greater deflection for a given size outer beam and (2) a purely vertical active collector travel, since $\theta_3 = 0$. For these reasons, mock-up work was confined to the Case III configuration to verify the results of the analysis.

In fabricating the mock-ups of the Case III configuration, Nb-1Zr tubing was used for both the outer and inner tubular beams. Nb-1Zr was chosen for two reasons.

1. Nb-1Zr has a Youngs modulus about equal to that of the refractory alloys used in the actual transducer.
2. Nb-1Zr tubing was readily available, in various sizes, for test purposes.

Three mock-ups were fabricated for testing. The first mock-up used a brazed assembly with an outer tubular beam of 0.187 inch O.D., 0.137 inch I.D. and an inner tubular beam of 0.096 inch O.D., 0.086 inch I.D.. Initial testing yielded erratic results. Investigation showed that the braze joint holding the outer and inner beams together had failed and the inner beam had become loose. A second mock-up was made using the same size inner and outer beams but the assembly was welded together. Test results obtained from the second mock-up indicated that for an applied force of one pound, an inner beam deflection of about 0.0002 inch was obtained.

The third mock-up used a welded assembly with an outer tubular beam of 0.125 inch O.D., 0.075 inch I.D. and an inner tubular beam of 0.063 inch O.D. and 0.051 inch I.D.. The inner beam deflection was monitored by a Distance Meter capable of accurate measurement of distances from 50 microinches to 0.5 inch depending on the probe used. A probe is electrically connected to the instrument and brought into proximity with the flattened end of the inner beam (active collector surface). The capacitance formed between the probe and the inner beam is calibrated in terms of distance. The probe used had a full scale range of 0.005 inch with an accuracy of $\pm$0.0001 inch. A typical force versus deflection characteristic is shown in Figure 150. The data indicate that application of a

one pound force resulted in an inner beam deflection of about 0.0007 inch. The force versus deflection curve was linear within 3 percent of full scale deflection corresponding to a one pound force. There appeared to be no detectable hysteresis effect.

As a final check, to determine whether any low-frequency resonant effects could produce large scale beam motion, the mock-up was installed on a vibration table and subjected to vibrations based on procedure XIV of MIL-E-5272C(ASG). The procedure involved the following test parameters.

0 to 10 cps,	0.20 inch double amplitude
10 to 20 cps,	$\pm$ 1.0g
20 to 90 cps,	0.05 inch double amplitude
90 to 2000 cps,	$\pm$ 20g

Prior to testing of the complete mock-up, the probe of the Distance Meter was vibrated by itself to check if the probe might exhibit any resonance at the frequencies of interest. The probe used for the vibration test had a full scale range of 0.010 inch with an accuracy of $\pm$ 0.0002 inch. The decreased accuracy of this probe was acceptable for this test since a qualitative idea of the resonant behavior of the beam was all that was desired. The probe exhibited no resonant points at the frequencies used for the test.

Results of the vibration tests of the beam in air showed that the Case III beam configuration had relatively broad resonant peaks between 220-250 cps, 700-820 cps, and 1400-1600 cps, and a sharply defined resonance at about 330 cps. Should these resonant

peaks exist while the beam is in operation, the transducer output would be in considerable error. However, in operation the beam will be immersed in liquid metal, and therefore, subject to greatly increased damping conditions. For this reason, the resonant motion of the beam will be certainly minimized if not eliminated completely.

Based on the results of the analysis and the experimental data obtained from the mock-up assemblies, the Case III configuration was chosen as a viable basis for the differential transducer design.

9.0 Transducer Signal Conditioner

The signal conditioning instrument with the built in d.c. voltmeter is shown in the photograph in Figure 152. The associated schematic diagram (CCC Dwg. No. KMY1316) is shown in Figure 151 along with the physical layout shown in Figure 153.

The system is basically composed of three main control systems; namely, the heater control circuits, the constant current diode control circuits, and the pressure computing amplifiers. Each circuit will be described in detail.

9.1 Heater Control

The emitter heater control circuit derives its input signal from a thermocouple mounted on the emitter. The thermocouple signal is a 1 to 22 mv signal which corresponds to a 100°F to 2220°F emitter temperature. This thermocouple signal is fed into the inverting input of a linear integrated operational amplifier (LA1) after being filtered for noise pick-up by R64, C5, and R22. This input is summed with the desired input potentiometer setting (emitter temperature) from potentiometer, R_{19}, whose reference voltage is derived from a 6.2V zener diode, CR_9, (T.C. = 0.002%/C°) for a stable reference. The amplifier is operated open loop for increased control accuracy and feeds another gain and emitter follower stage (Q7 and Q5) coupled together by the two diodes, CR7 and CR8. This output feeds the input voltage to the inverter comprised of Q6, Q11 and T2. The invertor oscillates at a basic frequency of about 800 Hz corresponding to the following relationship:

$V = 4Bm\ AFN\ X\ 10^{-8}$

where V = input voltage

Bm = flux density in gausses

A = core area in cm^2

F = output frequency

N = number of turns

With this relationship, the output frequency will be proportional to the input voltage amplitude. The output of the transformer, T2, feeds a diode (CR10, CR11, CR 12, CR 13) full wave rectified bridge circuit whose d.c. output will be proportional to the frequency and input amplitude to the invertor. Capacitor C6, is for proper filtering and feed amplifier Q10, which feeds the Darlington stages, Q8 and Q9, for the high current output control to the heater via the fuse, XF1.

Since the emitter heater is electrically connected to the emitter, isolation is required throughout the circuit. Hence, the use of the invertor circuit for transformer isolation and the use of the separate, isolated, unregulated power supply (T3, CR14, CR15, R25, C7) for powering the heater only and the use of the transformer coupled (T1) power supplies (+15V, -15V) to supply the regulated voltages for the operational amplifier and the associated circuits of the heater circuit only. With the high control circuit amplifier gains used (LA1≈45000) the emitter temperature was controlled to well within $\pm$ 5°F for input power changes, long term drift, and chamber ambient temperature changes. Thus for example, as the emitter temperature attempts to change above the desired setting (usually

about 2100°F) the positive thermocouple signal is summed with the negative reference signal and the amplifier's output reduces, the output of Q7 increases, the output of Q5 increases, the output of the F.W.R. increases, the output of Q10 decreases, the output of Q8 decreases, the output of Q9 decreases and the resulting heater power decreases. Current limiting is accomplished by the use of the 1.5A fuse inserted with the heater. The emitter thermocouple voltage and the heater voltage can be monitored directly by the built in d.c. voltmeter with the meter selector switched placed in the appropriate positions.

9.2 Constant Current Control

A constant current regulated circuit maintains the sum of the active and reference collector currents constant by sensing the voltage analog sum R33, feeding it into LA3 (inverting side) via R37, and comparing it with the "sum of currents" adjustment, R52, into the non-inverting input to LA3. The output of the open loop amplifier, LA3, feeds an emitter follower output, Q12, for increased current capability up to 200 ma. With the high loop gain which is used the sum of the currents is held constant to better than 0.5% f.s. throughout the pressure input test range. System stability is maintained by the use of high frequency roll off capacitors, C11 on the output stage and C15, together with C12 and R35 for the integrated circuit operational amplifier, LA3. Long term stability and accuracy is achieved by use of wire wound 0.5% sense resistors for the sum of currents measurements.

In the "Auto" mode the sum of the currents regulator is in normal operation using the isolated, regulated power supplies. With switch, S3, in the MANUAL position the sum of the currents can be adjusted manually without the use of an automatic regulator using the same "sum of currents" potentiometer on the front panel. The manual switch also switches the power supply biasing resistors, R48 and R49, to provide for higher output currents on the -15V output and disconnects the positive supply altogether.

9.3 Pressure Computing Amplifiers

The computing integrated operational amplifier, LA4, produces an output signal which is proportional to the transducer pressure. The active and reference collector currents are monitored by use of R32 and R26 series resistors to monitor the voltage analog of the current. These voltage analogues are monitored by use of R27 and R30 feeding into a computing amplifier, LA2, which computes the difference between the two currents (i_a - i_c). This difference analog signal is then fed into the inverting input of operational amplifier, LA4. In order to compensate for the initial unbalance in the active and reference collector currents (I_a and I_r) of the diode, a zero adjust is necessary for the pressure computing amplifier in order to null out this initial offset potential and not create a fixed error. The pressure output signal is a 0 to 5.0VDC, low output impedance signal (0 to 80 psia equivalent) whose gain and linearity are adjustable with panel mounted potentiometers. The linearity adjustment is required in order to compensate for the non-linear pressure transducer (diode) differential current signal.

A non-linear amplifier gain characteristic is achieved through the use of a diode (CR24) in the feedback network of an operational amplifier. Since the forward breakdown impedance of a diode changes non-linearly , the gain of the amplifier changes in a similar fashion since the gain is directly proportional to the amplifier's feedback resistance. To obtain the desired output characteristics both the "gain" and "linearity" adjustments must be used since they are a function of each other. D.C. isolation is achieved in the computational circuits through the use of transformer coupling (T3) to the regulated, ± 15.0 VDC power supplies.

9.4 External Instrumentation

For monitoring various voltages and voltage analogue's of current, a built in d.c. voltmeter was built into the front panel as shown in Figure No. 152. Various parameters can be measured by use of the meter select switch as can be noted from the photograph. External jacks are provided for monitoring with an external meter or recorder. When plotting "space charge" curves of diode voltage vs. active collector or reference collector current for various pressures the external jacks were used for recorder inputs. The pressure voltage analog plots vs. actual pressure were made using the external jacks for pressure output.

10.0 Vacuum Test Facility

The initial concept and design for the Vacuum Test Facility was discussed in Section 4.1.1. Early in the program, the facility was used for performance of tests on the initial set of pressure capsules (see Section 4.1) and preliminary tests on thermionic diode sensor mock-ups. Figure 154 shows this early Vacuum Test Facility configuration.

As the program advanced into the area of complete transducer design and test, the function of the Vacuum Test Facility became to provide the means for evaluating the operation of the complete transducer. While the basic Facility of Figure 154 did not change, additions were made to achieve transducer operation and evaluation. These additions included (1) fitting of individual ion pumps to two test chambers, (2) installation of an argon manifold supply, (3) installation of transducer pressurization systems with automatic pressure cycling capacity and (4) installation of automatic safety systems to protect the transducer from high-temperature oxidation damage in the event of failures in the pressurization system.

Figure 155 presents, in schematic form, two chambers of the Vacuum Test Facility set up to operate the absolute pressure transducers. The transducer is enclosed in a heated, high-vacuum chamber. Radiant heat is supplied by a set of cylindrical resistance heaters fabricated of Nb-1Zr material. The test zone is large enough to assure uniform heating and provide space for heat shields used to control end effects. The test head contains the pressure and electrical feedthrough connections needed for operation of the transducer. Since all support is from this test head, the transducer can be installed quickly.

Early test experience indicated the desirability of being able to operate individual test chambers independent of the facility itself. This was achieved by fitting individual ion pumps (20 liters per second) to each test chamber. During initial bake-out runs to 1800°F, the 200 liter per second ion pump, common to all chambers, may be used for maximum pumping. Once operating temperature and pressure conditions are attained, the chamber is valved off (V16, V25) and run on its own ion pump.

A manifold system is used for the argon supply. Four supply tanks feed into a manifold separated from a second plenum by a high-pressure valve. A spare tank feeds into the second plenum. This tank is normally closed and the system runs on the four tank supply. When these tanks need replacement, Valve V3 is closed and the system is run off the spare tank. The four tanks are replaced, the manifold cleaned by backfilling and evacuating through V1 and the tanks are turned on. Valve V3 is opened, charging the spare argon tank which is then turned off. The system is then back on the four tank supply.

The pressurization systems used for operating the transducers have an automatic pressure cycling capability of 20 cycles per hour. A timer-actuated solenoid valve (SV1, SV2) is used to pressurize the pressure capsule for 1 1/2 minutes (3 minute pressure cycle). The valving allows connection of the pressure gauge (G3) and a room temperature transducing cell (T1) into the system to monitor the pressure and obtain an electrical signal for the X-Y recorder used in the evaluation testing. The system for testing the differential pressure transducer is valved so that the pressure

and vacuum ports can be switched, allowing pressurization of either side of the pressure capsule.

The Vacuum Test Facility includes three safety systems designed to protect the transducer from high-temperature oxidation damage in the event of failures in the argon pressurization system, the mechanical vacuum pump used for evacuation of the transducer during pressure cycling, or the vacuum test chamber.

1. Argon pressurization system - The pressurization system must be monitored to check excessive oxygen content in the argon gas and any air leakage into the pressure system. The oxygen content (parts per million) of the argon entering the pressurization system is monitored by a Lockwood-McLorie oxygen analyzer. Past experience indicated that the normal oxygen content of the argon is under 5 PPM. The electrical output of the ozygen analyzer (about 0.5 millivolt per PPM) is in turn monitored by a meter-relay system with an adjustable high set-point which is set at about 2.5 millivolts. If the oxygen content of the argon reaches 5 PPM, the meter-relay system is activated and performs two functions.
   (a) The test chamber heater is de-energized to allow rapid cool-down of the transducer.
   (b) The three-way solenoid valve used in the pressure cycling system is de-energized. In the de-energized condition, this valve connects the transducer to the mechanical vacuum pump. Thus no high-oxygen-content argon would be introduced into the transducer.

The Lockwood-McLorie monitors the argon for the chambers by feeding argon from both pressure systems, through flowmeters, to the oxygen analyzer. The two flowmeters are adjusted so that (1) the proper pressure conditions are met for the operation of the analyzer and (2) the flows from the two pressure systems are about equal.

2. Mechanical vacuum pump used for evacuation of the transducer during pressure cycling - A check must be made to insure that the pump is operating. If the pump stops, ambient air will be introduced into the transducer, which is operating at 1800°F. Oxidation and failure of the pressure capsule will follow. Operation of the pump is monitored by a centrifugal switch mounted directly on the pump shaft. A standard industrial type switch is used, modified so that switch actuation occurs at the speed of the vacuum pump (about 600 RPM). At speed, the switch is open. If the pump stops for any reason, the switch closes and performs two functions.

   (a) The test chamber heater is de-energized to allow rapid cool-down of the transducer.

   (b) A normally-closed solenoid valve in the exhaust line between the transducer and the pump is de-energized. This isolates the transducer from the mechanical pump and blocks backstreaming from the pump.

3. Vacuum chamber - Vacuum integrity must be maintained in the test chamber inside of which the transducer operates. Failure of any of the vacuum seals would introduce air into the chamber, resulting in oxidation and failure of the pressure capsule. The integrity of the test chamber is monitored by a relay connected to the circuit breaker of the ion pump power supply. Loss of chamber vacuum increases the current drawn by the pump and trips the circuit breaker, de-energizing the safety relay. In turn, the test chamber heater is de-energized to allow rapid cool-down of the transducer.

For both oxygen content of the argon and test chamber vacuum, a problem in any chamber results in corrective actions being taken in both chamber systems. This is due to the fact that the Lockwood-McLorie and the ion pump power supply work with both chambers in common and cannot trace a safety signal to a particular chamber. For the third safety, separate chamber controls are used since each chamber has its own mechanical vacuum pump. The three safety operations have one thing in common: any alarm condition results in the test chamber heater being de-energized.

11.0 Transducer Test Program

During the course of the transducer effort, testing program emphasis shifted from preliminary testing of representative pressure capsule configurations (described in Section 4.1) to a series of tests designed to prove out the fabrication techniques used in the transducer and finally, to evaluate the performance of the finished transducer.

Seven experimental devices (T-1 through T-7) were fabricated and tested in the initial stages of the program. Once the fabrication techniques had been developed, four absolute transducers (A-1 through A-4) and two differential transducers (D-1 and D-2) were built for performance testing.

Operating lifetimes of over 2,000 hours were exhibited by the test units. While some changes in transducer pressure-output parameters were associated with temperature excursion tests, it appeared that in the absence of the temperature excursion tests, the pressure-output data could have remained within a $\pm$ 5 percent envelope around a 0-5 volt full scale output over the entire test period. With some additional work to minimize temperature effects, the testing indicated that a viable transducer design is at hand.

11.1 Experimental Test Devices

Table 12 presents a listing of the seven experimental devices (T-1 through T-7) along with information on the test configuration, test purpose, duration and temperature of test, and cause of failure. The first two devices were designed specifically

TABLE 12
EXPERIMENTAL TEST DEVICES

NO.	TEST CONFIGURATION	TEST PURPOSE	TEST HOURS	TEST TEMP. (°F)	SENSOR FAILURE MODE
T-1	Mechanical actuation (micrometer drive)	Development of proper material and fabrication techniques for sensor	20	1800	Open circuit heater
T-2	Mechanical actuation (micrometer drive)	Development of proper material and fabrication techniques for sensor	20	1800	Faulty braze between emitter housing and Lucalox base
T-3	Pressure actuation (C-129Y capsule)*	Development of proper material and fabrication techniques for sensor and integration with capsule	50	1800	Faulty braze between emitter housing and Lucalox base, open-circuit heater
T-4	Pressure actuation (C-129Y capsule)*	Evaluation of sensor design. Demonstration of pressure-output performance over ambient temperature range.	1500	1000-1800	Decrease in emission
T-5	Pressure actuation (FS-85 capsule)*	Evaluation of sensor design. Demonstration of pressure-output performance over ambient temperature range.	850	1000-1800	Decrease in emission
T-6	Pressure actuation (FS-85 capsule)*	Refine sensor design to increase operating life. Demonstration of pressure-output performance over ambient temperature range.	2700	1000-1800	Decrease in emission
T-7	Pressure actuation (C-129Y capsule)*	Refine sensor design to increase operating life. Demonstration of pressure-output performance over ambient temperature range.	2000	1000-1800	Open circuit heater due to accidental current surge

*Same C-129Y capsule used in T-3, T-4 and T-7; 3550 total operating hours
Same FS-85 capsule used in T-5 and T-6; 3550 total operating hours

to investigate sensor fabrication techniques and used a simulated active collector surface driven by a micrometer head mounted outside the vacuum test chamber. The next five devices were designed to investigate mating of the sensor to a pressure capsule. The double-convolution C-129Y and FS-85 pressure capsules used in the initial deflection tests (see Section 4.1) were used in devices T-3 through T-7. The first six devices included a secondary reference collector, isolated in the middle of the reference collector surface. This secondary reference collector was intended as a monitor of emitter temperature. The current through this collector would be used to indicate any shift in the reference emitter from the space-charge limited mode to the emission-limited mode. In the event of the emitter becoming emission-limited, the emitter temperature would be automatically raised until space-charge limited operation is regained.

In all cases the test was suspended because of problems encountered in the thermionic diode sensor. More detailed treatments of each test device are included in the following test chronology.

The procedure used to evaluate the performance of test devices consisted of the following steps.

1. The emitters were activated by applying about 15 volts to the diode with the emitters at 2280°F as measured by the thermocouple installed on the emitter housing. The

emission currents increased to a stable level at which point the emitter temperature was lowered to the operating level of 2100°F. For an emitter-collector spacing of about 0.006 inch, the stable current level is about 45 milliamperes for an applied voltage of 15 volts.

2. The space-charge characteristics were determined by measuring the active and reference collector currents as a function of increased voltage. These data served two purposes. When plotted on log-log coordinates with emitter-collector distance as a parameter related through theoretical space-charge formulae, the data indicated the reference collector and active collector distances. The data also indicated any emission limiting effects (poisoning) occuring at applied voltages up to about 20 volts. Since the thermionic sensor must operate in the space-charge limited region, any emission-limited condition will introduce error into the output signal and must be avoided.

3. Using the data of (2) above, an upper limit was placed on the applied voltage to insure that no poisoning effect was present. With this pre-determined applied voltage at zero pressure, pressure-output current (i_a-i_r) characteristics were obtained for chamber temperatures of 1800, 1600, 1400, 1200 and 1000°F while the emitter temperature was maintained at 2100°F. As the pressure was changed, the applied voltage was varied to keep the sum (i_a+i_r) constant at its zero pressure value. For the transducer test units, the active collector distance was

adjusted to be equal to the reference collector distance at room temperature prior to installation in the Vacuum Test Facility. However, at 1800°F, motion of the pressure capsule caused the active collector distance to change. Since no further adjustment was made, the difference current ($i_a - i_r$) was not zero at zero pressure.

The first test device (T-1) was constructed using the heater assembly of Figures 156 and 157 in conjunction with the ceramic base shown in Figure 158. This first heater assembly (Figure 156) consisted of the alumina coil form, a bare tungsten heater and molybdenum power leads. The tungsten/molybdenum connection was made by plasma-spraying the joint with tungsten. The heater assembly was then inserted in the emitter housing cavity and pieces of alumina were placed between the heater and the walls on all four sides and at the bottom of the cavity (see Figures 99 and 100). Figure 157 shows the assembly before the casting operation. After casting, the emitters were brazed into their cavities and the complete sensor, shown in Figure 159, was assembled. Three metal-ceramic joints were used in the complete assembly. These included:

1. Mounting of the encapsulated heater assembly (molybdenum) to the Lucalox ceramic base,
2. Mounting of the Nb-1Zr support plate to the Lucalox ceramic base and
3. Mounting of the reference collector surface to the Lucalox ceramic base.

All the above joints must, of course, maintain mechanical stability. In addition, joining operations (1) and (2) must take place at a low enough temperature (below 2300°F) to prevent damage to the thermionic emitters. The reference collector may be mounted at a higher temperature since this operation takes place prior to mounting of the encapsulated heater assembly (see Figure 158). For the first test assembly, tungsten/yttria was used (1) as the metallizing material for the posts on which the encapsulated heater assembly was brazed, (2) as the metallizing material for the braze between the ceramic base and its Nb-1Zr support plate and (3) to establish the reference collector surface. A nickel/niobium/titanium braze material was used to make both the heater assembly/ceramic and the ceramic/support plate joints.

The assembly of Figure 159 was mounted on a vacuum flange equipped with a micrometer head, installed in a chamber of the Vacuum Test Facility and baked-out to 1800°F with a chamber pressure of 3×10^{-8} torr. At this point, the encapsulated heater was energized and emitter activation was begun. After about 20 hours of operation, during which time the emission currents from both emitters were close to the values predicted by space-charge theory, the heater developed an open circuit. Preliminary examination indicated that the open circuit occurred in the first heater turn around the alumina coil form, which included one of the plasma-sprayed joints. Efforts to disassemble the heater and determine exactly where the failure occurred were unsuccessful.

The failure of the heater of T-1 indicated the use of rhenium wire instead of tungsten wire to improve the high-temperature characteristics of the heater and its external leads. The use of rhenium would bring about the following improvements.

1. A rhenium/rhenium weld joint would replace the tungsten/molybdenum plasma-sprayed joint, resulting in a stronger, more stable connection.
2. The improved ductility of rhenium would minimuze the breakage problem caused by bending the external heater leads after casting. Mounting the encapsulated heater assembly on the ceramic base required that sharp bends be made in the heater power leads so that the wires could be inserted in the proper holes in the ceramic base. However, after the casting operations, the molybdenum wires became brittle and subject to breakage during the bending operation.

To implement these refinements, both 0.010 and 0.012 inch diameter rhenium wire was obtained for the external leads and a heater design was developed using 0.003 inch diameter rhenium wire. However, wire embrittlement and breakage problems encountered in the fabrication of the heater indicated that the development of the pure rhenium heater would take too long to be of value in the program. As a second choice, heaters of 0.003 inch diameter W-3Re wire (see Figure 100) were ordered. Until these heaters were received, work continued using the tungsten heater and rhenium external leads.

The next two test devices, T-2 and T-3, contained a tungsten heater with rhenium external leads. T-2 used 0.010 inch diameter rhenium wire; T-3 used 0.012 inch diameter rhenium wire. The tungsten/rhenium connection was welded and appeared much stronger than the plasma-sprayed tungsten/molybdenum connection used in T-1.

The T-2 unit incorporated the micrometer head fixture to control the motion of a simulated active collector. Initial emitter activation indicated that the emission currents from both emitters were close to the values predicted by space charge theory. After bake-out, the active and reference collector currents became erratic, forcing suspension of the test and removal of the unit to determine the cause of the problem.

The T-3 unit consisted of the thermionic diode sensor installed inside the C-129Y double convolution pressure capsule. The C-129Y capsule, which had been used in the initial deflection tests, was modified to allow for argon pressurization of the T-3 unit in the Vacuum Test Facility. Following the initial bake-out, an electrical short was observed between the C-129Y capsule and the emitter housing of the thermionic sensor. The unit was removed from the vacuum chamber and dismantled. In both the T-2 and T-3 units, faulty braze joints were found between the emitter housing and the Lucalox ceramic base. The resultant cocking of the emitter housing on the Lucalox base caused the erratic data of T-2 and the short circuit in T-3. In addition, hairline cracks were noticed at the base of the Lucalox posts upon which the emitter housing was mounted. To resolve these problems, it was decided to move the position of the Lucalox posts so that each post had a central hole.

Previously, the holes had been used to contain the wiring to the thermionic diode sensor. Reinforcing wires were placed in the holes and brazed in place. Enough of the wire extended out the top of the posts to mechanically hold down the mounting tabs of the emitter housing. For added structural integrity, the wire was brazed to the mounting tab.

Two new Lucalox bases, incorporating the reinforcing wires, were prepared for use in T-2 and T-3. During re-assembly of the T-3 unit, the heater developed an open-curcuit inside the casting, requiring the preparation of a new encapsulated heater assembly. At this time, the W-3Re heaters had been obtained and were used with 0.012 inch diameter rhenium external leads. The new heater exhibited good ductility during assembly and the W-3Re/rhenium weld joint appeared sound. The T-2 unit was re-assembled with its original pure tungsten heater assembly.

Both T-2 and T-3 were installed in the Vacuum Test Facility and following initial bake-out, underwent emitter activation. The active collector and reference collector currents of T-2 were found to be lower than expected. The activation process was continued but no appreciable increase in current was obtained. A possible reason for this condition could have been a deterioration of the emitters brought about by handling when rebuilding T-2.

During emitter activation, transducer T-3 exhibited an electrical short-circuit between the C-129Y capsule and the emitter housing of the thermionic sensor. The electrical short appeared

to have occurred in the spacing between the hole in the C-129Y capsule (0.216 inch I.D.) and the emitter housing (0.206 inch O.D.). A slight change in alignment of the thermionic diode sensor in the pressure capsule coupled with any shifts in alignment at 1800°F could have resulted in the electrical short circuit. T-3 was disassembled. The C-129Y capsule was modified as described below and a new thermionic diode sensor was fabricated to resolve the shorting problem. The new unit was denoted T-4.

The thermionic sensor of T-4 used a W-3Re heater with 0.012 inch diameter rhenium external leads. The heater exhibited good ductility during assembly and the W-3 Re/rhenium spot-welded joint appeared sound.

In addition, transducer T-4 incorporated the following changes from T-3.

1. The hole in the C-129Y capsule was opened to 0.250 inch I.D.
2. The Lucalox ceramic base outside diameter was increased to 0.236 inch. Since the outside diameter of the emitter housing remained at 0.206 inch, the Lucalox base served as an insulator between the pressure capsule and the emitter housing.
3. The three wires running through the Lucalox which were used to position the emitter housing were replaced by 0.015 inch diameter Nb-1Zr wires, that had one end flattened to form a bolt head, and the other end threaded. Holes

were drilled in the emitter housing mounting tabs and the Nb-1Zr wires were passed through the housing mounting tabs and the holes in the Lucalox. The flattened heads of these wires were used to exert pressure on the housing mounting tabs. The threaded ends of the wires leaving the Lucalox end of the assembly were held with Nb-1Zr nuts. This method of assembly resulted in a more stable mounting of the emitter housing on the Lucalox base. One of the Nb-1Zr "bolts" was used as the electrical connection to the emitters.

4. To monitor the emitter temperature, a Pt/Pt-13 Rh thermocouple was spot-welded to the emitter housing.

Because of the relatively successful fabrication of T-4, future test devices concentrated on transducer models using pressure capsules instead of the micrometer head fixture used in T-2. Accordingly, tests on T-2 were suspended and another test unit, T-5, was fabricated incorporating the FS-85 double convolution pressure capsule previously tested using the optical measuring technique. In all respects, T-5 was identical to T-4.

Figure 160 presents the space-charge data gathered from T-4. The data is plotted on log-log coordinates with emitter-collector distance as a parameter. The current scale was obtained from the space-charge current density, assuming an emitter of 0.125 inch diameter. The reference collector spacing was seen to be about 0.006 inch while the active collector spacing was about 0.0045 inch. A severe emission-limited condition existed for i_r above an applied

voltage of 18 volts. An operating voltage of 16 volts was chosen for the pressure - output current tests. An operating pressure range of 0 to 50 inches of mercury was chosen for T-4. Figure 161 presents the pressure-output current characteristics for T-4. Figure 162 shows the device heater power necessary to maintain the emitters at 2100°F as the test chamber temperature was varied.

Analysis of the i_a and i_r data indicated that the relatively large shifts in the output current characteristics with temperature as shown in Figure 161 could be caused by thermal expansion effects between the pressure capsule (active collector) and the Lucalox base of the thermionic sensor. Both i_a and i_r were observed to decrease with increasing temperature. For given pressure and voltage conditions, this decrease in current can be attributed to an increase in the collector spacing. When referred to the chamber temperature, the most probable explanation for this shift is that both the C-129Y capsule and the Lucalox posts on which the emitter housing was mounted experienced thermal expansions. These expansions would result in increased collector distances and decreased values of i_a and i_r respectively.

Figure 163 shows the experimental values of i_a and i_r as functions of chamber temperature at zero pressure and an applied voltage of 16 volts. In the temperature range of interest (1000 to 1800°F), the coefficients of thermal expansion of both niobium, the main component of C-129Y, and alumina, the main component of Lucalox, vary linearly with temperature.

The active and reference collector distances also vary linearly with temperature if the coefficients of thermal expansion vary linearly. If the values for i_a and i_r corresponding to 1000 and 1800°F are accepted as valid, interpolated current values for 1200, 1400 and 1600°F may be obtained from theoretical space-charge relations involving voltage, current and distance. These theoretical relations are represented graphically by the distance lines of Figure 160. Scaling off linear distance changes on the space-charge plots resulted in the interpolated current values shown in Figure 163. Close agreement was observed between the experimental and interpolated current values, with the exception of the 1200°F value for i_r. It appeared that this experimental value was probably in error.

Correction factors were calculated to adjust the curves of Figure 161 to an 1800°F reference. Table 13 presents the values of i_a and i_r measured at 16 volts and zero pressure for the various test temperatures. The changes in i_a and i_r with temperature were used to compute an $(i_a - i_r)$ correction. A correction was not obtained at 1200°F since the experimental value for i_r appears to be in error. Applying the corrections of Table 13 to the measured values of $(i_a - i_r)$ shown in the curves of Figure 161 resulted in the curves shown in Figure 164. The sensitivity of the transducer (change in current with change in pressure) appeared to decrease for increasing temperature because the decrease in i_a due to thermal expansion of the capsule is greater than the change in Young's modulus of the capsule material with temperature.

TABLE 13

TEST DEVICE T-4 OUTPUT CURRENT CORRECTIONS

	(i_a)		(i_r)		$(i_a - i_r)$
TEMP °F	EXP. ma	CORRECTION ma	EXP. ma	CORRECTION ma	CORRECTION ma
1800	97	0	47	0	0
1600	113	16	51	4	12
1400	132	35	54	7	28
1200	159	62	52	-	--
1000	189	92	61	14	78

Unfortunately, the data gathered on T-5 using the FS-85 capsule yielded erratic results. After T-4 and T-5 had been in continuous operation about 1500 and 850 hours respectively, both test devices exhibited some losses in emission from the emitters used in the reference circuit. To a lesser extent, the same effect was noticed in the active emitter circuits.

Investigation showed that three possible problem areas could have accounted for the loss in emission. One was the braze joint holding the secondary reference collector in the Lucalox section of the sensor. During operation, the braze material could have reacted with the emitter. The second was the platinum thermocouple used to monitor the emitter temperature. The emission could have been degraded by platinum migration over the emitter surfaces. Lastly, the loss in emission could have been due to an over-extended activation procedure which resulted in excessive loss of impregnant material from the emitters. In addition to these fabrication and operation aspects it was clear that the emitters could be a problem area and procedures should be developed to assure that proper quality control be maintained on the emitters.

To investigate the problem areas mentioned above, T-5 was disassembled and the FS-85 pressure capsule was fitted with a new thermionic diode sensor to form a new test unit, T-6. The thermionic diode sensor had the following features.

1. The sensor did not include the secondary reference collector.
2. The Pt/Pt-13 Rh thermocouple was replaced by a W-5 Re/W-26 Re thermocouple. This thermocouple was spot-welded to the emitter housing.

3. The emitters were pre-activated in vacuum (about 10^{-6} torr) at 2280°F for 25 minutes before assembling the sensor. In the Vacuum Test Facility, another 20 minute pre-activation period at 2280°F was completed. Current was drawn from the emitters during the second pre-activation procedure.

4. The Nb-1Zr "bolts" used to hold down the emitter housing to the Lucalox base were rhenium-plated. The plating was done to avoid any possible reaction between the columbium and the Lucalox.

T-4 was disassembled and the C-129Y pressure capsule was fitted with a new thermionic diode sensor to form a new test unit, T-7. The sensor was identical to the sensor prepared for T-6 except that a secondary reference collector was included. It was intended that comparison of data collected on T-6 and T-7 would indicate whether the secondary reference collector has any detrimental effects on sensor operating life. If the testing indicated that the secondary reference collector should not be used, the W-5 Re/W-26 Re thermocouple could be used in the final design to indicate and control the emitter temperature.

As indicated in Table 12, 2700 and 2000 test hours were accumulated on T-6 and T-7 respectively. During the testing, two complete sets of pressure-output tests were run on both T-6 and T-7. The tests consisted of three pressure cycles at 1800, 1600, 1400, 1200, 1000, 1200, 1400, 1600, and 1800°F. Space-charge

data taken before and after the temperature runs were used to indicate the active and reference collector distances and any emitter poisoning that might be present. For the first tests on both T-6 and T-7, the supply voltage for zero pressure was 10 volts for all test temperatures. The use of a constant zero-pressure supply voltage for all temperatures, coupled with any shifts in the pressure capsule (active collector) with temperature, resulted in different sum-of-the-currents ($i_a + i_r$) values at each temperature. Complete sets of pressure-output current ($i_a - i_r$) data from T-6 and T-7 are presented in Figures 165 through 172. Figures 165 through 168 relate to T-6 and Figures 169 through 172 relate to T-7. For both transducers, the data are presented in the following sequence; initial space-charge data, pressure-output data for decreasing temperatures, pressure-output data for increasing temperatures and final space-charge data.

From the initial space-charge data shown in Figures 165 and 169, an operating voltage of about 10 volts was chosen for T-6 and T-7. This voltage resulted in no apparent poisoning effect in either sensor. To obtain about 0.001 inch pressure capsule deflection, full scale pressures of 50 inches of mercury and 60 psia were chosen for T-6 and T-7, respectively.

Table 14 presents the various current parameters with 10 volts applied to the sensor at zero pressure. The data of Table 14 indicated that the major portion of the zero shift with temperature

in the output current (i_a-i_r) was due to shifts in the active collector distance probably related to thermal expansion effects. As the temperature decreased, the pressure capsule contracted and the active collector distance decreased, resulting in an increase in i_a. The effect was more pronounced in T-6 than in T-7, shown by comparing the shifts with temperature of the data of Figures 166 and 167 (T-6) with the shifts with temperature of the data of Figures 170 and 171 (T-7).

Figures 165 and 168, the two sets of space-charge data on T-6, indicated that the active collector distance decreased from a little under 0.004 inch prior to the temperature tests to about 0.0035 inch following the temperature tests. Space-charge runs taken about two weeks later showed that the active collector distance had decreased still further to about 0.0032 inch. At that time, T-6 was removed from the test chamber to adjust the active collector distance to a value closer to that of the reference collector (about 0.005 inch). The thermionic sensor was shimmed to adjust the active collector distance and T-6 was re-installed in the test chamber.

The pressure-output tests were repeated on both T-6 and T-7. However, instead of using a constant zero-pressure voltage at all temperatures, a constant sum-of-the-currents ($i_a + i_r$) value was used for all temperatures. The thermal expansion effects mentioned above were minimized since any increases in current (especially i_a) were restricted by the constant (i_a+i_r) requirement. In addition,

TABLE 14

ZERO PRESSURE TEST PARAMETERS;
CONSTANT APPLIED VOLTAGE, 10 VOLTS

Test Temp °F	T-6		T-7	
	$i_a + i_r$ ma	$i_a - i_r$ ma	ia + ir ma	ia - ir ma
1800	89.4	24.6	74.0	21.7
1600	95.9	31.8	77.8	24.7
1400	107.1	43.0	79.4	27.5
1200	126.7	58.4	82.0	28.9
1000	146.7	74.6	85.4	30.6
1200	138.7	65.2	83.2	26.7
1400	122.6	51.3	80.8	25.4
1600	110.9	41.3	75.8	23.0
1800	104.1	36.3	67.9	21.1

the tests were more representative of final transducer operation since the signal conditioning system operation is based on maintaining a constant ($i_a + i_r$) value.

Complete sets of pressure-output current ($i_a - i_r$) data from these second tests on T-6 and T-7 are presented in Figures 173 through 187. Figures 173 through 176 relate to T-6 and present the data in the following sequence; initial space-charge data, pressure-output data for decreasing temperatures, pressure-output data for increasing temperatures and final space-charge data. Figures 177 through 187 relate to T-7 and present the data in the following sequence; initial space-charge data, pressure-output-temperature data (Figures 178 through 186) and final space-charge data. Each temperature test on T-7 is presented separately since the data corresponding to each temperature test are not distinguishable when plotted on one format.

There was a marked improvement in zero shift indicated by comparing the pressure-output data of Figures 173 through 187 with those of Figures 165 through 172. Table 15 presents the various zero-pressure parameters using a constant sum-of-the-currents value (70 ma) for each temperature.

The improvement in zero shift is evident by comparing the (i_a-i_r) values of Table 15 with those of Table 14. Using Table 14 data, the spreads in (i_a-i_r) values with temperature for T-6 and T-7 were 50.0 and 9.5 milliamperes, respectively. Using the sum-of-the-currents value as the reference parameter, the spreads in (i_a-i_r) values with temperature, from Table 15, decreased to 20.6 and 2.4 milliamperes for T-6 and T-7, respectively.

TABLE 15

ZERO PRESSURE TEST PARAMETERS;
CONSTANT SUM-OF-THE-CURRENTS, 70 ma

Test Temp °F	T-6		T-7	
	$i_a + i_r$ ma	$i_a - i_r$ ma	$i_a + i_r$ ma	$i_a - i_r$ ma
1800	70.0	17.2	70.0	24.3
1600	70.0	23.0	70.0	23.6
1400	70.0	28.1	70.0	24.7
1200	70.0	32.9	70.0	24.3
1000	70.0	37.8	70.0	23.2
1200	70.0	33.4	70.0	22.5
1400	70.0	28.3	70.0	24.3
1600	70.0	24.7	70.0	22.3
1800	70.0	23.5	70.0	23.6

Two further objectives of the test program were to determine the effect of the secondary reference collector on operating life and to check the operation of the heater control loop of the electrical signal conditioning system. Test data did not indicate any definite effect of the secondary reference collector on operating life. However, tests performed with the initial breadboard signal conditioning system showed that the secondary reference collector could not be used to accurately control the emitter temperature.

Originally it was intended to have the secondary reference collector current serve as an indication of the continuous operation of the thermionic diode sensor in the space charge limited mode. Initial tests run on the signal conditioning breadboard with T-7 showed that the secondary reference collector current actually consisted of two components. The first component was the expected current flowing between the emitter and the secondary reference collector.

The second component was a current flowing between the reference collector and the secondary reference collector due to the difference in the voltages applied to the two elements. While the voltage applied to the secondary reference collector was constant, the voltage applied to the reference collector varied. Its value was determined not by emitter temperature, but by the constant sum-of-the-currents ($i_a + i_r$) condition. This second component therefore prevented accurate operation of the heater control loop with the secondary reference collector current as the input.

Rather than undertaking a re-design to eliminate the current between the reference collector and the secondary reference collector, the testing was continued using the output of thw W-5Re/W-26Re thermocouple mounted on the emitter housing as the heater control loop input. Use of this thermocouple to maintain a 2100°F emitter temperature also assured continuous space-charge limited operation since the thermionic sensor operated at supply voltages for which the onset of emission-limited conditions occurs at temperatures well below the 2100°F level.

Using test transducer T-7, operation of the heater control loop was checked with the W-5Re/W-26Re thermocouple as the input. The emitter temperature was programmed to 2100°F and held within 10°F over an ambient temperature range of 1000 to 1800°F.

Unfortunately, test transducer T-7 developed an open-circuit heater shortly after the emitter temperature tests. Examination of the T-7 sensor showed that the open circuit occurred inside the casting in the emitter housing, making repairs impossible. The open-circuit appeared to result from an inadvertant heater current surge which took place while adjustments were being made on the signal conditioning breadboard.

The signal conditioning breadboard was then connected to test transducer T-6 and the emitter temperature tests repeated. The heater control loop achieved satisfactory emitter temperature control (at 2100°F within 10°F) over an ambient temperature range of 1000 to 1800°F. At that point, it was decided to suspend testing because the emission levels of the T-6 sensor had decreased from about 30 ma to less than 15 ma.

The following conclusions were drawn from the test results.

1. T-7 (C-129Y) exhibited much less zero shift with temperature than T-6 (FS-85) during both test series (see Tables 14 and 15). From the results of the initial deflection tests (see Section 4.1), the W-25 Re material chosen for the final pressure capsule design will improve upon the performance of the C-129Y test unit T-7.
2. Hysteresis effects in the pressure-output data for both T-6 and T-7 were noticeable only at temperatures above 1400°F and, in some instances, 1600°F.
3. The secondary reference collector was eliminated from the transducer and replaced by the W-5Re/W-26Re thermocouple as a monitor of space-charge limited operation.
4. The hours of successful operation accumulated by T-6 and T-7 indicated that the fabrication changes used on these units had solved the problems encountered in test units T-4 and T-5.
5. Work was concluded on the series of experimental test devices. Testing shifted to performance evaluation of more complete transducer assemblies (see Figures 4 and 5).

11.2 Final Transducer Testing

As part of the final transducer test program, four absolute transducers (A-1 through A-4) and two differential transducers (D-1 and D-2) were built. In each case, the transducer included the Nb-1Zr main housing, the W-25Re pressure capsule, the thermionic diode sensor and, for the differential transducer, the differential beam assembly. The testing was performed in the Vacuum Test Facility (see Section 10.0) and was done in two phases; the first phase involving transducers A-1, A-2, D-1 and D-2, and the second phase involving transducers A-3 and A-4.

During the first phase of testing, mechanical and electrical problems in both the transducers and the Test Facility limited operation of the differential transducers to the extent that long-term operating data could not be obtained. However, operation of the differential beam assembly at 1800°F was demonstrated.

Extensive testing of A-1 and A-2 brought to light a further problem area centered on the impregnated emitters and involving three facets; initial quality control and impregnation of the emitters, brazing of the emitters into the emitter housing, and grinding or machining of the emitters. Briefly, the operating histories of A-1 and A-2 were as follows:

Absolute Transducer 1: A total of 5200 hours of operation were accumulated on A-1. The first 2000 were concerned mainly with pressure cycling tests at temperatures of 1000 to 1800°F.

The last 3000 hours were devoted to creep tests and general life tests on the emitter characteristics. A decrease in emission was noticed in the reference emitter after about 2000 hours of operation. The emission was restored somewhat by raising the diode voltage but then fell back to low values. Full-scale testing was suspended after about 4,000 hours and continued spot-checks on the active emitter indicated that its emission level did not change significantly over the 5200 hours of operation. The reference emitter had been ground when the sensor was assembled, to establish the proper distance between it and the reference collector surface on the Lucalox base. The active emitter had not been machined.

Absolute Transducer 2: A total of 1100 hours of operation at 1800°F were accumulated on A-2. After about 400 hours of operation, some decrease in emission was noticed, particularly in the active emitter. During the testing, the decrease in emission became worse and was accompanied by onset of emission limit conditions at about 9 volts. The decrease in emission of the reference emitter was not pronounced; however, emission limit conditions were observed at about 10-11 volts. As with A-1, the reference emitter had been ground; the active emitter was not.

The behavior of A-1 and A-2 focused attention upon the impregnated emitters. The successful operation of the active emitter of A-1 and the reference emitter of A-2 supported the choice of the impregnated emitter for the transducer. However, the emission problems encountered in the overall testing indicated that the emitter characteristics had to be more precisely defined and a more

rigid quality control procedure had to be instituted to assure these characteristics. The emitter tests described below resulted in the quality control and fabrication procedures spelled out in Section 5.1.

In discussions with Philips Metalonics, the grinding of the surface of the reference emitter was brought out. Philips has evidence that grinding is very injurious to the emitter surface. 500X photomicrographs were taken of the surface of an impregnated emitter. A uniform pore distribution was shown with a maximum distance between pores of about 10 microns. Since the migration of barium at 1100°C is about 100 microns, the emitter is more than capable of providing a uniform work-function surface for the transducer application. The emitter was then ground and a second photomicrograph taken. The grinding operation smeared the surface to the extent that practically none of the pores were left open. Etching restored the pore structure somewhat but it was not nearly as uniform or close-spaced as the original surface of the emitter. It was recommended that no grinding at all be done on the emitters. Normally, a light polishing of the emitter surface is performed to remove the natural matte finish. This operation should also be eliminated.

In addition to grinding and machinging, the brazing of the emitters into the emitter housing was also discussed. The braze is a very critical operation and a minimum of braze alloy should be used to prevent braze coverage or contamination of the emitter surface and the resulting degradation of emission capability.

To evaluate the grinding and brazing problems, metallographic examinations were performed on the following emitters.

T-2 emitters (active and reference)

T-6 emitters (active and reference)

A-1 emitters (active and reference)

A-2 emitters (active and reference)

5 unused emitters from stock (Ser. Nos. 2, 6, 7, 8, 9)

2 unused emitters from recent order (Ser. Nos. 5, 20)

All the results of the photomicrographic evaluation will not be presented here. Typical photomicrographs showing the normal open pore structure and the possible effects of grinding and brazing are presented in Figure 102.

In general, the photomicrographs showed the deleterious effects of the grinding and brazing operations performed in assembly of the thermionic sensor. The value of eliminating the final polishing operation was also demonstrated.

All four emitters of T-2 and T-6 showed varying degrees of braze alloy coverage of the emitter surfaces. Presence of the braze alloy resulted in poor pore structure and virtual elimination of the affected areas as emitting surfaces.

Inspection of the photomicrographs of the reference emitters of T-2 and T-6 showed relatively large areas of small grain structure, probably caused by the grinding operation. The grinding apparently smeared the surface and the smeared platelets then recrystallized during operation of 2100°F into the small grain structure shown in the photos. This resulted in a very poor pore structure with almost all the pores closed.

The central portion of the active emitter of A-1 (about 70% of the emitter surface) showed a normal uniform open-pore structure, and accounted for the successful 5200 hour operation of this emitter. The outer edge of the emitter showed a small grain structure that apparently was caused by a grinding operation. This structure had been observed before in the reference emitters of T-2 and T-6.

The entire surface of the reference emitter of A-1 showed the small grain structure described above, and is indicative of the grinding operation performed on the reference emitters.

The active emitter of A-2 was essentially the same as the active emitter of absolute transducer 1 except the central portion was about 50% of the emitter surface and the pores appeared partially closed, probably due to polishing.

The reference emitter of A-2 showed a surface that appeared to have been contaminated with braze alloy prior to grinding. The grinding removed the diffused zones to various depths and made focusing of the 500X photomicrographs almost impossible. The result was a poor pore structure and virtual elimination of the majority of the surface area as emitting surface.

Photomicrographs of the old unused emitters (Nos. 2, 6, 7, 8, 9) showed some of the possible results of the final polishing of the emitter surface. The emitters all had lathe turned surfaces which resulted in projecting tool marks and a disruption of the uniform pore structure. In addition, final lapping or polishing was shown to cause a certain amount of smearing of tungsten over the surface.

In the majority of cases, these operations did not destroy the value of the emitter. However, for emitter No. 7, a large percentage of the surface area was smeared with tungsten and the polishing had pulled out particles of metal at a number of locations. The value of this particular emitter is quite questionable. It was for this reason that Philips dropped the above procedures when preparing the new lot of emitters from which emitters 5 and 20 were taken.

Photomicrographs of the more recent unused emitters (Nos. 5, 20) showed the value of dropping the final machining operations. Both emitters displayed good open pore structures with little or no smeared tungsten on the emitter surface. There were some scratches on the emitters, apparently a result of rubbing the emitters on alumina paper to remove the excess aluminates after impregnation. The scratches did not affect the pore structure to the extent that the efficiency of the emitter would be degraded and the scratches could be eliminated by specifying that all excess impregnant be removed by ultrasonic water bath only.

In one of the early diode sensor tests, no current could be drawn from the emitter during activation. A possible explanation for this was that the emitter was not impregnated. To establish the extent of impregnation, a series of etch tests were performed. For this test, the emitter is measured and weighed, after which the tungsten matrix is etched out, leaving the impregnant as a free-standing mass. The amount of impregnant is a general indication of the optimum lifetime of the emitter. The etchant used is a 50/50 mixture of HF and HNO_3 diluted with water to prevent too violent an etching action.

The first etch tests were performed on four emitters taken from stock. The emitters were chosen for having maximum and minimum calculated weight/volume ratios. The two maximum ratio emitters showed very little, if any, impregnant after etching (0.7 and 1.6 milligrams compared to 4.3 and 6.4 milligrams for the two minimum ratio emitters). Calculated values for the partial densities of the emitters were 86% for the low impregnant emitters and about 79% for the normally impregnated emitters. The design figure (Philips Metalonics) is 79-82%.

Further etch tests were performed on the emitters from absolute transducers A-1 and A-2 and two emitters (Ser. Nos. 5 and 20) from a more recent shipment. Table 16 presents the results of these etch tests in terms of emitter weight before and after etching.

The results tended to clarify the life tests quite well. The following conclusions were drawn.

1. The decrease in emission noticed in Abs. 1, reference, may be traced to the relatively small amount of impregnant in the emitter.
2. The rapid degradation noticed in Abs. 2, active, may be traced to the fact that no noticeable amount of impregnant was found in the emitter.
3. The slight decrease in emission in Abs. 2, reference, may be traced to the incomplete impregnation of the emitter (3.9 mgm).
4. The results show clearly that impregnation is as important to satisfactory emitter operation as brazing and grinding have been shown to be. All three requirements must be met.

TABLE 16

EMITTER ETCH TEST RESULTS

Emitter	Before Etch Weight (gm)	After Etch Weight (gm)
Abs. 1, active	0.1067 (a)	0.0007 (b)
Abs. 1, reference	0.1263	0.0025 (c)
Abs. 2, active	0.1296	(d)
Abs. 2, reference	0.1335	0.0039 (e)
No. 5 new	0.1310	0.0059 (e)
No. 20 new	0.1305	0.0067 (e)

(a) During removal of the emitter, a portion of the emitter was lost. Therefore 0.1067 gm. does not represent the entire weight before etching.

(b) During etching and handling, a large amount of the impregnant was lost. We estimate that at least half of the impregnant was lost. This result is not critical, since operation of Abs. 1 for over 5,000 hours indicated the presence of a good amount of impregnant.

(c) After etching, the top of the impregnant pellet was found to be loose. Removing the top showed that the center of the pellet was hollow, accounting for the relatively small weight of impregnant (0.0025 gm).

(d) After etching, no trace of any impregnant was found.

(e) After etching, the impregnant pellet was broken. A homogeneous pellet was found, in contrast with the result on Abs. 1, reference, (c) above. The impregnant pellets of Nos. 5 and 20 were the same size as the emitter pellet before etching, indicating complete impregnation.

There appeared to be no doubt that brazing the emitters into the emitter housing was the most reliable mounting technique. The one problem area in the brazing operation is contamination of the emitter surface by braze alloy. With reference to Figure 188, the original braze configuration permitted contamination in three ways;

1. Braze permeation through the emitter,
2. Braze wetting action up the side and across the emitter face, and
3. Evaporation of braze components and condensation on the emitter face.

Braze permeation through the emitter was eliminated by quality controls which assure fully impregnated emitters. Braze wetting action and evaporation-condensation effects were eliminated by a change in emitter configuration, shown in Figure 188. Both braze wetting and braze evaporants were directed away from the emitter face. Using this revised emitter (see Figure 101) and braze configuration, thermionic sensors were fabricated for the final test transducers, A-3 and A-4. These transducers also used new Nb-1Zr main housings and W-25Re pressure capsules.

Prior to actual operation of A-3 and A-4, a Transducer Test Program was developed to establish guidelines for the evaluation testing. The complete Test Program is presented in Appendix C. The basic test conditions to be included were the following.

1. 2,000 hour life at 1600°F basic operating temperature.

2. Temperature excursions between 1000 and 1600°F.

3. Spot checks at 1800°F.

11.2.1 Absolute Transducer 3

Prior to final assembly, Absolute Transducer 3 (A-3), without its thermionic diode sensor, was installed in the Vacuum Test Facility for stress relief exercising. The W-25Re pressure capsule was cycled between 0-80 psia at 1800°F for 2000 cycles at a 20 cycle/hour rate. Following the cycling, the transducer was removed from the test chamber and checked. It was found to be leak-tight and room-temperature pressure-deflection data agreed with data taken before cycling (80 psia resulted in a deflection of about 0.003 inch).

Following pre-activation of the emitters, the thermionic diode sensor was assembled and installed in the pressure capsule with a room-temperature active emitter-collector distance of 0.006 inch. The complete transducer A-3 was then installed in the Vacuum Test Facility and a 15 minute activation at 2280°F was performed on the emitters. During activation, 10 volts was applied to the diode and the active and reference collector currents at the end of the activation period were 41.9 and 43.5 milliamperes respectively. The emitter temperature was then lowered to its 2100°F operating value; 10 volts was maintained on the diode and space-charge data were taken to determine when the active and reference currents stabilized. The space charge data indicated that the reference current was stabilized immediately after activation (about 40 ma. at 10 volts).

The active current was observed to rise from about 38 ma to about 44 ma (at 10 volts) within 25 hours following activation. Checks on the reference current showed an emission limit condition at about 16 volts. No emission limit condition was observed in the active current for voltages up to about 18 volts and transducer pressures up to 80 psia. At 80 psia, active space charge currents up to 200 ma were drawn with no emission limiting effects. The expected "ten volt effect" was observed in both the active and reference currents. This effect is an apparent slight decrease in emission capability due to dissociation effects on the collector surface. On the space charge plots, the effect shows up as a slight dip which corrects itself as the voltage is increased to about 12 volts. Figure 189 is a set of typical space charge data taken on the X-Y recorder. The theoretical curves corresponding to spacings of .003-.006" are shown dotted. The reference current (I_r) and active current (I_a) data are shown solid. For low voltages, the experimental currents do not agree with the values predicted by Childs' Law because of emission effects. The emission limit on I_r and the ten volt dip are evident.

The data indicated that to avoid both emission limit effects and the ten volt region, the operating voltage on the diode would have to be less than 10 volts. For testing of A-3, the control parameter (constant sum-of-the-currents I_a and I_r) was set at 60 ma, corresponding to a diode voltage of about 8 volts at zero pressure.

During the first 350 hours of operation, the chamber temperature was 1800°F. At that point it was decided to lower the basic test temperature to 1600°F (see Appendix C).

The first 440 hours of operation were spent on monitoring the space charge characteristics and checking the operation of the signal conditioning system with the transducer. By the end of this period, the signal conditioner had been checked out for transducer operation between 1000 and 1800°F. The conditioner successfully maintained (1) the emitter temperature at 2100°F over the ambient temperature range and (2) the 60 ma sum-of-the-currents over the 0-80 psia pressure range and the ambient temperature range.

Testing of A-3 was continued until an open-circuit failure of the emitter heater ended the test. In all, 1718 hours of operation were accumulated, the last 1275 of which were part of the main test program. A chronological breakdown of the testing is presented in Table 17. The test history of A-3 is contained in Figures 190 through 199.

At the start of testing, the constant sum-of-the-currents control parameter was set at $I_a + I_r = 60$ milliamperes, corresponding to a diode voltage of about 8 volts at zero-pressure. The signal conditioner was originally set up at 1600°F with a zero-pressure output of about +0.1 volt and full-scale output of about 5.15 volts. Pressure-output data was evaluated against a $\pm$5 percent envelope around a 0-5 volts full-scale linear response.

Figures 190 and 191 present variations, with test time, in the zero-pressure values of the active and reference collector currents (I_a and I_r) and the signal conditioner output. There appeared to be three regions of stability, separated by the temperature excursion tests. The most pronounced shift occurred around 1190 clock hours, with the zero-pressure output shifting from about -0.5 volt to about -1.5 volt. This shift is also evident in the

TABLE 17

TEST CHRONOLOGY, ABSOLUTE TRANSDUCER 3

Clock Hours (A)	Test (B)	Figure
443	1600°F operation	192
467	Temperature excursion test (C)	192
498	1600°F operation	192
564	1800°F Spot Check	193
566	1600°F operation	193, 194
665	1800°F Spot Check	193
668	1600°F operation	193, 194
948	Temperature excursion test (C)	195
983	1600°F operation	196
1163	1600°F operation	197
1307	Temperature excursion test (C)	198
1340	1600°F operation	197
1619	Temperature excursion test (C)	199
1668	1600°F operation	197
1718	Heater failure	

(A) Refers to an electric timer running since activation of the sensor of Absolute Transducer 3.

(B) During testing, transducer was continuously cycled between 0-80 psia once every three minutes.

(C) Tests run at 1600, 1400, 1200, 1000, 1200, 1400, 1600°F.

data of Figure 190. Both currents changed at that time, I_r increasing and I_a decreasing. The large negative zero-shift was due to the decrease in the $(I_a - I_r)$ parameter which established the signal conditioner output.

Figure 192 presents the data up to the first 1800°F spot check at 564 clock hours. These data include the first temperature excursion test (1600-1000-1600°F) started at 467 clock hours. The pressure-output curves reproduced quite well and fell well within the $\pm$5% envelope. For the temperature excursion test, the 1600°F output data appeared to be a little higher (about 0.1 volt) than the data for the lower temperatures.

Figures 193 and 194 present the results of the two 1800°F spot checks and the following 1600°F time periods. As shown in Figure 193, 1800°F operation resulted in a large positive zero-shift (about 1 volt) accompanied by an apparent drop in gain, resulting in the 80 psia point approaching the $\pm$5% envelope. Analysis of the space-charge data showed the reason for this behavior. No essential change was noticed in I_r. However, the zero-pressure data indicated an increase in active collector current, resulting in the observed large positive zero-shift. However, the 80 psia data indicated a smaller increase in active collector current, resulting in the observed smaller shift in full-pressure output. To conclude that the full-scale pressure capsule deflection is less at 1800°F than at 1600°F is not realistic and it appeared that an effect not shown in the space-charge data was responsible. To avoid any possible damage to the sensor and assure the maximum amount of valid information on transducer operation, it was decided to forgo any future 1800°F operation.

Again with reference to Figure 193, 1600°F data taken immediately after (2-3 hours) 1800°F operation yielded anomalous results. The curves appeared to take a small negative zero-shift but exhibited increased gain at full-scale conditions. After several hours, however, the pressure-output curves returned to the conditions of Figure 192. The periods of time after the 1800°F spot checks yielded data outlined in Figure 194. The envelope broadened somewhat with data between the two 1800°F spot checks (566-665 clock hours) concentrated in the upper portion of the envelope and data taken between the second 1800°F spot check and the second temperature excursion test (668-948 clock hours) concentrated in the lower portion of the envelope.

With the second temperature excursion test (948-983 clock hours), considerable shifting of the pressure-output curves took place (see Figure 195). Generally, the only noticeable effect in the space-charge data was an increase in both active and reference collector currents as the temperature decreased from 1600 to 1000°F. Although the signal-conditioner system maintained the sum-of-the-currents constant, the non-linearity of the space-charge curves introduced the wandering of the pressure-output curves of Figure 195.

Following the second temperature excursion, the transducer was observed to have taken a definite negative zero-shift of about 0.4-0.5 volt. The envelope is shown in Figure 196. Again using space-charge data to investigate this shift, it was found that while a small increase had taken place in I_r, the values for I_a had dropped to a greater extent, accounting for a decrease in $I_a - I_r$

and the resultant negative zero-shift. Comparing Figure 196 to Figure 192, little difference is seen in the envelope of the curves. Consistent operation was obtained in both cases with the negative zero-shift of Figure 196 an apparently permanent effect.

One of the obvious aspects of the data was that changes in currents and zero-shifts seemed to occur after changes in the system (1800°F operation, temperature excursions). In addition, space-charge data did not prove conclusive. Both emitters showed no signs of emission limit effects and appeared to be operating properly.

At about 1190 clock hours the most pronounced zero shift occurred, with the zero-pressure output changing from about -0.5 volt to about -1.5 volts. The change in the pressure-output curve is shown in Figures 196 and 197. After 1200 hours, the 1600°F characteristic appeared to stabilize quite well (Figure 197) up to the end of testing at 1718 hours.

Space-charge data taken around the time of the shift at 1200 hours showed a marked decrease in active collector current and a less pronounced change in reference collector current. Both emitters appeared to be operating properly and showed no signs of emission limit effects.

The results of the final two temperature excursion tests are shown in Figures 198 and 199 and are in basic agreement with positive zero-shifts resulting from decreased temperature. Space-charge data showed increases in both active and reference collector currents as the temperature decreased. The positive zero-shift was caused by the predominant increase in active collector current I_a.

It became apparent that spacing changes inferred from the space-charge data were not realistic and could not reasonably explain the anomalous shift at 1200 hours or the zero-shift/temperature effects.

A more likely explanation for the temperature effects may be found from consideration of the collector surfaces. Changes in work-function of these surfaces may result from temperature excursions and current levels. These work-function changes, in turn, cause shifts in the current-voltage characteristics and the signal conditioner output.

11.2.2 Absolute Transducer 4

Prior to final assembly, Absolute Transducer 4 (A-4), without its thermionic diode sensor, was installed in the Vacuum Test Facility for stress relief exercising. The W-25Re pressure capsule was cycled between 0-80 psia at 1800°F for 120 hours using two modes; manual cycling (once an hour) during the working day and automatic cycling (20 times an hour) overnight. Manual cycling consumed 33 hours (33 cycles) while automatic cycling was performed for 87 hours (1740) for a total of 1773 pressure cycles. Following the cycling, the transducer was removed from the chamber and checked. It was found to be leak-tight and room-temperature pressure-deflection data agreed with data taken before cycling (80 psia resulted in a deflection of about 0.003 inch).

Following pre-activation of the emitters, the thermionic diode sensor was assembled and installed in the pressure capsule with a room-temperature active emitter-collector distance of 0.006 inch. The complete transducer A-4 was then installed in Vacuum

Test Facility and a 15 minute activation at 2280°F was performed on the emitters. During activation, 10 volts was applied to the diode and the active and reference collector currents at the end of the activation period were 37.8 and 18.5 milliamperes respectively. The emitter temperature was then lowered to its 2100°F operating value; 10 volts was maintained on the diode and space-charge data were taken to determine the active and reference current characteristics. Following a weekend of operation, the active and reference currents appeared to have stabilized at values of about 37 and 19 milliamperes respectively (at 10 volts).

Space charge data on both currents showed no emission limit conditions; the expected "ten volt effect" was observed in both currents. Active current data was run up to about 21 volts and 100 milliamperes at zero-pressure and 17.5 volts and 137 milliamperes at 80 psia. The zero-pressure active collector distance appeared to be about 0.006 inch. Reference current data was run up to about 33 volts and 100 milliamperes. Space charge curves indicated a reference collector distance of 0.0085 inch, accounting for the relatively low value of reference current in the absence of emission limit conditions. Reviewing the fabrication of the sensor and the procedures used for installation in the transducer failed to turn up any reason for the large reference collector distance. It appeared that the question could be resolved only by removal of the transducer from the test chamber and inspection of the sensor. However, this course of action would run the risk of damaging the sensor by exposure to air. Instead, it was decided to continue the testing and have the signal conditioner system offset the large

difference between I_a and I_r and establish a zero-output for zero-pressure through the use of the zero control.

Initial data on A-4 were collected with laboratory heater and space-charge circuitry. After about 120 hours of operation, the signal conditioner was installed and about 100 hours were spent checking operation with the transducer. Because of the low value of reference current and the necessity of operating the diode at less than 10 volts, the control parameter (constant sum-of-the-currents) was set at $I_a + I_r = 50$ milliamperes, corresponding to a diode voltage of about 9 volts at zero pressure.

Figures 200 and 201 present typical pressure-output and space-charge characteristics taken at the end of this 220 hour period. The signal conditioner was adjusted as best as possible for zero, gain and linearity conditions. Figure 201 contains theoretical space-charge curves corresponding to various emitter-collector distances. At low operating voltages, correlations with Childs' Law were not obtained due to emission effects. Correlation was obtained at higher voltages (above 15 volts).

Transducer A-4 was operated for a total of 2240 hours, the last 2020 of which constituted the main test program. During the testing, the transducer was continuously cycled between 0-80 psia once every three minutes, resulting in about 40,000 pressure cycles at 1600°F without mechanical failure. A chronological breakdown of the testing is presented in Table 18. The test history of A-4 is contained in Figures 202 through 212.

TABLE 18

TEST CHRONOLOGY, ABSOLUTE TRANSDUCER 4

Clock Hours (A)	Test (B)	Figure
1168	1600°F operation	202, 205, 208
1191	Temperature excursion test (C)	202, 205, 209
1236	1600°F operation	202, 205, 208
1618	Temperature excursion test (C)	202, 205, 210
1667	1600°F operation	202, 205, 208
1955	1600°F operation	203, 206, 211
2585	1600°F operation	204, 207, 212
3188	1600°F operation (end of 2000 hour test)	204, 207, 212

(A) Refers to an electric timer running since activation of the sensor of Absolute Transducer 3.

(B) During testing, transducer was continuously pressure cycled (0-80 psia) once every three minutes.

(C) Tests run at 1600, 1400, 1200, 1000, 1200, 1400, 1600°F.

Because of the low value of reference current and the necessity of operating the diode at less than 10 volts, the constant-sum-of-the-currents control parameter was set at $I_a + I_r = 50$ milli-amperes, corresponding to a diode voltage of about 9 volts at zero pressure. At the start of testing, the signal conditioner was adjusted as best as possible for zero, gain and linearity at 1600°F and a full-scale output of 5 volts. Pressure-output data was evaluated against a ± 5 percent envelope around a 0-5 volts full-scale linear response.

Figures 202, 203 and 204 present variations, with test time, in the zero-pressure values of the active and reference collector currents. The signal conditioner zero-pressure output is shown in Figures 205, 206 and 207.

The transducer displayed good stability over the 2000 hour period at 1600°F. Figures 202, 203 and 204 show the active and reference collector currents. Aside from a slight increase in I_a following the second temperature excursion test (1618 - 1667 hours), both currents were quite stable. This is also reflected in Figures 205, 206 and 207, which show the output zero-shift. The increase in I_a after the second temperature test resulted in the zero-shift going positive and remaining there for the rest of the test period, inside a $\pm$ 5 percent envelope.

Space-charge data taken through the 2000 hour test period showed no abnormalities in either the active or reference current traces. It was evident that the work done on developing proper fabrication and quality control procedures for the emitters and the thermionic sensor was successful and resulted in a sensor exhibiting good reliability and life.

Further proof of transducer stability was shown in the pressure-output envelopes of Figures 208, 211 and 212. The earliest test results of Figure 208 showed an envelope that agreed quite well with the ± 5 percent envelope, shown dotted in the figure. The envelope was broadened somewhat due to the positive zero-shift following the second temperature test. Data taken before the second temperature test are concentrated in the lower portion of the envelope of Figure 208 while data taken afterward are concentrated in the upper portion.

The pressure-output envelopes of Figures 211 and 212 agreed quite well with the upper portion of the envelope of Figure 208, indicating stable transducer operation over the 2000 hour period at 1600°F.

The results of the two temperature excursion tests (Figures 209 and 210) were in basic agreement with the temperature tests of A-3. Positive zero-shifts resulted from decreased temperatures. For A-4, the magnitudes were greater than exhibited by A-3, but this was probably due to the large unbalance between the active and reference currents. Space charge data showed the zero-shifts to be due almost entirely to increases in active collector current . The reference collector current remained fairly constant. During the second temperature excursion test, the increasing temperature portion (1200-1400-1600°F) showed zero-shifts higher than expected, with the 1200°F zero point being more positive than the 1000°F point. At 1400°F, the first run showed a shift in the pressure-output curve during the test. A second 1400°F run was performed

which is included in Figure 210. No apparent reason was found for this behavior and at 1600°F, the zero-point agreed reasonably with the value before the temperature test. At 1700 hours, a 1400°F test was run as a check and a more realistic zero-shift was obtained.

Changes in transducer pressure-output parameters both during and after temperature excursions were encountered with both A-3 and A-4. Spacing changes inferred from space-charge data were not realistic and could not reasonably explain the temperature effects. The basic conclusion was that non-repeatable temperature effects were due to changes in collector surface conditions. It appeared that transducer operation must be established in a regime where (1) the collector work function is constant or (2) changes in the collector work-function are repeatable and may be compensated.

In the absence of the temperature excursion tests, the pressure-output data could have remained within a $\pm$5 percent of 5 VFS envelope for the entire 2000 hour period. If the temperature effects were minimized, it appeared that a viable transducer design was demonstrated.

SUMMARY OF RESULTS

The program leading to the development of a high-temperature liquid-metal pressure transducer was conducted along several lines of activity. Prior to a test program involving the final transducer design configuration, considerable effort was concentrated in the areas of material selection, fabrication procedures, liquid-metal compatibility and development of the test facilities necessary to conduct these studies.

The basic transducer design called for the use of a refractory-alloy pressure capsule to transform the liquid metal pressure into a mechanical displacement. This displacement is then monitored by a thermionic diode sensor whose output indicates the pressure.

Construction of test pressure capsules using four candidate alloys (C-129Y, FS-85, T-222 and W-25 Re) allowed for the development of suitable fabrication techniques for the capsule and the evaluation of the capsule operational characteristics.

The inherent difficulties involved in normal machining of the refractory alloys and the known harmful effects of oxygen in refractory metals exposed to liquid alkali metals require that fabrication of the pressure capsules use electrical discharge machining and electron beam welding.

Extended testing of the four candidate materials, using the pressure capsule configuration, was performed in a high-vacuum environment (10^{-8} torr) with high-purity argon used for pressurization. The testing yielded the following results.

1. Hysteresis effects at temperatures up to 1800°F were negligible for full scale deflections up to about 0.001 inch.
2. The increase in full scale deflection with temperature generally followed the predicted change based on literature values of Young's modulus.
3. Zero shift data generally showed that the W-25Re capsule was the most stable.
4. There is a definite need for extended pressure cycling to obtain stable pressure-deflection characteristics.

Based on the results of these initial deflection tests, W-25Re was chosen as the alloy for the pressure capsule.

Work on the metal-ceramic seal configurations necessary to provide electrical connections into the transducer concentrated on the development of joints capable of maintaining integrity under 1800°F conditions and liquid metal attack. The final configuration involved the use of a high-purity alumina (Lucalox) material in conjunction with Nb-1Zr alloy metal structures. The Lucalox was metallized with a tungsten/yttria compound and the braze material was a Ni/Nb/Ti mixture.

Compatibility testing performed on capsules of the four refractory alloys and a representative metal-ceramic seal configuration demonstrated the ability of the test samples to maintain their integrity under liquid metal attack. The testing was conducted for 500 hours and used liquid potassium at a temperature of 1800°F (corresponding to a vapor pressure of about 80 psia).

To establish a reliable operating life of over 2000 hours, the critical design areas of the thermionic diode sensor were the electrical heater configuration used to hold the emitter temperature at 2100°F and the emitters themselves. The heater assembly, incorporating both emitters, was designed to withstand shock and vibration loading and provide improved heat transfer between the electric heater and the emitters.

The fabrication technique involved casting of the heater into a cavity of the emitter housing. An alumina/beryllia mixture was used, resulting in a homogeneous cast structure. A W-3Re heater with spot welded rhenium leads gave the flexibility required to assemble the sensor.

The most critical part of the thermionic diode sensor is the emitter. Philips Type B impregnated emitters were chosen for this application since they are capable of sufficient emission capacity at the relatively low temperature used (2100°F). Extensive testing and evaluation revealed the necessity for stringent quality control requirements. To obtain operating lifetimes of over 2000 hours for the emitters, the following requirements must be met.

1. The emitter must be checked by weighing before and after impregnation to verify that it is fully impregnated.
2. No machining of any kind should be done to the emitting surface. All excess impregnant should be removed by ultrasonic water bath only.

3. Brazing of the emitters into the emitter housing should not disturb the uniform, open pore structure of the emitter. To check this, microscopic examinations (at least 500X) should be made of the emitter surface both before and after brazing.

The final stages of the program involved the design and construction of an electrical signal conditioning system to automatically control the operation of the transducer. A system was developed and operated with final transducer test units over a period of 2000 hours.

The signal conditioner maintained emitter temperature at 2100 $\pm$ 5°F over all conditions of time and chamber temperature and controlled the operation of the thermionic diode sufficiently to maintain the sum of the active and reference currents within $\pm$ 0.5% of full scale. The conditioner output was adjustable and set at 5 volts dc for full scale.

During the 2000 hour test program, some temperature effects were noticed in the pressure-output parameters of the test transducers. However, it appeared that these effects could be due to surface conditions of the collector electrodes of the sensor and as such, appeared amenable to compensation.

The basic design and fabrication of the transducer (both pressure capsule and thermionic diode sensor) were shown to be reliable and capable of consistent operation over a period exceeding 2000 hours.

REFERENCES

1. W. B. Nottingham; "The Thermionic Diode as a Heat-to-Electrical-Power Transducer", Direct Conversion of Heat to Electricity, ed. by J. Kaye and J. A. Welsh, M.I.T. Summer Session, July 1959, Chapter 2.

2. R. J. Roark; "Formulas for Stress and Strain", Third ed., McGraw-Hill Book Co., Inc., 1954, p. 192-231.

3. Ibid. p. 100.

4. C. L. Bartberger; "The Magnetic Field of a Plane Circular Loop", Journal of Applied Physics, Vol. 21, No. 21, Nov. 1950, p. 1108.

5. W. B. Nottingham: "Thermionic Emission", Encyclopedia of Physics, Vol. XXI, Electron Emission Gas Discharges, ed. by S. Flugge, Springer-Verlag, 1956, p. 1-175.

6. I. Langmuir: "The Effect of Space Charge and Residual Gases on Thermionic Currents in High Vacuum", Physical Review, Vol. II, No. 6, Dec. 1913, p. 450.

7. C. Herring and M. H. Nichols: "Thermionic Emission", Reviews of Modern Physics, Vol. 21, No. 2, April 1949, p. 185-270.

BIBLIOGRAPHY

R. E. Engdahl: First Quarterly Report, Pressure Measuring Systems for Closed Cycle Liquid Metal Facilities. NASA CR-54140, July 2, 1964.

R. E. Engdahl: Second Quarterly Report, Pressure Measuring Systems for Closed Cycle Liquid Metal Facilities. NASA CR-54193, September 28, 1964.

A. J. Cassano: Third Quarterly Report, Pressure Measuring Systems for Closed Cycle Liquid Metal Facilities. NASA CR-54276, December 28, 1964.

A. J. Cassano: Fourth Quarterly Report, Pressure Measuring Systems for Closed Cycle Liquid Metal Facilities. NASA CR-54371, April 5, 1965.

A. J. Cassano: Fifth Quarterly Report, Pressure Measuring Systems for Closed Cycle Liquid Metal Facilities. NASA CR-54439, June 28, 1965.

A. J. Cassano: Sixth Quarterly Report, Pressure Measuring Systems for Closed Cycle Liquid Metal Facilities. NASA CR-54763, October 18, 1965.

A. J. Cassano: Seventh Quarterly Report, Pressure Measuring Systems for Closed Cycle Liquid Metal Facilities. NASA CR-54899, January 25, 1966.

A. J. Cassano: Eighth Quarterly Report, Pressure Measuring Systems for Closed Cycle Liquid Metal Facilities. NASA CR-54960, April 8, 1966.

A. J. Cassano: Ninth Quarterly Report, Pressure Measuring Systems for Closed Cycle Liquid Metal Facilities. NASA CR-72055, August 1, 1966.

A. J. Cassano: Analysis of Two High-Temperature Liquid Metal Pressure Measuring Systems. Aerospace Conference Proceedings, IEEE Transactions on Aerospace, Vol. AS-3, No. 2, June 1965, p. 466.

A. J. Cassano and R. E. Engdahl: Pressure Transducer for Liquid Metal Applications. Proceedings of the Conference on Application of High Temperature Instrumentation to Liquid-Metal Experiments, September 28-29, 1965. Argonne National Laboratory Report ANL-7100.

APPENDIX A

VARIABLE IMPEDANCE SENSOR

The variable impedance concept for detecting pressure element motion is based on the use of two air-core pancake-coil inductors whose impedance is varied by th motion of a conductive surface (diaphragm). The diaphragm is initially mid-way between the two inductors. Under pressure, the diaphragm approaches one of the coils and moves further away from the other. The inductances decrease and increase, respectively, from their zero-pressure values. In addition to coil inductance L, there also exists a capacitance C between the coil and the pressure actuated diaphragm. These parameters are introduced into a balanced ac impedance bridge whose output becomes pressure-dependent. Of primary improtance is the parametric determination of coil inductance as a function of diaphragm position.

A-1 Pancake Coil Inductance

An exact analytical evaluation of the pancake coil inductance is not readily accomplished. However, image theory offers a valid, reasonably accurate model from which the inductance can be determined.

Using image theory, the field existing between a current element and a conducting material is developed by postulating the existence of a second current element of equal strength and opposite direction (image element). Within the material, the fields due to the two elements have opposing normal components and the location of the image is determined by the plane along which these normal components

tend to cancel out. If the diaphragm were a perfect conductor, its interior would be field-free and image theory would allow for an exact solution. The induction field of the coil would be zero at the diaphragm surface and a 100% strength image coil would have a position equal to the coil-diaphragm distance.

The fact that an actual diaphragm has a finite conductivity allows the field to penetrate into the diaphragm. This penetration may be treated as a modification to the infinite conductivity situation in one of two ways.

1. The field attenuation occurring within the diaphragm may be considered to involve an "effective skin depth" relative to an induction field with normal H components. In this context, the term "skin depth" refers to a general field penetration phenomena and should not be confused with the common definition involving penetration of electromagnetic waves with tangetial H components. Although there may be a relationship between the two, the definition of this relationship is beyond this work.
2. The presence of a weakened image field may be postulated. This also allows for field penetration into the diaphragm. However, there is no basis upon which an estimate of the image efficiency may be obtained.

Figure 213 presents the geometry of the problem (employing the skin depth approach) in cylindrical coordinates where δ_e denotes the effective skin depth at which the normal fields tend to cancel.

To develop the analytic expression for inductance, the coil and its image will be considered to be concentric separate loops, each carrying the same current. Since the distances involved are negligible compared to wavelength, the current in the image coil may be taken as the same as that in the pancake coil.

Bartberger (Reference 4) presents the following formulae for the axial field component of a plane circular loop of wire in cylindrival coordinates z, ρ, θ (referred to the plane of the coil as z = o).

$$H_z = \frac{H_o}{S_b^3}\left[\Phi_1 - \left(\frac{\rho}{a}\right)\Phi_2\right] \qquad \text{(A1)}$$

$$\left.\begin{aligned}\Phi_1 &= \frac{1}{\pi}\int_o^{\pi} \frac{d\theta}{(1-b\cos\theta)^{3/2}} \\ \Phi_2 &= \frac{1}{\pi}\int_o^{\pi} \frac{\cos\theta\, d\theta}{(1-b\cos\theta)^{3/2}}\end{aligned}\right\} \text{ tabulated in Bartberger (Reference 4)} \qquad \text{(A2)}$$

where

$$b = \frac{2a\rho}{a^2 + z^2 + \rho^2}$$

a = radius of loop

$$S_b^2 = \frac{a^2 + z^2 + \rho^2}{a^2}$$

H_o = field at center (z = ρ = o) of loop (A-3)

$$H_o = \frac{i_o}{2a}$$

i_o = current in loop

Therefore:

$$H_z = \frac{i_o a^2}{2(a^2 + z^2 + \rho^2)^{3/2}}\left[\Phi_1 - \left(\frac{\rho}{a}\right)\Phi_2\right] \qquad \text{(A-4)}$$

Referring to Figure 213, the total axial field in the plane of the pancake coil, related to the n^{th} turn, will consist of components due to the pancake coil itself (for which z = o in the above formulae) and due to the image coil (for which $z = 2z_e$ in the above formulae). These components will be in opposition so that the total field related to the n^{th} turn will be

$$H_n(\rho) = \frac{i_o a_n^2}{2}\left[\frac{\Phi_1' - \left(\frac{\rho}{a_n}\right)\Phi_2'}{(a_n^2+\rho^2)^{3/2}} - \frac{\Phi_1'' - \left(\frac{\rho}{a_n}\right)\Phi_2''}{(a_n^2+4z_e^2+\rho^2)^{3/2}}\right] \qquad (A\text{-}5)$$

where the primes denote pancake coil integrals and the double primes denote image coil integrals. The total field related to the pancake coil is

$$H_z(\rho) = \sum_{n=1}^{N} H_n(\rho) \qquad (A\text{-}6)$$

where N is the total number of turns.

The flux linked by the m^{th} turn is:

$$\phi_m = \int_0^{A_m} B_z 2\pi\rho d\rho = 2\pi\mu_o \int_0^{A_m} H_z \rho d\rho \qquad (A\text{-}7)$$

where μ_o is the permeability of the vacuum space and $2\pi\rho d\rho$ is the differential area in cylindrical coordinates. The voltage generated in the m^{th} turn is

$$V_m = \frac{d\phi_m}{dt} = j\omega\phi_m \qquad (A\text{-}8)$$

since $\phi_m = \phi_{max} e^{j\omega t}$ is a time varying parameter.

The total voltage generated in the pancake coil is

$$V_T = \sum_{m=1}^{N} V_m \qquad \text{(A-9)}$$

The reactance of the pancake coil is

$$X_C = \frac{V_T}{jI_o} \qquad \text{(A-10)}$$

and the inductance is $L = X_C/\omega$ or

$$L = \pi\mu_o \sum_{m=1}^{N} \int_0^{a_m} \sum_{n=1}^{N} a_n^2 \left[\frac{\Phi_1' - \left(\frac{\rho}{a_n}\right)\Phi_2'}{(a_n^2 + \rho^2)^{3/2}} - \frac{\Phi_1'' - \left(\frac{\rho}{a_n}\right)\Phi_2''}{(a_n^2 + 4z_e^2 + \rho^2)^{3/2}} \right] \rho\, d\rho \qquad \text{(A-11)}$$

Attempts to determine, by slide rule calculations, the inductance of a single turn pancake coil in the presence of a conducting diaphragm have indicated that Equation A-11 can be practically solved only by computer techniques. Two alternatives presented themselves. One was to use the computer and the other was to establish the inductance by experiment. It was felt that the experimental approach was preferable.

A.2 Experimental Program

The main objective of the experimental program was the determination of pancake coil inductance as a function of diaphragm position. In addition, it was expected that the program would result in data that would verify the basic premise of the analysis; the

presence of an image coil whose position is determined by a skin-depth phenomena. The discussion that follows expands upon this last statement.

Image theory has been proposed as a valid method of determining the coil inductance. Of prime importance is the distance between the pancake coil and the image coil. This distance is in turn determined by a skin depth phenomena experienced in the diaphragm. At some effective skin depth (which may be postulated to be some multiple of a unit skin depth) inside the diaphragm, the induction field of the pancake coil will tend to zero and the pancake and image coils become equidistant from this plane. This phenomena is dependent upon the resistivity of the diaphragm material. As an example, consider a perfectly conducting diaphragm (resistivity = 0). The field does not enter the diaphragm at all and has its zero value at the diaphragm surface. For this case the pancake coil to image coil distance will be twice the pancake coil to diaphragm distance. In addition, the pancake coil inductance will vary between a value of zero when the distance is zero and a finite value, e.g. L_∞, corresponding to complete absence of a diaphragm. The inductance L will tend to this value as the spacing increases. Although the exact shape of the curve is uncertain, Figure 214 indicates the general trend. The fact that $L = 0$ at $d_c = 0$ for $\rho r I = 0$ means that the pancake and image coils are so close to each other that their axial fields cancel out in the plane of the pancake coil.

Now, an important point must be made. The pancake coil inductance is determined by the opposing interaction of two acial induction fields; one due to the pancake coil itself and the other due to the image coil. The strength of the image field is governed by the distance between the coils. This distance is determined by two parameters; the diaphragm spacing and the effective skin depth as established by the diaphragm resistivity. However, the sum of diaphragm spacing and effective skin depth is the important thing. In other words, two diaphragms of different resistivities will result in the same pancake coil inductance if the diaphragm spacing is adjusted to compensate for the difference in effective skin depth. As resistivity increases, skin depth increases. Referring to Figure 214, the inductance L_2 for a spacing d_{c2} with a zero resistivity diaphragm would correspond to the same inductance L_2 caused by a diaphragm with zero spacing and an effective skin depth of 1/2 d_{c2} determined by a finite resistivity $\rho r2$. This statement applies also to inductance L_3 where a diaphragm with zero spacing would have an effictive skin depth of 1/2 d_{c3} determined by resistivity $\rho r3$. If a diaphragm of very low resistivity (e.g. copper) is used, the $\rho r1 = 0$ curve will be approached. Using this curve, an effort may be made to determine correlations between effective skin depth and resistivity. Using the standard formula for unit skin depth as a function of resistivity, an effort will be made to determine whether the effective skin depth postulated above is a constant multiple of the unit skin depth.

The use of diaphragms of various resistivities should result in a series of parallel curves intersecting the ordinate at larger values of inductance for larger values of resistivities. This procedure will give an estimate of inductance change with diaphragm temperature. A temperature change will result in a resistivity change affecting skin depth and inductance even at constant spacing.

A 20 turn single-layer pancake coil (I.D. = 3/16 inch, O.D. = 9/16 inch, AWG 32 heavy Formvar insulated magnet wire) was fabricated and encapsulated in the surface of a block of lucite. Diaphragm mock-ups of various materials covering a range of resistivity values and thicknesses (copper, 1.7 X 10^{-6} ohm-cm, 0.015 inch; cupro-nickel, 39 X 10^{-6} ohm-cm, 0.031 inch; monel, 49 X 10^{-6} ohm-cm, 0.015 inch; K-monel, 58 X 10^{-6} ohm-cm, 0.021 inch) were prepared and mounted on polystyrene rods. A test fixture was constructed to allow mounting of the diaphragm samples in a support slide and positioning of the samples at various distances from the coil by means of a vernier micrometer. Figure 215 shows the test fixture.

Initial testing of the coil on the basis of impedance measurements proved inconsistent. This testing involved the use of a radio frequency signal generator and a calibrated oscilloscope to obtain current and voltage parameters. Parallel resonance phenomena introduced by the impedance characteristics of the instruments made this method inconclusive. The resonance problem was eliminated by using a Q-meter instrument for further testing.

In addition to obtaining the inductance-distance characteristics, efforts were made to determine:

1. System sensitivity to small changes in coil-diaphragm distance,
2. System error introduced by coil-diaphragm angular misalignment,
3. System response to changes in diaphragm diameter and
4. System error introduced by coil-diaphragm zero spacing error.

Typical inductance-distance curves using diaphragms of various resistivities and the pancake coil described above are shown in Figures 216 through 218 Coil - diaphragm distances of up to 0.070 inch are shown. For greater distances, the curves tended to flatten out and approach an inductance value of 4 microhenries at 0.2 inch, independent of diaphragm material. It appears that the skin depth change with resistivity, upon which the analytical model of the variable impedance device is based, is a minimal effect. There is no definite displacement of the curves with increasing resistivity. To ascertain whether the results might reflect instrumentation and set-up errors, known spacing and alignment errors were introduced in later tests with the following results.

Pancake-coil response to changes of 0.001 inch (5 percent of an assumed total diaphragm travel of 0.002 inch) in coil - diaphragm distance was measured. Tests run at distances of 0.010, 0.030, and 0.060 inch showed a change of less than 1 percent in the measured inductance. This percentage change was independent of diaphragm material, thickness and diameter. It therefore appears that the system is relatively insensitive to small changes in spacing.

Spot checks made on the effect of coil - diaphragm angular misalignment showed inductance changes of 2-3 percent for an alignment error of 1 degree. However, a 1 degree error is easily noted by visual observation and the normal experimental run is made with errors well below this 1 degree value. It therefore appears that misalignment is not a cause of the inconclusive results of Figures 216 through 218.

Tests conducted using 1, 1-1/2 and 2 inch diameter diaphragms of copper, cupronickel, monel and K-monel failed to yield any consistent inductance change with diaphragm diameter. These materials represent a range of resistivities corresponding to the values expected in operating a refractory alloy up to 1800°F.

Using a dial indicator to ascertain the coil-diaphragm zero spacing, it was possible to repr oduce the zero spacing results within 5-15 percent. It should be remembered that although the actual zero spacing may be determined to better than 0.001 inch with the dial indicator, the Q-meter is operating with the lowest possible Q-value for the pancake-coil. This makes a relatively large operator error quite possible. It is felt that this difficulty in reading the Q-meter at very small coil - diaphragm distances is the most likely cause of the inconclusive results concerning the reproducibility of the induction at zero spacing.

APPENDIX B

THERMIONIC DIODE RELATIONS

B.1 Derivation of Expression for Space Charge Potential V_e

The emission limit relation for critical temperature T_c is:

$$I_c = 120\ T_c^2 \exp\left(-\frac{e\phi_e}{KT_c}\right) \tag{B-1}$$

As the temperature increases above T_c, the space charge potential V_e develops and the current becomes

$$T = 120\ T^2 \exp\left[-\frac{e(\phi_e + Ve)}{KT}\right] \tag{B-2}$$

Nottingham (Ref. 5) suggests that an equation of the following form is a more useful empirical equation:

$$I = B \exp\left(-\frac{e\phi}{KT}\right) \tag{B-3}$$

where (B) is a thermionic constant determined by experiment to fit the observed data and ϕ is called the "work-factor" with values 5 to 15 percent higher than the values of the work function ϕ_e, depending on the emitter material. Using this formulation, the current equations become

$$I_c = B \exp\left(-\frac{e\phi}{KT_c}\right) \tag{B-4}$$

and

$$I = B \exp\left[-\frac{e(\phi + Ve)}{KT}\right] \tag{B-5}$$

Taking natural logarithms and substracting Equation B4 from B5 yields

$$\ln I - \ln I_c = -\frac{e(\phi + Ve)}{KT} + \frac{e\phi}{KT_c}$$

$$\text{or} \quad \frac{KT}{e} \ln\left(\frac{I}{I_c}\right) = -V_e + \phi\left(\frac{T}{T_c} - 1\right)$$

and

$$V_e = \phi \frac{\Delta T}{T_c} - \frac{KT}{e} \ln\left(\frac{I}{I_c}\right) \tag{B-6}$$

where $\Delta T = T - T_c$ is the increase in temperature above T_c. Experiments have shown that I exceeds I_c by only a small amount ($\Delta I = I - I_c$) for considerable increase in temperature (i.e. $I/I_c \approx 1$). Using the series expansion for the natural logarithm.

$$\ln \chi = (\chi-1) - \frac{1}{2}(\chi-1)^2 + \frac{1}{3}(\chi-1)^3 - \cdots \qquad 0 < \chi < 2 \tag{B-7}$$

and neglecting terms higher than first order

$$\ln\left(\frac{I}{I_c}\right) \cong \left(\frac{I}{I_c} - 1\right) = \frac{\Delta I}{I_c} \tag{B-8}$$

Assuming, for calculation purposes, $\phi \approx \phi_e$

$$V_e \cong \phi_e \frac{\Delta T}{T_c} - \frac{KT}{e} \frac{\Delta I}{I_c} \tag{B-9}$$

B.2 Error Analysis - Current Density Dependence on Temperature

Since e/k = 11600, the relation for the current from Equation 4 of text becomes

$$I = AT^2 \exp\left[-\frac{11600\ (\phi_e + V_e)}{T}\right] \tag{B-10}$$

Taking the partial derivative with respect to temperature

$$\frac{\partial I}{\partial T} = AT^2 \exp\left[-\frac{11600(\phi_e+V_e)}{T}\right](-11600)\left[\frac{T\frac{\partial}{\partial T}(\phi_e + V_e) - (\phi_e+V_e)}{T^2}\right] \tag{B-11}$$

$$+ \exp\left[-\frac{11600\ (\phi_e + V_e)}{T}\right] 2\ AT$$

and substituting Equation B-10 into B-11

$$\frac{\partial I}{\partial T} = I\left[\frac{11600(\phi_e+V_e) - 11600T\,\frac{\partial}{\partial T}(\phi_e + V_e)}{T^2}\right] + \frac{2I}{T}$$

The change in current may be expressed as

$$\frac{\Delta I}{I} \cong \left[\frac{11600(\phi_e + V_e)}{T^2} - \frac{11600}{T}\,\frac{\partial}{\partial T}(\phi_e + V_e) + \frac{2}{T}\right]\Delta T \qquad \text{(B-12)}$$

To evaluate $\frac{\partial}{\partial T}(\phi_e + V_e)$, consider from B9 above

$$V_e \cong \phi_e\,\frac{(T-T_c)}{T_c} - \frac{T(I - I_c)}{11600\ I_c} \qquad \text{(B-13)}$$

Differential yields

$$\frac{\partial V_e}{\partial T} = \frac{\phi_e}{T_c} - \frac{(I - I_c)}{11600\ I_c} \qquad \text{(B-14)}$$

Reference 6 shows that with changes in temperature

$\frac{I - I_c}{I_c} < .1$ or $\frac{I - I_c}{11600\ I_c} < 10^{-5}$. For $\phi_e = 2.1$ ev and

$T_c = 1420°K$, $\frac{\phi_e}{T_c} = 1.5 \times 10^{-3}$ and

$$\frac{\partial V_e}{\partial T} \cong \frac{\phi_e}{T_c} \qquad \text{(B-15)}$$

Experimental results (Reference 7) have yielded values for

$\partial\phi_e/\partial T$ of $\pm 5 \times 10^{-5}$ ev/°K. Therefore

$$\frac{\partial}{\partial T}(\phi_e + V_e) \cong \frac{\partial V_e}{\partial T} \cong \frac{\phi_e}{T_c} \qquad \text{(B-16)}$$

and

$$\frac{\Delta I}{I} \cong \left[\frac{11600\ (\phi_e + V_e)}{T^2} - \frac{11600\ \phi_e}{TT_c} + \frac{2}{T}\right]\Delta T \qquad \text{(B-17)}$$

If the right side of Equation B17 is evaluated using Equation B9 and, assuming the following parameters,

$T = 1520°K$, $T_c = 1420°K$, $\Delta T = 100°K$

$\phi_e = 2.1$ ev and $\frac{\Delta I}{I_c} = .1$, it is found that

$$\left[\frac{11600(\phi_e + V_e)}{T2} - \frac{11600\phi_e}{T_c \ T}\right] << \frac{2}{T} \qquad \text{(B-18)}$$

Equation B17 then becomes

$$\frac{\Delta I}{I} \tilde{=} \frac{2\Delta T}{T} \qquad \text{(B-19)}$$

This indicates that the percentage change in current is about twice the percentage change in temperature.

B.3 Error Analysis - Current Density Dependence on Emitter Work Function.

The space charge current relation based on emitter parameters is

$$I = AT^2 \exp\left[\frac{-e(\phi_e + V_e)}{KT}\right] \qquad \text{(B-20)}$$

Using Equation 5 of text and the potential energy diagram of Figure 1, curve C

$$V_e = V_c + \phi_c - \phi_e - V \qquad \text{(B-21)}$$

Then, substituting B21 in B20

$$I = AT^2 \exp\left[-\frac{e\ (V_c + \phi_c - V)}{KT}\right] \qquad \text{(B-22)}$$

and

$$\frac{\partial I}{\partial \phi e} = 0 \qquad \text{(B-23}$$

Thus, the current is not affected by change in emitter work function.

B.4 Error Analysis - Current Density Dependence on Mechanical Distance

The space charge limited current given by the Langmuir-Child equation (Equation 1 in text) and assuming $d \approx x_c$ is

$$I = 2.34 \times 10^{-6} \frac{V_c^{3/2}}{d^2} \qquad \text{(B-24)}$$

Therefore

$$\frac{\partial I}{\partial d} = -2(2.34 \times 10^{-6}) \frac{V_c^{3/2}}{d^3} = -2 \frac{I}{d}$$

and

$$\frac{\Delta I}{I} \cong -2 \frac{\Delta d}{d} \qquad \text{(B-25)}$$

The percentage change in current is about twice the percentage change in emitter-collector distance.

B.5 Error Analysis - Current Density Dependence on Collector Work Function.

Using Equations B21 and B24 above, the space charge current becomes

$$I = 2.34 \times 10^{-6} \frac{(V_e + \phi_e + V - \phi_c)^{3/2}}{d^2} \qquad \text{(B-26)}$$

Then differentiating

$$\frac{\partial I}{\partial \phi_c} = -\frac{3}{2} (2.34 \times 10^{-6}) \frac{V_c^{1/2}}{d^2} = \frac{3}{2} \frac{I}{V_c}$$

and

$$\frac{\Delta I}{I} \cong -\frac{3}{2} \frac{\Delta \phi_c}{V_c}$$

The percentage change in current is about 1.5 times the percentage change in collector work function referenced to the diode driving potential V_c.

B.6 Error Analysis - Current Density Dependence on Applied Voltage.

Using the same technique as in B.5 above

$$\frac{\partial I}{\partial V} = \frac{3}{2}\frac{I}{V_C}$$

and

$$\frac{\Delta I}{I} = \frac{3}{2}\frac{\Delta V}{V_C} \qquad \text{(B-28)}$$

The percentage change in current is about 1.5 times the percentage change in applied voltage referenced to the diode driving potential V_C.

APPENDIX C

PRESSURE TRANSDUCER TEST PROGRAM

OBJECT

The test program will establish the operating characteristics of the 80 psia pressure transducer developed under contract NAS 3-4170. The transducer ambient temperature range will be 1000-1600°F.

GENERAL

The transducers will be pressurized with high-purity argon. Transducer test pressures will be monitored by a room temperature transducing cell (accuracy better than 0.2% of full scale). The transducer output signal (0-5 volts) will be obtained from the transducer electrical signal conditioning system. Test pressure and transducer output data will be correlated by an X-Y recorder (accuracy of 0.2% of full scale). The transducer ambient temperature will be monitored by a W-5Re/W-26Re thermocouple in the vacuum test chamber and adjacent to the transducer housing.

PRE-TEST PROCEDURES

The pre-test procedures are intended to establish the proper operating conditions for the thermionic diode sensor. Prior to installation of the sensor, the transducer is installed in the vacuum test chamber for stress-relief exercising of the pressure capsule. The chamber temperature is raised to 1800°F and the pressure is not allowed to exceed 5×10^{-6} torr. The pressure capsule is exercised for 100 hours using two modes; manual cycling (vacuum-full scale pressure) once an hour and automatic cycling (vacuum-full

scale pressure) every three minutes. Full scale pressure is 80 psia. Following exercising, the transducer is removed from the test chamber for installation of the sensor.

1. Pre-activate the emitters, after installation in the molybdenum emitter housing, in vacuum (about 10^{-6} torr) at 2280°F for 25 minutes. The emitter housing will be mounted on its ceramic base and the lead wires preformed through the ceramic. During pre-activation, the emitter housing is set about 1/8 inch off the ceramic base and a molybdenum shim is inserted between the reference emitter and collector.
2. Assemble the thermionic diode sensor by fastening the emitter housing down on the ceramic base. Install the sensor in the transducer and adjust the active collector distance to about 0.006 inch.
3. Install the transducer in a vacuum test chamber. Raise the test chamber temperature until the thermocouple indicates a transducer ambient temperature of 1800°F. The chamber pressure should not be allowed to exceed 5×10^{-8} torr.
4. Energize the sensor heater and raise the emitter temperature to 2280°F as measured by the W-5Re/W-26Re thermocouple installed on the emitter housing. Apply 10 volts to the diode to draw active and reference collector currents. For an emitter-collector distance of about 0.006 inch, the current level is 40 milli-amperes minimum. Maintain sensor operation at 2280°F emitter temperature and 10 volts for 15 minutes, after which lower the emitter temperature to its operating level of 2100°F.

5. Connect the transducer signal conditioning system and determine the diode space-charge characteristics by measuring the active and reference collector currents as a function of increased voltage. Vary the voltage from 0 to 15 volts and, using the X-Y recorder, plot the results on cartesian coordinates with emitter-collector distance as a parameter related through theoretical space-charge formulae. Using the space-charge plots, determine the active collector and reference collector distances. Also determine whether any emission limiting effects (poisoning) occur at applied voltages up to 15 volts. This poisoning effect shows up as a limit on the current that may be drawn from the emitter. As the voltage is increased the current not only doesn't increase, but may even decrease. Since the thermionic sensor must operate in the space-charge limited region, any emission-limited condition will introduce error into the output signal and must be avoided.

6. The 1800°F space-charge characteristics should indicate that the active and reference collector distances are about equal (within .001 inch). If not, remove the transducer from the test chamber, install a new pre-activated thermionic diode sensor and readjust the active collector distance so that it is equal to the reference collector distance as determined by the space-charge data. Install the transducer in the test chamber and perform the pre-test procedures leading to the space-charge tests of (5) above to determine the active collector and reference

distances. Repeat the procedure until the active collector and reference collector distances are shown to be about equal ($i_a \cong i_r$) by the space-charge data.

7. Continue 1800°F operation with about 10 volts applied to the diode until steady-state operation has been achieved. This condition will be reached when no further increases are noticed, with time, in the active and/or reference collector currents. The currents should be stable for at least twelve hours. During this period, space-charge data should be collected (5) above to monitor operation of the emitters.
8. When the 1800°F space-charge characteristics indicate that steady-state emission has been achieved and the active and reference distances are about equal, so that $i_a \cong i_r$, obtain a set of pressure-output data by varying the transducer pressurization from zero to full scale and back to zero. Full scale pressure is 80 psia. The signal conditioning system should be adjusted for zero pressure output and a full scale output of about 5 volts. The pressure-output data will be used to correlate the data obtained during the main part of the test program.

TEST PROGRAM

1. Following emitter activation and adjustment of the active collector distance (if necessary), the transducer is ready for the main part of the test program. During testing, the basic ambient temperature will be set at 1600°F and the test chamber pressure should not be allowed to exceed 10^{-7} torr.

2. Vary the transducer pressurization from zero to full scale and back to zero. Full scale pressure is 80 psia. Monitor the pressure and transducer output with the X-Y recorder. From the test results, evaluate the transducer accuracy, including the effects of linearity, hysteresis, sensitivity, zero shift and repeatability, by comparing the pressure-output characteristics with a $\pm$ 5% envelope drawn around a 0-5 volts full-scale linear response.
3. Repeat (2) above at capsule temperatures of 1400, 1200, 1000, 1200, 1400 and 1600. In addition to transducer accuracy, evaluate the zero shift due to capsule temperature change.
4. Using a solenoid operated valve to switch the transducer from the argon pressurization line to the vacuum line, pressure cycle (vacuum-full scale pressure-vacuum) the transducer once every three minutes. For the 2000 hour life test program, continue the pressure cycling for 400 hours. The transducer is cycled between 0-80 psia. Perform pressure-output spot checks during the test using the X-Y recorder. Evaluate the transducer accuracy as a function of test time.
5. Repeat steps 2, 3 and 4 above five times for the 2000 hour life test program.
6. During the 2000 hour test, establish an ambient temperature of 1800°F once during each 100 hours of testing and obtain pressure-output for this condition. Compare the data obtained at 1800°F with that obtained at the other test temperatures.

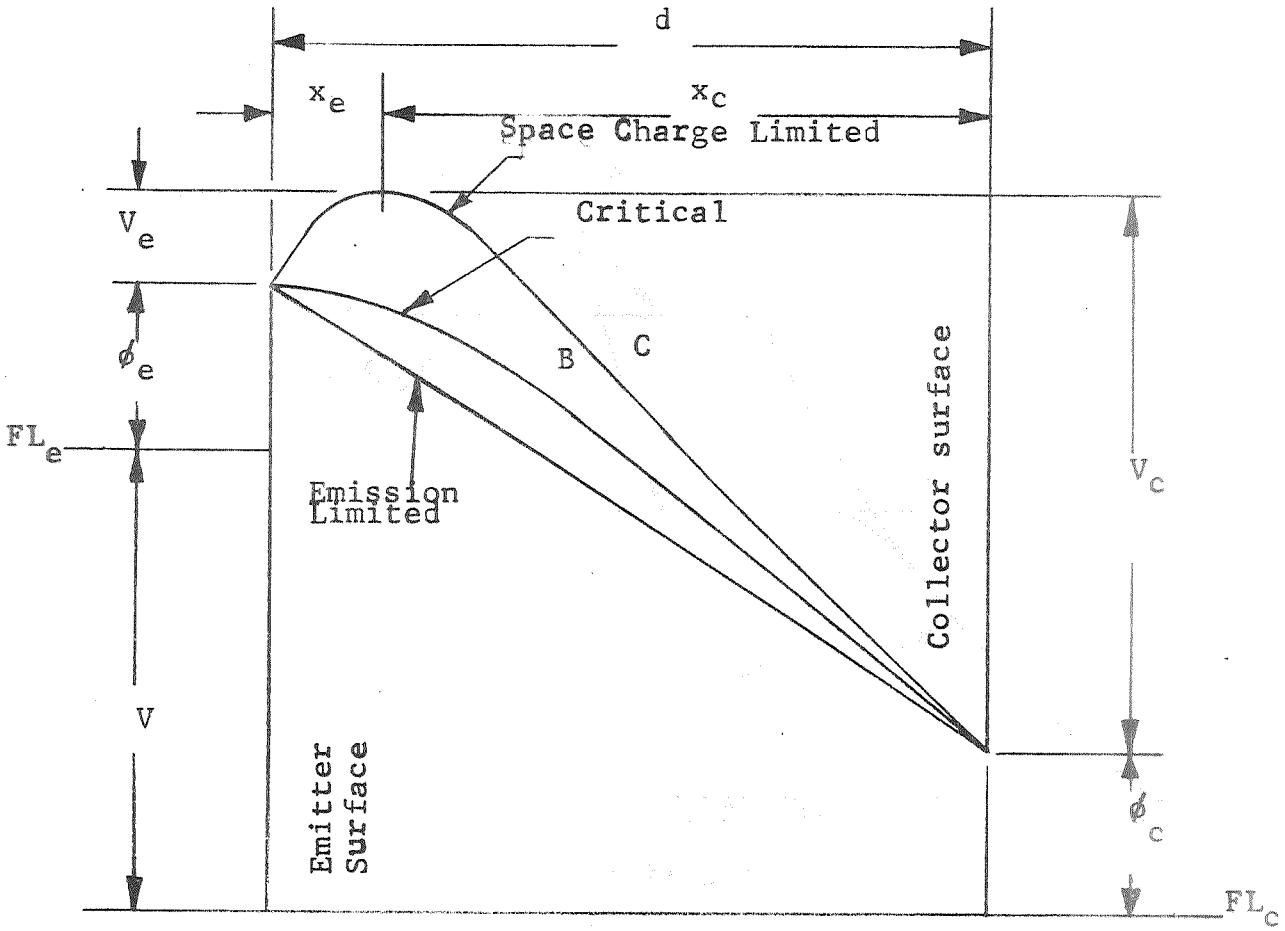


Figure 1

Electron Potential Energy Diagram

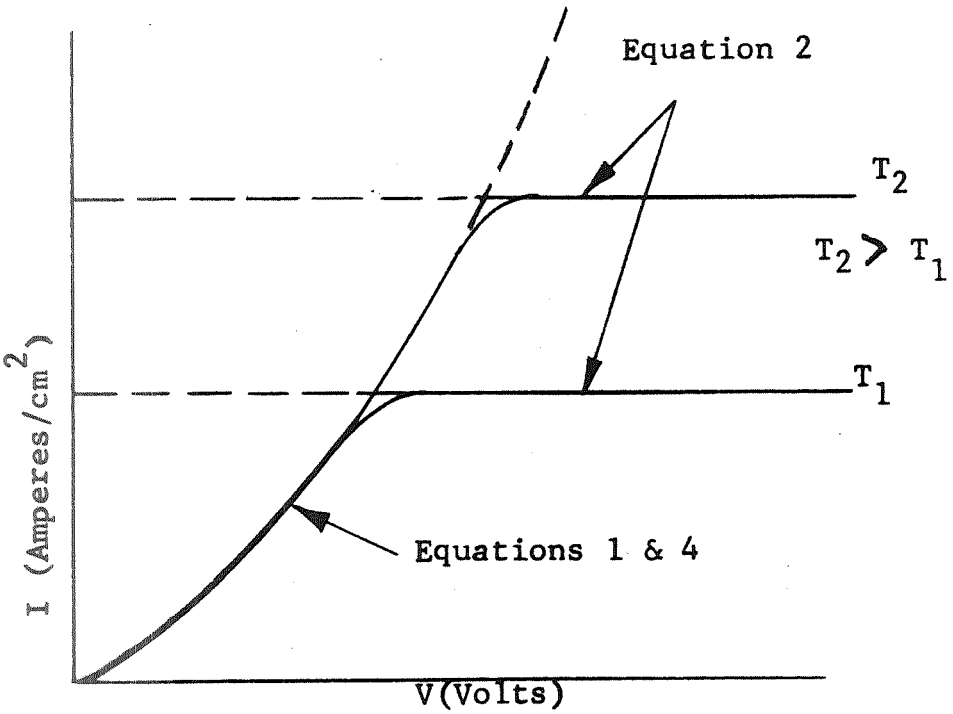


Figure 2

Current-Voltage Relation at Constant Temperature

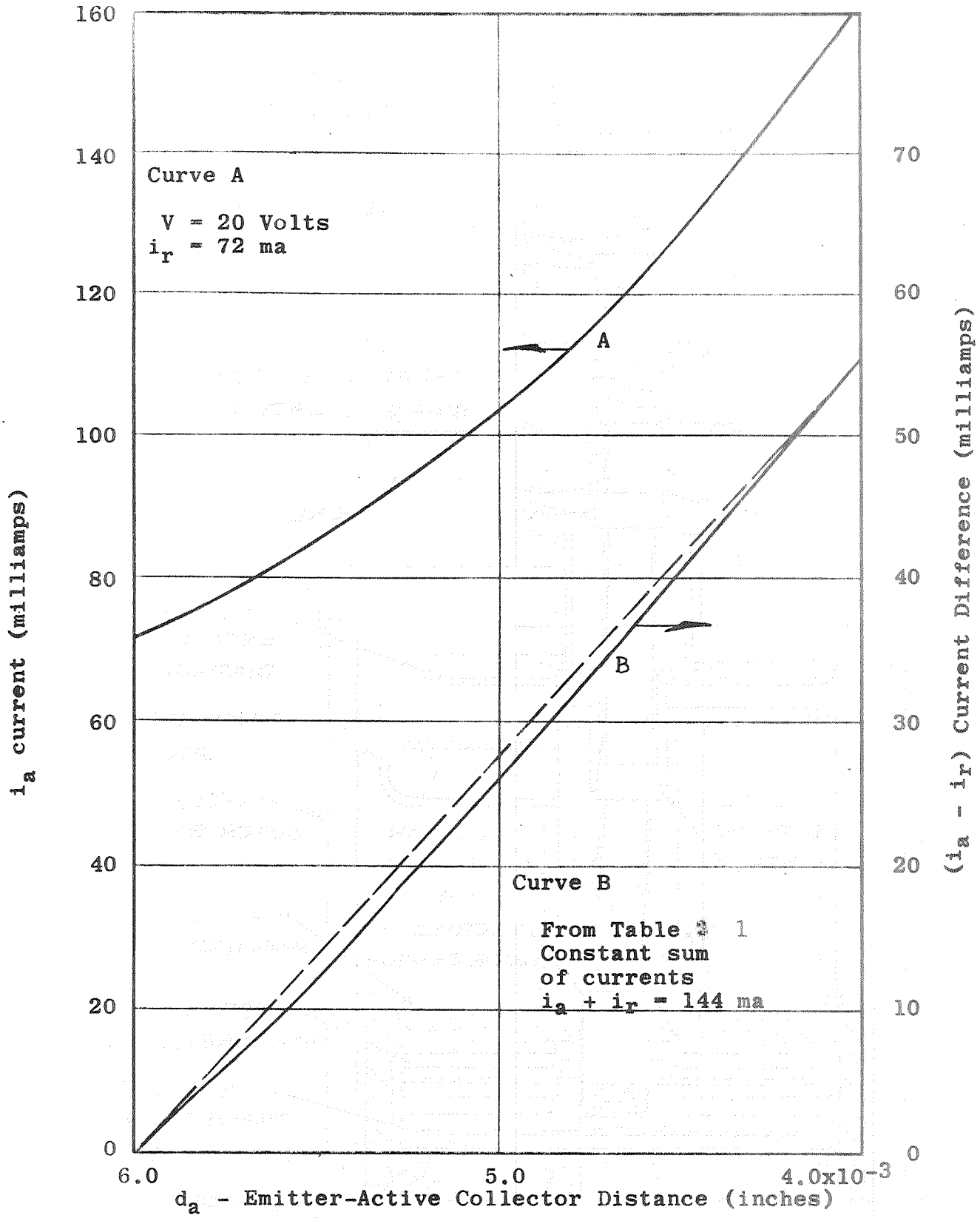


Figure 3
Thermionic Output
Signal Curves

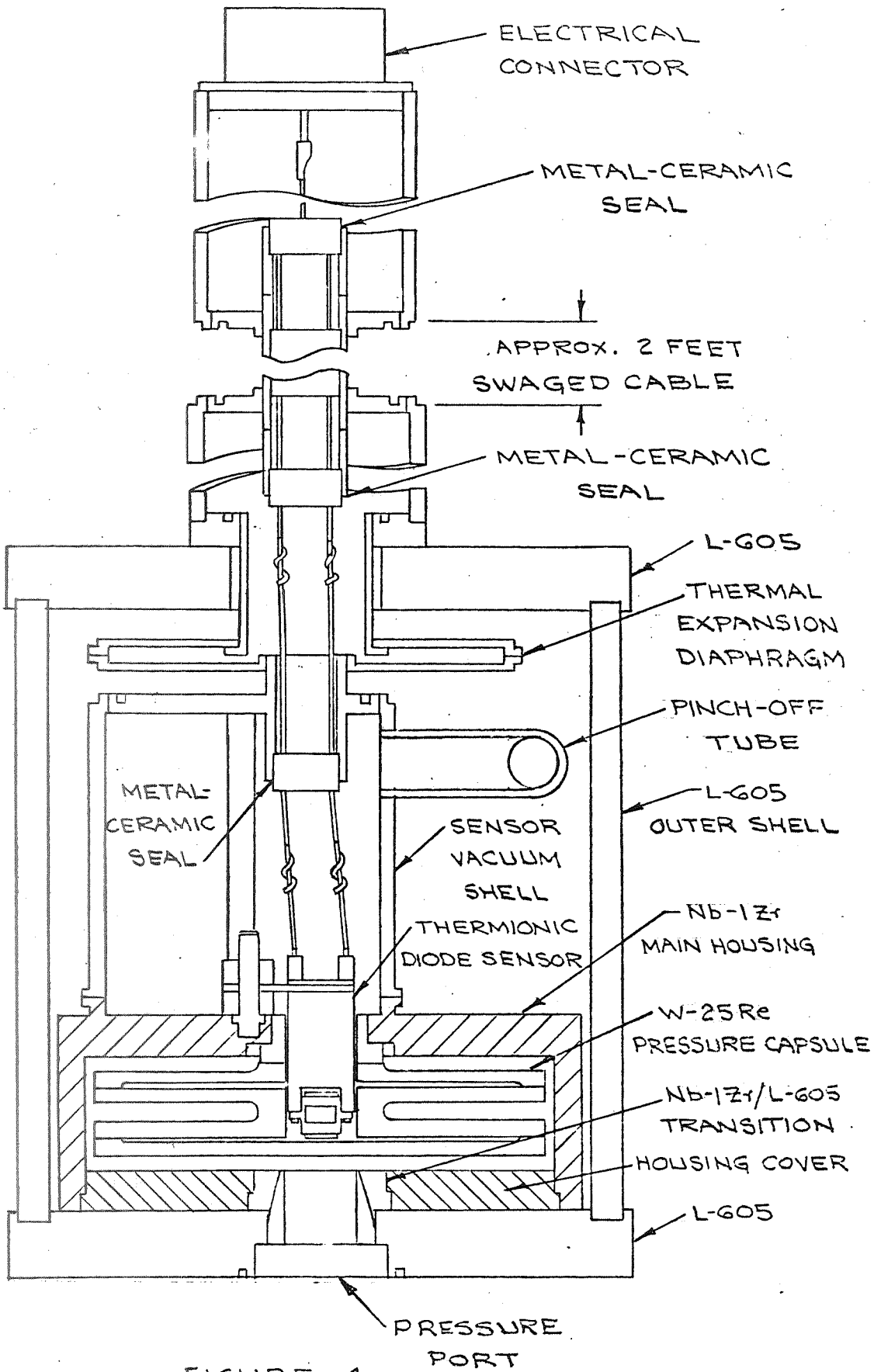


FIGURE 4

ABSOLUTE PRESSURE TRANSDUCER

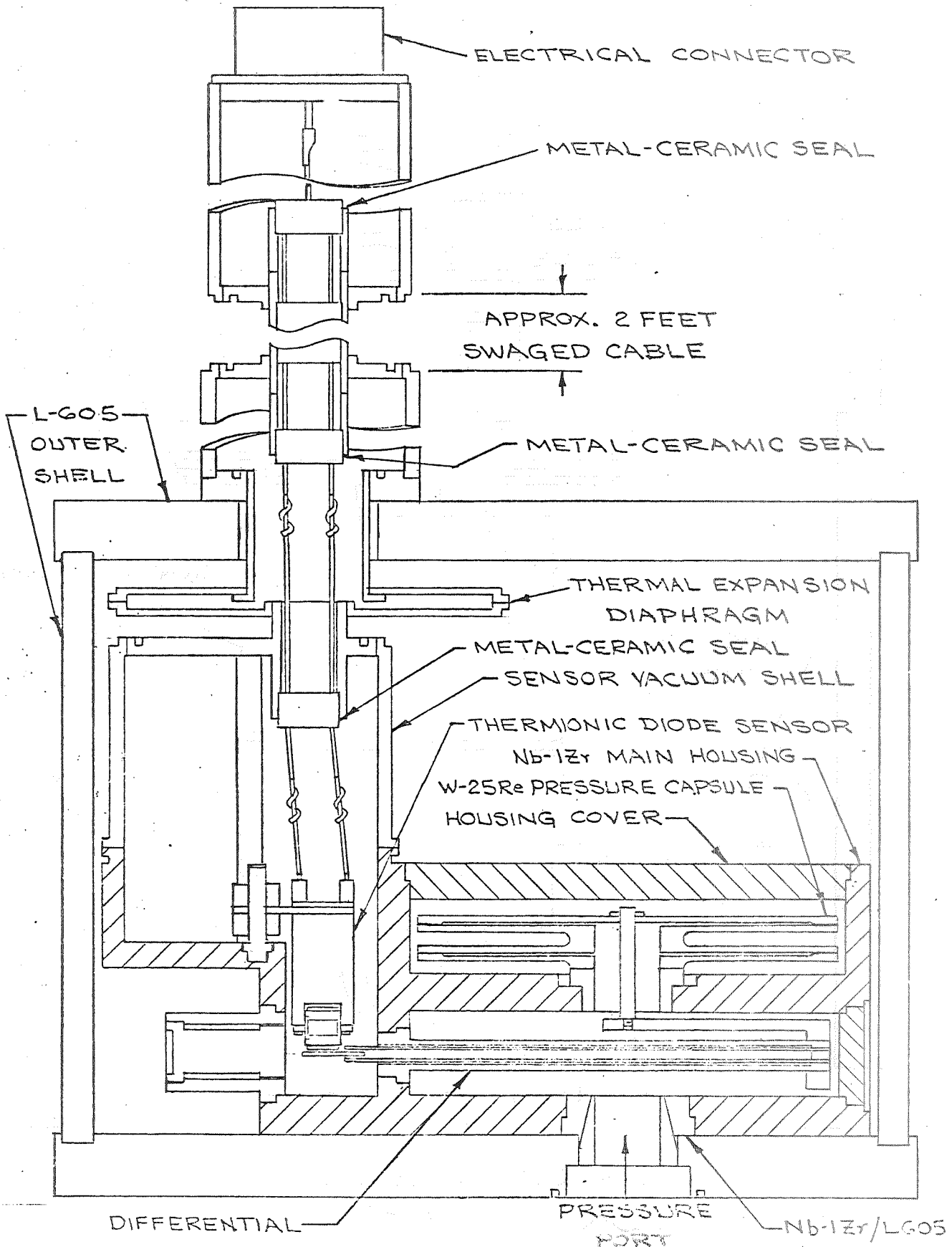


FIGURE 5

DIFFERENTIAL PRESSURE TRANSDUCER

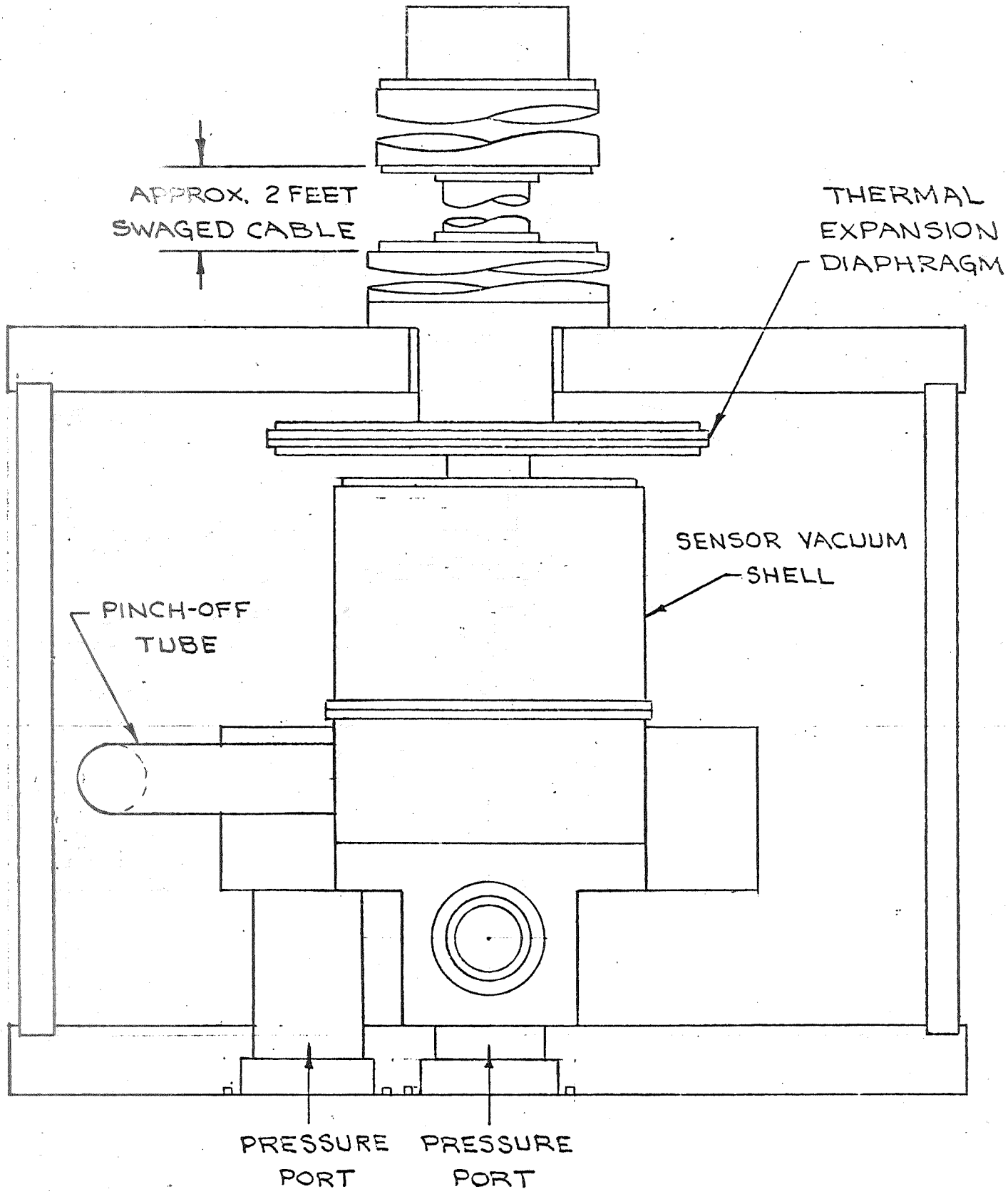
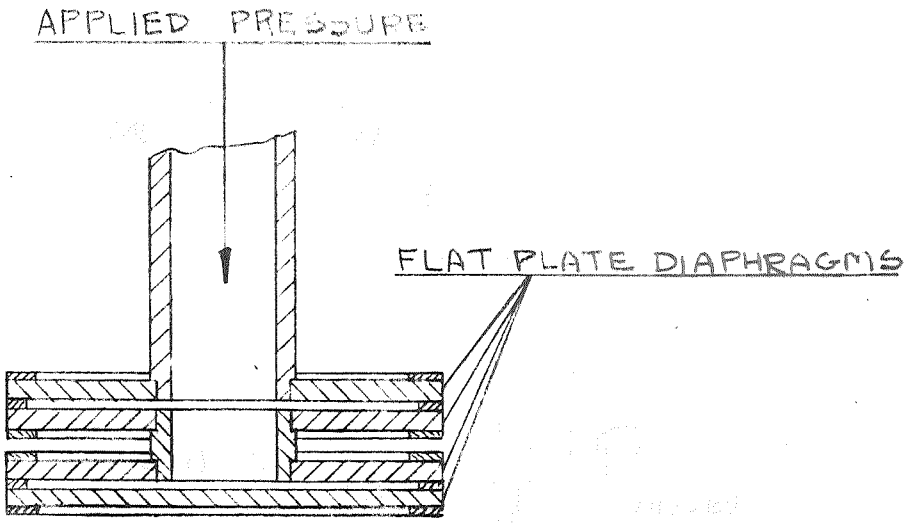
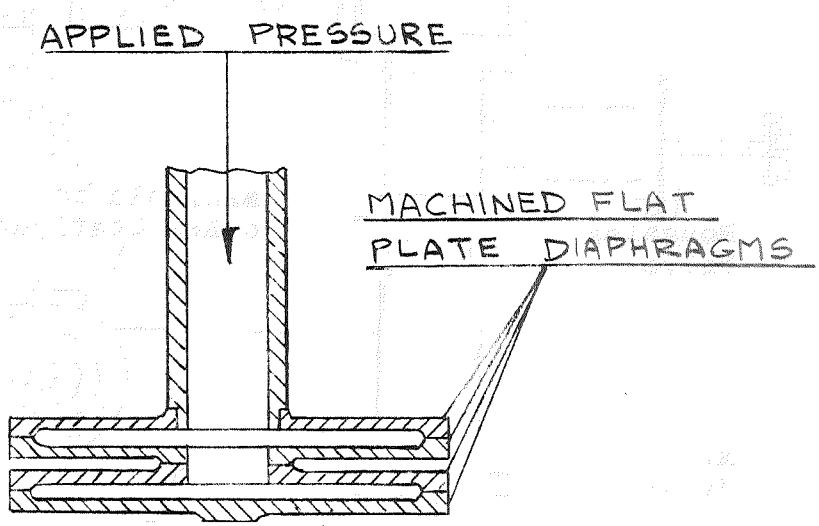


FIGURE 6

DIFFERENTIAL PRESSURE TRANSDUCER



Ring/Plate Diaphragm Design



Machined Diaphragm Design

Figure 7

Test Pressure Capsule Configurations

-

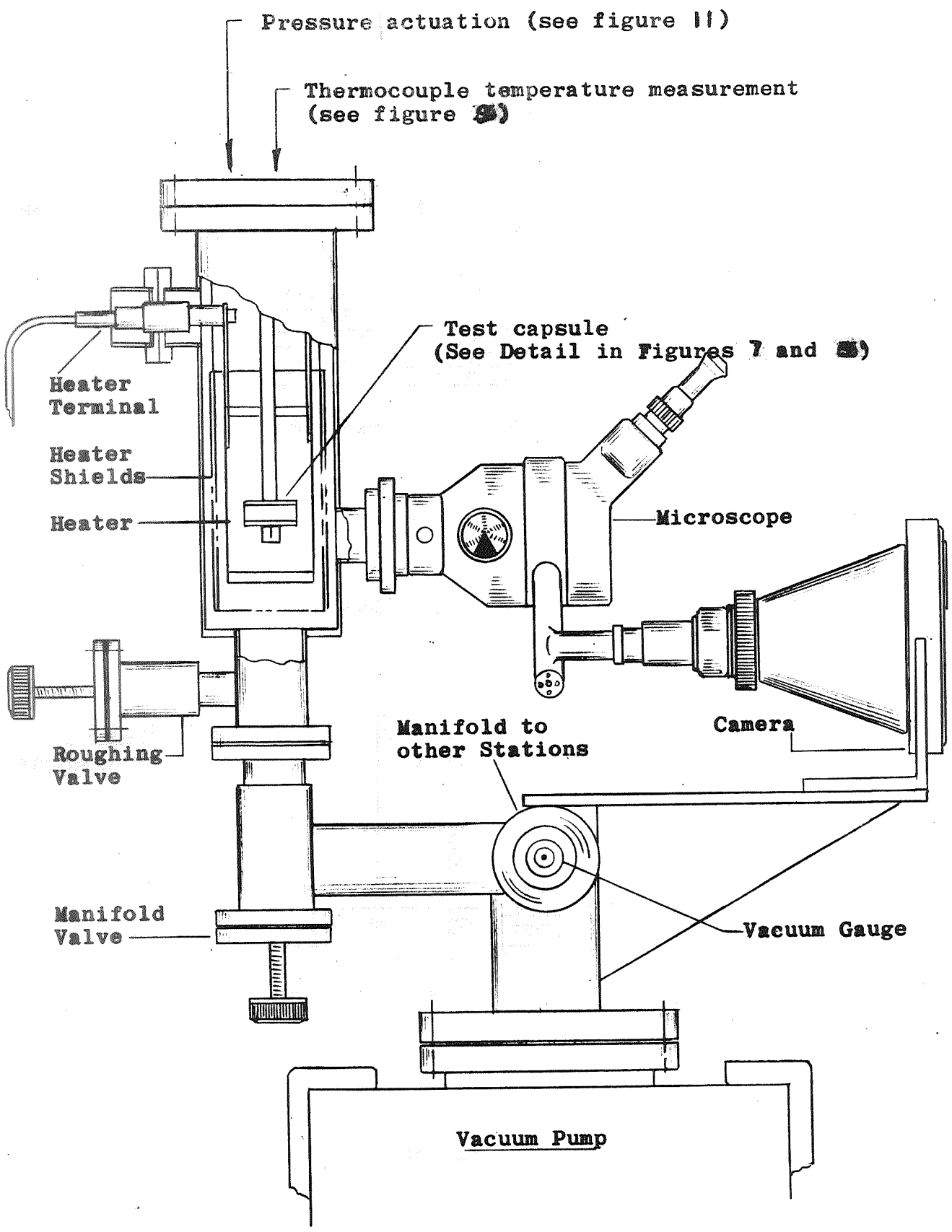


Figure 3

Test Facility for Fuel Element

Vacuum Test Facility Test Station

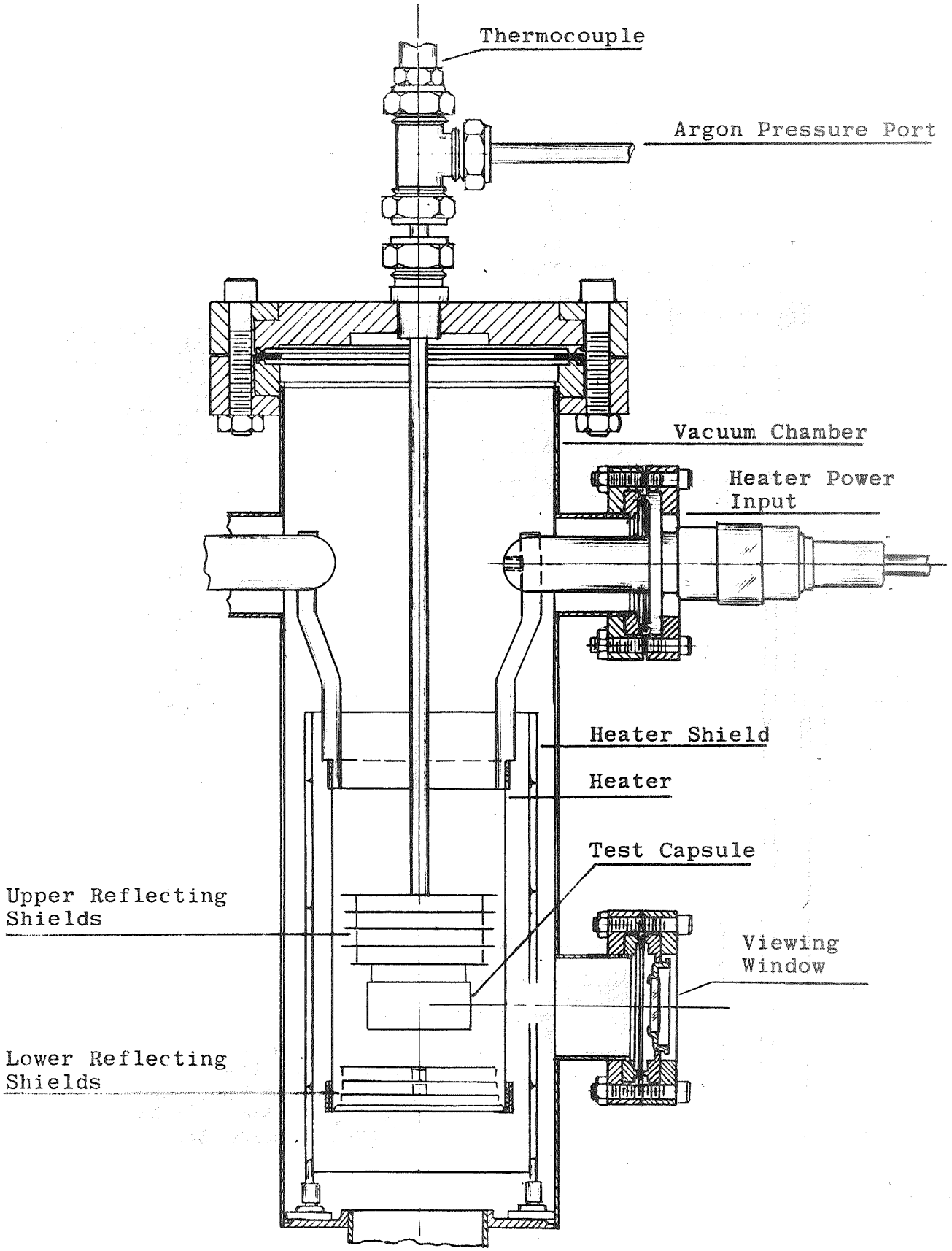


Figure 1

Vacuum Test Chamber For Pressure

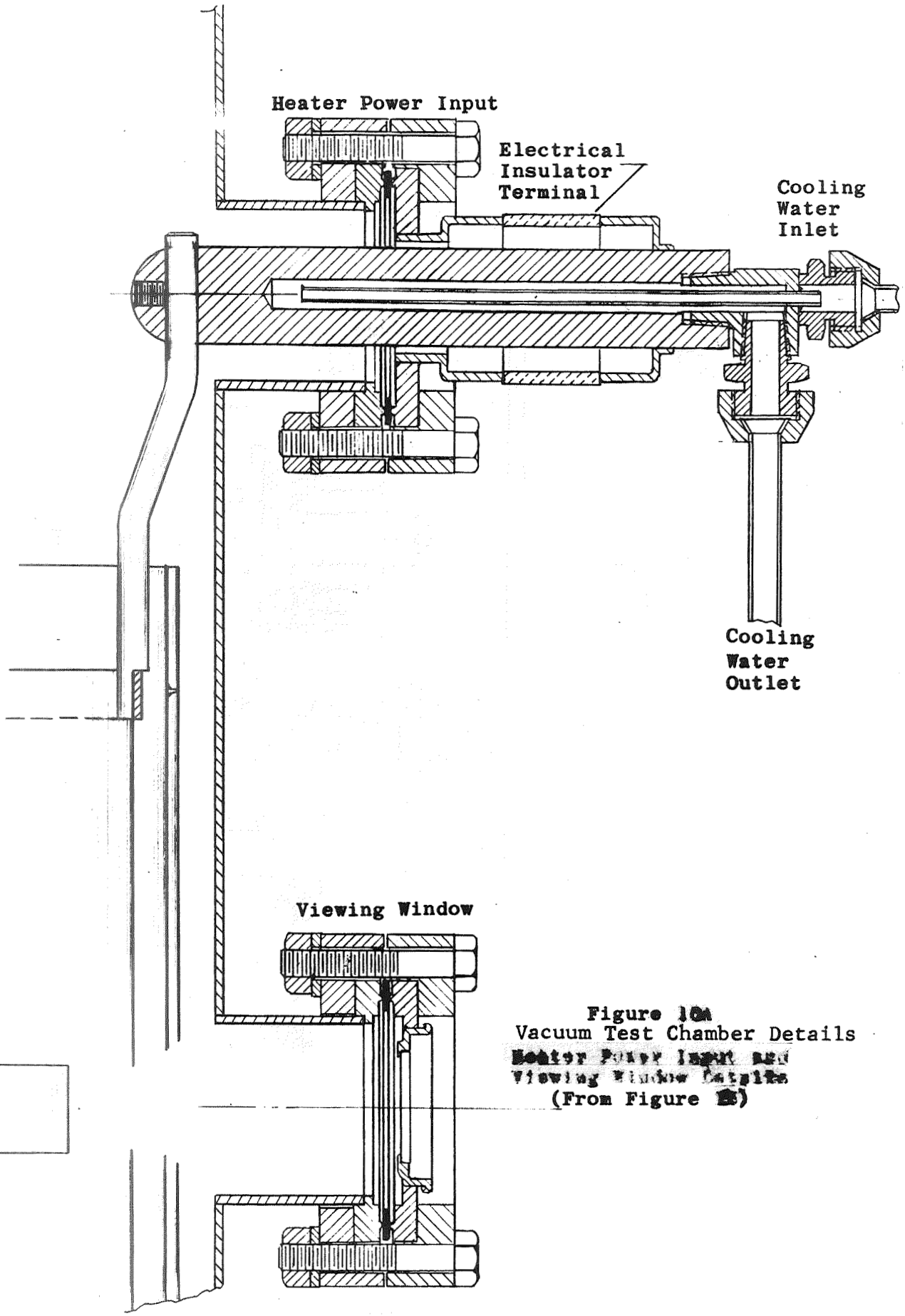


Figure 10A
Vacuum Test Chamber Details
Heater Power Input and
Viewing Window Details
(From Figure 8)

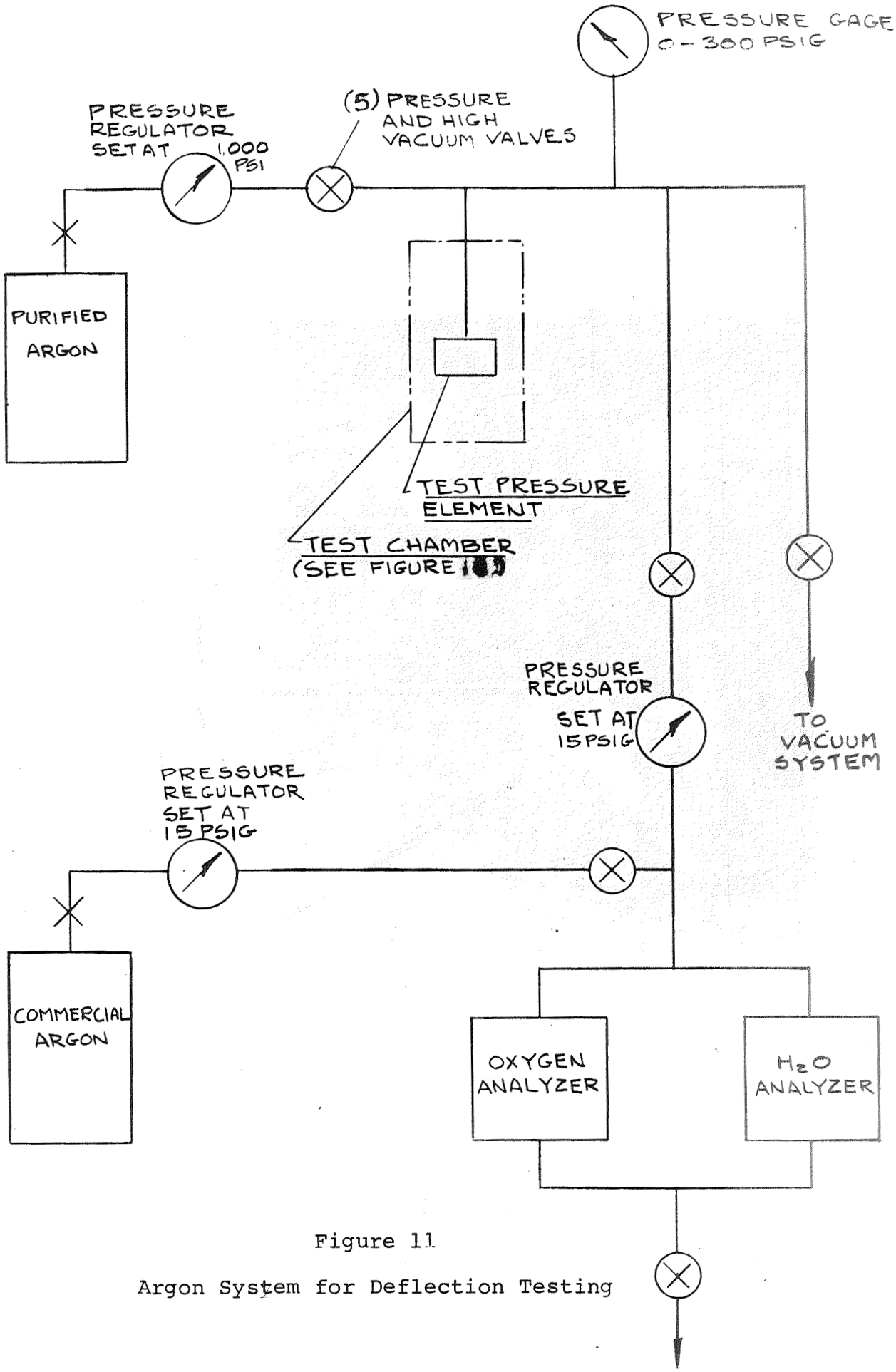


Figure 11

Argon System for Deflection Testing

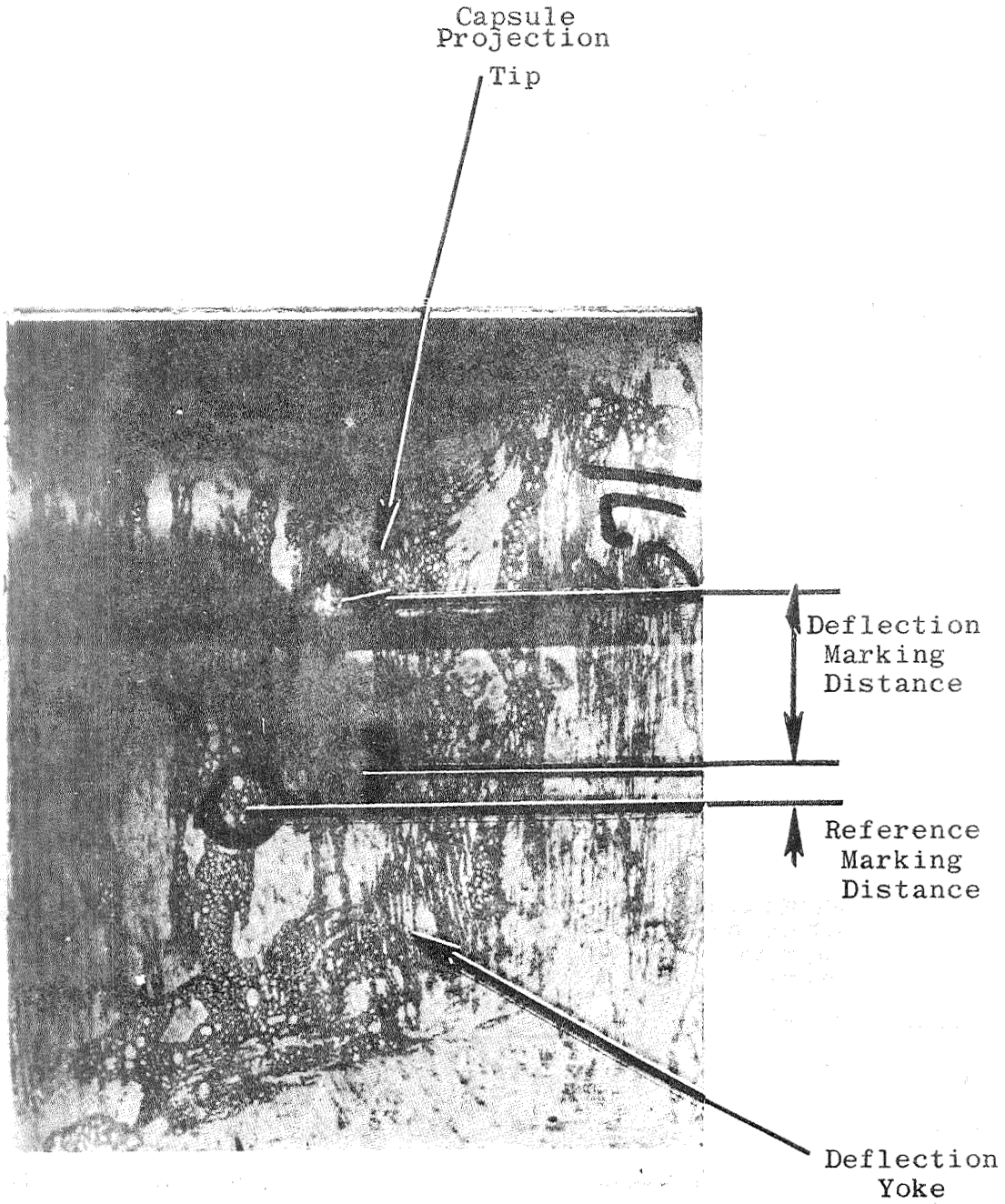


Figure 12

Typical Metallographic Plate

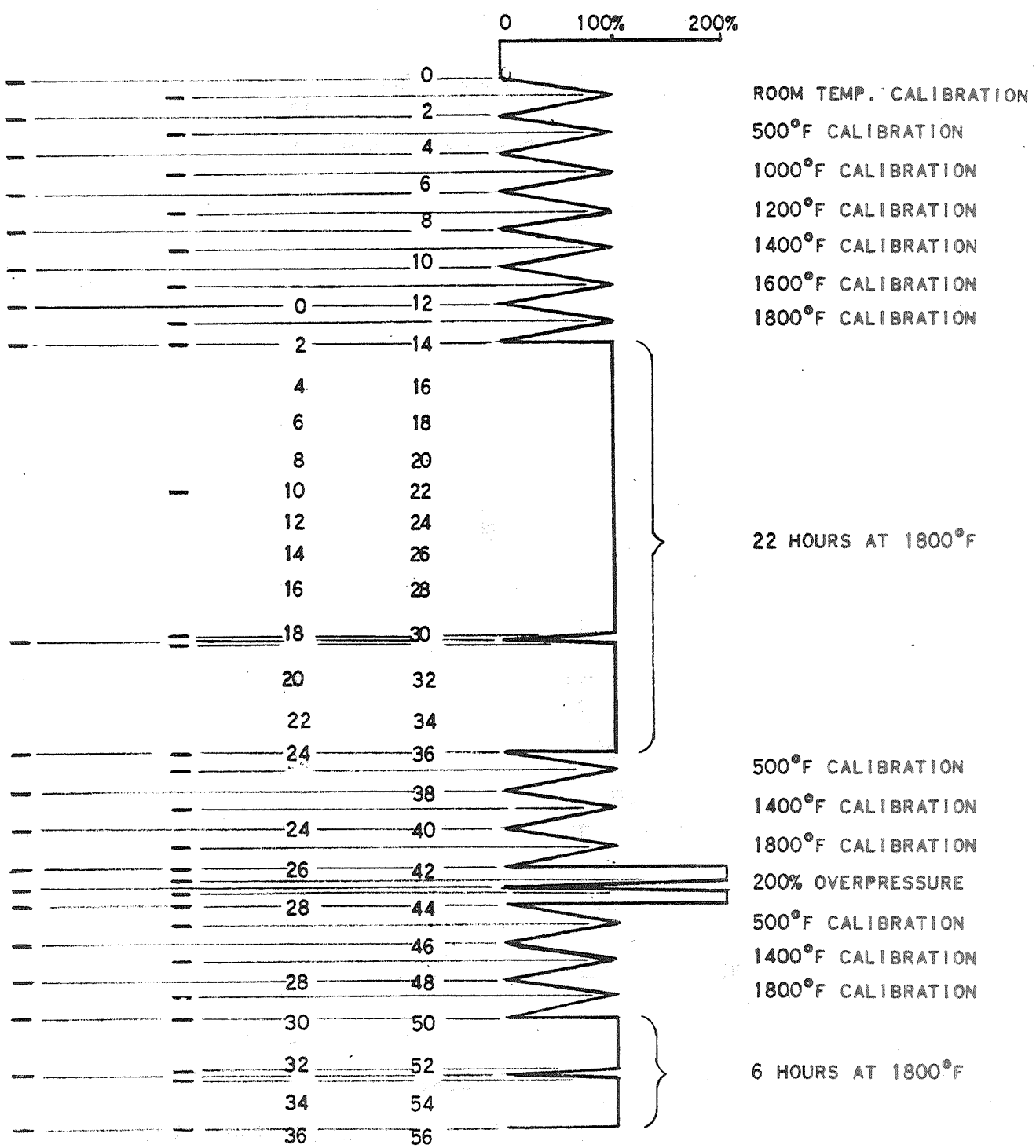


FIGURE 13

DEFLECTION TEST CHRONOLOGY

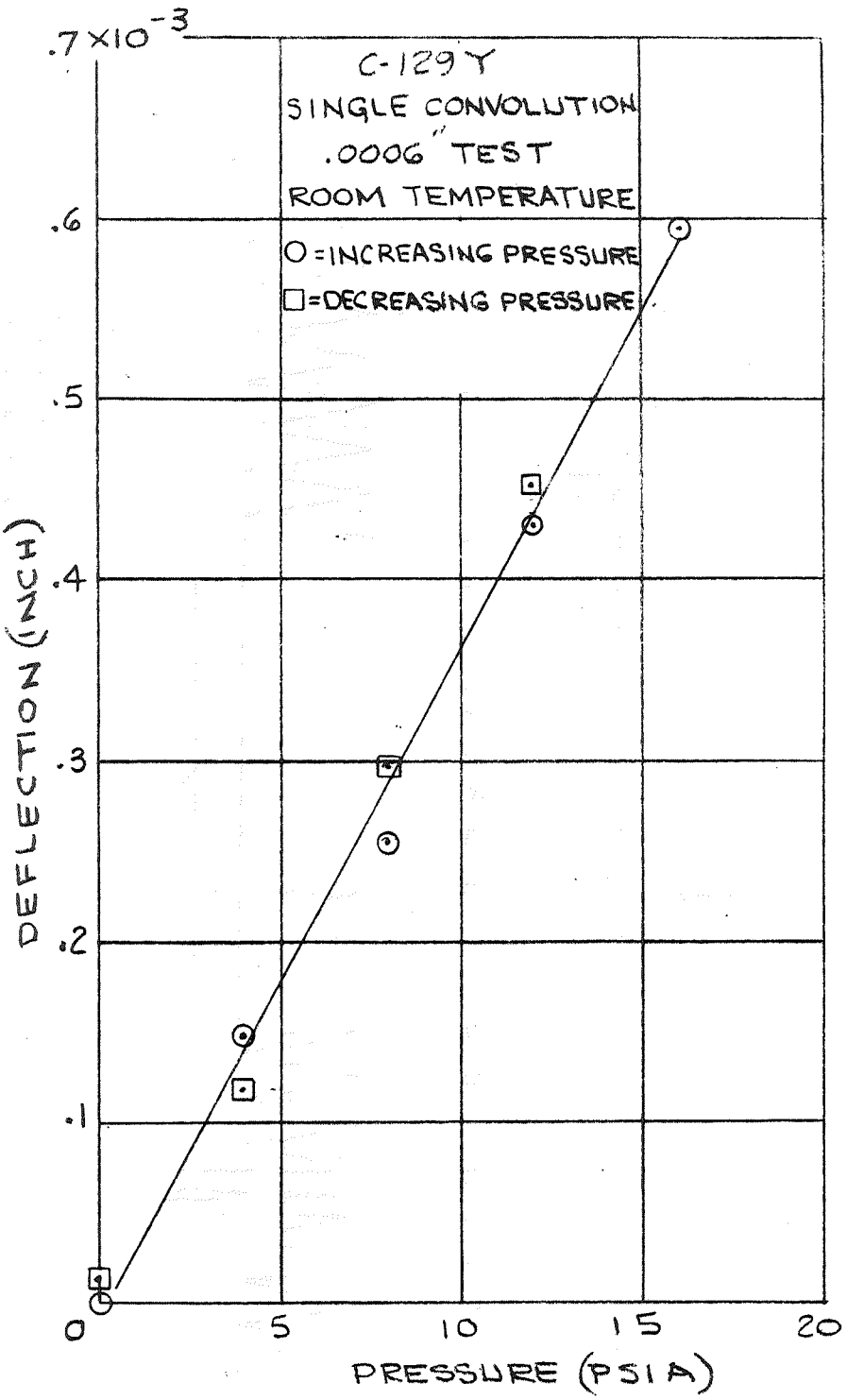


FIGURE 14

C-129Y PRESSURE-DEFLECTION, ROOM TEMPERATURE

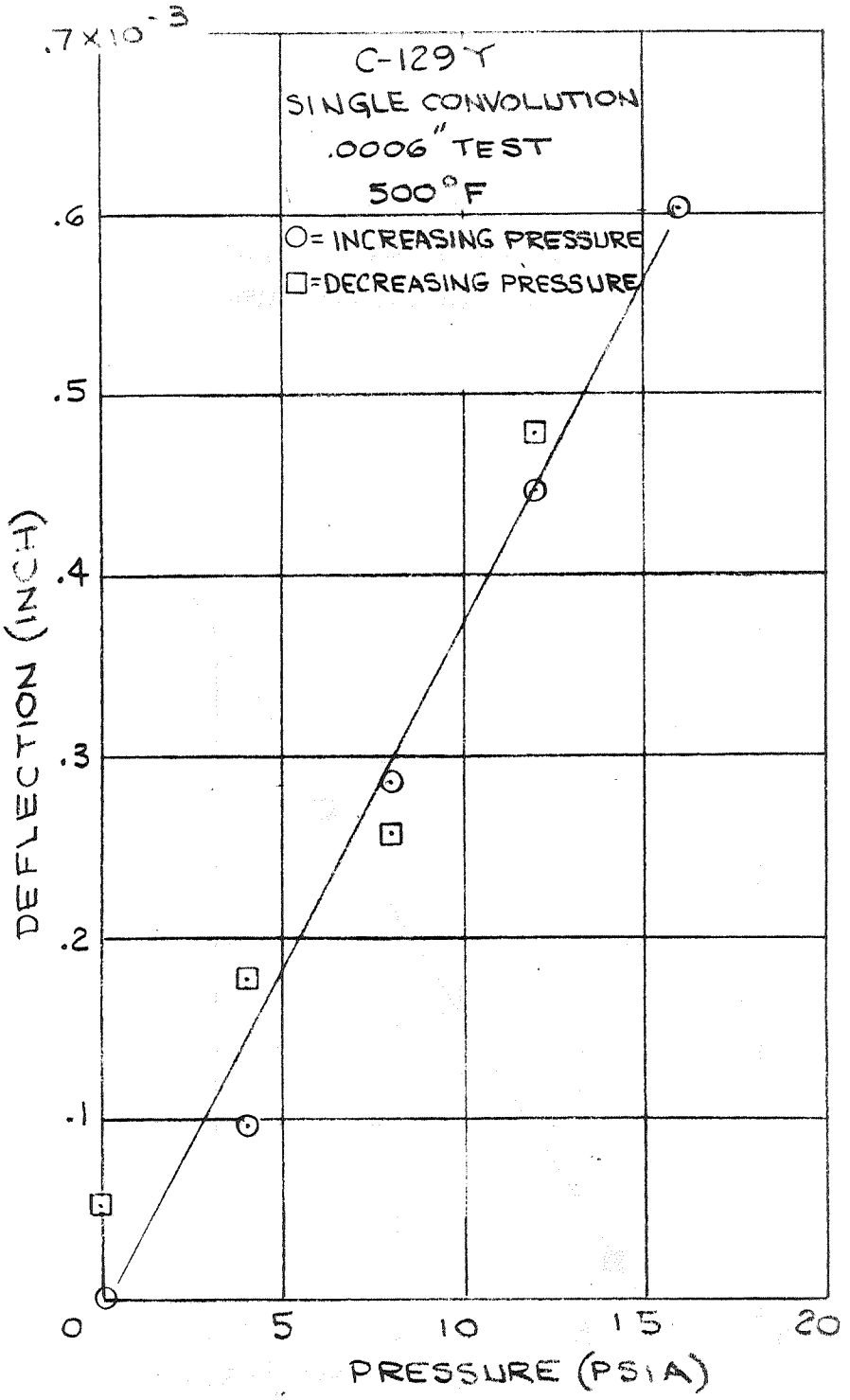


FIGURE 15

C-129Y PRESSURE-DEFLECTION, 500°F

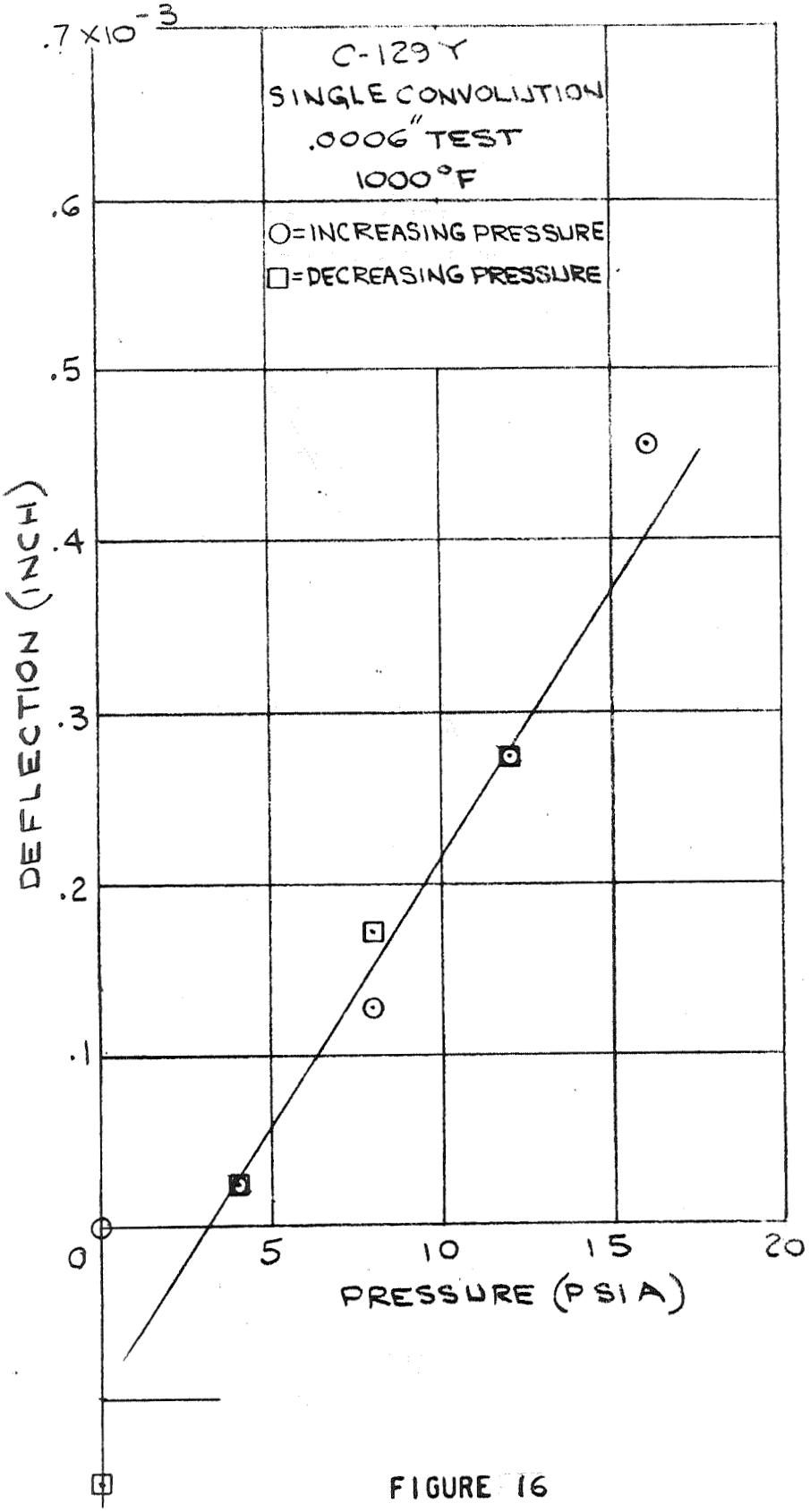


FIGURE 16

C-129Y PRESSURE-DEFLECTION, 1000°F

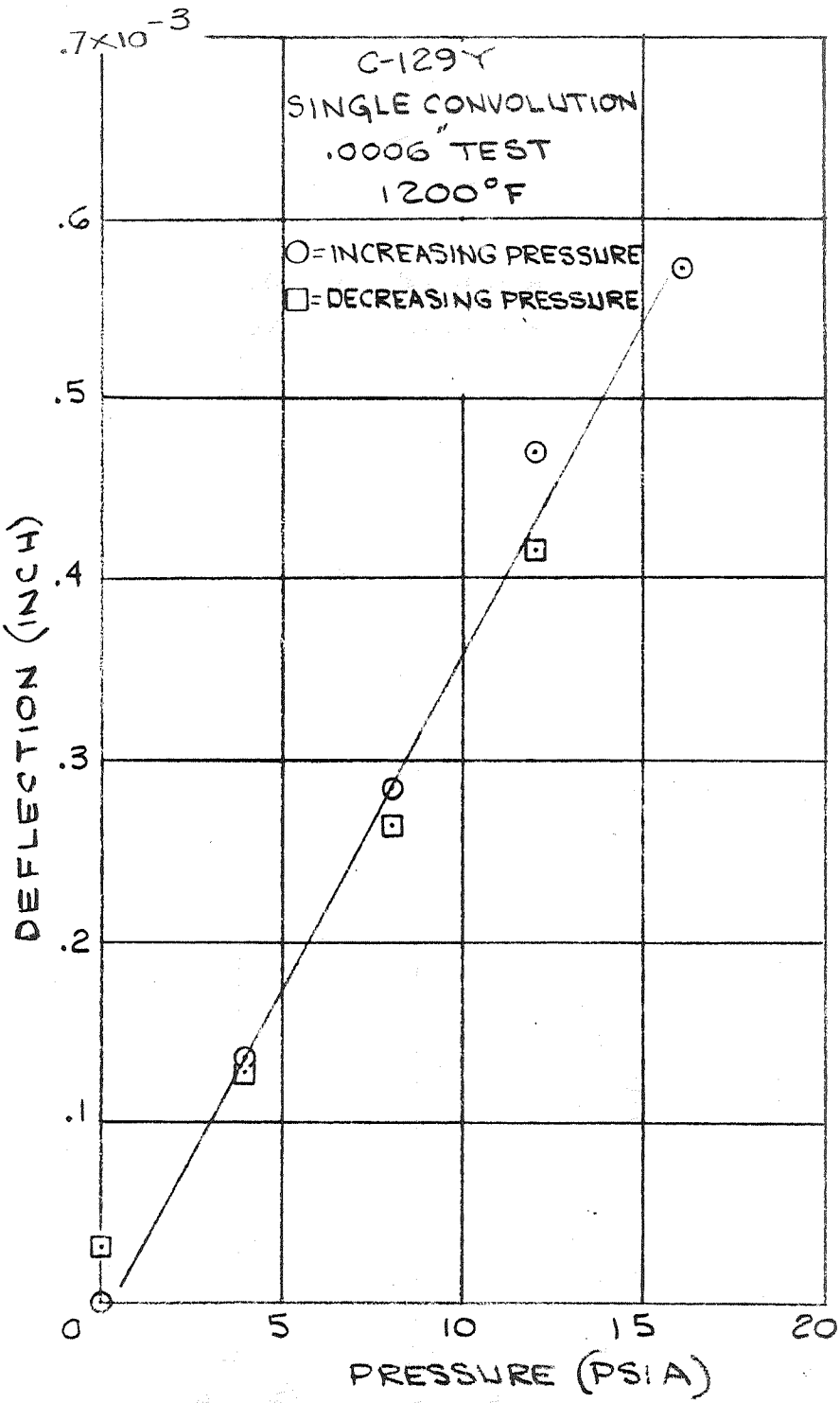


FIGURE 17

C-129Y PRESSURE-DEFLECTION, 1200°F

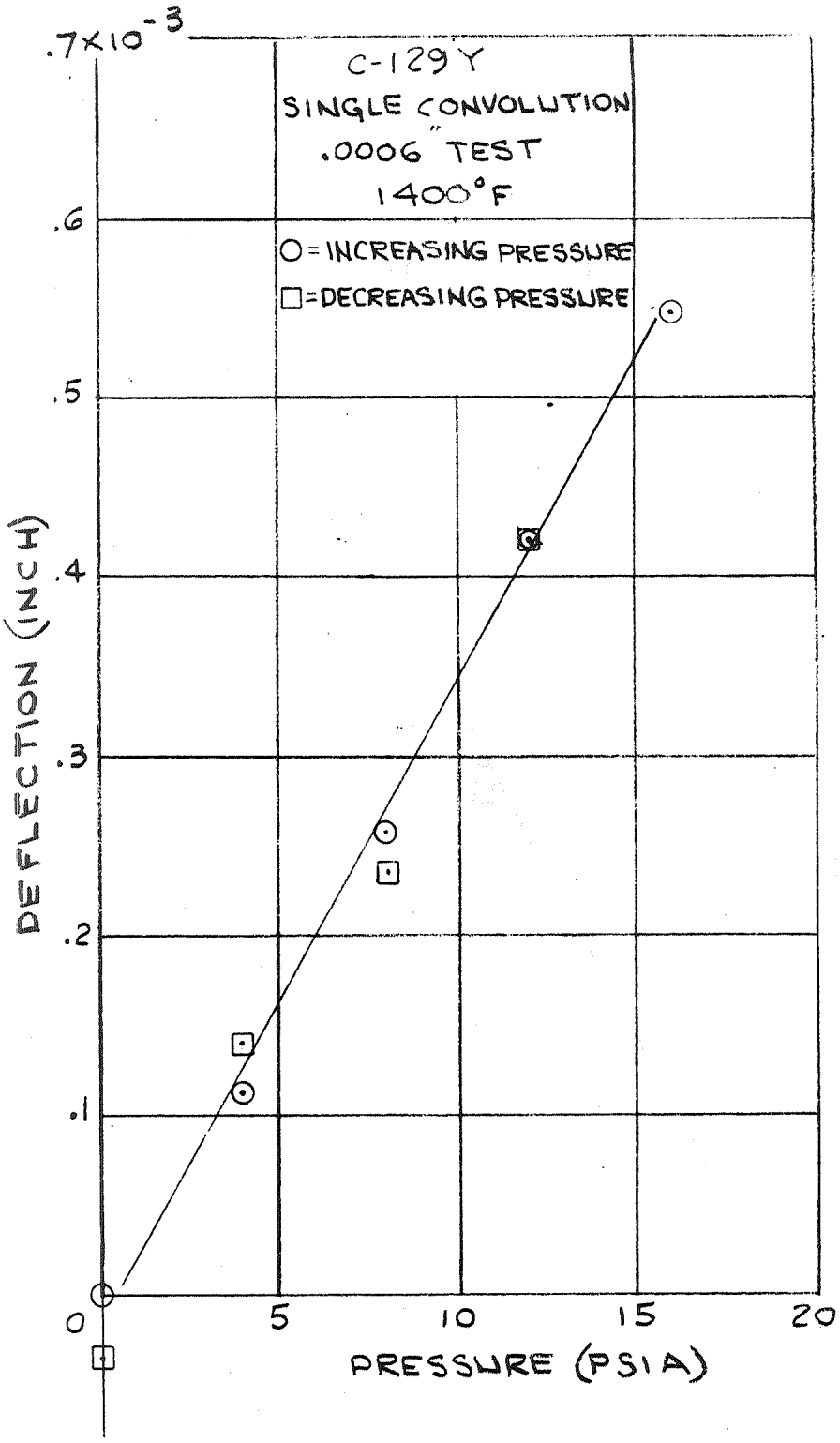


FIGURE 18

C-129Y PRESSURE-DEFLECTION, 1400°F

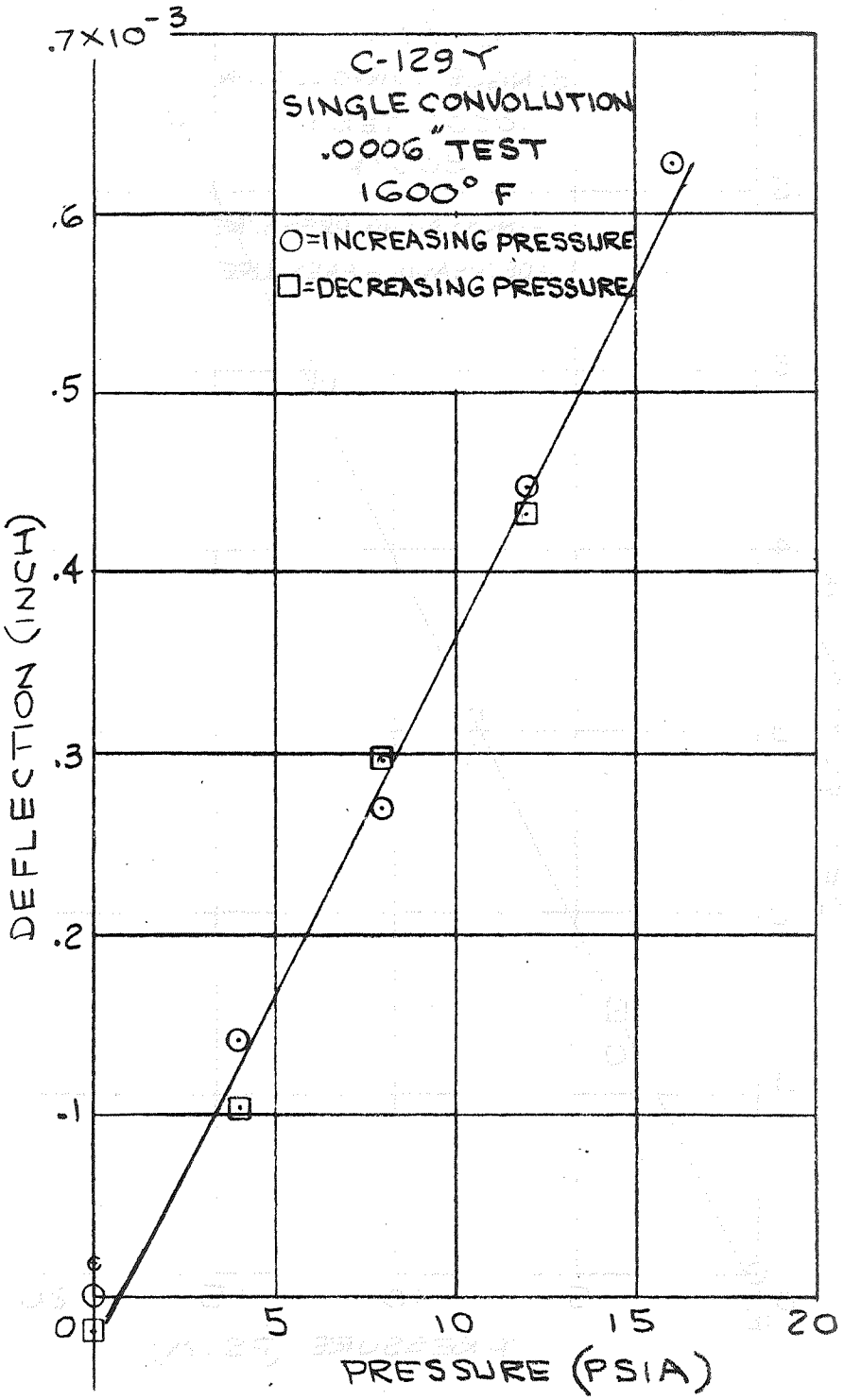


FIGURE 19

C-129 PRESSURE-DEFLECTION, 1600°F

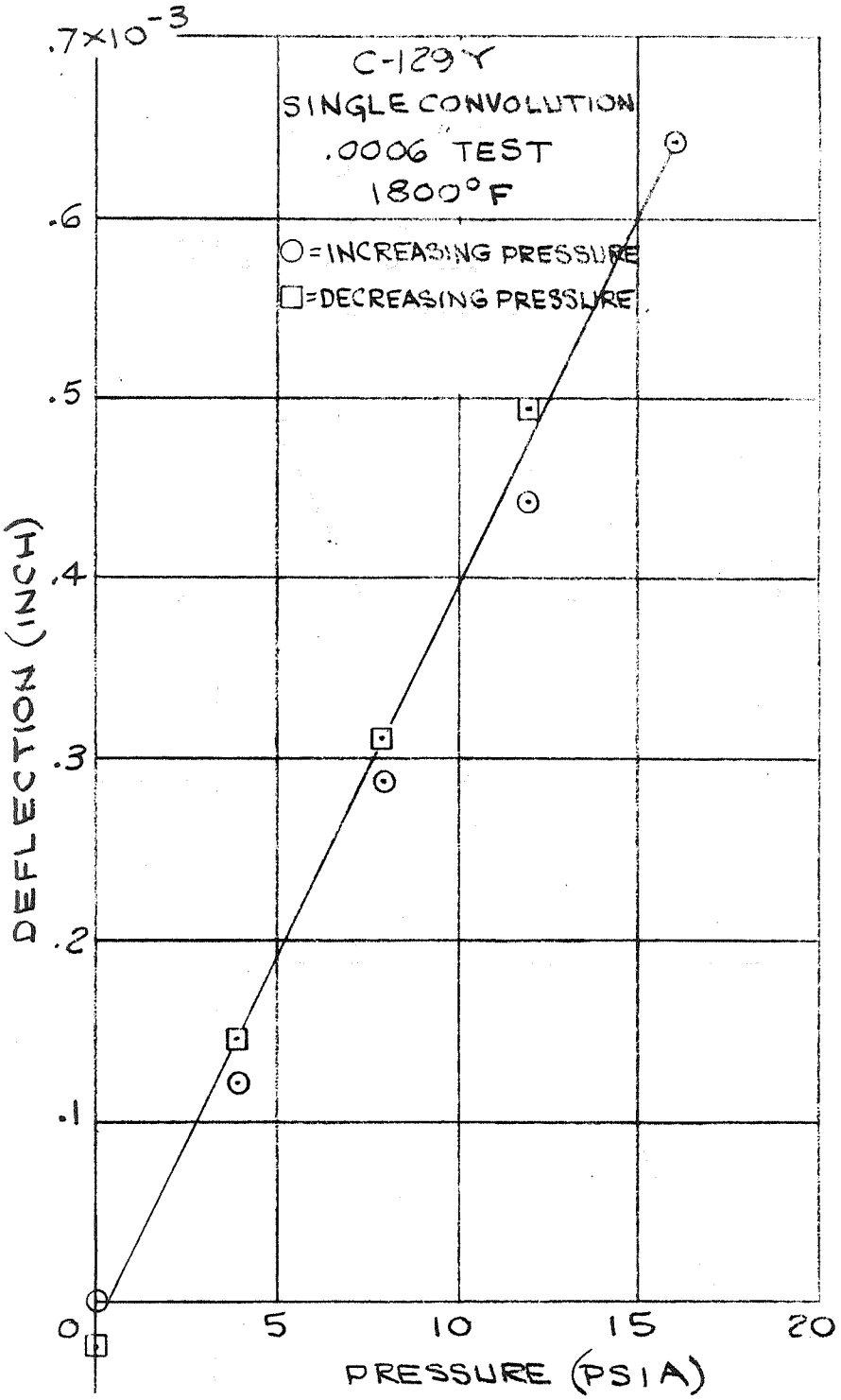


FIGURE 20

C-129Y PRESSURE-DEFLECTION, 1800°F

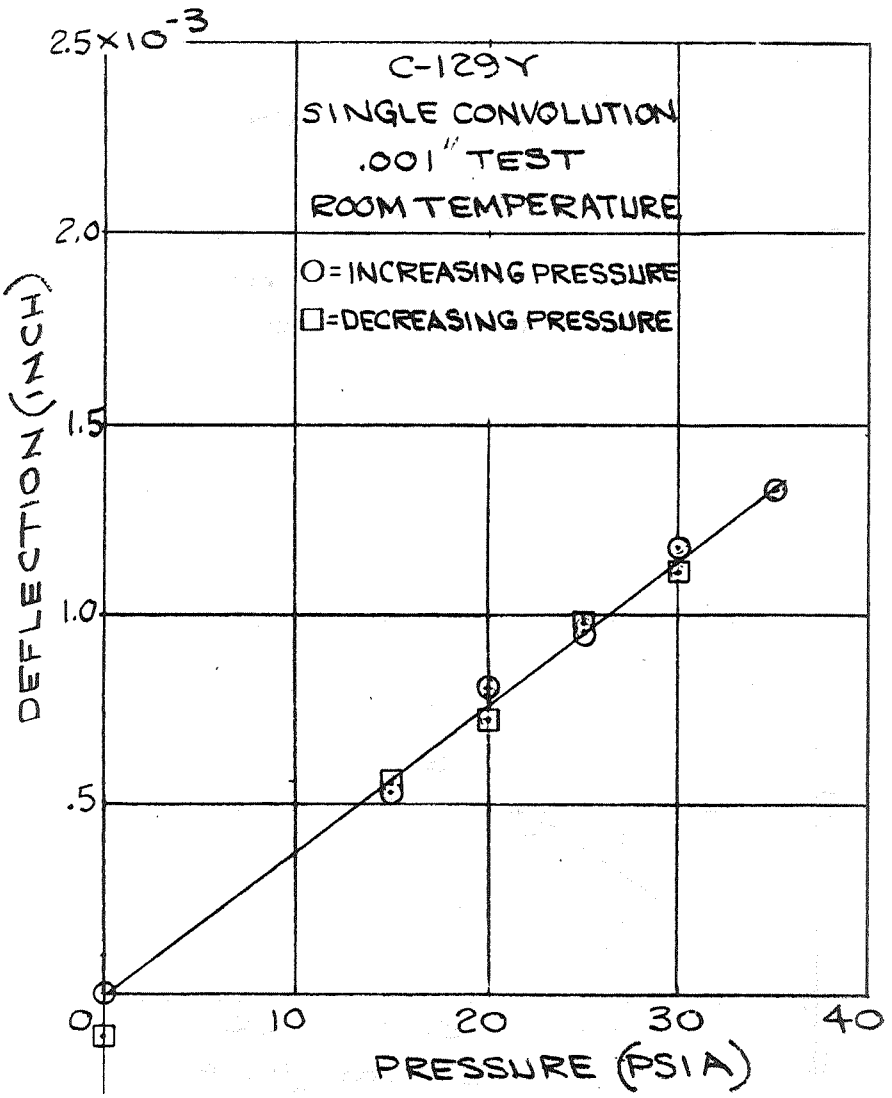


FIGURE 21

C-129Y PRESSURE-DEFLECTION, ROOM TEMPERATURE

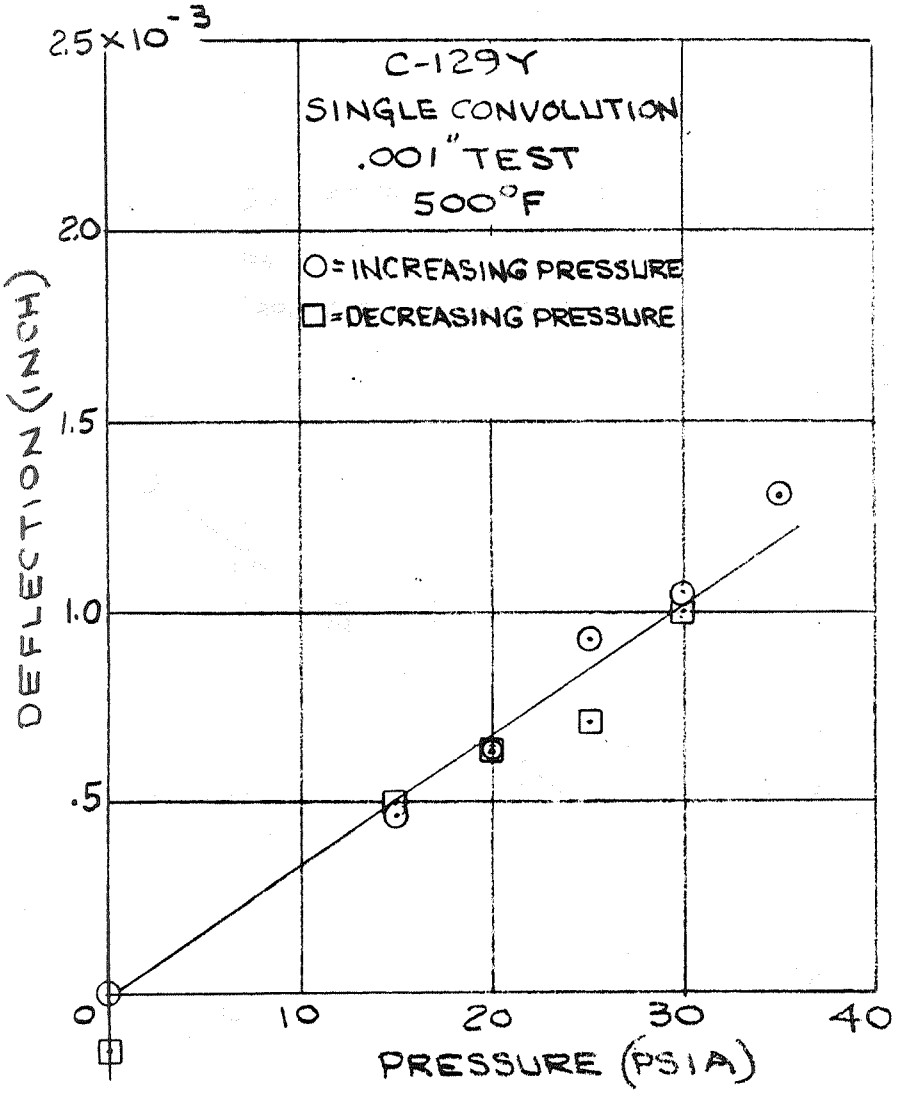


FIGURE 22

C-129Y PRESSURE-DEFLECTION, 500°F

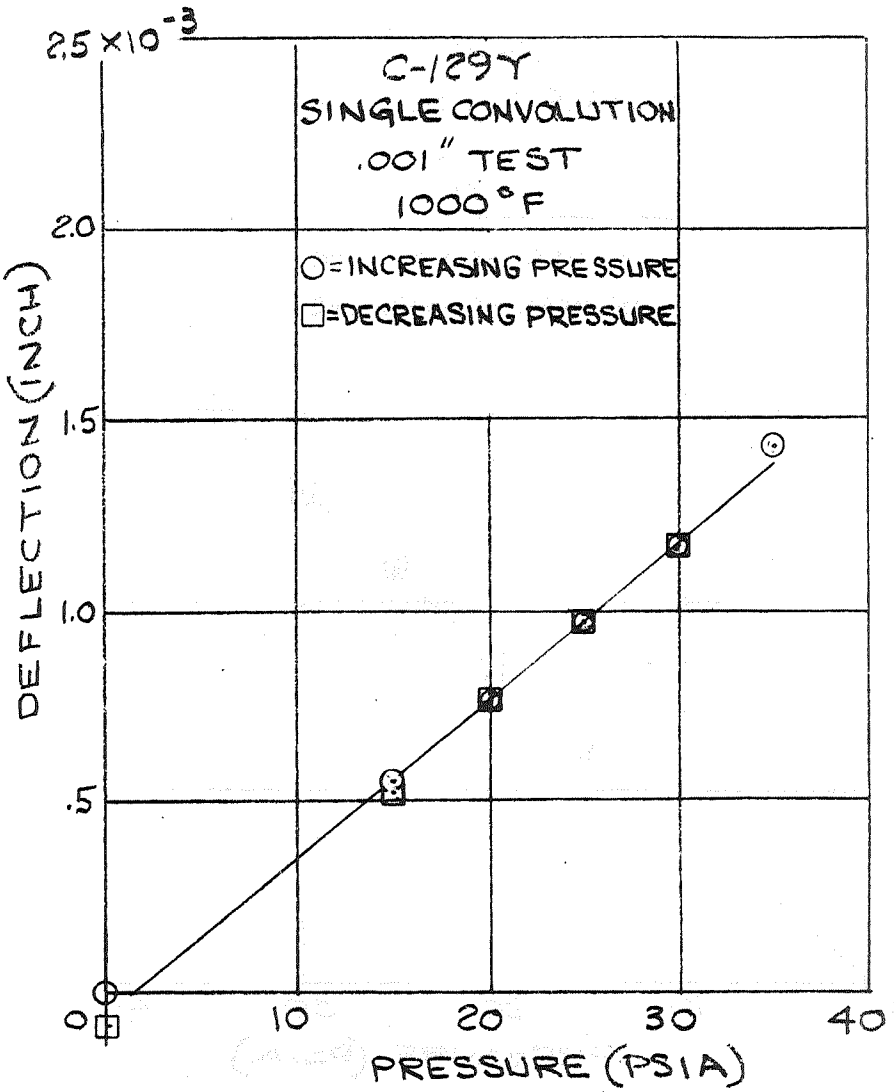


FIGURE 23

C-129Y PRESSURE-DEFLECTION, 1000°F

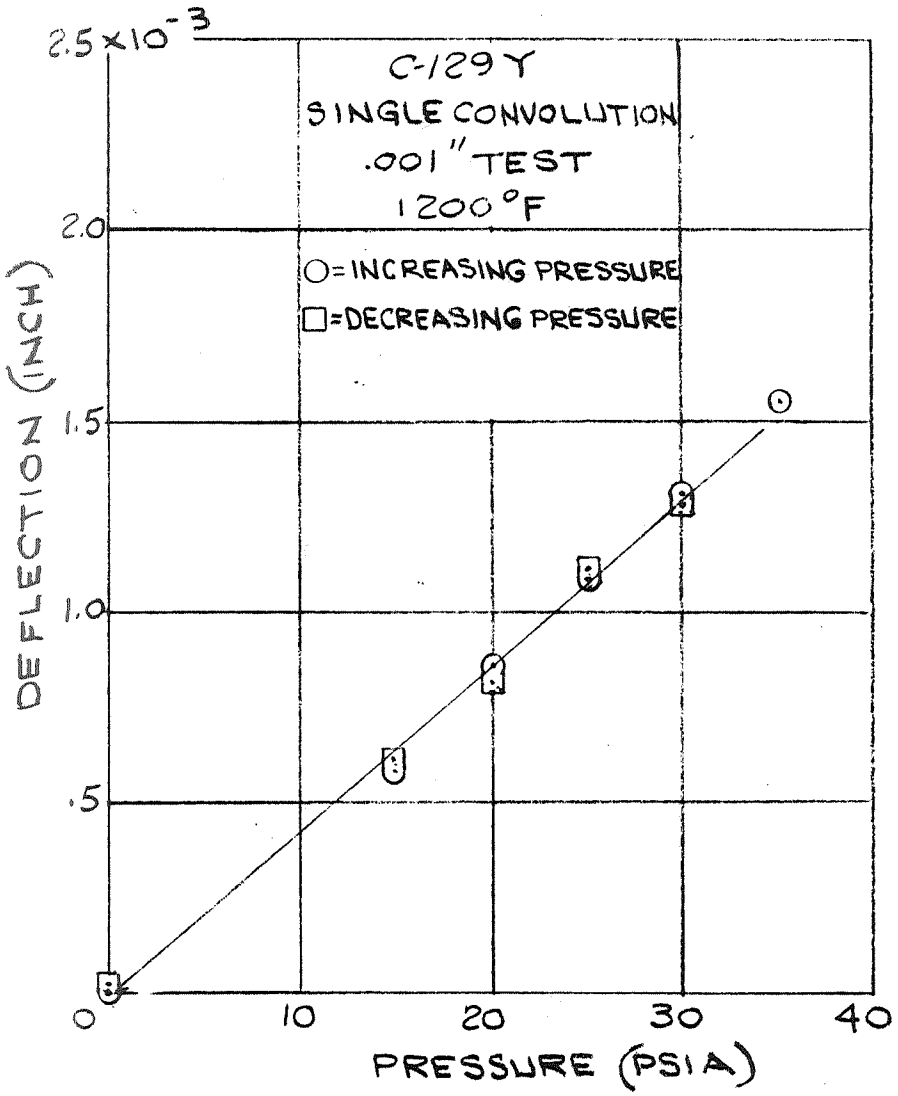


FIGURE 24

C-129Y PRESSURE-DEFLECTION, 1200°F

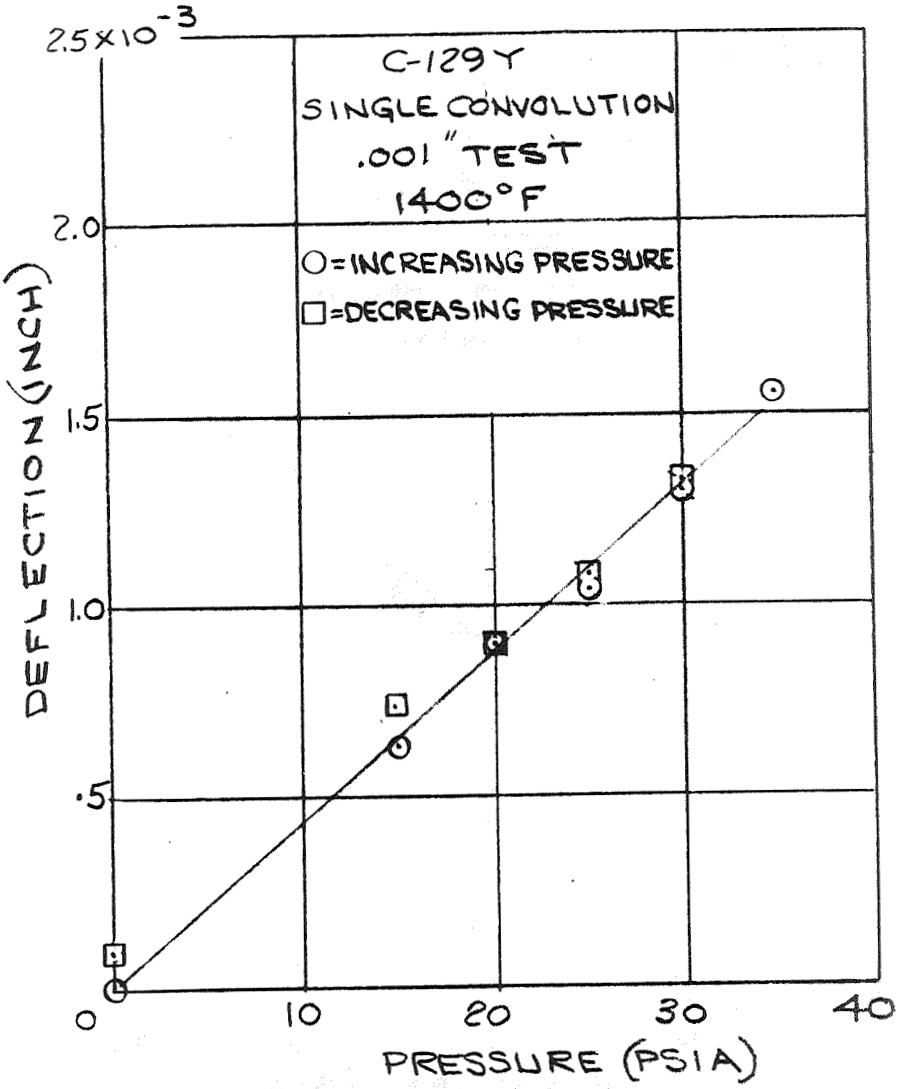


FIGURE 25

C-129Y PRESSURE-DEFLECTION 1400°F

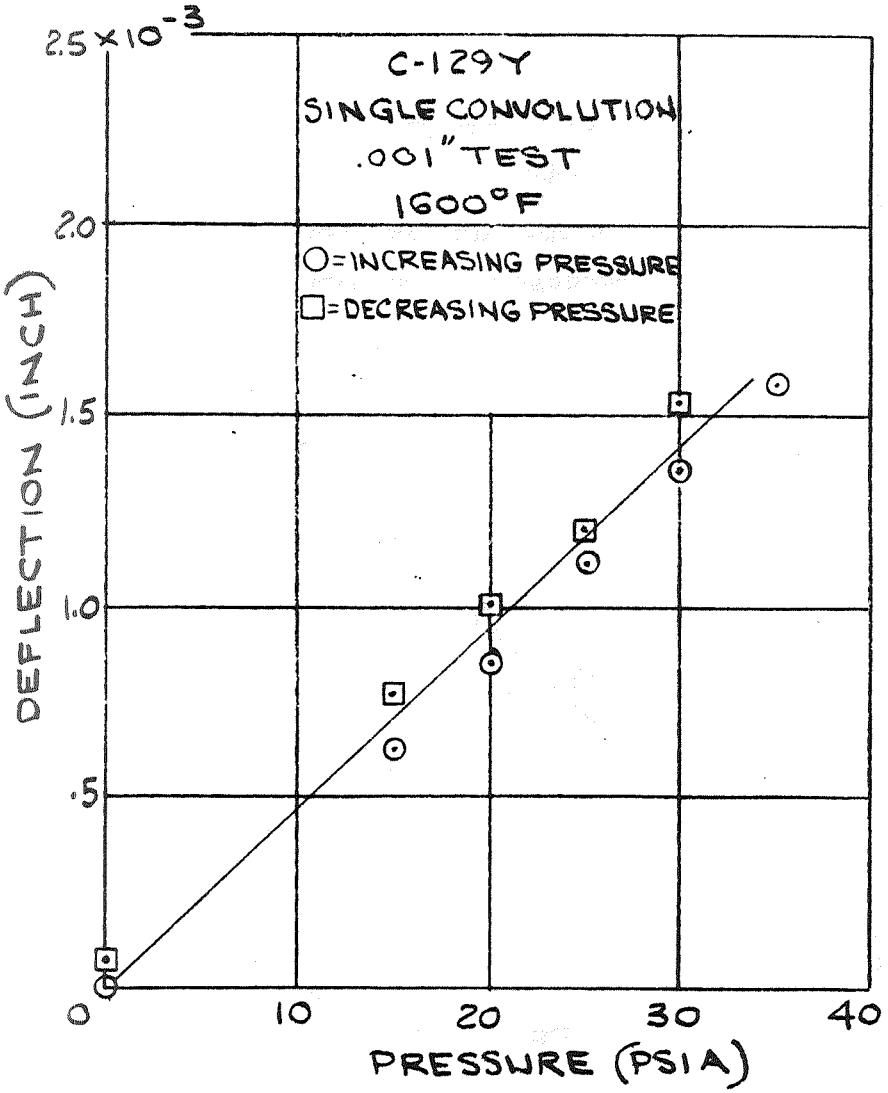


FIGURE 26

C-129Y PRESSURE-DEFLECTION, 1600°F

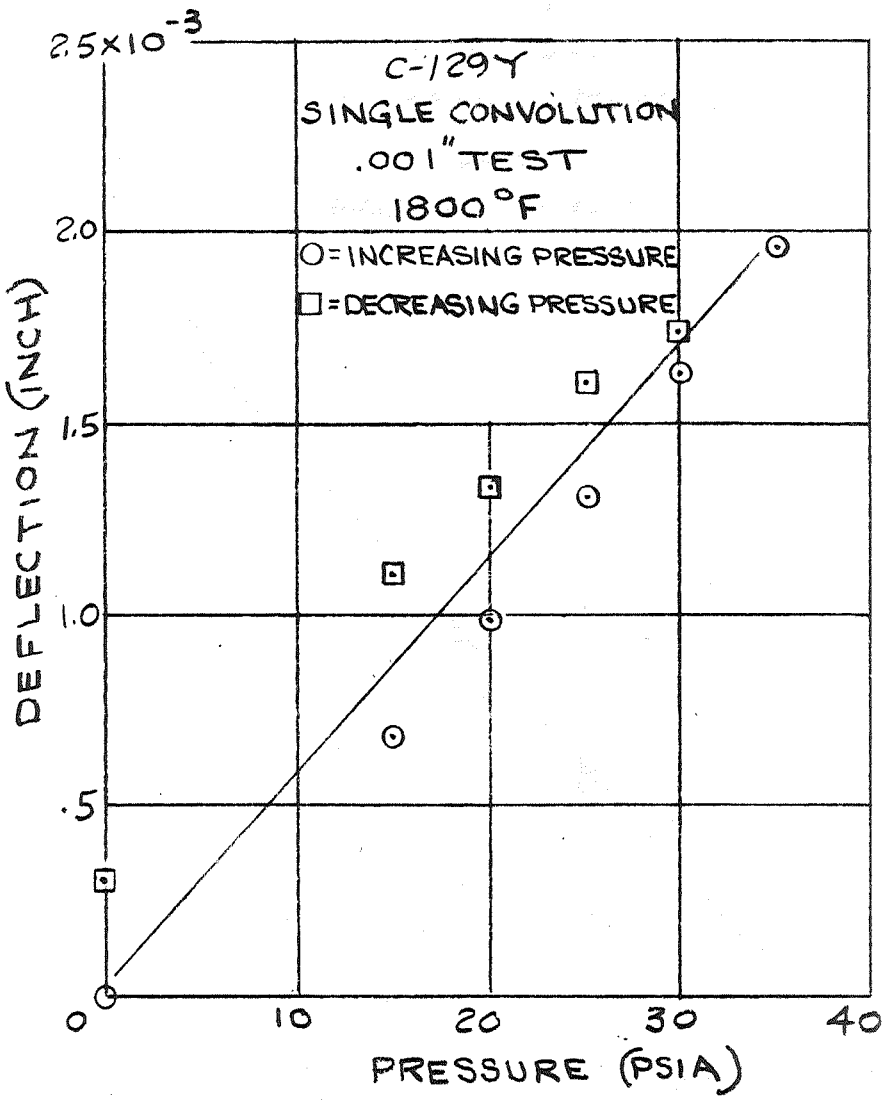


FIGURE 27

C-129Y PRESSURE-DEFLECTION, 1800°F

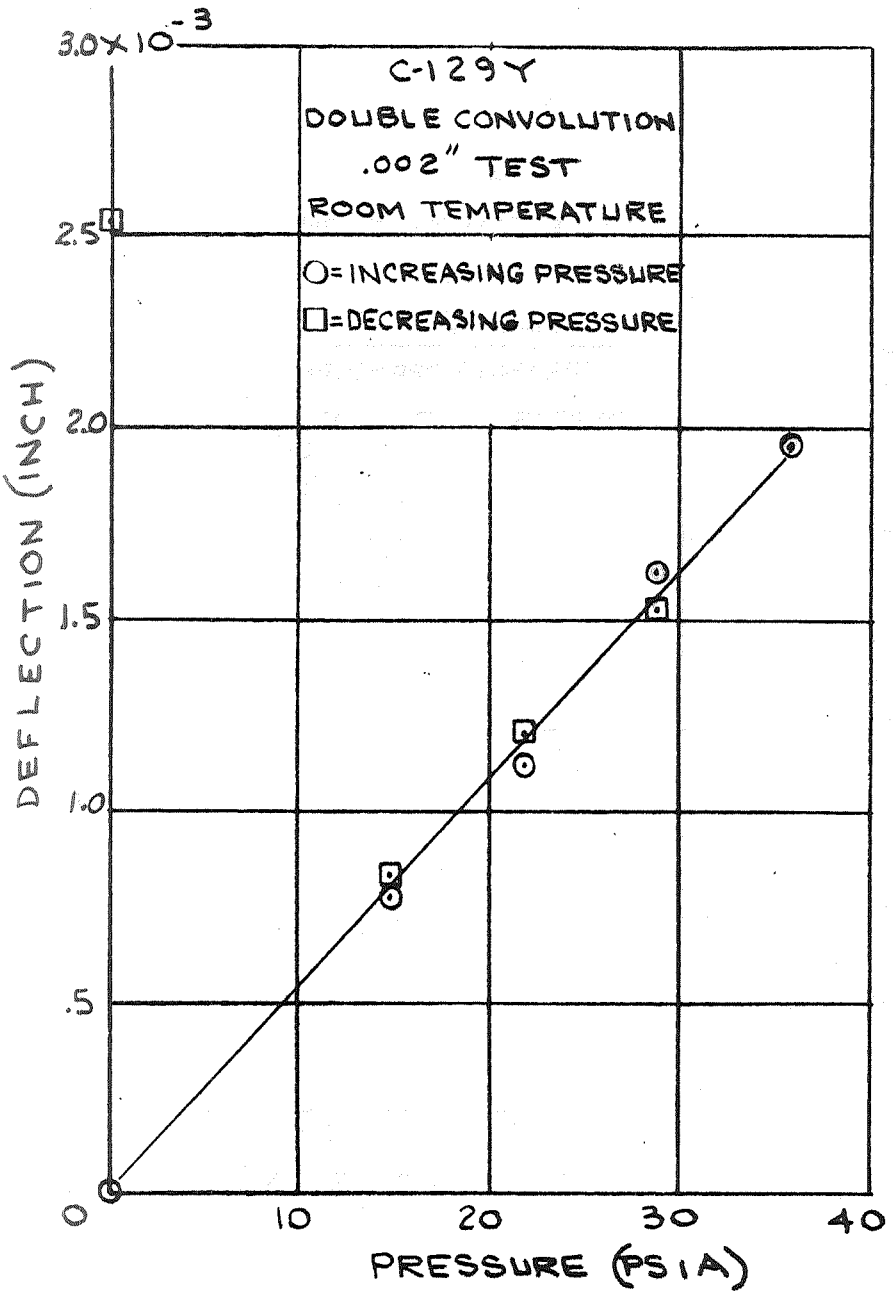


FIGURE 28

C-129Y PRESSURE-DEFLECTION, ROOM TEMPERATURE

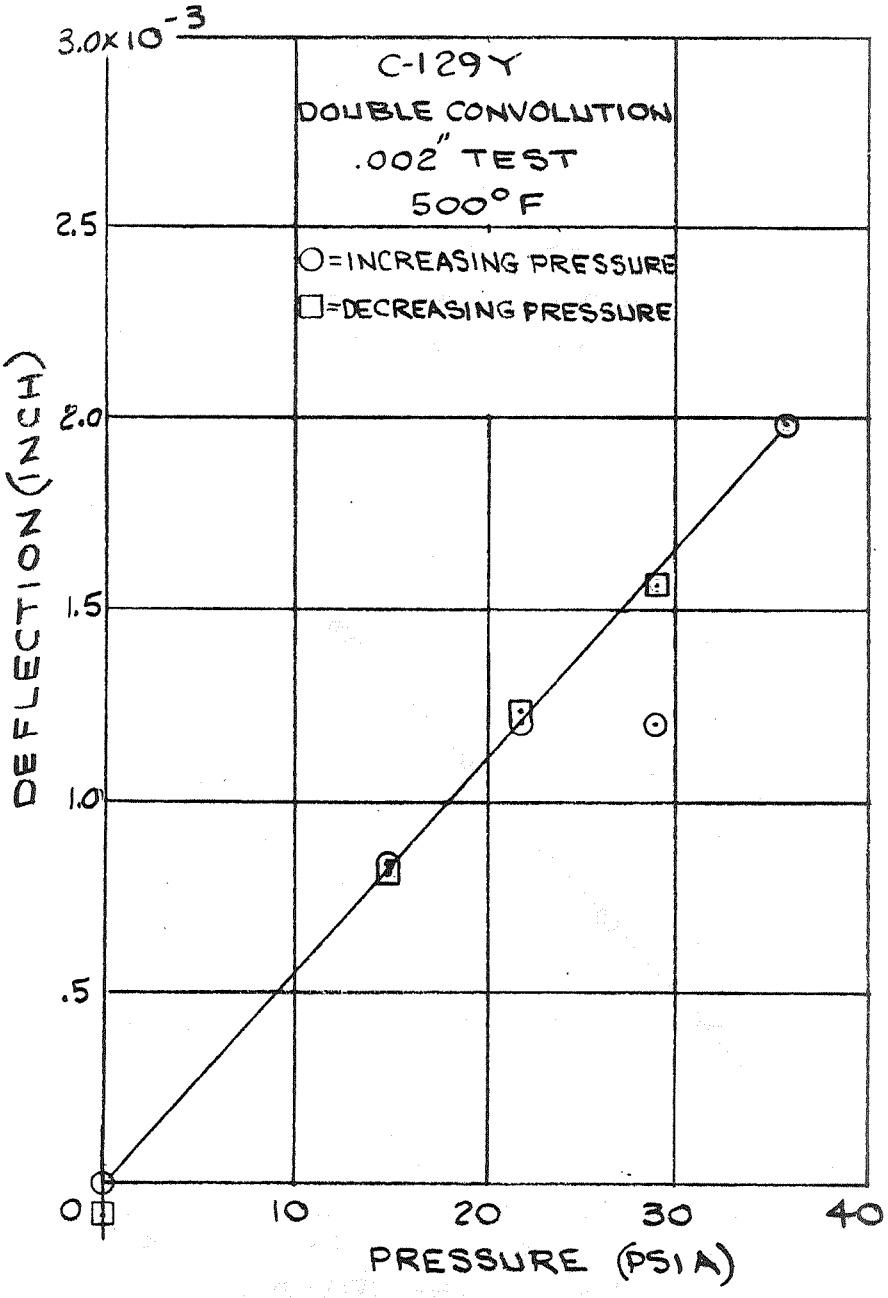


FIGURE 29

C-129Y PRESSURE-DEFLECTION, 500°F

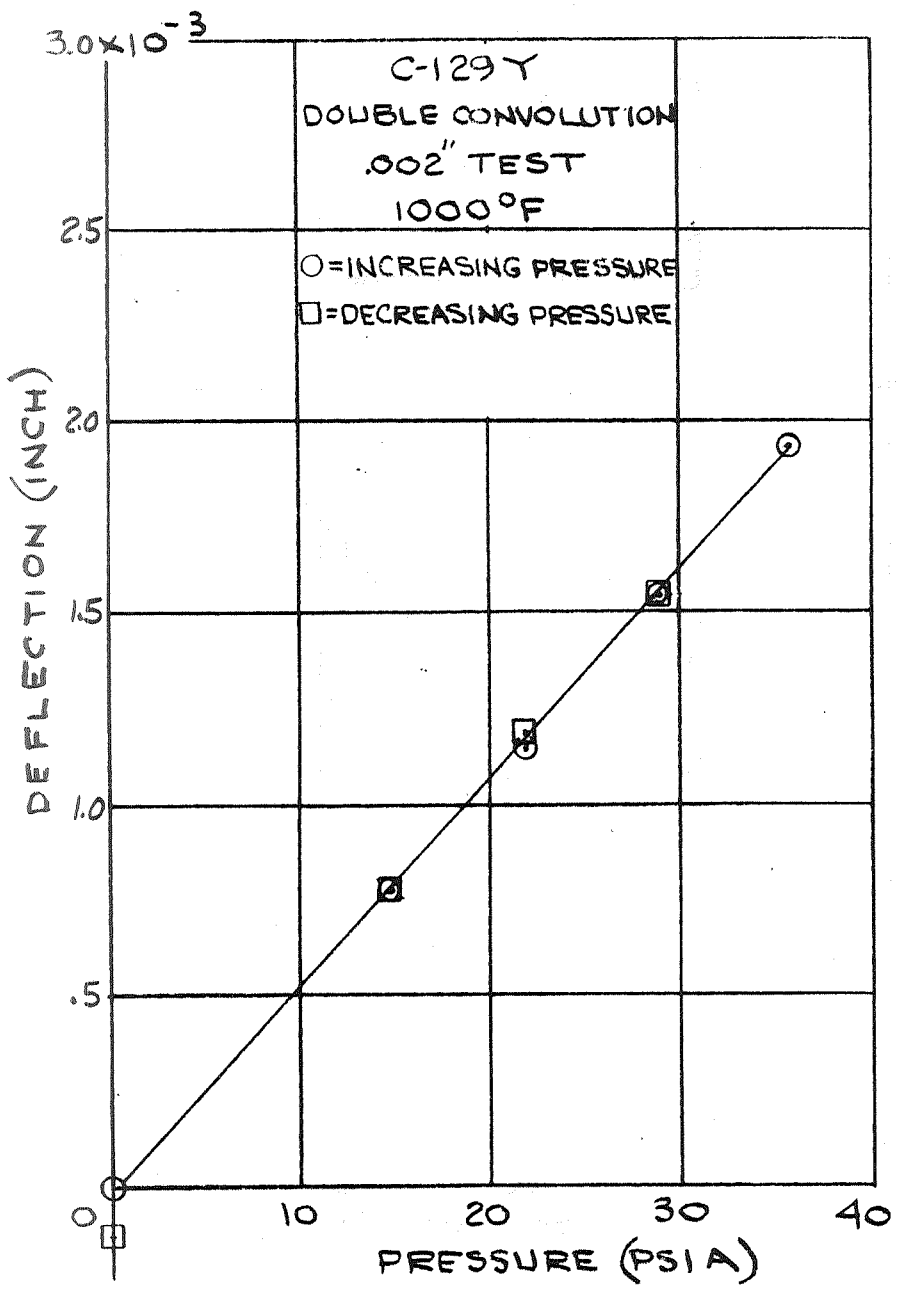


FIGURE 30

C-129Y PRESSURE-DEFLECTION, 1000°F

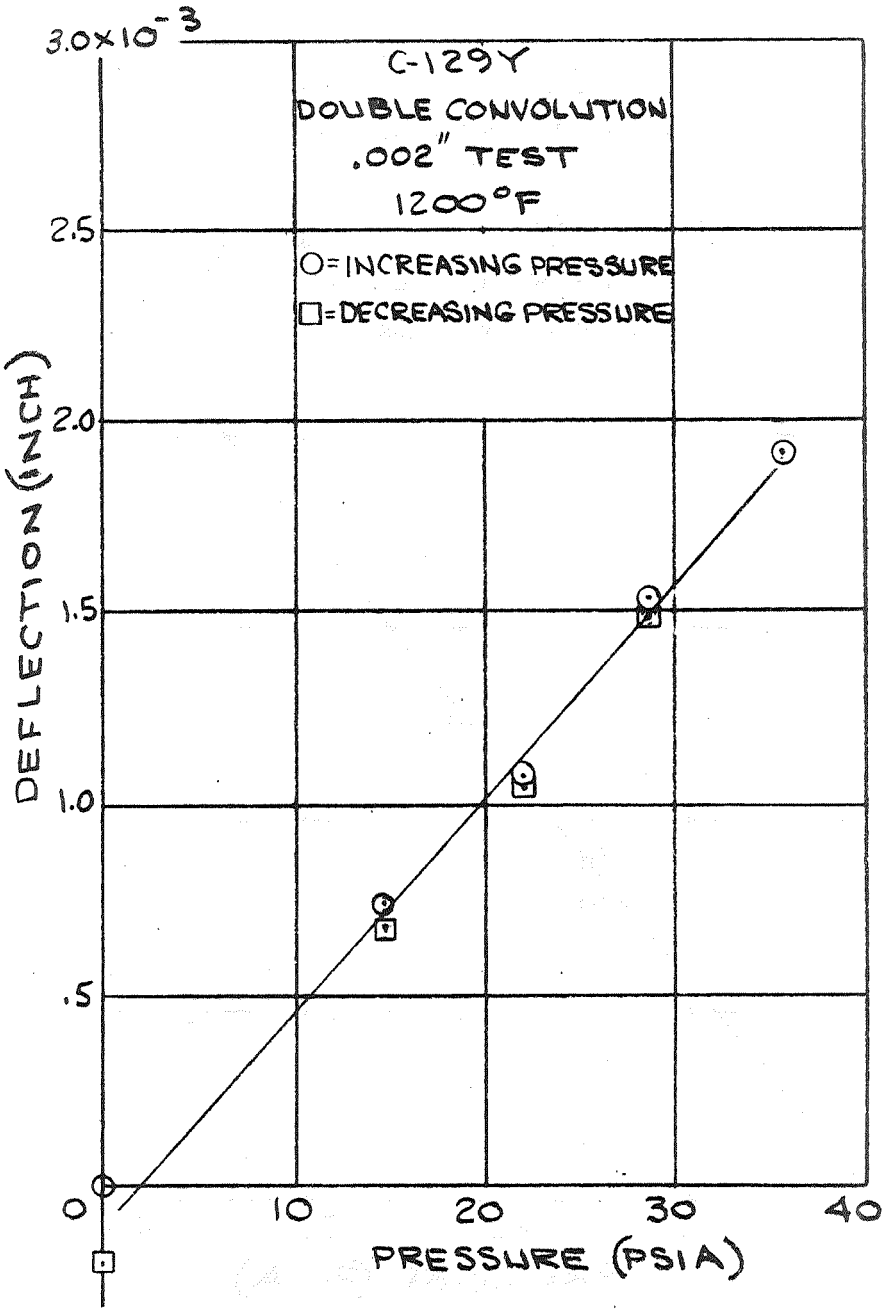


FIGURE 31

C-129Y PRESSURE-DEFLECTION, 1200°F

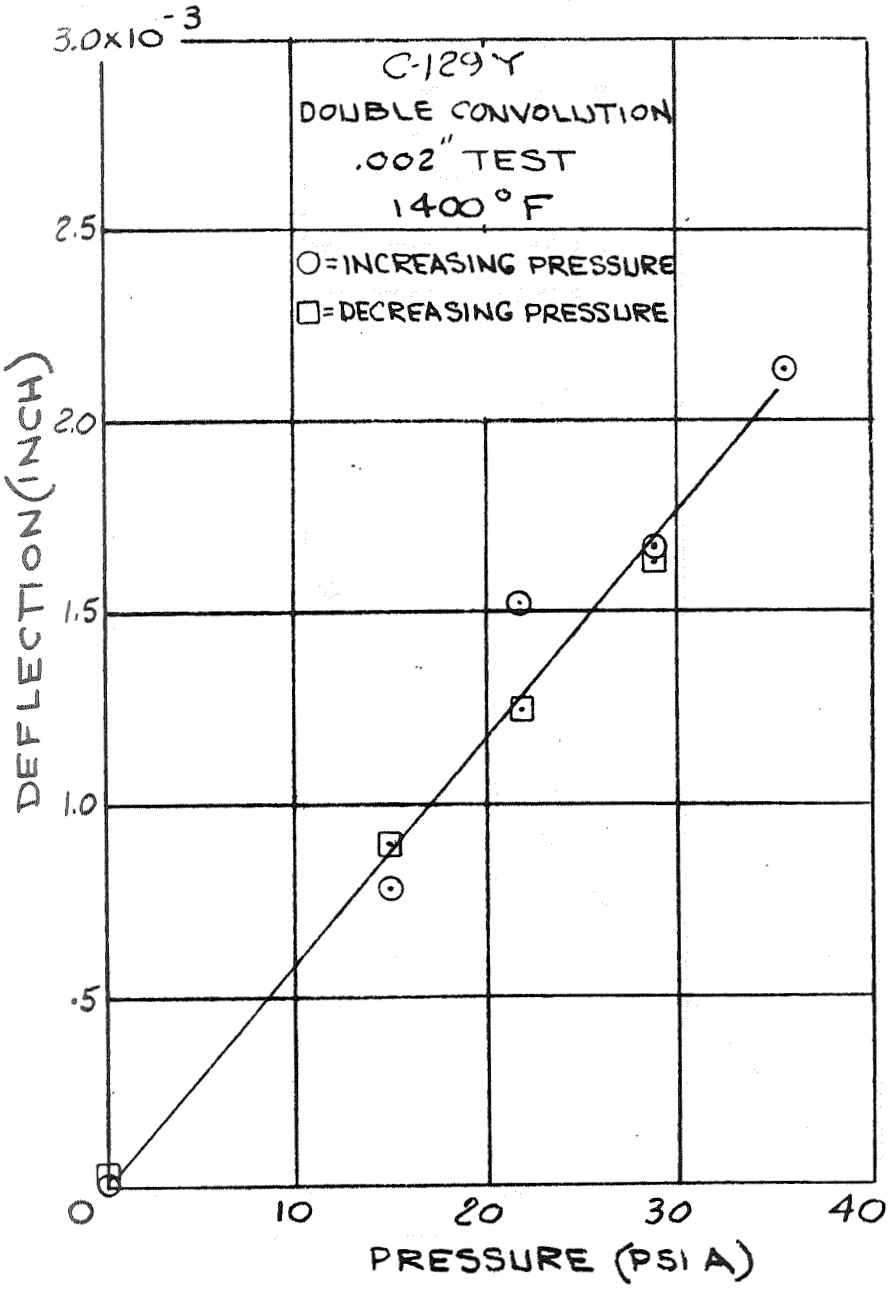


FIGURE 32

C-129Y PRESSURE-DEFLECTION, 1400°F

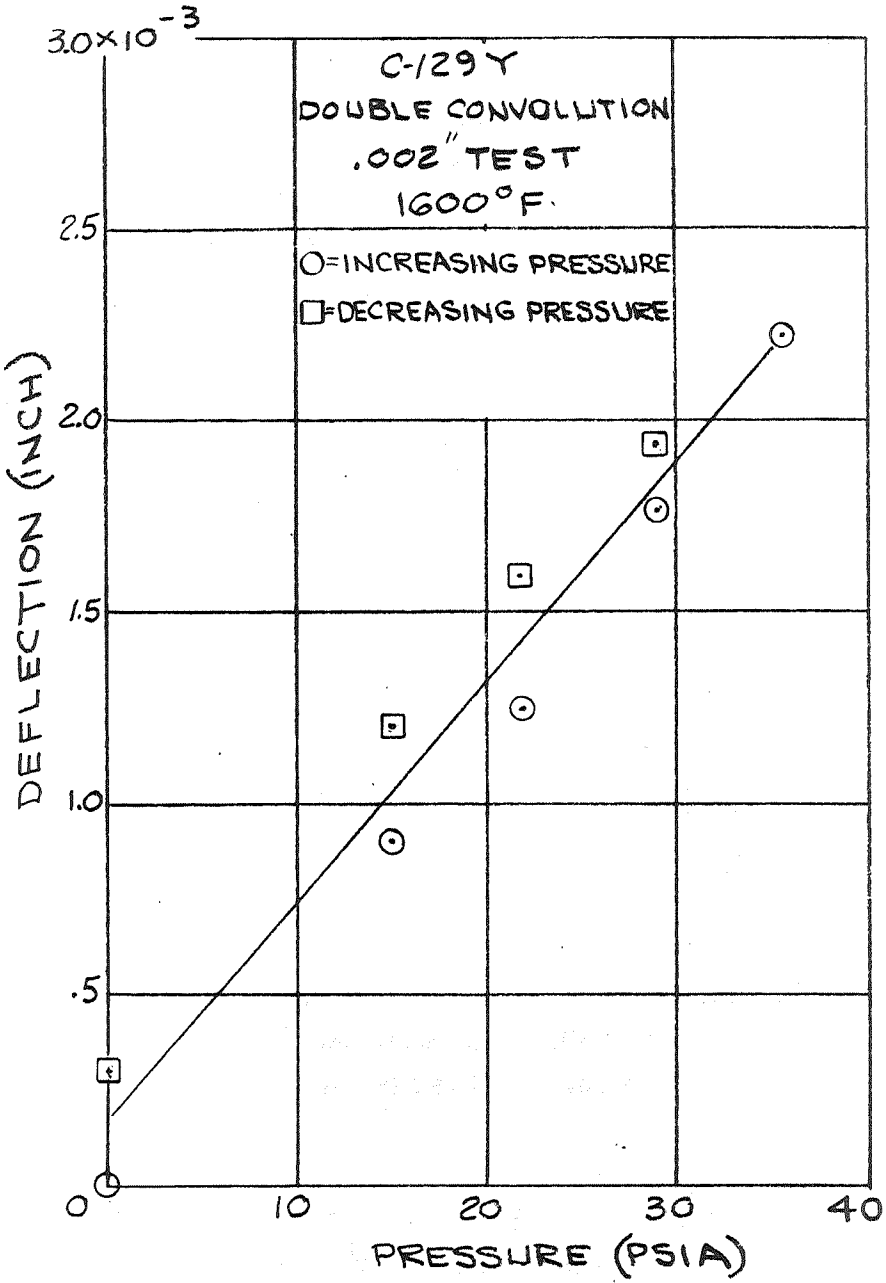


FIGURE 33

C-129Y PRESSURE-DEFLECTION, 1600°F

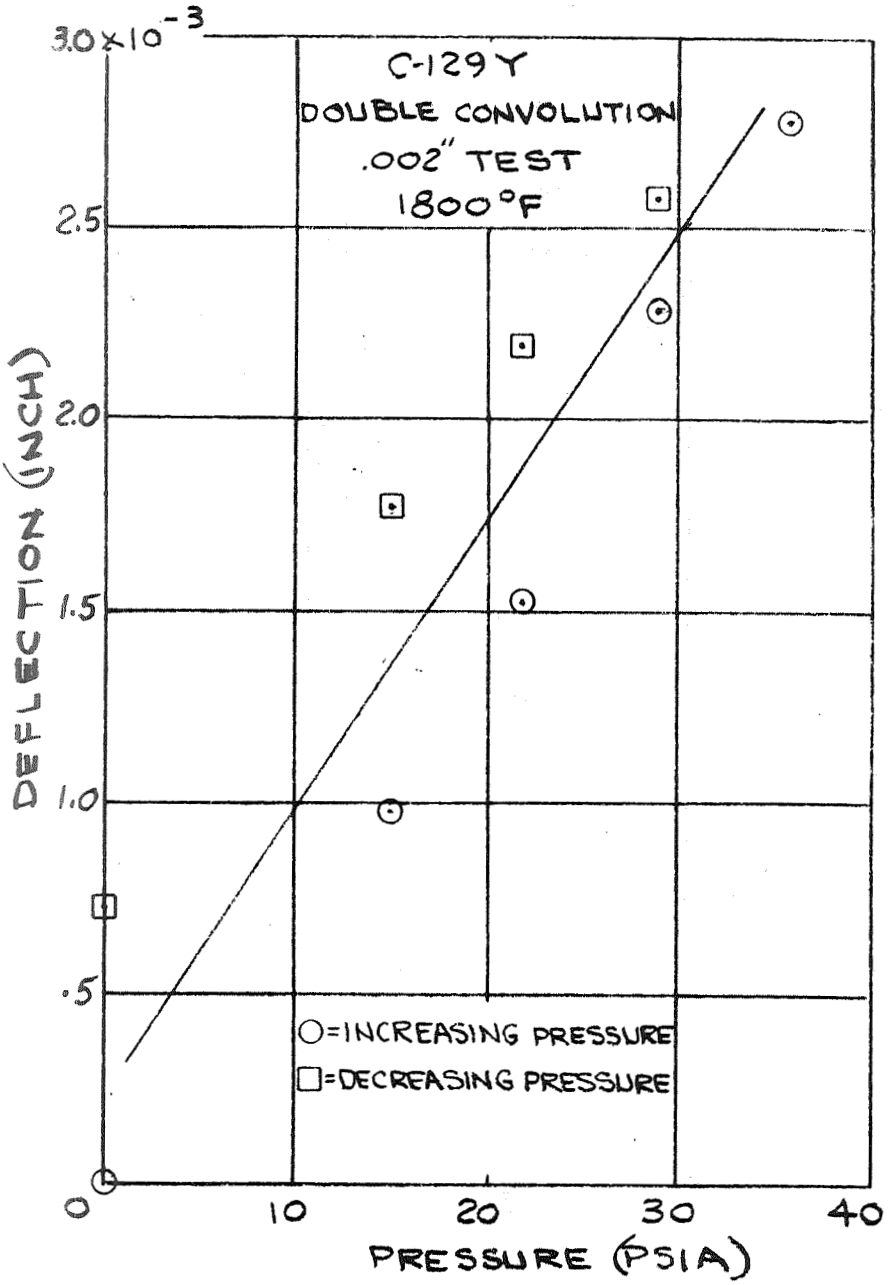


FIGURE 34

C-129Y PRESSURE-DEFLECTION, 1800°F

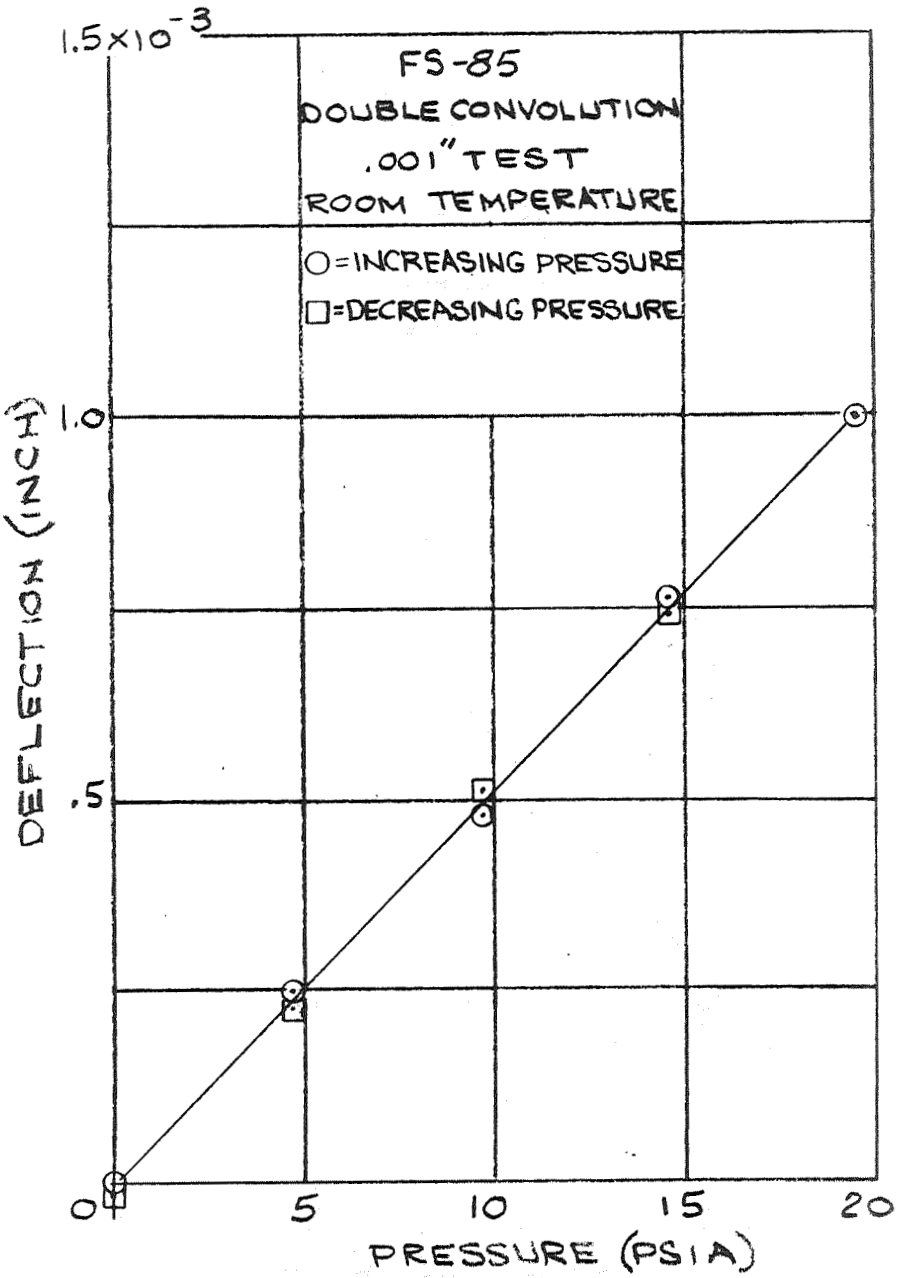


FIGURE 35

FS-85 PRESSURE-DEFLECTION, ROOM TEMPERATURE

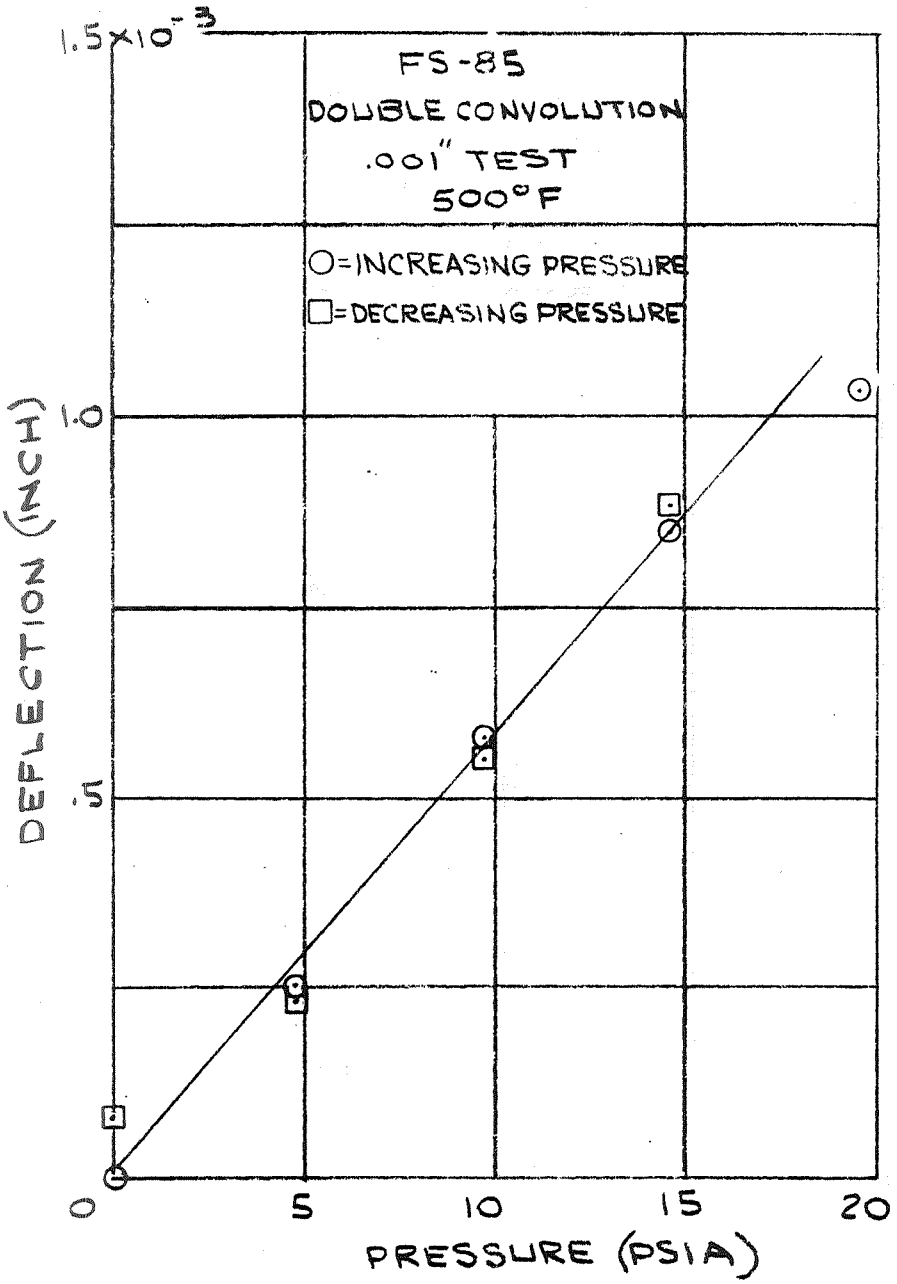


FIGURE 36

FS-85 PRESSURE-DEFLECTION, 500°F

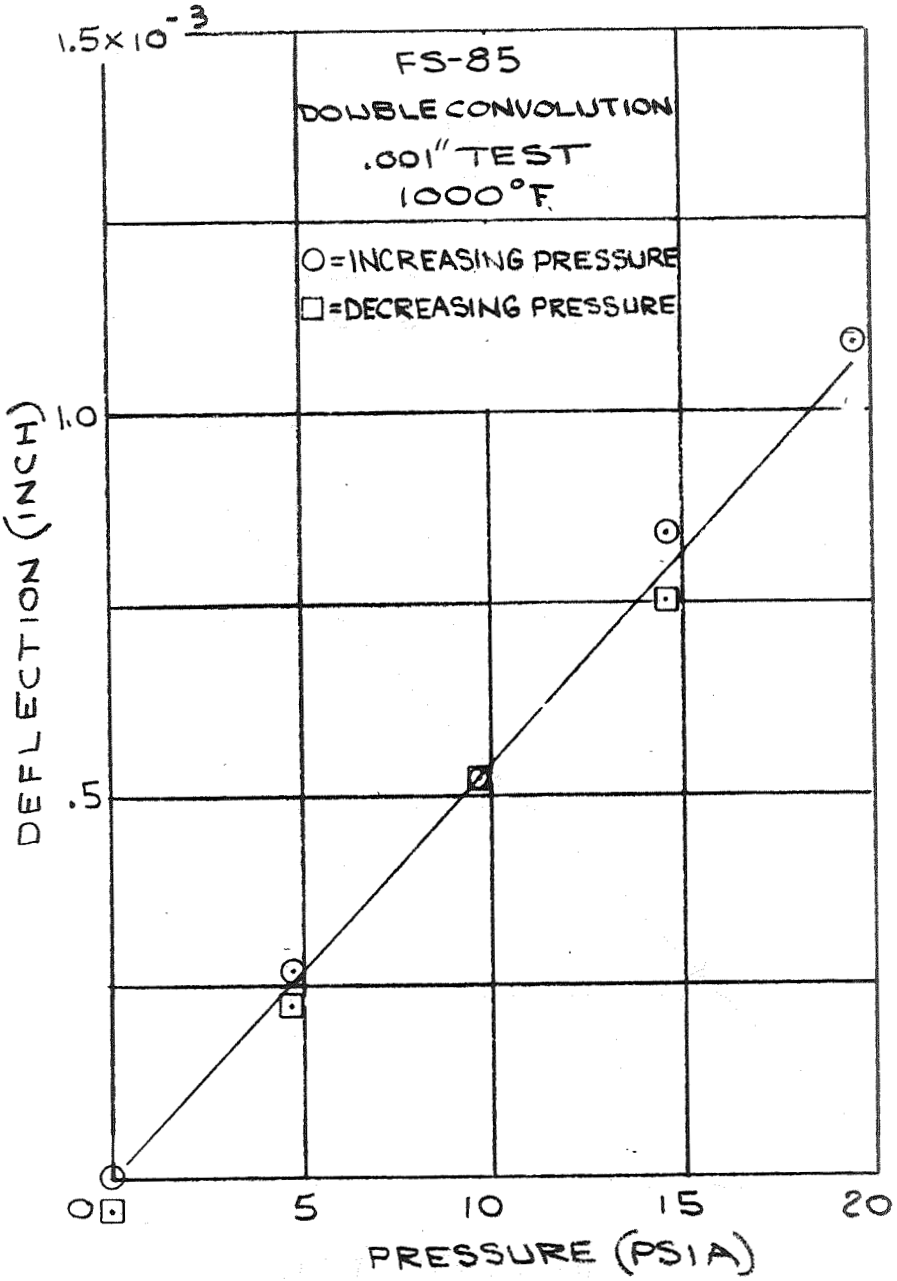


FIGURE 37

FS-85 PRESSURE-DEFLECTION, 1000°F

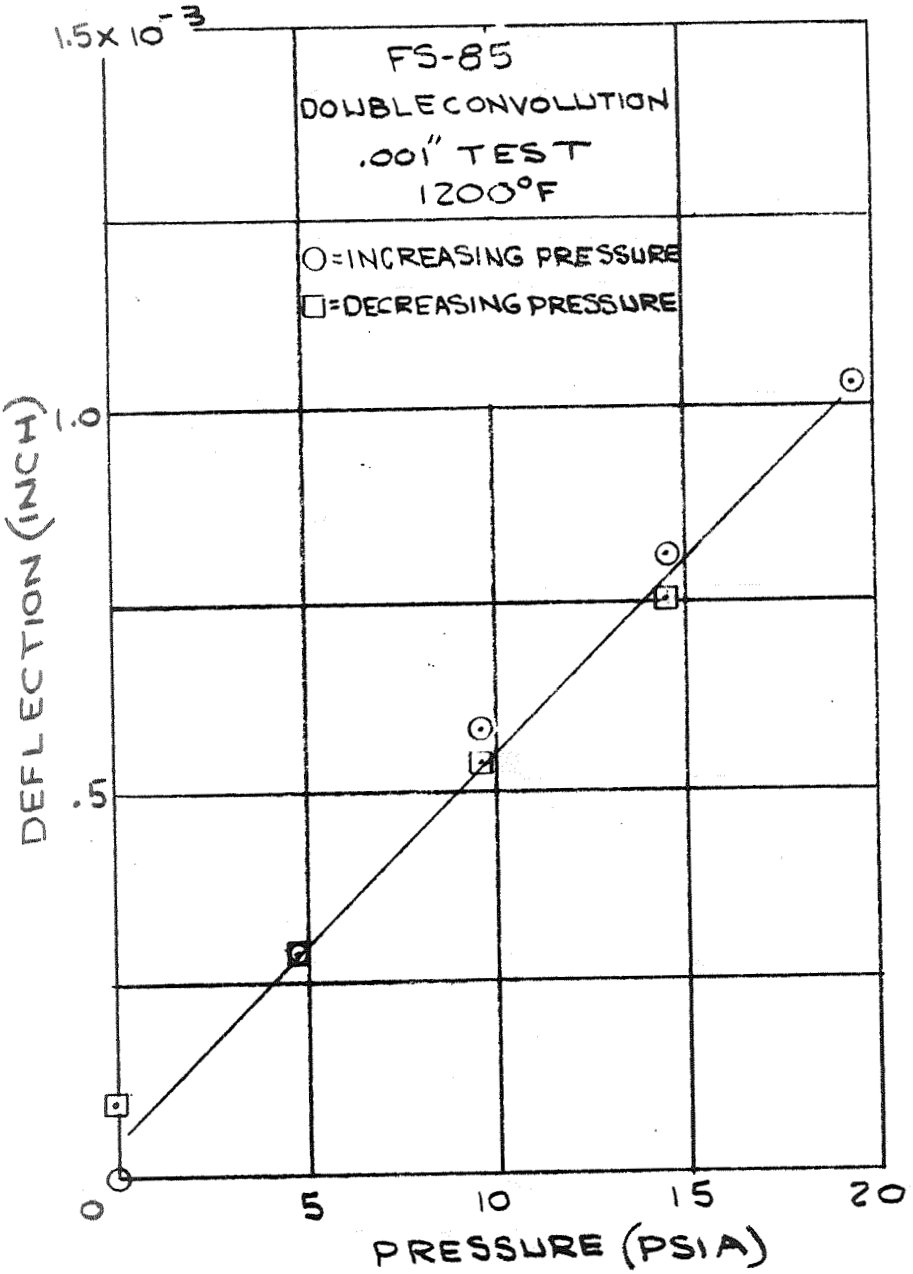


FIGURE 38

FS-85 PRESSURE-DEFLECTION, 1200°F

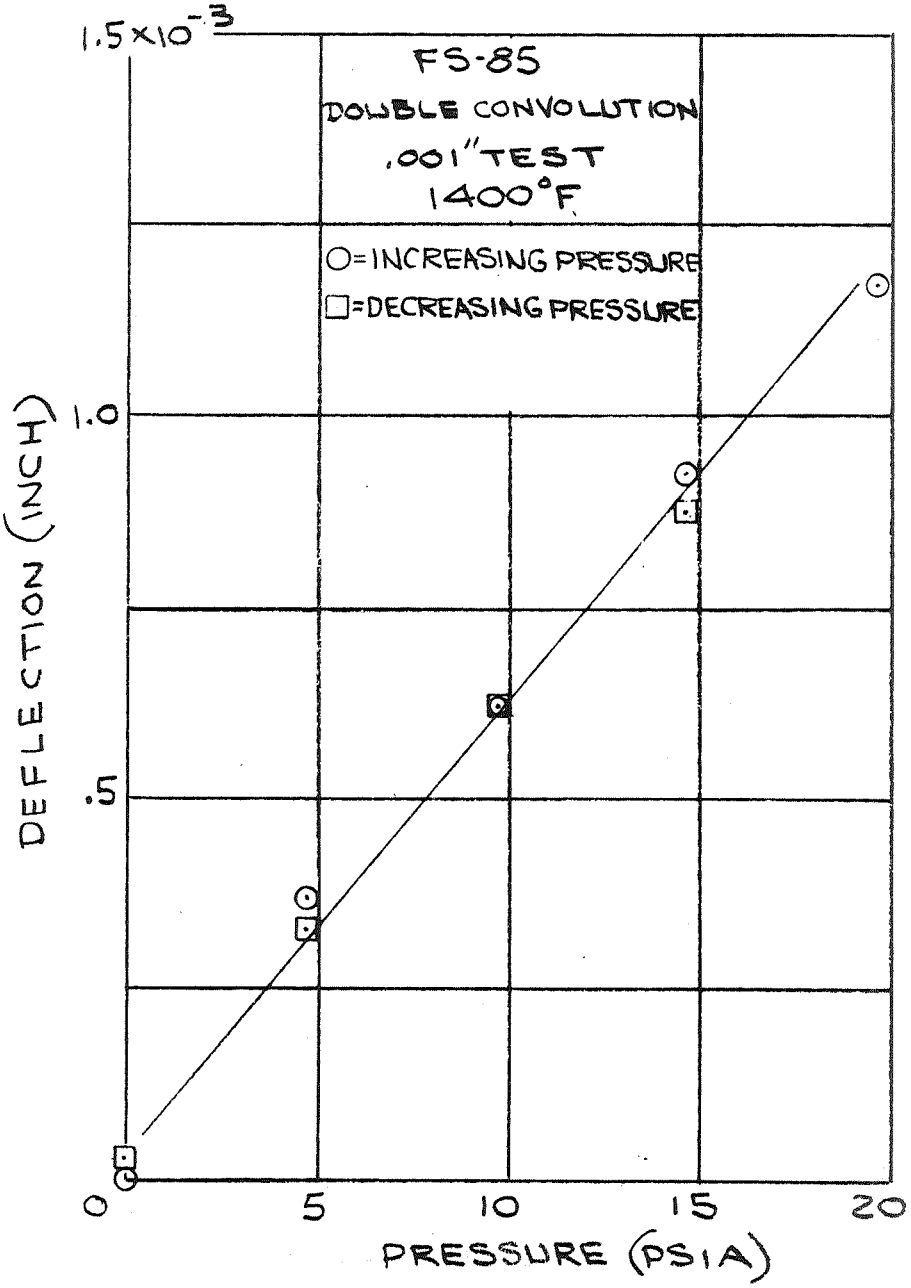


FIGURE 39

FS-85 PRESSURE-DEFLECTION, 1400°F

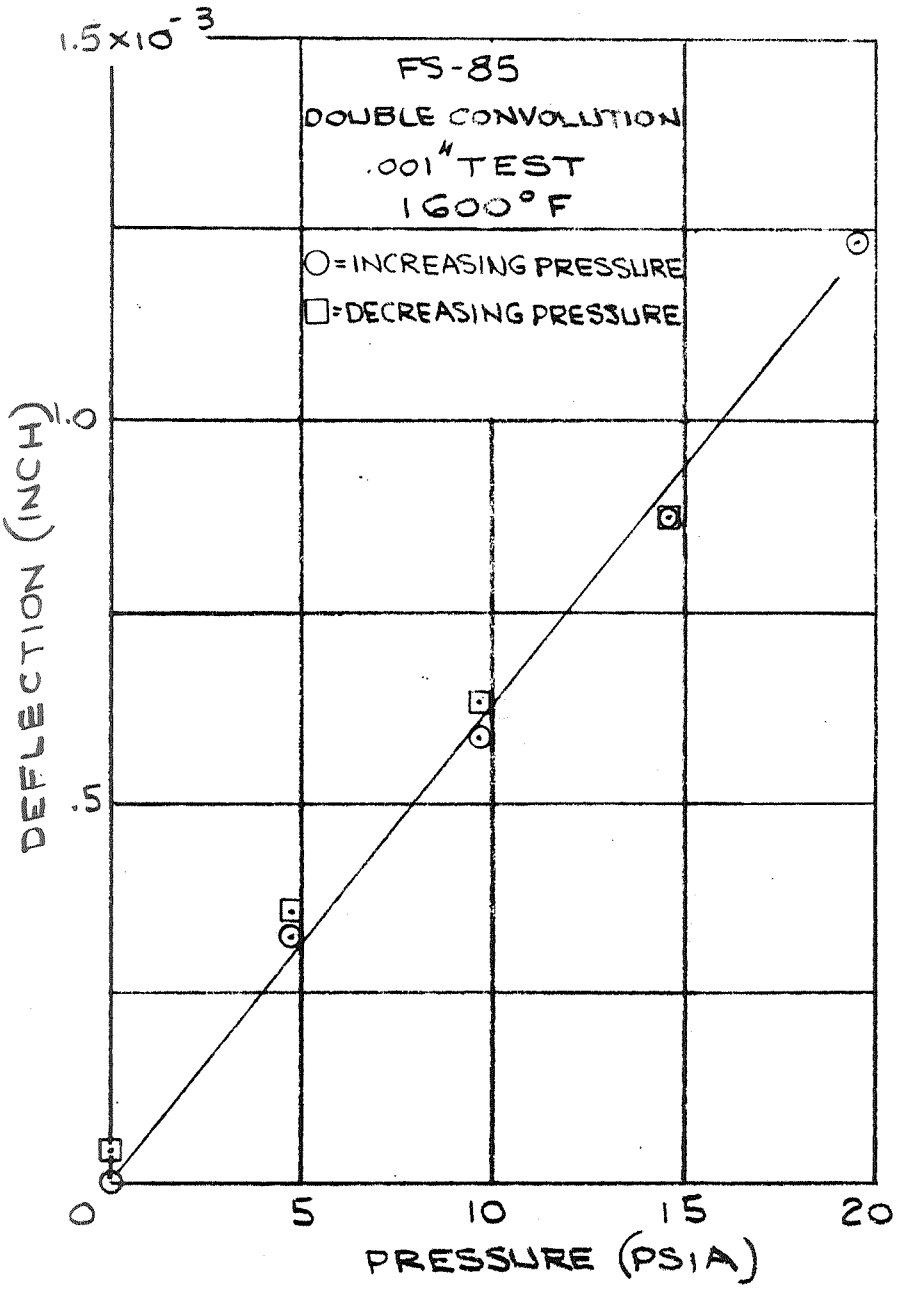


FIGURE 40

FS-85 PRESSURE-DEFLECTION, 1600°F

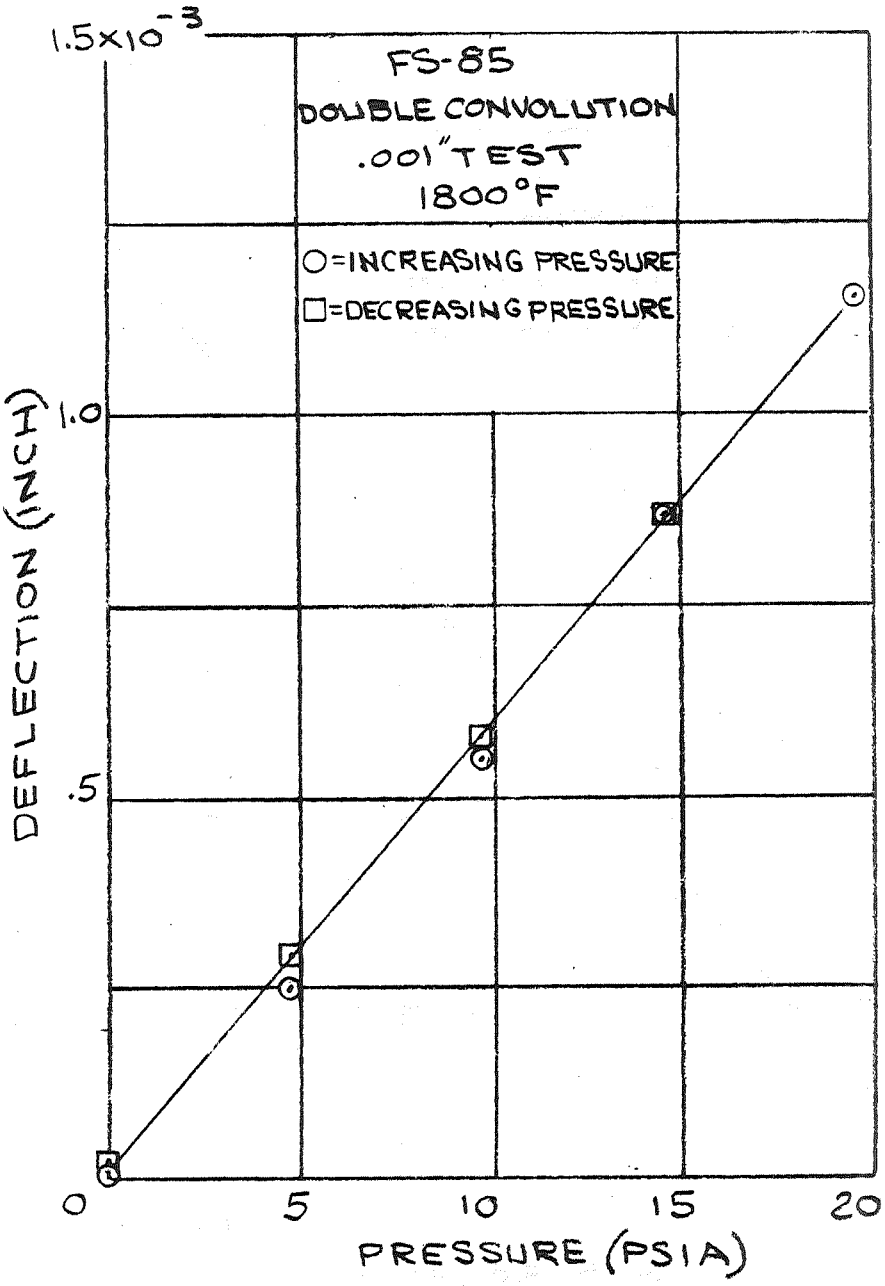


FIGURE 41

FS-85 PRESSURE-DEFLECTION, 1800°F

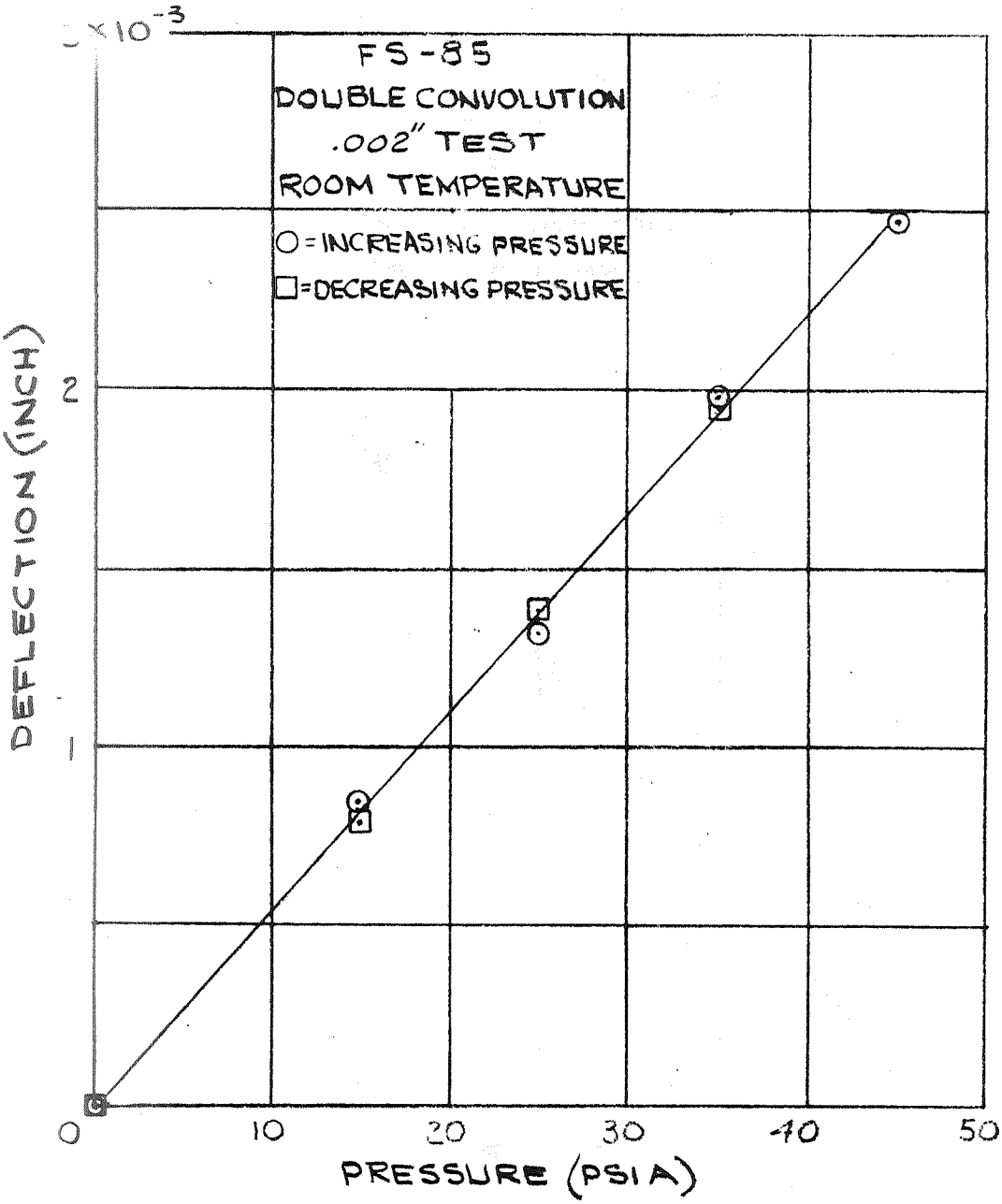


FIGURE 42

FS-85 PRESSURE-DEFLECTION, ROOM TEMPERATURE

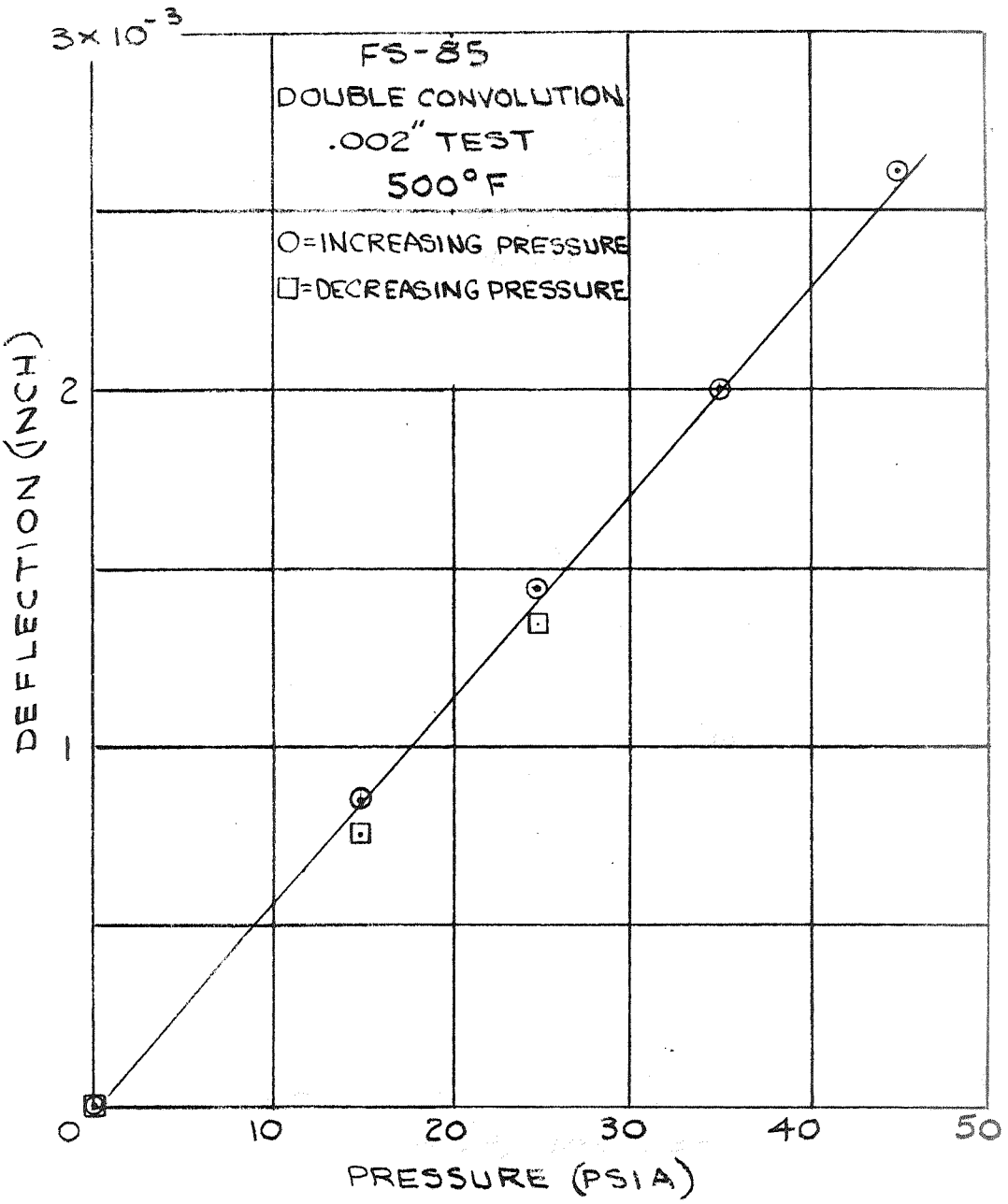


FIGURE 43

FS-85 PRESSURE-DEFLECTION, 500°F

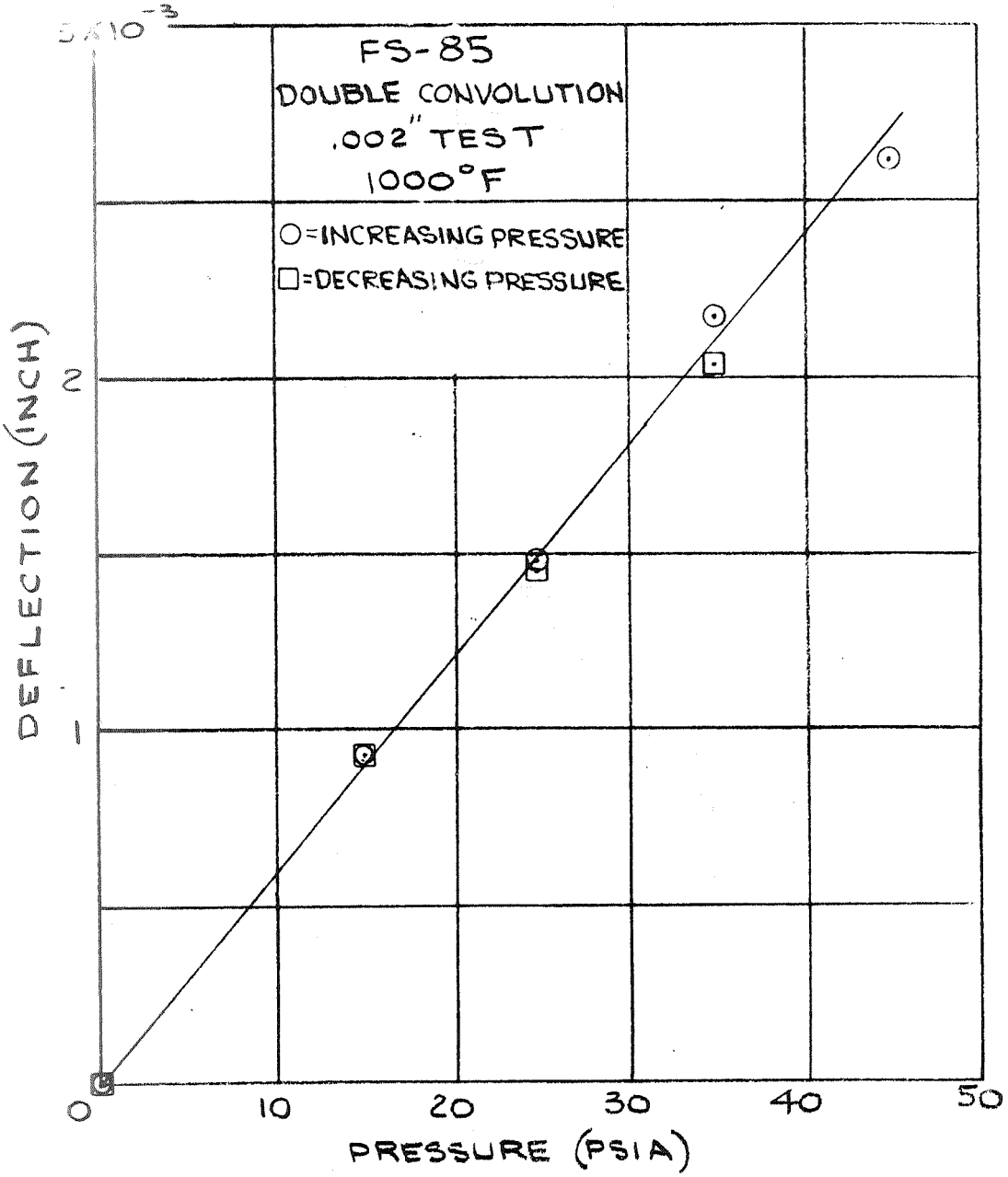


FIGURE 44

FS-85 PRESSURE-DEFLECTION, 1000°F

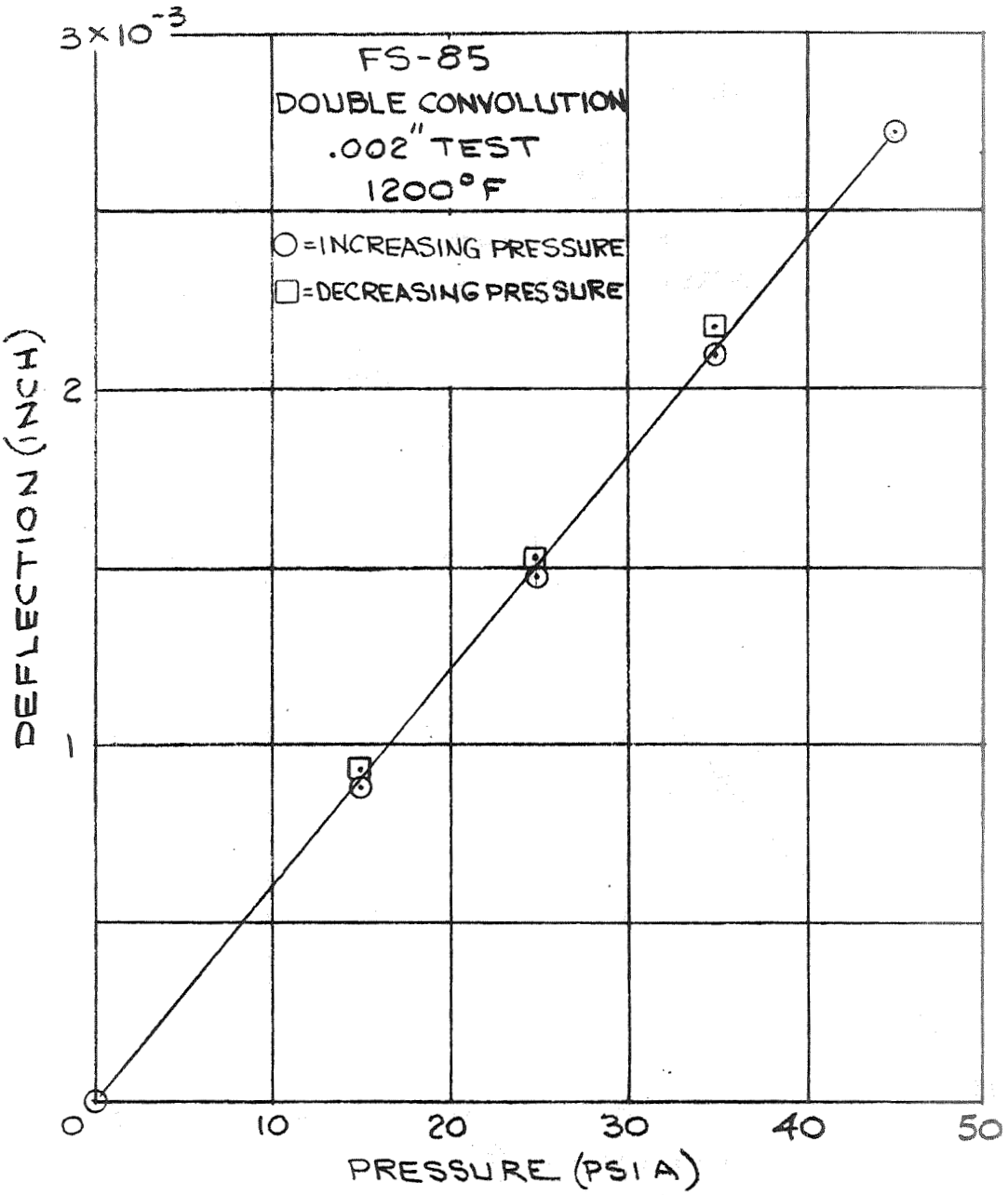


FIGURE 45

FS-85 PRESSURE-DEFLECTION, 1200°F

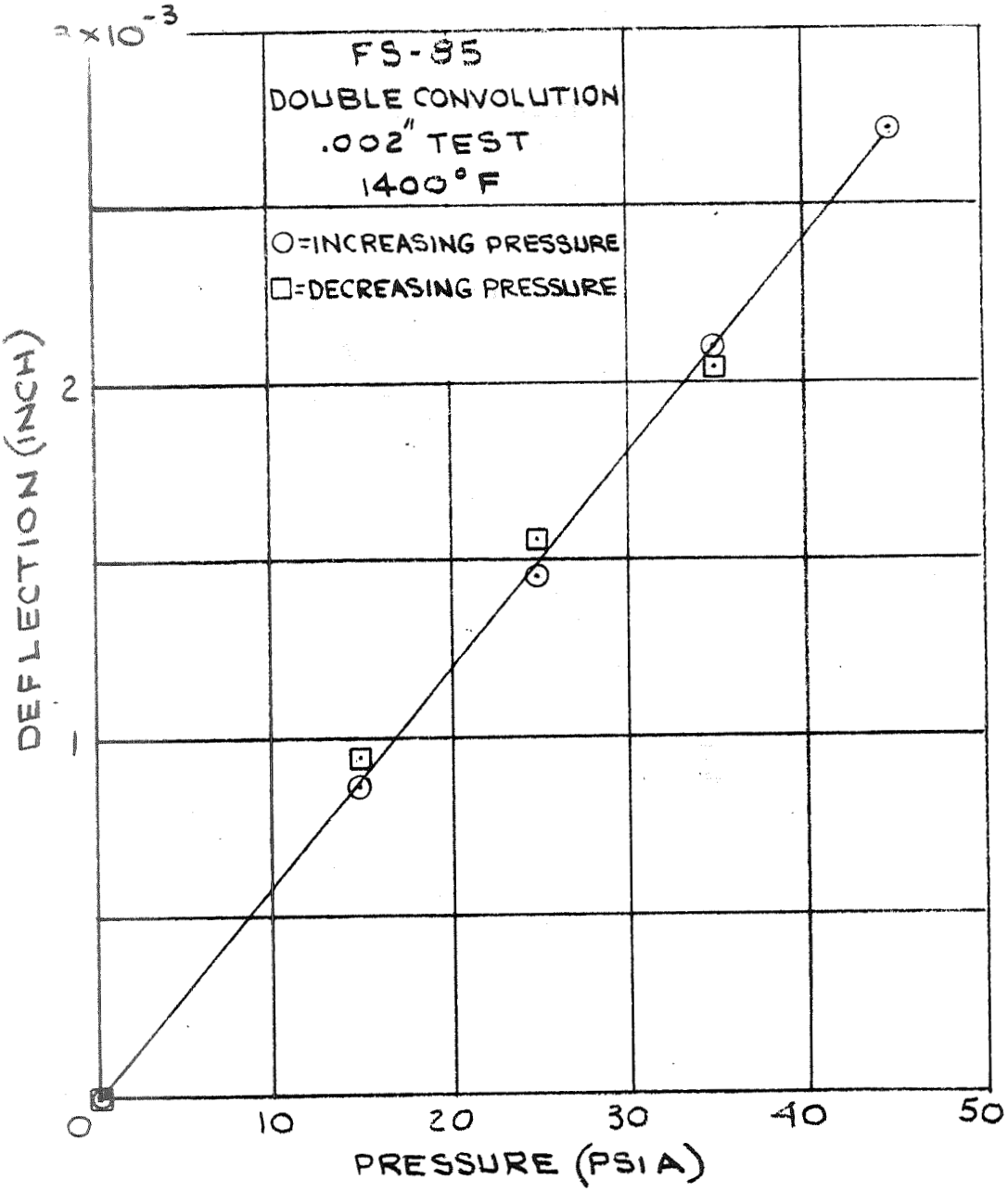


FIGURE 46

FS-85 PRESSURE-DEFLECTION, 1400°F

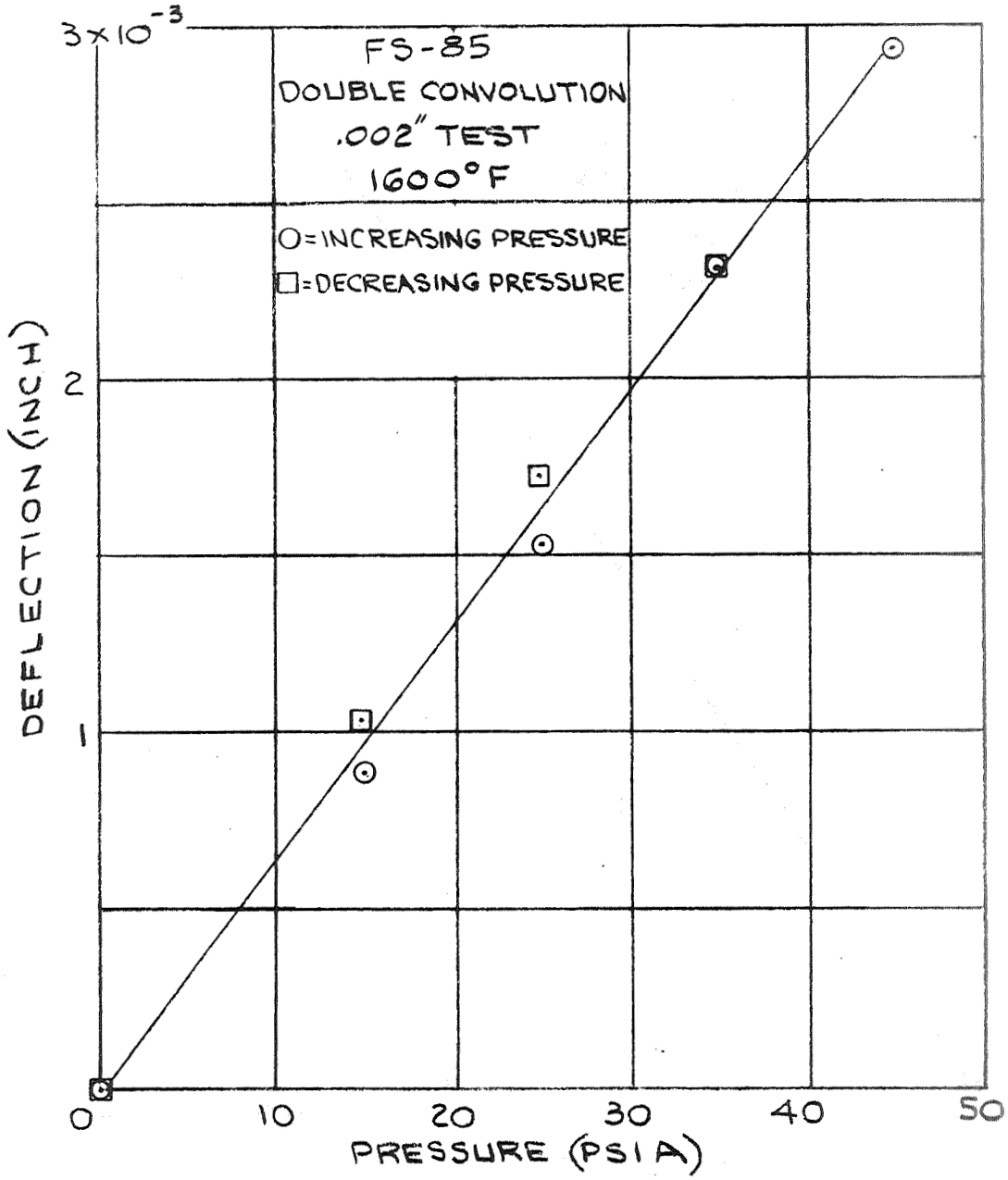


FIGURE 47

FS-85 PRESSURE-DEFLECTION, 1600°F

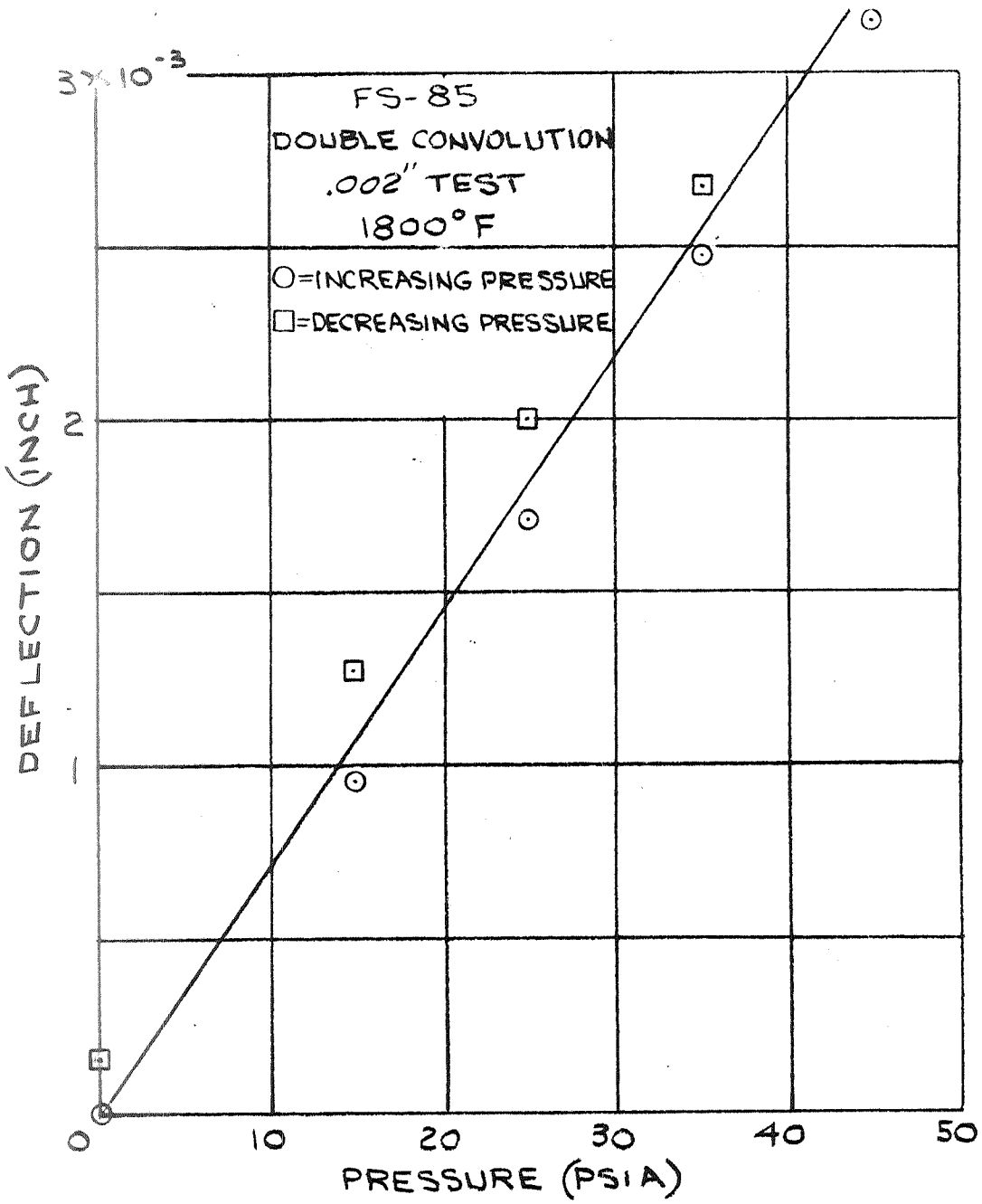


FIGURE 48

FS-85 PRESSURE-DEFLECTION, 1800°F

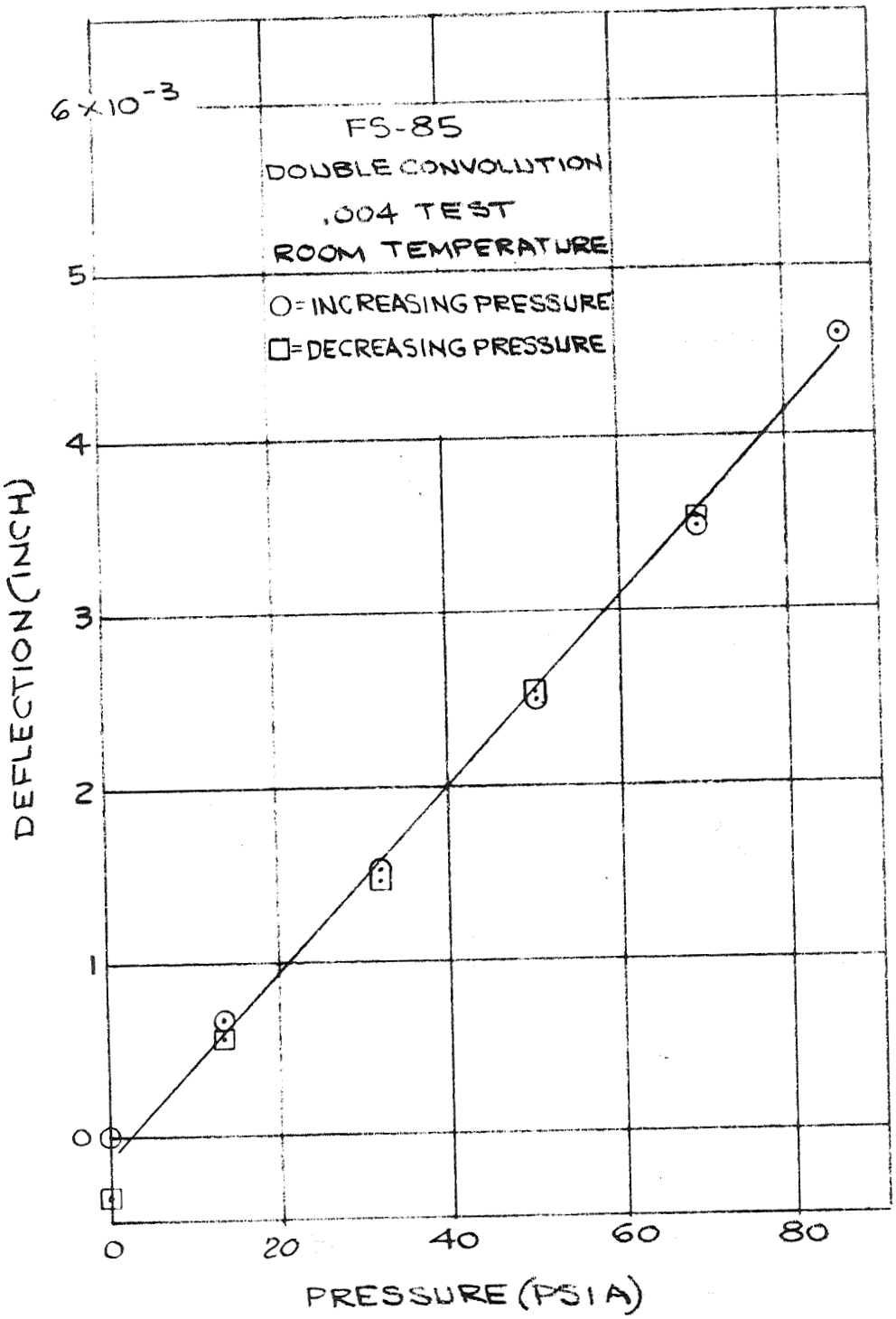


FIGURE 49

FS-85 PRESSURE-DEFLECTION, ROOM TEMPERATURE

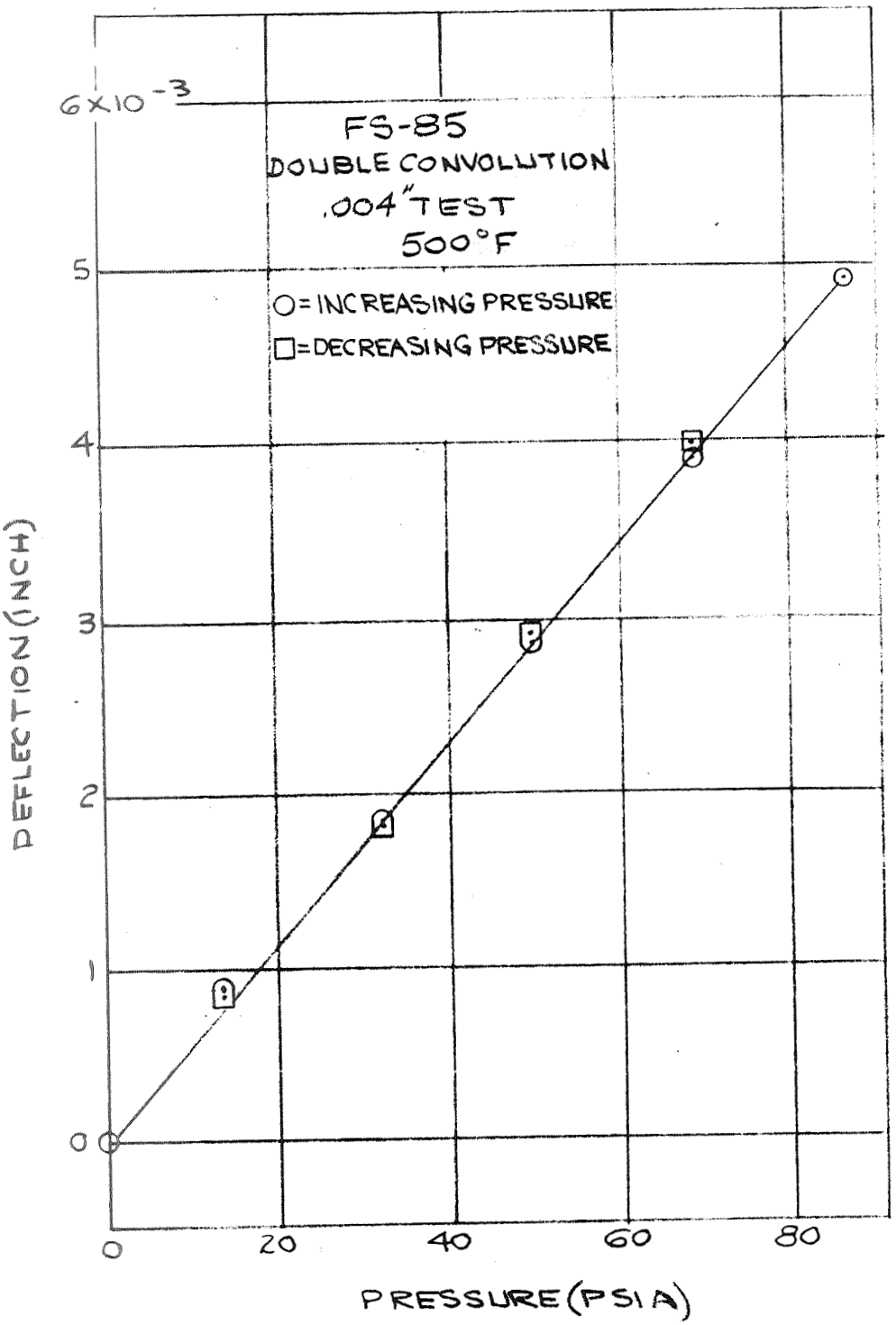


FIGURE 50

FS-85 PRESSURE-DEFLECTION, 500°F

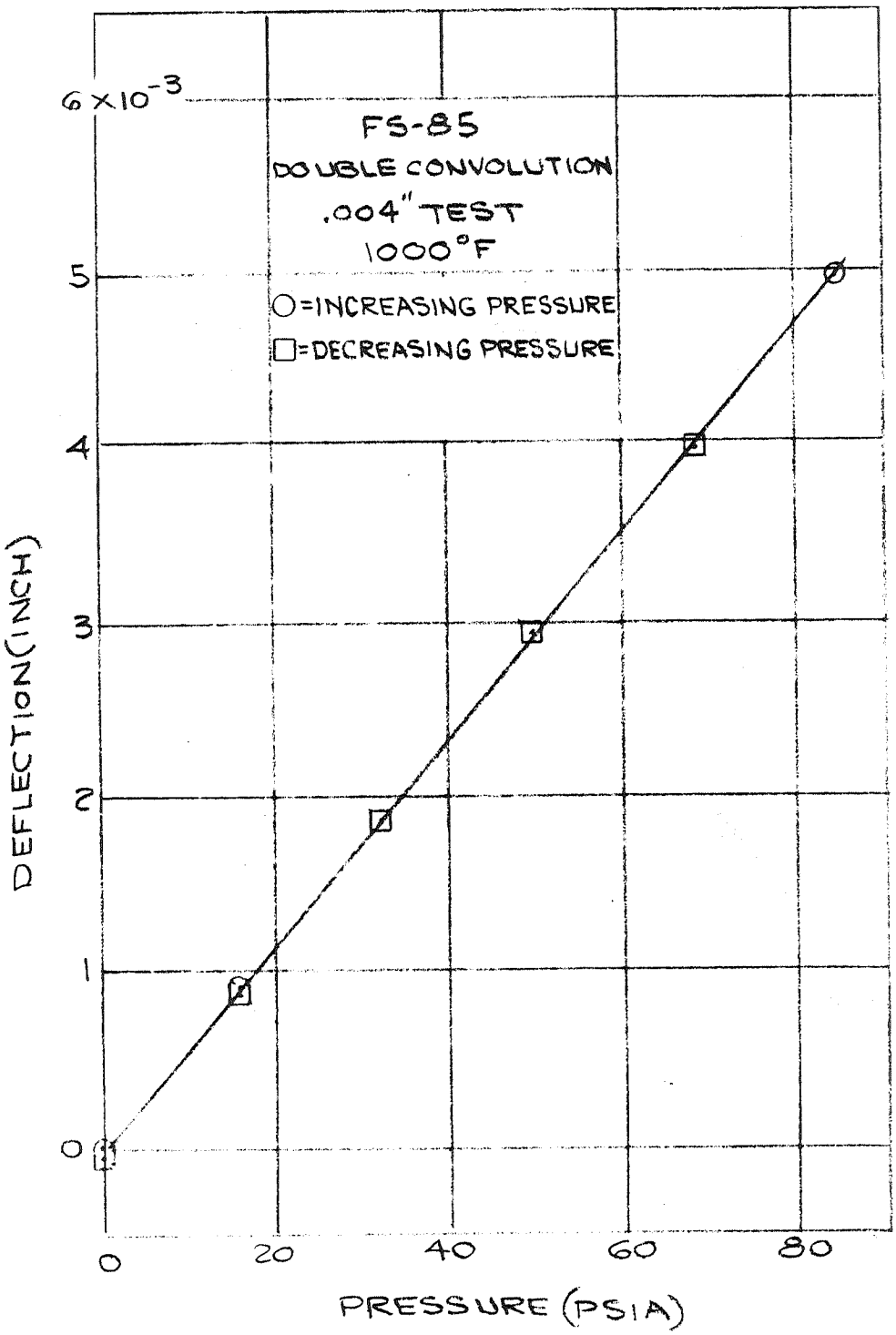


FIGURE 51

FS-85 PRESSURE-DEFLECTION, 1000°F

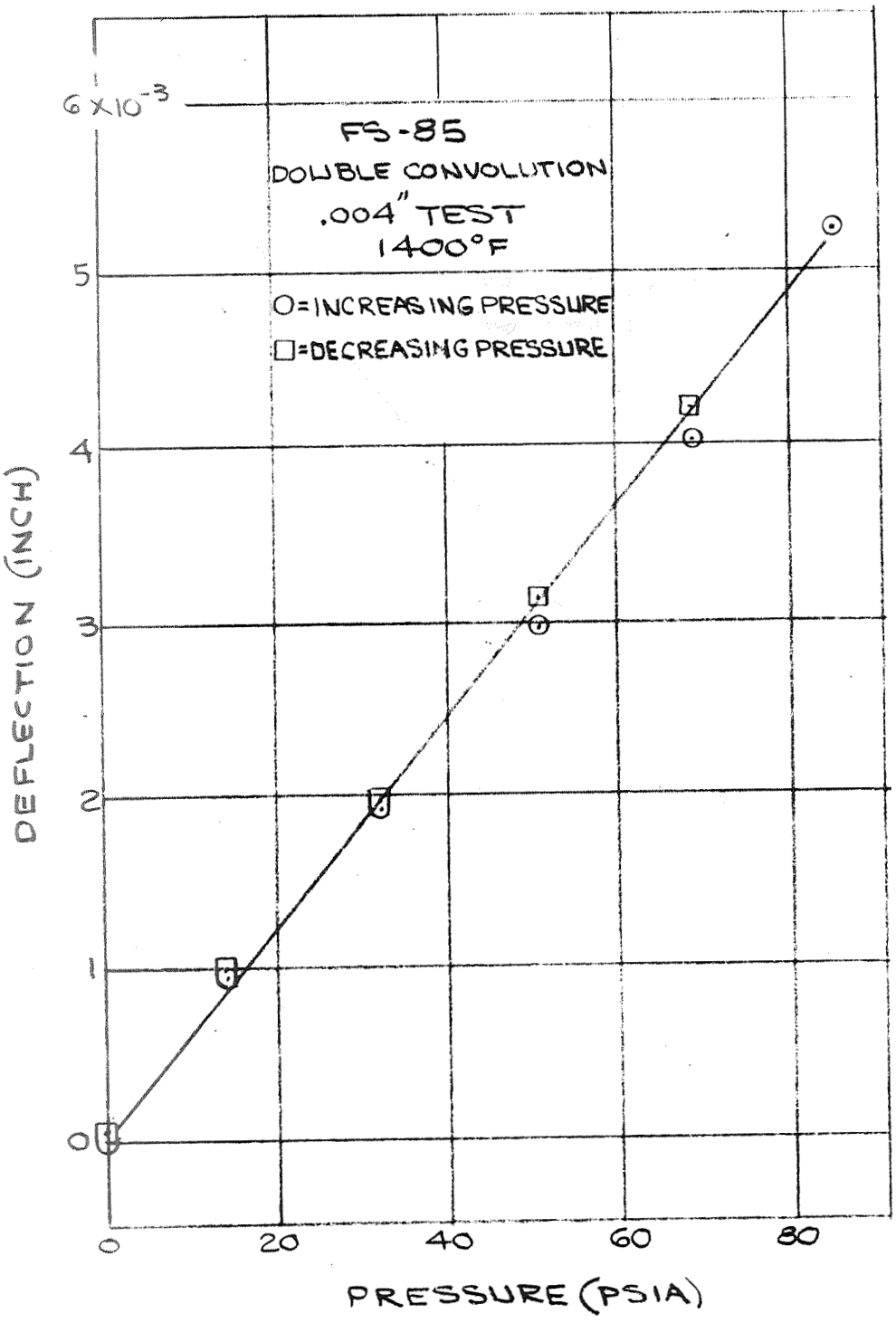


FIGURE 52

FS-85 PRESSURE-DEFLECTION, 1400°F

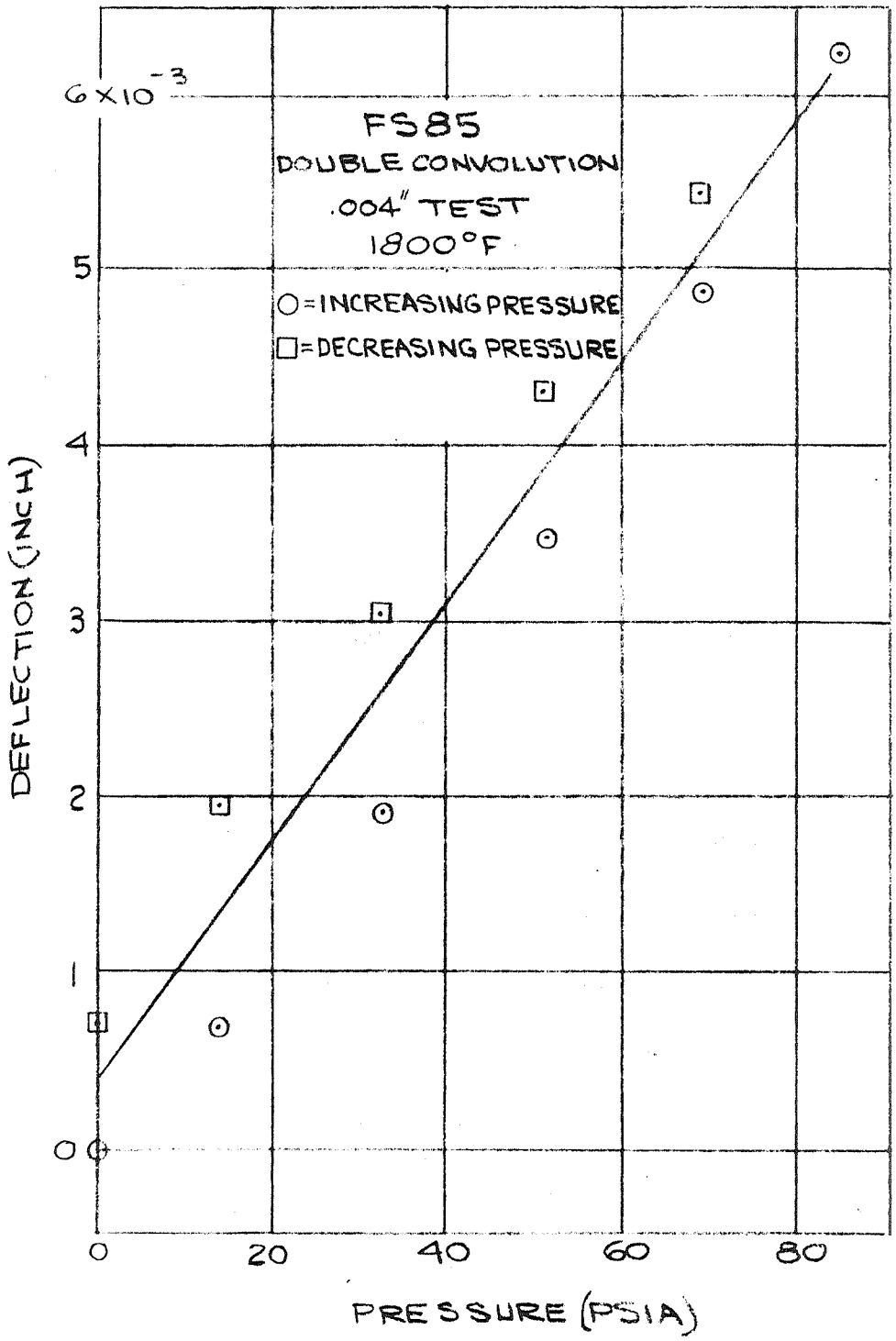


FIGURE 53

FS-85 PRESSURE-DEFLECTION, 1800°F

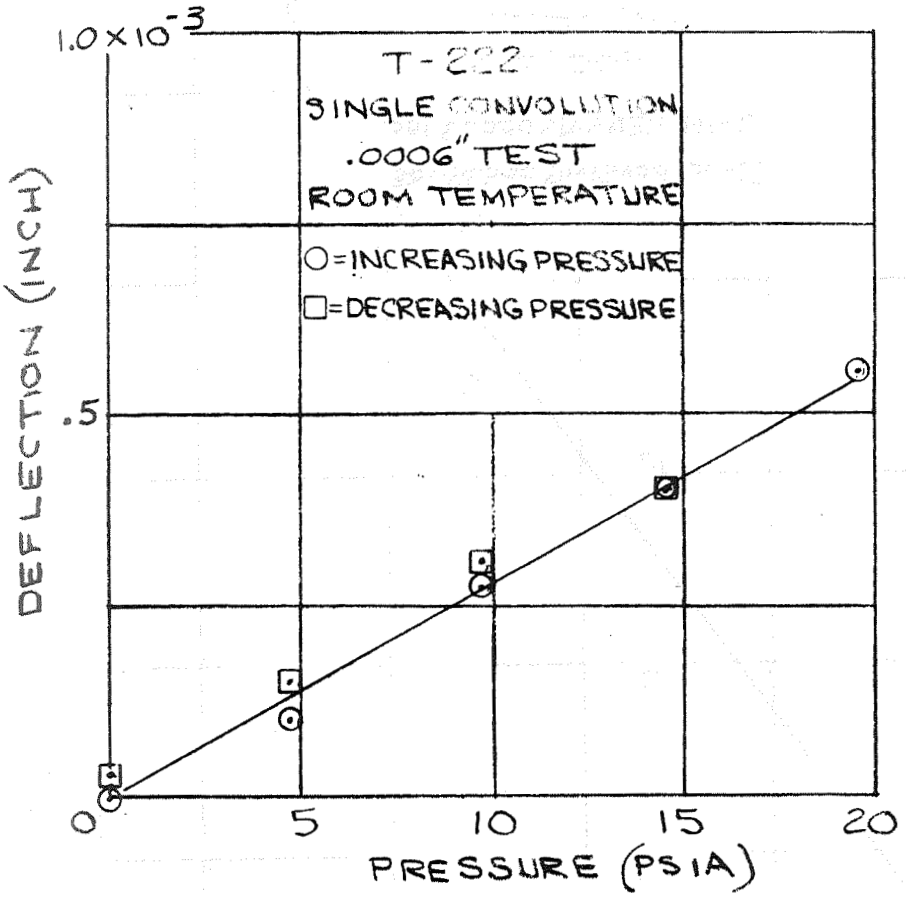


FIGURE 54

T-222 PRESSURE-DEFLECTION, ROOM TEMPERATURE

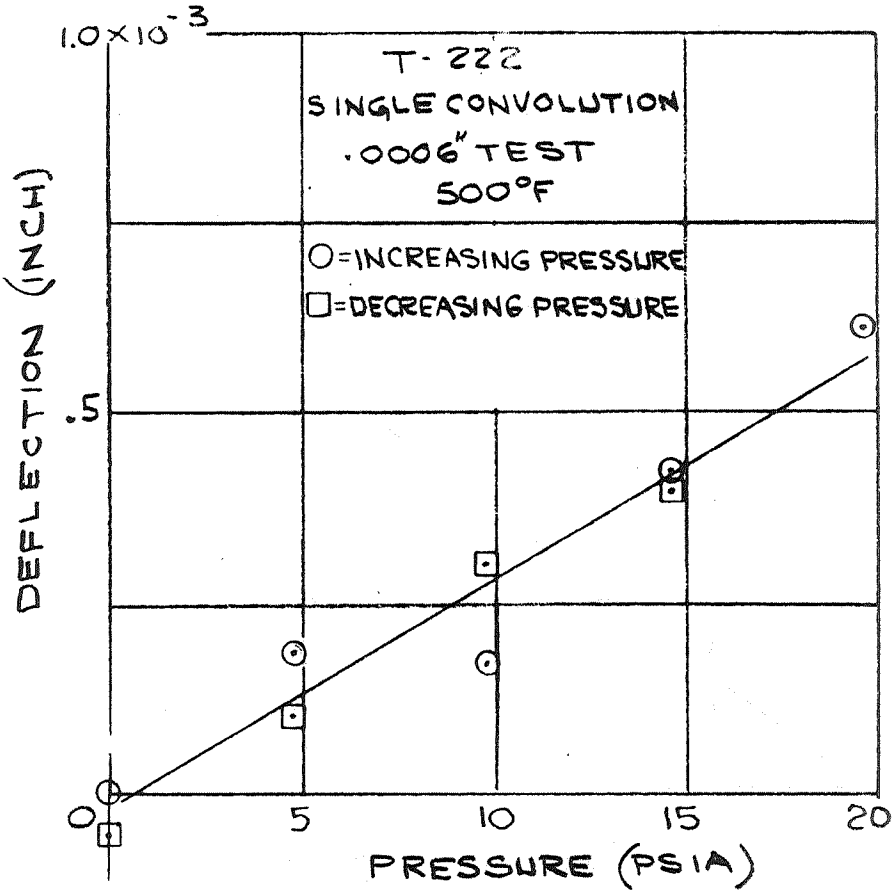


FIGURE 55

T-222 PRESSURE-DEFLECTION, 500°F

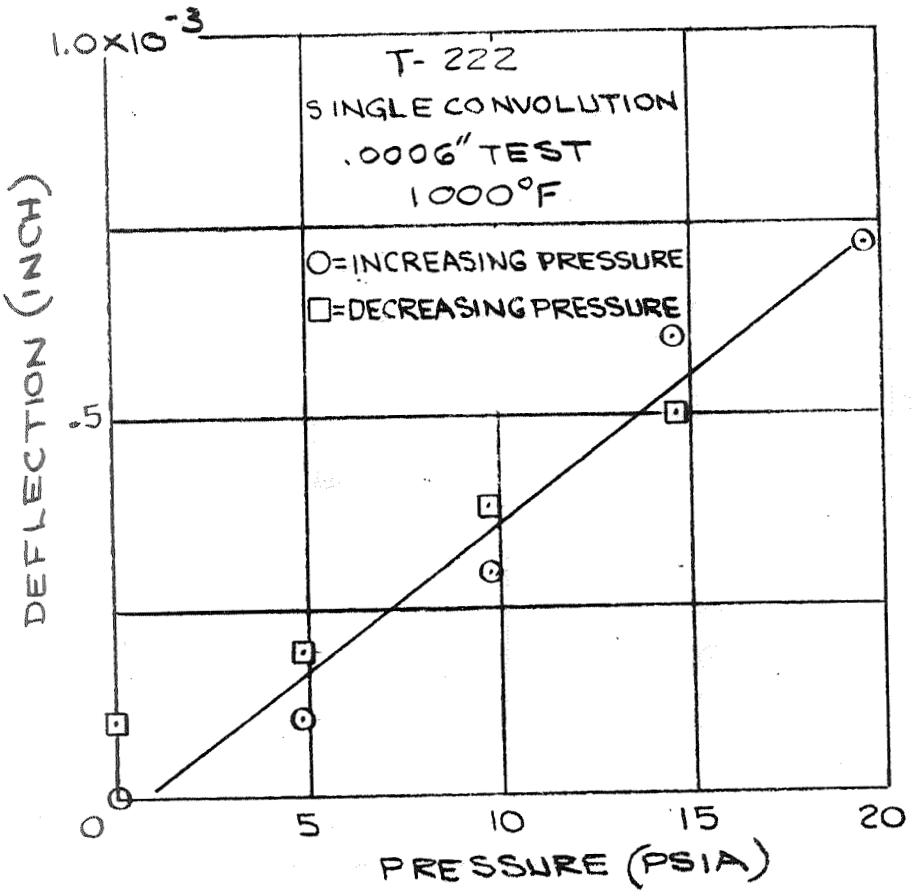


FIGURE 56

T-222 PRESSURE-DEFLECTION, 1000°F

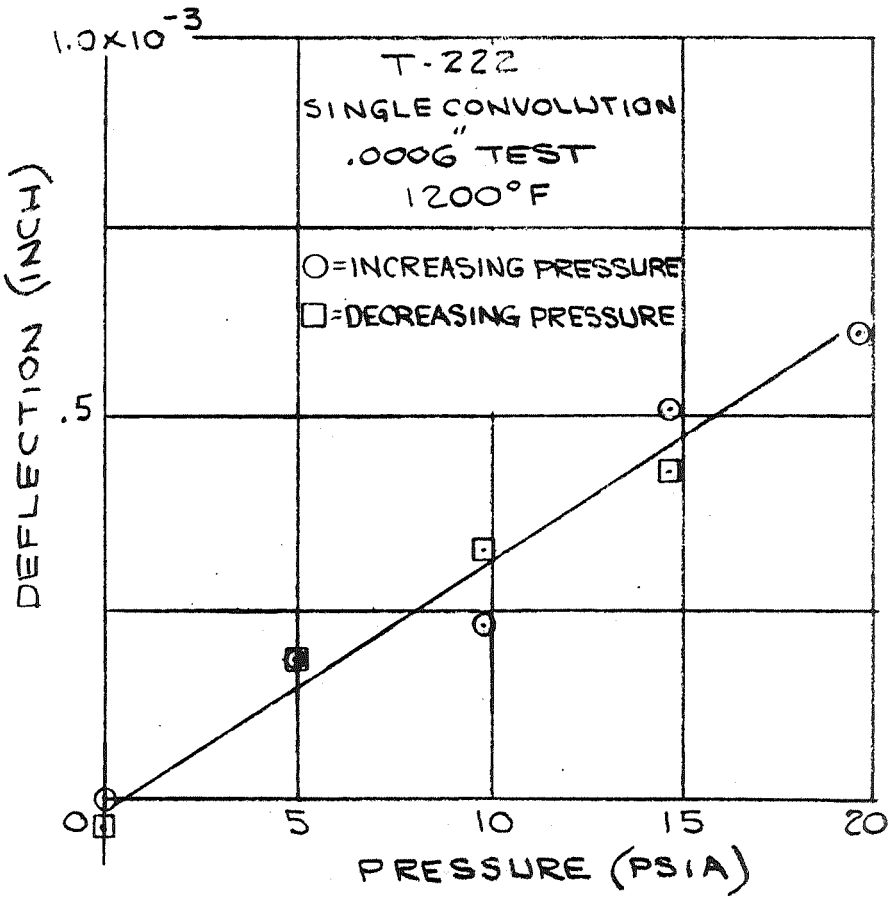


FIGURE 57

T-222 PRESSURE-DEFLECTION, 1200°F

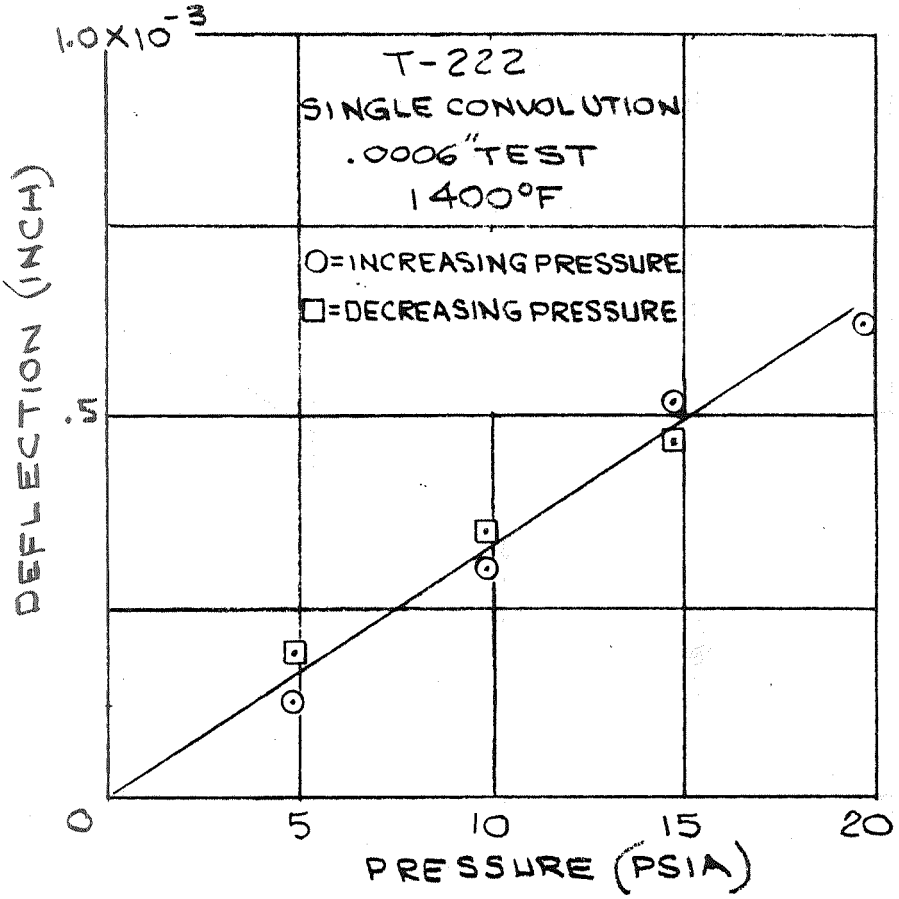


FIGURE 58

T-222 PRESSURE-DEFLECTION, 1400°F

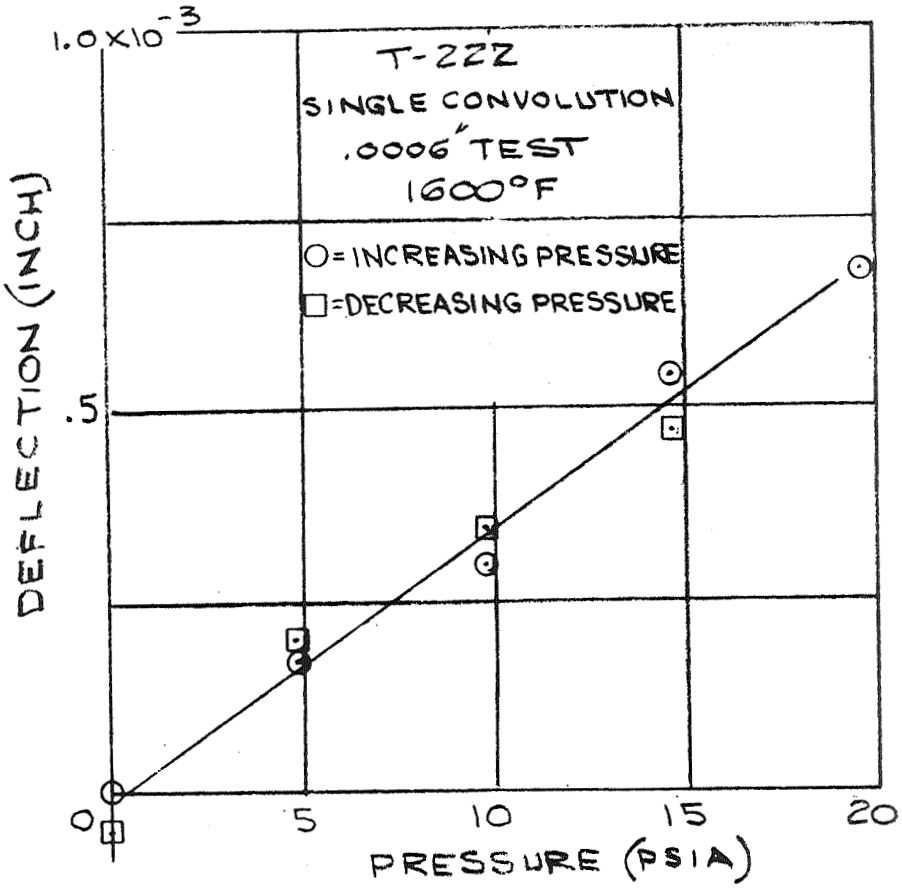


FIGURE 59

T-222 PRESSURE-DEFLECTION, 1600°F

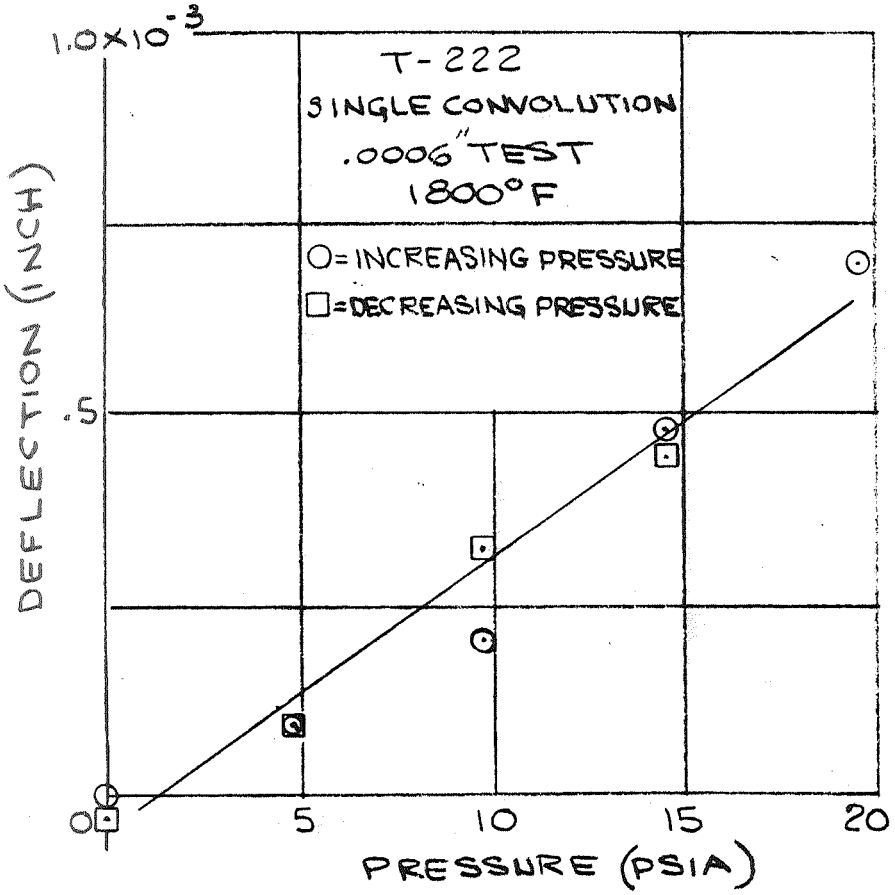


FIGURE 60

T-222 PRESSURE-DEFLECTION, 1800°F

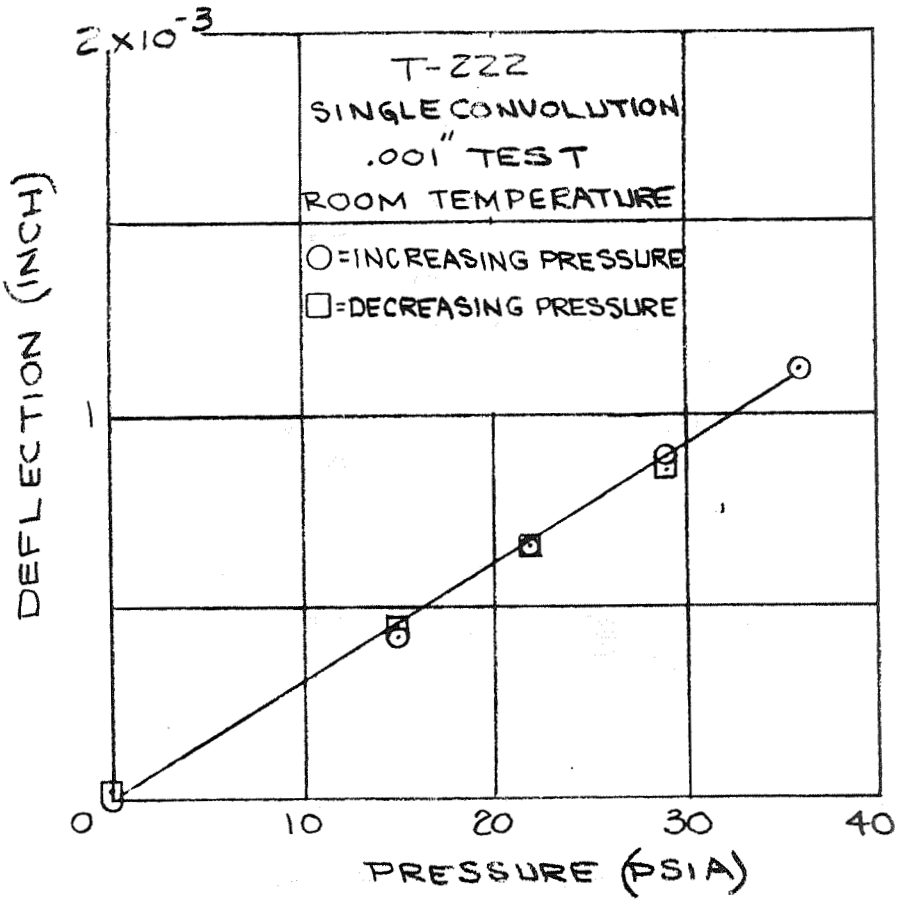


FIGURE 61

T-222 PRESSURE-DEFLECTION, ROOM TEMPERATURE

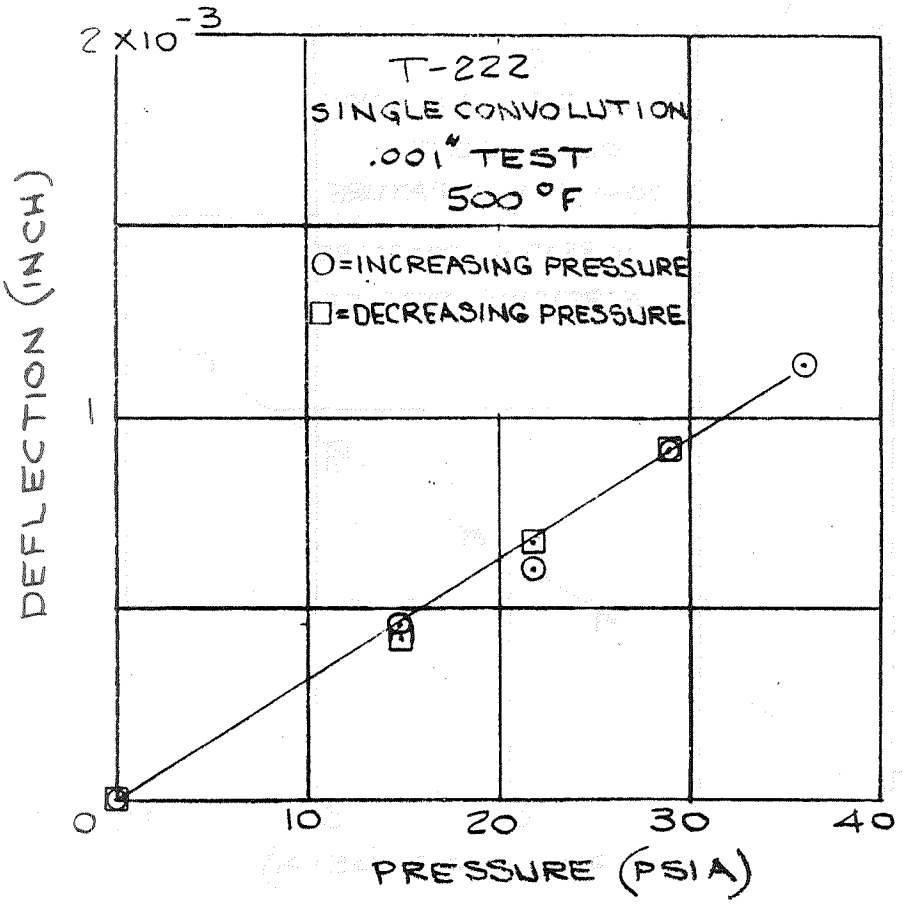


FIGURE 62

T-222 PRESSURE-DEFLECTION, 500°F

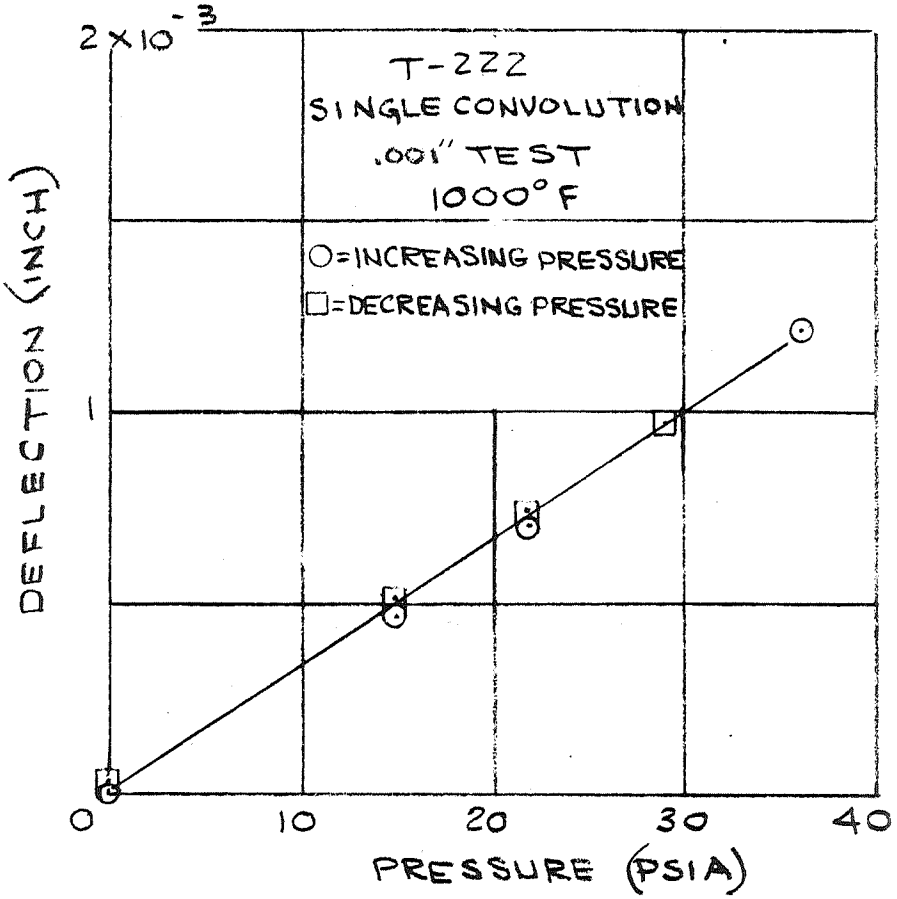


FIGURE 63

T-222 PRESSURE-DEFLECTION, 1000°F

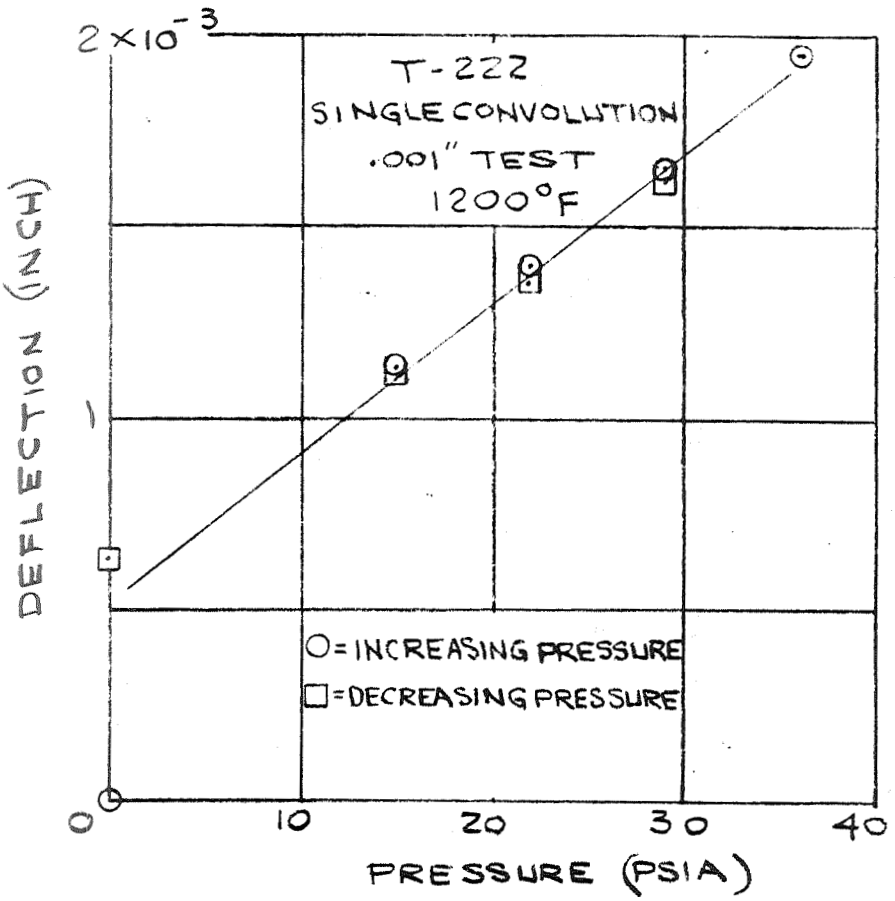


FIGURE 64

T-222 PRESSURE-DEFLECTION, 1200°F

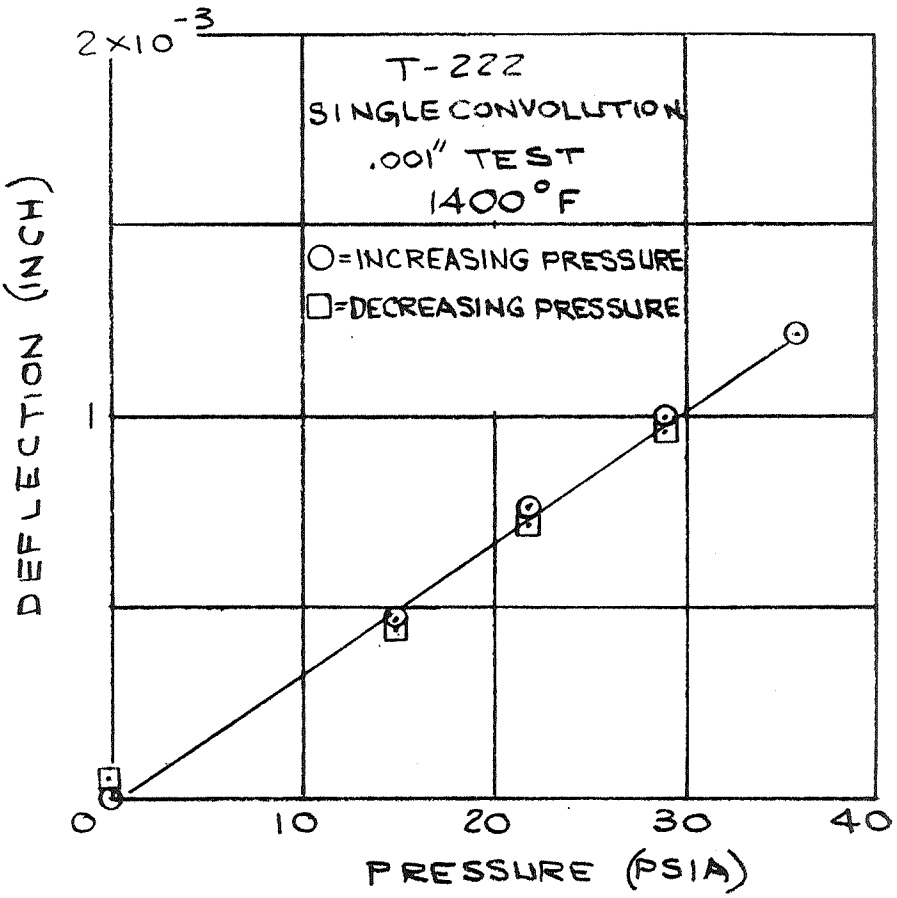


FIGURE 65

T-222 PRESSURE-DEFLECTION, 1400°F

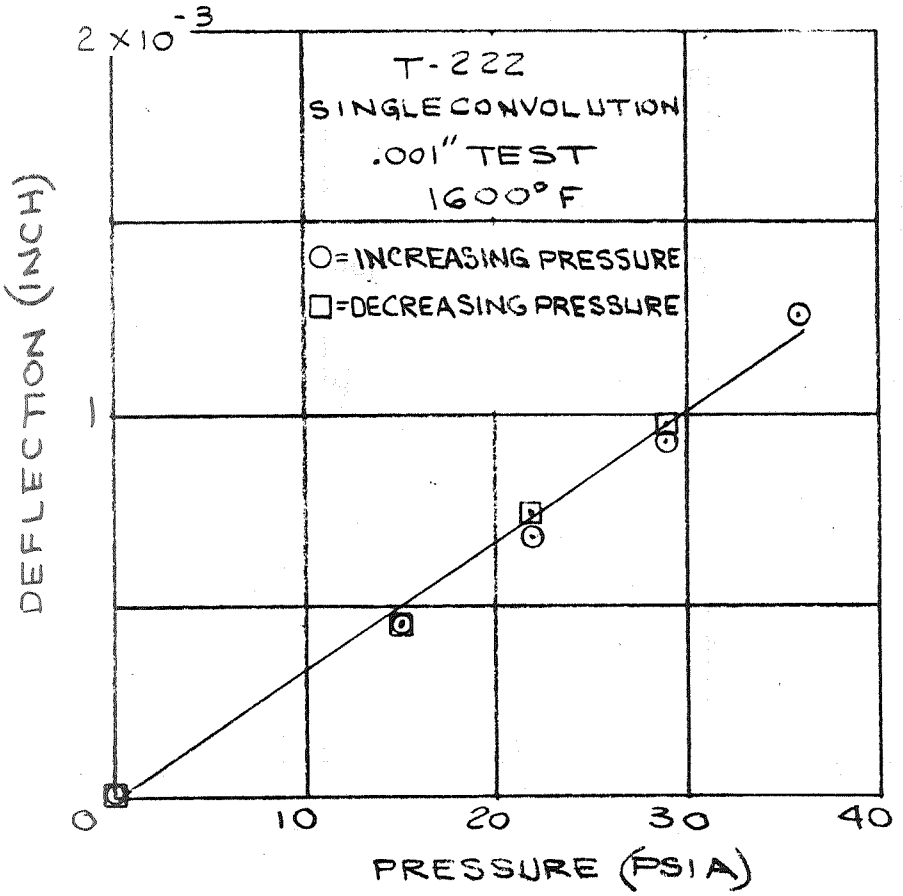


FIGURE 66

T-222 PRESSURE-DEFLECTION, 1600°F

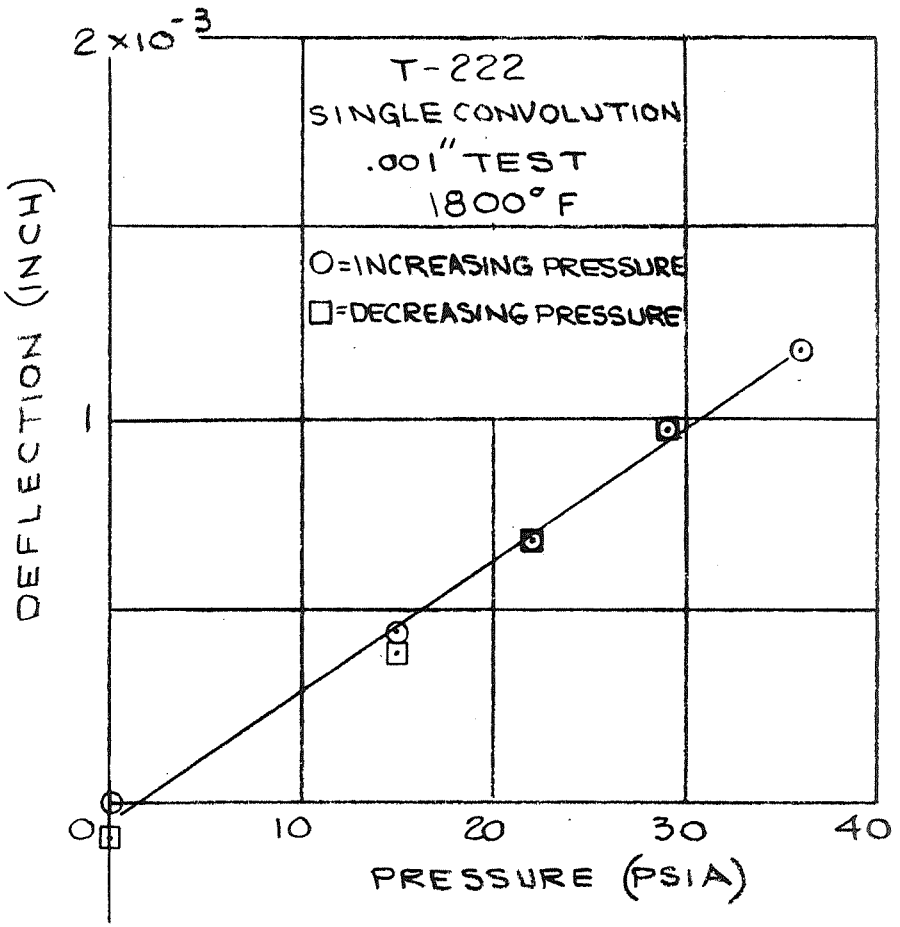


FIGURE 67

T-222 PRESSURE-DEFLECTION, 1800°F

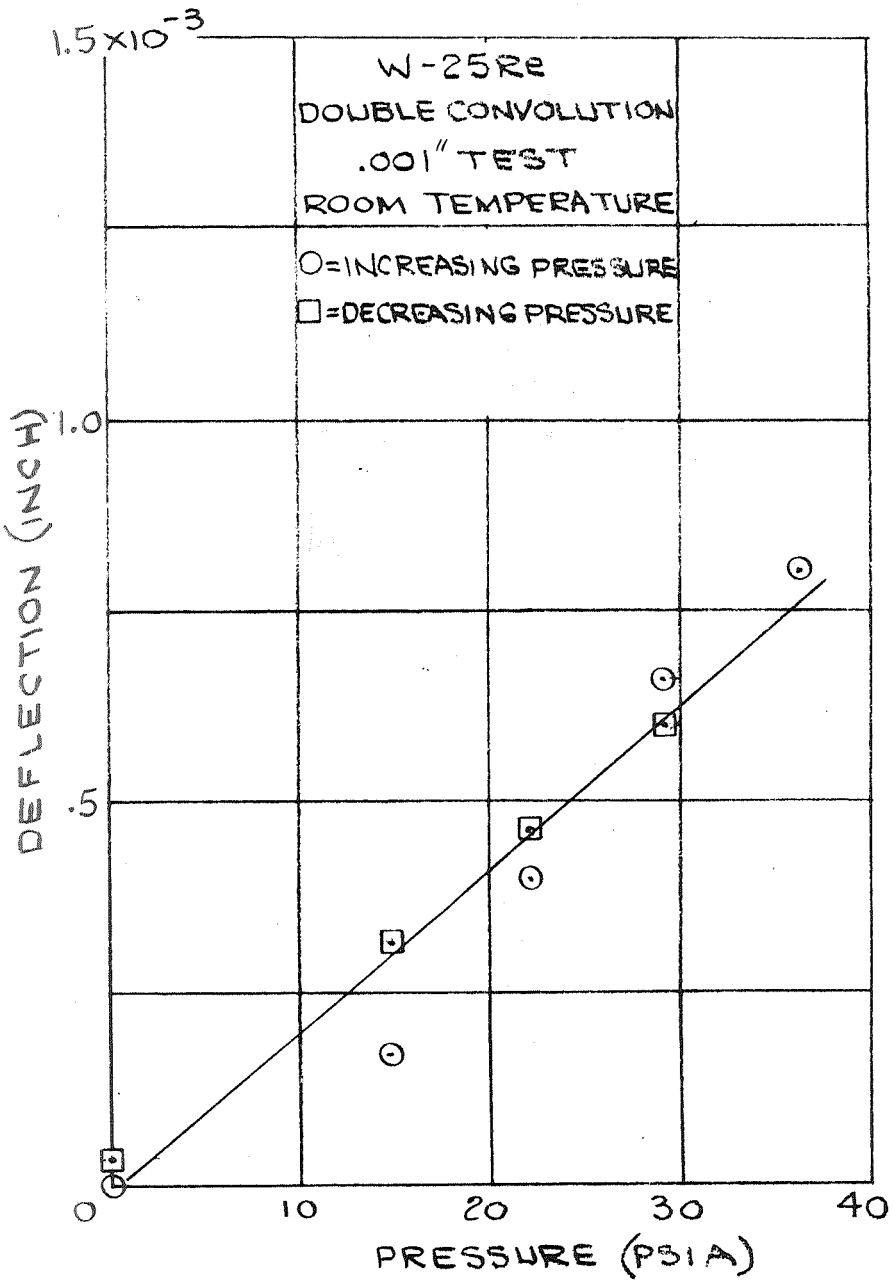


FIGURE 68

W-25Re PRESSURE-DEFLECTION, ROOM TEMPERATURE

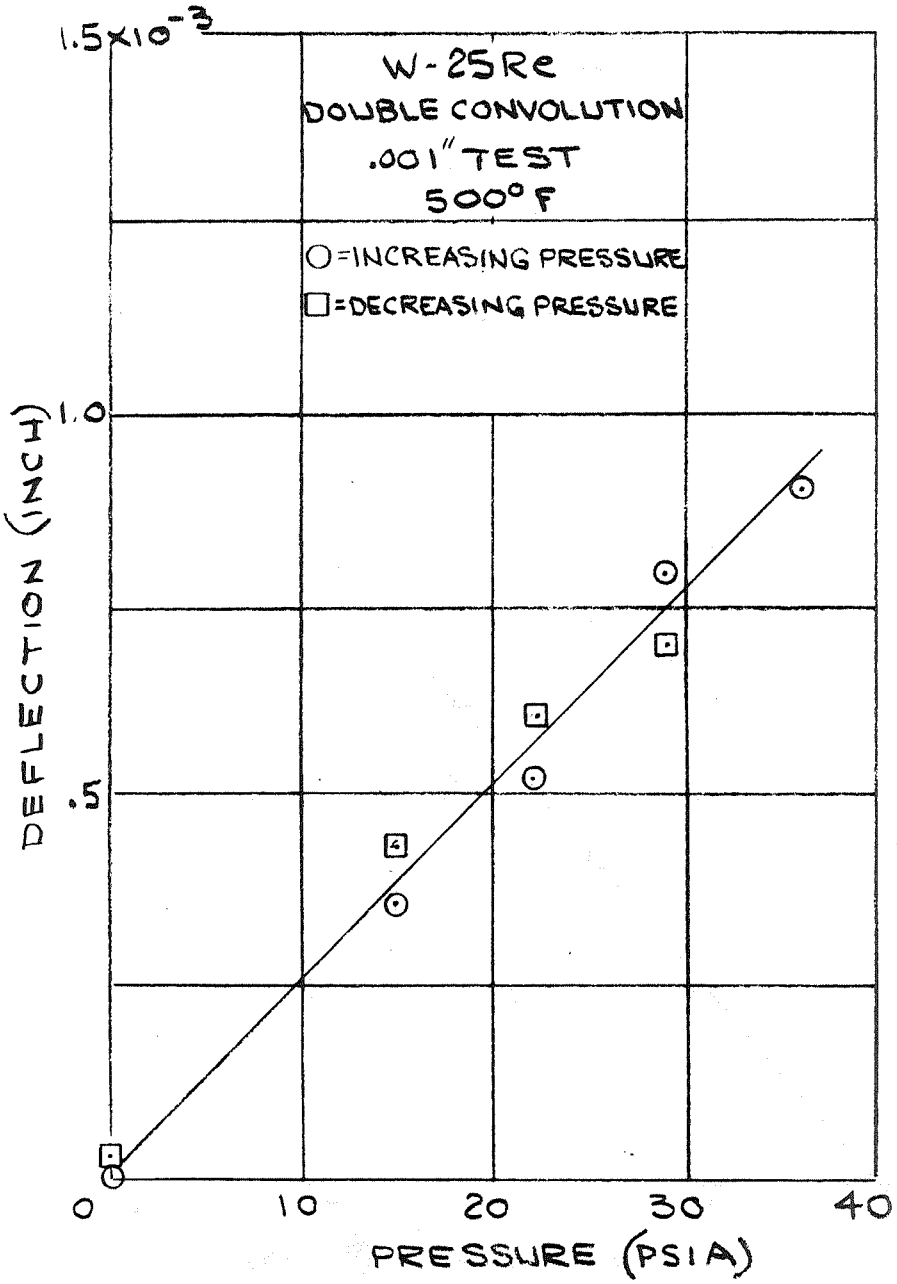


FIGURE 69

W-25Re PRESSURE-DEFLECTION, 500°F

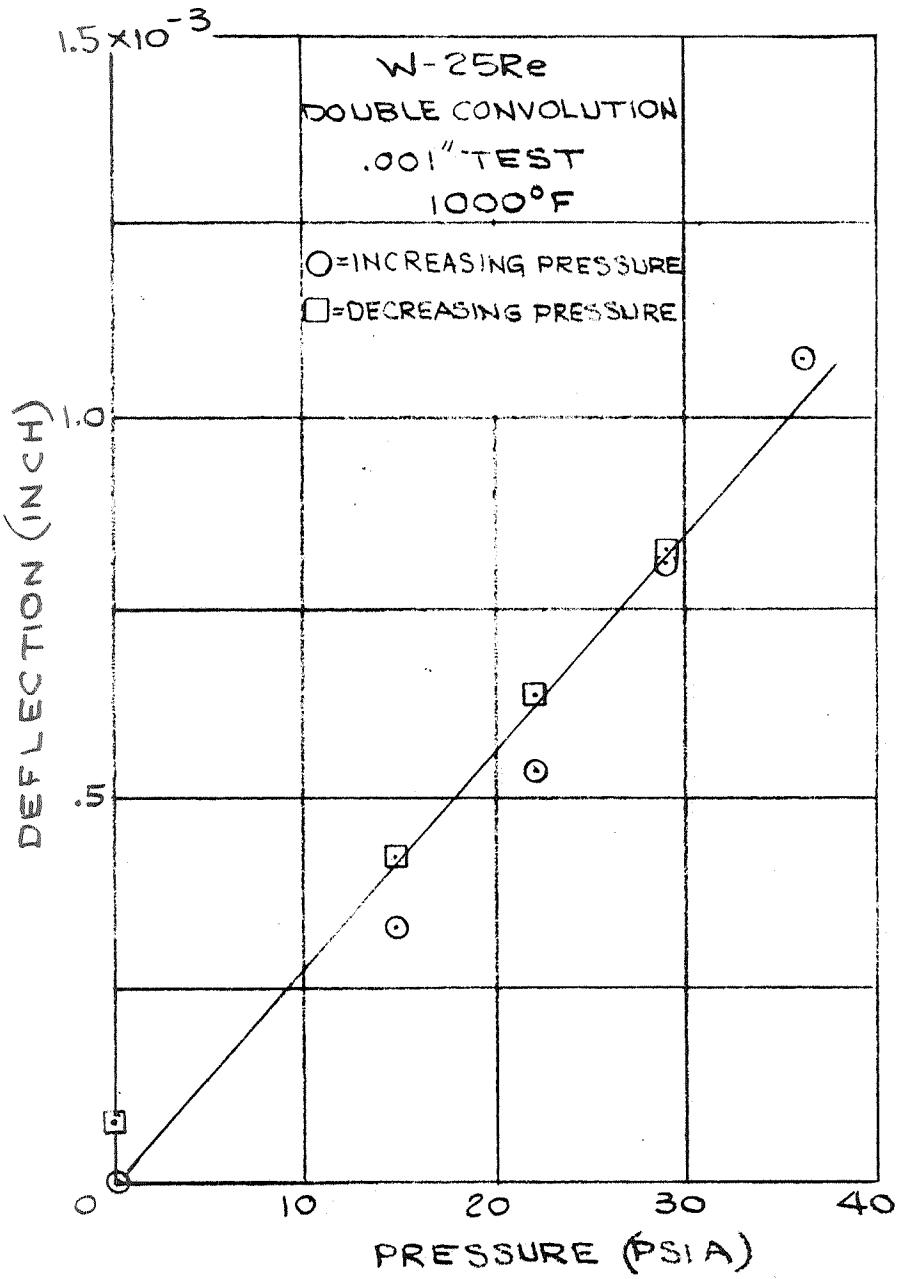


FIGURE 70

W-25Re PRESSURE-DEFLECTION, 1000°F

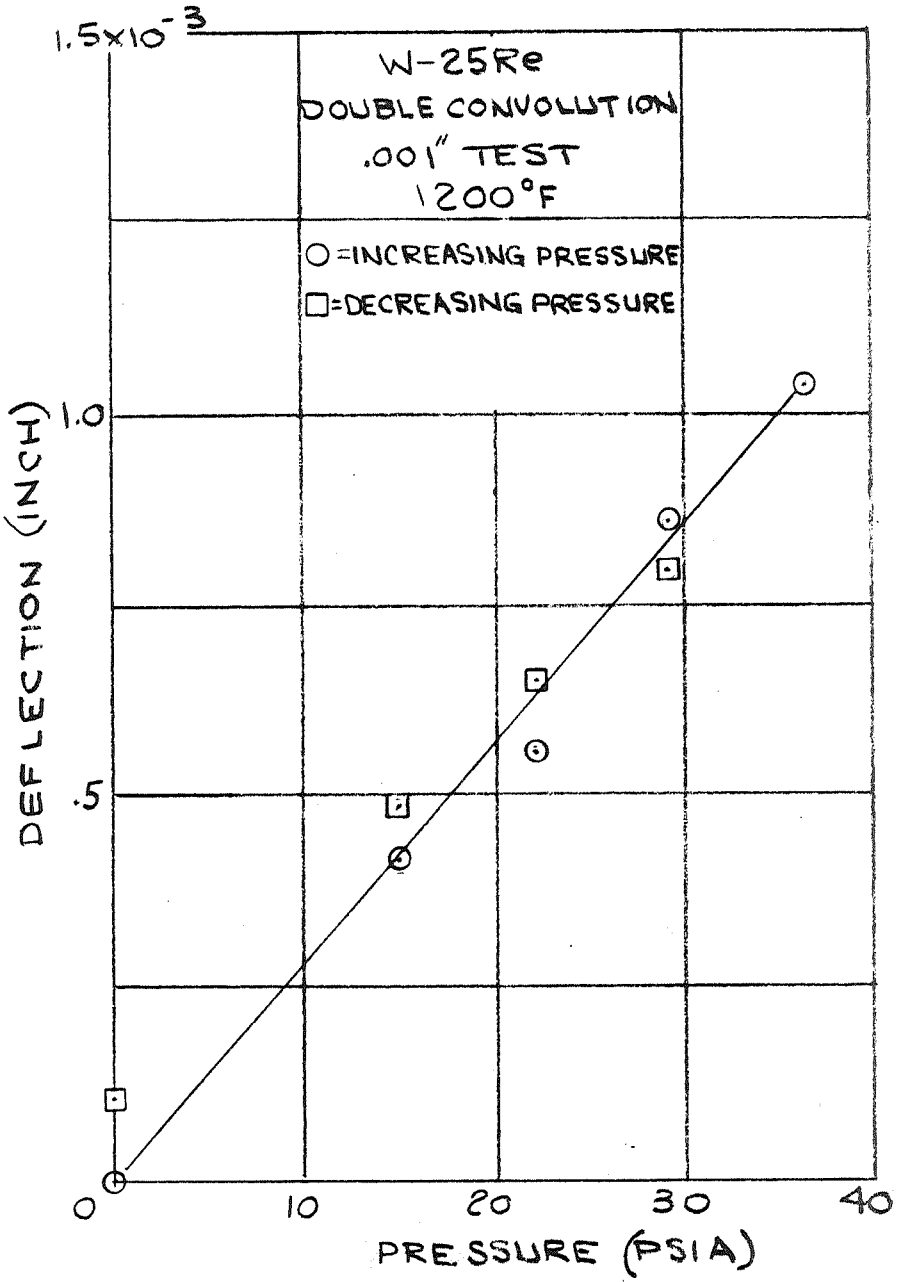


FIGURE 71

W-25Re PRESSURE-DEFLECTION, 1200°F

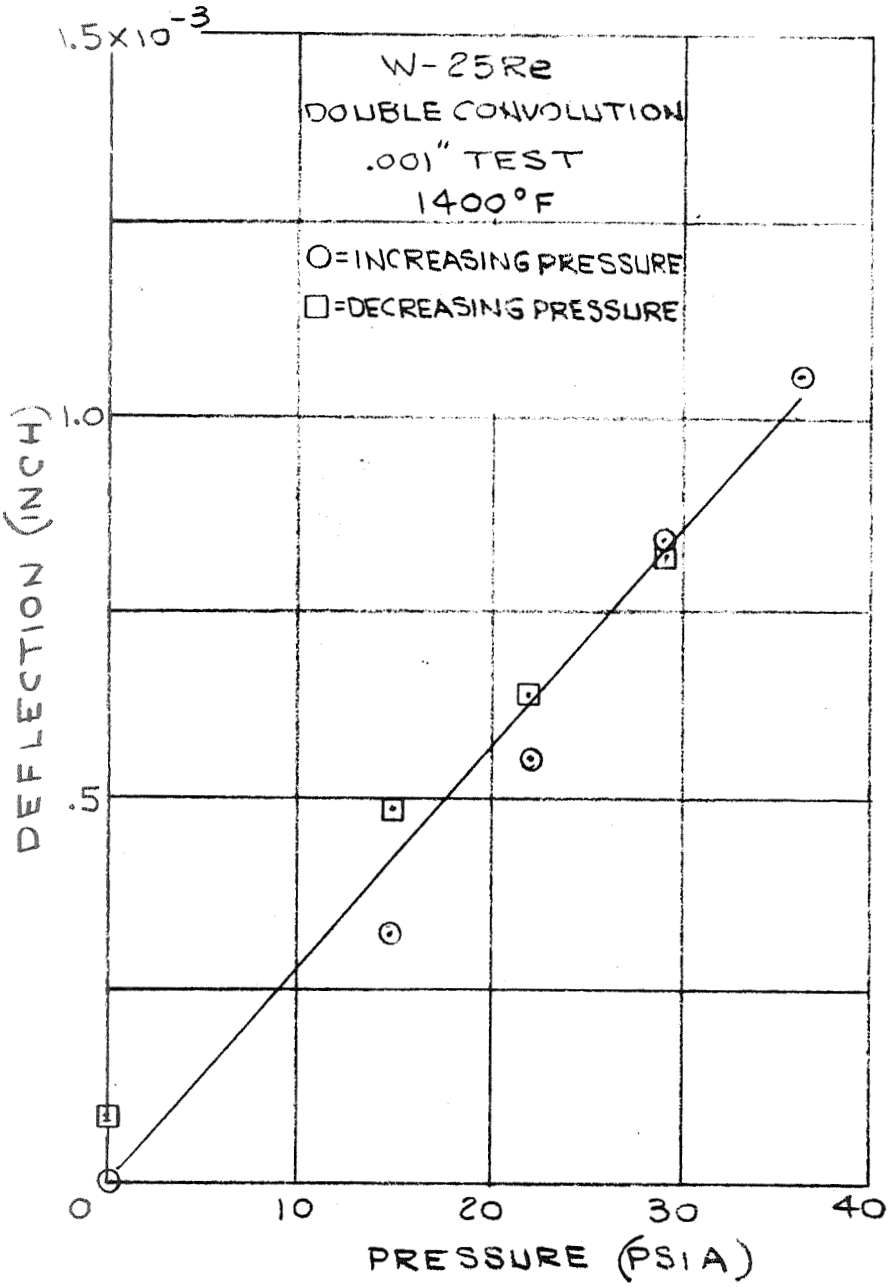


FIGURE 72

W-25Re PRESSURE-DEFLECTION, 1400°F

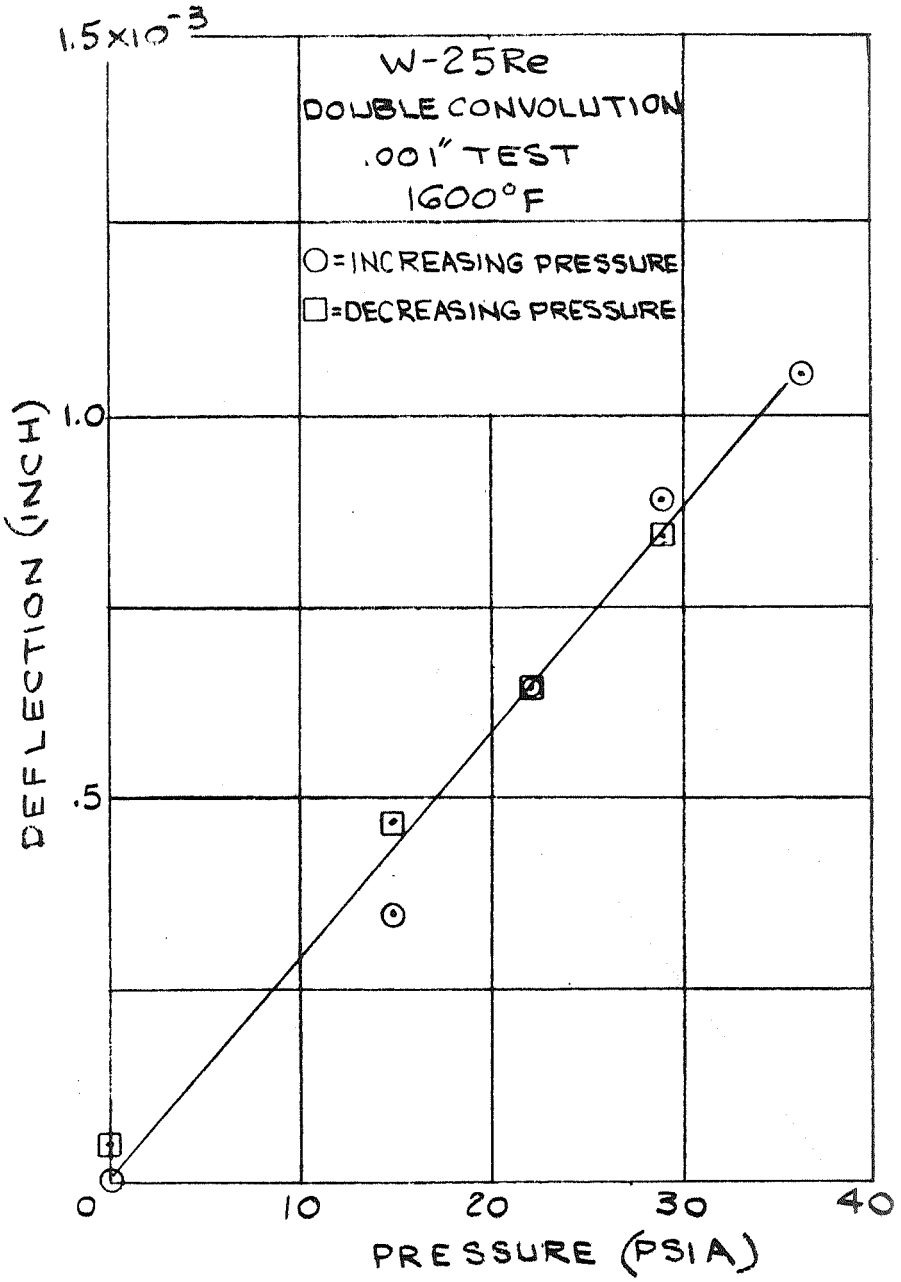


FIGURE 73

W-25Re PRESSURE-DEFLECTION, 1600°F

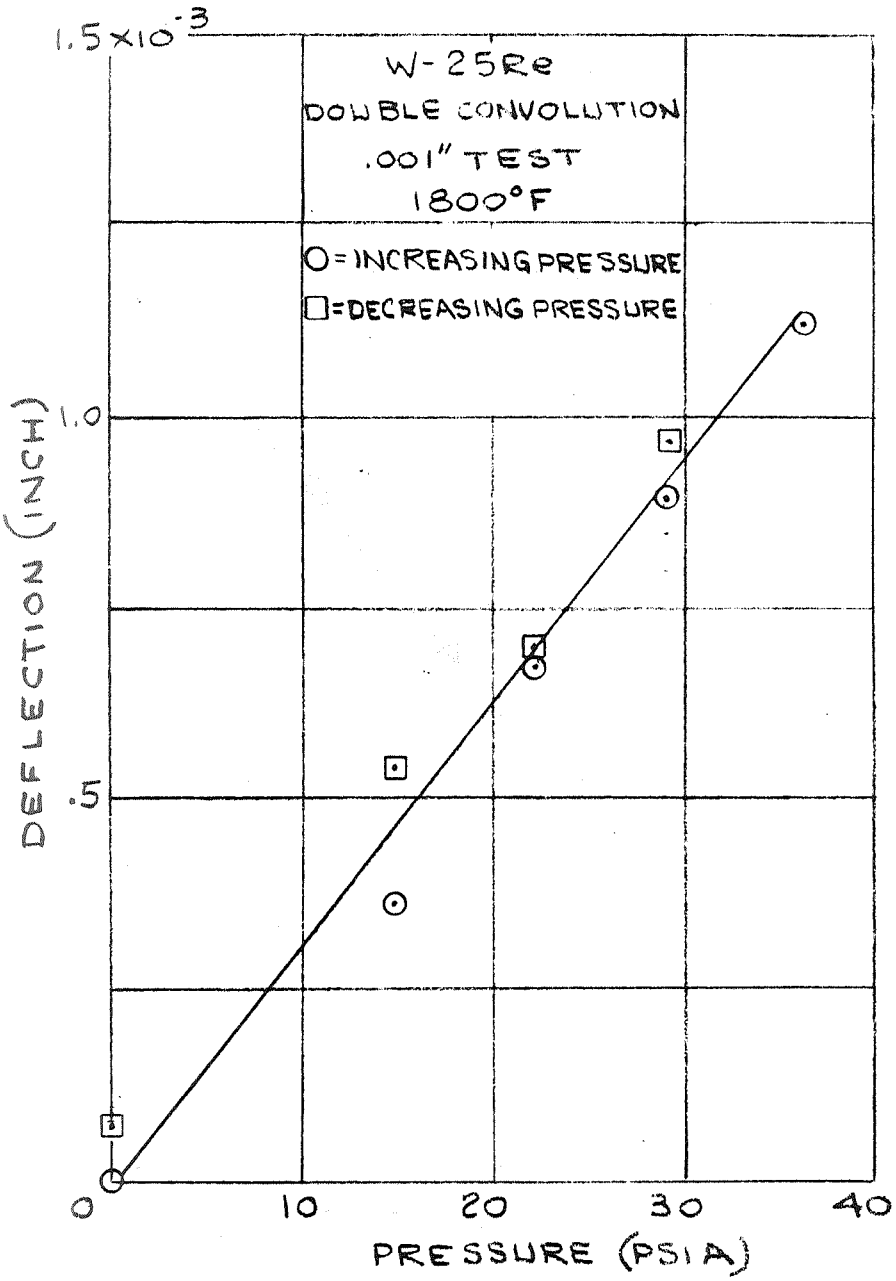


FIGURE 74

W-25Re PRESSURE-DEFLECTION, 1800°F

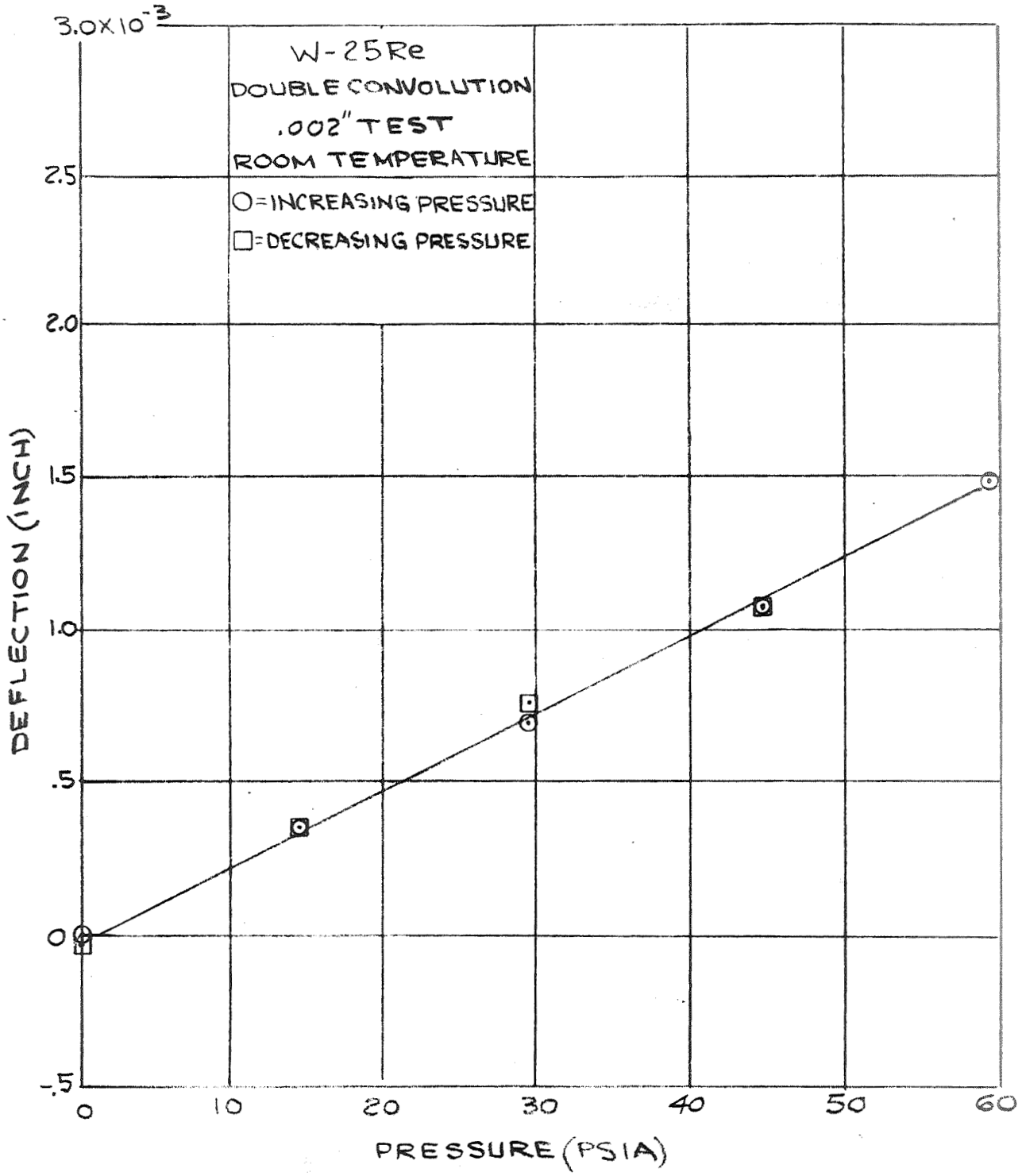


FIGURE 75

W-25Re PRESSURE-DEFLECTION, ROOM TEMPERATURE

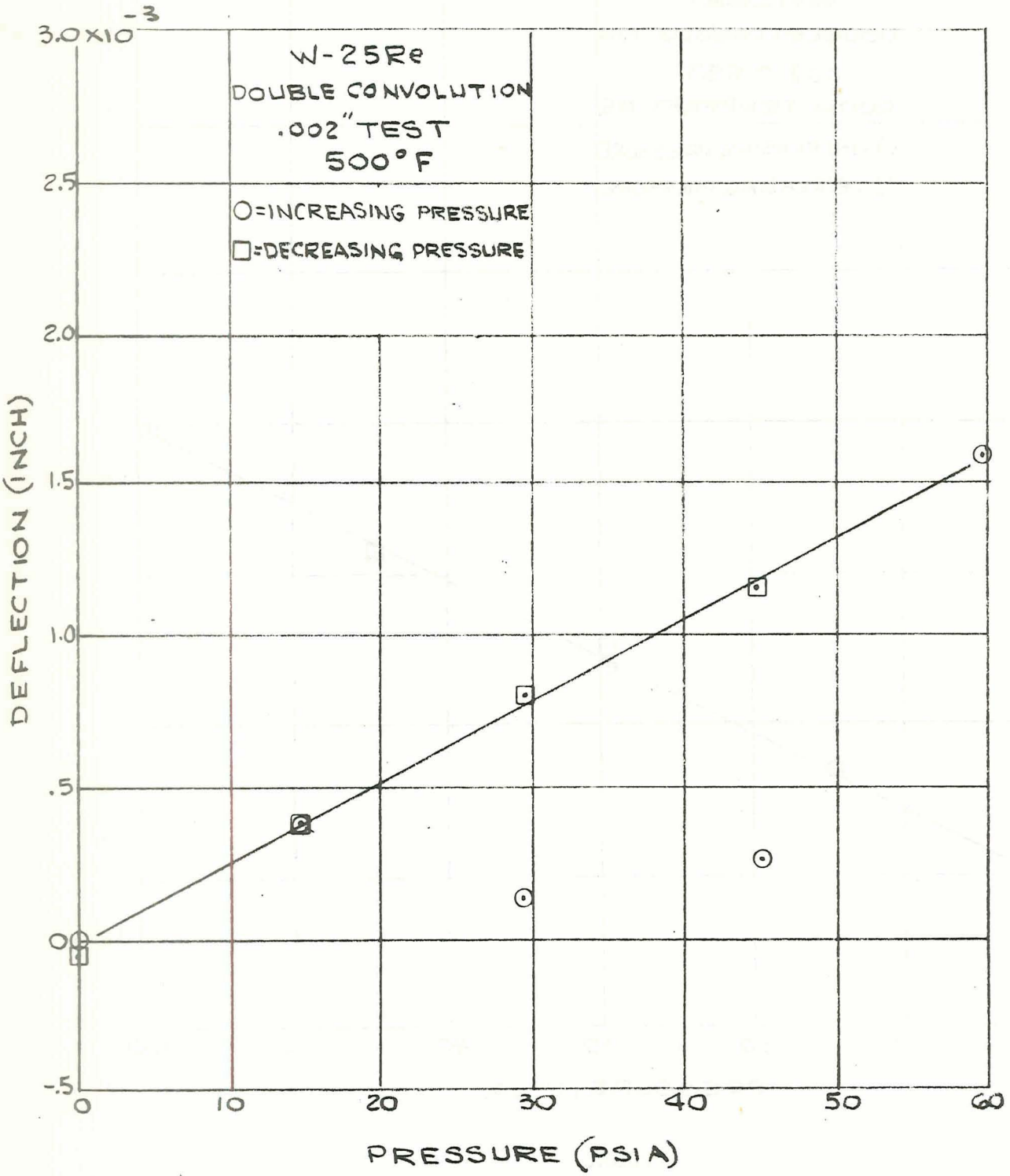


FIGURE 76

W-25Re PRESSURE-DEFLECTION, 500°F

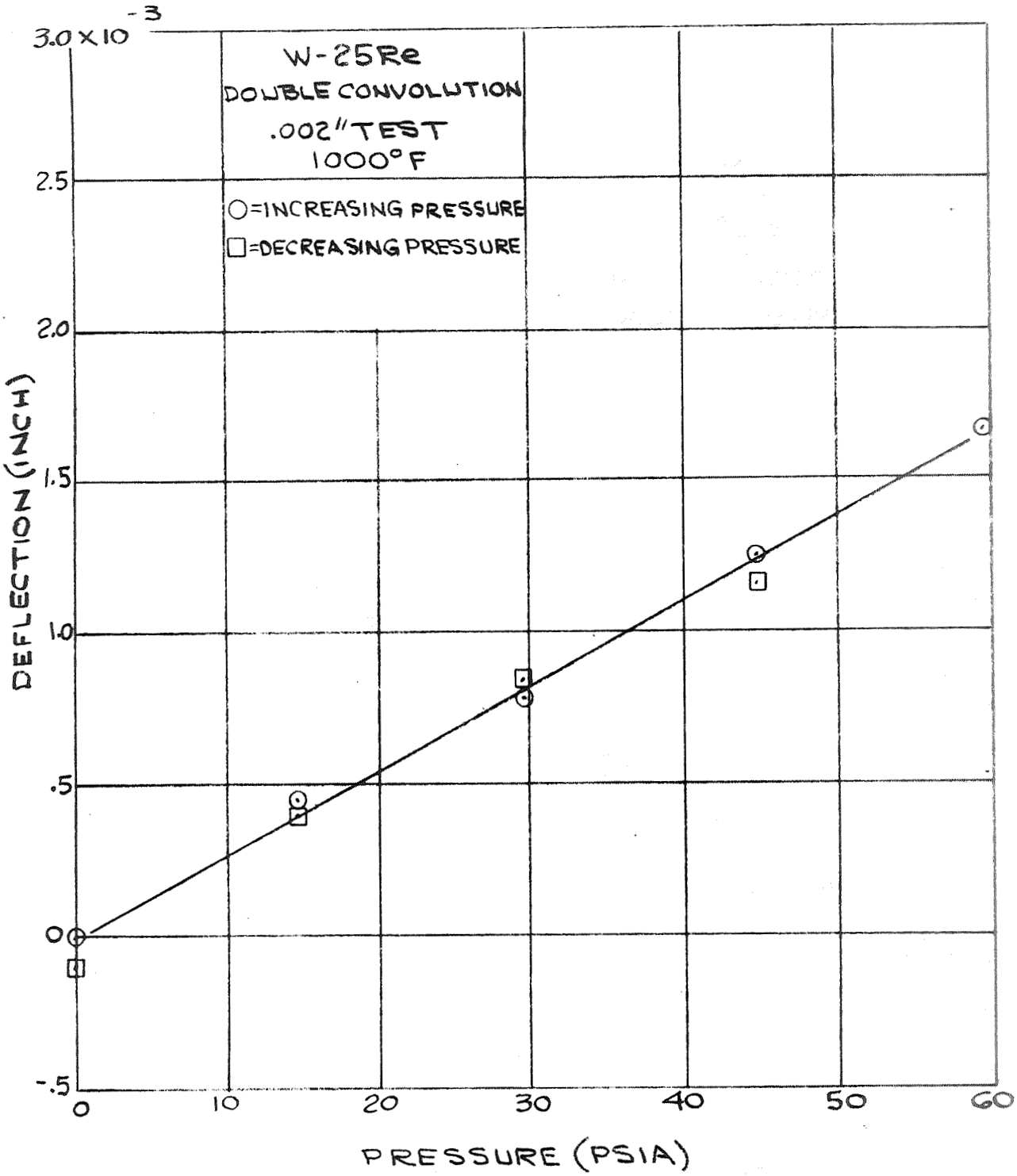


FIGURE 77

W-25Re PRESSURE-DEFLECTION, 1000°F

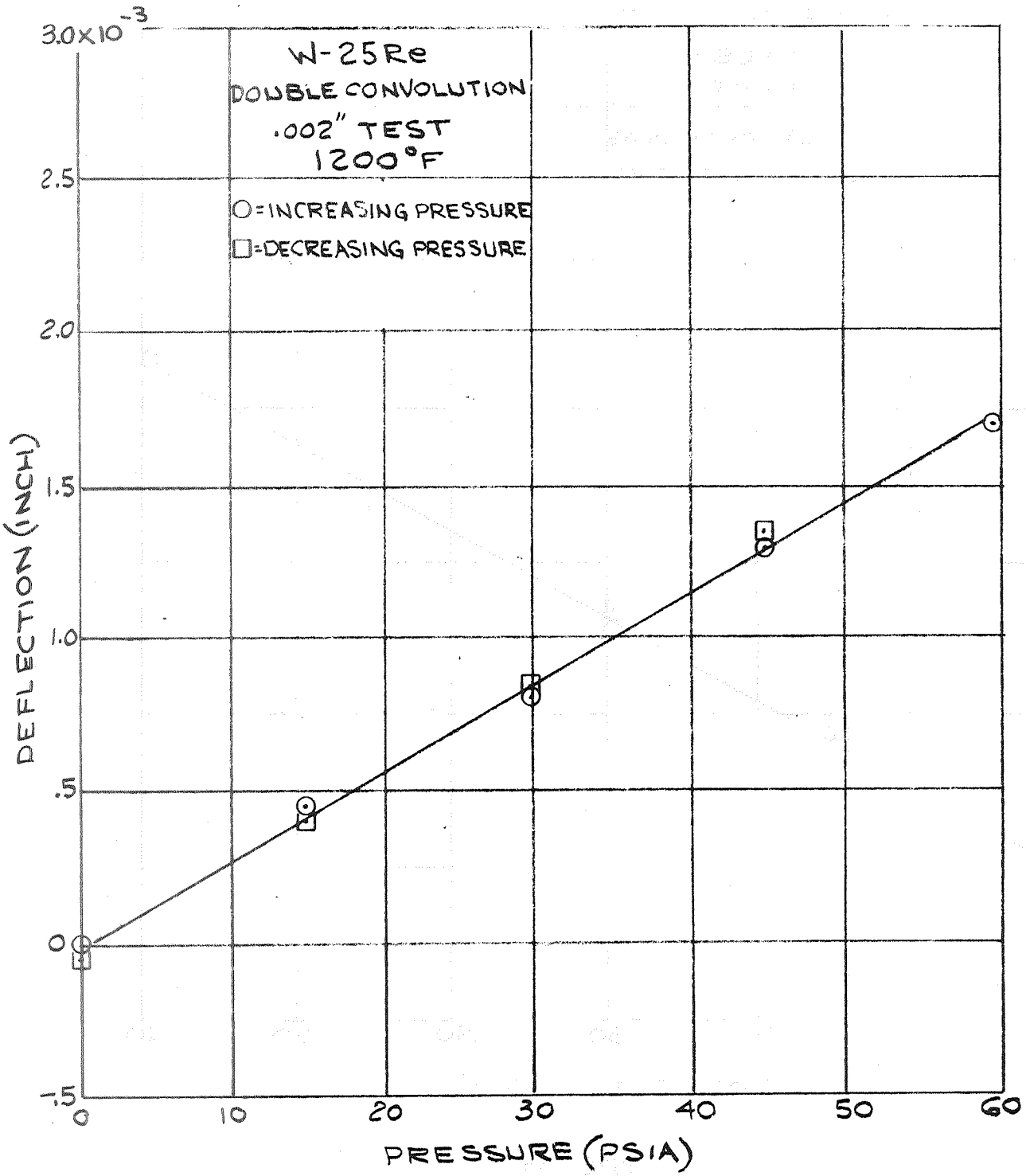


FIGURE 78

W-25Re PRESSURE-DEFLECTION, 1200°F

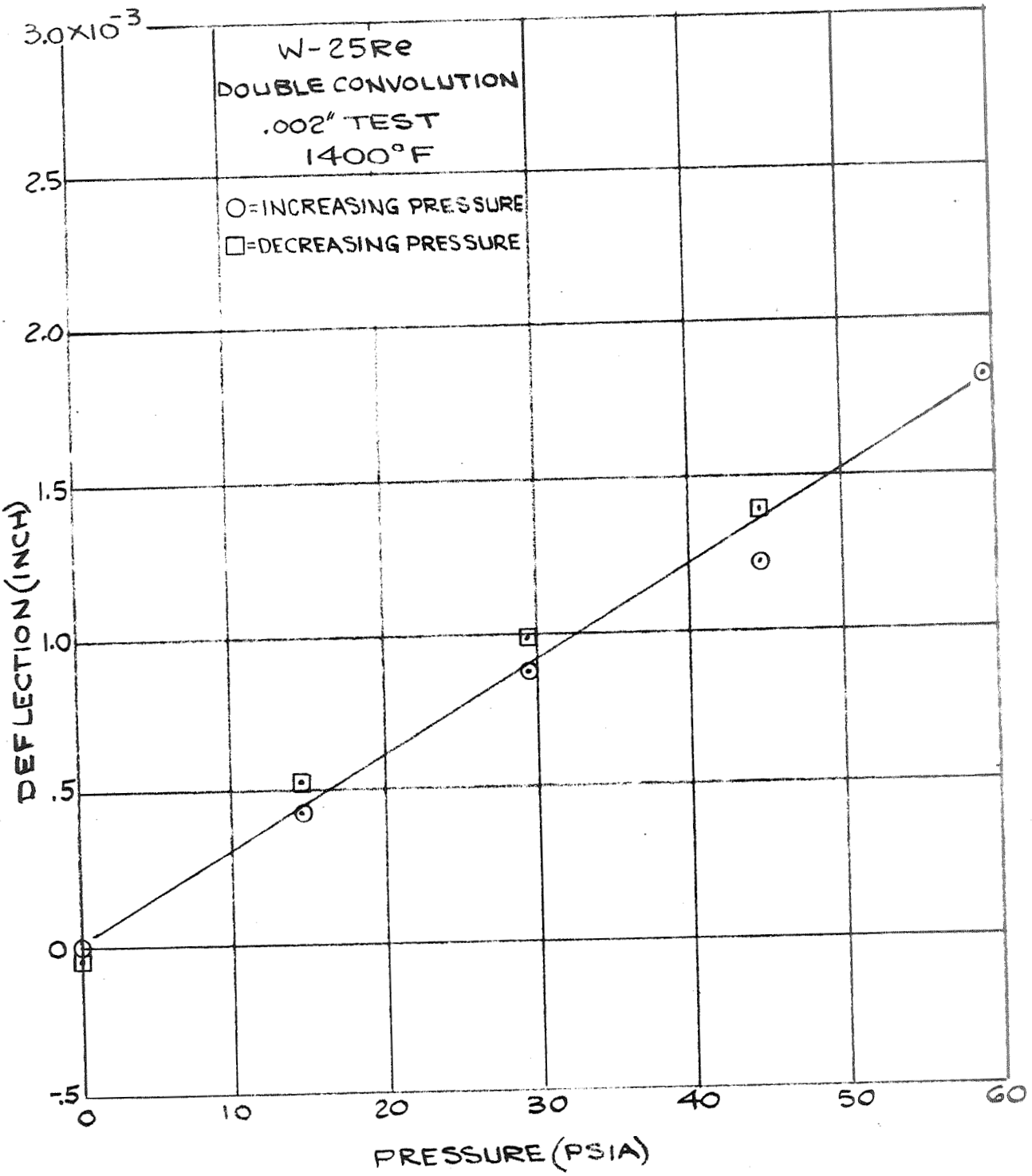


FIGURE 79

W-25Re PRESSURE-DEFLECTION, 1400°F

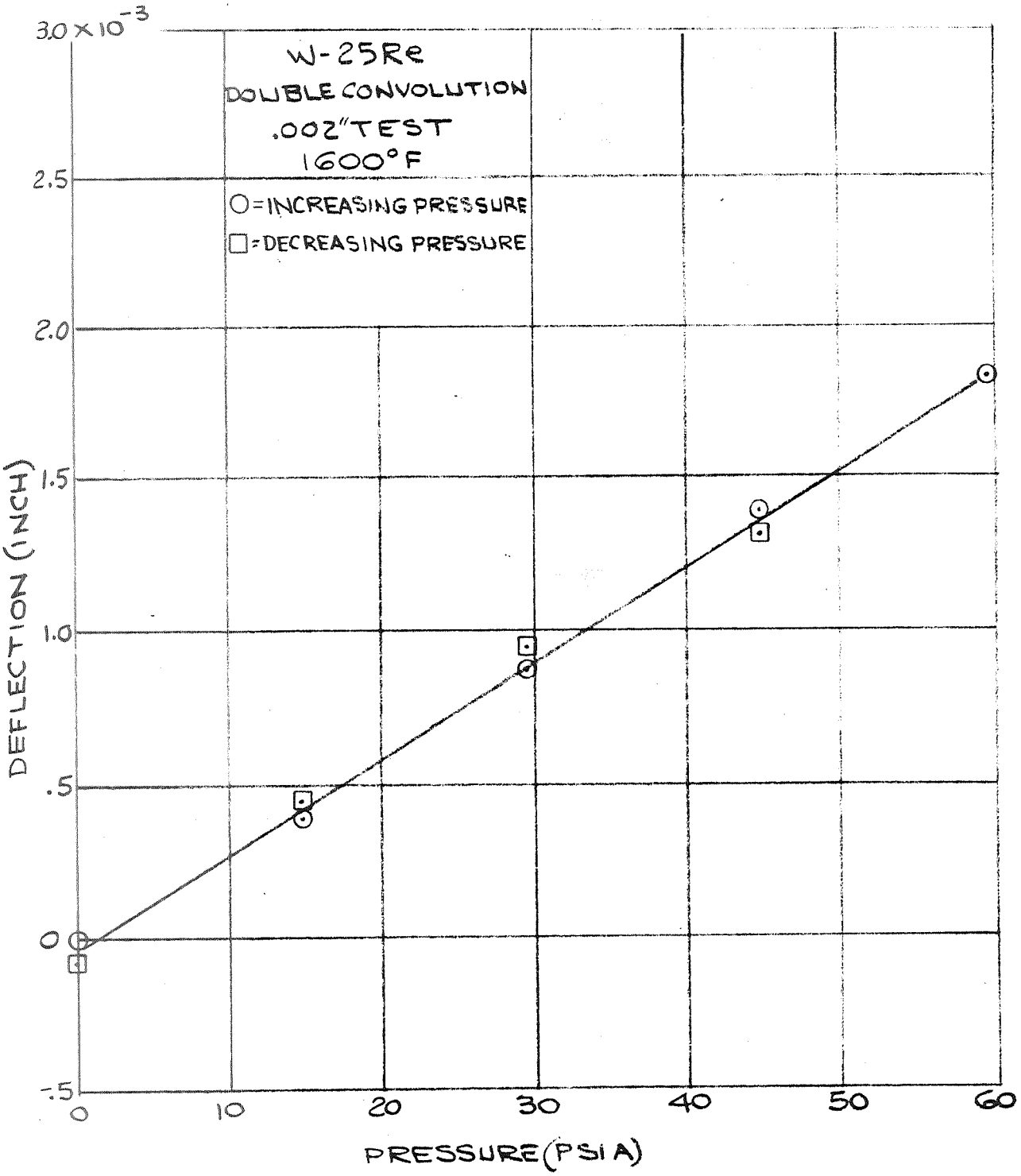


FIGURE 80

W-25Re PRESSURE-DEFLECTION, 1600°F

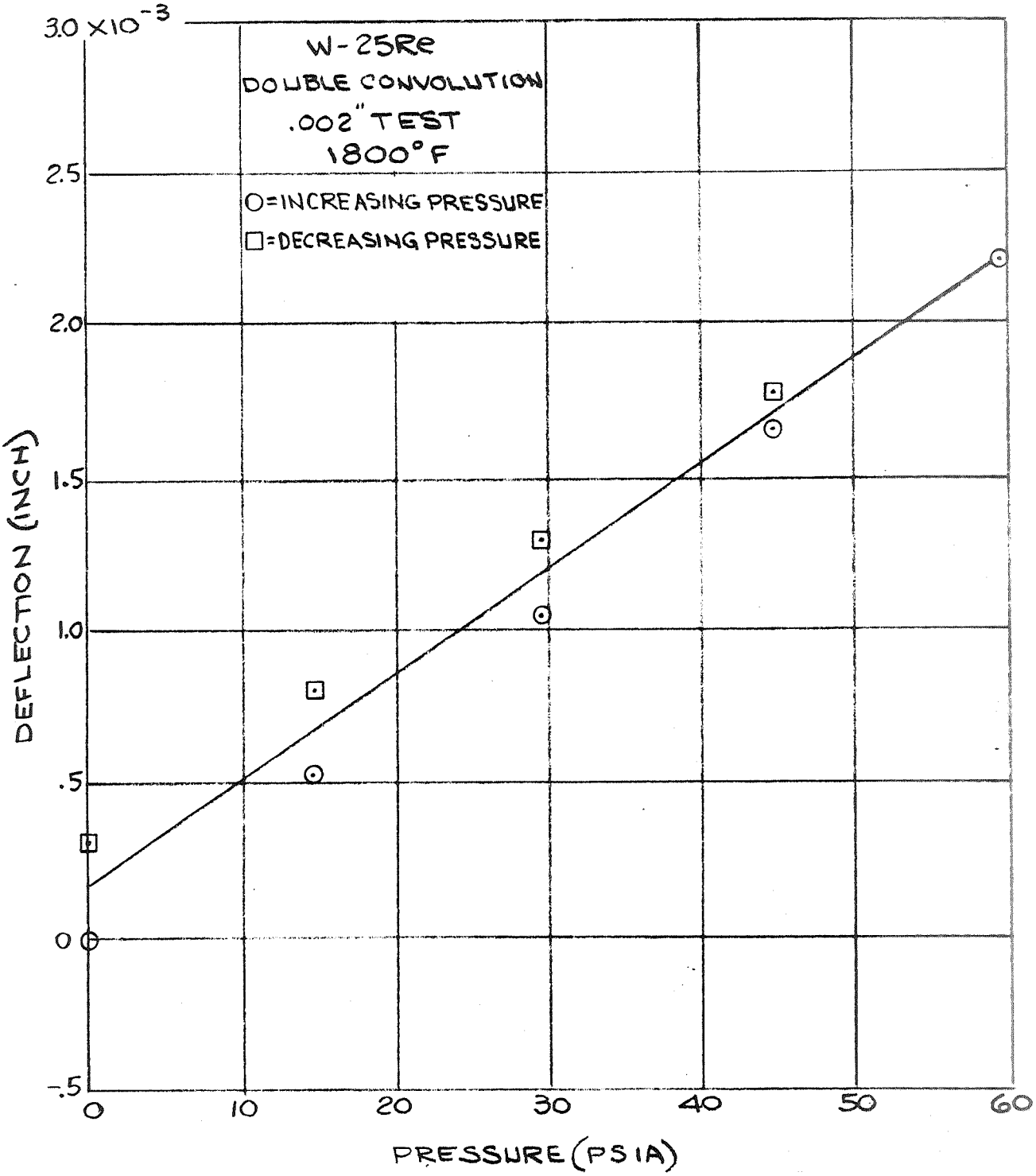


FIGURE 81

W-25Re PRESSURE-DEFLECTION, 1800°F

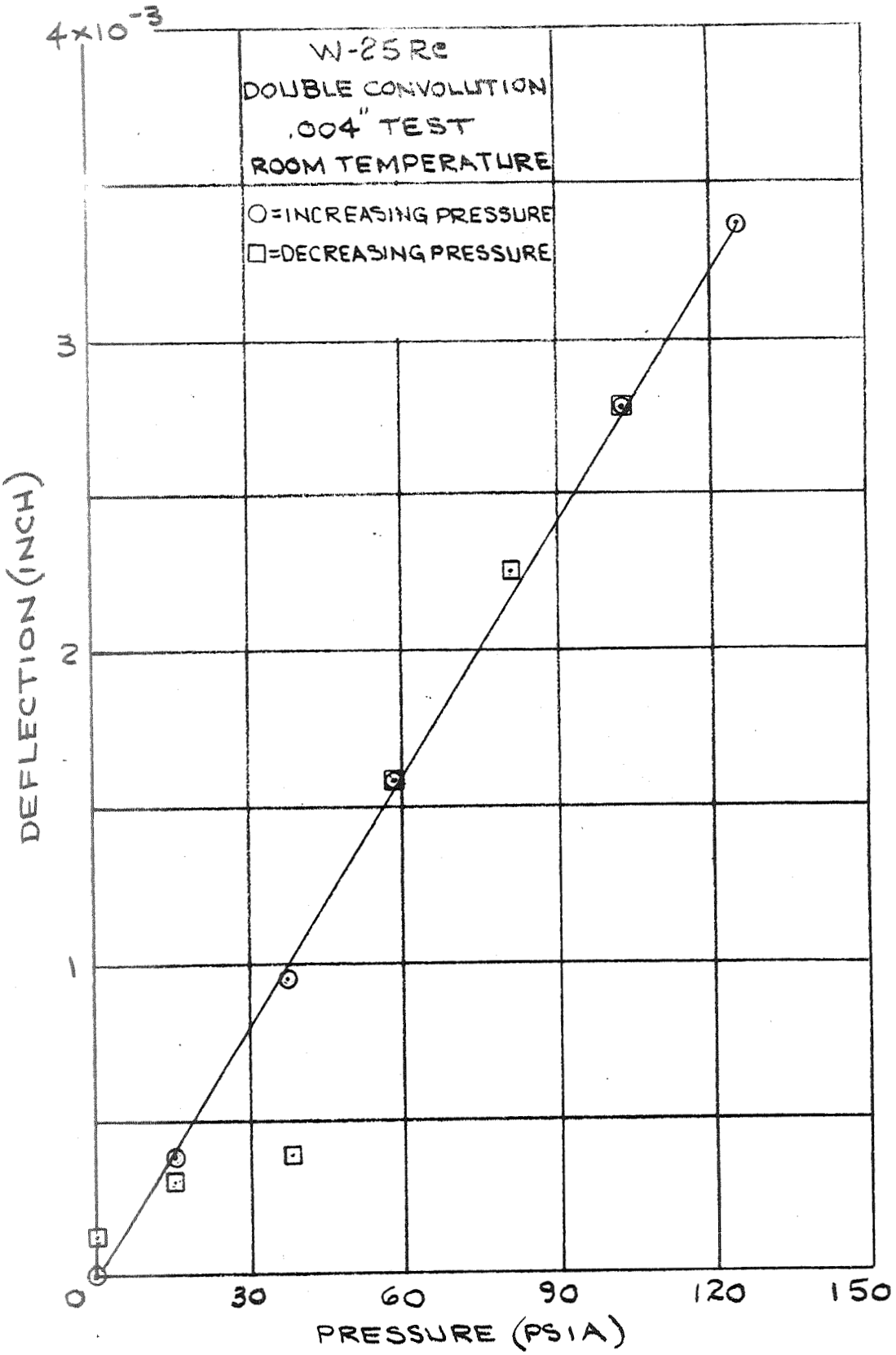


FIGURE 82

W-25Re PRESSURE-DEFLECTION, ROOM TEMPERATURE

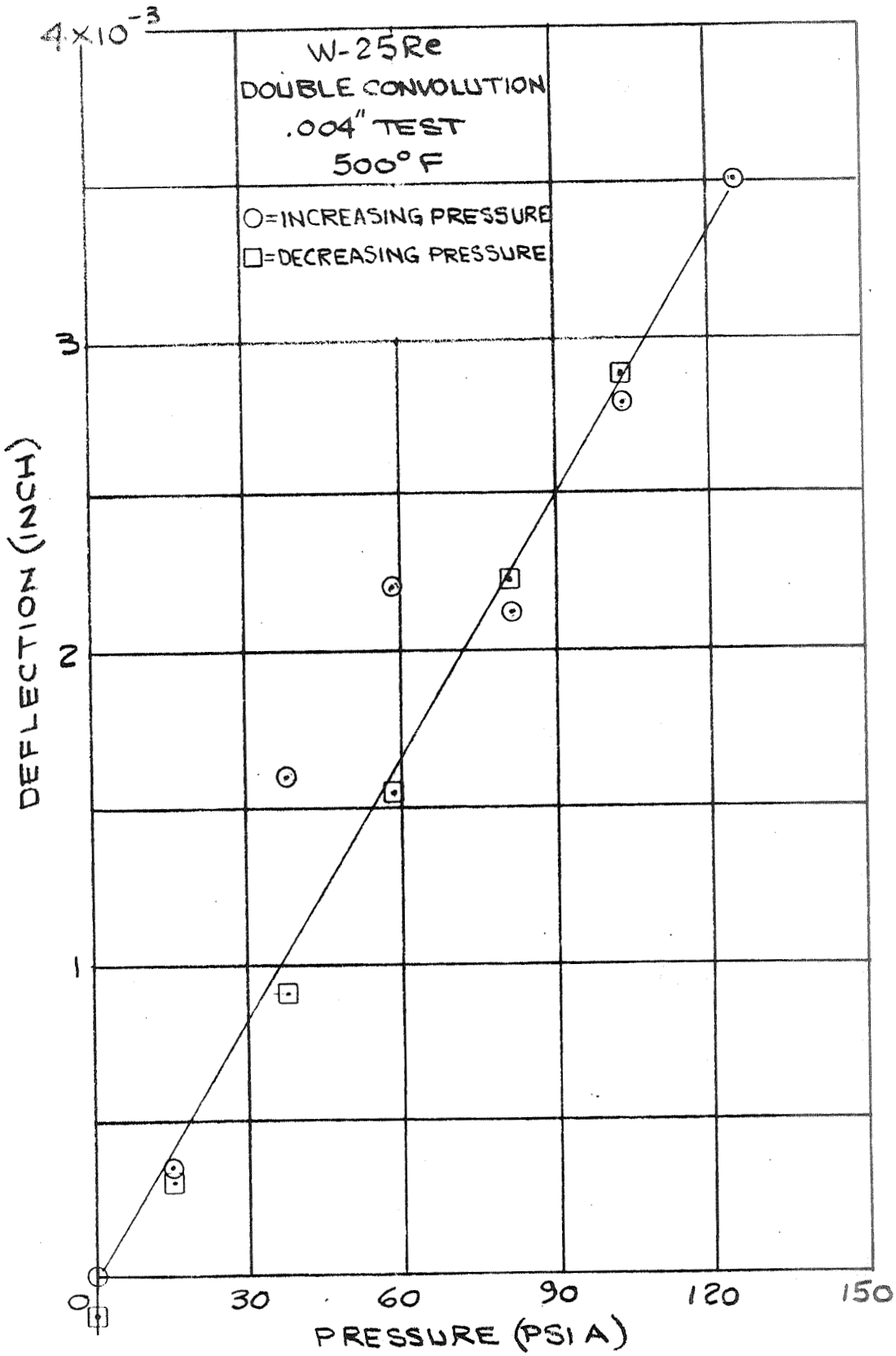


FIGURE 83

W-25Re PRESSURE-DEFLECTION, 500°F

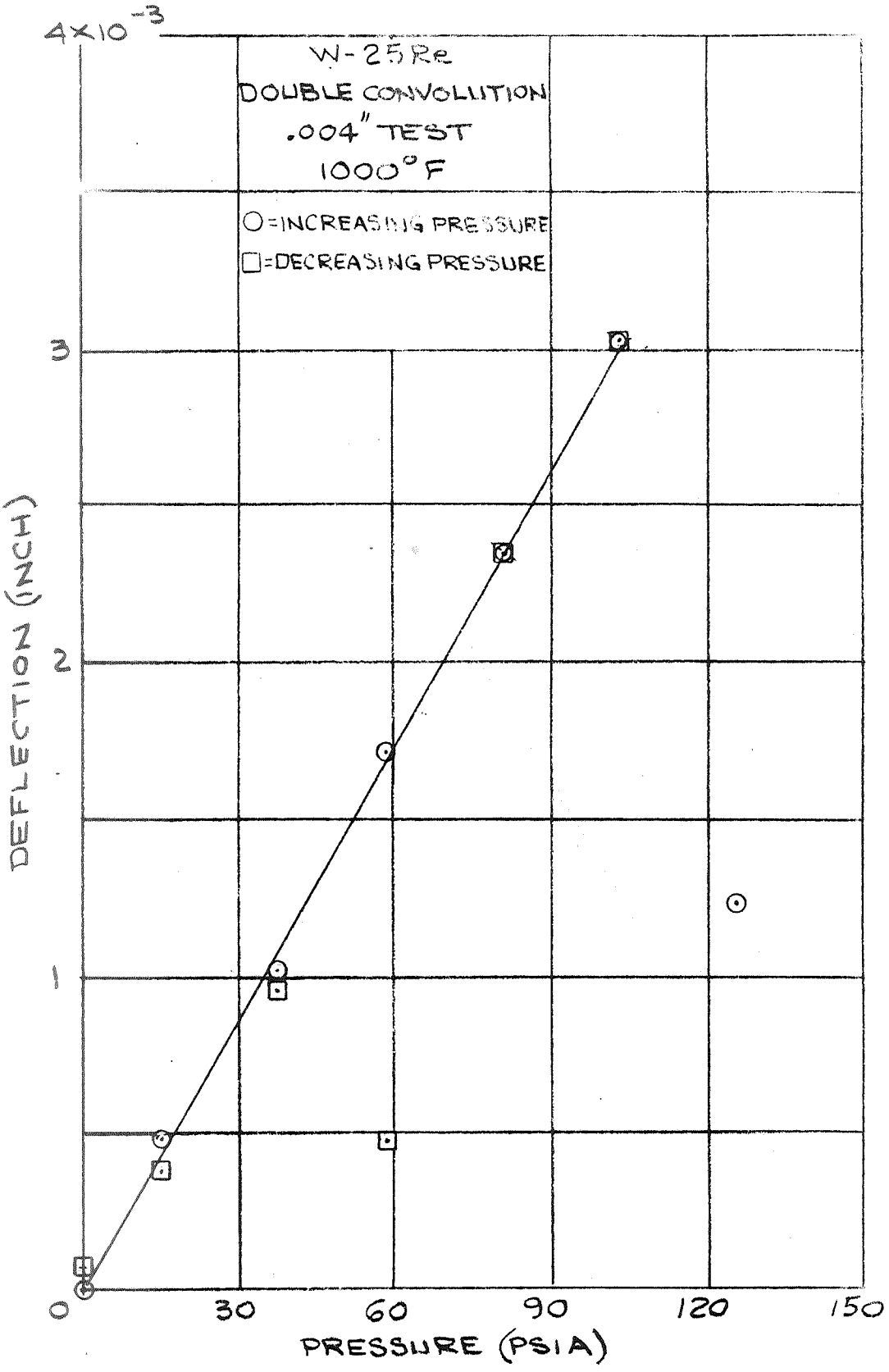


FIGURE 84

W-25Re PRESSURE-DEFLECTION, 1000°F

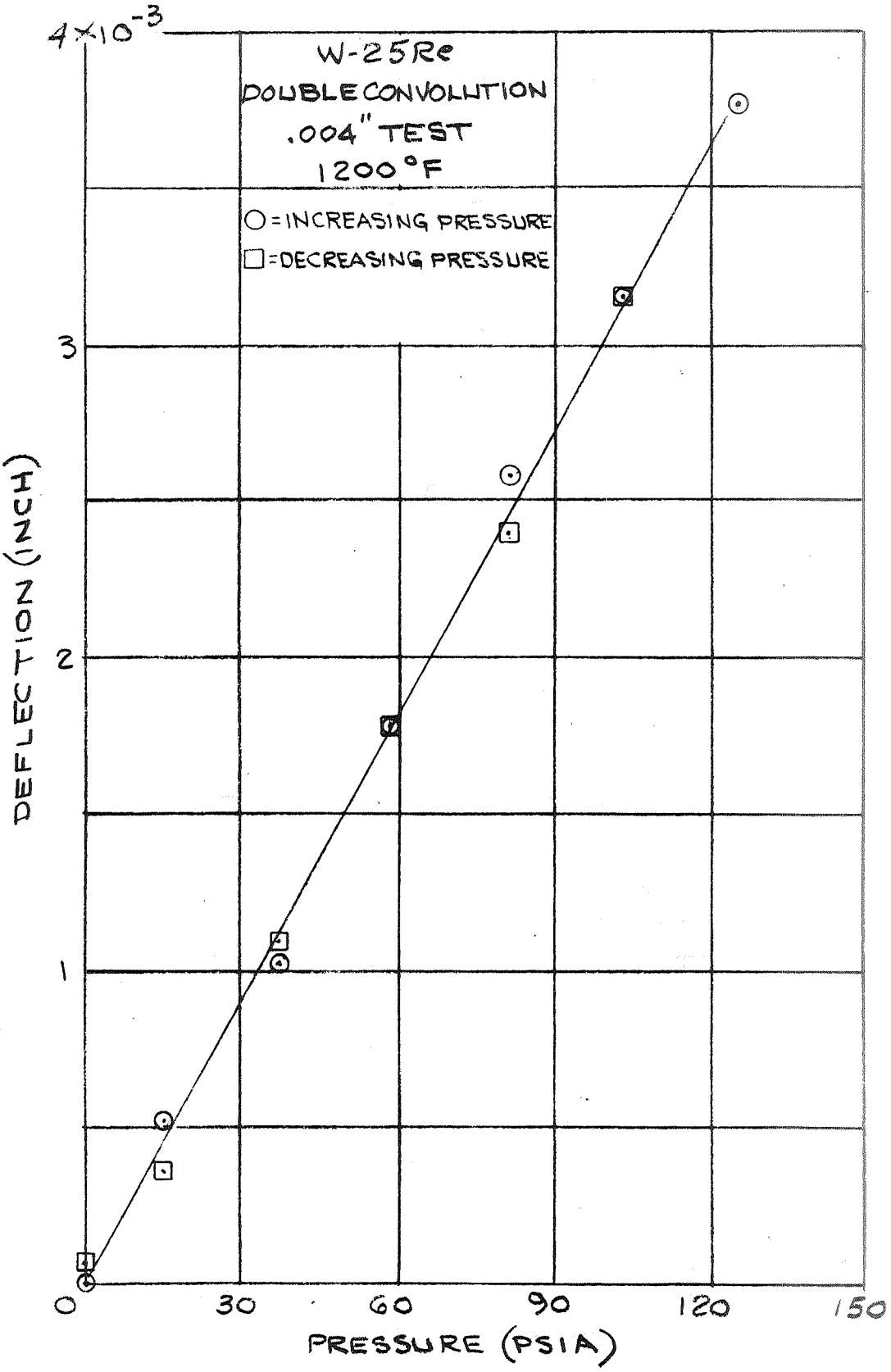


FIGURE 85

W-25Re PRESSURE-DEFLECTION, 1200°F

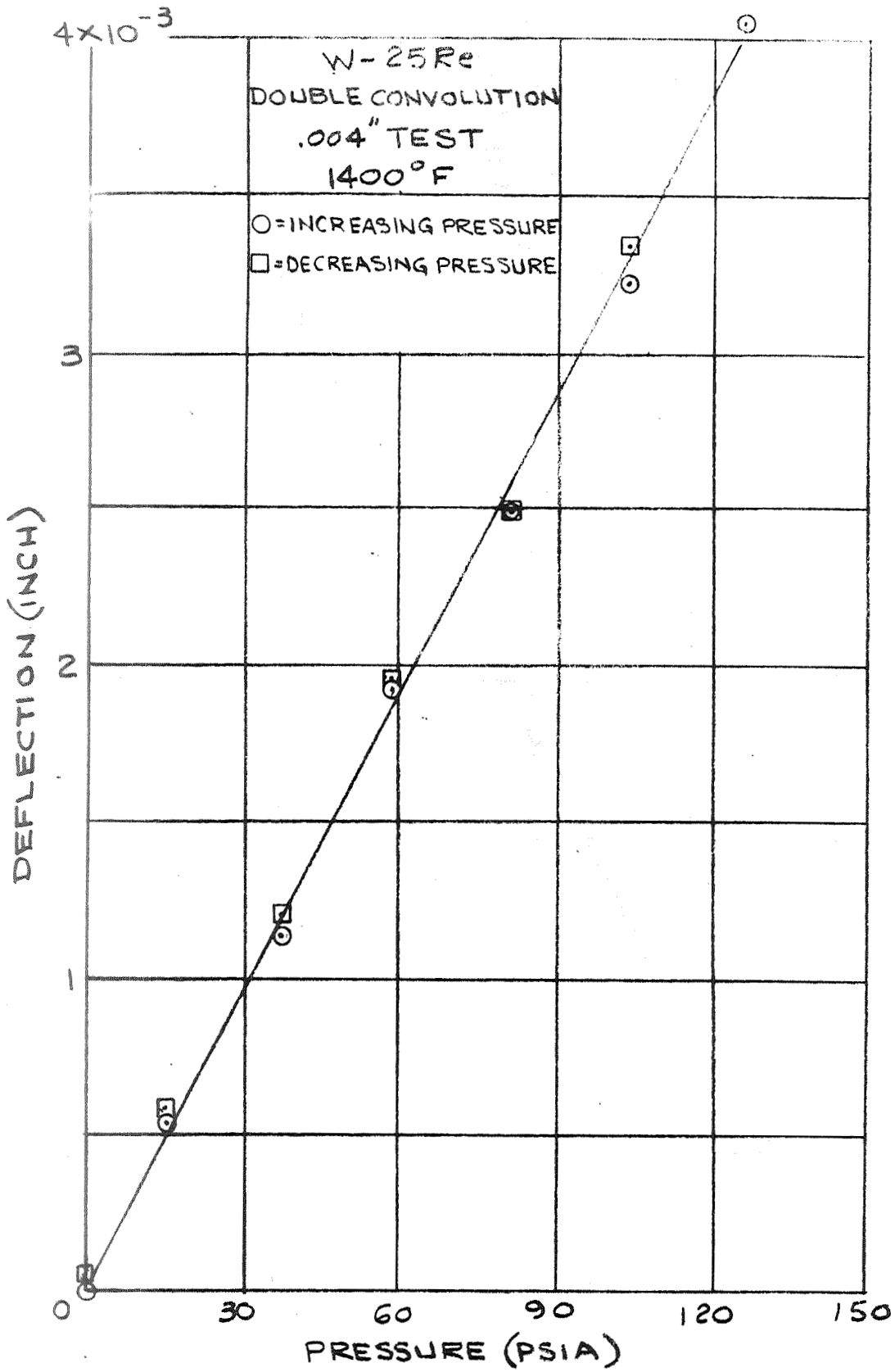


FIGURE 86

W-25Re PRESSURE-DEFLECTION, 1400°F

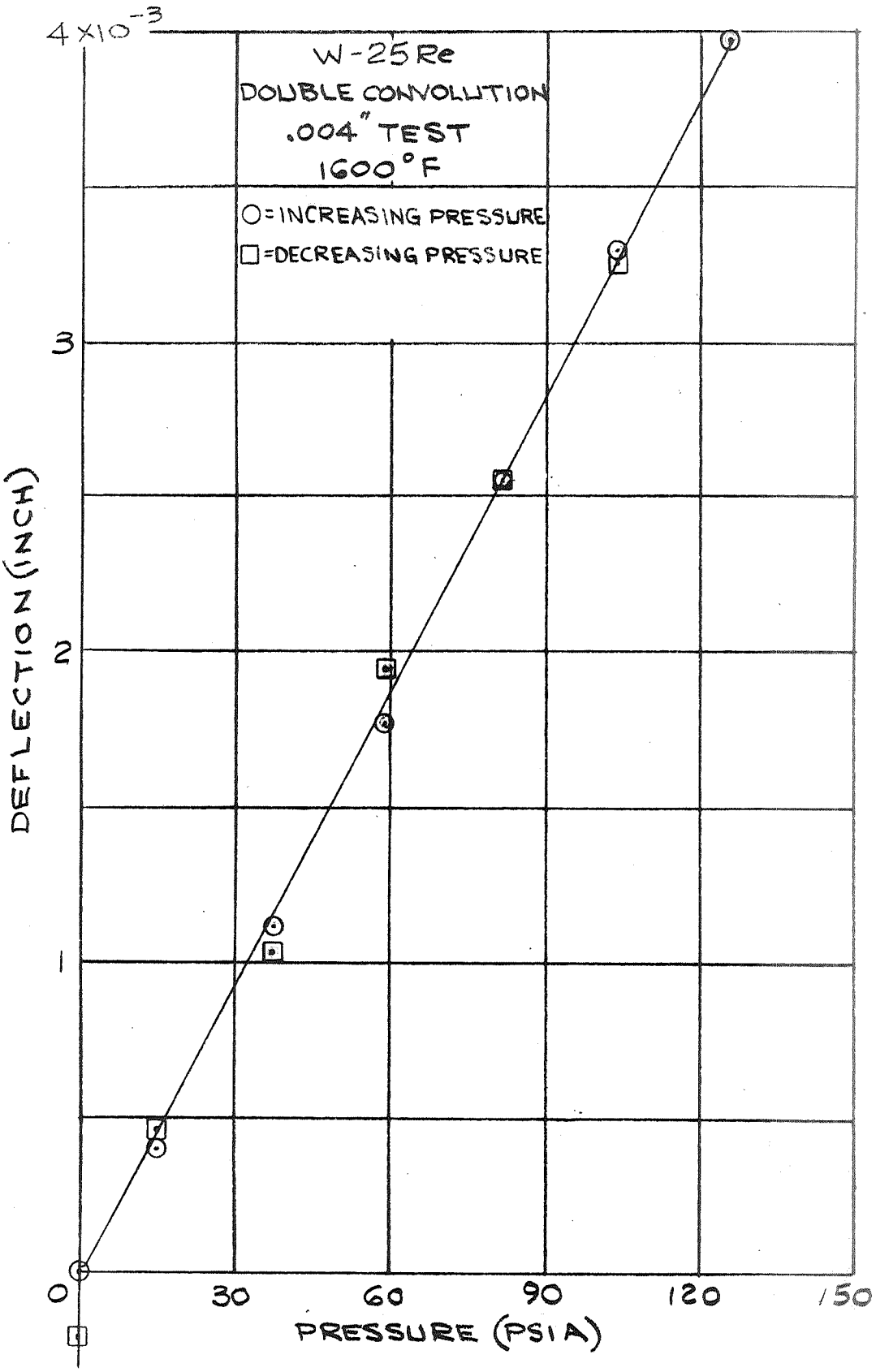


FIGURE 87

W-25Re PRESSURE-DEFLECTION, 1600°F

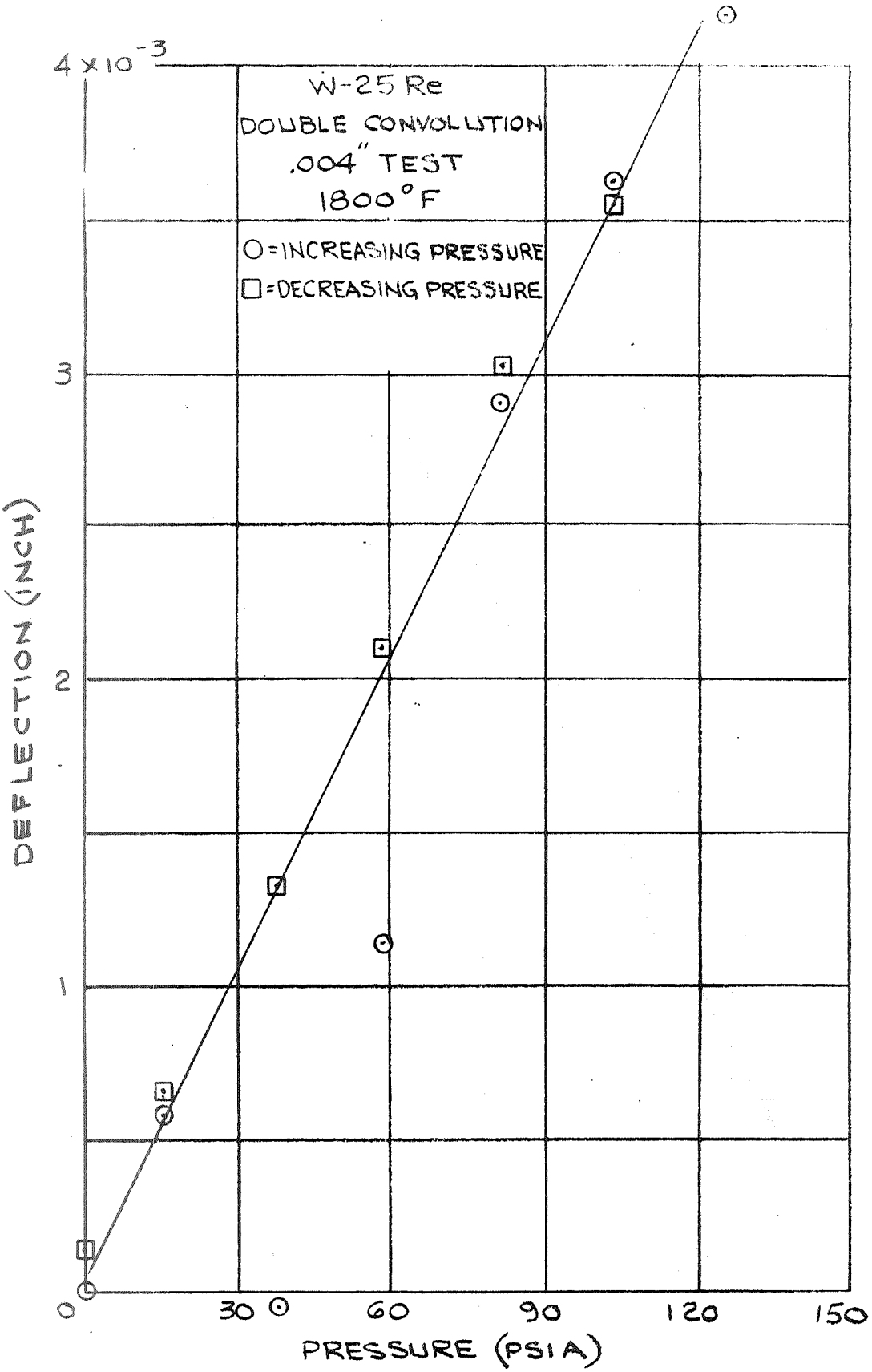


FIGURE 88

W-25Re PRESSURE-DEFLECTION, 1800°F

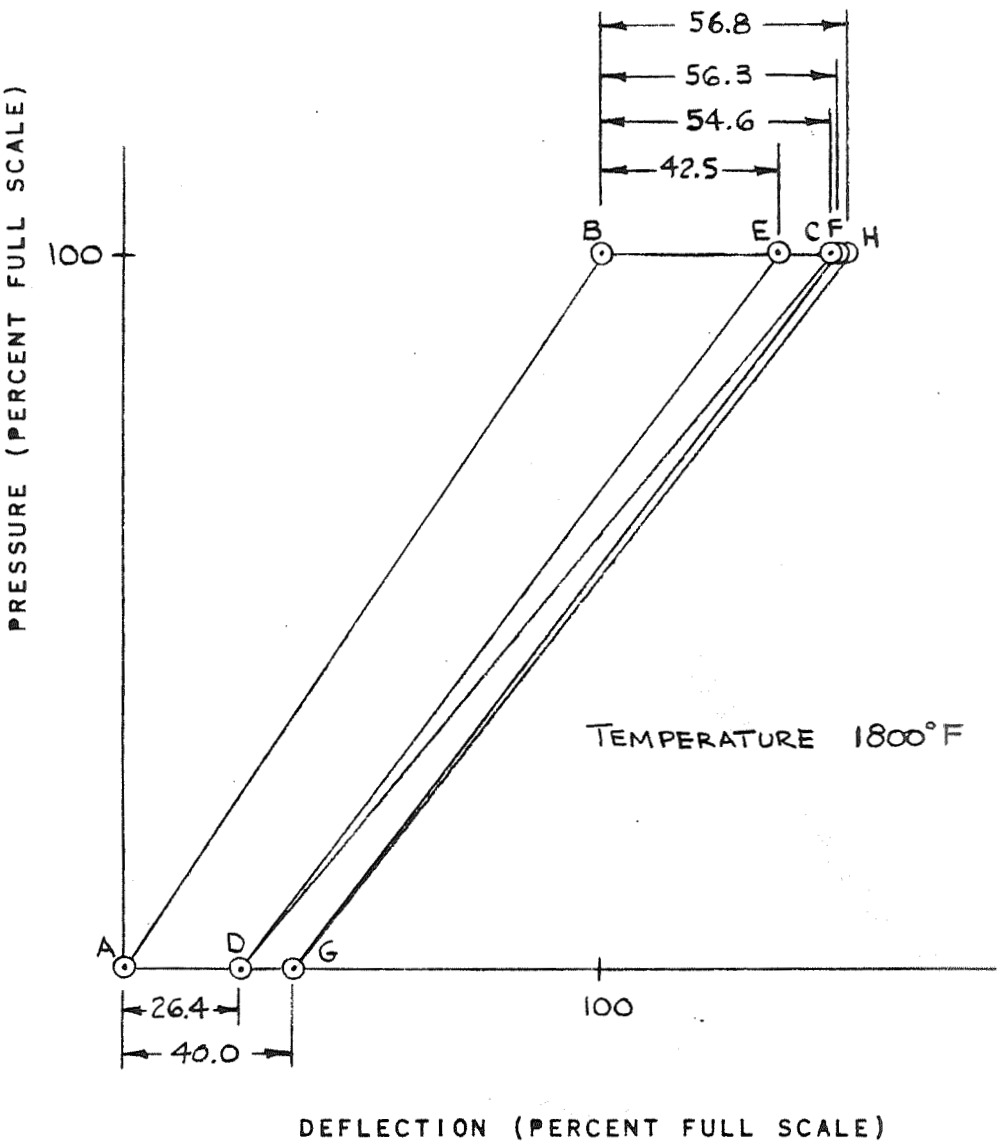


FIGURE 89

C-129Y FINAL TIME TEST PROCEDURE

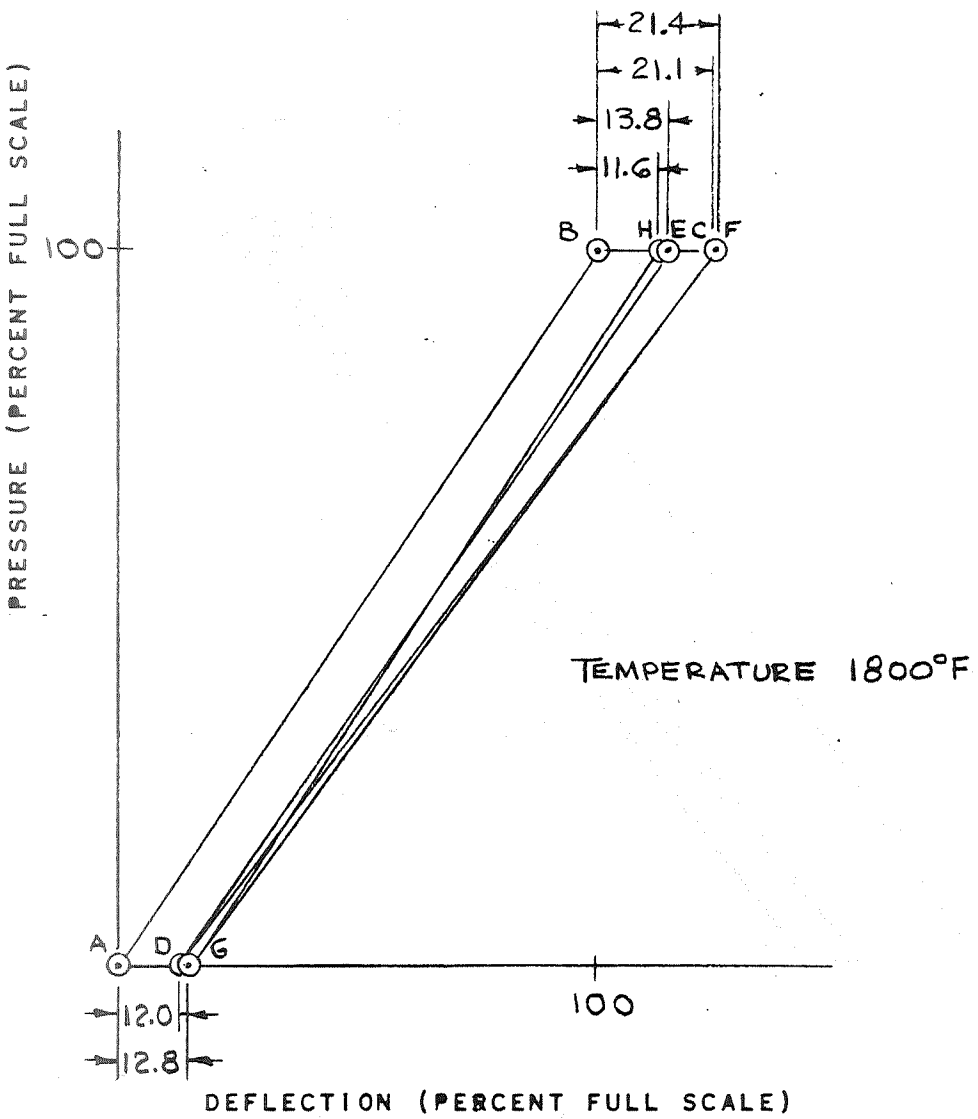


FIGURE 90

FS-85 FINAL TIME TEST PROCEDURE

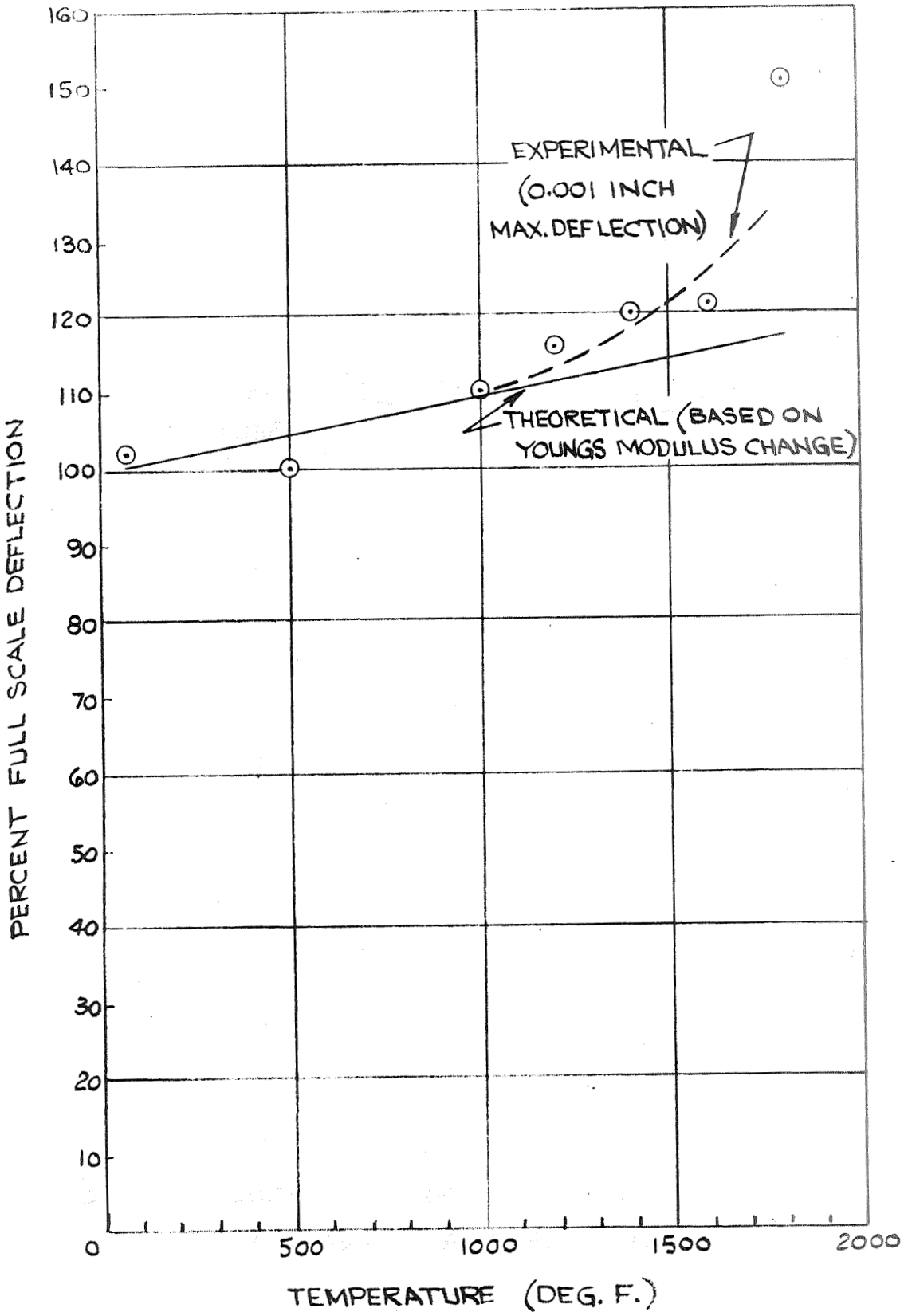


FIGURE 91

C-129Y FULL SCALE DEFLECTION-TEMPERATURE CURVES

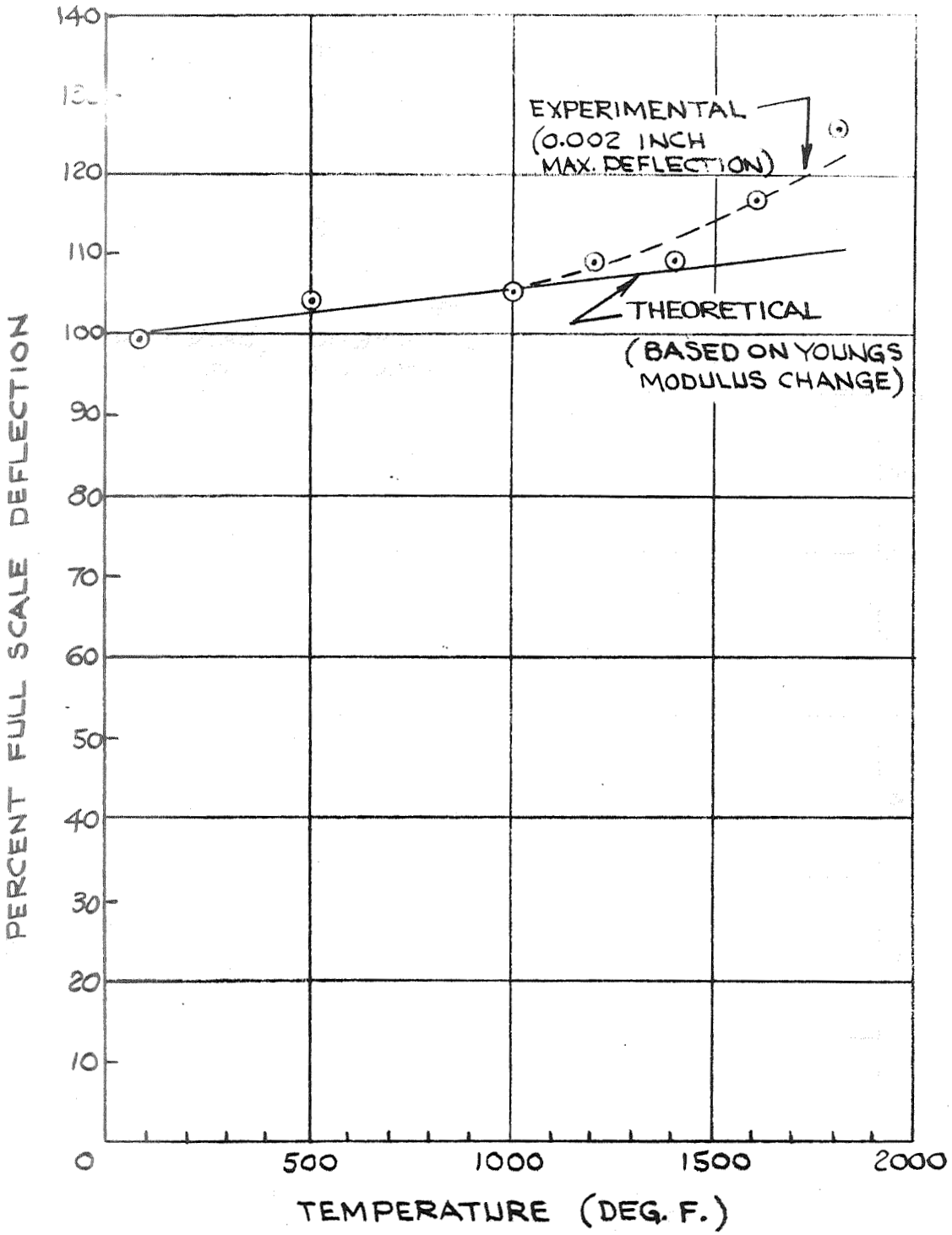


FIGURE 92

FS-85 FULL SCALE DEFLECTION-TEMPERATURE CURVES

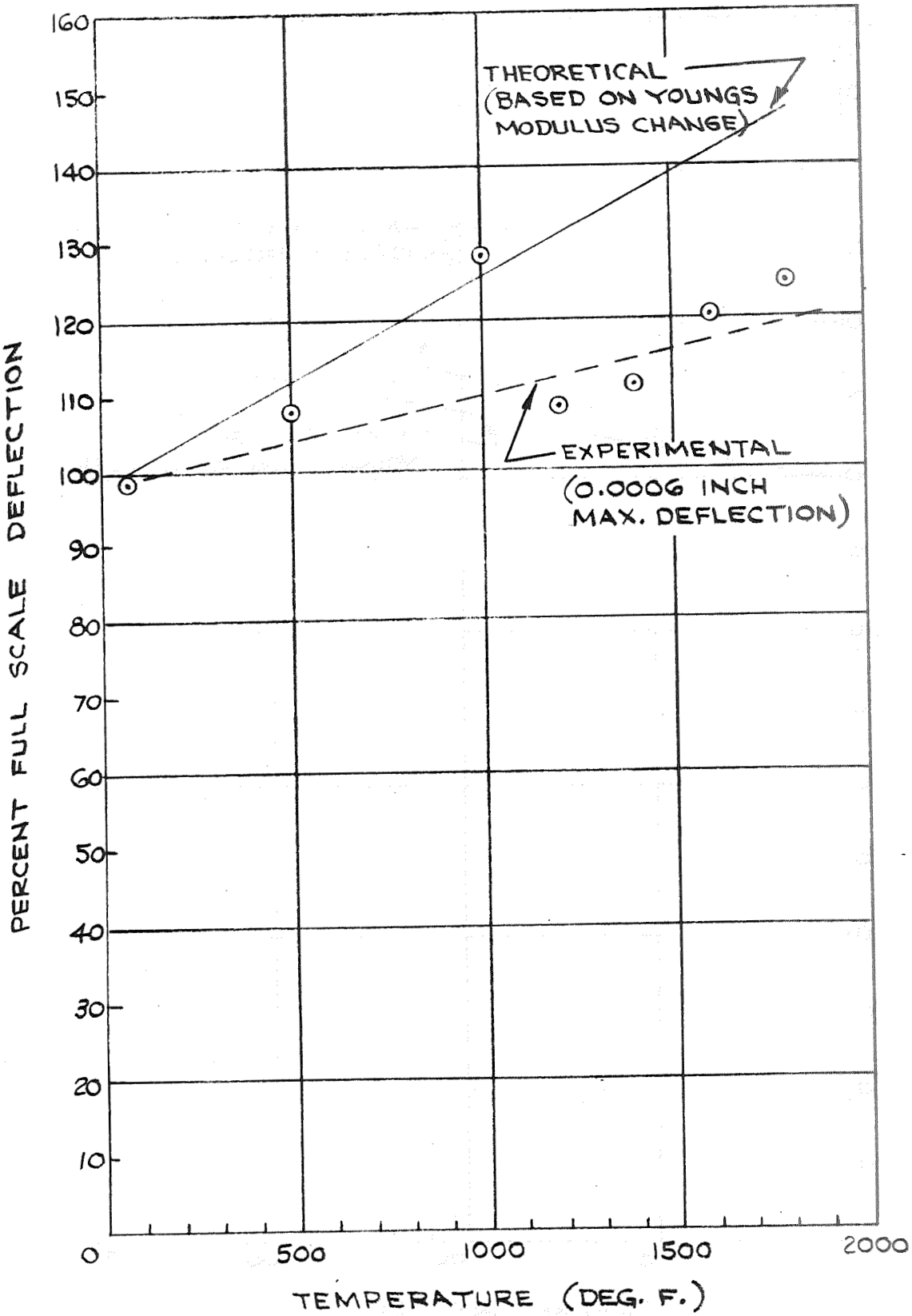


FIGURE 93

T-222 FULL SCALE DEFLECTION-TEMPERATURE CURVES

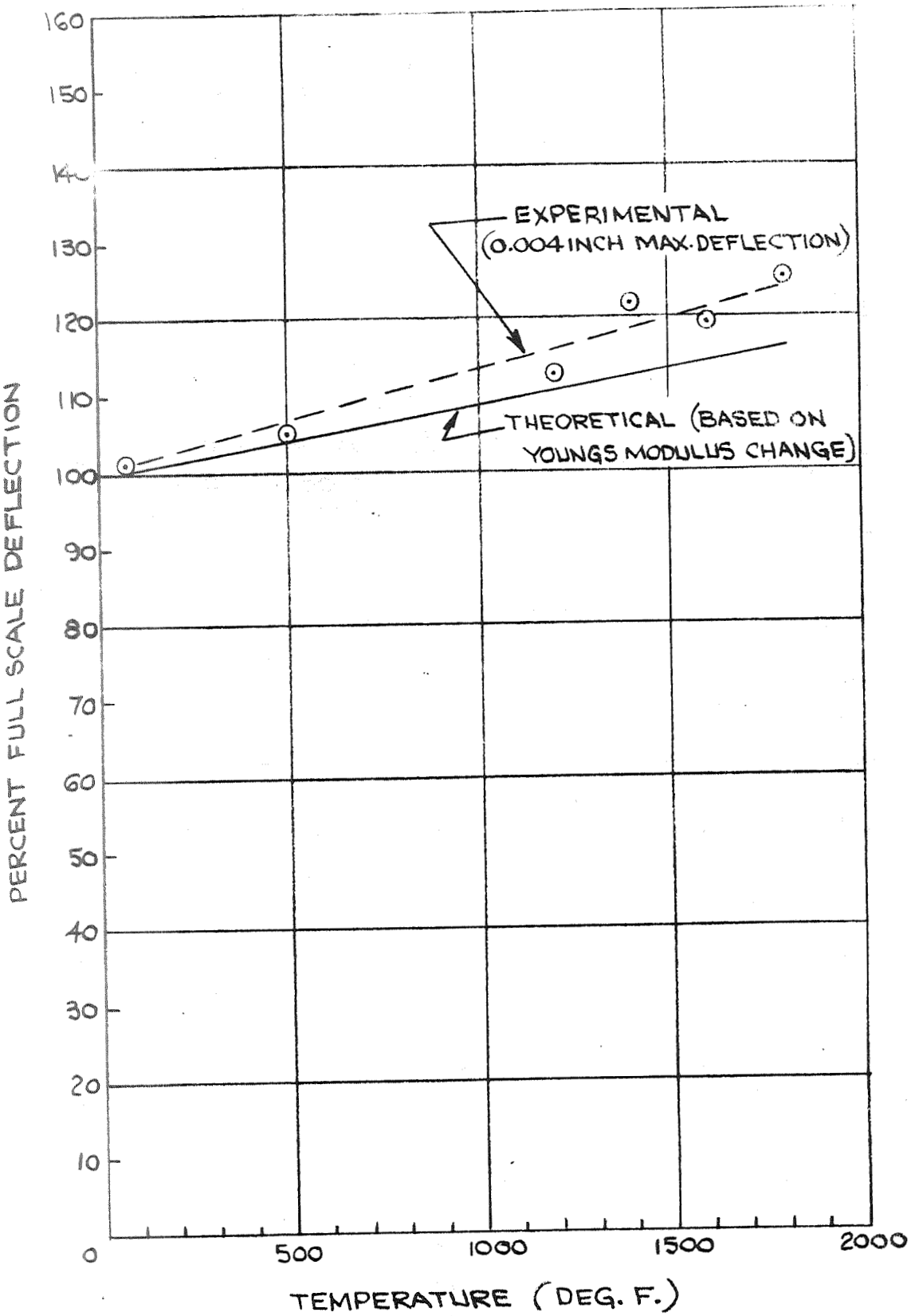


FIGURE 94

W-25Re FULL SCALE DEFLECTION-TEMPERATURE CURVES

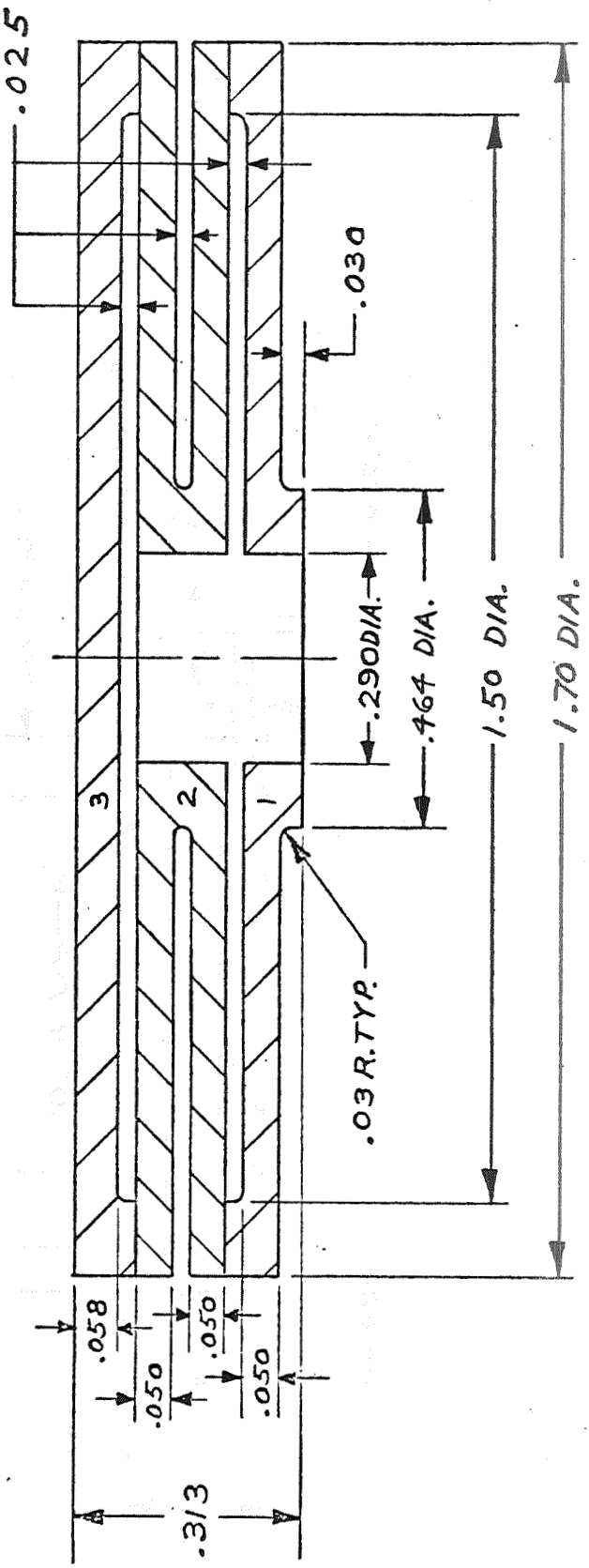


FIGURE 95

ABSOLUTE PRESSURE CAPSULE

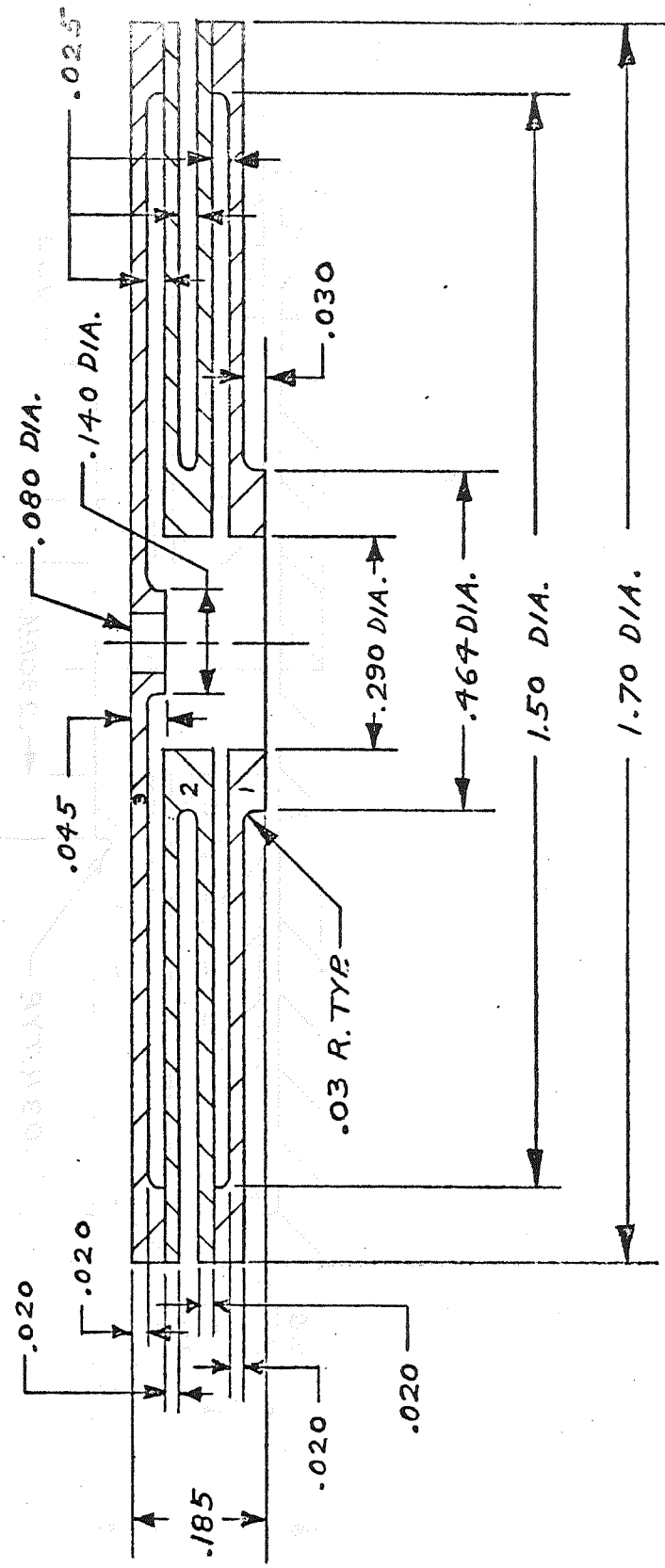


FIGURE 96

DIFFERENTIAL PRESSURE CAPSULE

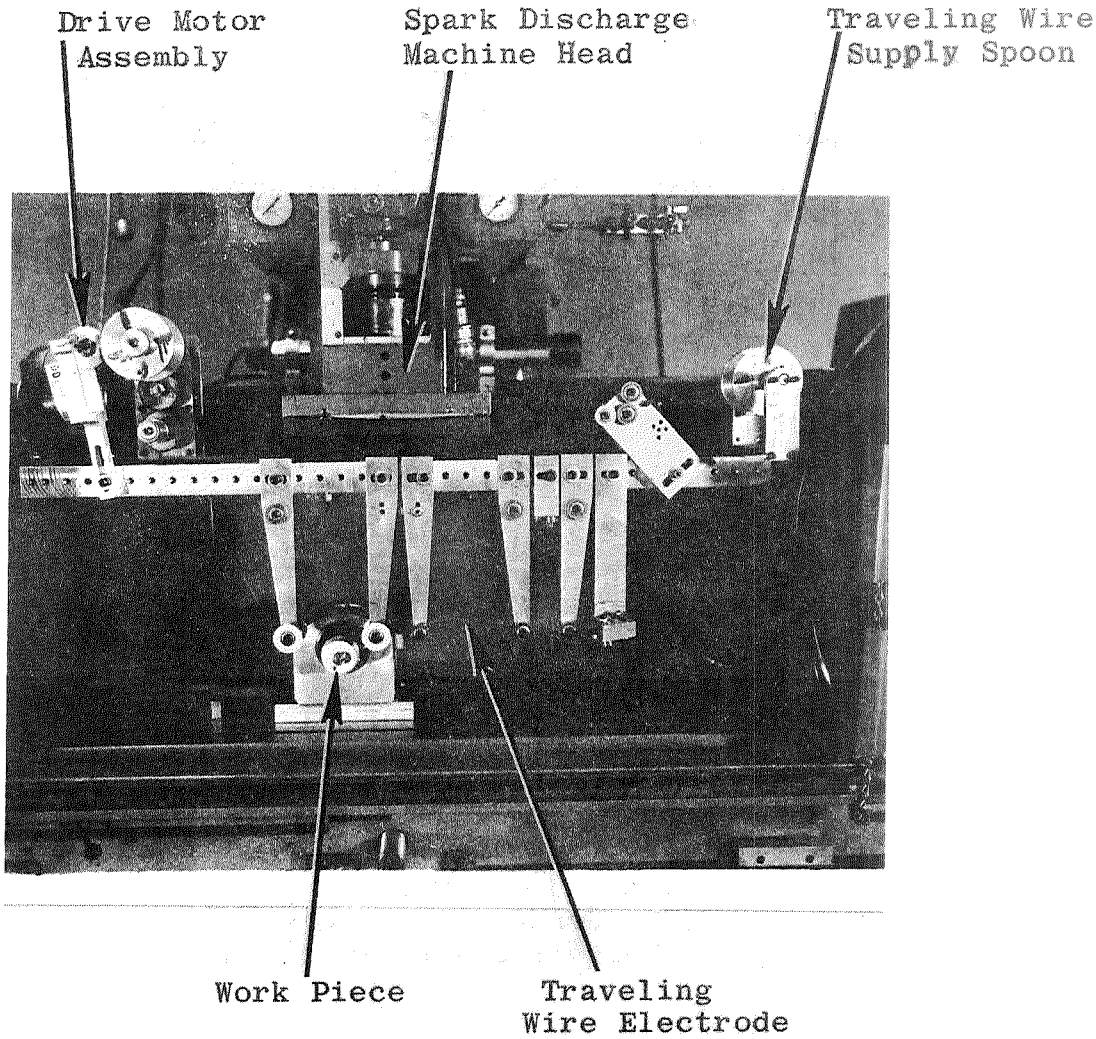


FIGURE 97

Spark Discharge Machining Set-Up

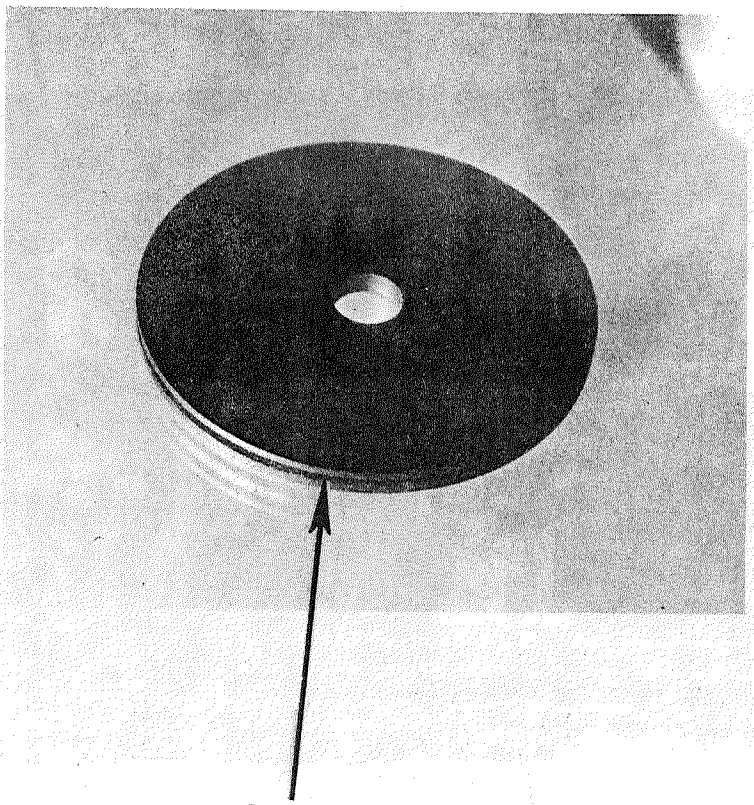


FIGURE 98

5 PSID Pressure Capsule Convolution

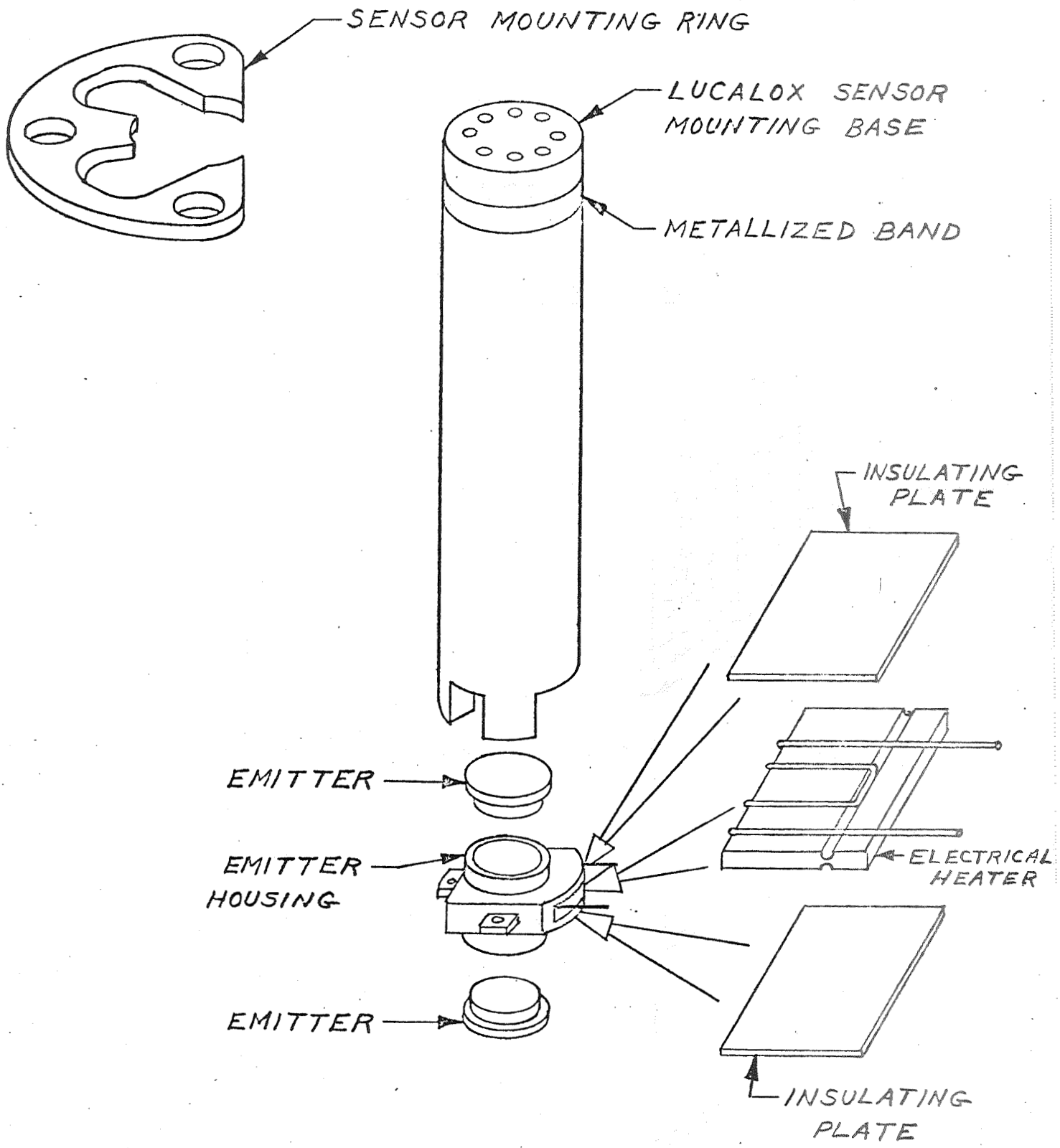
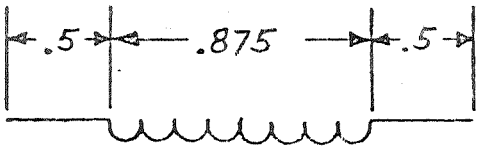


FIGURE 99

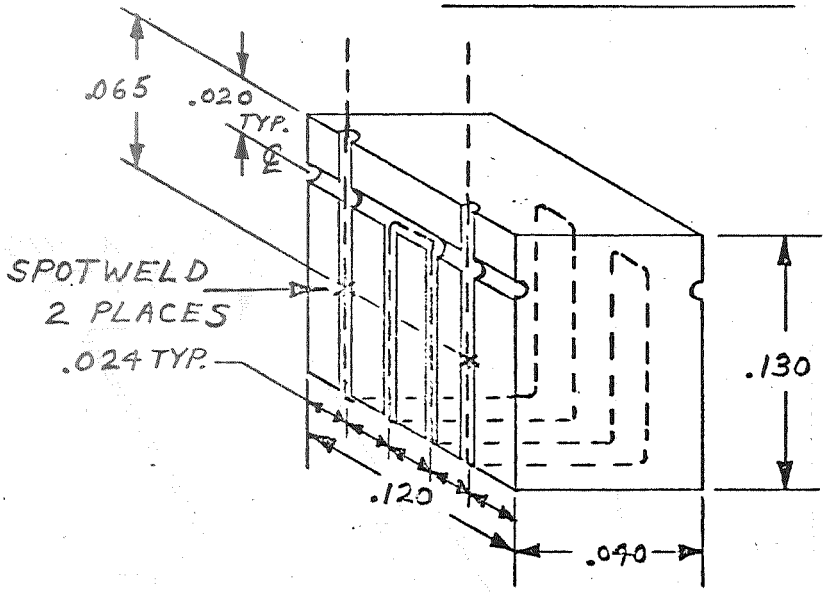
THERMIONIC DIODE SENSOR

HEATER



MATERIAL : .003" DIA. W-3Re
MANDREL : .004" DIA.
UNDEVELOPED LGTH. : $2\frac{5}{16}$"

HEATER CORE



ALL SLOTS ARE .015" WIDE x .012" DEEP

ALUMINA FILLERS

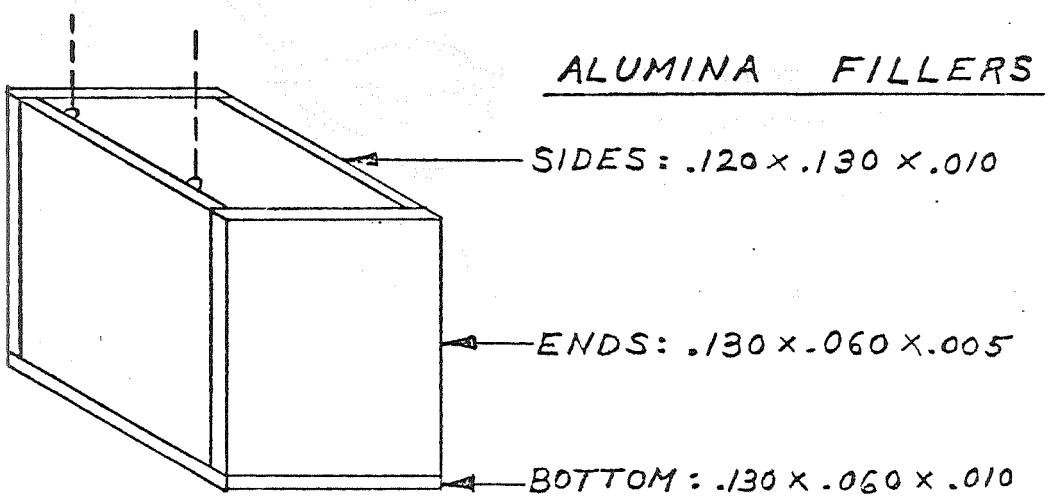


FIGURE 100

HEATER ASSEMBLY

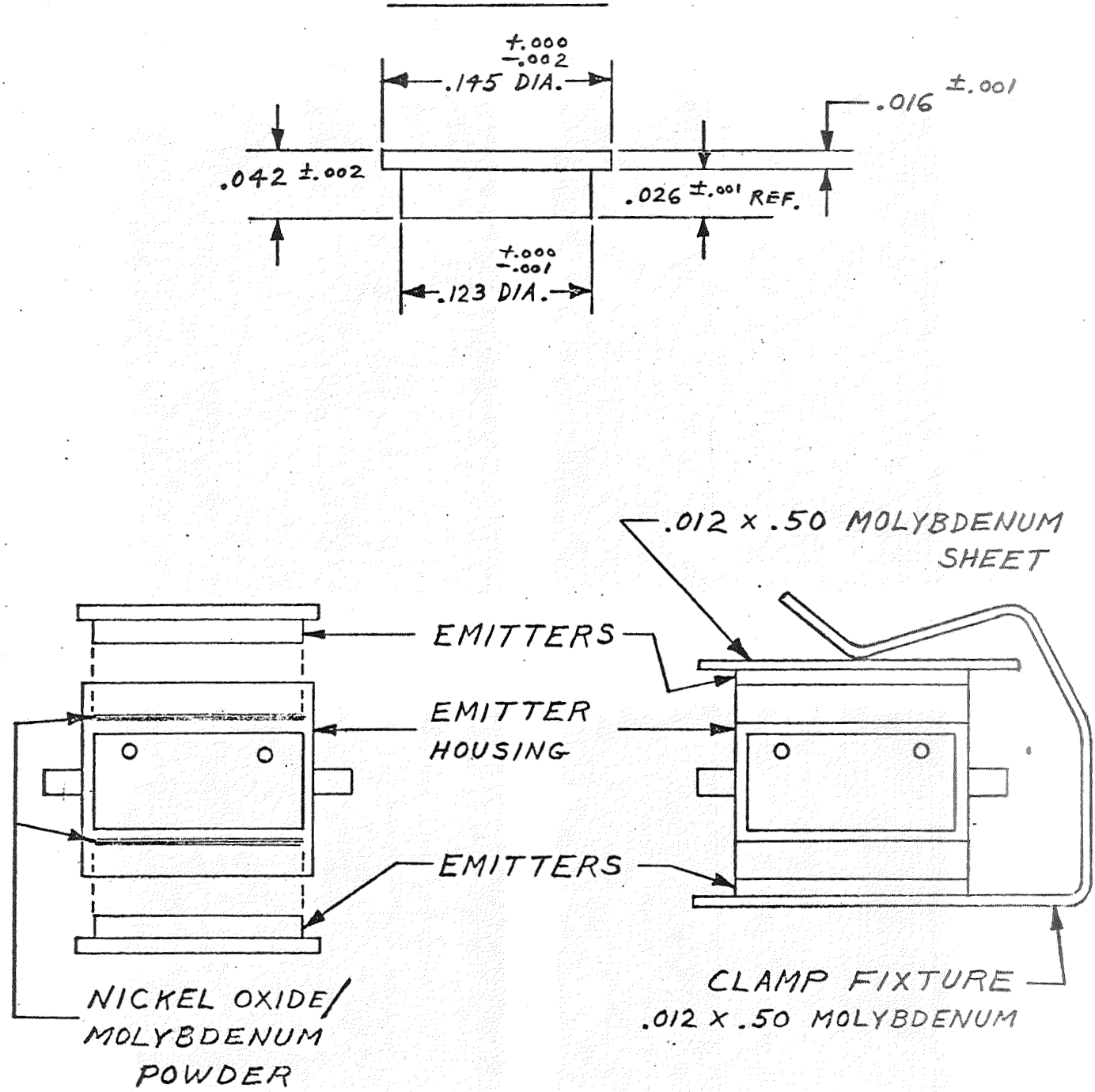
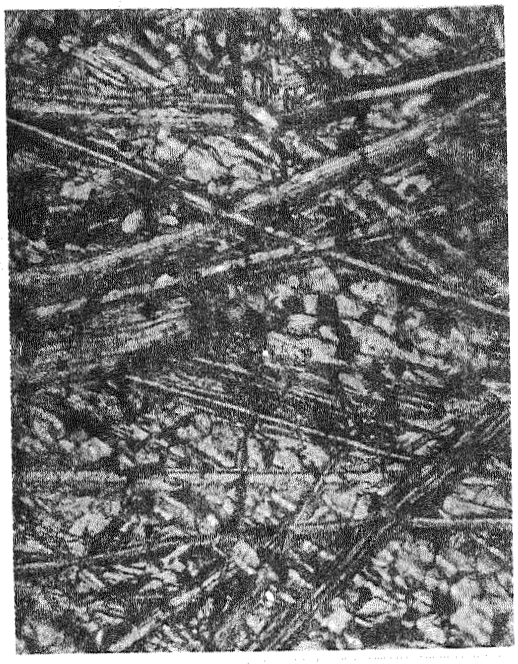


FIGURE 101

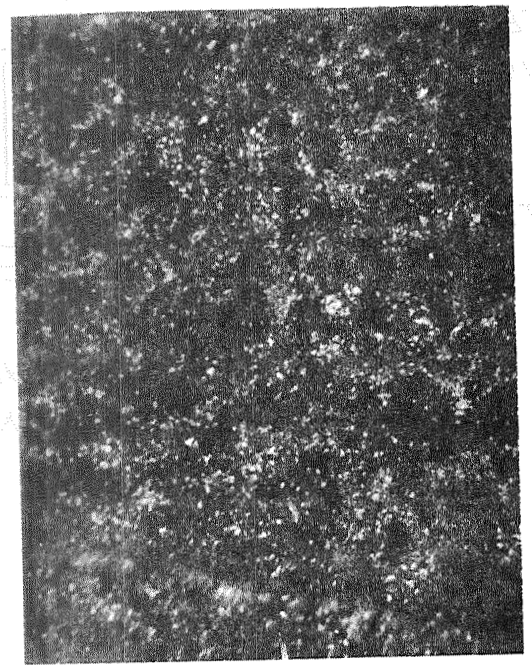
EMITTERS AND INSTALLATION



A. Uniform, open pore structure



B. Machined surface



C. Ground Surface



D. Braze-contaminated surface

FIGURE 102

Emitter Surface Photomicrographs

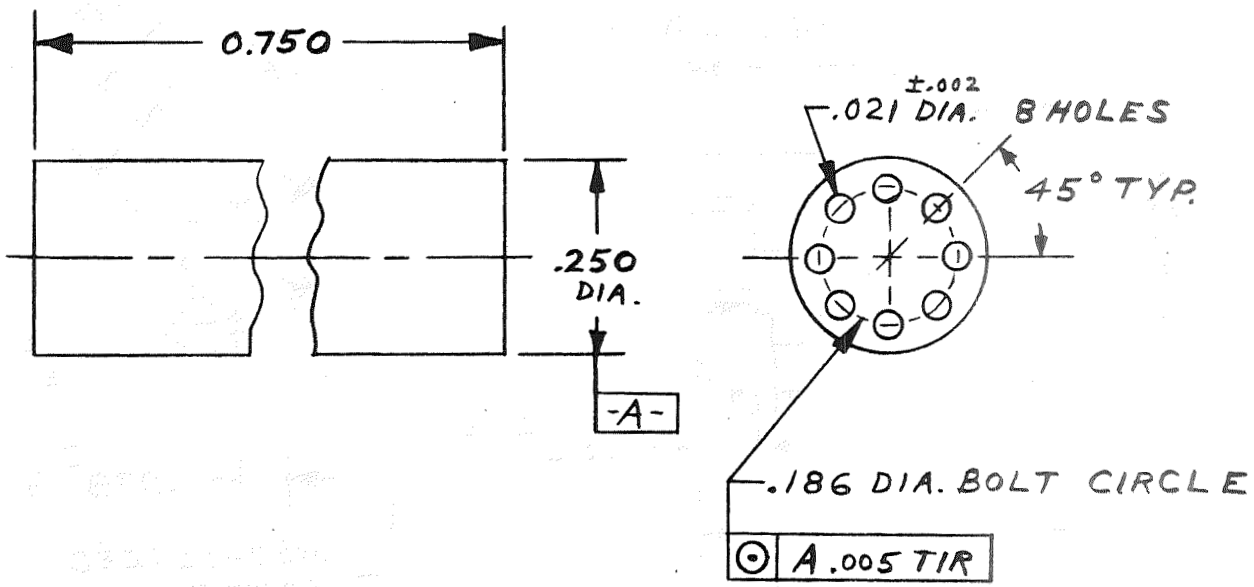


Figure 103

Lucalox Base Material

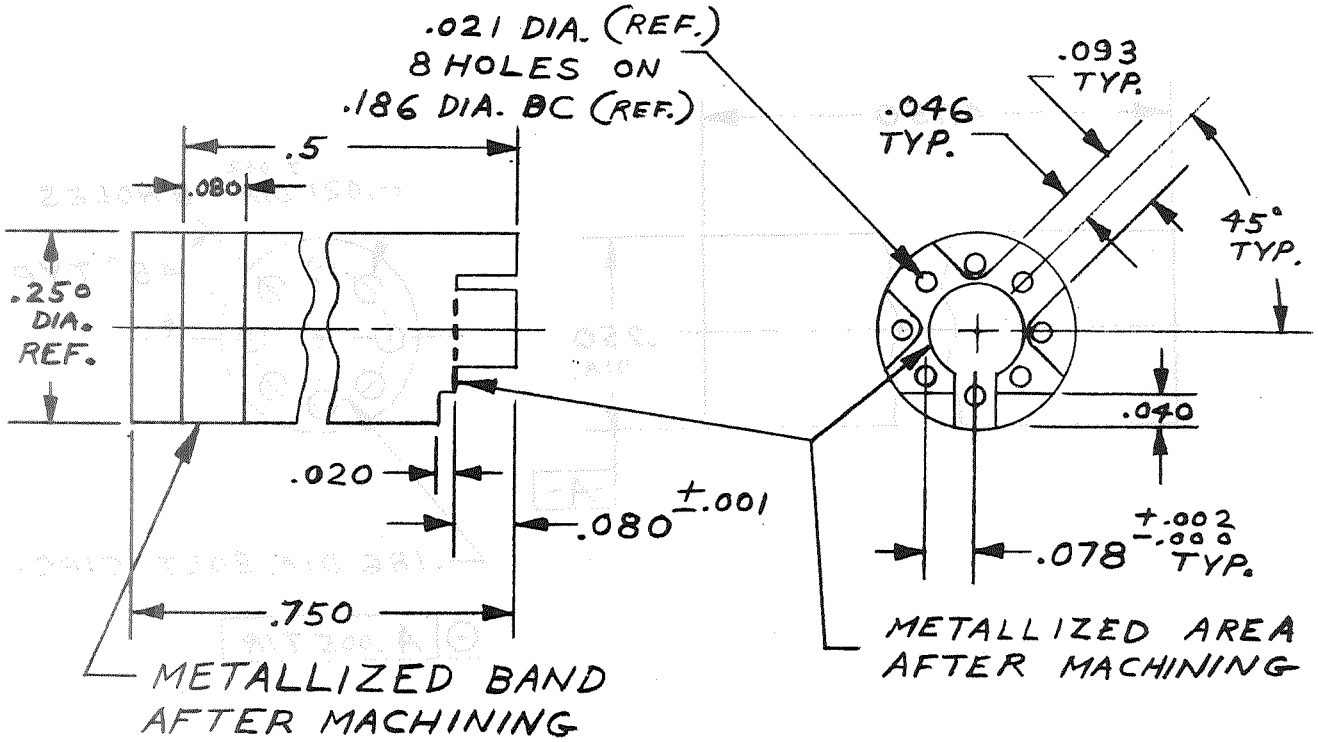


Figure 104

Finished Lucalox Sensor Base

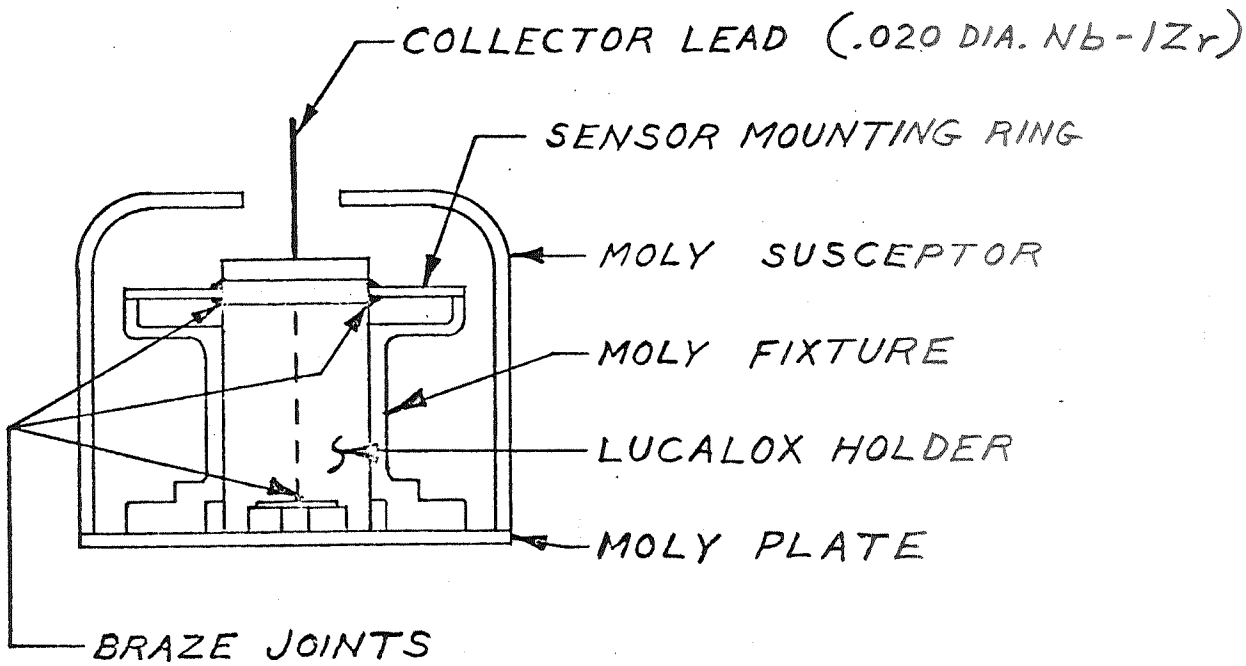
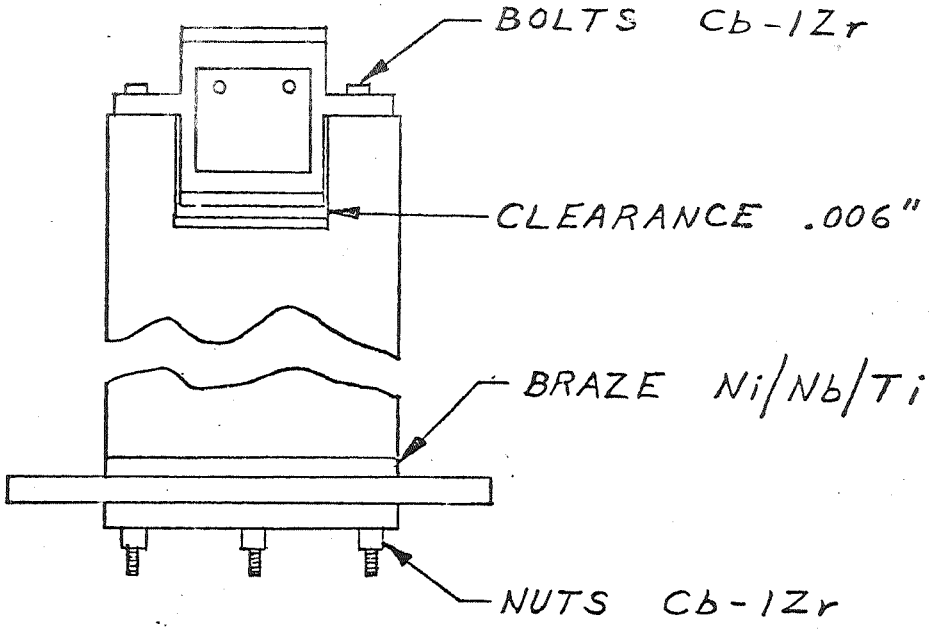


FIGURE 105

LUCALOX BRAZE SET-UP



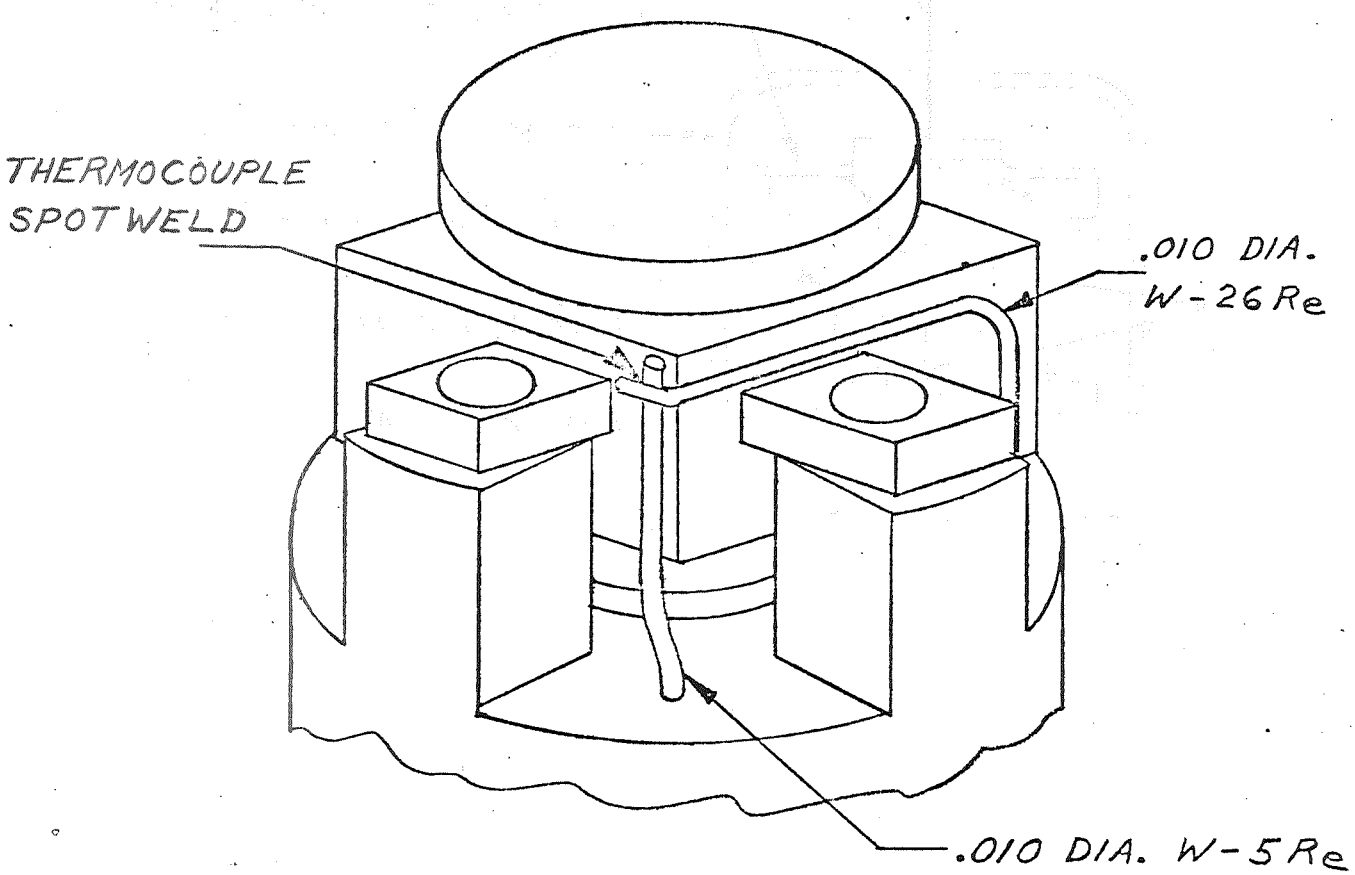


FIGURE 106

THERMIONIC DIODE SENSOR AND THERMOCOUPLE

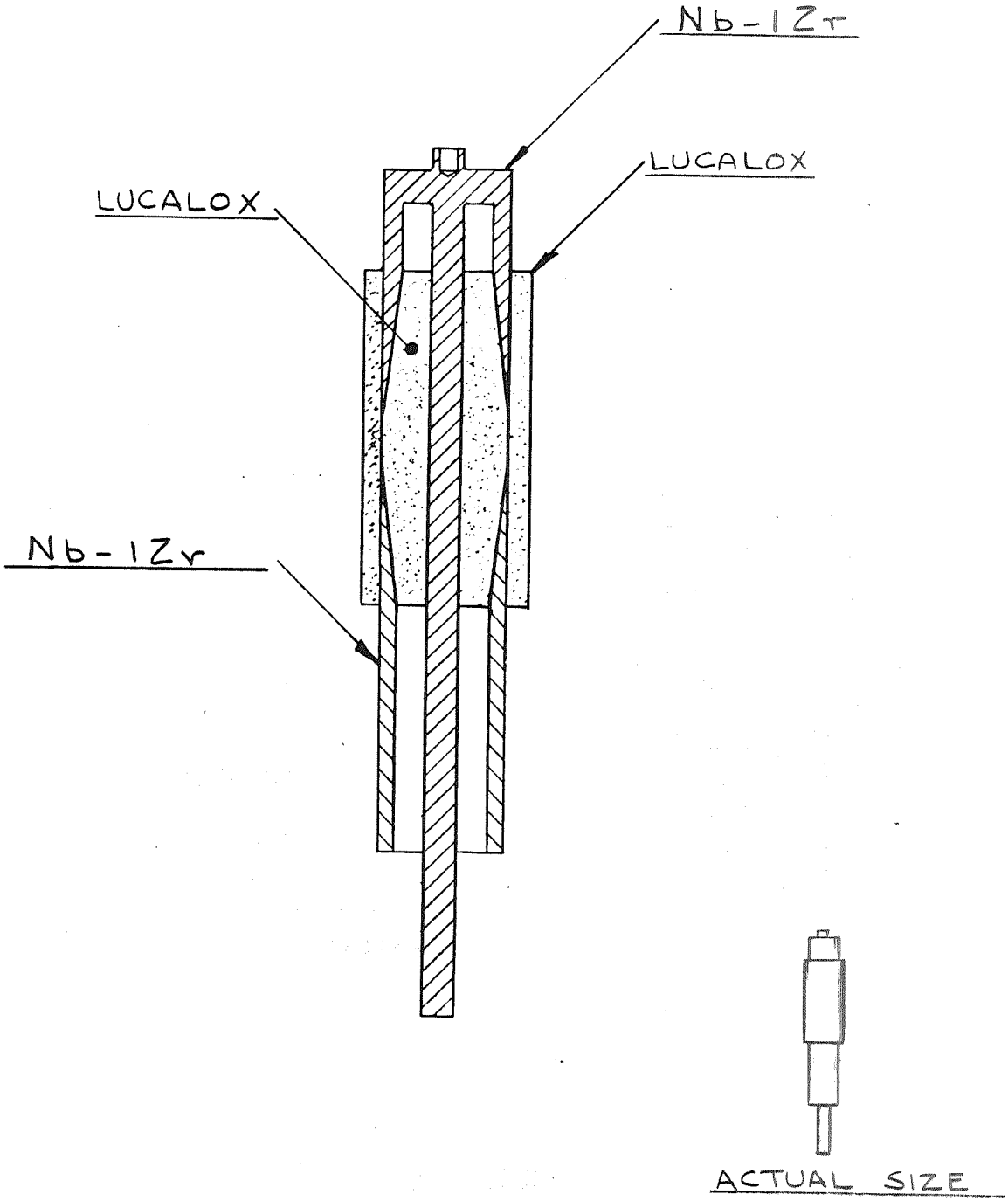


Figure 107

Electrical Terminal

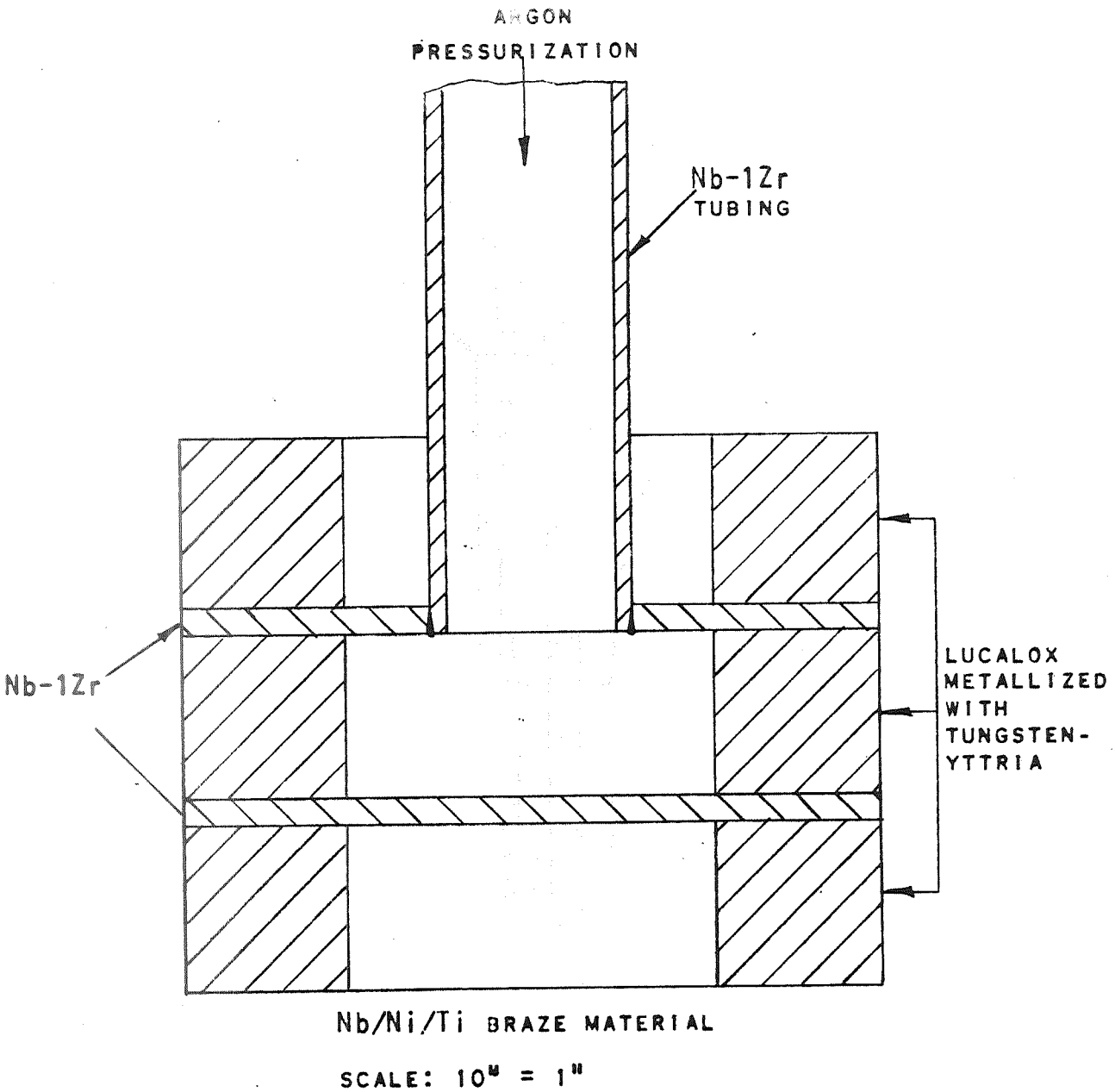


FIGURE 108

METAL-CERAMIC TEST UNIT

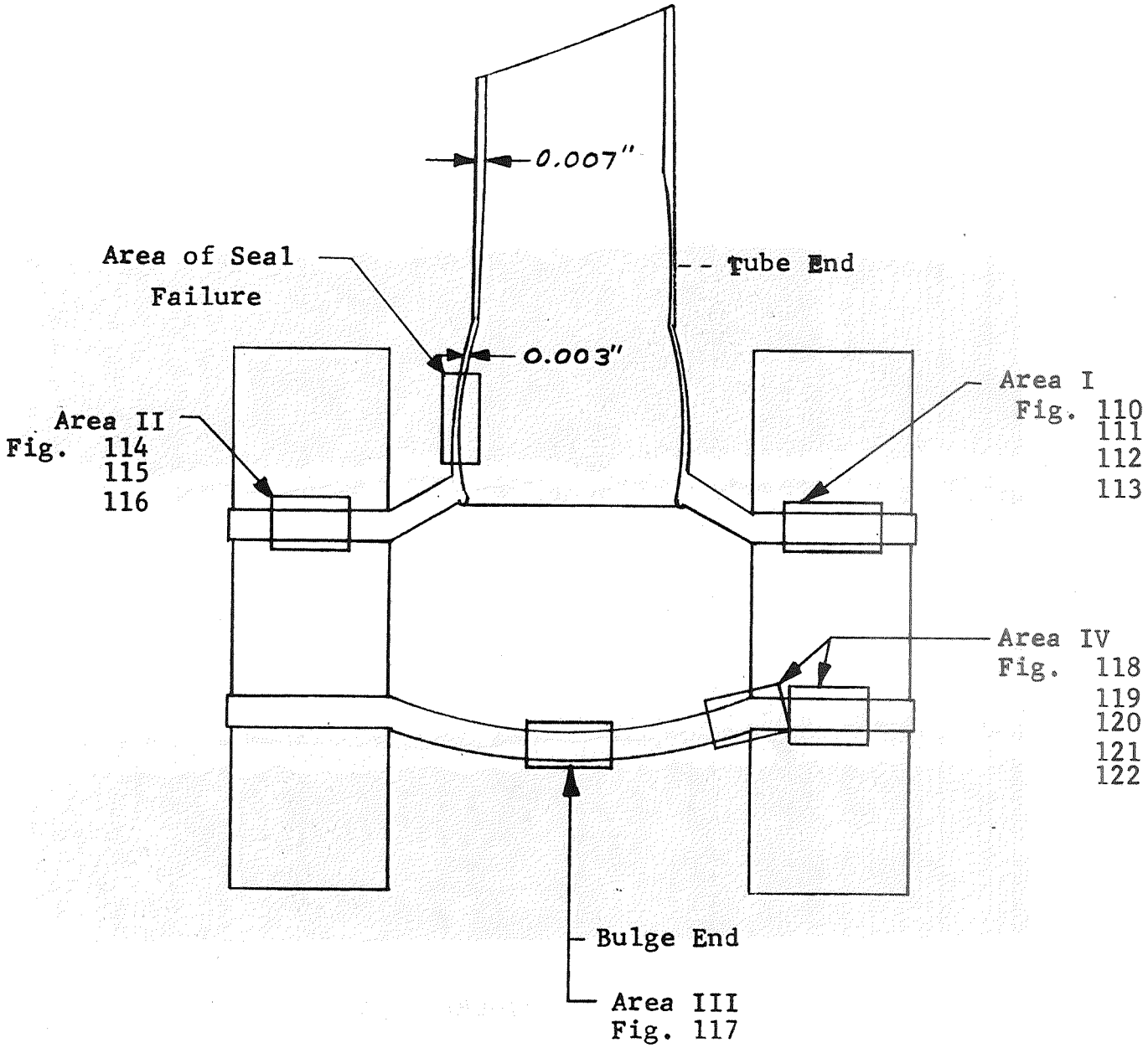


Figure 109

Metal-Ceramic Test Unit After Test

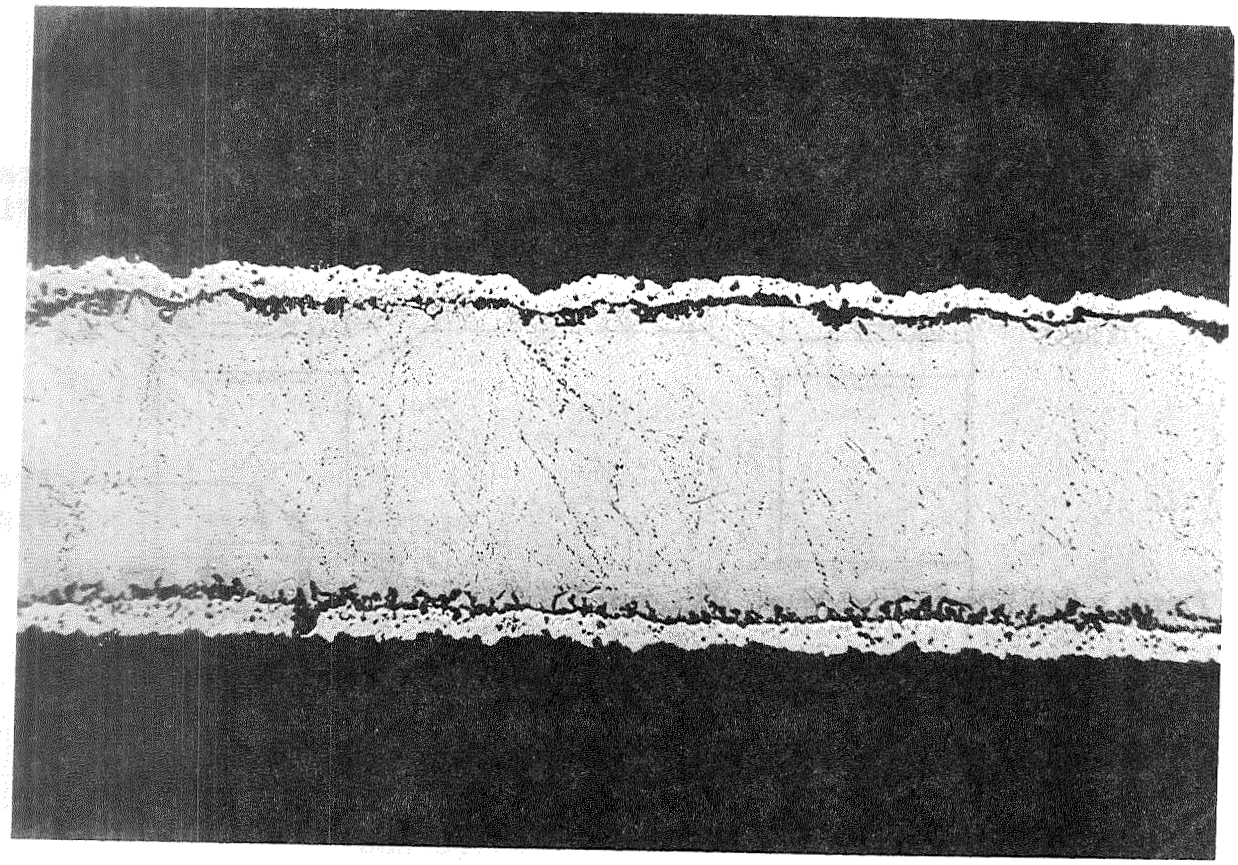


FIGURE 110

Ceramic to metal seal, tube end, unetched, 100X, Area I

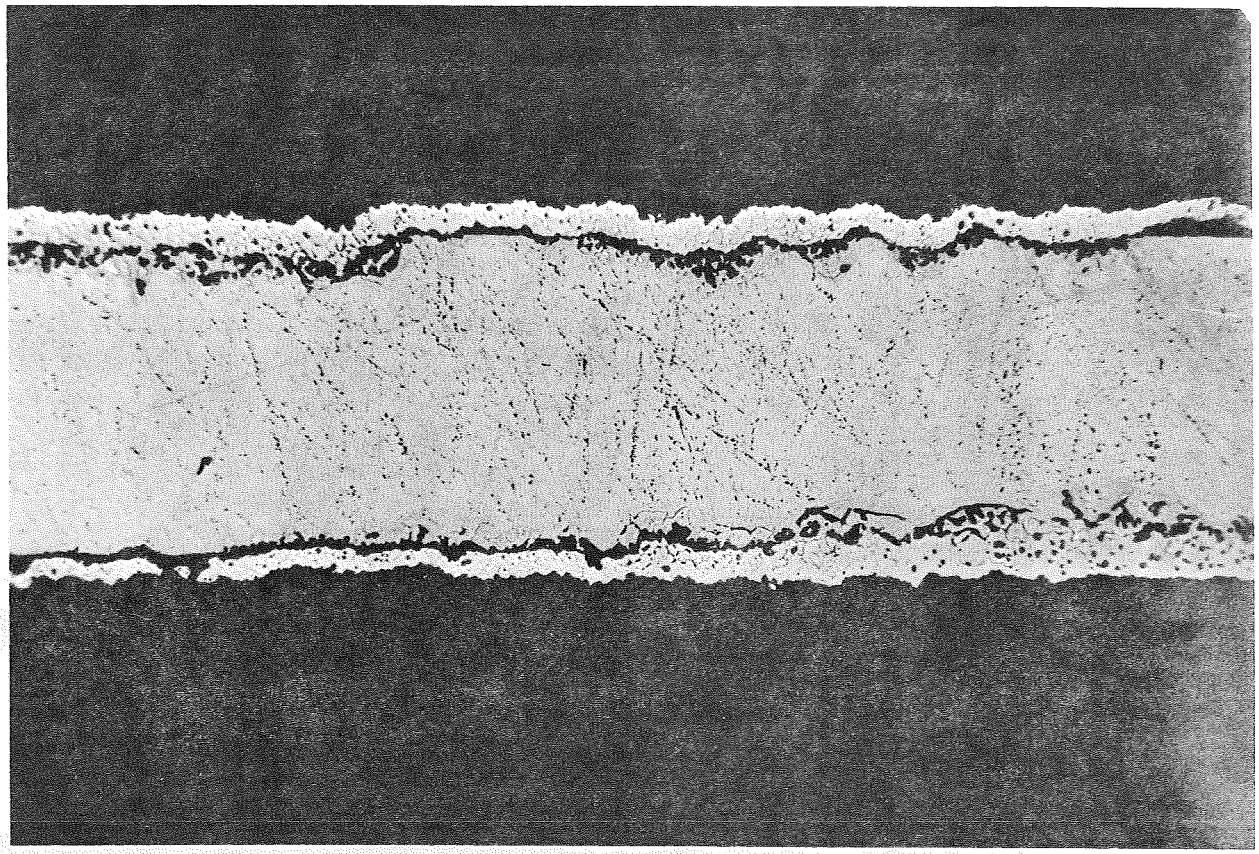


FIGURE 111

Ceramic to metal seal, tube end, unetched, 100X, Area I, site of Figures 112 and 113.

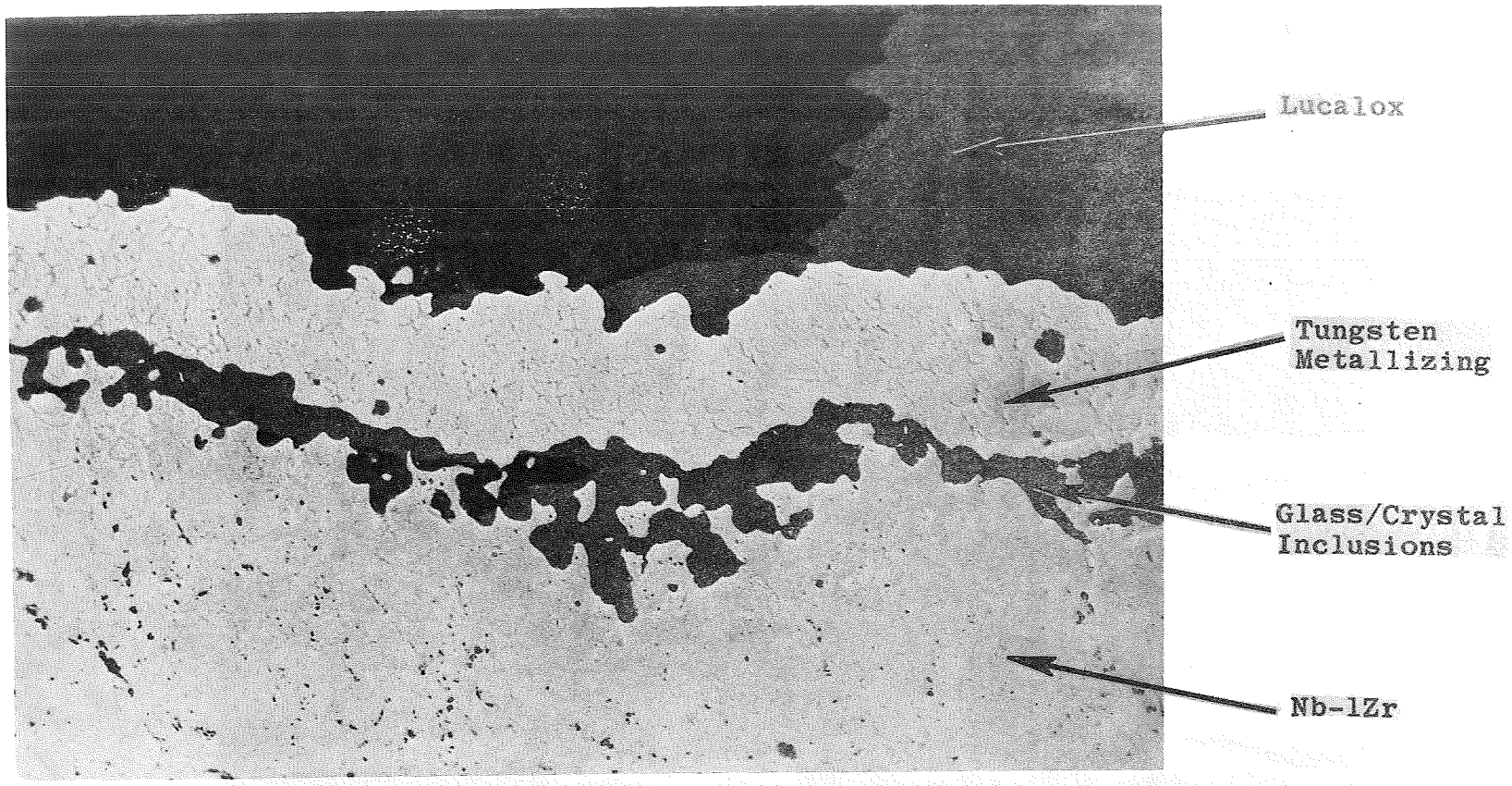


FIGURE 112

Tube end interface showing glass, etched, 500X, Area I

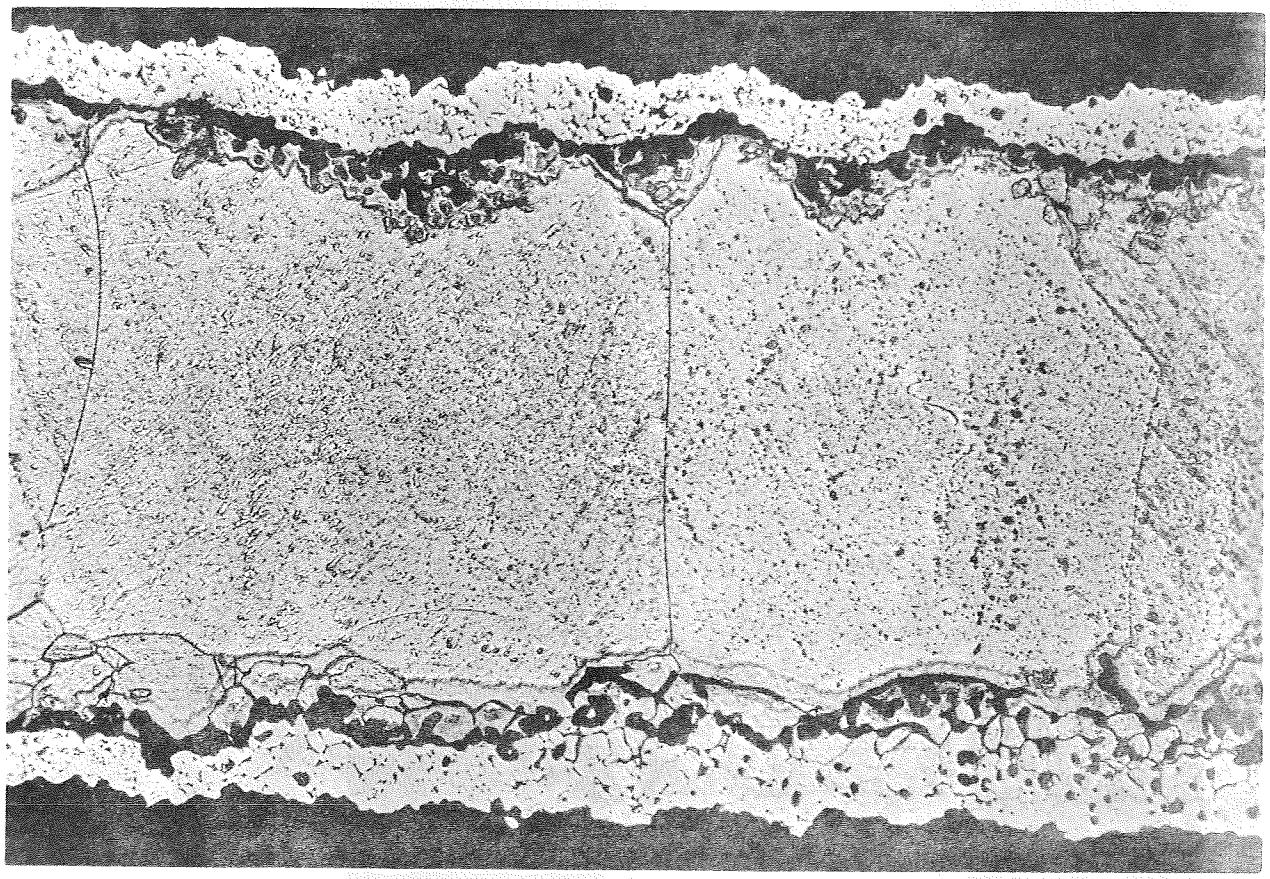


FIGURE 113

Tube end metal member showing large grain size, etched, 200X, Area I

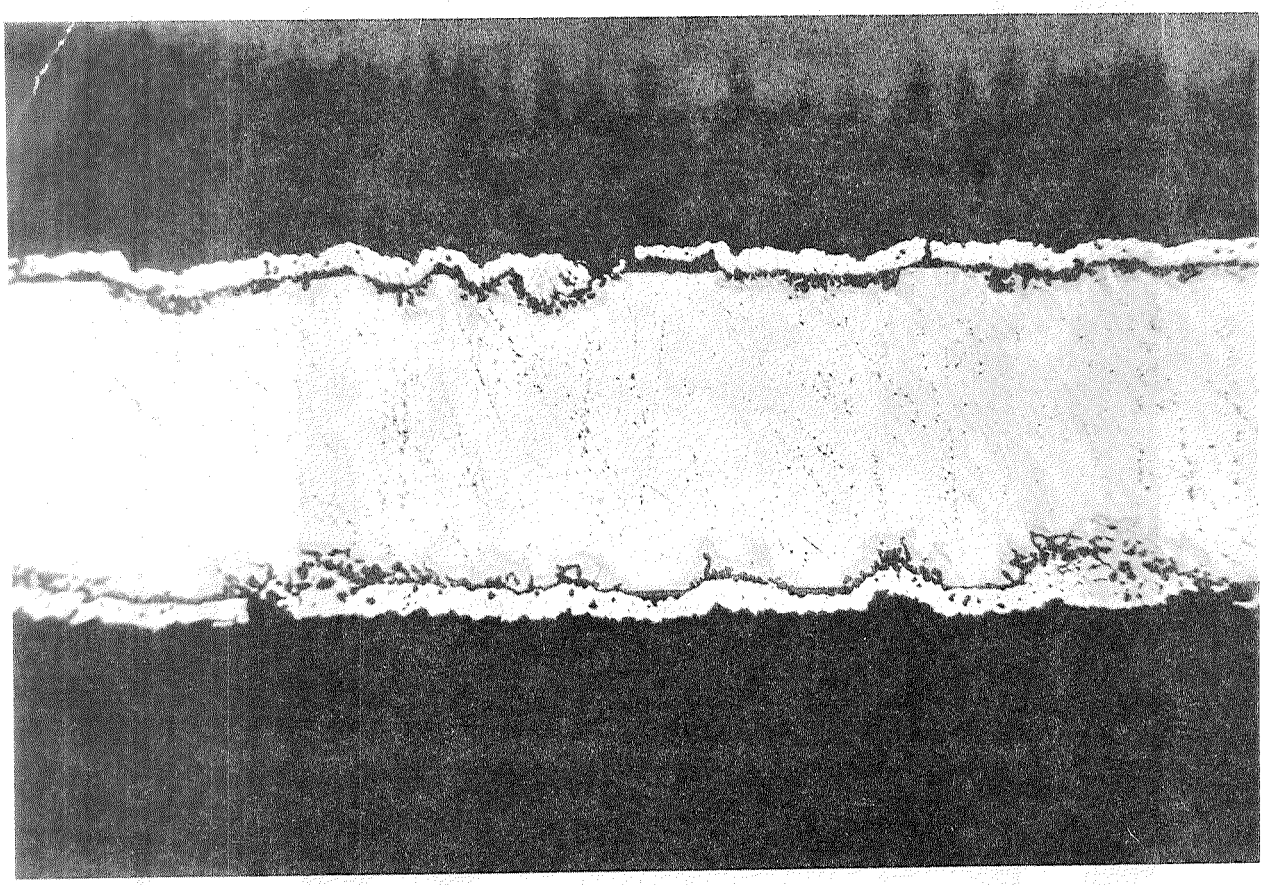


FIGURE 114

Ceramic to metal seal, tube end, unetched, 100X, Area II, site of Figures 115 and 116

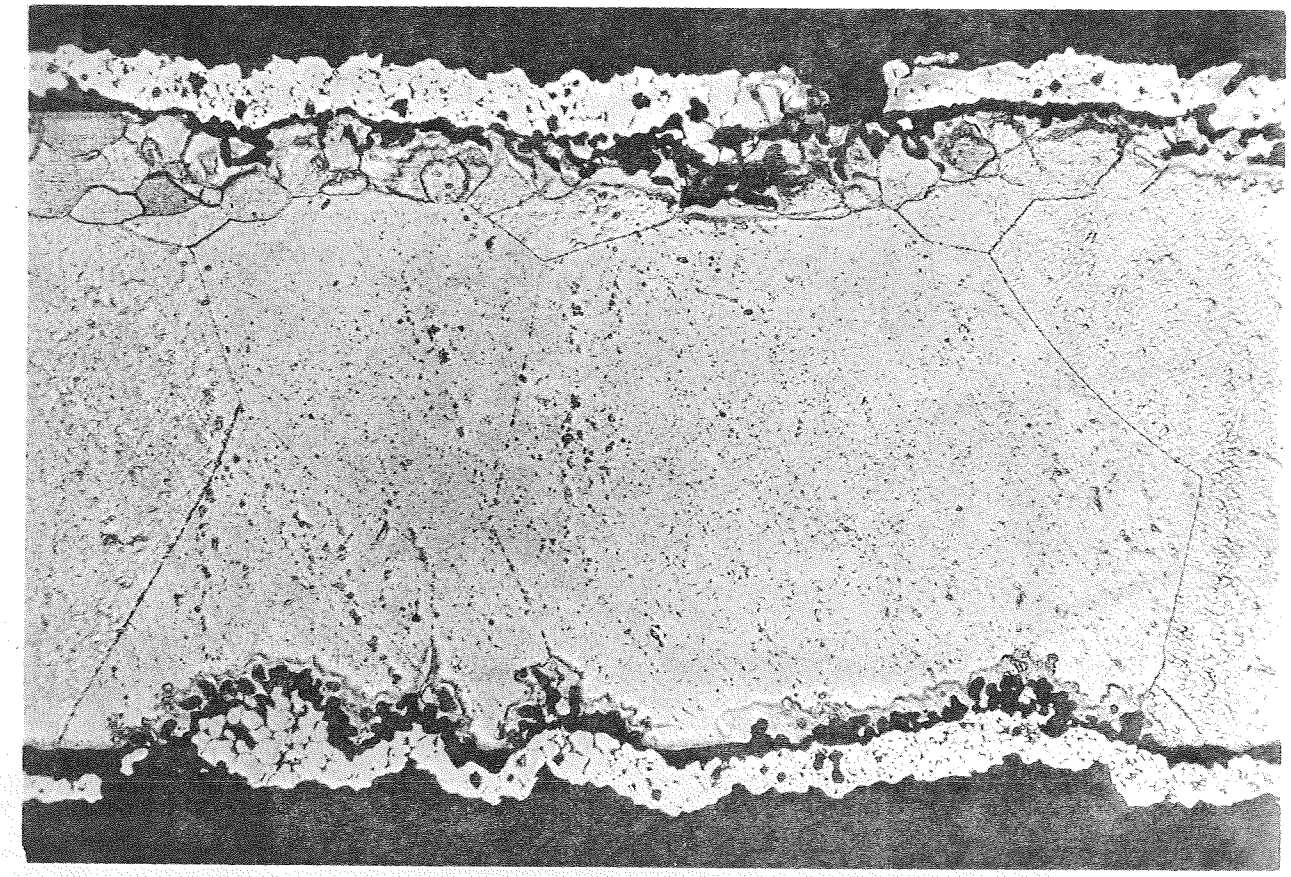


FIGURE 115

Tube end metal member showing large grain size, etched, 200X, Area II

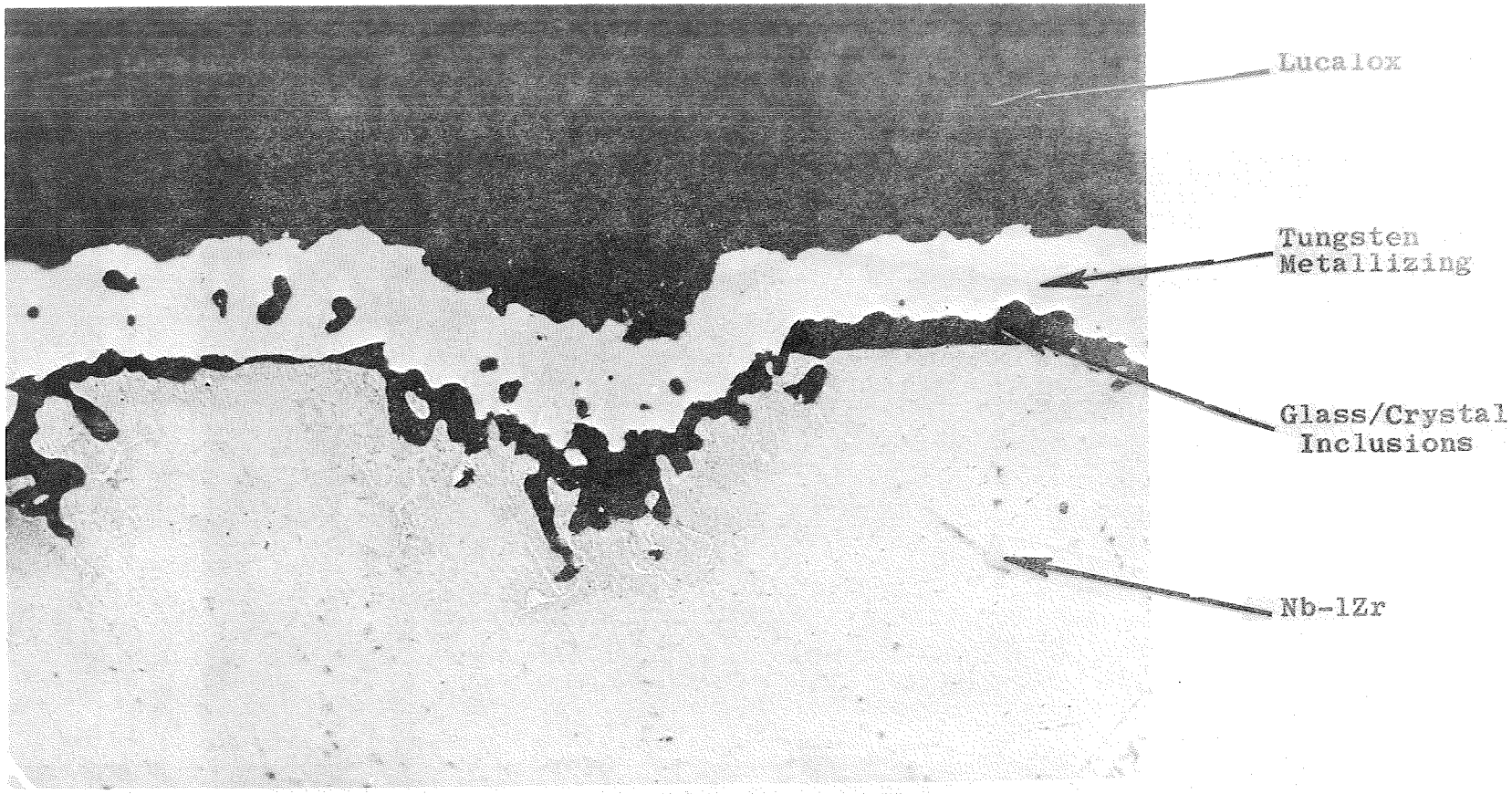


FIGURE 116

Tube end interface showing crystal-glass, oxygen attack, etched, 500X, Area II

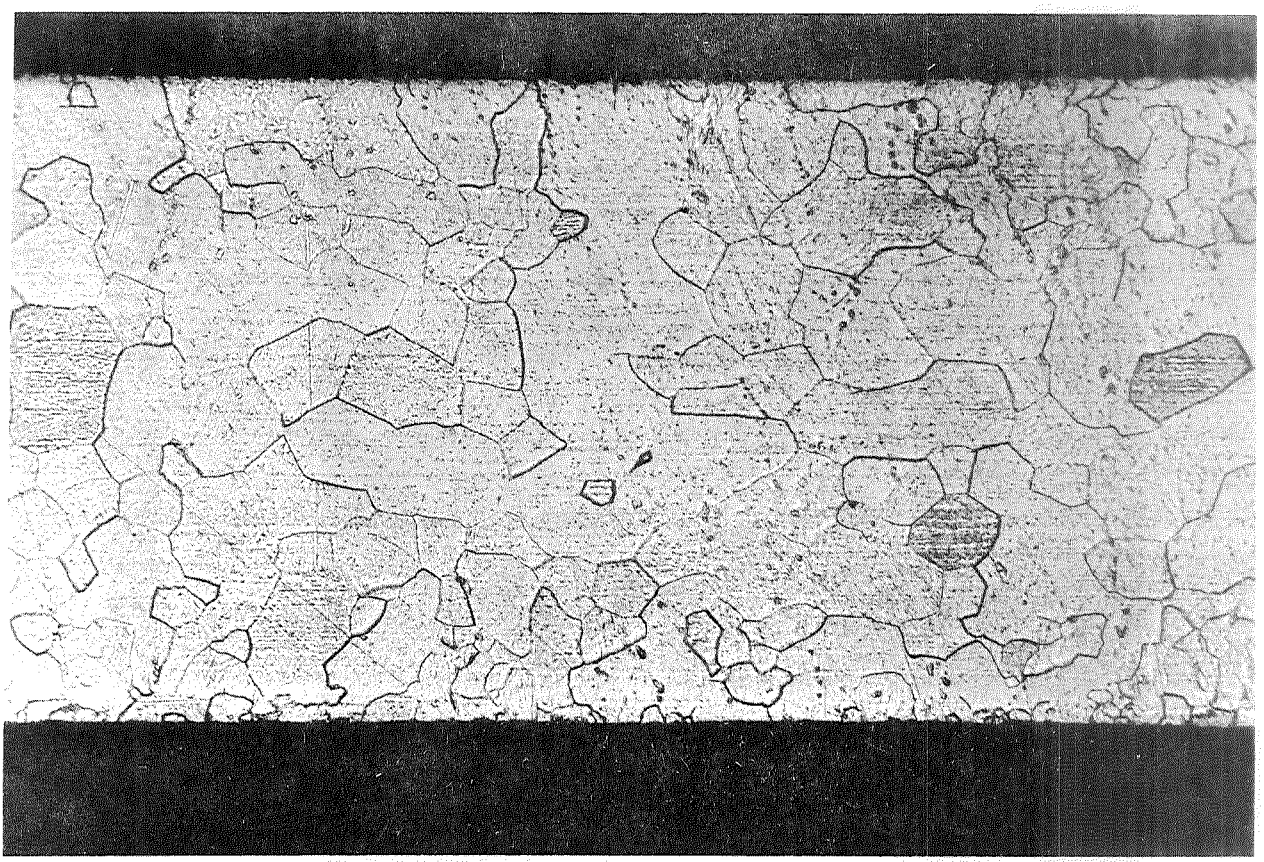


FIGURE 117

Bulged end, central portion of lower end plate, (Nb-1Zr), 200X, etched, Area III

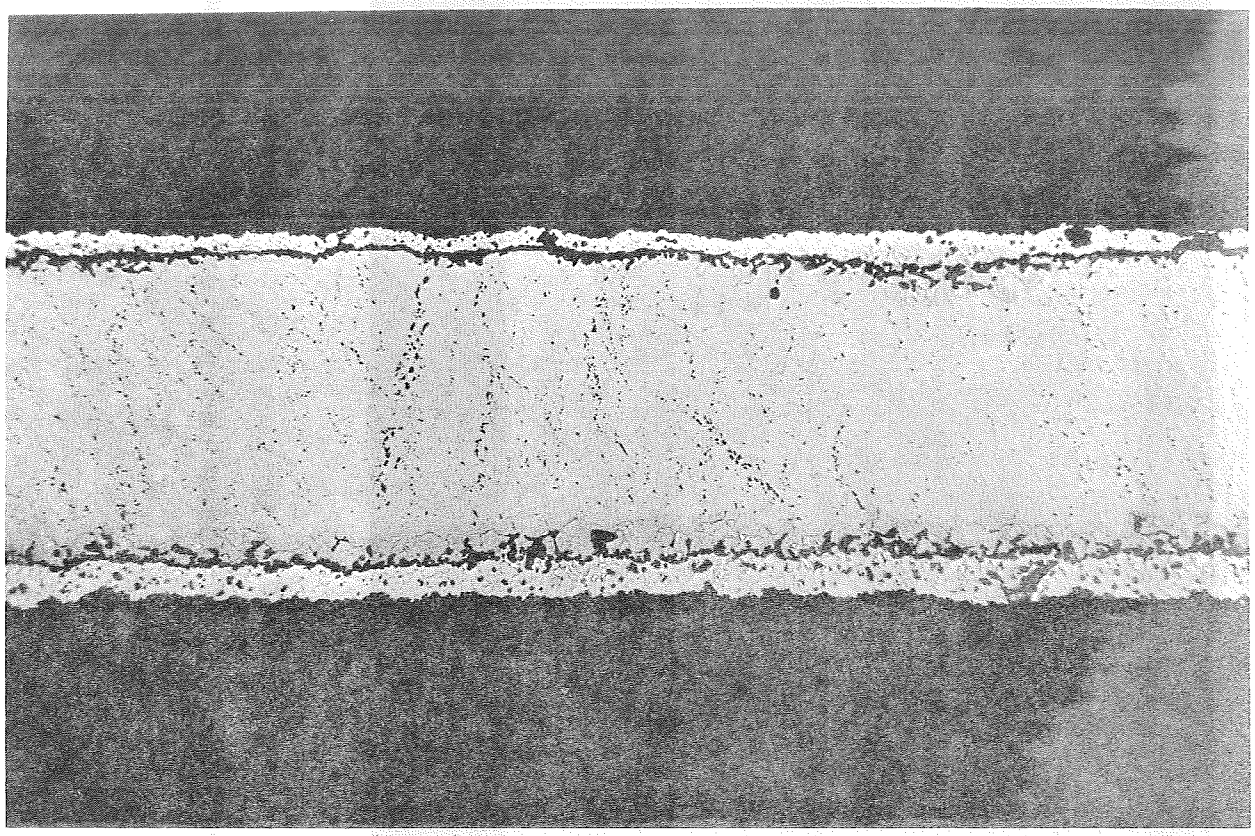


FIGURE 118

Ceramic to metal seal, bulged end, unetched, 100X, Area IV, site of Figures 120 and 121. Section across which X-ray probe is taken.

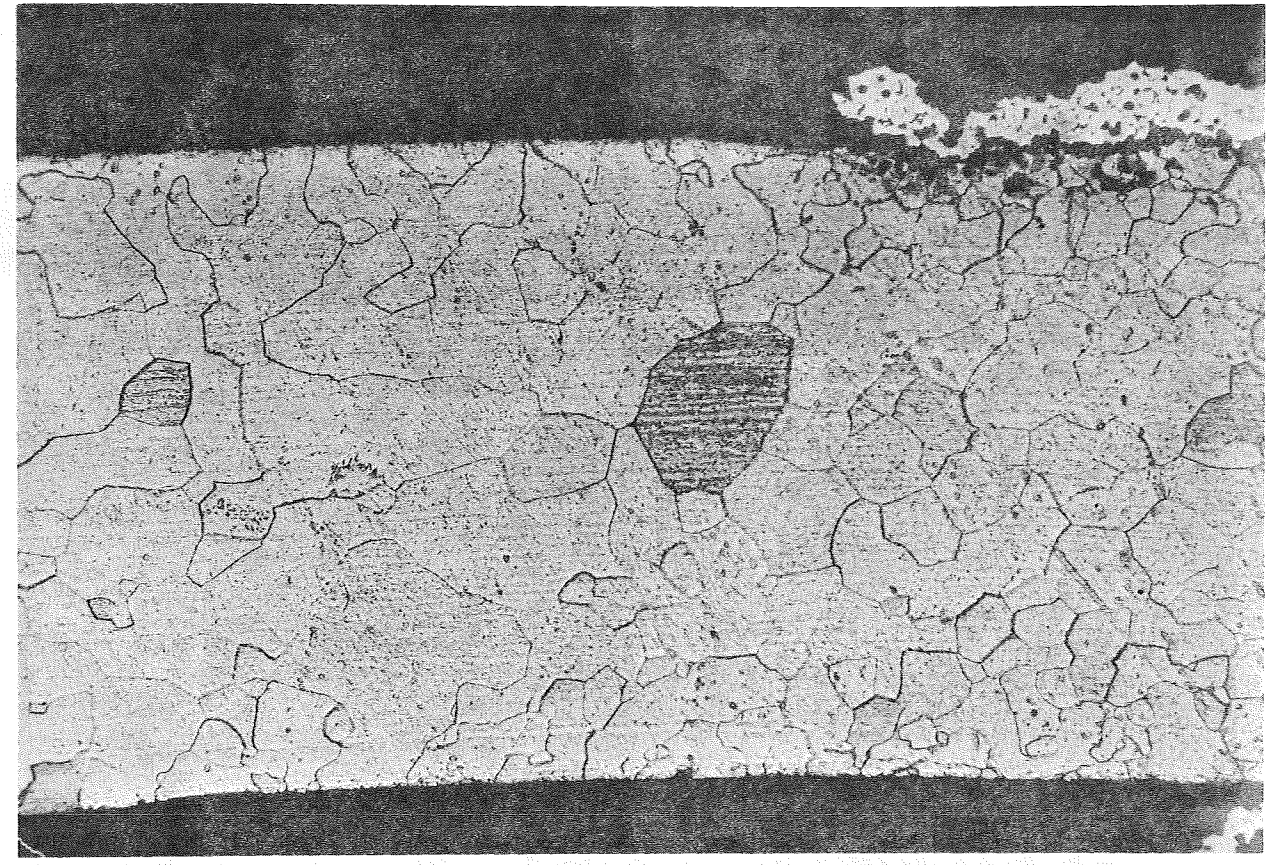


FIGURE 119

Bulged end metal member at braze meniscus area, etched, 200X, Area IV

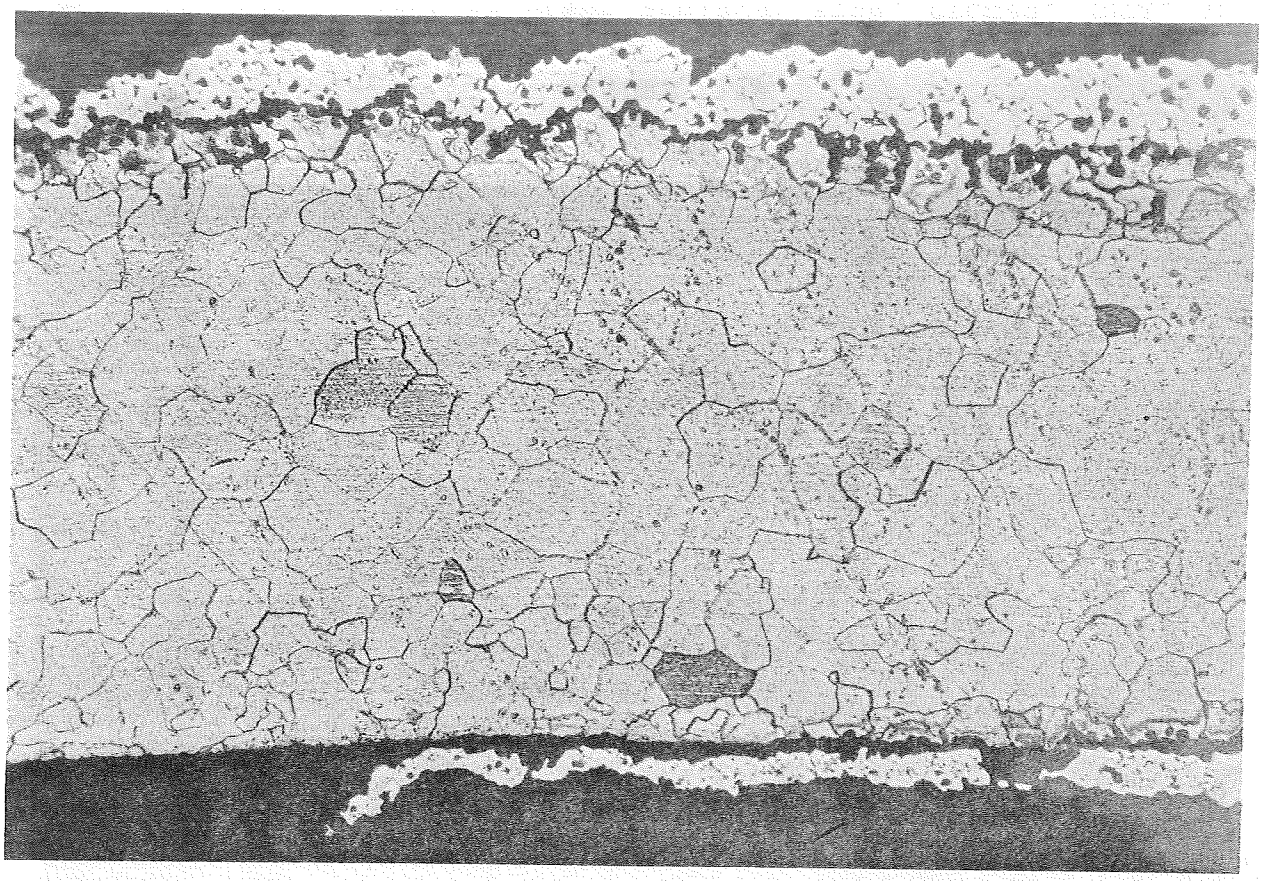


FIGURE 120

Bulged end metal member at braze meniscus area, etched, 200X, Area IV

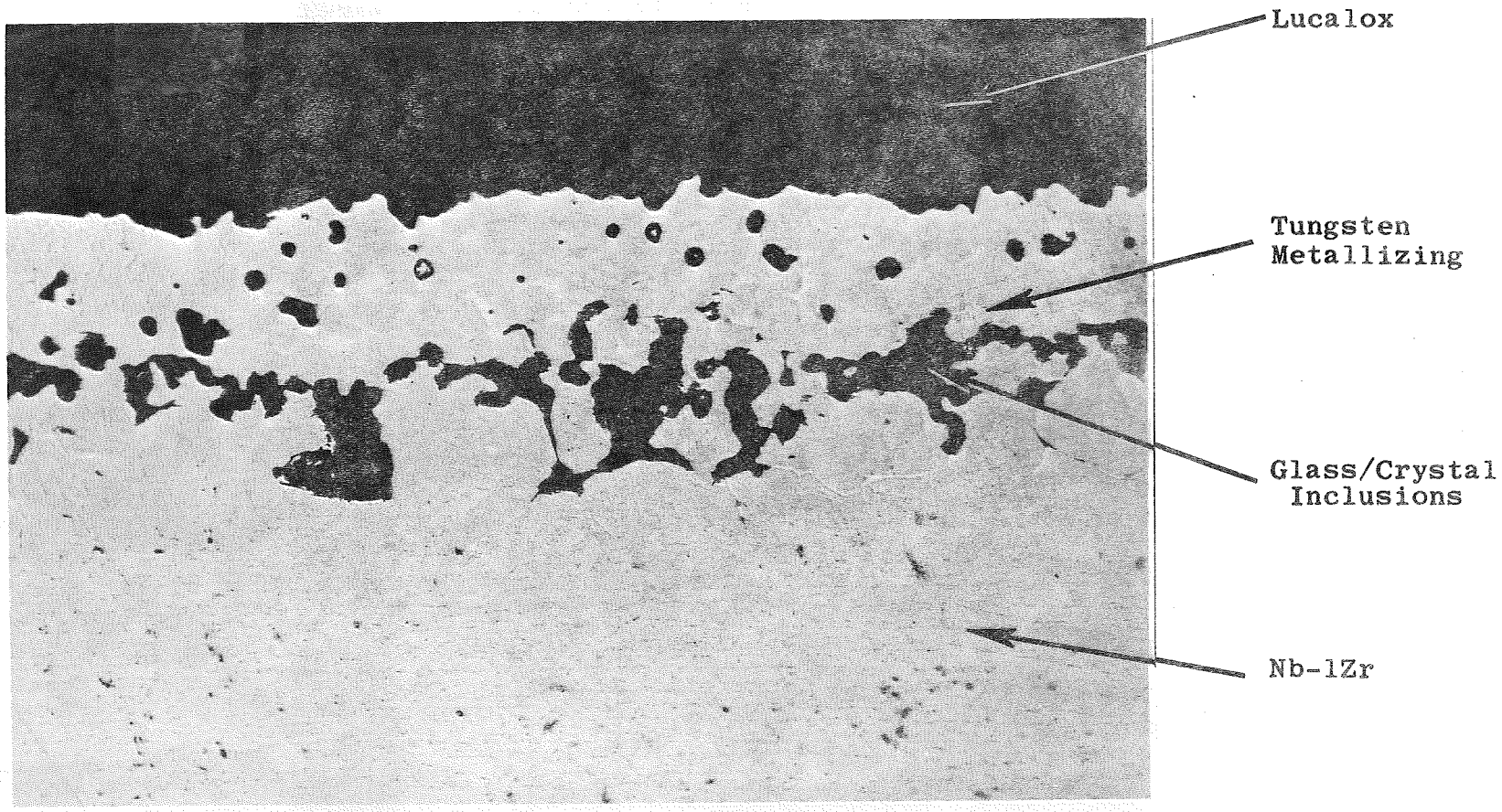


FIGURE 121

Bulged end interface showing crystal-glass, oxygen attack, etched, 500X, Area IV.

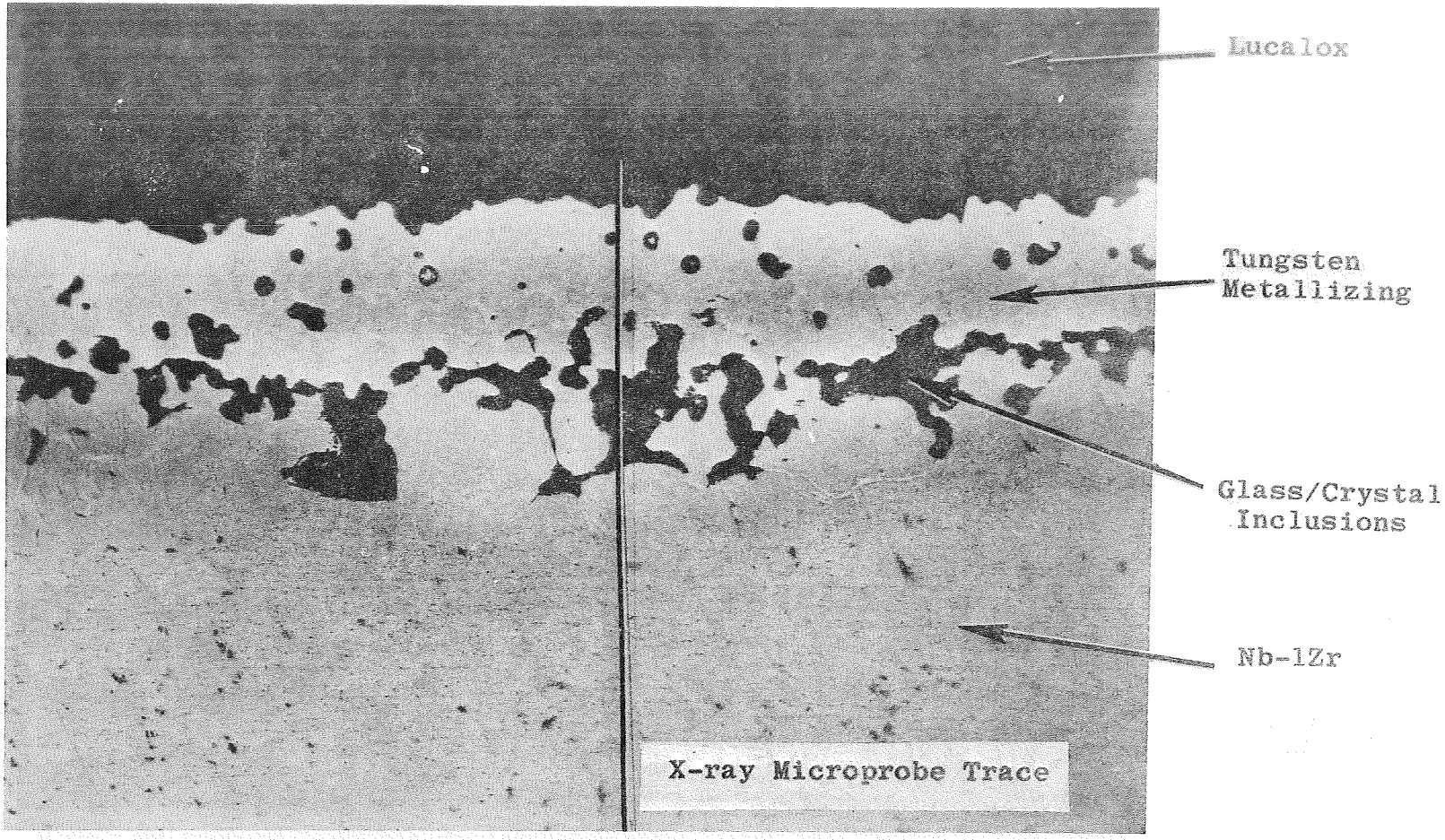
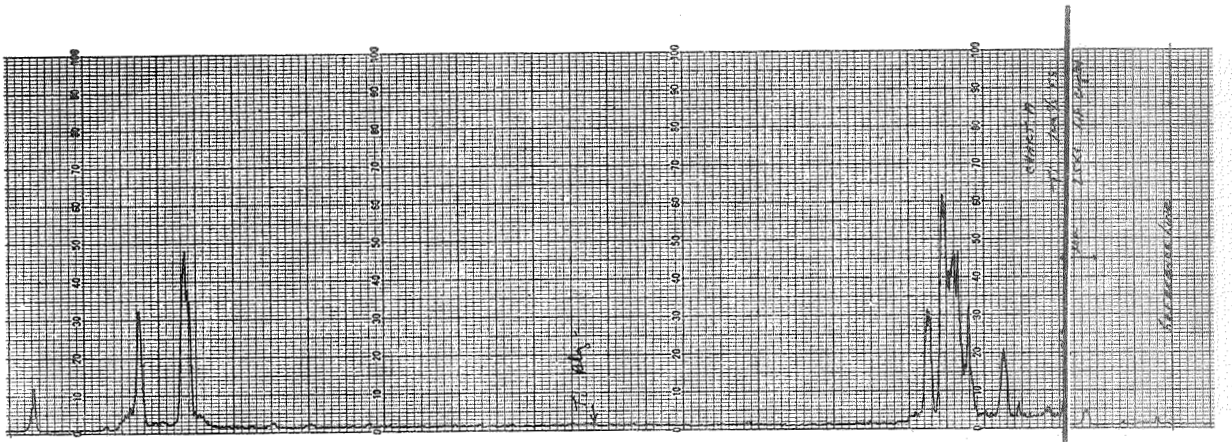


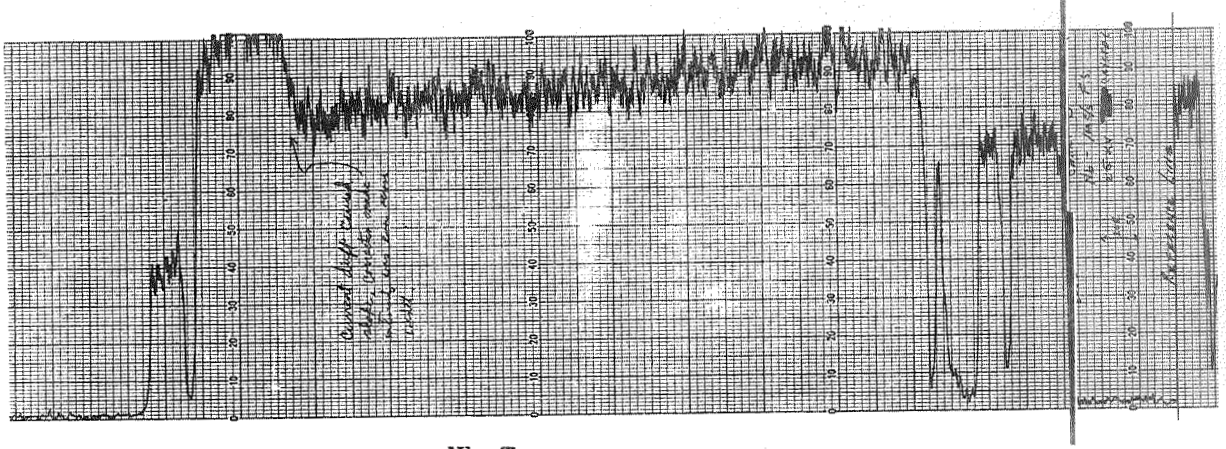
FIGURE 122

Bulged end interface showing crystal-glass, oxygen attack, etched, 500X, Area IV. Shows X-ray microprobe trace line.

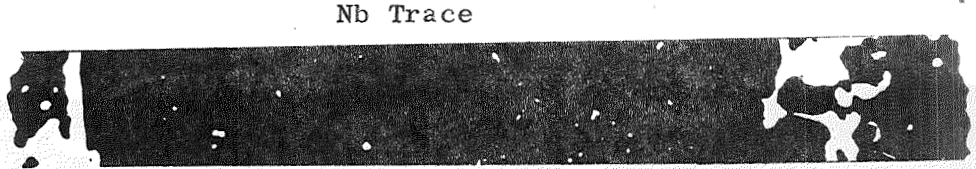


Ti Trace

Edge

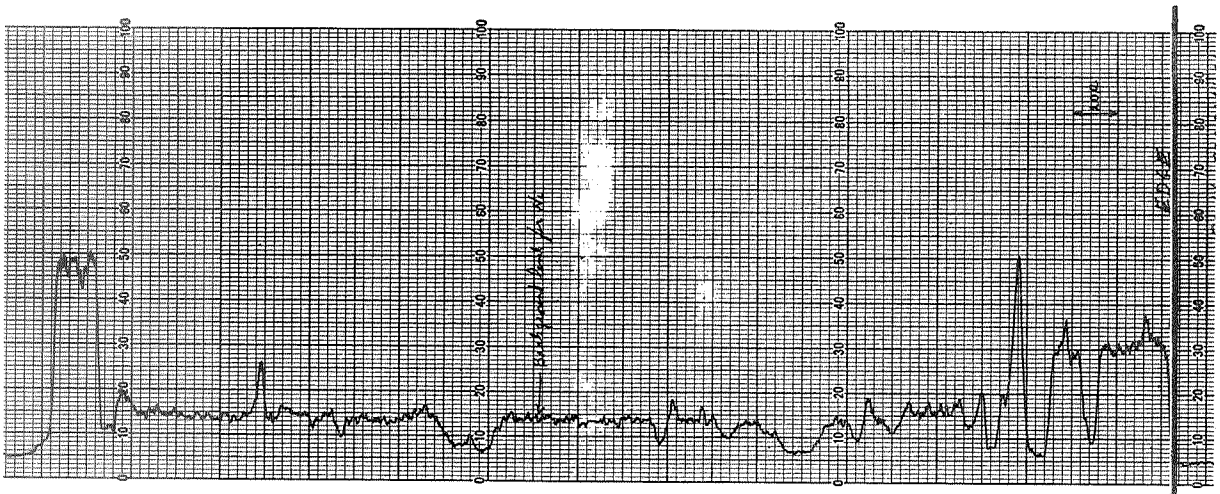


Nb Trace



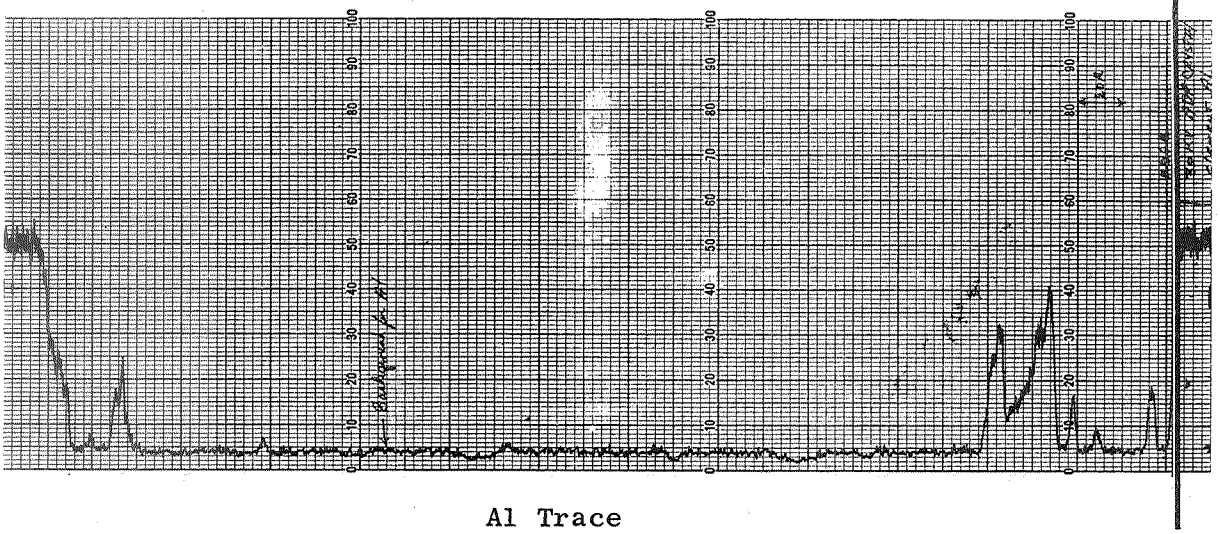
Negative Replica of Photomicrograph Cross-section.

Figure 123 X-ray Microprobe Traces of Metal-Ceramic Seal.
Lucalox Metallized with Tungsten-yttria, and Brazed to Nb-1Zr
with Ni/Nb/Ti Alloy.
Traces Recorded with LiF Crystal, 25KV Accelerating Potential.

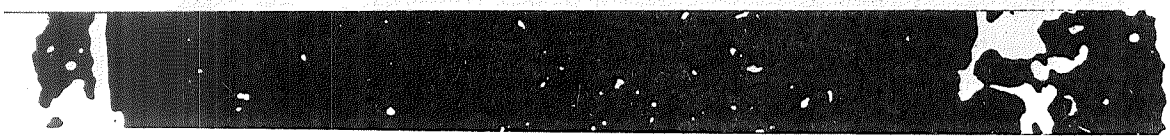


Ni Trace

Edge

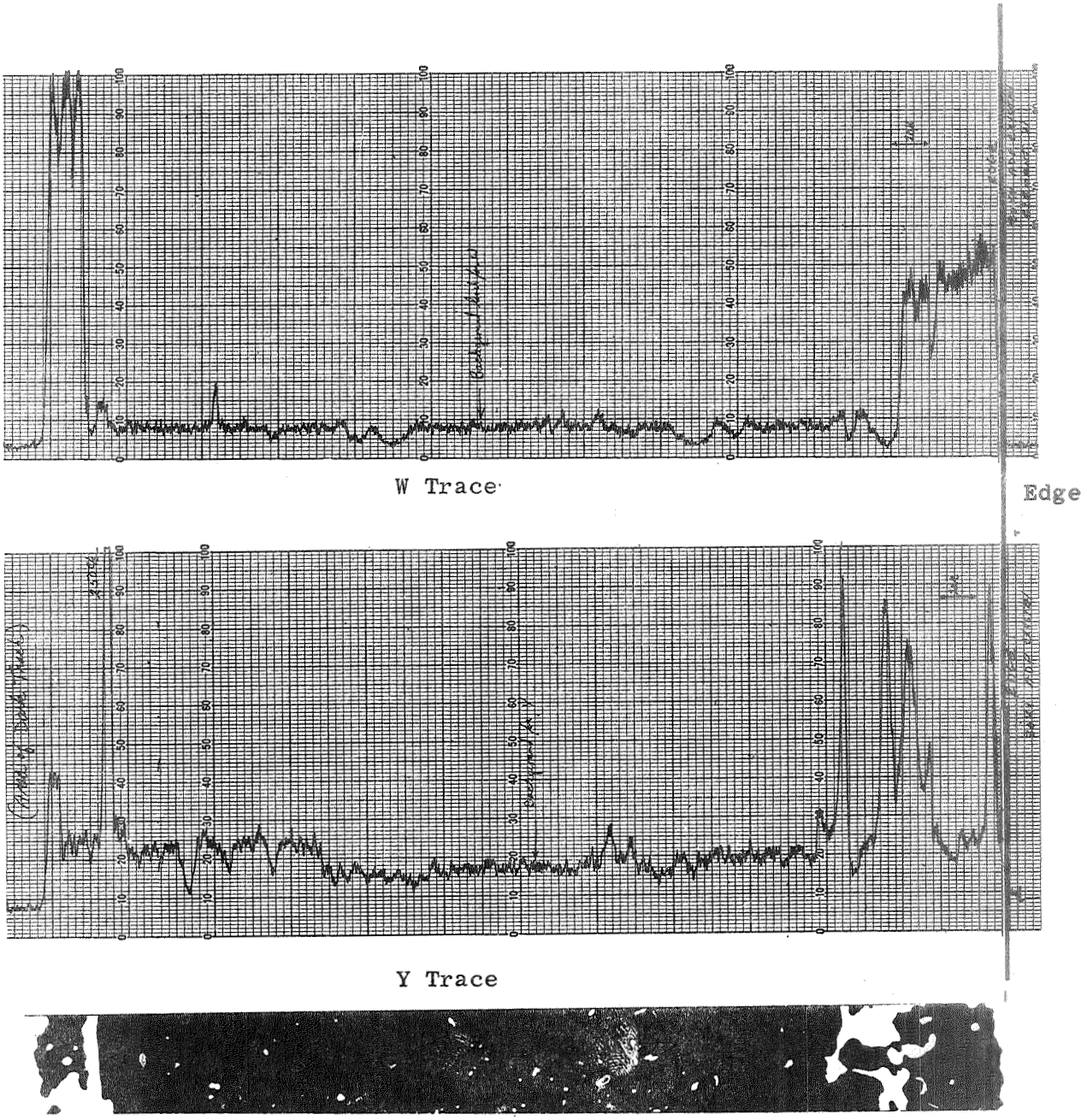


Al Trace



Negative Replica of Photomicrograph Cross-section.

Figure 124 X-ray Microprobe Traces of Metal-Ceramic Seal.
Lucalox Metallized with Tungsten-yttria, and Brazed to Nb-1Zr
with Ni/Nb/Ti Alloy.
Traces Recorded with ADP crystal, 30 KV accelerating potential.



Negative Replica of Photomicrograph Cross-section.

Figure 125 X-ray Microprobe Traces of Metal-Ceramic Seal.
Lucalox Metallized with Tungsten-yttria, and Brazed to Nb-1Zr
with Ni/Nb/Ti Alloy.
Traces Recorded with ADP Crystal, 30 KV Accelerating Potential.

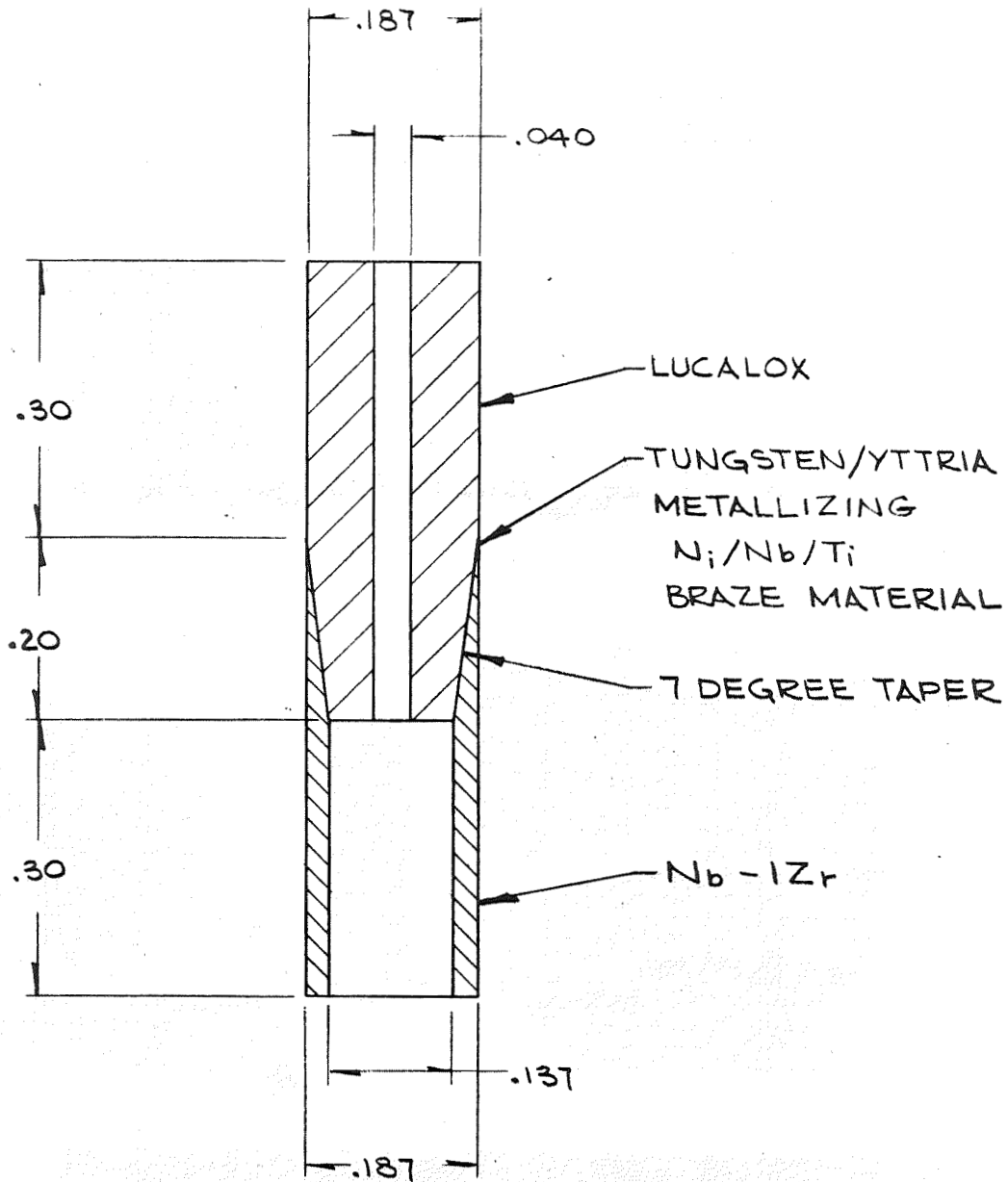


FIGURE 126

Metal-Ceramic Thermal Cycling Test Unit

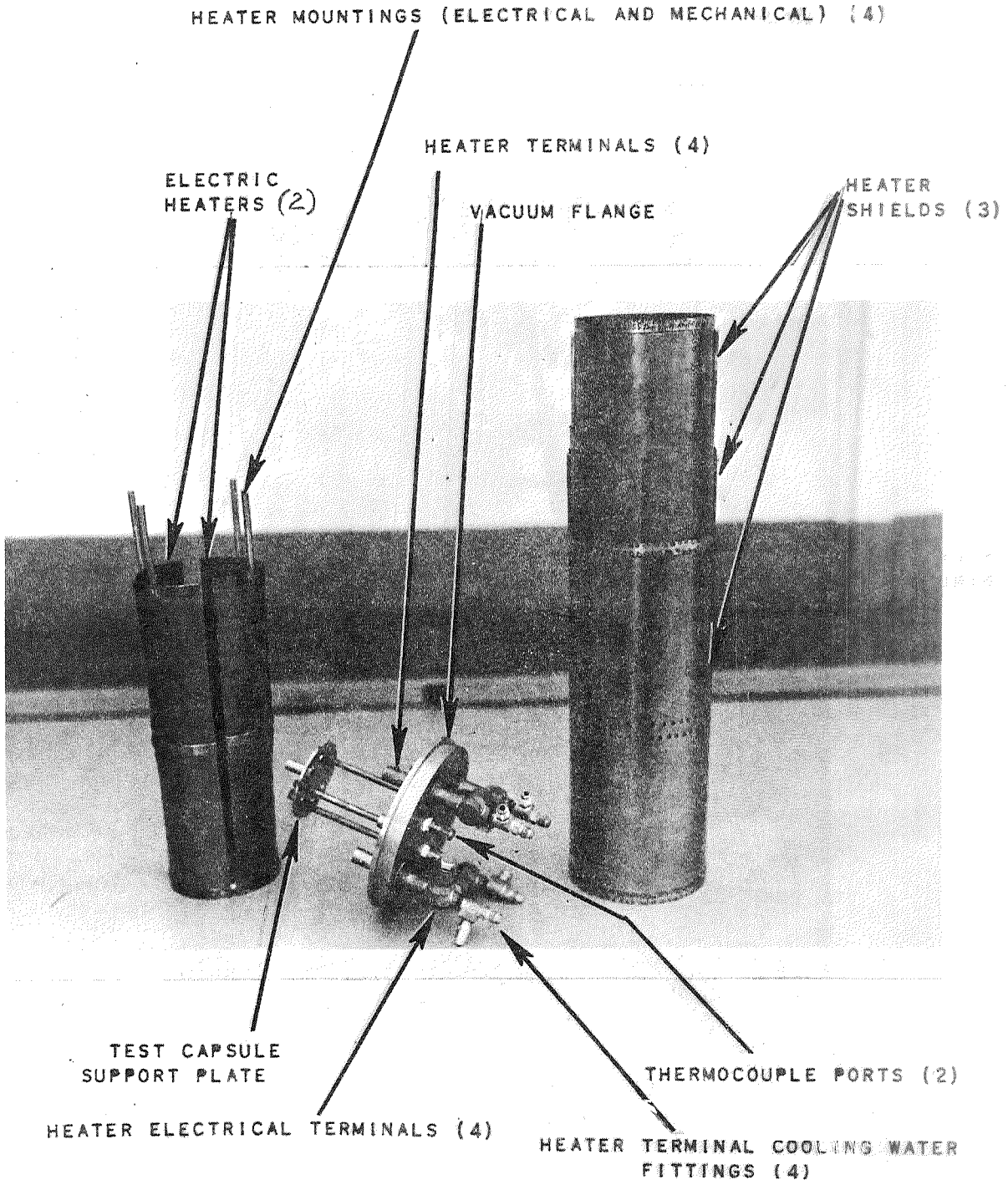


FIGURE 127

COMPATIBILITY TEST CHAMBER-INTERNAL COMPONENTS

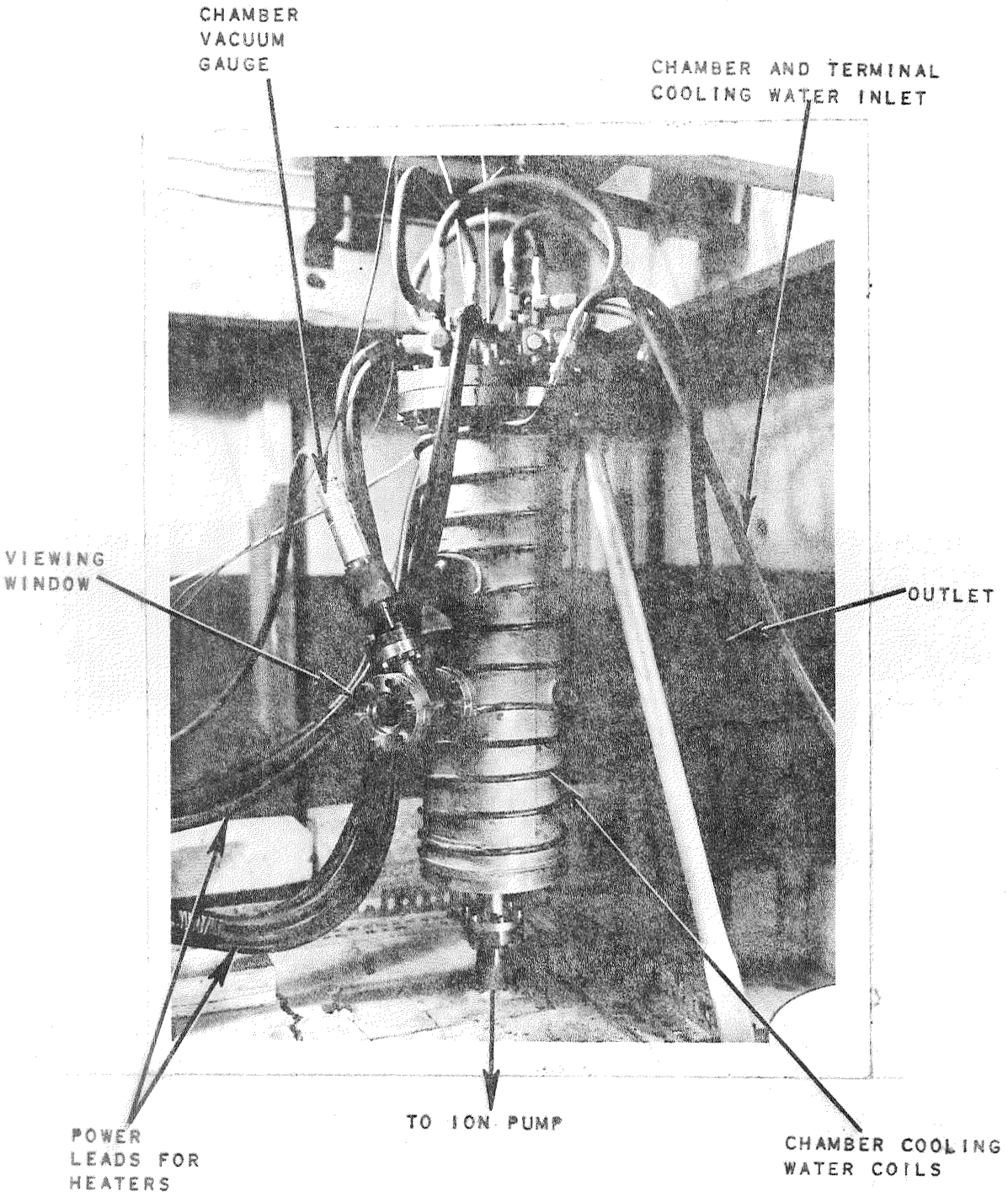


FIGURE .128

COMPATIBILITY TEST CHAMBER

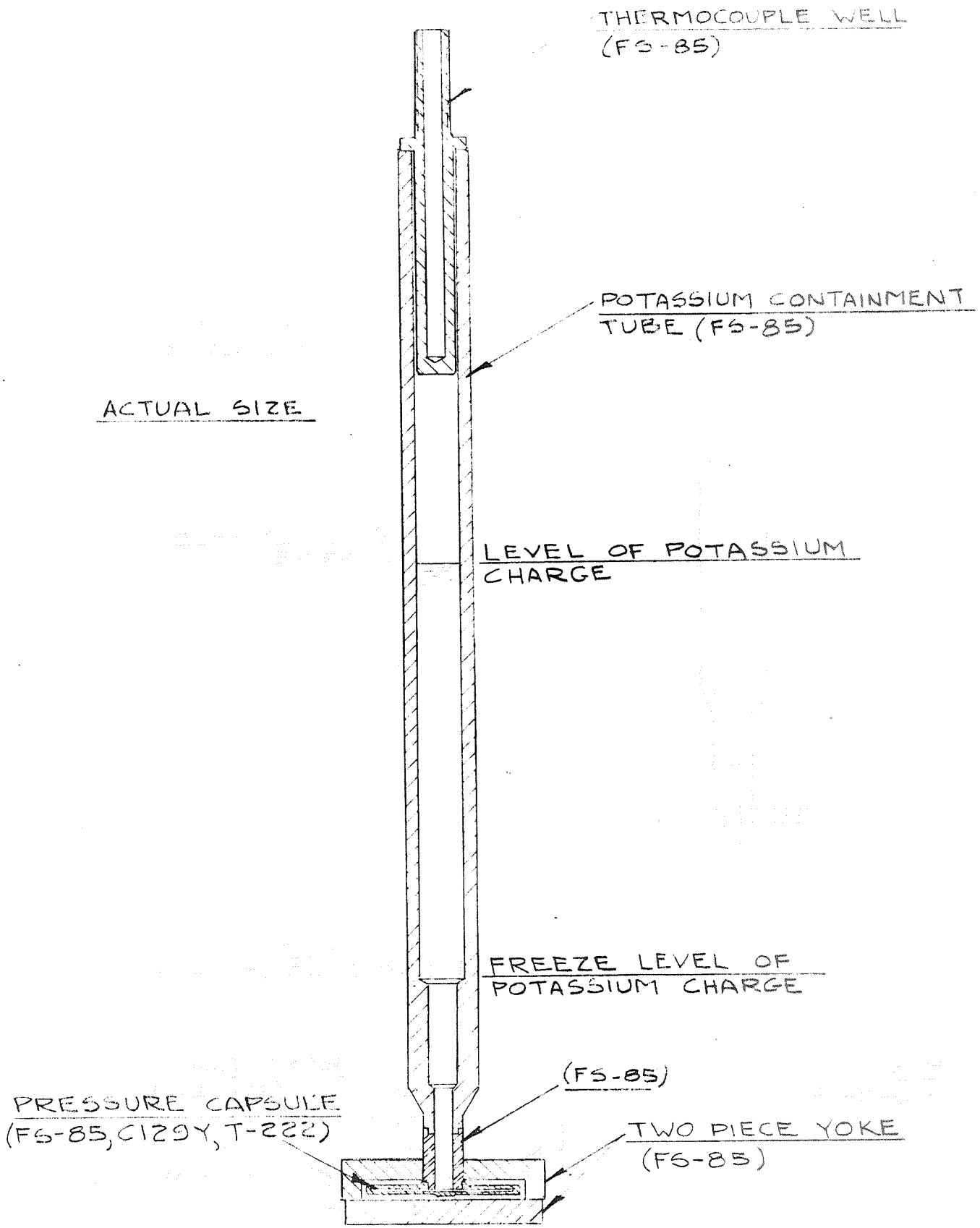


Figure 129

Compatibility Test Design for Columbium and Tantalum Capsules

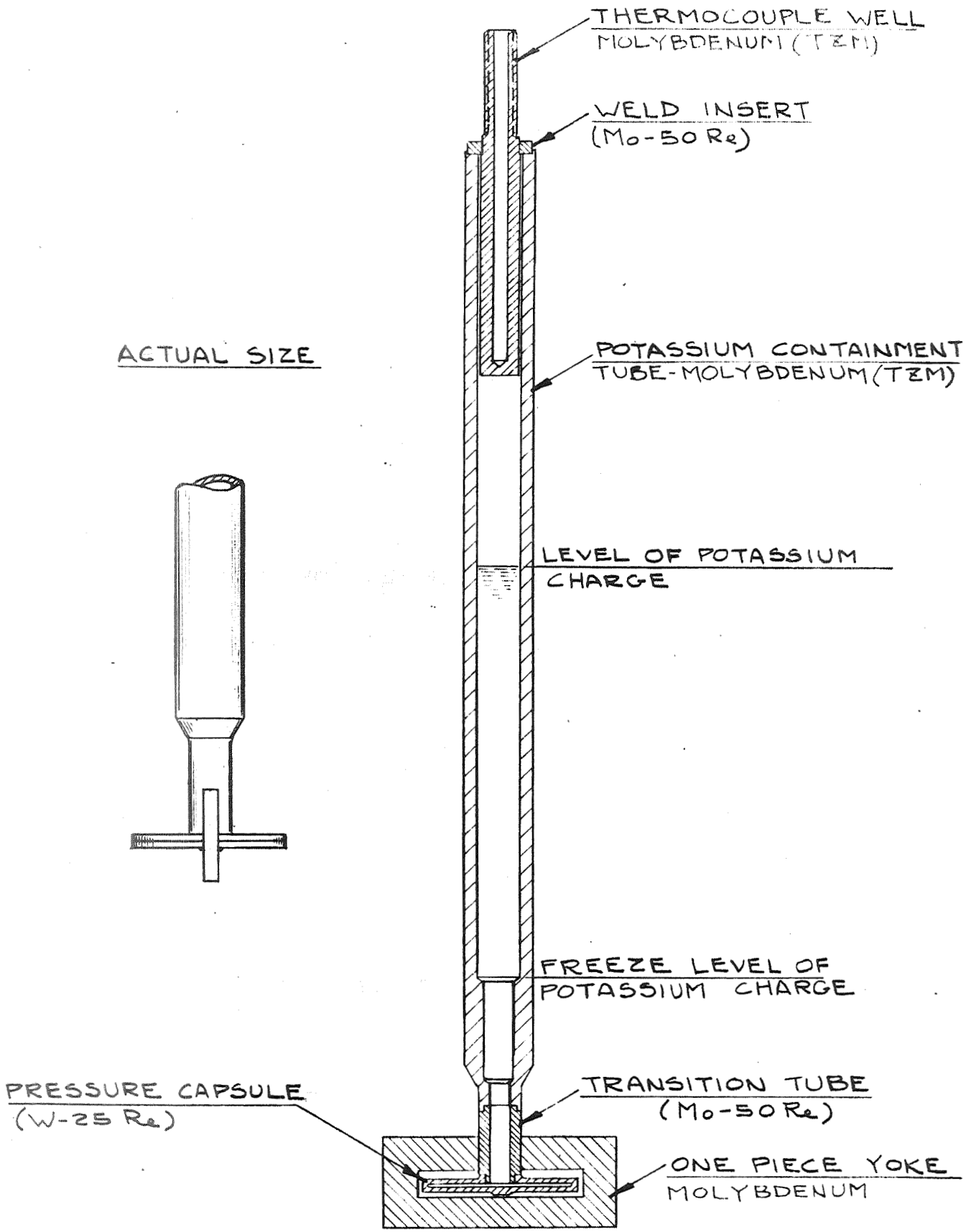


Figure 130

Compatibility Test Design for W-25Re Capsule

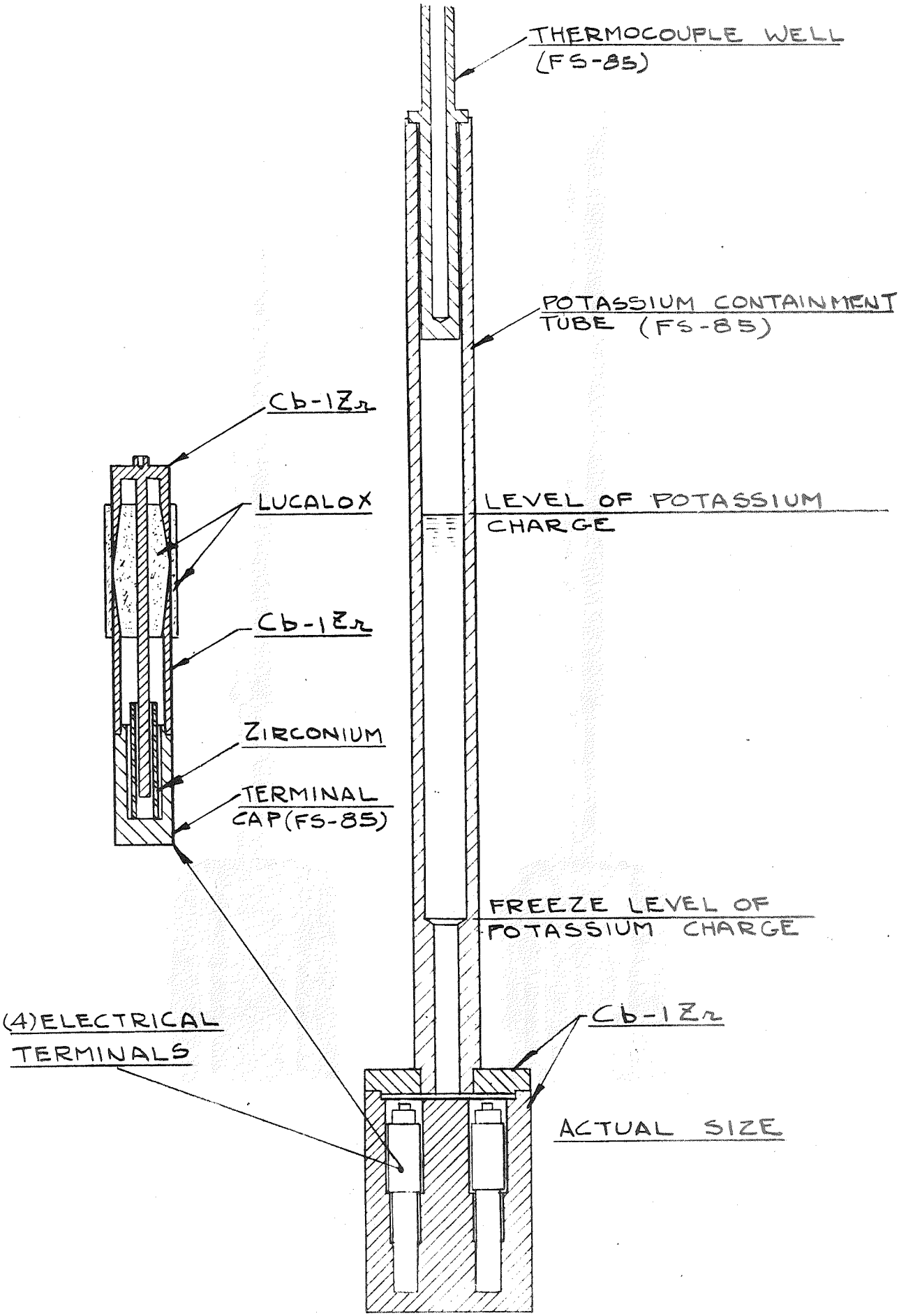


Figure 131

Compatibility Test Design for Electrical Terminals

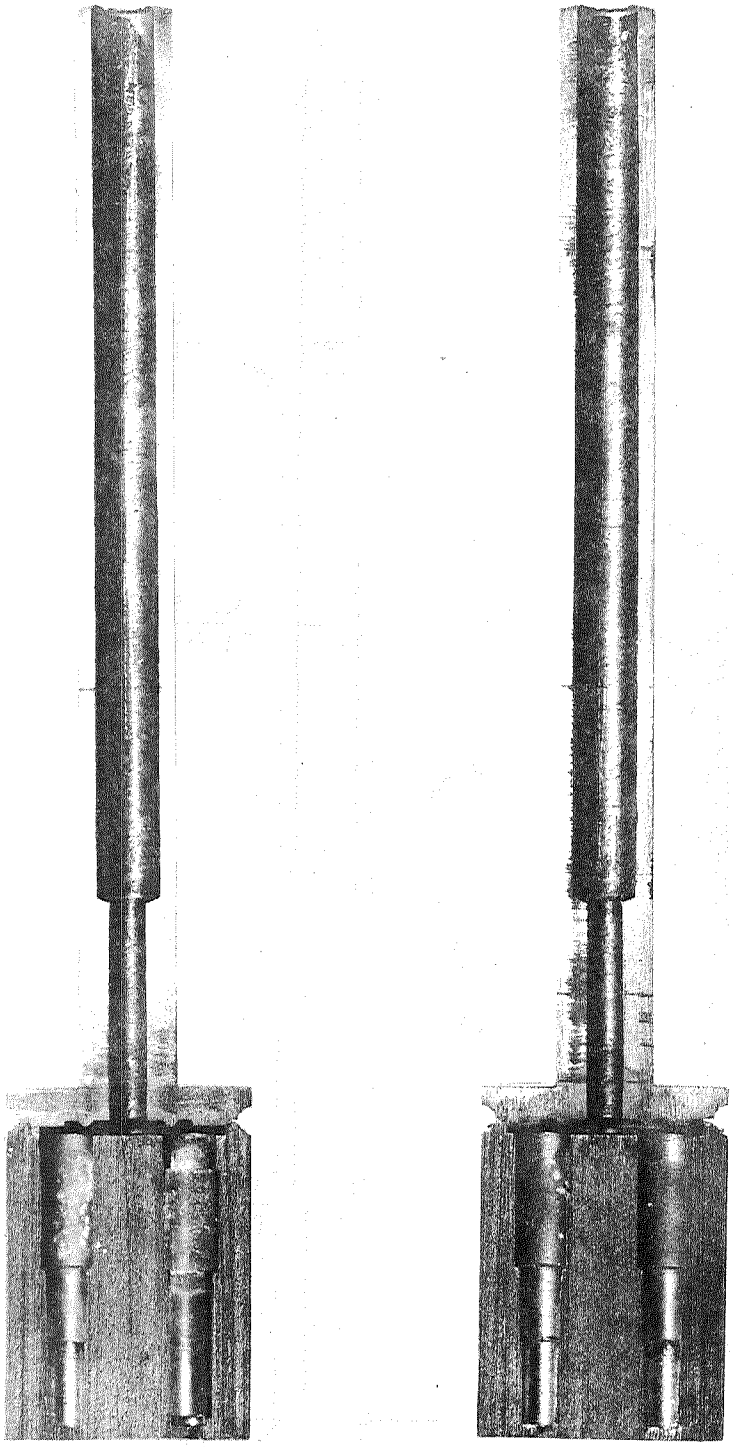


FIGURE 132

Terminal compatibility capsule in "as sectioned" condition after test with one terminal in place. (Full Scale)

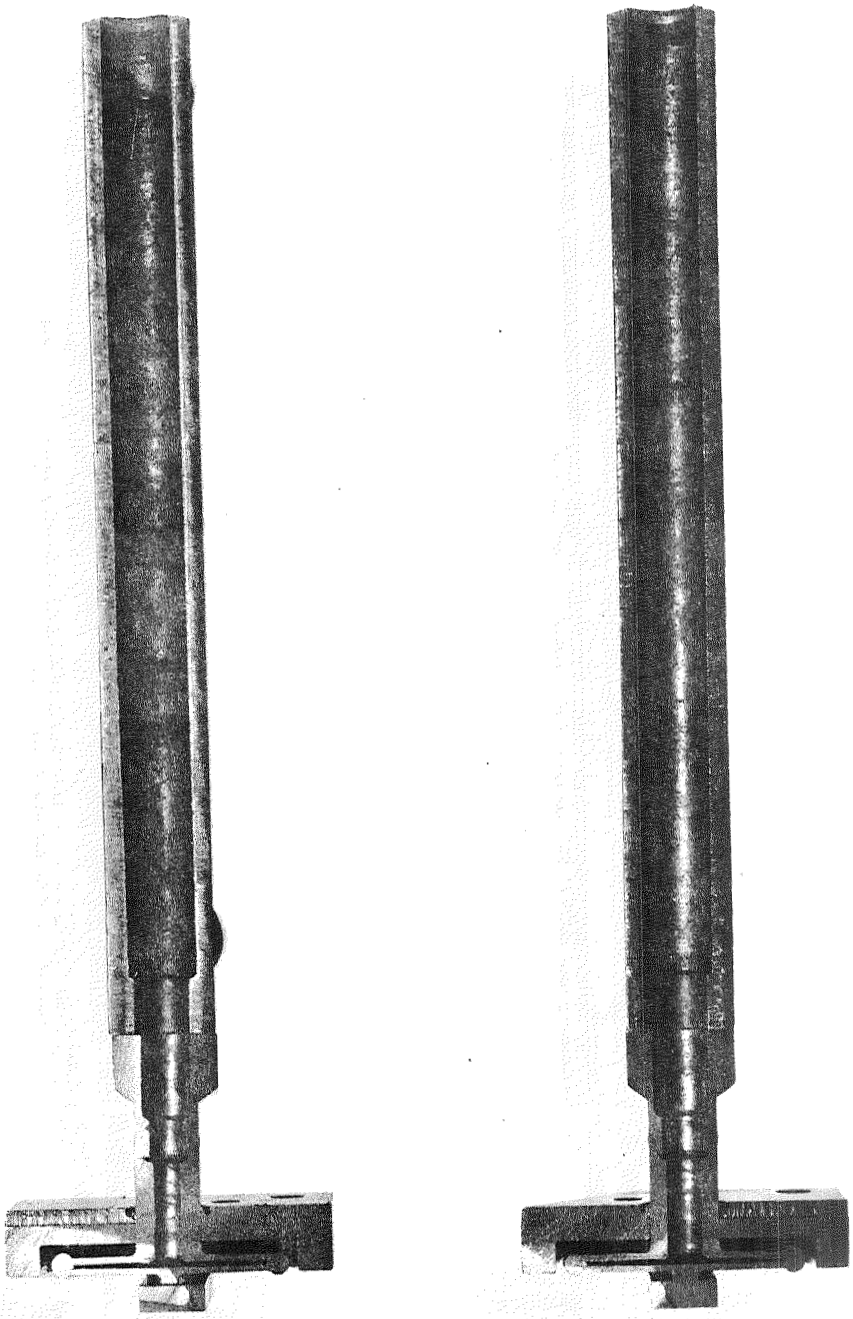


FIGURE 133

C-129Y compatibility capsule in "as sectioned" condition after test. (Full Scale)

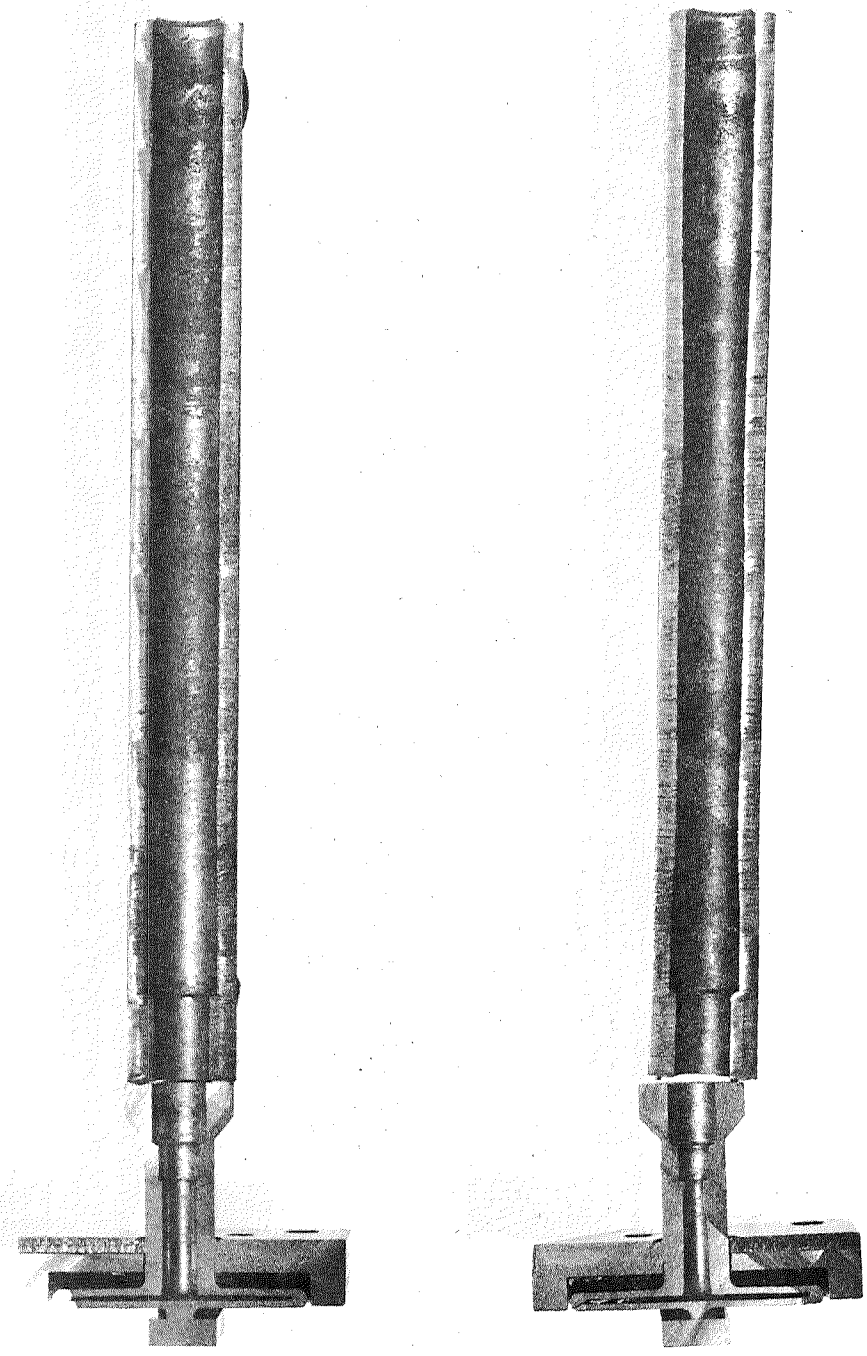


FIGURE 134

FS-85 compatibility capsule in "as sectioned" condition after test. (full scale)

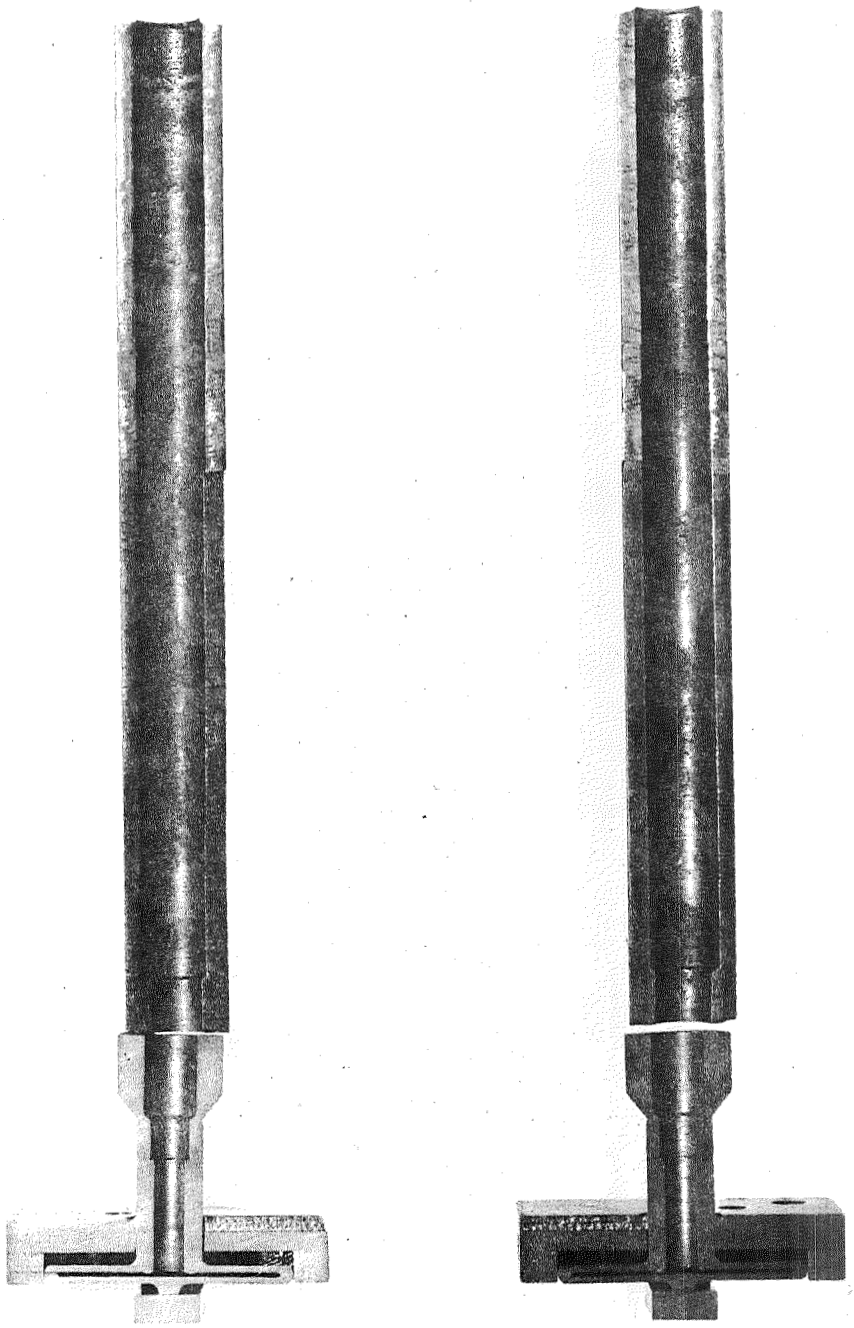


FIGURE 135

T-222 compatibility capsule in "as sectioned" condition after test. (Full Scale)

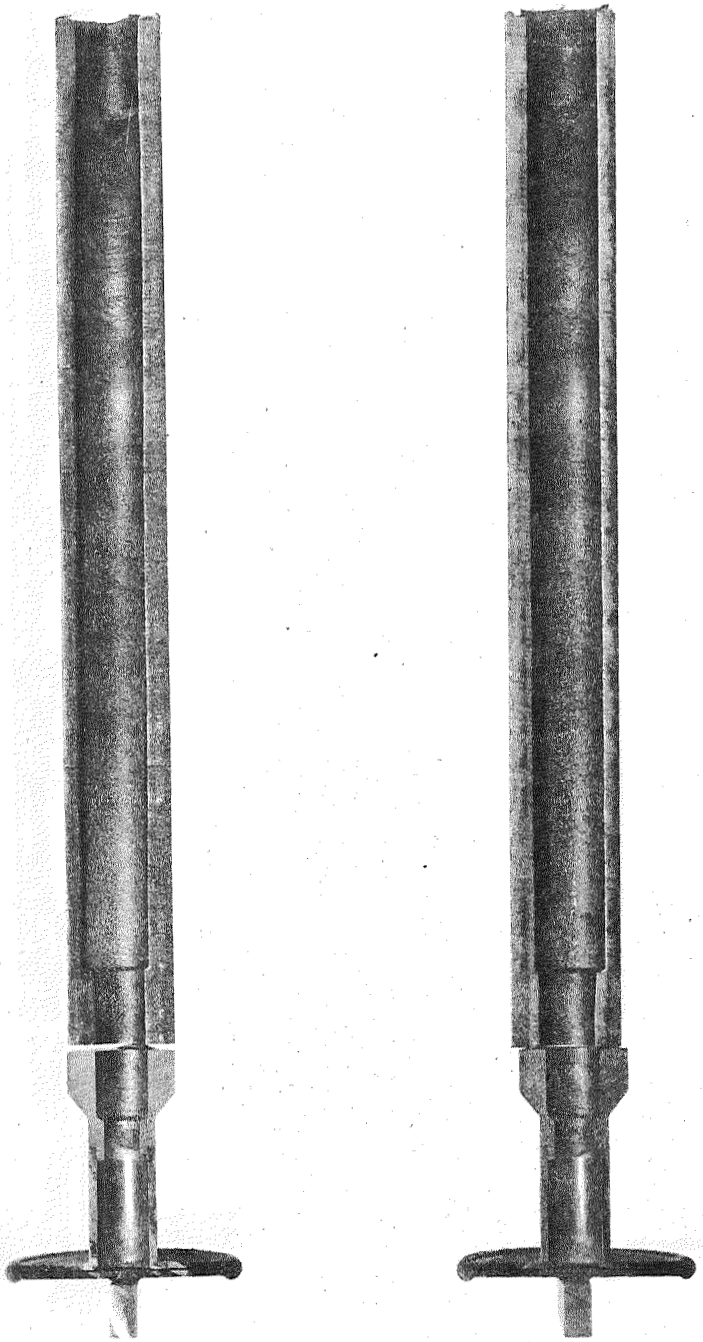


FIGURE 136

W-25 Re compatibility capsule in "as sectioned" condition after test. (Full Scale)

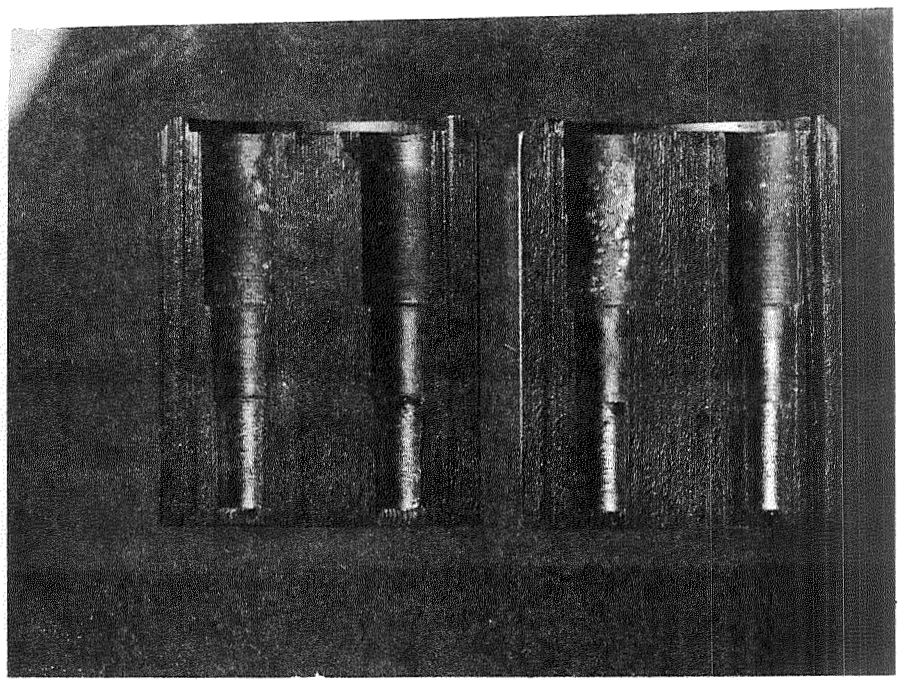


FIGURE 137

Lower portion of Terminal compatibility capsule in "as sectioned" condition after test with terminal removed.

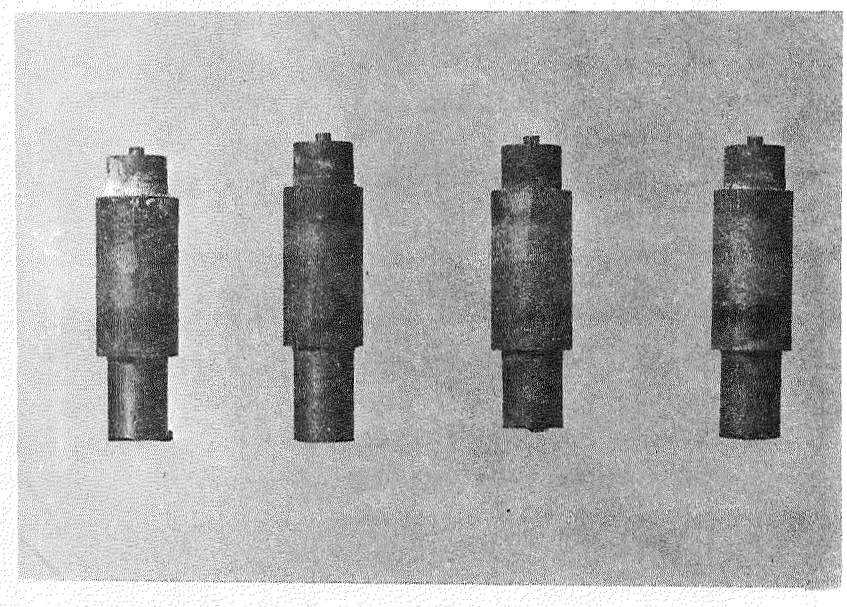


FIGURE 138

Electrical Terminals with lower end caps removed after test. (3X Magnification)

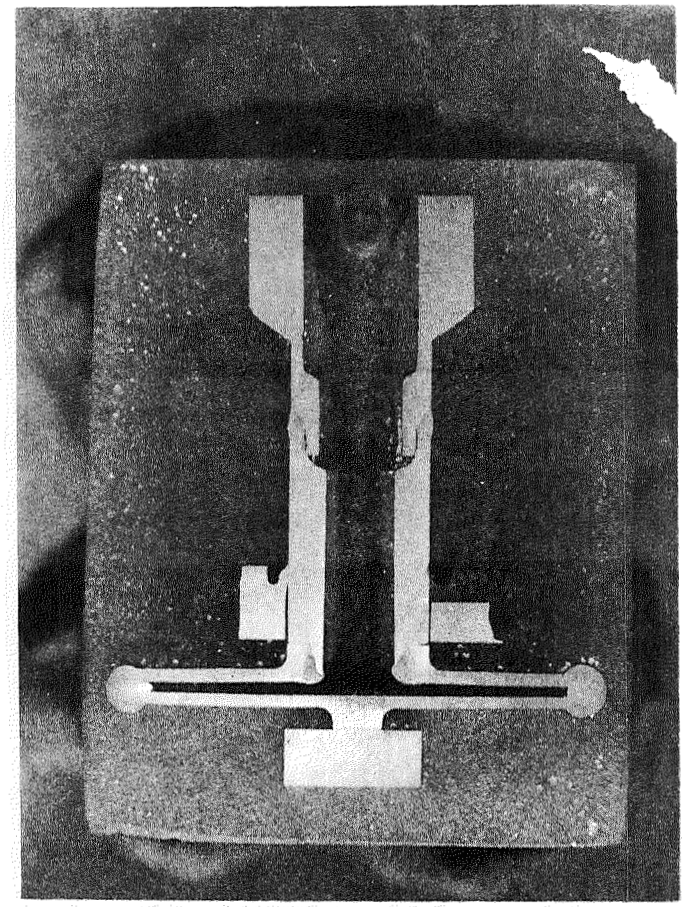


FIGURE 139

Photograph of C-129Y compatibility capsule after test with yoke removed. (3X Magnification)

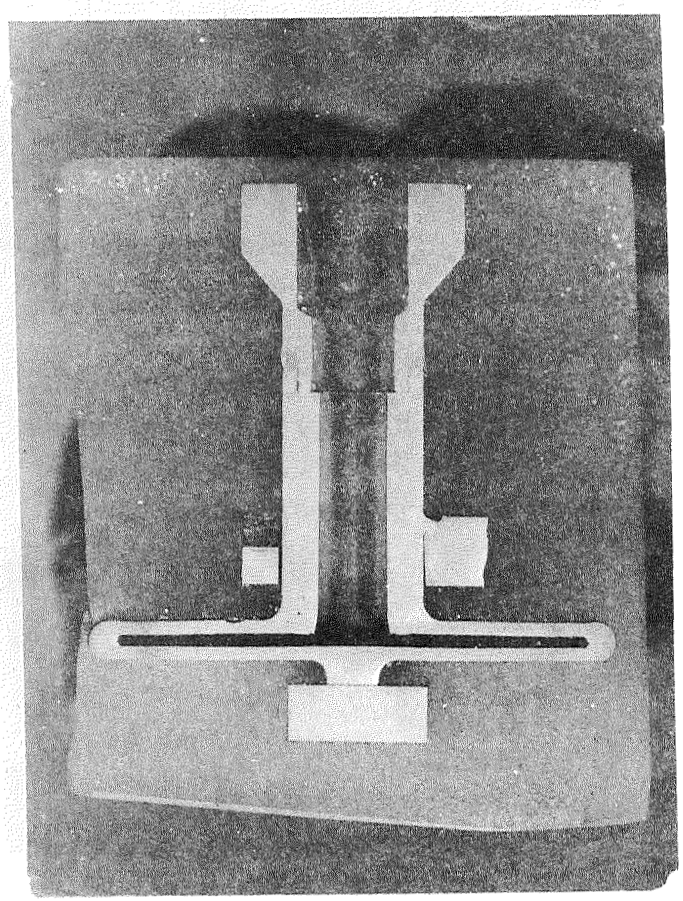


FIGURE 140

Photograph of FS-85 compatibility capsule after test with yoke removed. (3X Magnification)

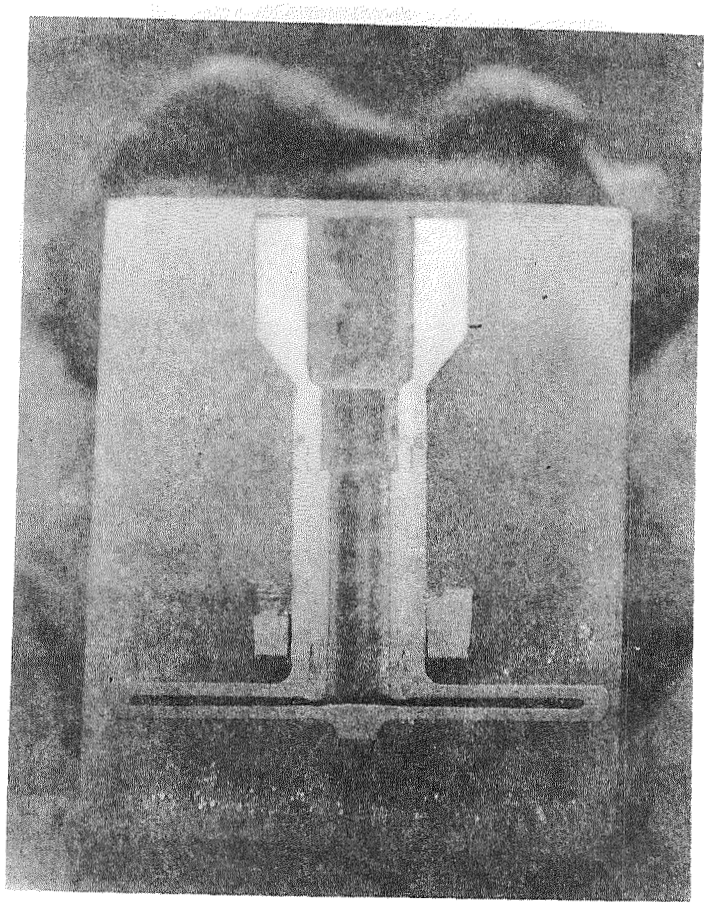


FIGURE 141

Photograph of T-222 compatibility capsule after test with yoke removed. (3X Magnification)

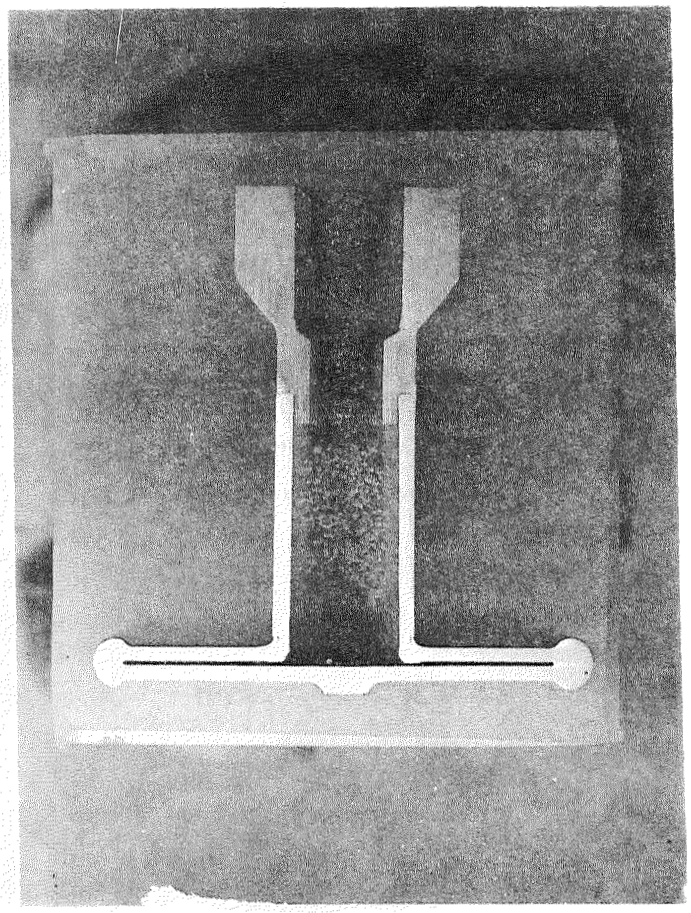


FIGURE 142

Photograph of W-25 Re compatibility capsule after test with yoke removed. (3X Magnification)

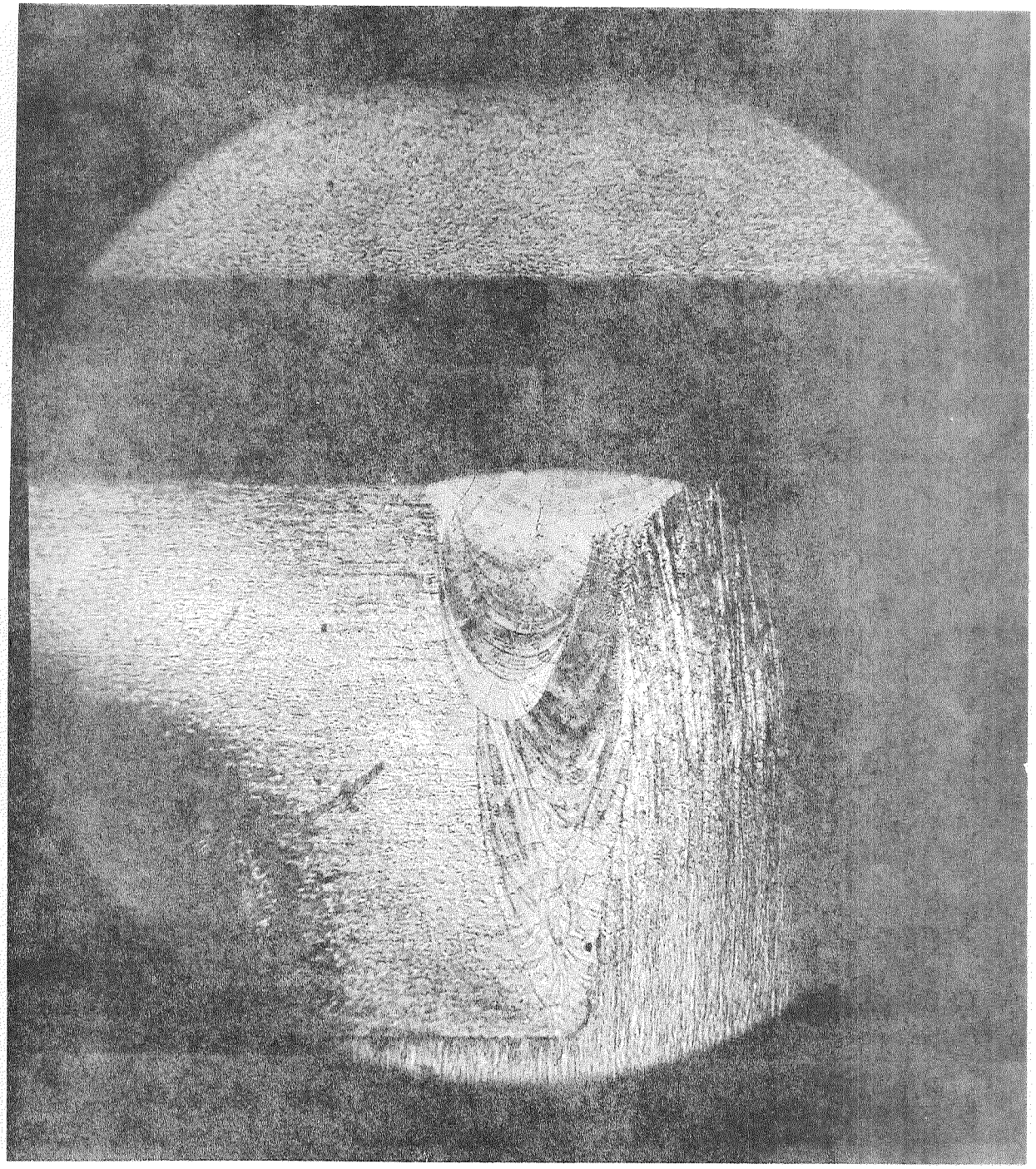


FIGURE 143

Photomicrograph of C-129Y compatibility capsule after test. Section shows electron-beam weld of C-129Y diaphragm to FS-85 tube, and portion of opposite diaphragm. (25X Magnification)

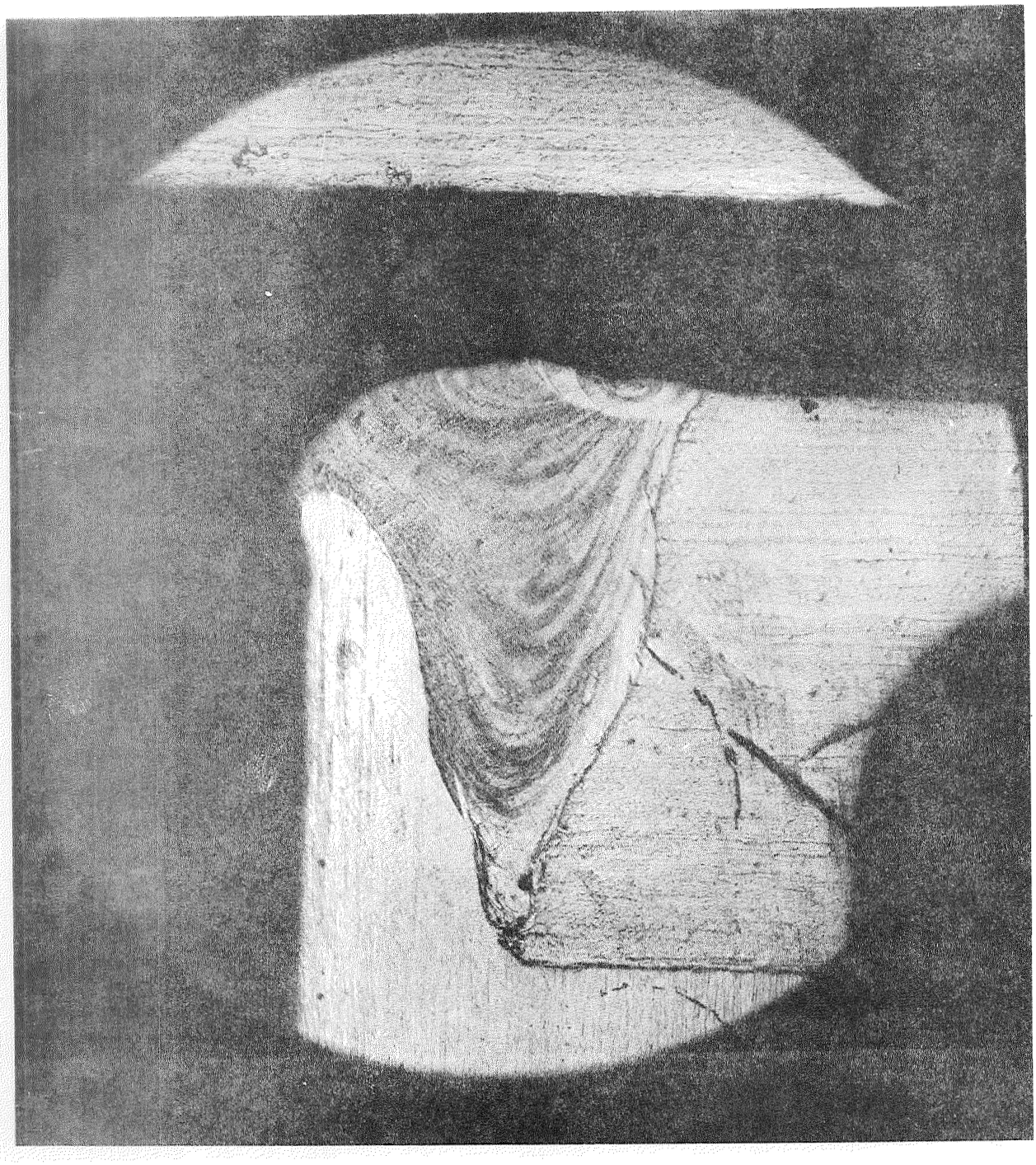


FIGURE 144

Photomicrograph of FS-85 compatibility capsule after test. (25X Magnification) Section shows electron-beam weld of FS-85 diaphragm to FS-85 tube, and portion of opposite diaphragm.



FIGURE 145

Photomicrograph of T-222 compatibility capsule after test. (25X magnification) Section shows electron-beam weld of T-222 diaphragm to FS-85 tube and portion of opposite diaphragm.

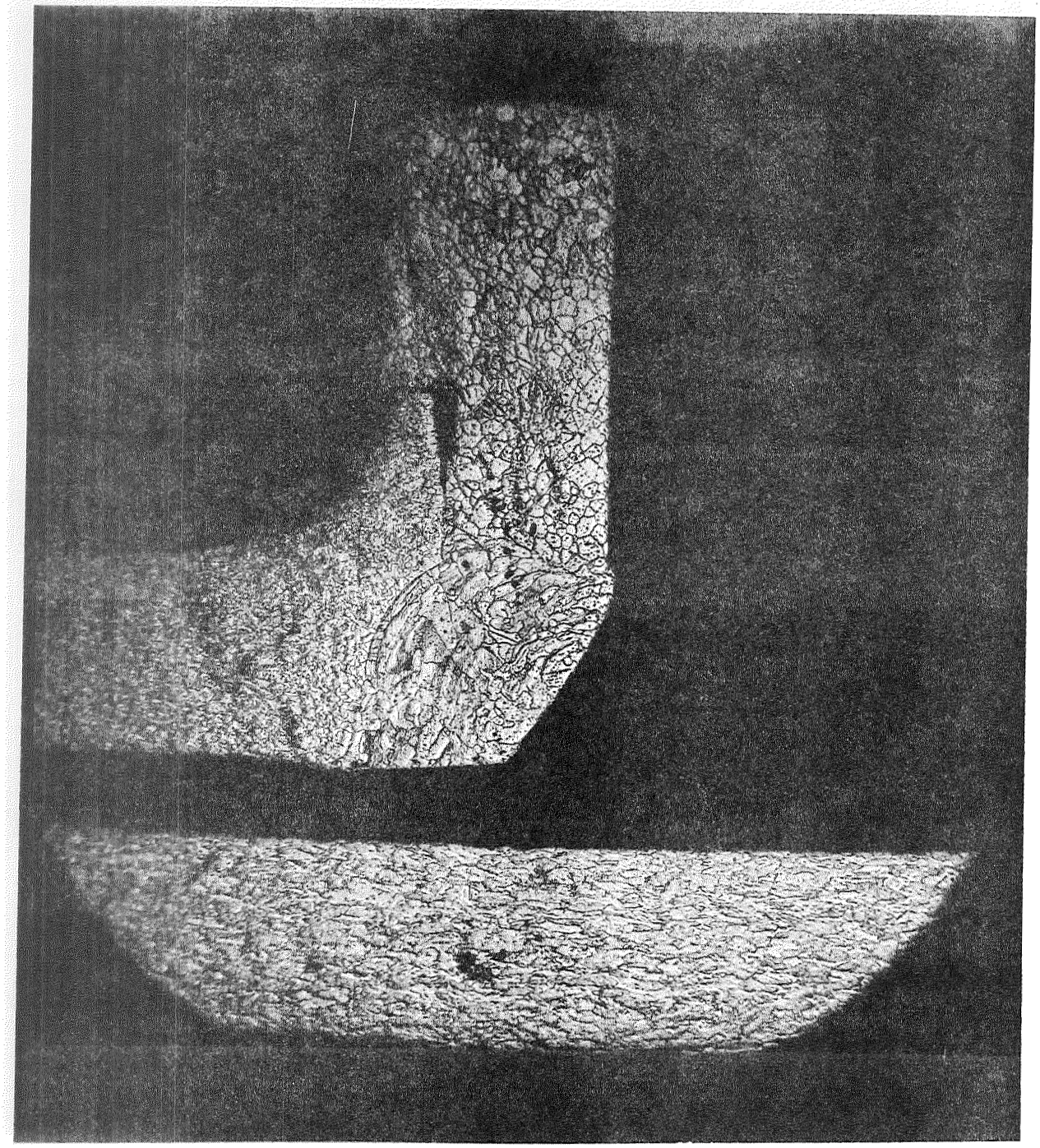


FIGURE 146

Photomicrograph of W-25 Re compatibility capsule after test. (25X magnification) Section shows electron-beam weld of W-25 Re diaphragm to MO-50 Re tube and portion of opposite diaphragm.

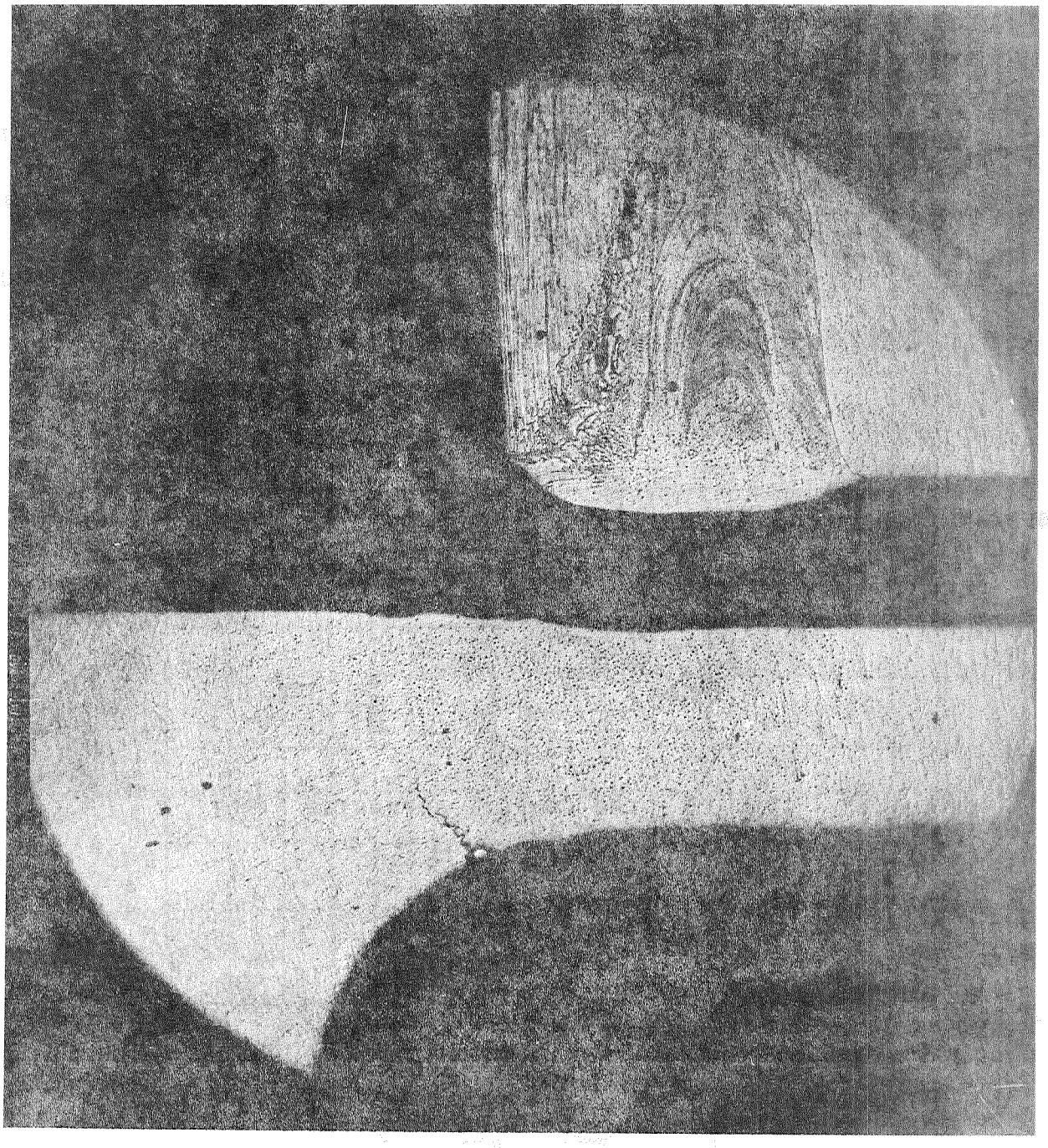
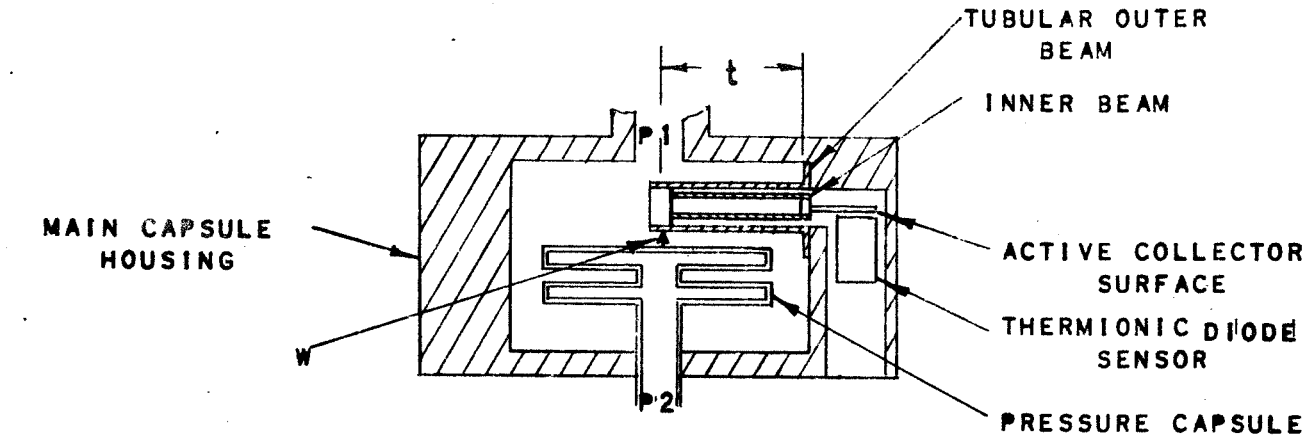
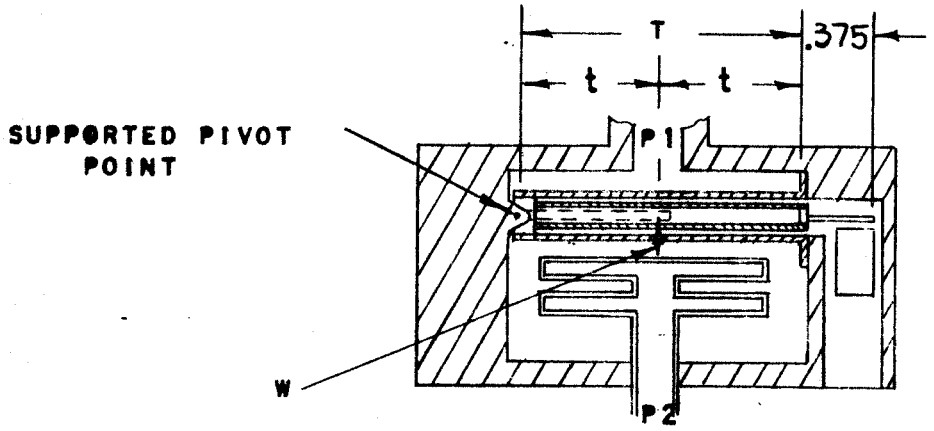


FIGURE 147

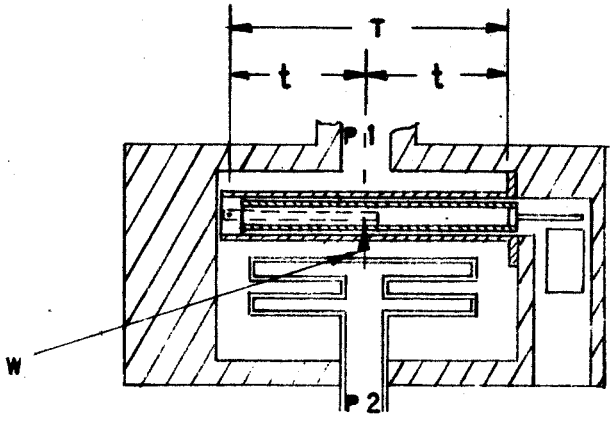
Intergranular crack in T-222 compatibility capsule at shoulder of boss in center of diaphragm. (25X magnification)



CASE I - CANTILEVER, END LOAD



CASE II - END COUPLE, SUPPORTED PIVOT



CASE III - END COUPLE AND END LOAD

FIGURE 148

DIFFERENTIAL PRESSURE TRANSDUCER CONFIGURATIONS

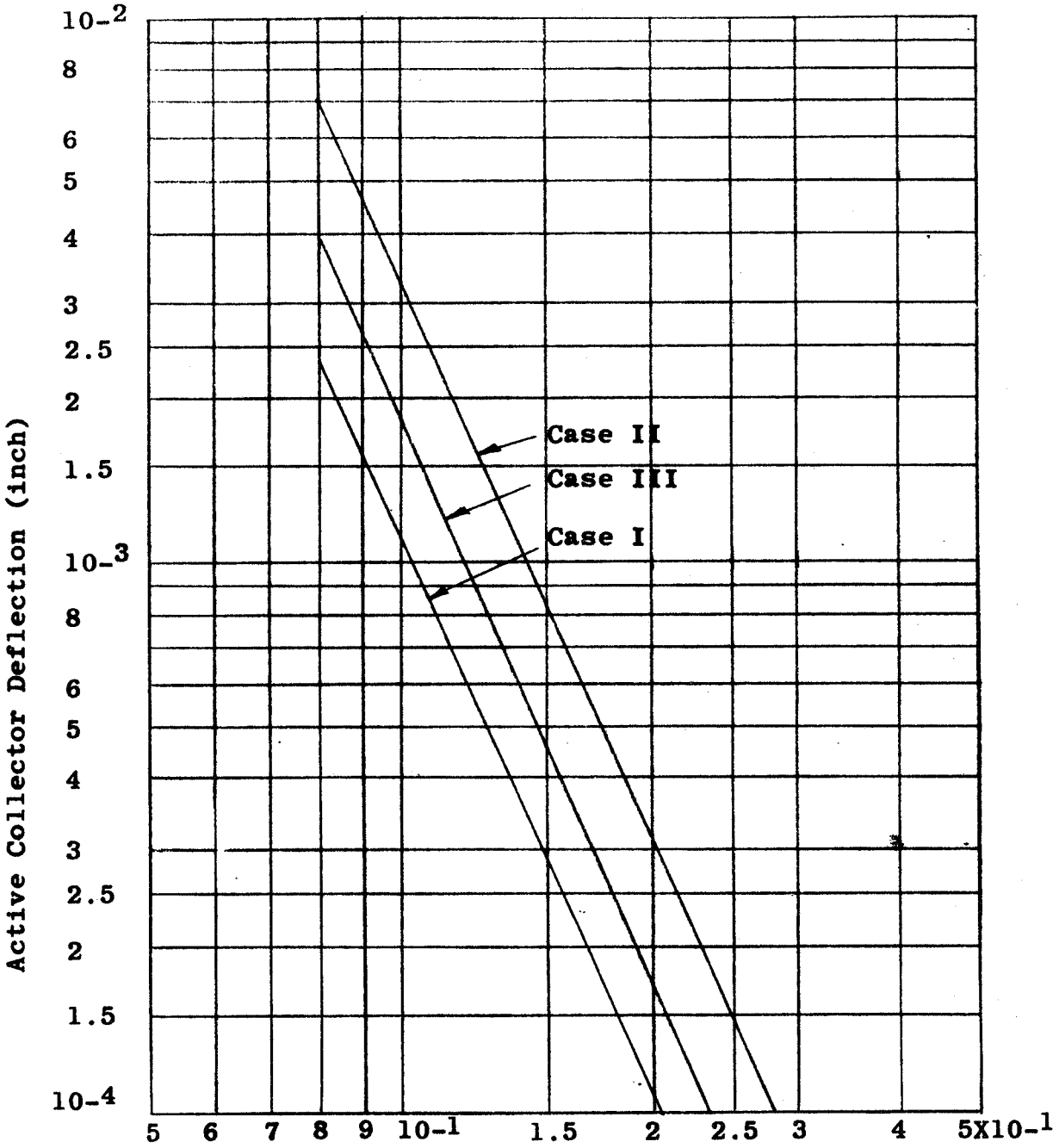


Figure 149

Differential Pressure Transducer

Deflection Characteristics

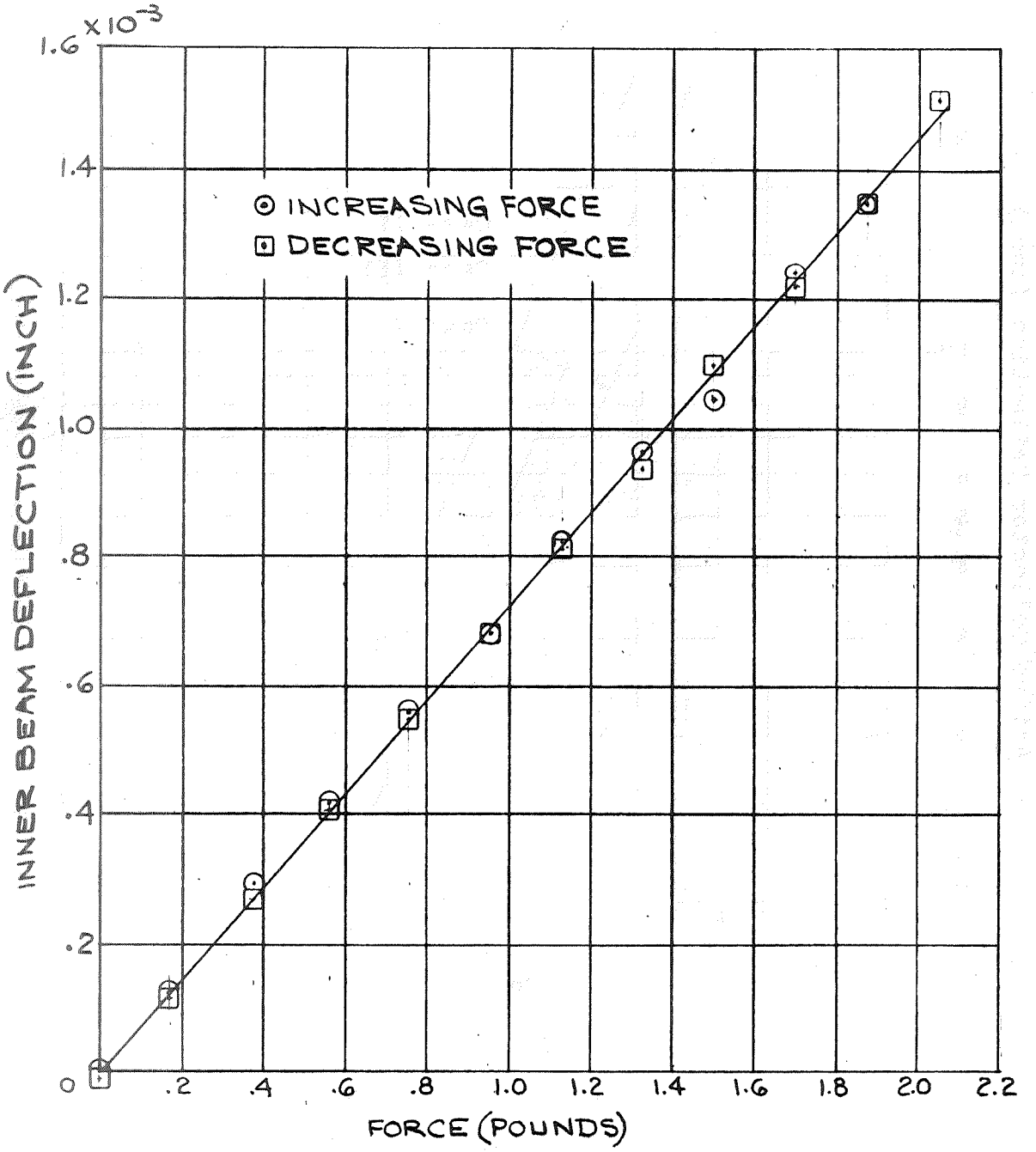
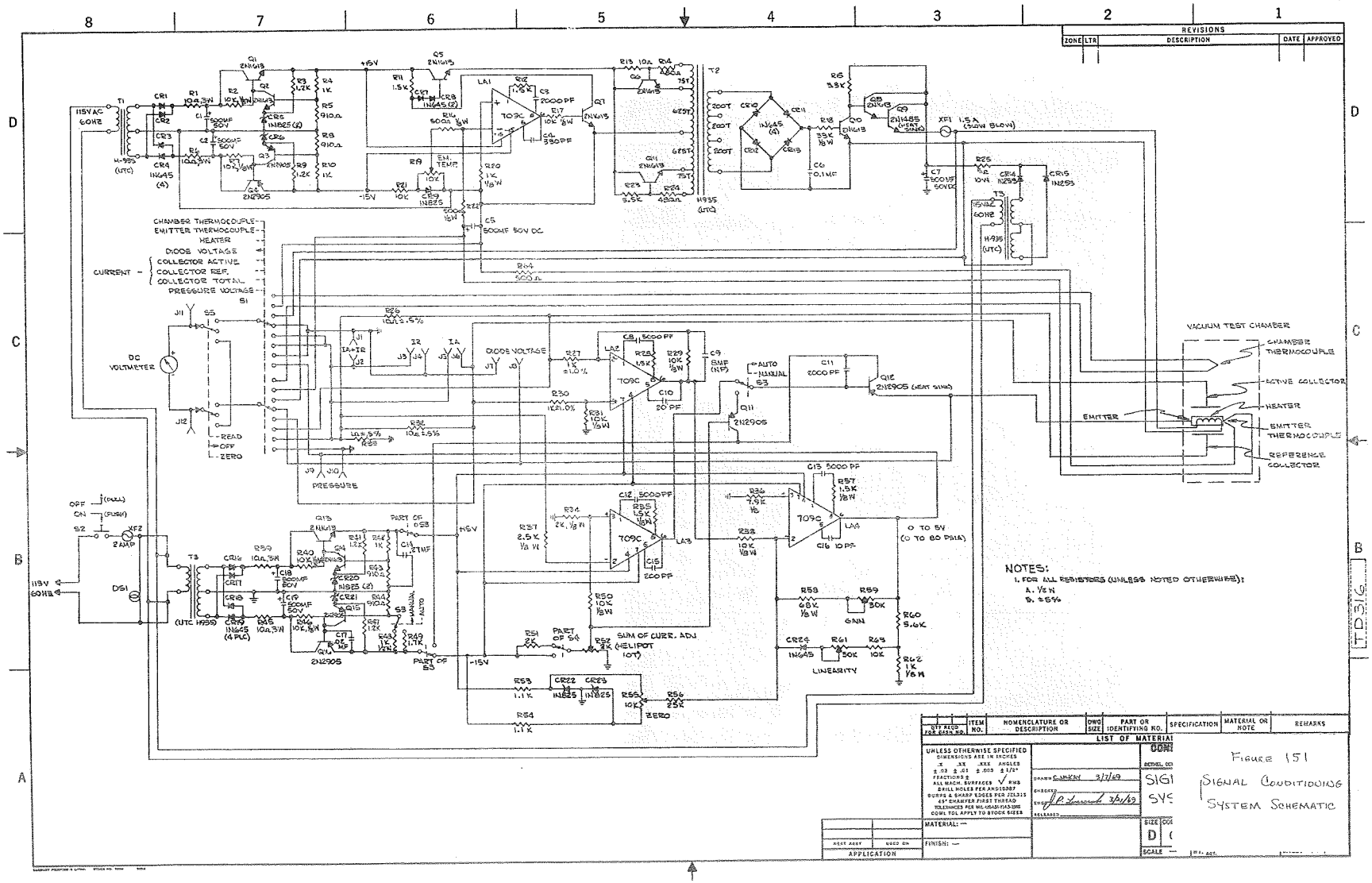


FIGURE 150
DIFFERENTIAL MOCKUP
FORCE-DEFLECTION CHARACTERISTIC


REVISIONS
ZONE | LTR | DESCRIPTION | DATE | APPROVED
115V AC 60HZ
CHAMBER THERMOCOUPLE
EMITTER THERMOCOUPLE
HEATER
DIODE VOLTAGE
CURRENT – COLLECTOR ACTIVE
COLLECTOR REF.
COLLECTOR TOTAL
PRESSURE VOLTAGE
DC VOLTMETER
- READ
- OFF
- ZERO
PRESSURE
DIODE VOLTAGE
VACUUM TEST CHAMBER
CHAMBER THERMOCOUPLE
ACTIVE COLLECTOR
HEATER
EMITTER
EMITTER THERMOCOUPLE
REFERENCE COLLECTOR
0 TO 5V (0 TO 80 PSIA)
NOTES:
1. FOR ALL RESISTORS (UNLESS NOTED OTHERWISE):
A. ½ W
B. ±5%
SUM OF CURR. ADJ
LINEARITY
ZERO
FIGURE 151
SIGNAL CONDITIONING SYSTEM SCHEMATIC

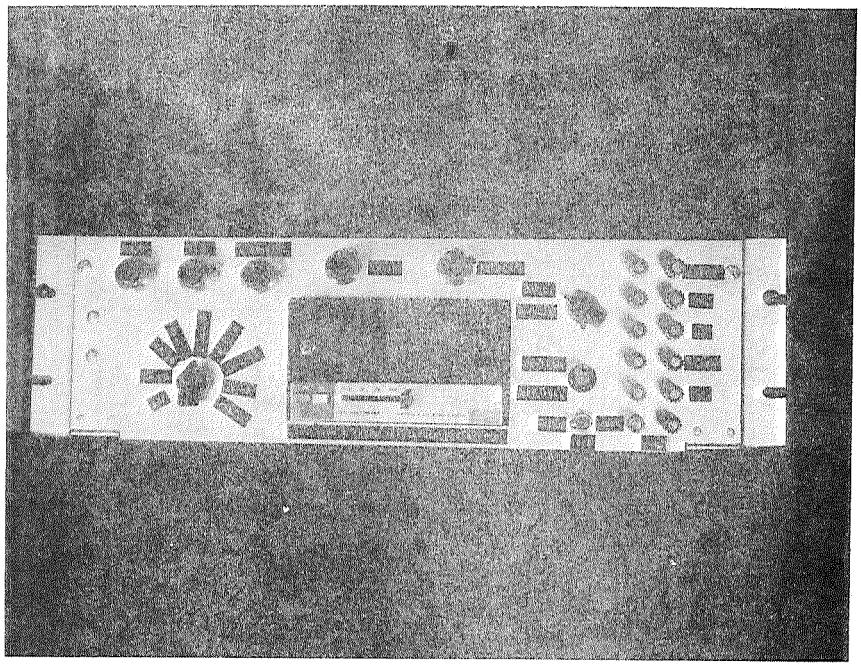


FIGURE 152

Electrical Signal Conditioner Panel

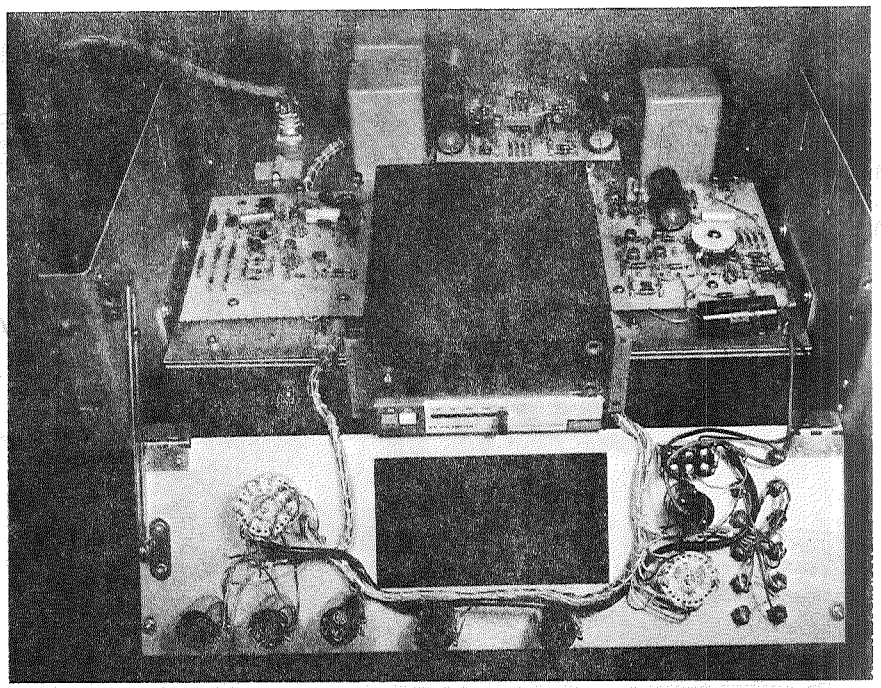


FIGURE 153

Electrical Signal Conditioner Layout

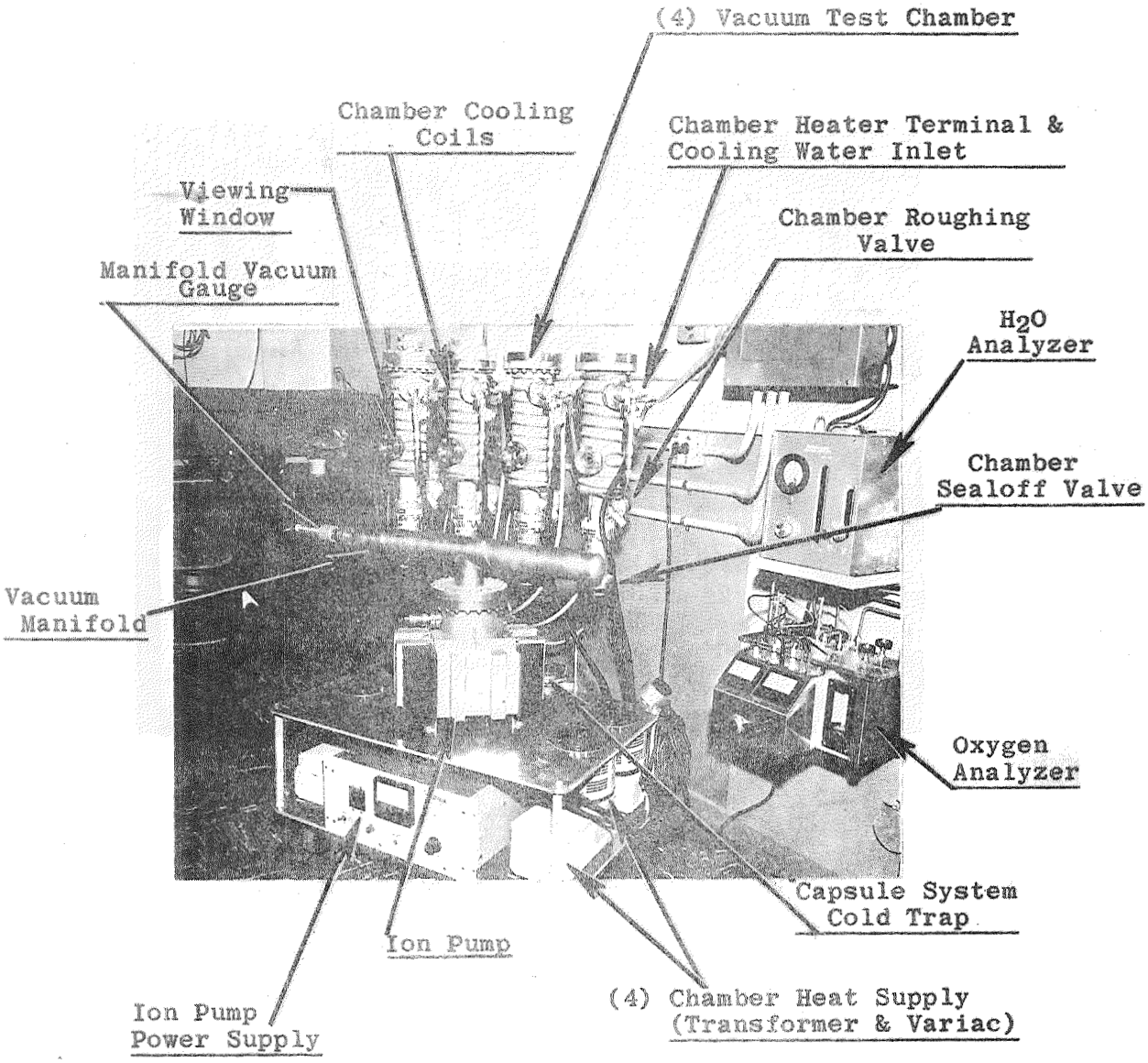


Figure 154

Early Vacuum Test Facility Configuration

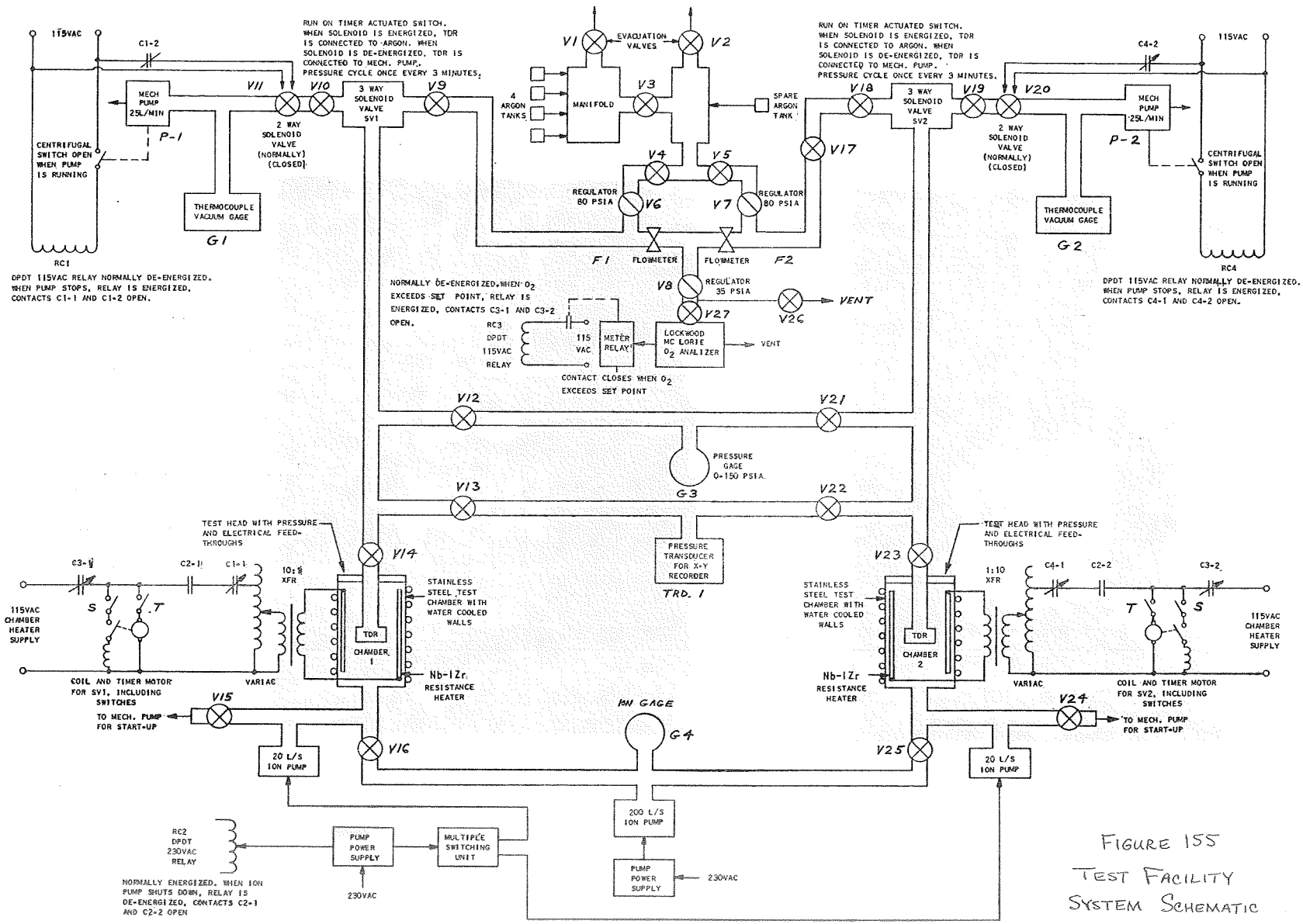


FIGURE 155
TEST FACILITY
SYSTEM SCHEMATIC
CHAMBERS 1 & 2

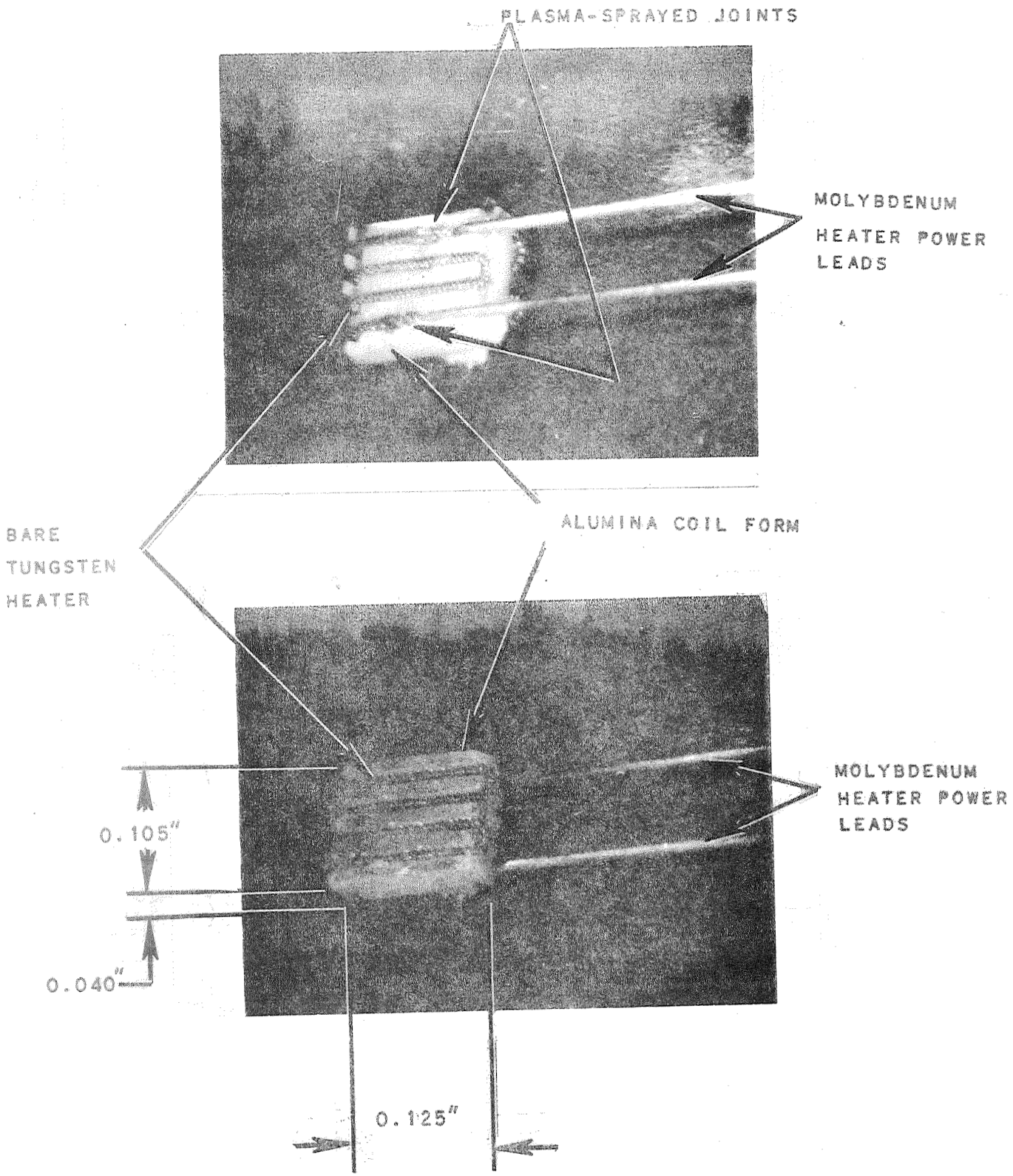


FIGURE 156

BASIC HEATER ASSEMBLY

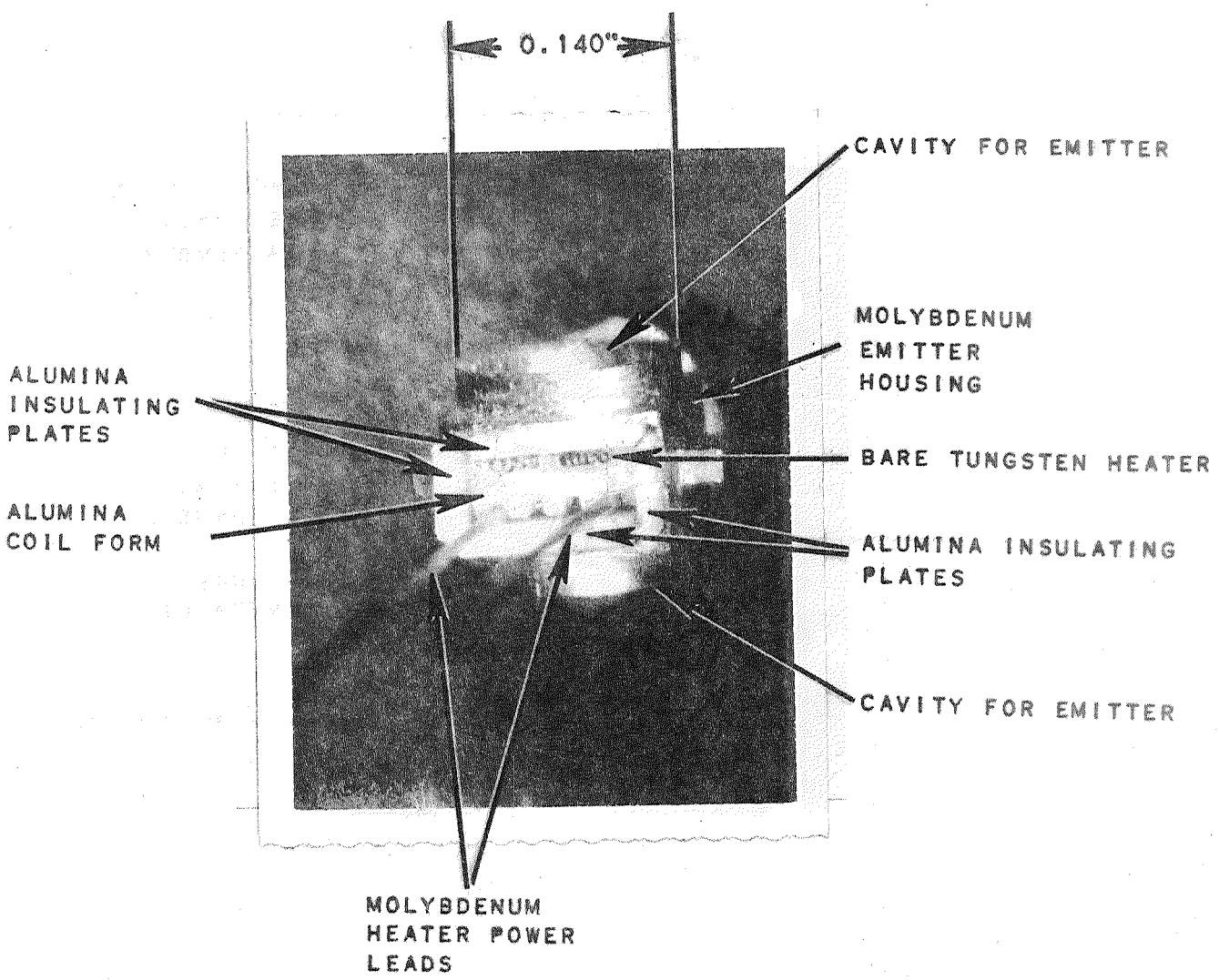


FIGURE 157
HEATER ASSEMBLY BEFORE CASTING

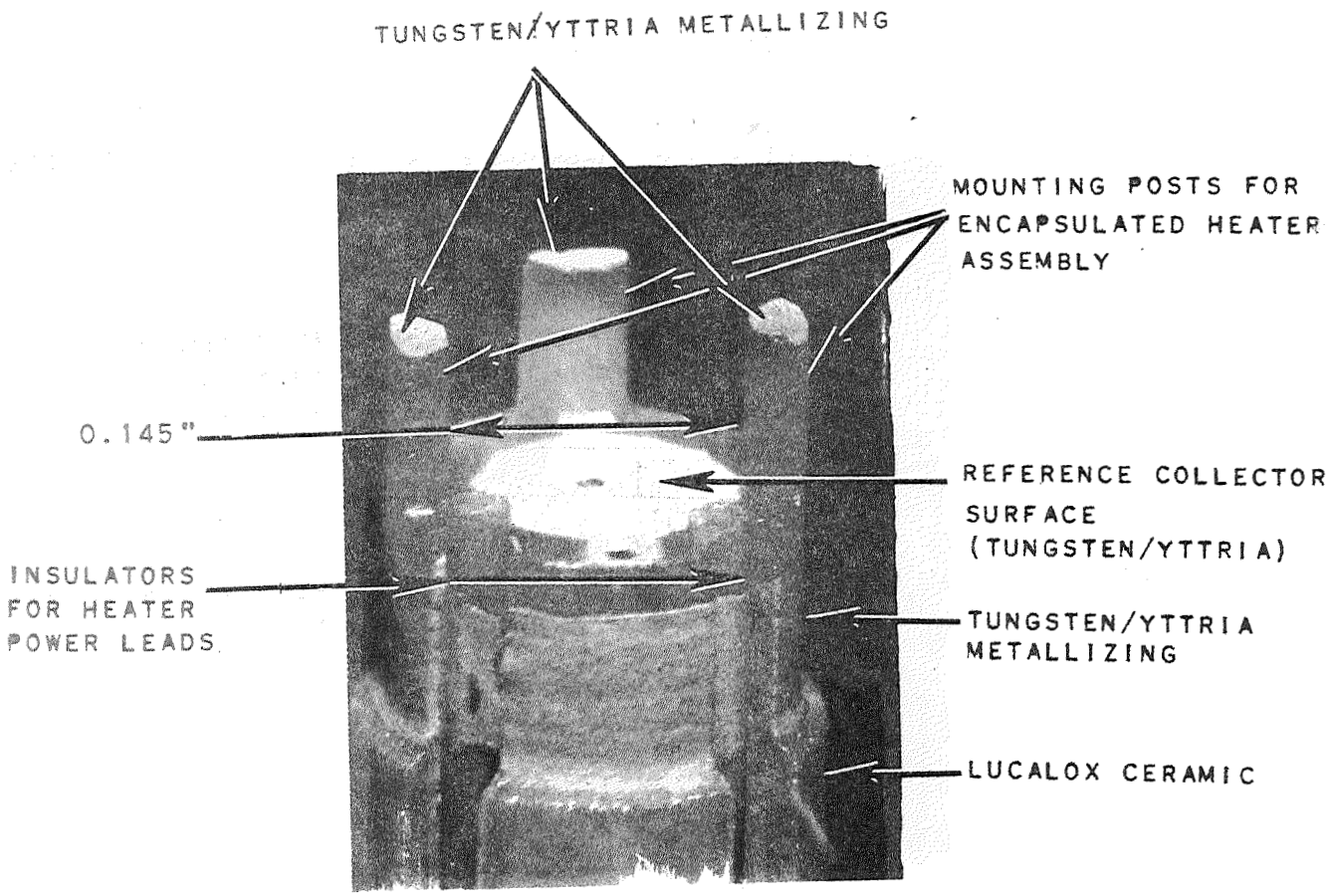


FIGURE 158

CERAMIC BASE

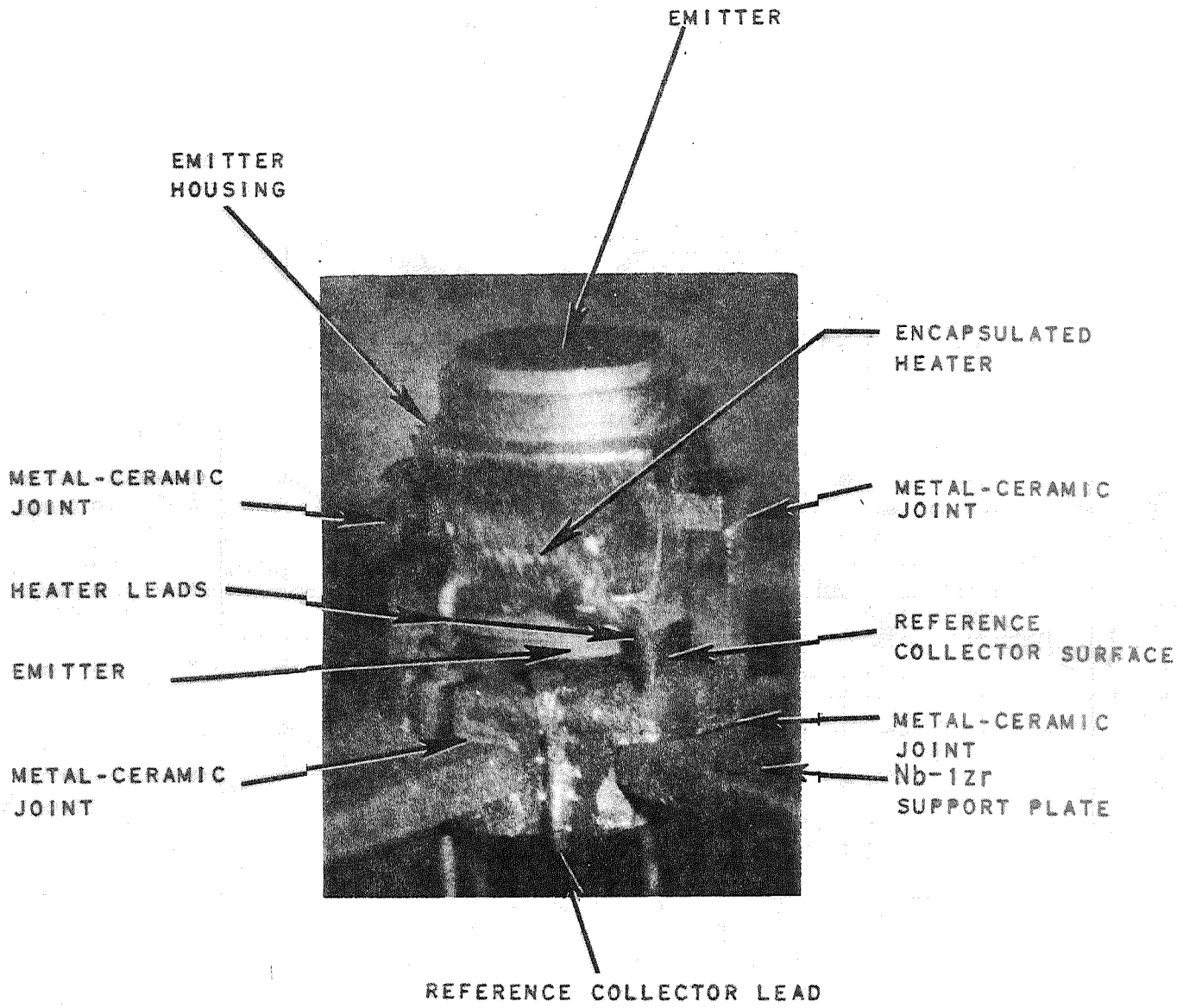
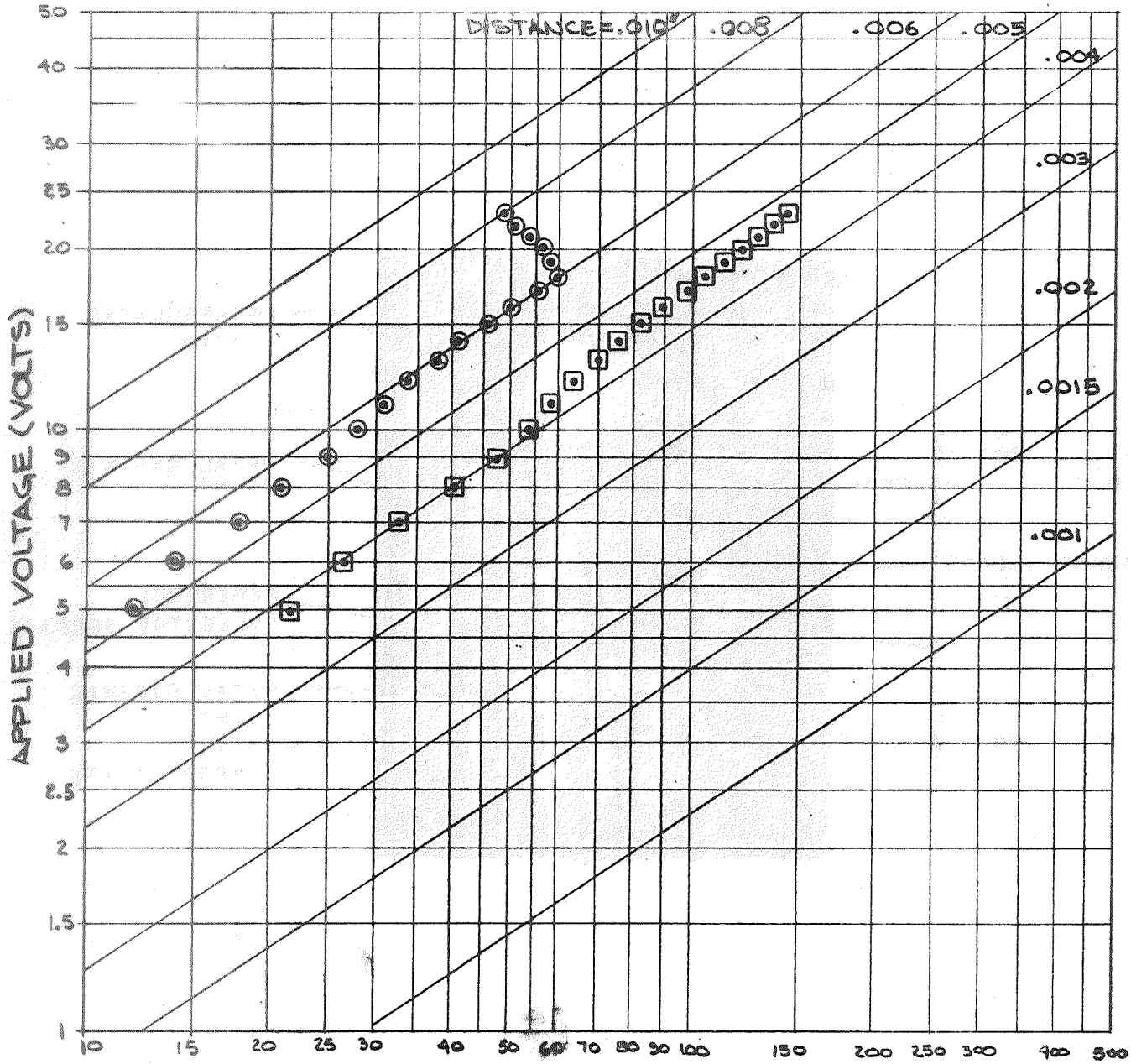


FIGURE 159

ENCAPSULATED HEATER-CERAMIC BASE-SUPPORT PLATE ASSEMBLY



CAPSULE TEMP. 1800° F

EMITTER TEMP. 2100° F

——— CALCULATED FROM EQ. 1, REF. 4

⊙ REFERENCE COLLECTOR, ZERO PRESSURE

⊡ ACTIVE COLLECTOR, ZERO PRESSURE

FIGURE 160

SPACE-CHARGE CHARACTERISTICS FOR T-4

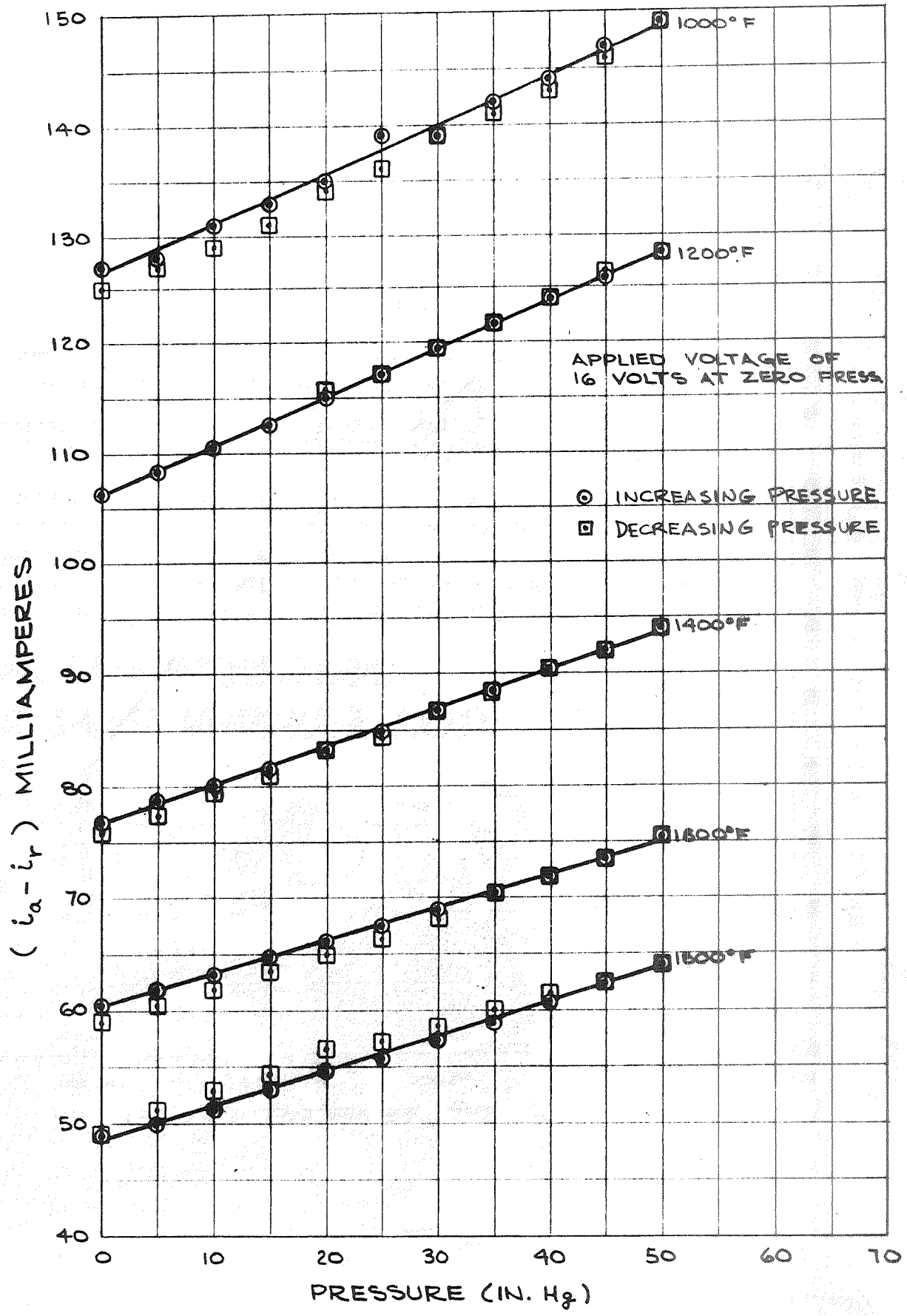


FIGURE 161

PRESSURE - OUTPUT CURRENT CHARACTERISTICS FOR T-4

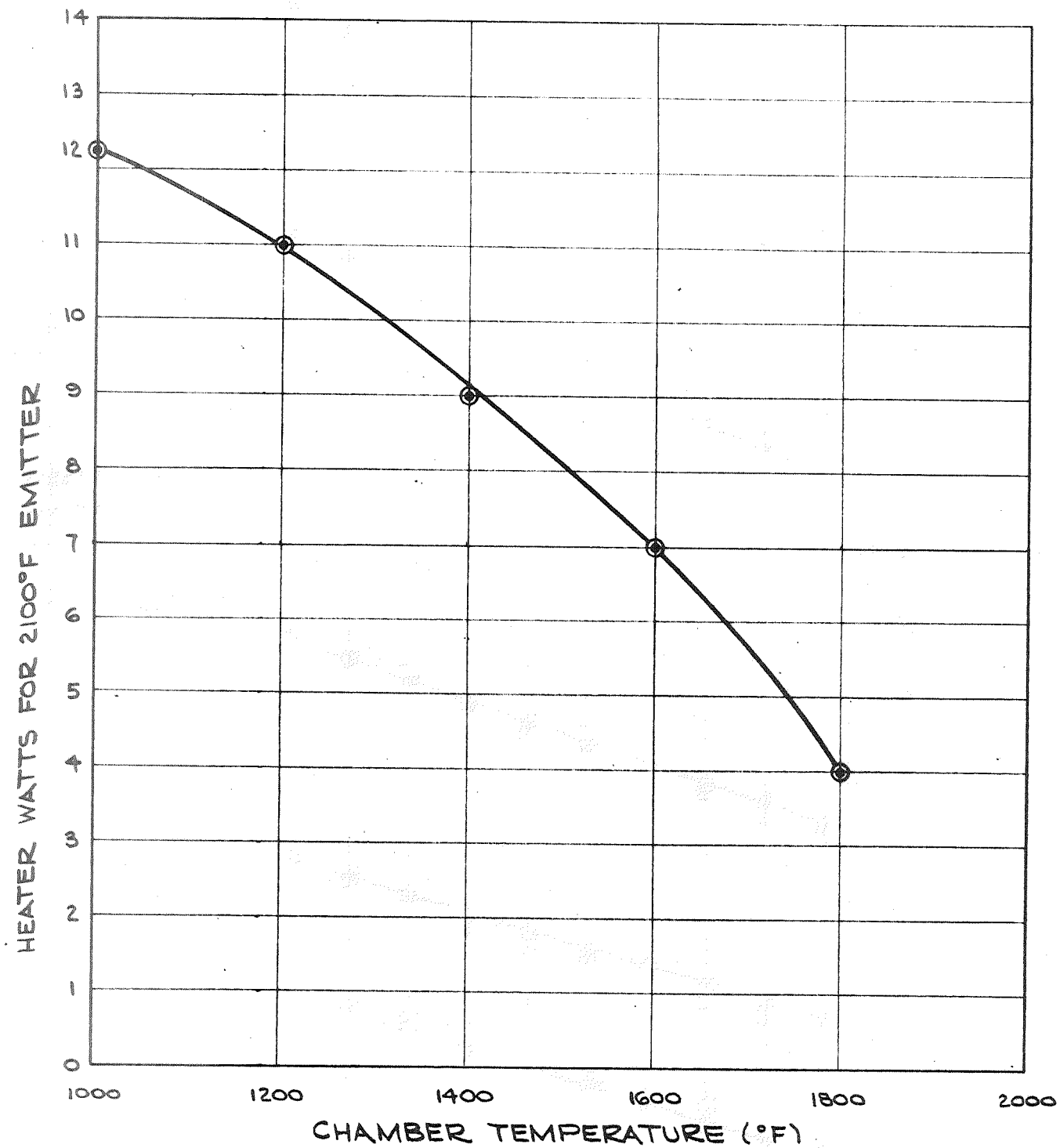


FIGURE 162

EMITTER HEATER POWER REQUIREMENTS FOR T-4

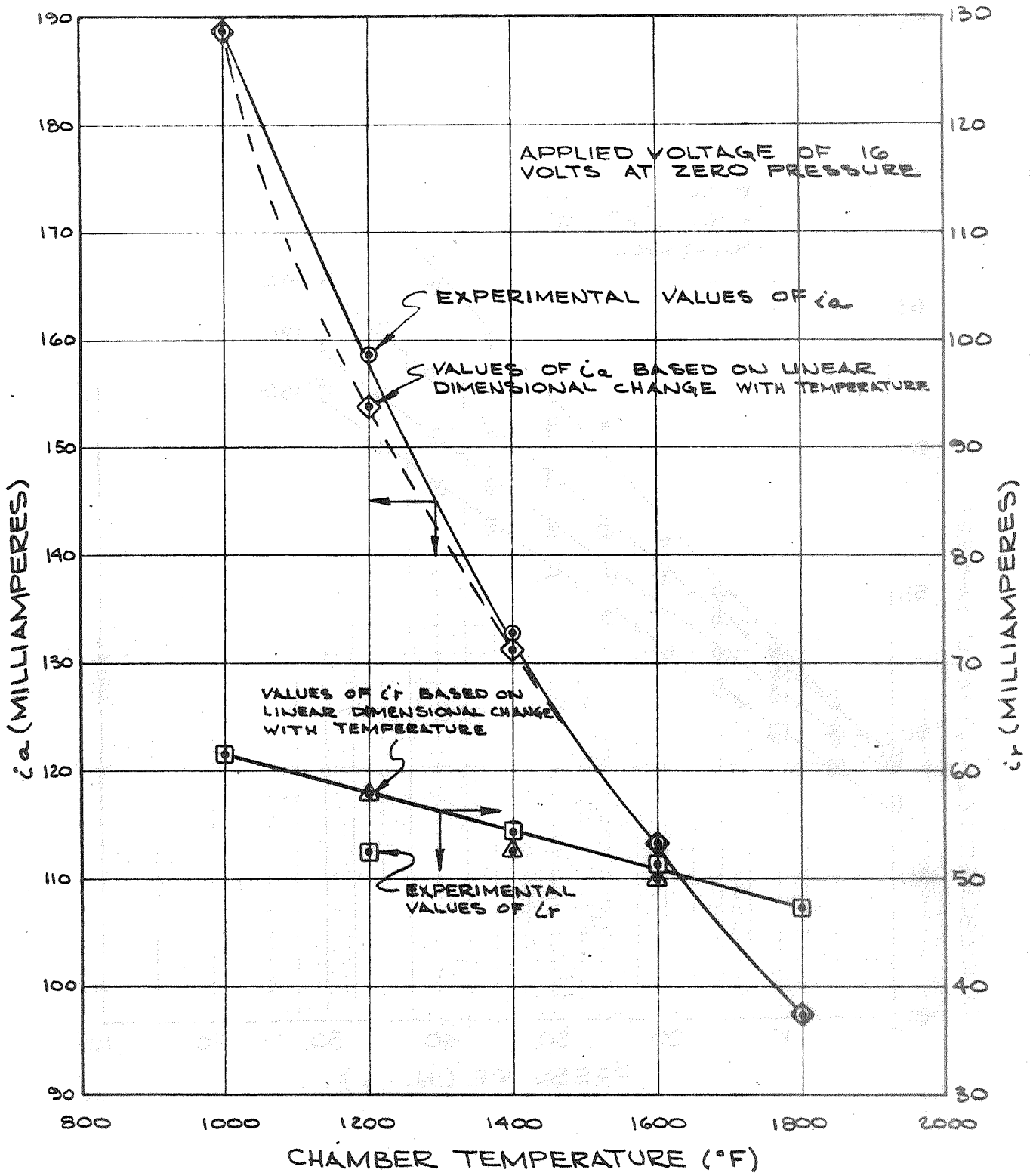


FIGURE 163

T-4 ACTIVE AND REFERENCE CURRENTS AS FUNCTIONS OF TEMPERATURE

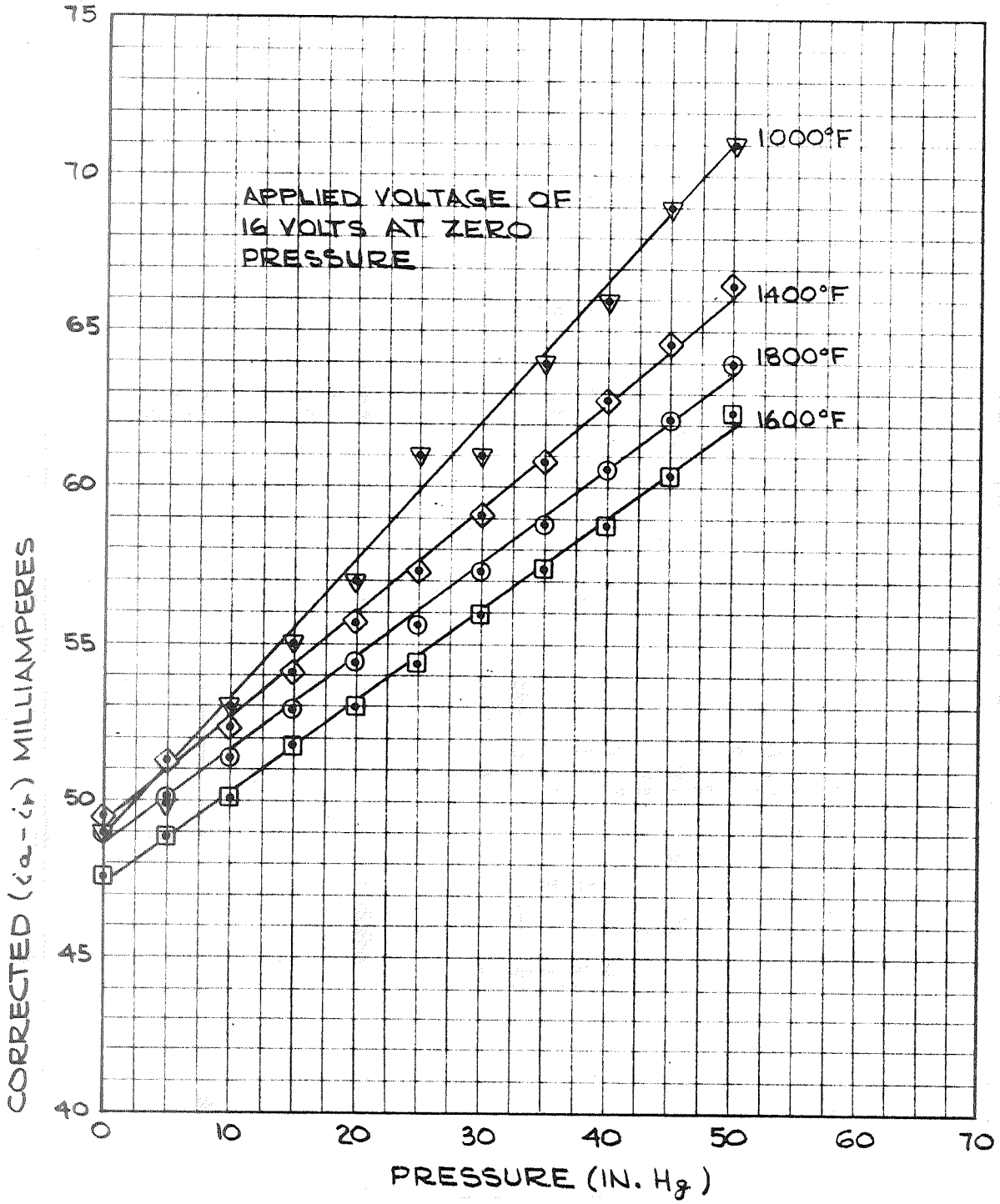


FIGURE 164

NORMALIZED PRESSURE - OUTPUT CHARACTERISTICS
FOR T-4

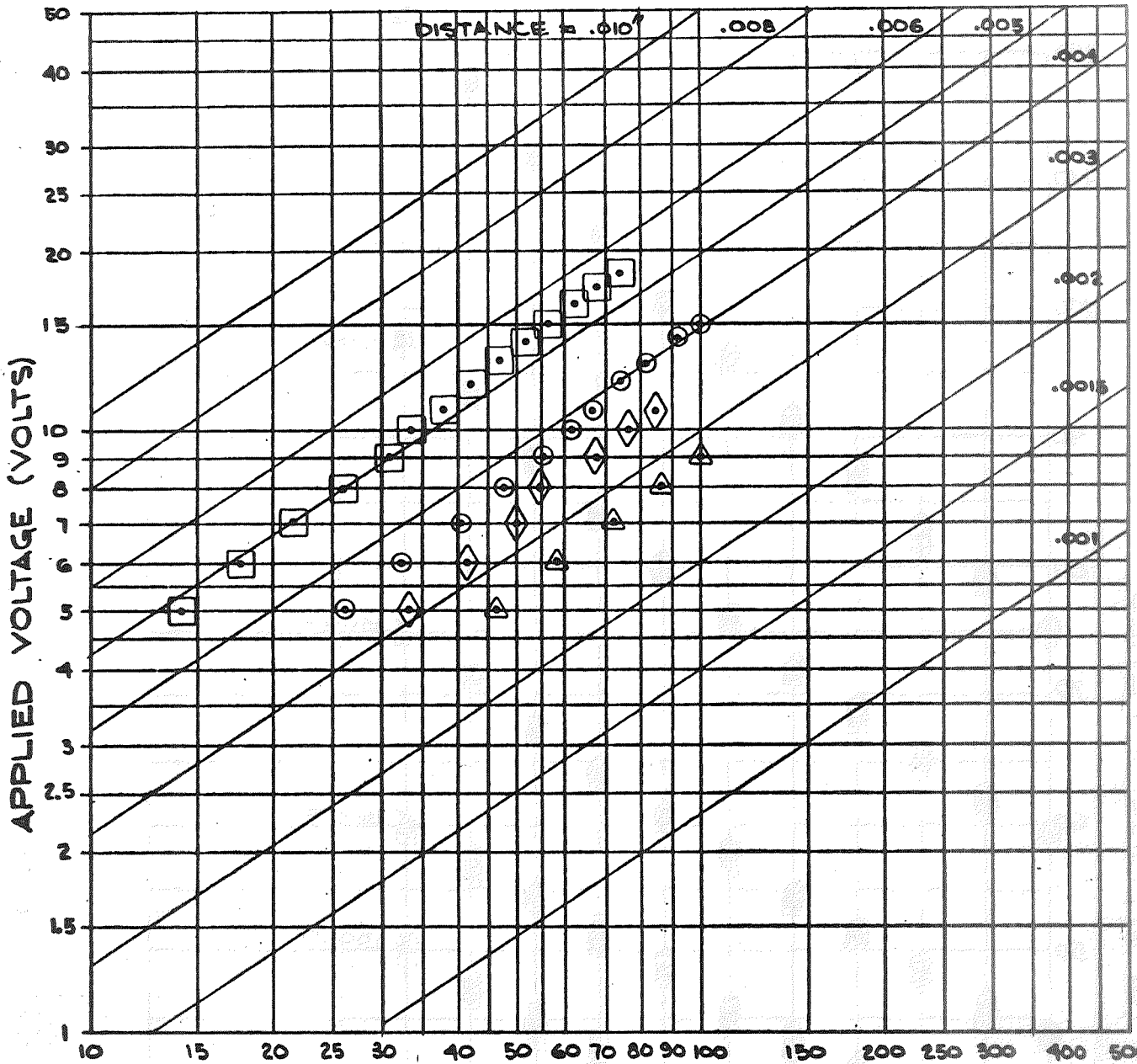


FIGURE 165

INITIAL SPACE-CHARGE DATA, T-6 (FS-85)

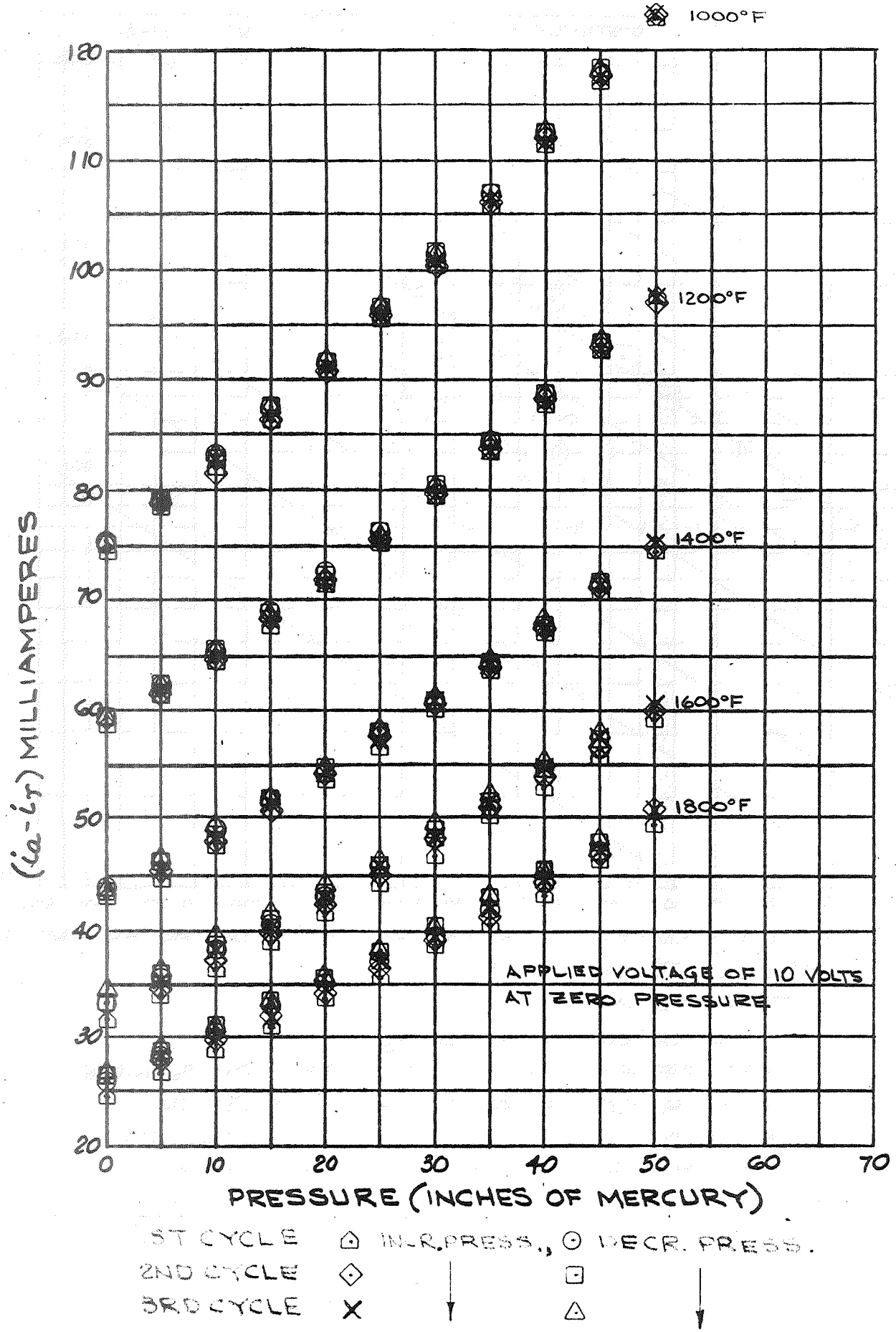


FIGURE 166

PRESSURE-OUTPUT DATA FOR DECREASING TEMPERATURE, 16(FS-85)

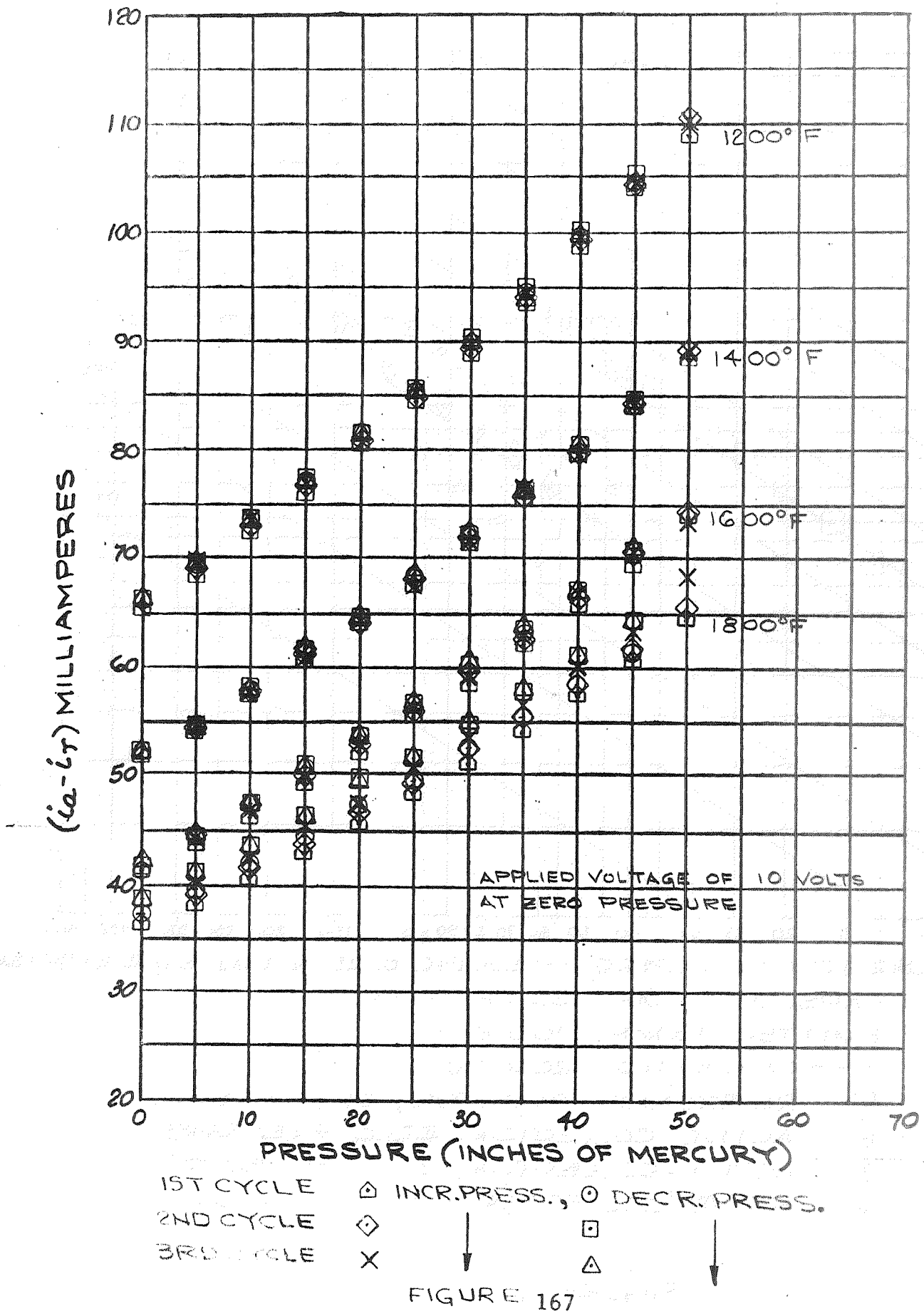


FIGURE 167

PRESSURE OUTPUT DATA FOR INCREASING TEMPERATURE, TG(FS-85)

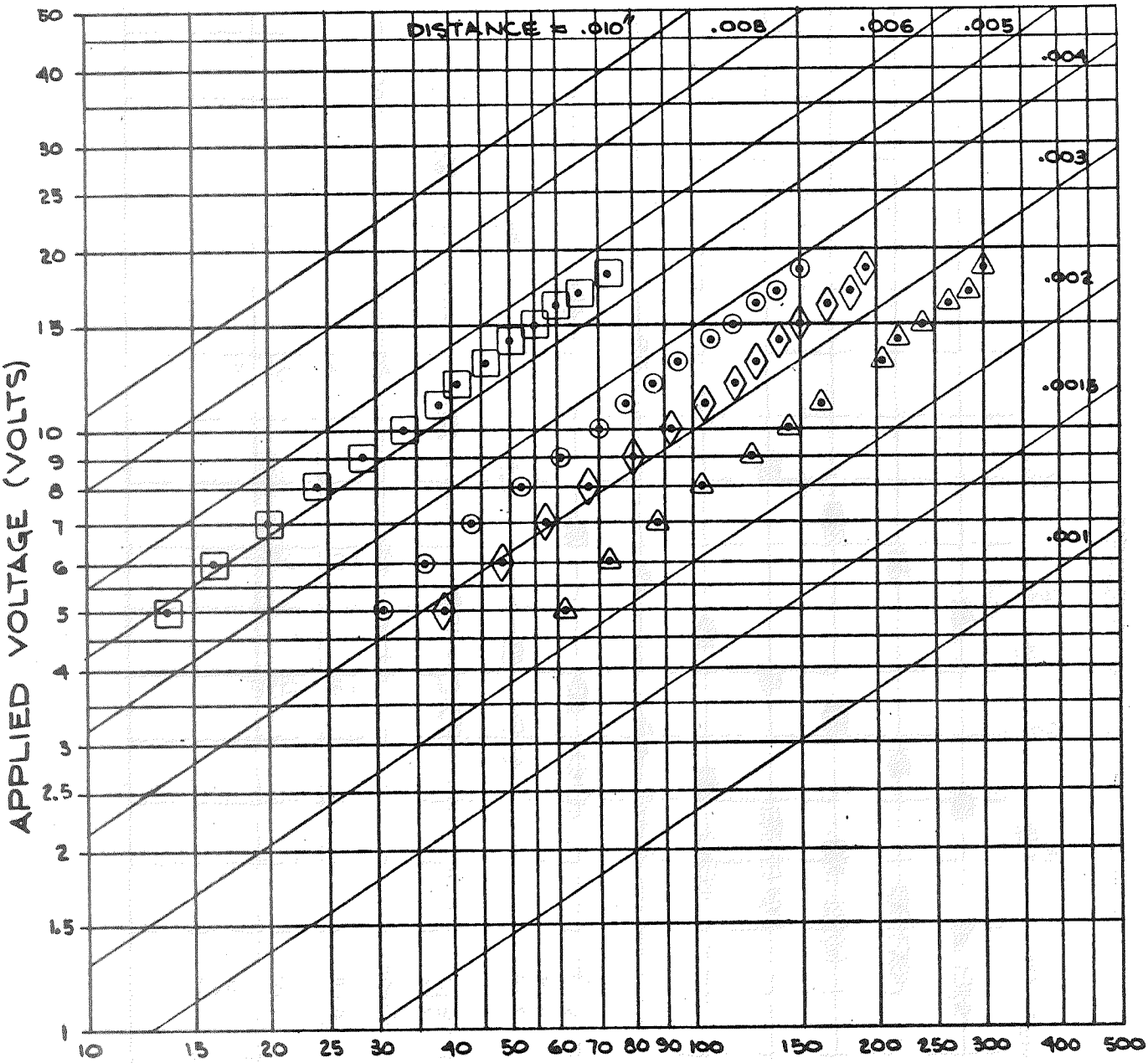


FIGURE 168

FINAL SPACE - CHARGE DATA, T-6 (FS-85)

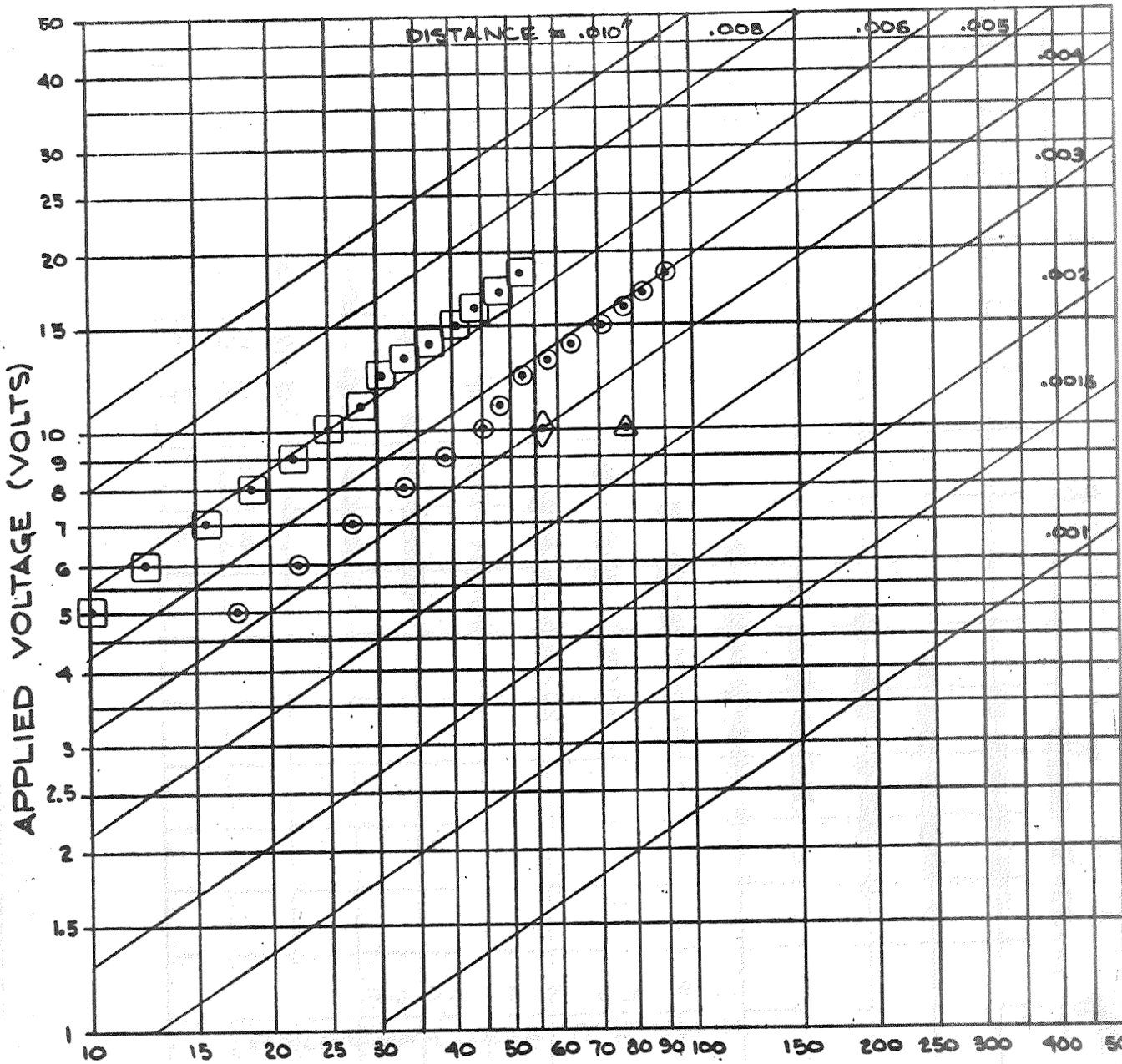


FIGURE 169

INITIAL SPACE - CHARGE DATA, T-7 (C-129Y)

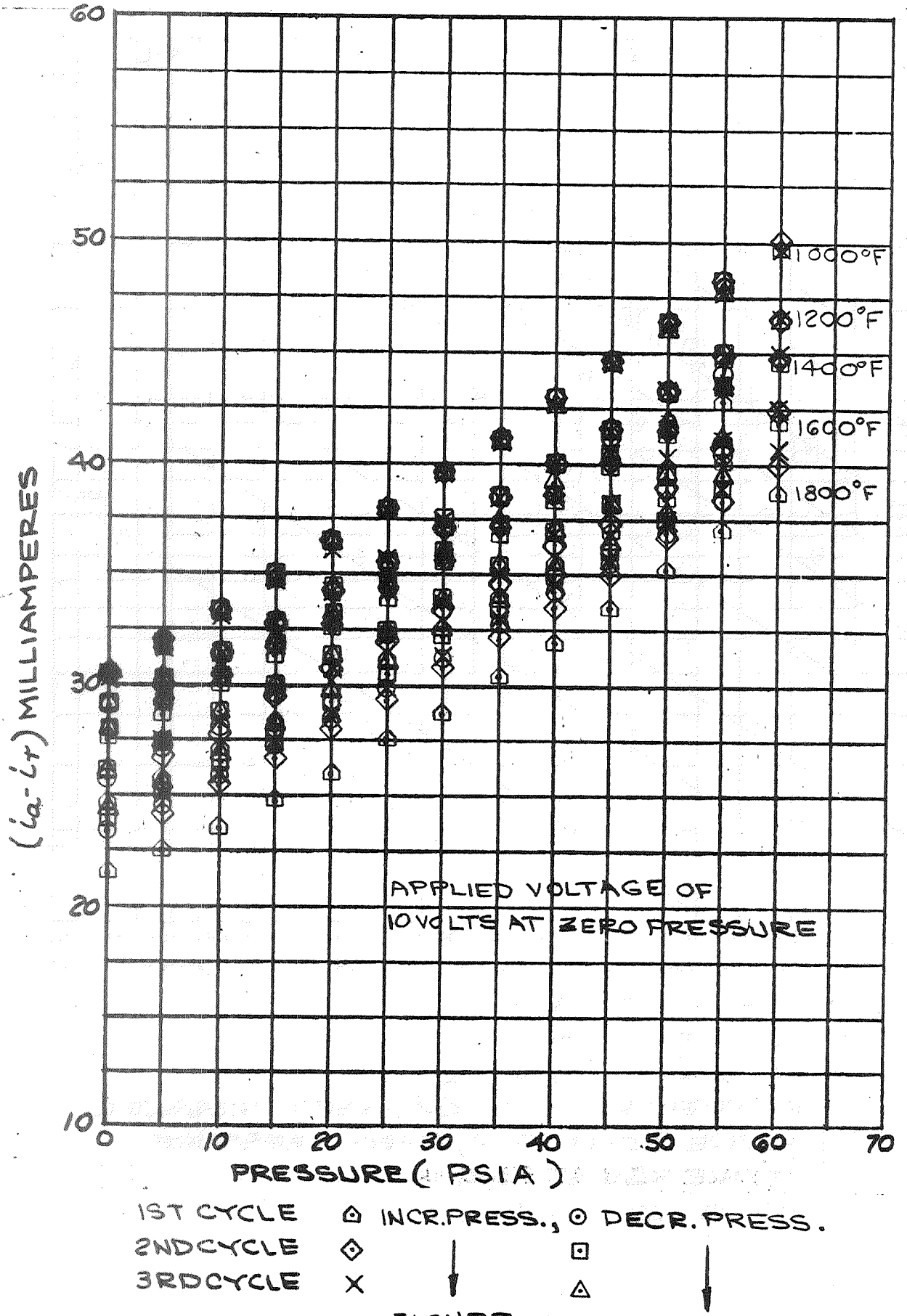


FIGURE 170

PRESSURE-OUTPUT DATA FOR DECREASING TEMPERATURE, T-7 (C-129Y)

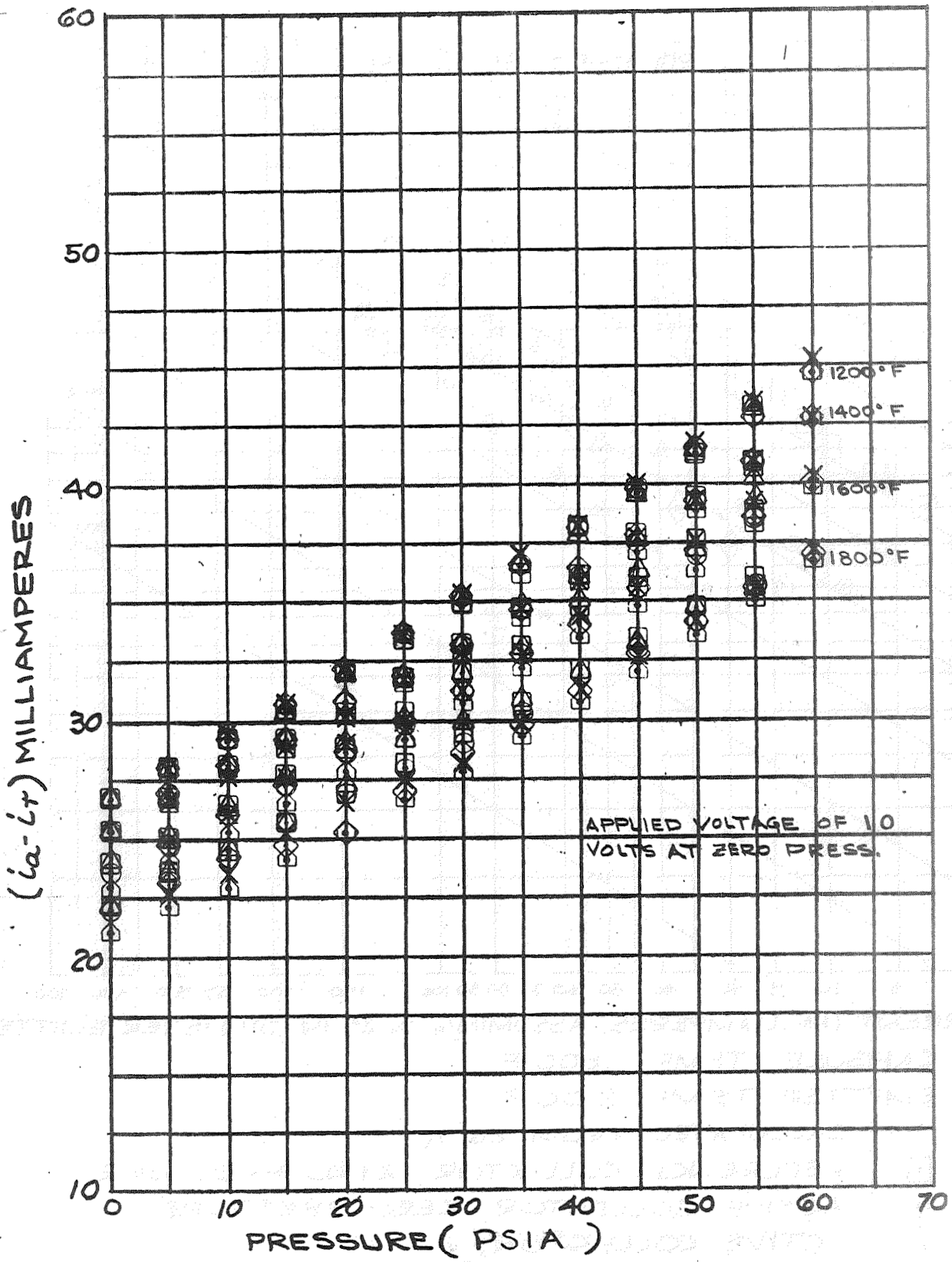


FIGURE 171

PRESSURE - OUTPUT DATA FOR INCREASING TEMP., T-7 (C-129Y)

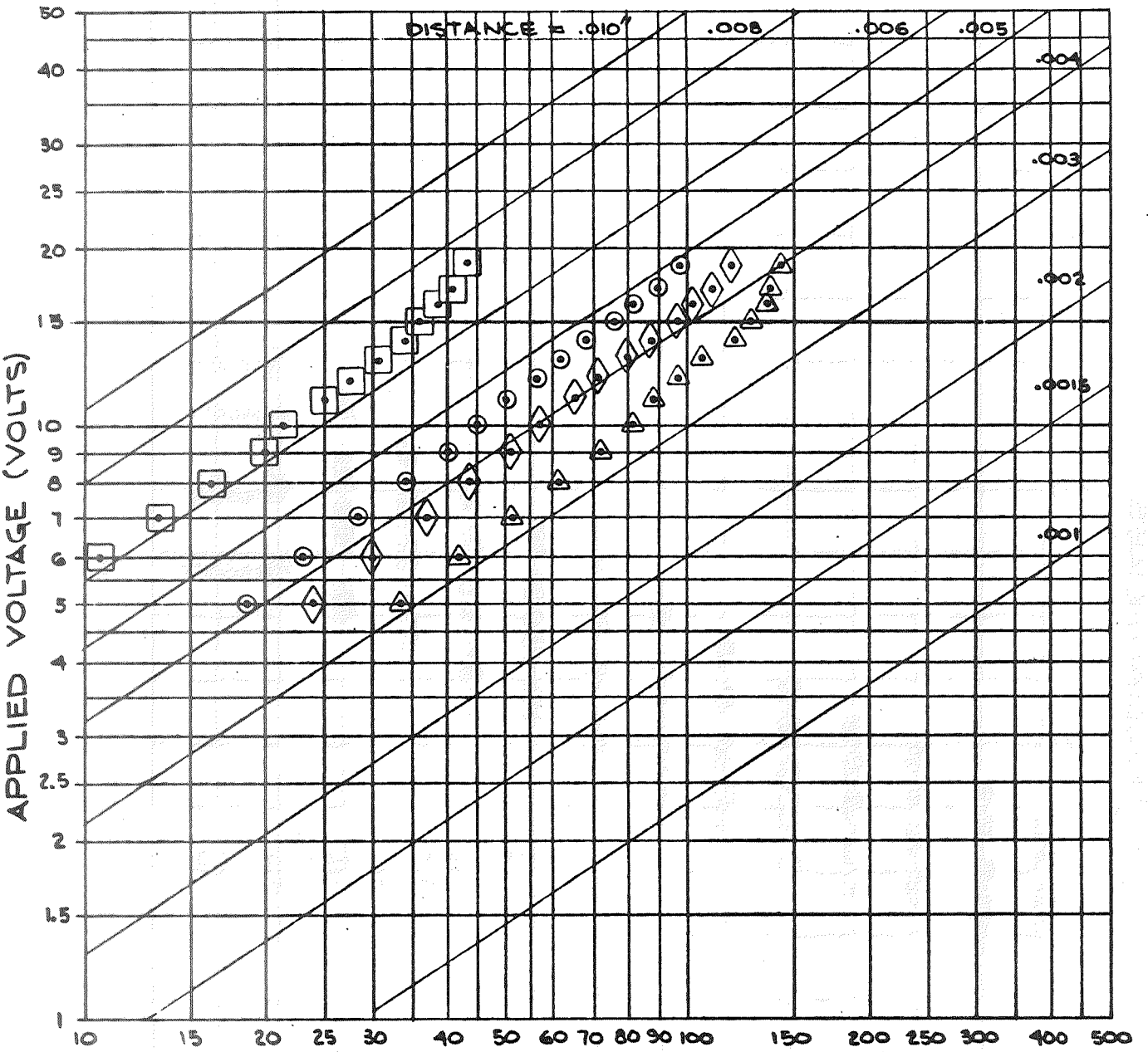


FIGURE 172

FINAL SPACE - CHARGE DATA, T-7 (C-129Y)

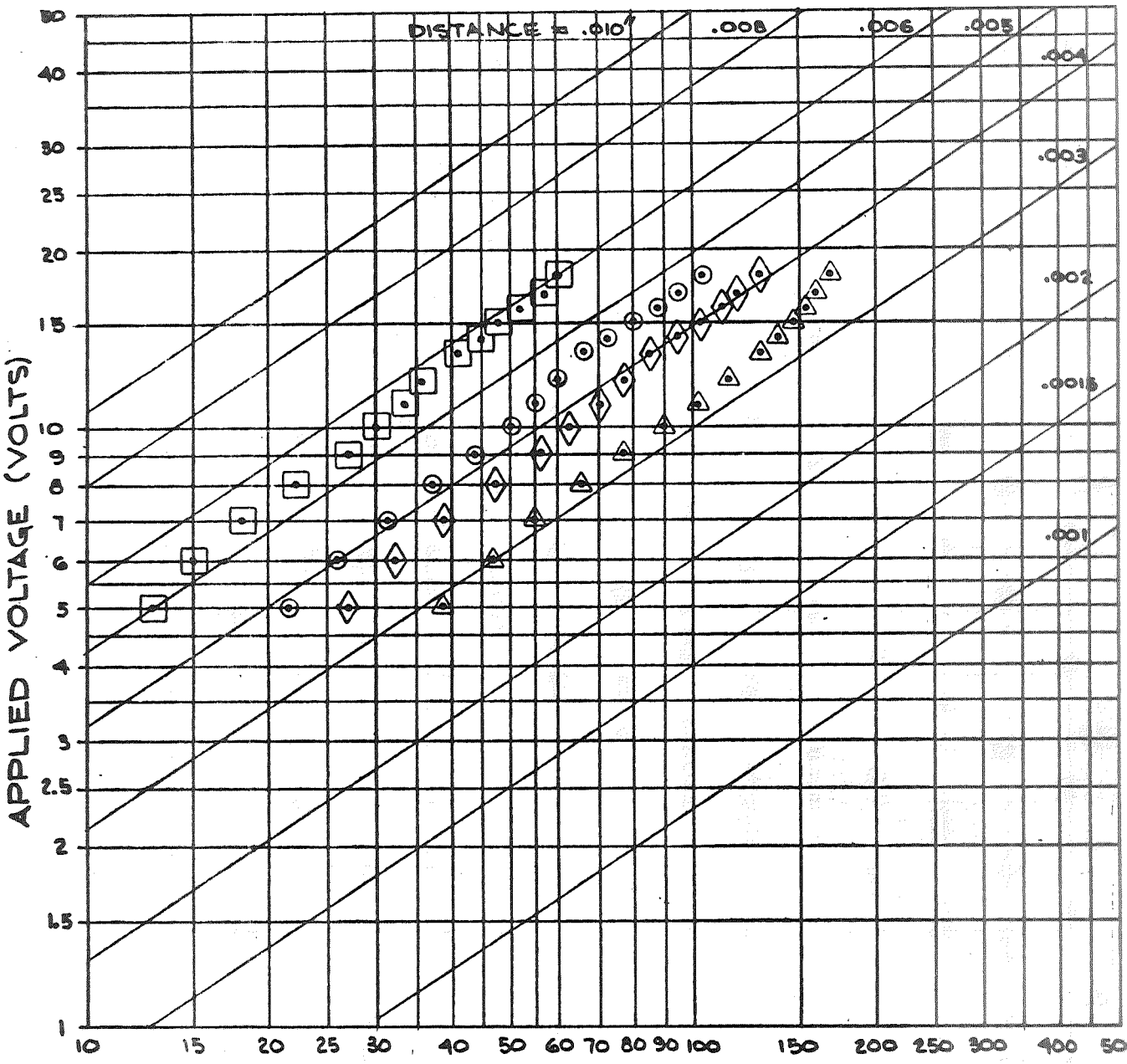


FIGURE 173

INITIAL SPACE-CHARGE DATA, T-6 (FS-85)

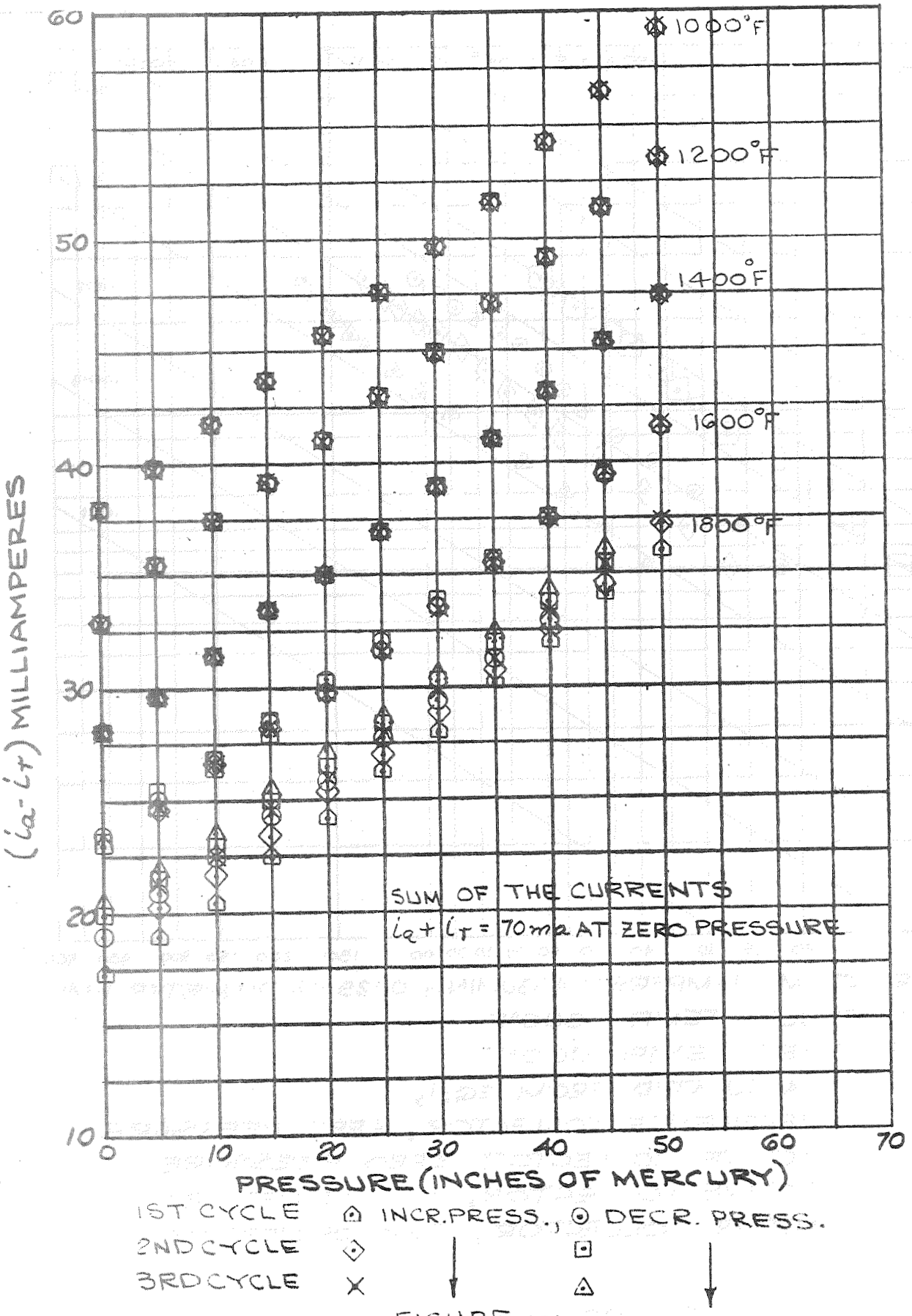


FIGURE 174

PRESSURE-OUTPUT DATA FOR DECREASING TEMPERATURE, T_6 (FS-85)

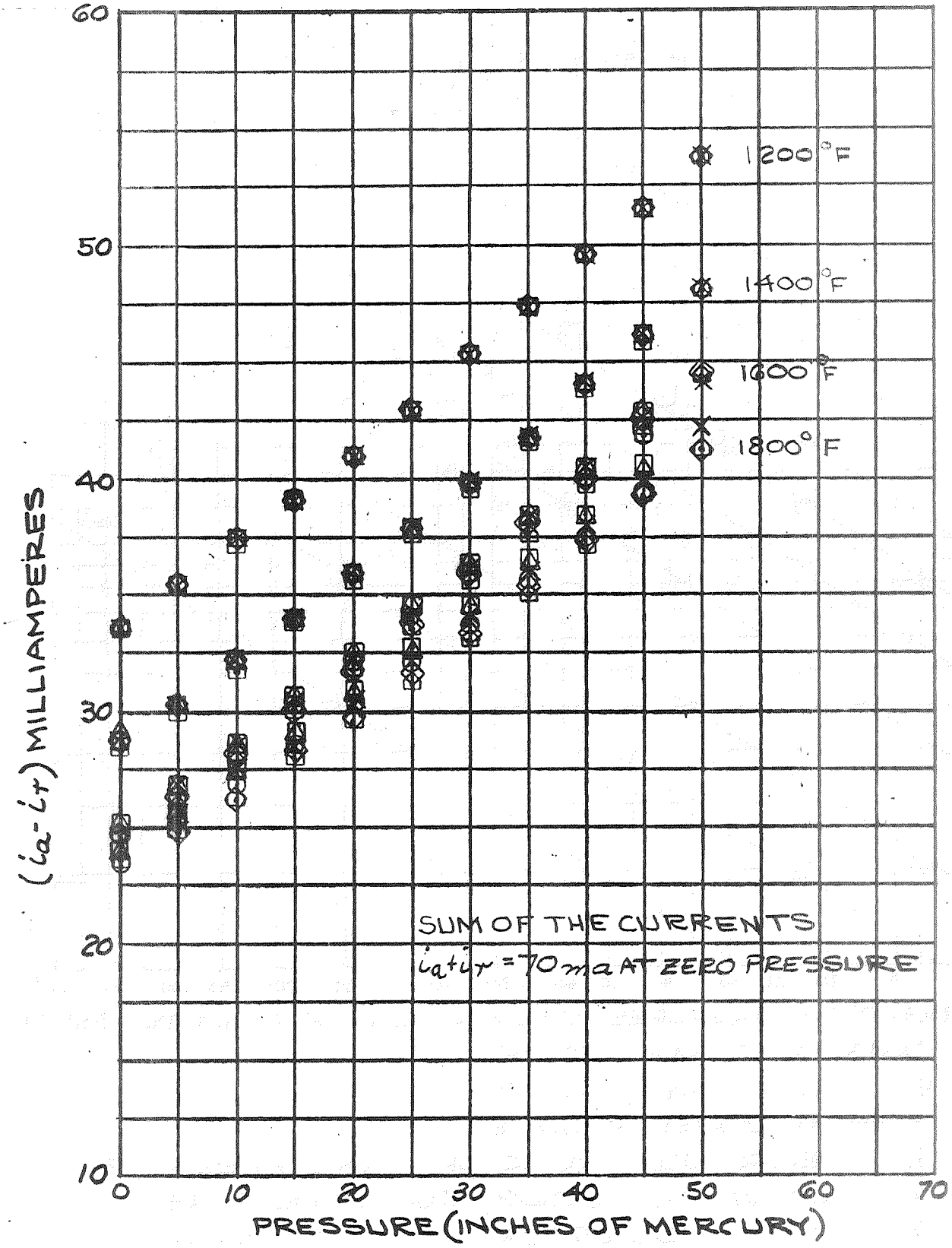


FIGURE 175

PRESSURE-OUTPUT DATA FOR INCREASING TEMPERATURE, TG (FS-35)

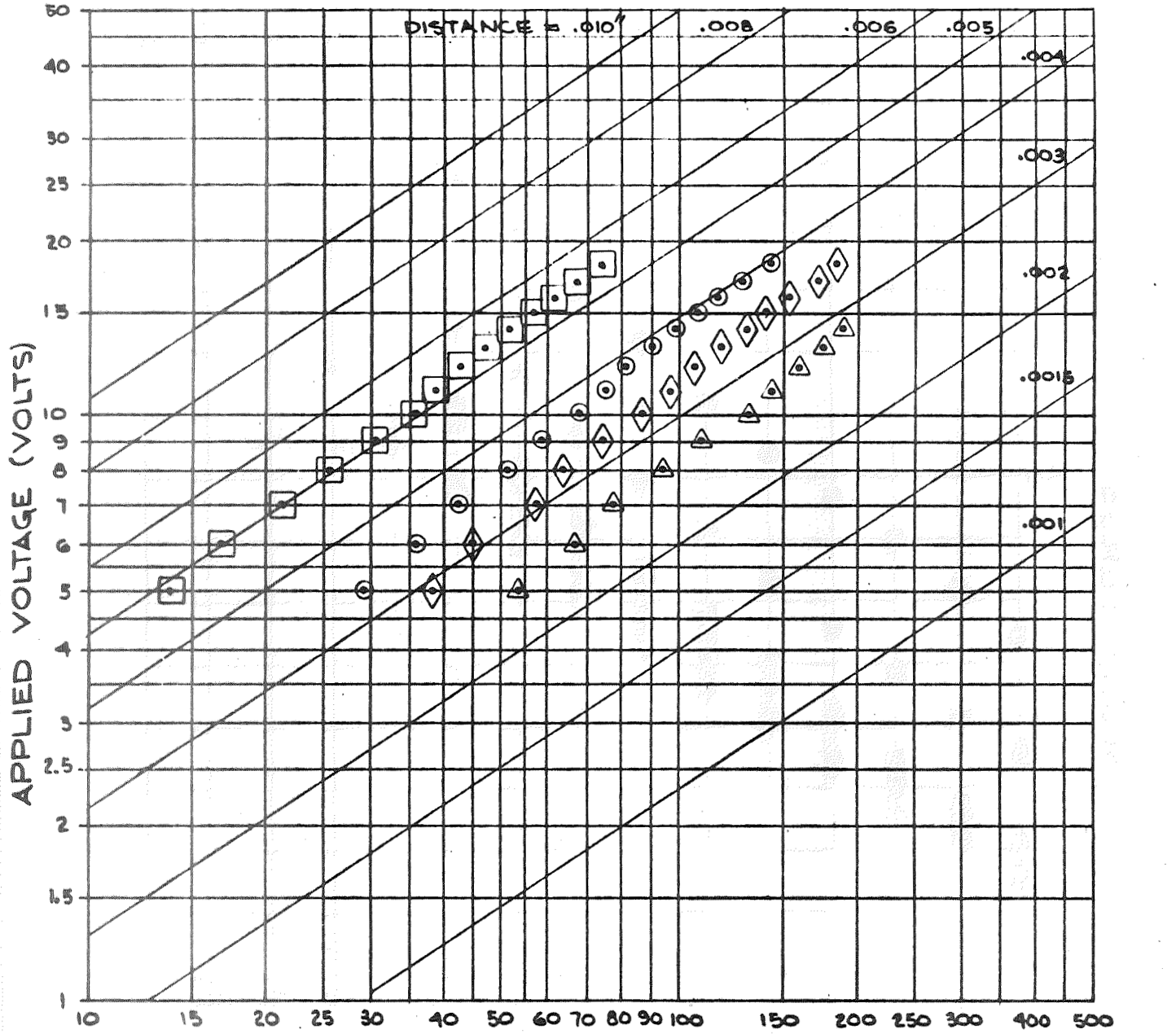


FIGURE 176

FINAL SPACE – CHARGE DATA, T-6 (FS-85)

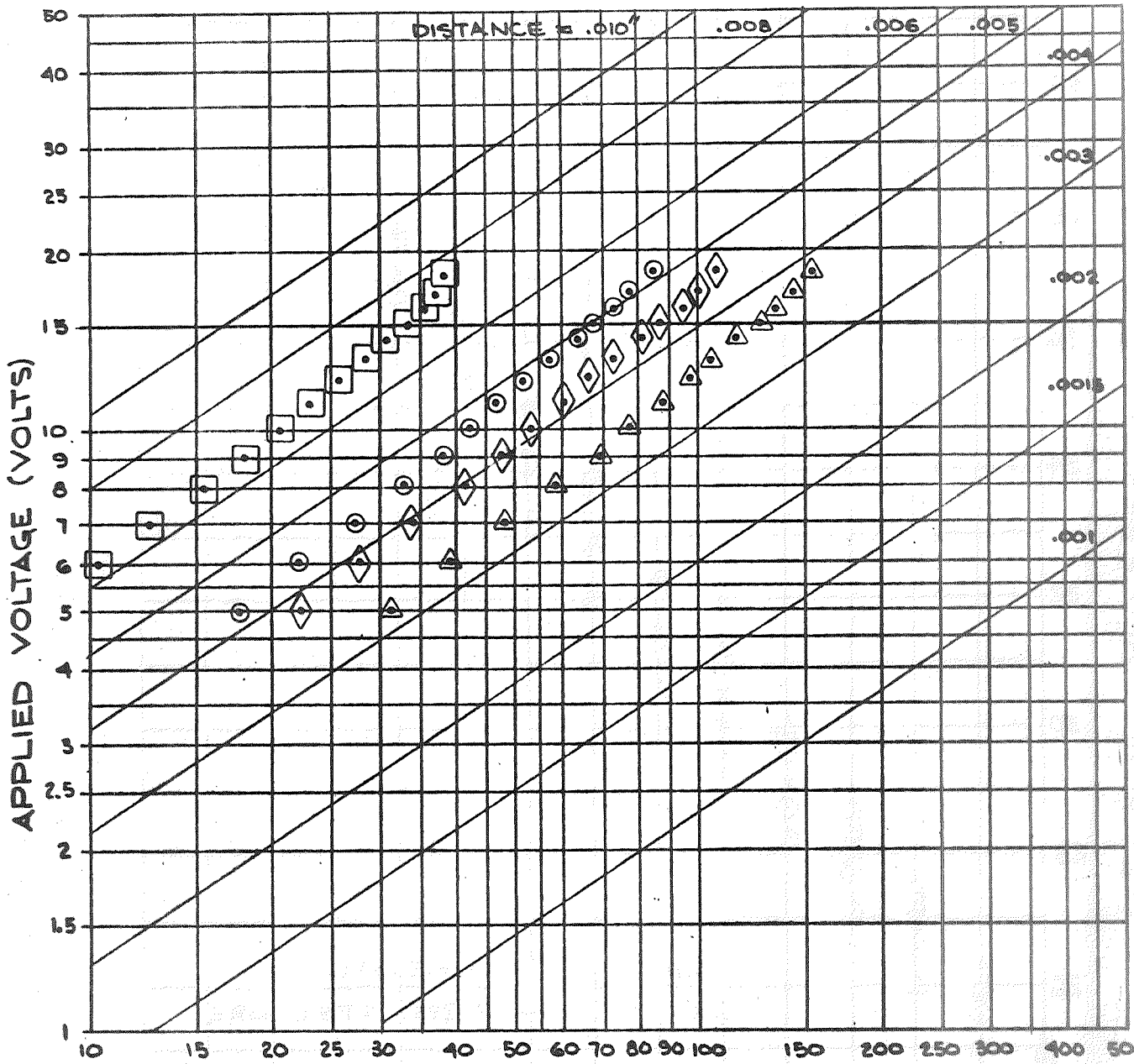


FIGURE 177

INITIAL SPACE - CHARGE DATA, T-7 (C-129Y)

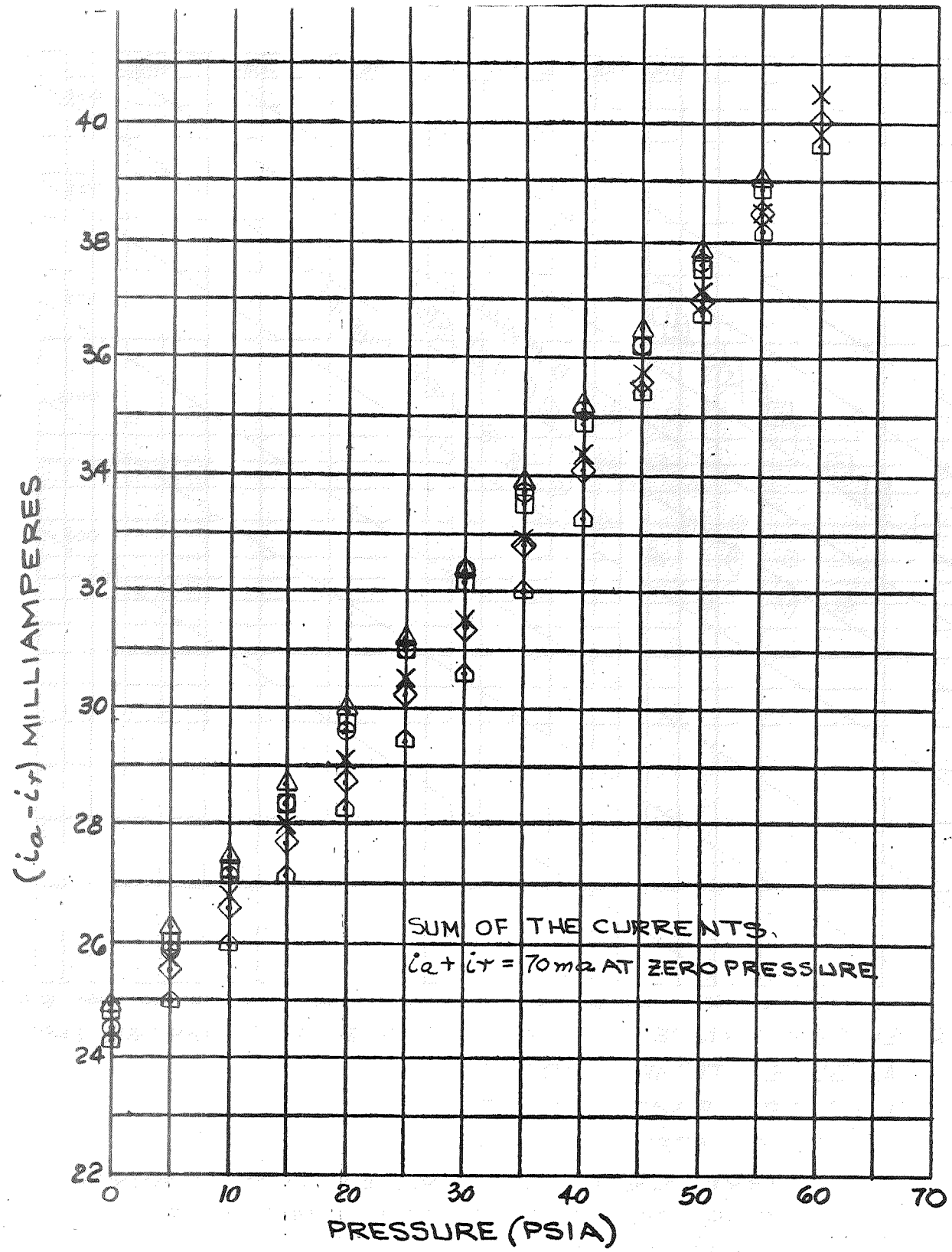


FIGURE 178

PRESSURE-OUTPUT DATA AT 1800°F, T-7 (C-129Y)

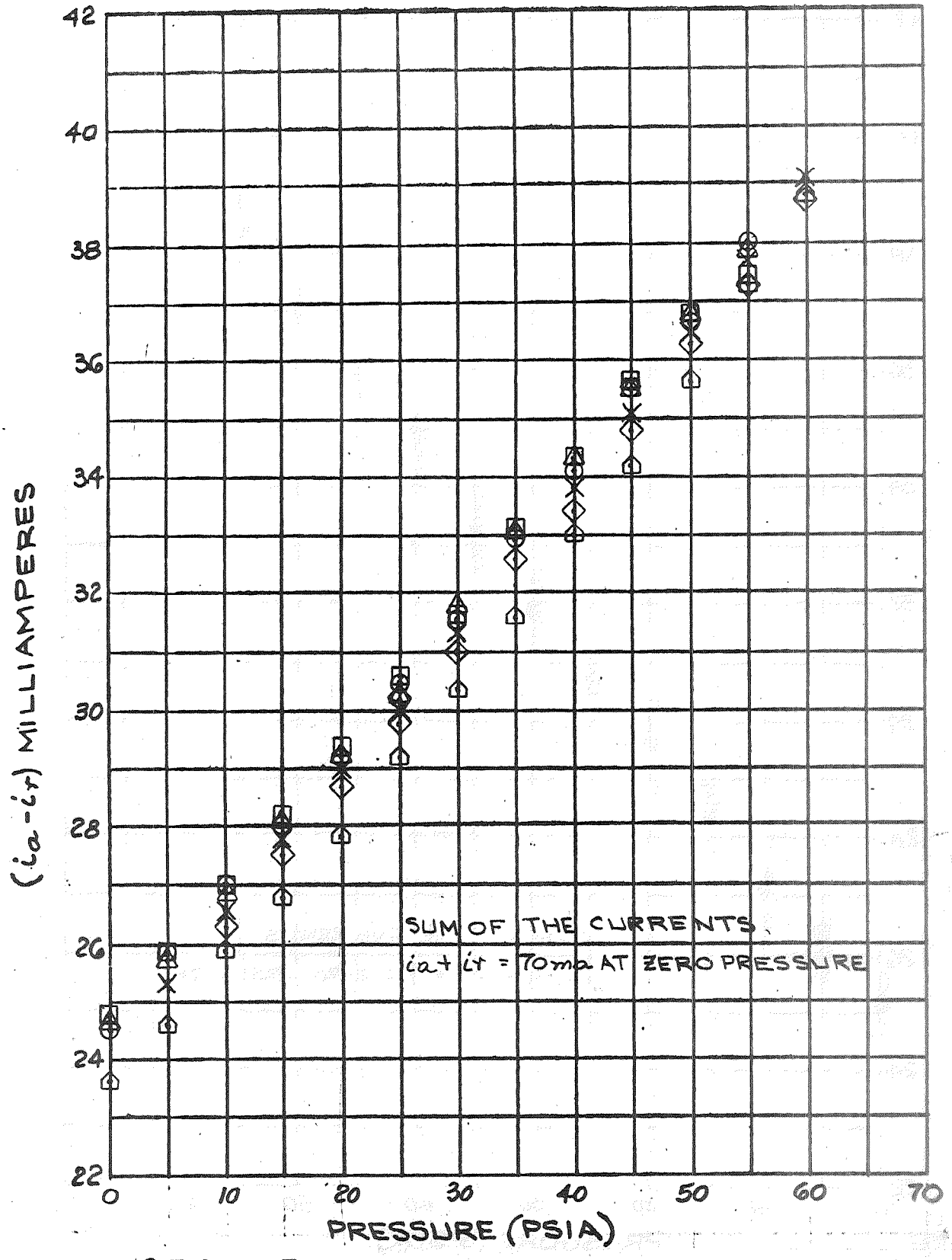


FIGURE 179

PRESSURE-OUTPUT DATA AT 1600°F, T-7 (C-129Y)

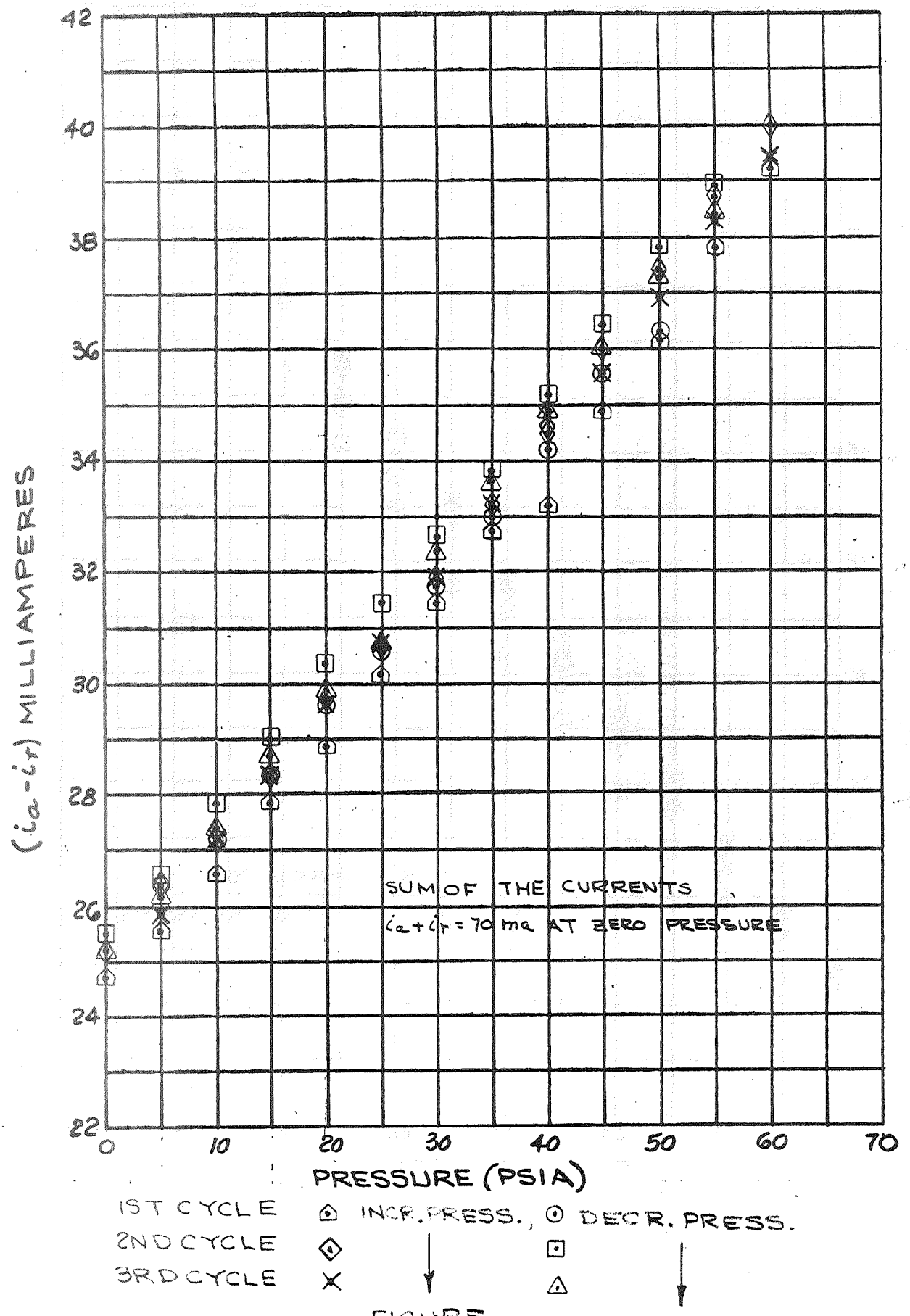


FIGURE 180

PRESSURE-OUTPUT DATA AT 1400°F, T-7(C-129Y)

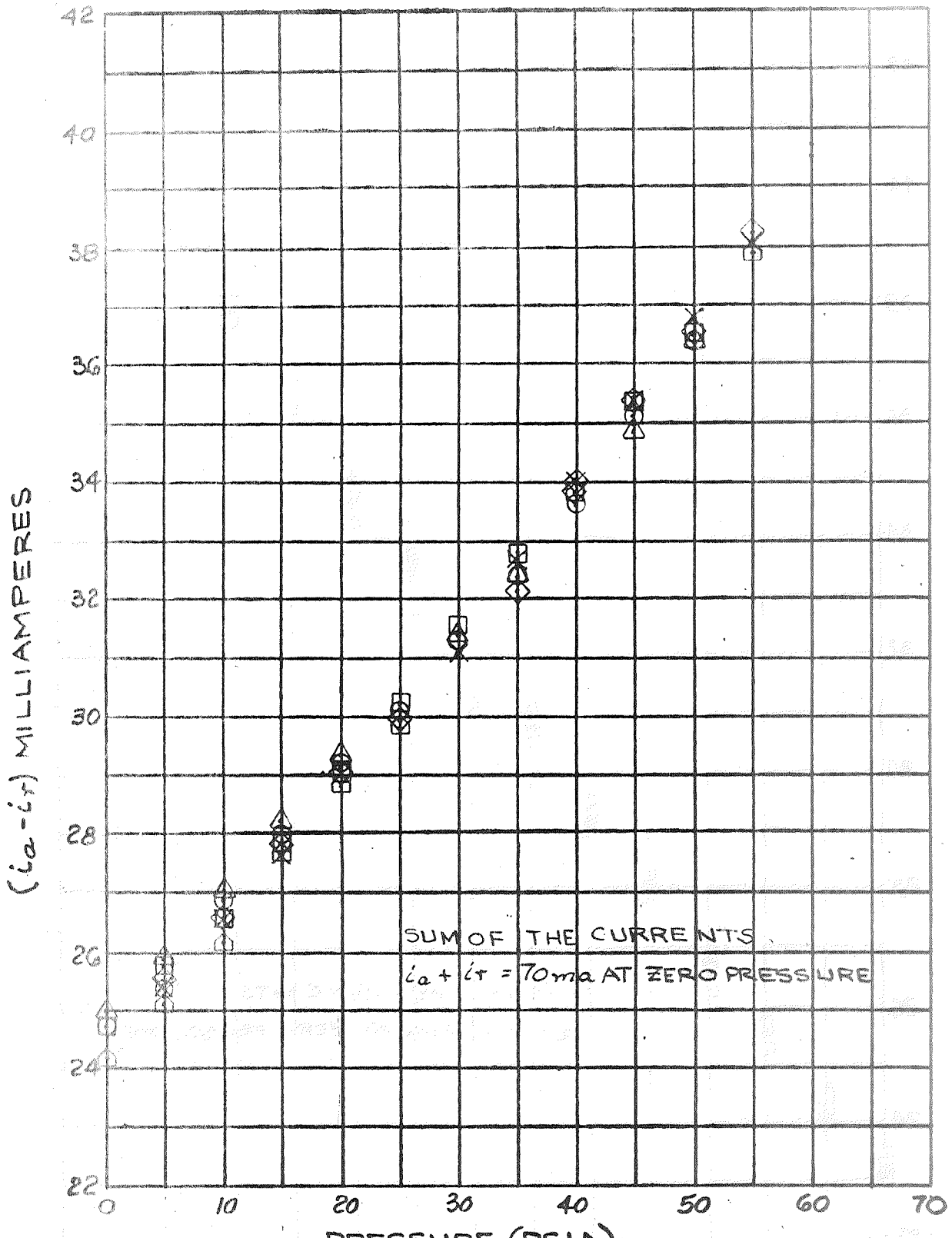


FIGURE 181

PRESSURE - OUTPUT DATA AT 1200°F, T-7 (C-129Y)

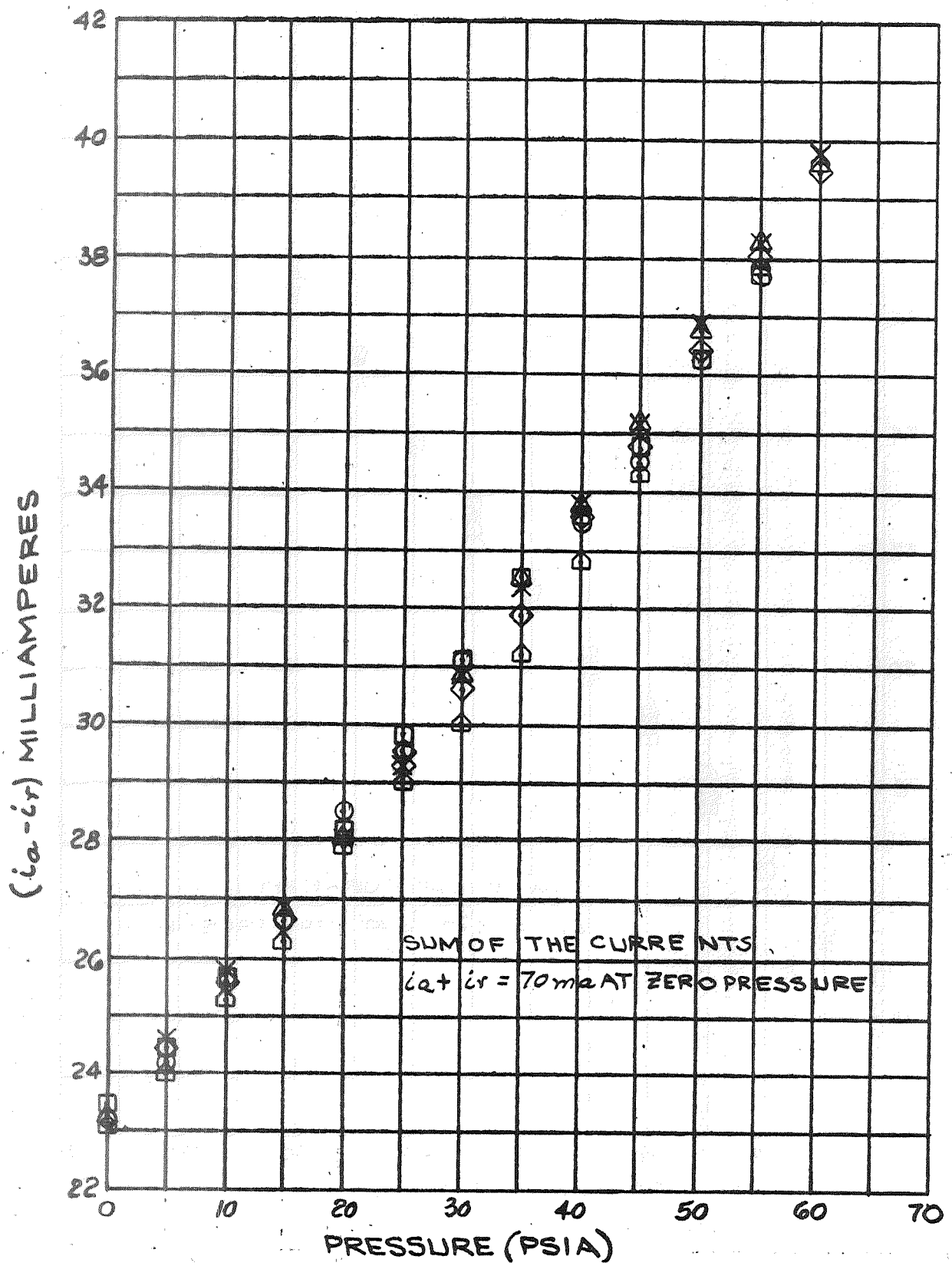


FIGURE 182

PRESSURE-OUTPUT DATA AT 1000°F, T-7 (C-129 Y)

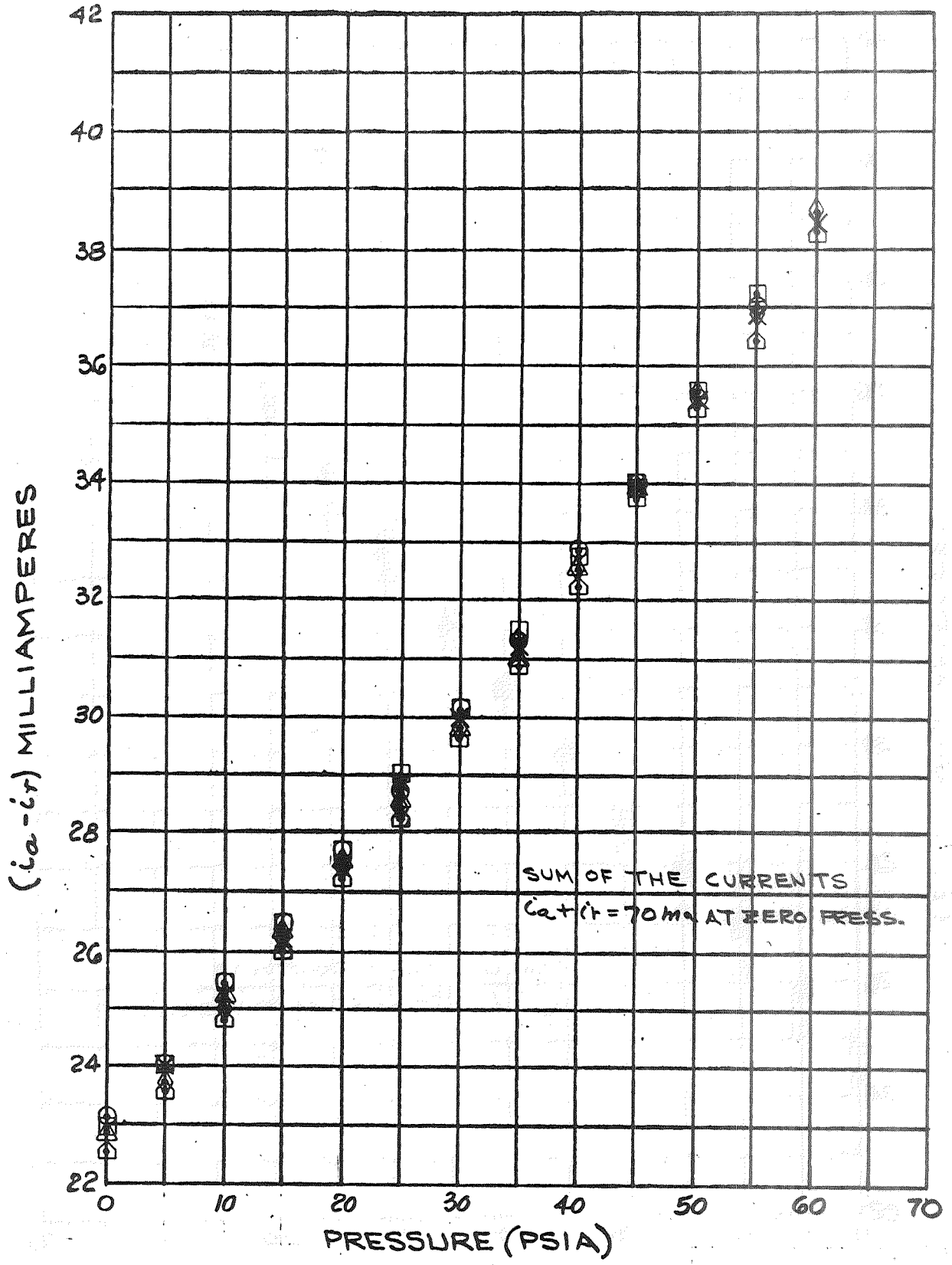


FIGURE 183

PRESSURE-OUTPUT DATA AT 1200°F, T-7 (C-129Y)

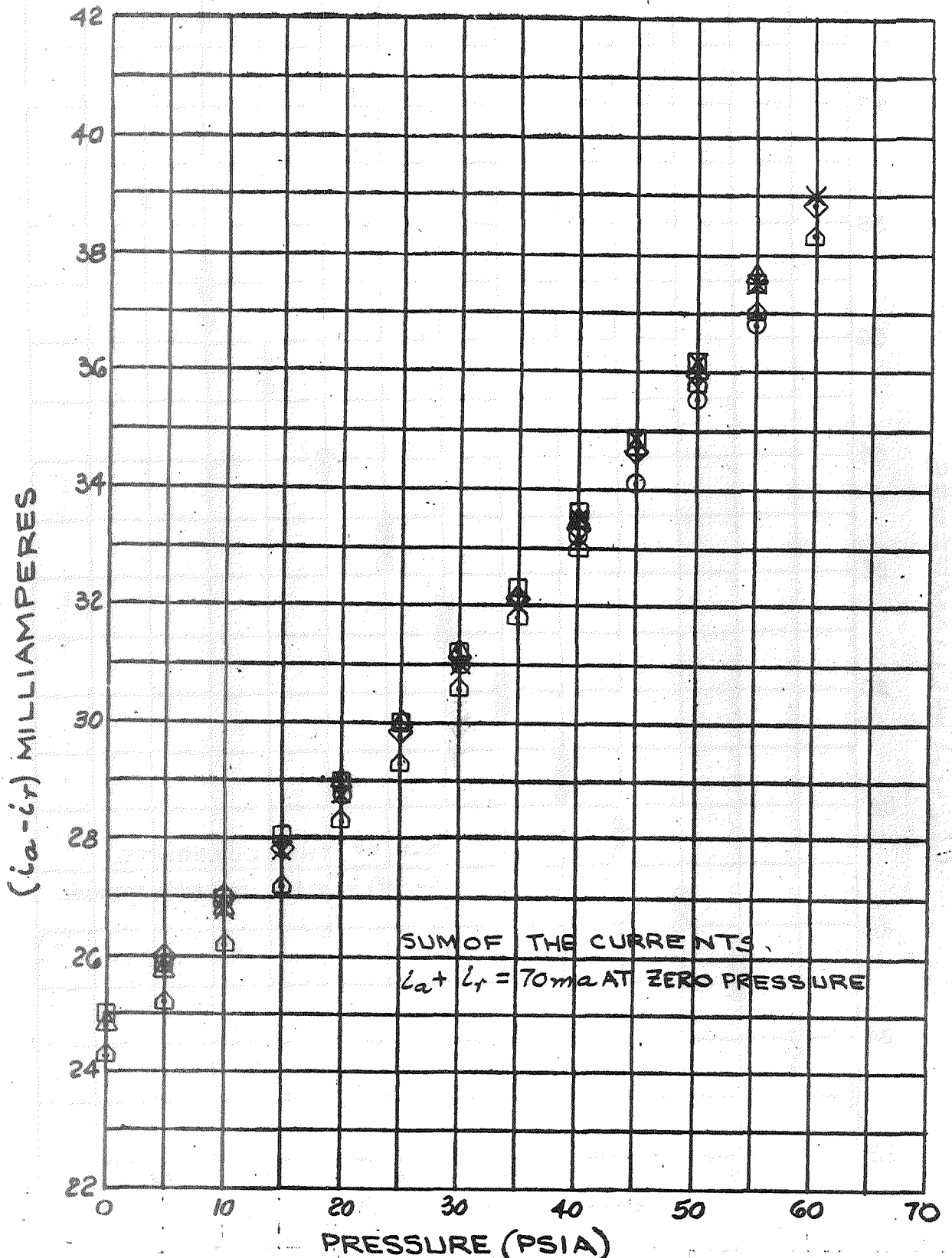


FIGURE 184

PRESSURE-OUTPUT DATA AT 1400°F, T-7 (C-129Y)

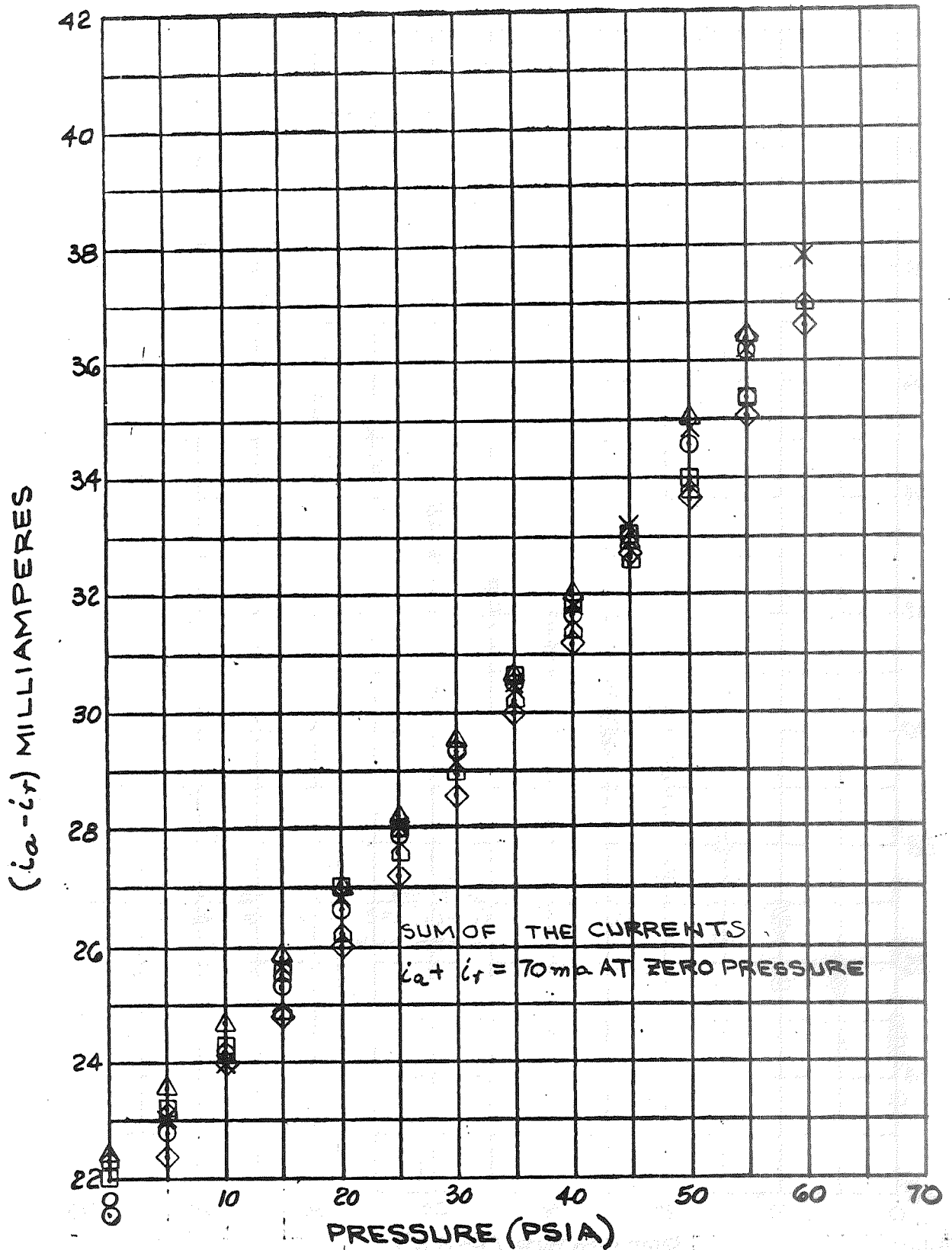


FIGURE 185

PRESSURE - OUTPUT DATA AT 1600°F, T-7 (C-129Y)

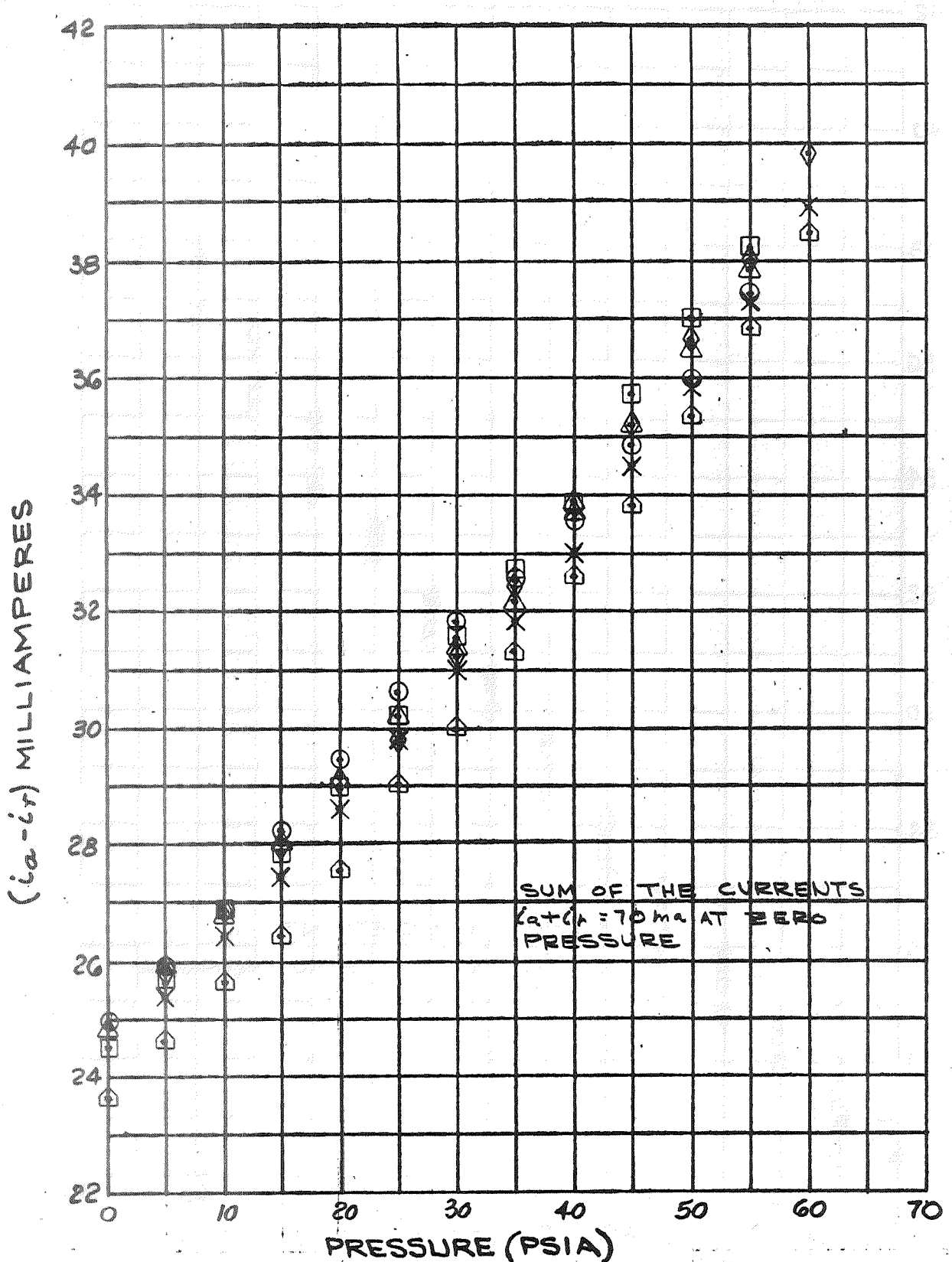


FIGURE 186

PRESSURE - OUTPUT DATA AT 1800°F, T-7 (C-129Y)

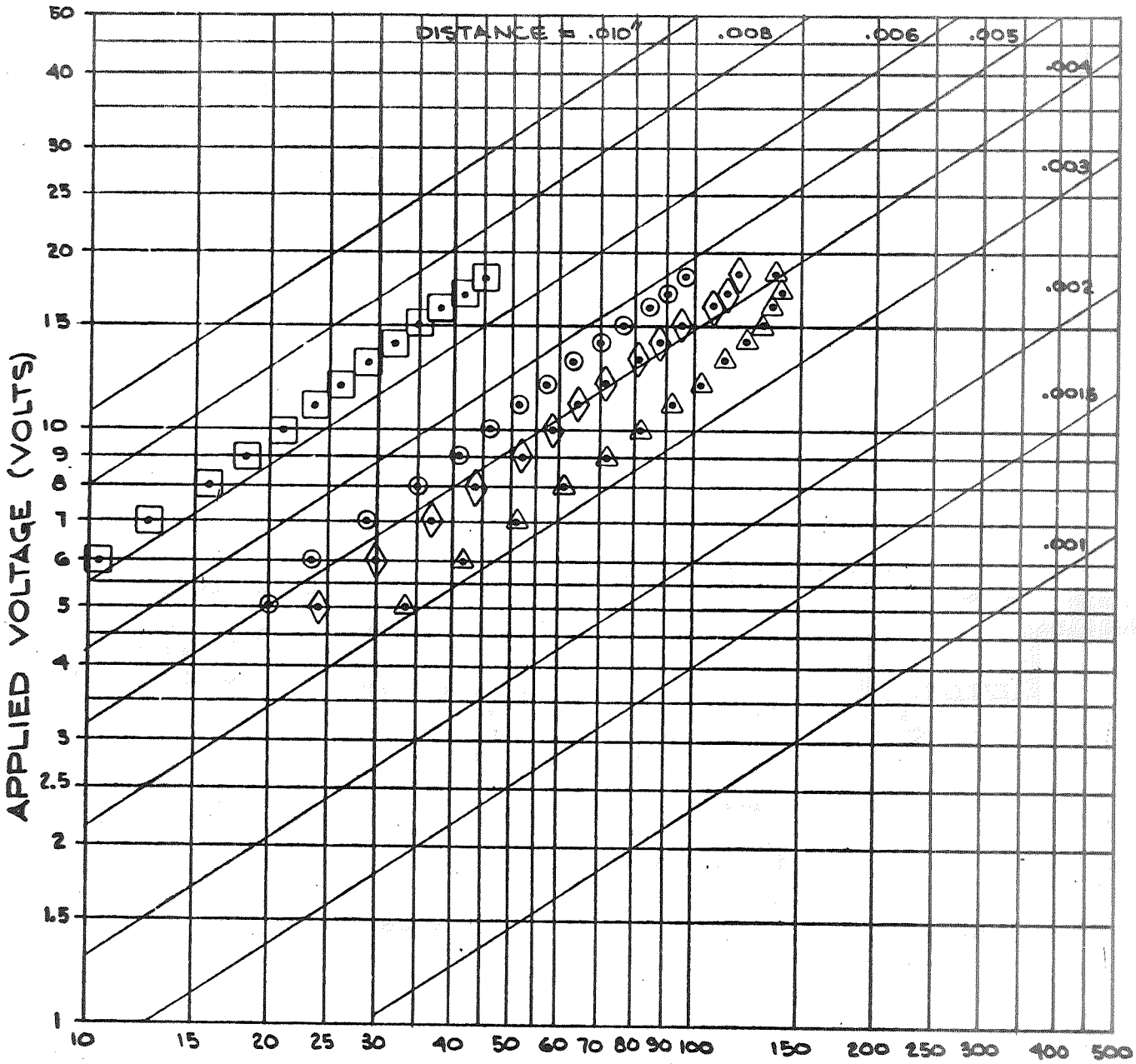


FIGURE 187

FINAL SPACE – CHARGE DATA, T-7 (C-129Y)

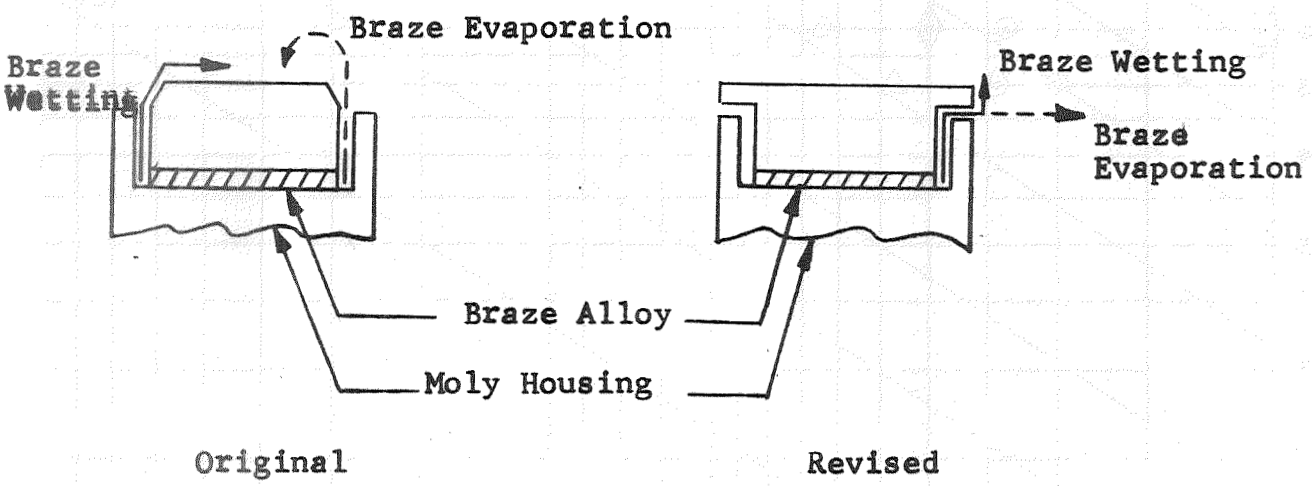


Figure 188

Emitter Braze Configuration

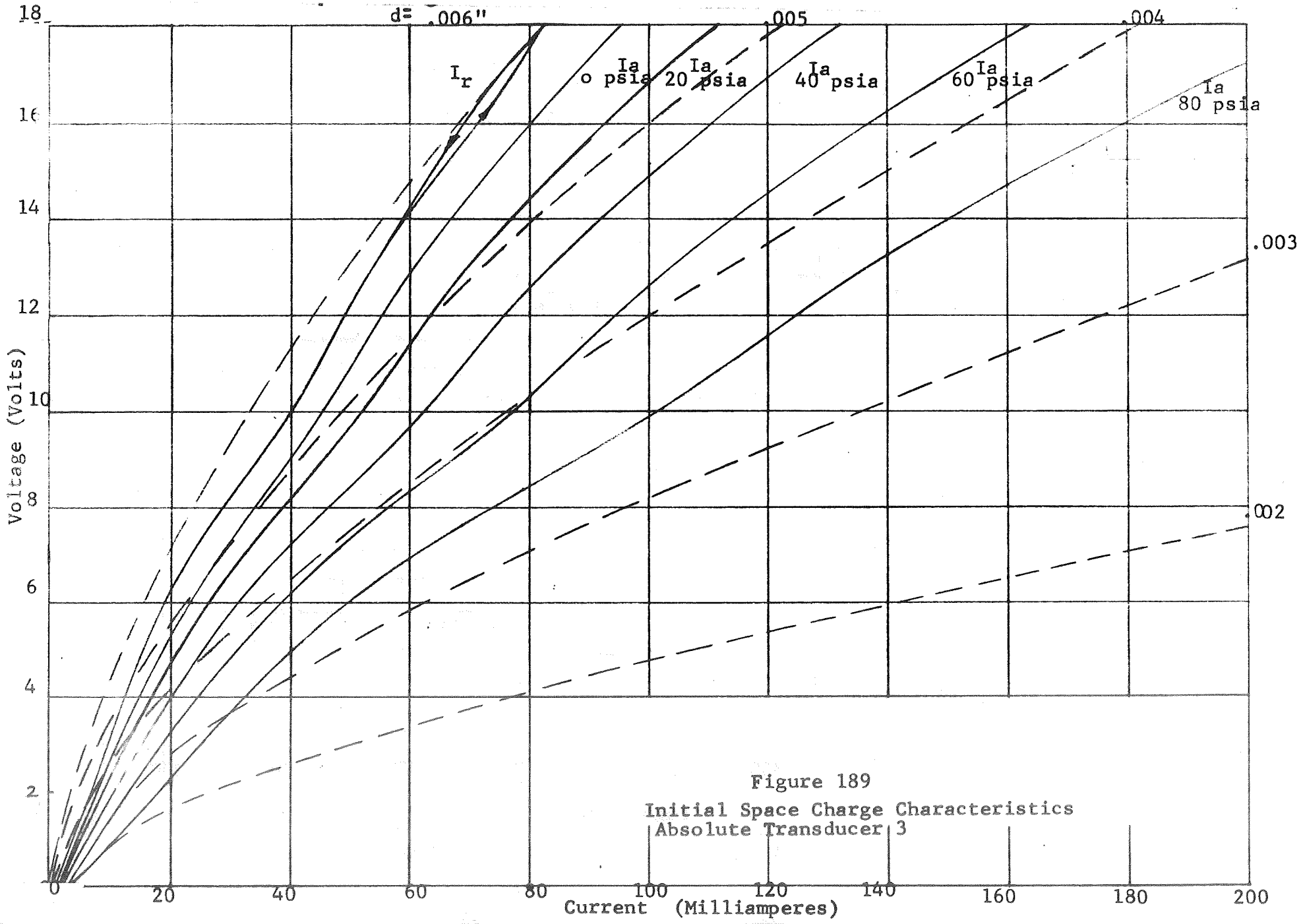


Figure 189

Initial Space Charge Characteristics
Absolute Transducer 3

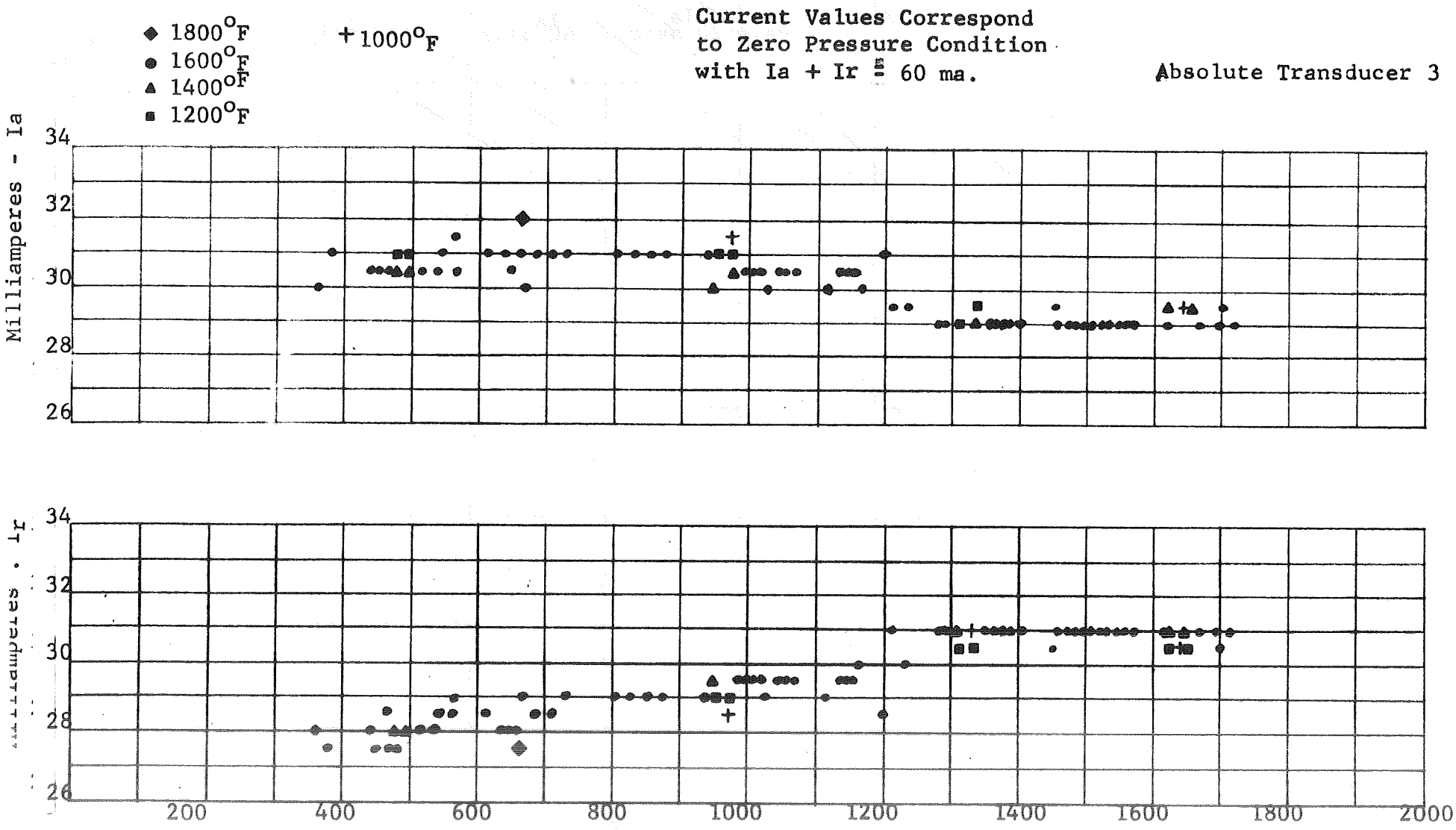


Figure 190

Active and Reference Current Characteristics

Absolute Transducer 3

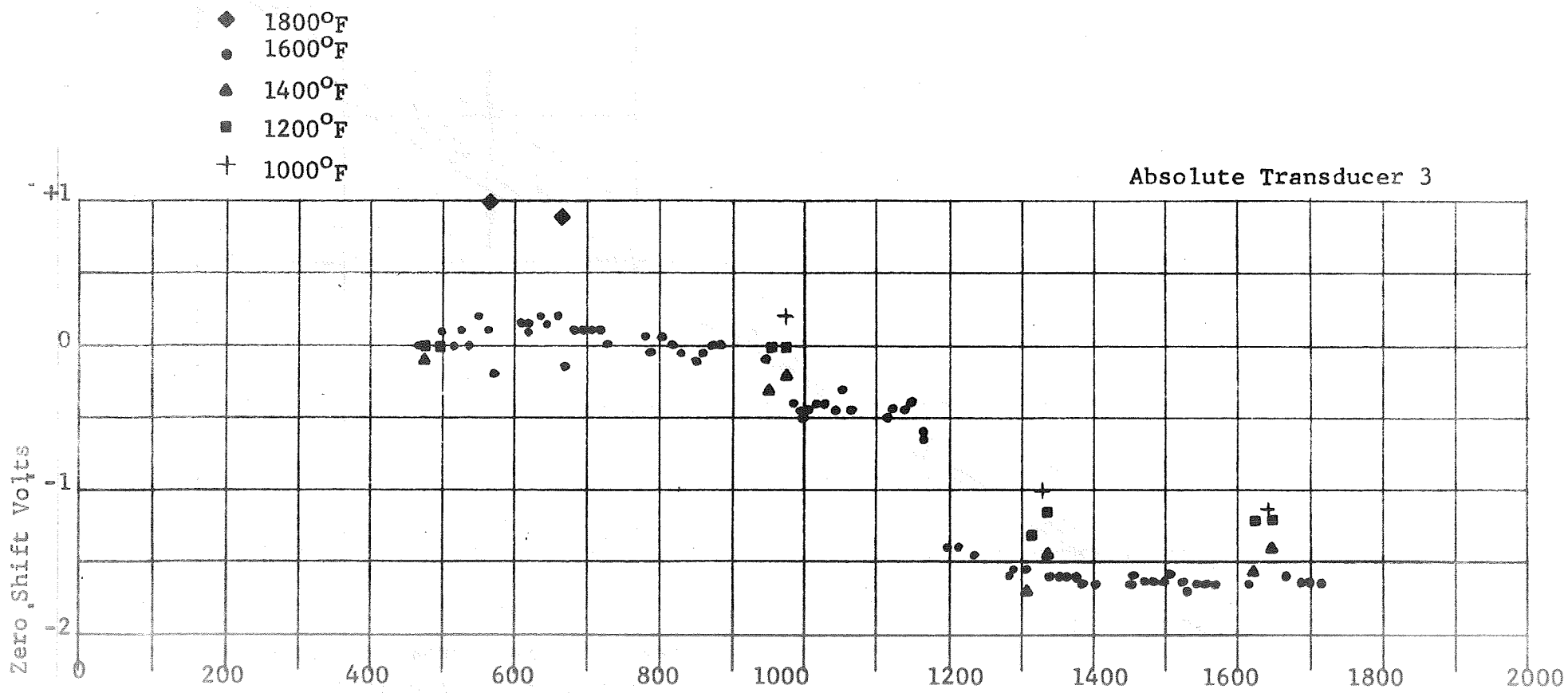


Figure 191

Zero-Shift Characteristics
Absolute Transducer 3

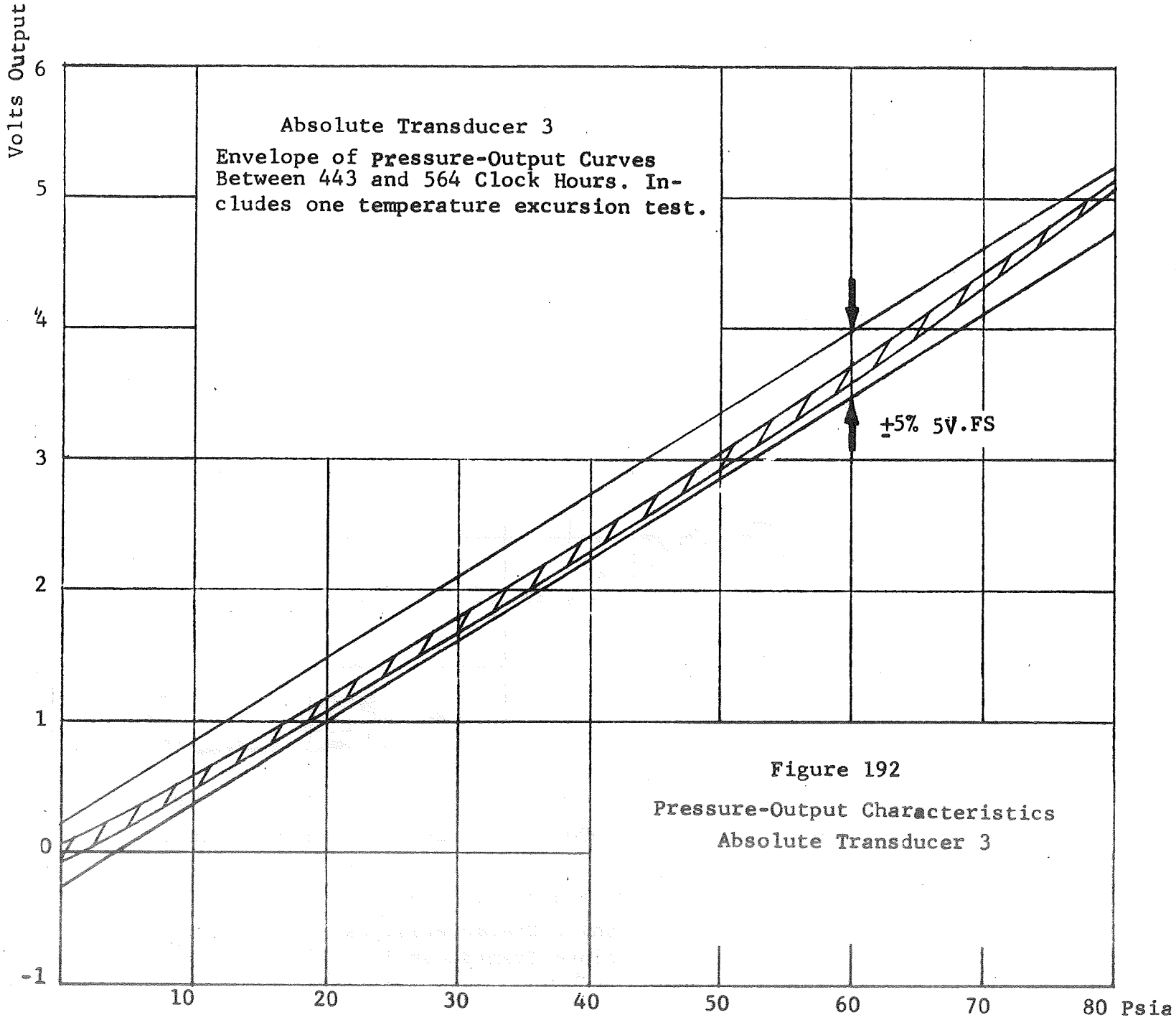


Figure 192

Pressure-Output Characteristics
Absolute Transducer 3

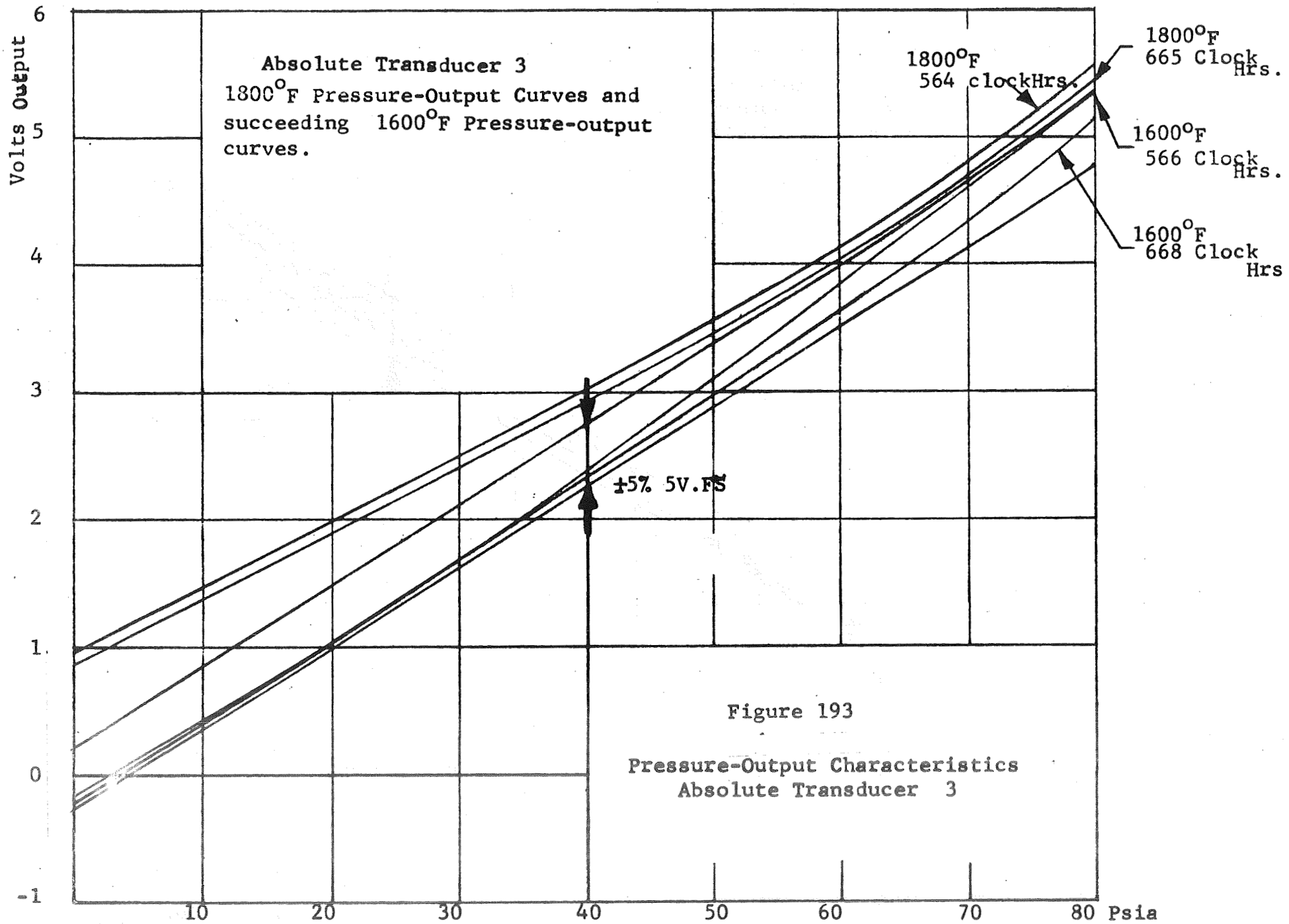


Figure 193

Pressure-Output Characteristics
Absolute Transducer 3

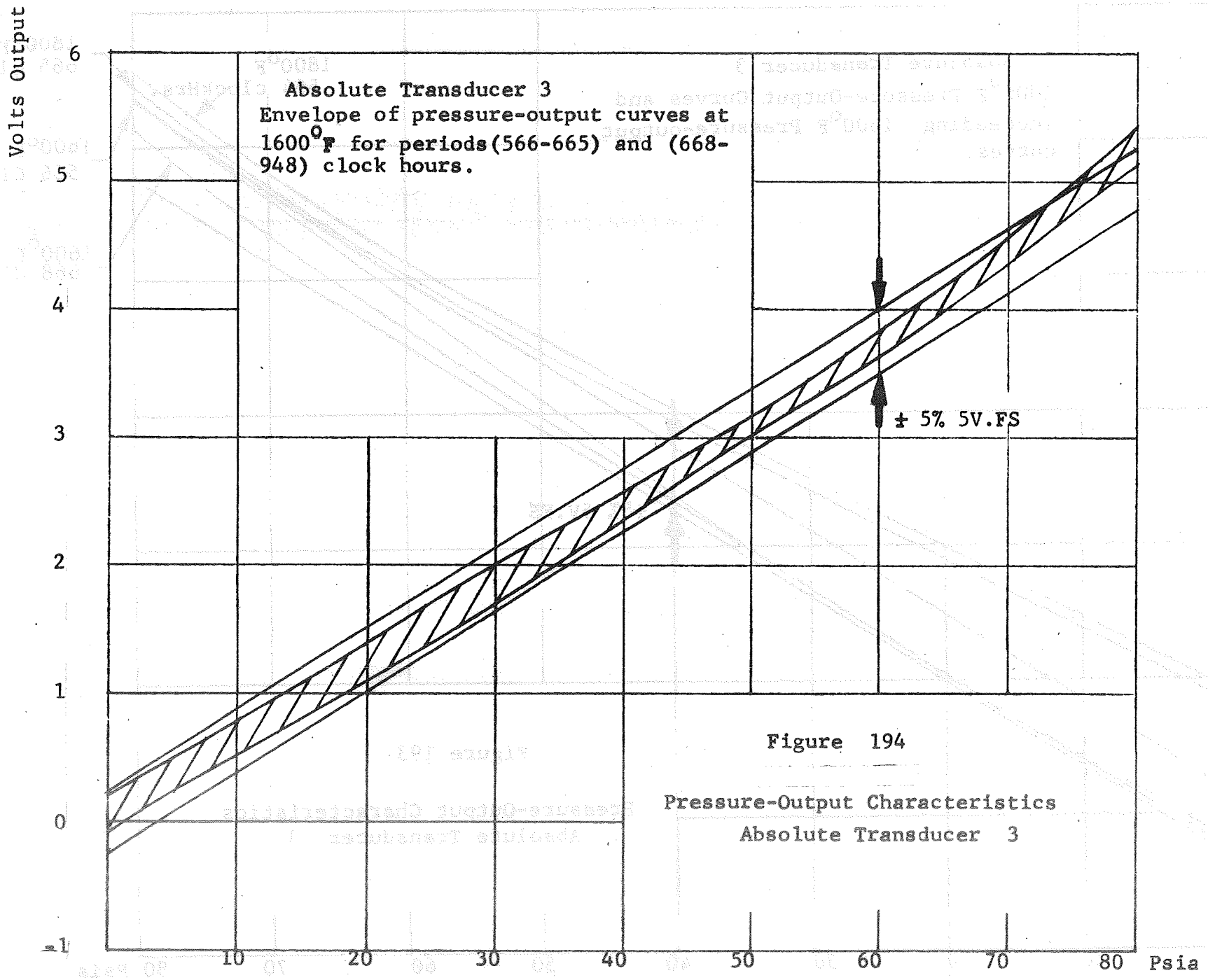


Figure 194

Pressure-Output Characteristics
Absolute Transducer 3

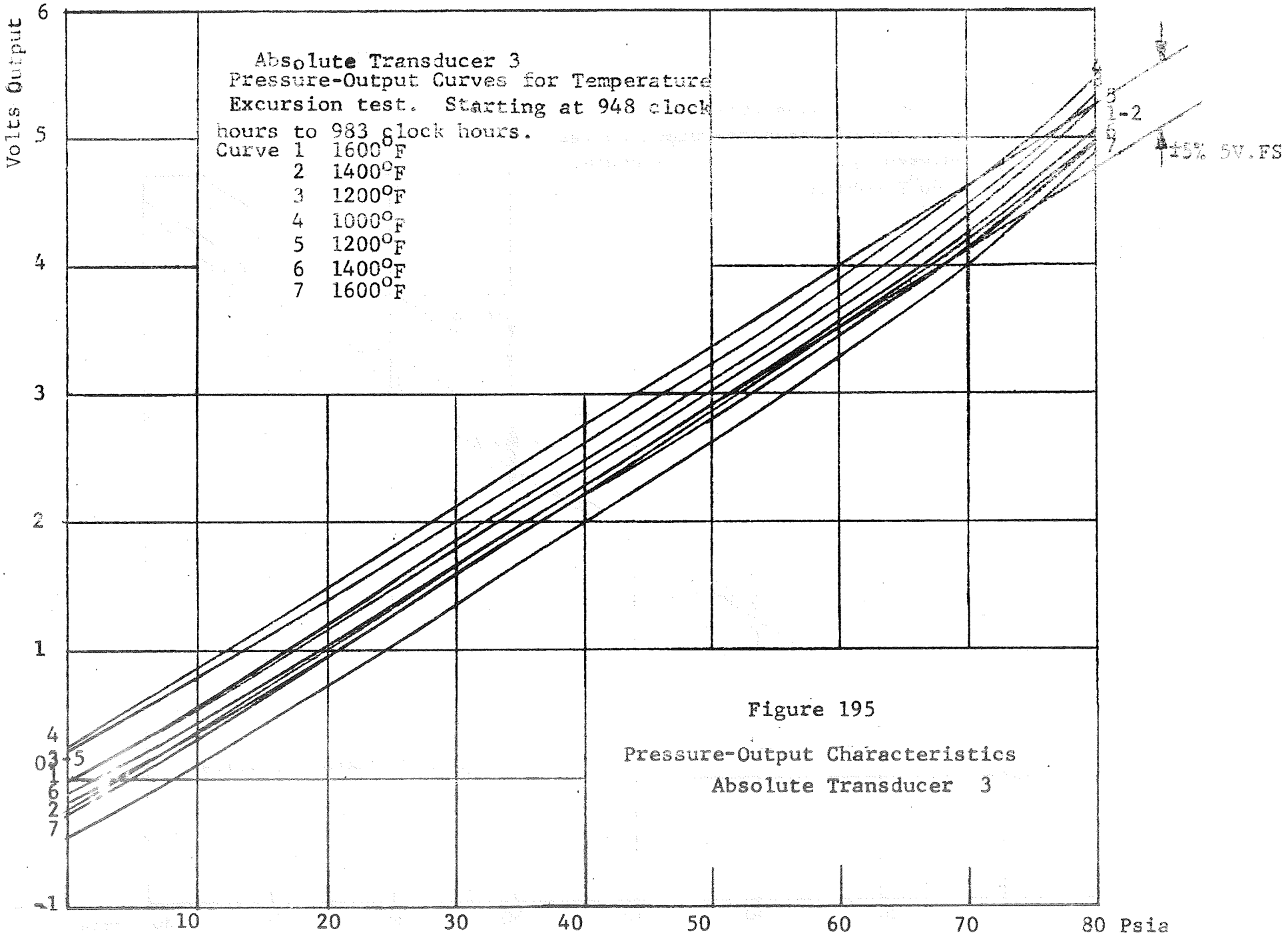


Figure 195

Pressure-Output Characteristics
Absolute Transducer 3

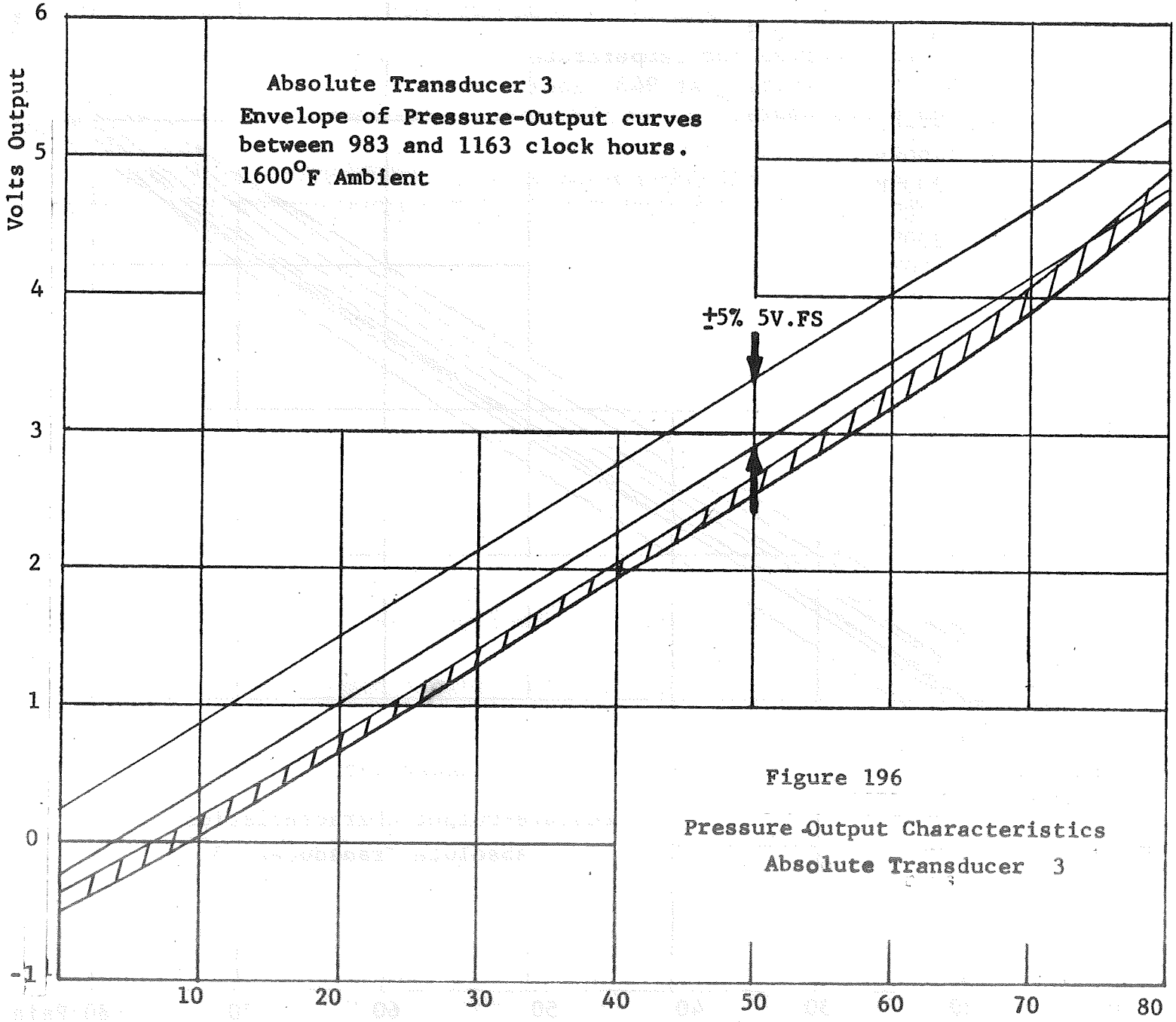


Figure 196

Pressure Output Characteristics

Absolute Transducer 3

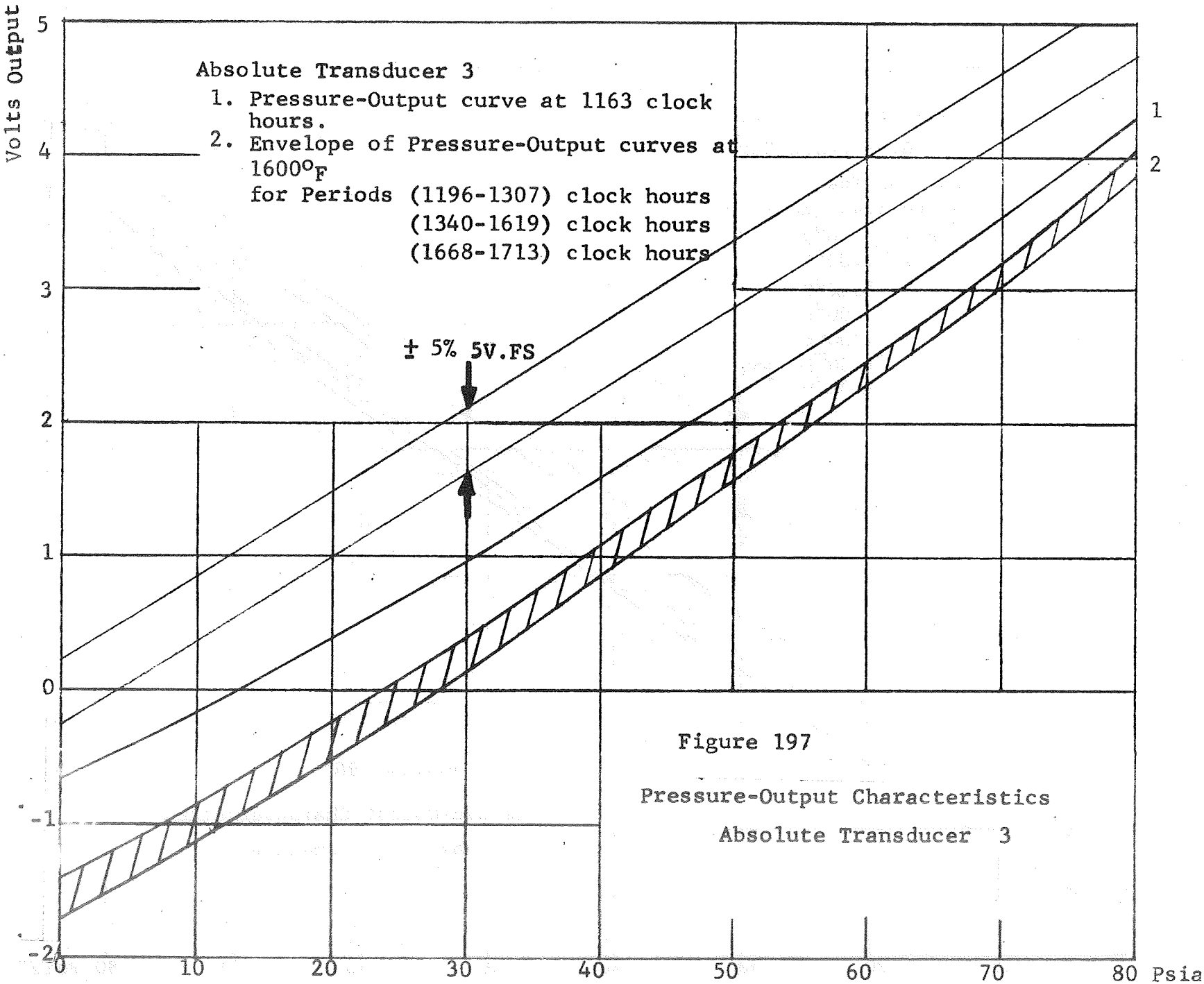


Figure 197

Pressure-Output Characteristics

Absolute Transducer 3

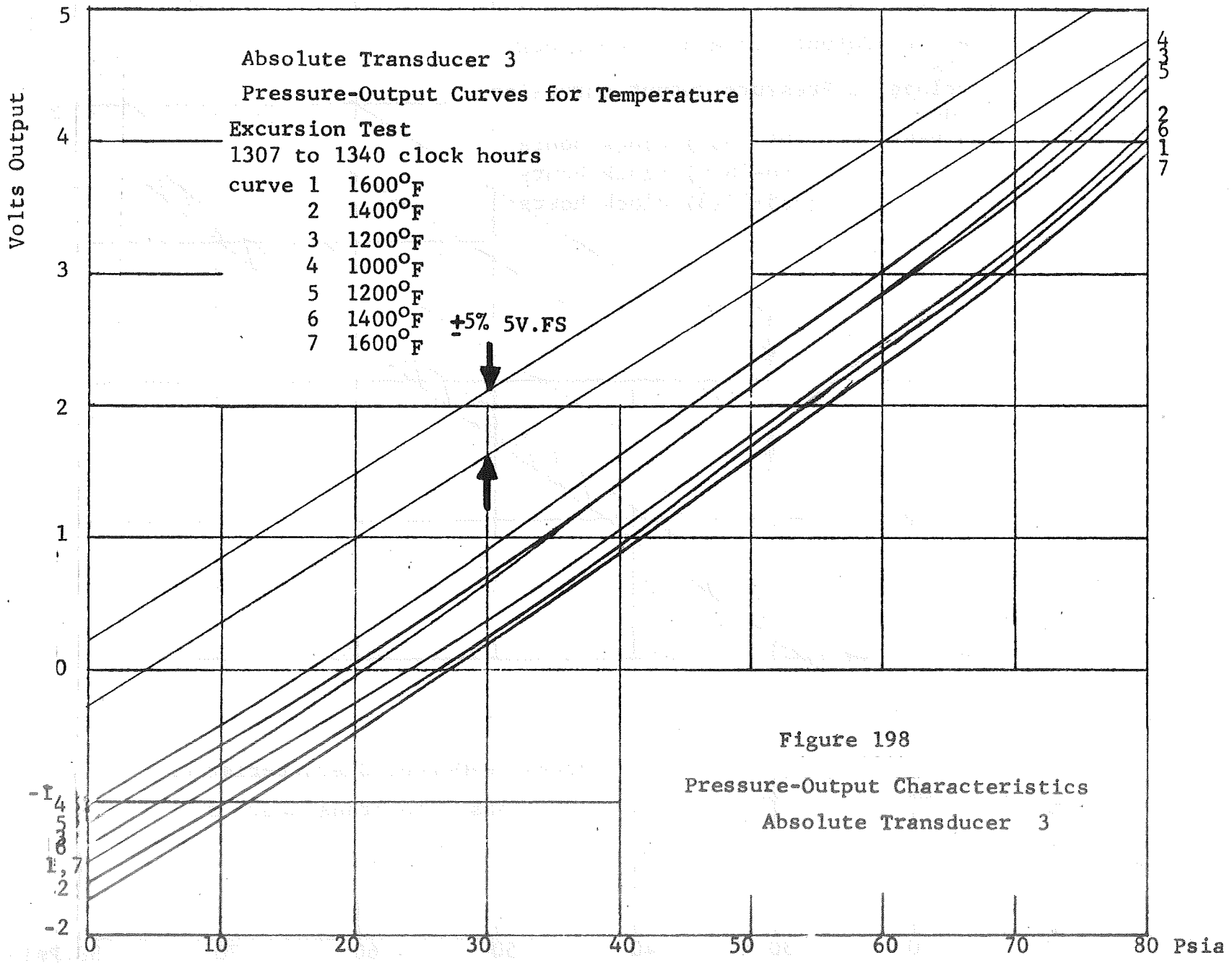


Figure 198

Pressure-Output Characteristics

Absolute Transducer 3

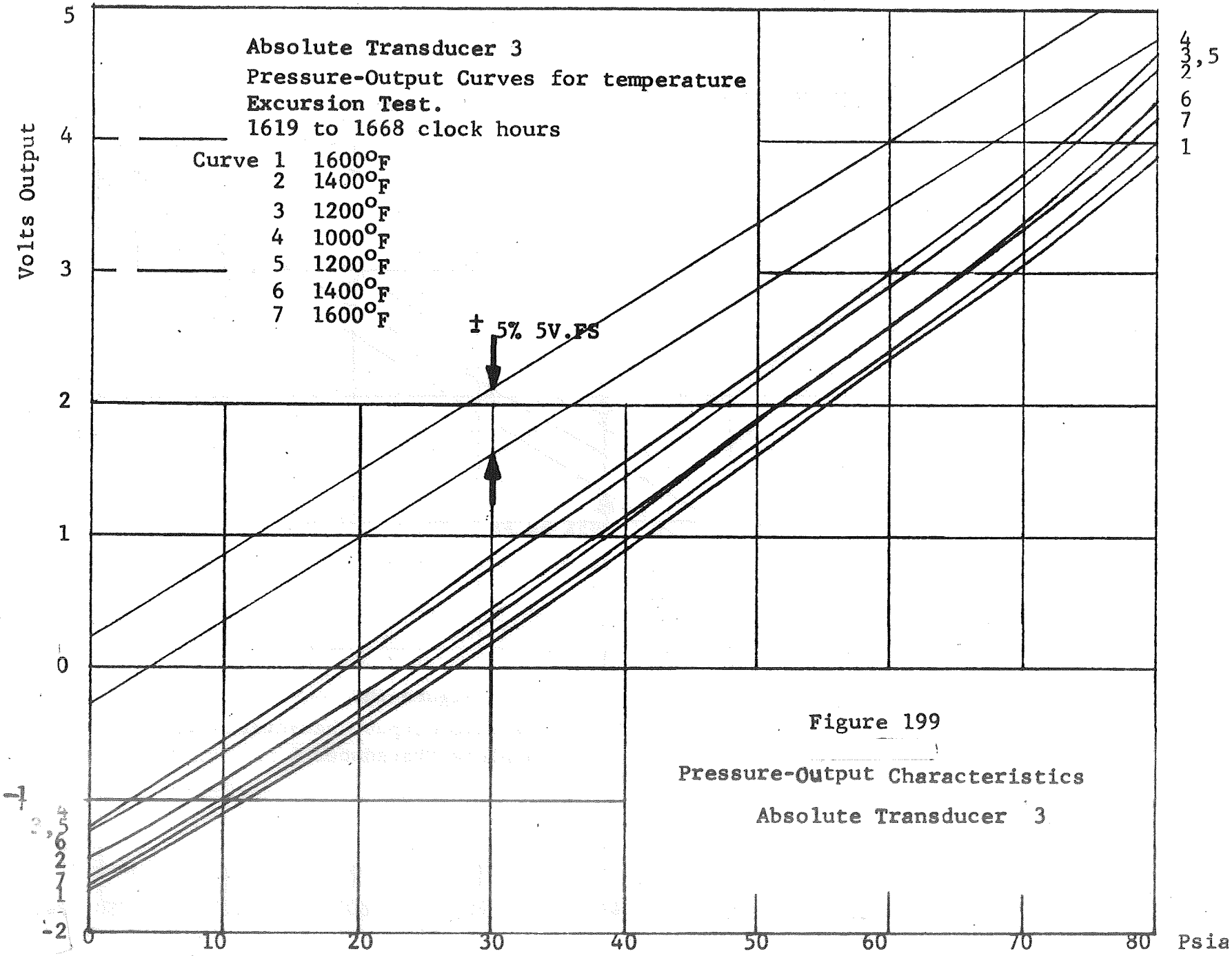


Figure 199

Pressure-Output Characteristics

Absolute Transducer 3

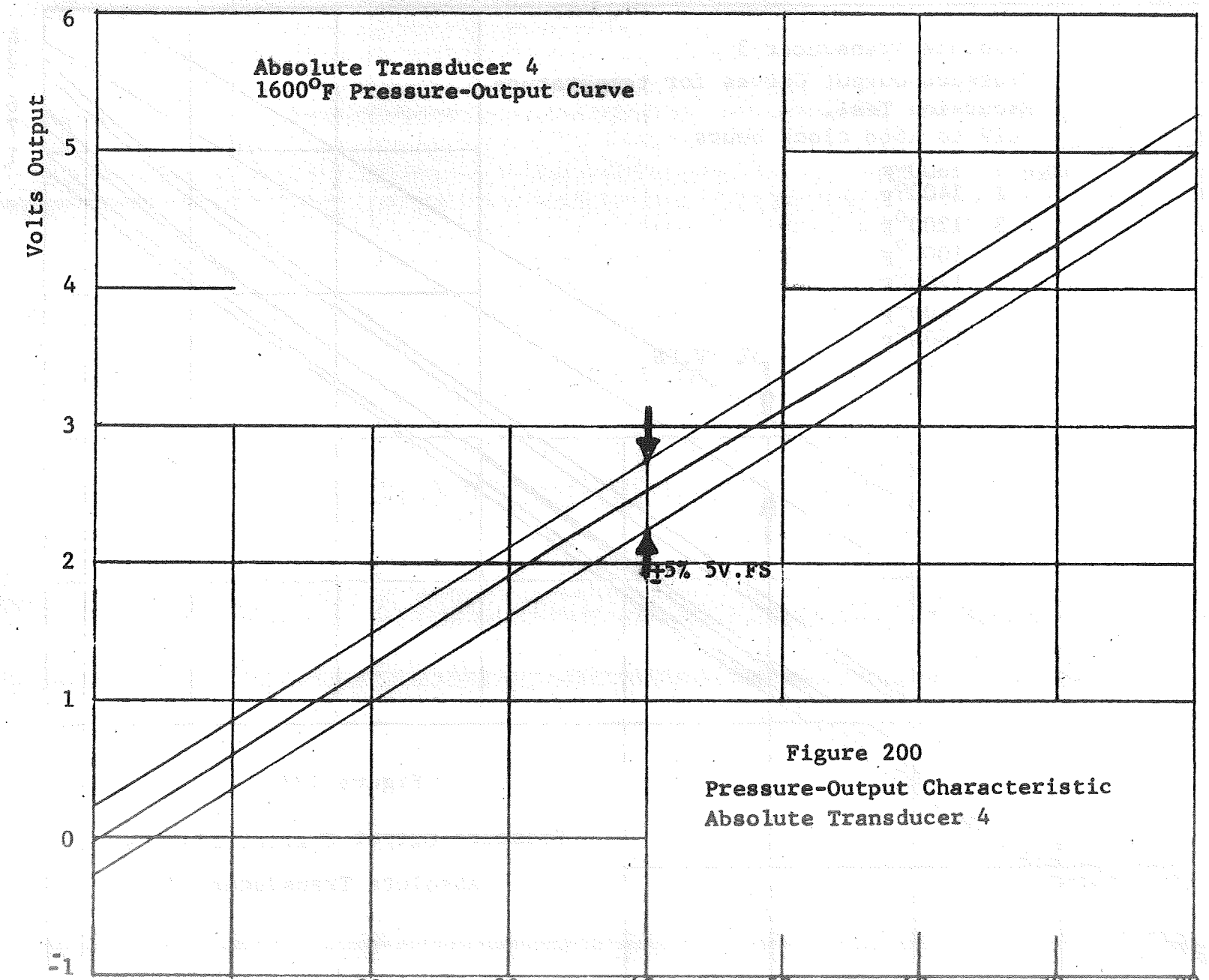


Figure 200
Pressure-Output Characteristic
Absolute Transducer 4

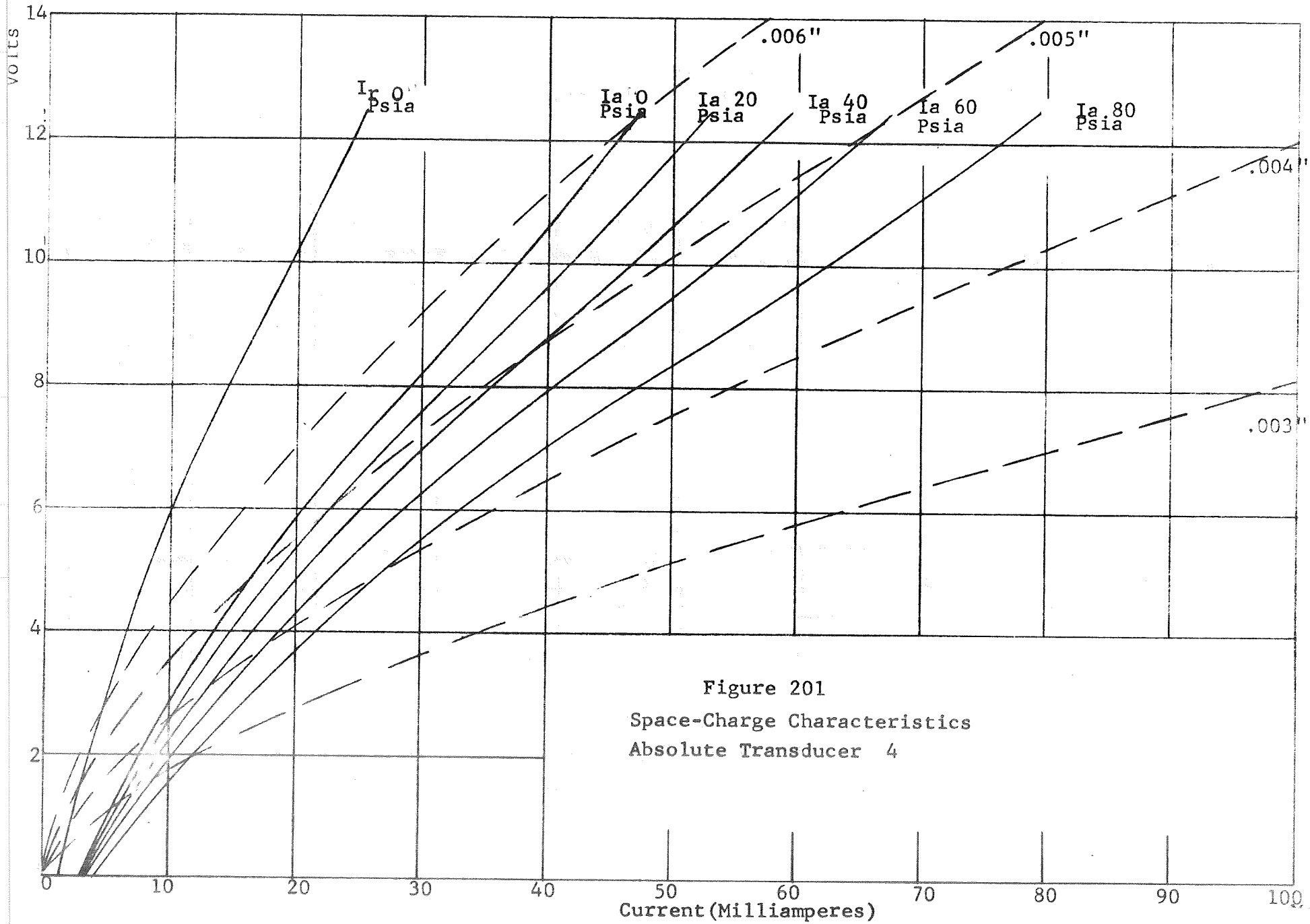


Figure 201

Space-Charge Characteristics

Absolute Transducer 4

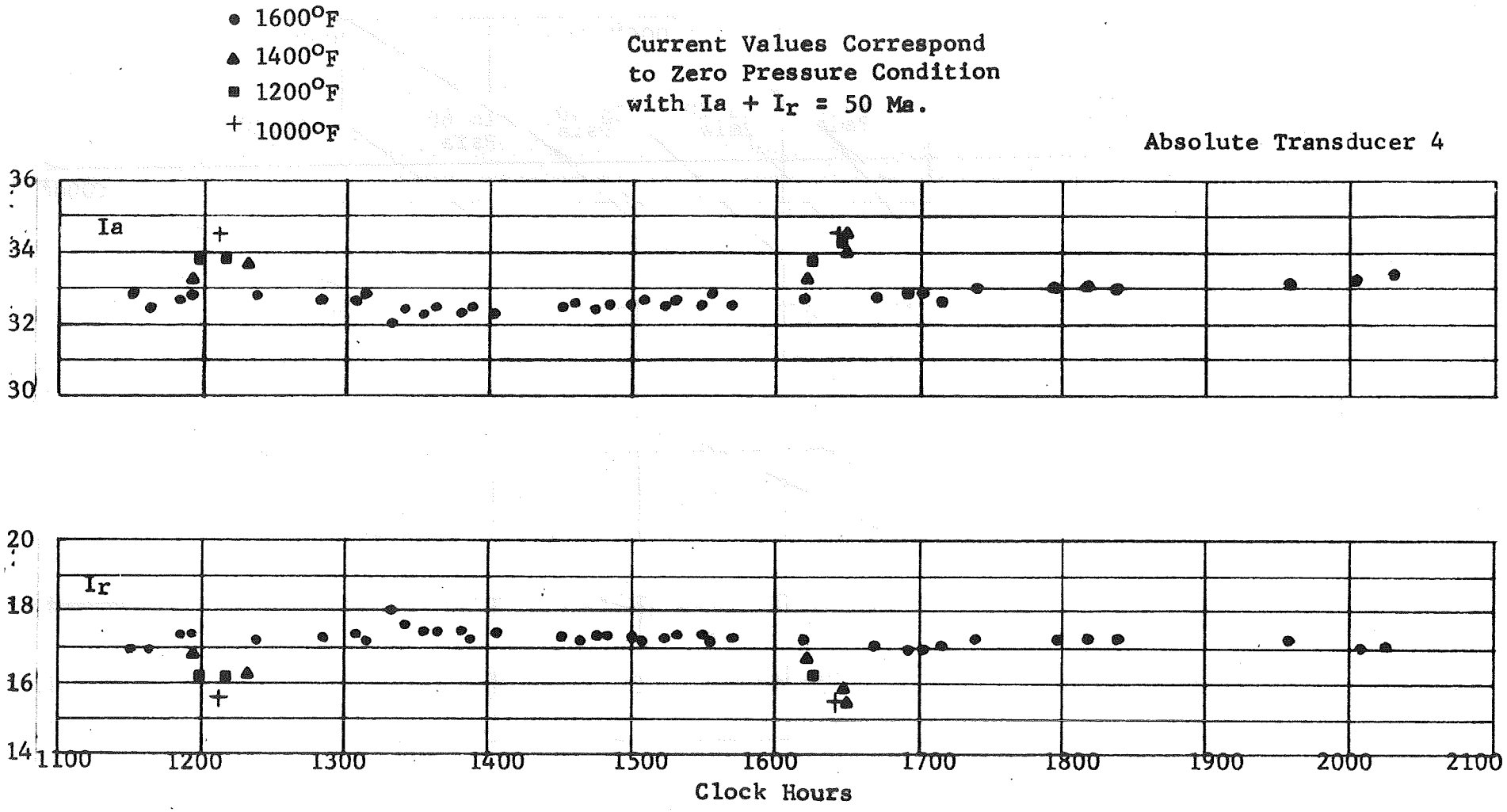


Figure 202
Active and Reference Current Characteristics
Absolute Transducer 4

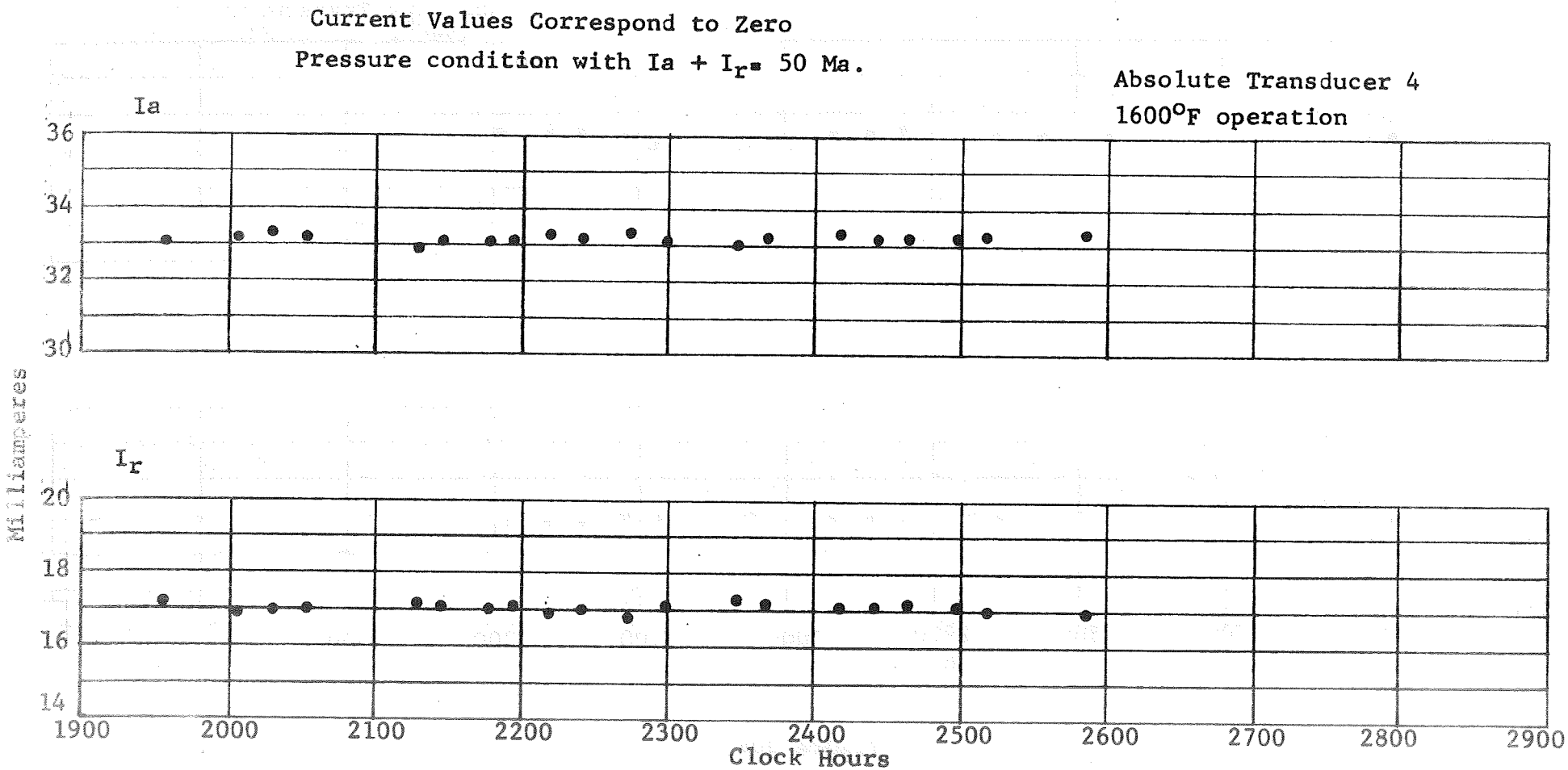


Figure 203

Active and Reference Current Characteristics
Absolute Transducer 4

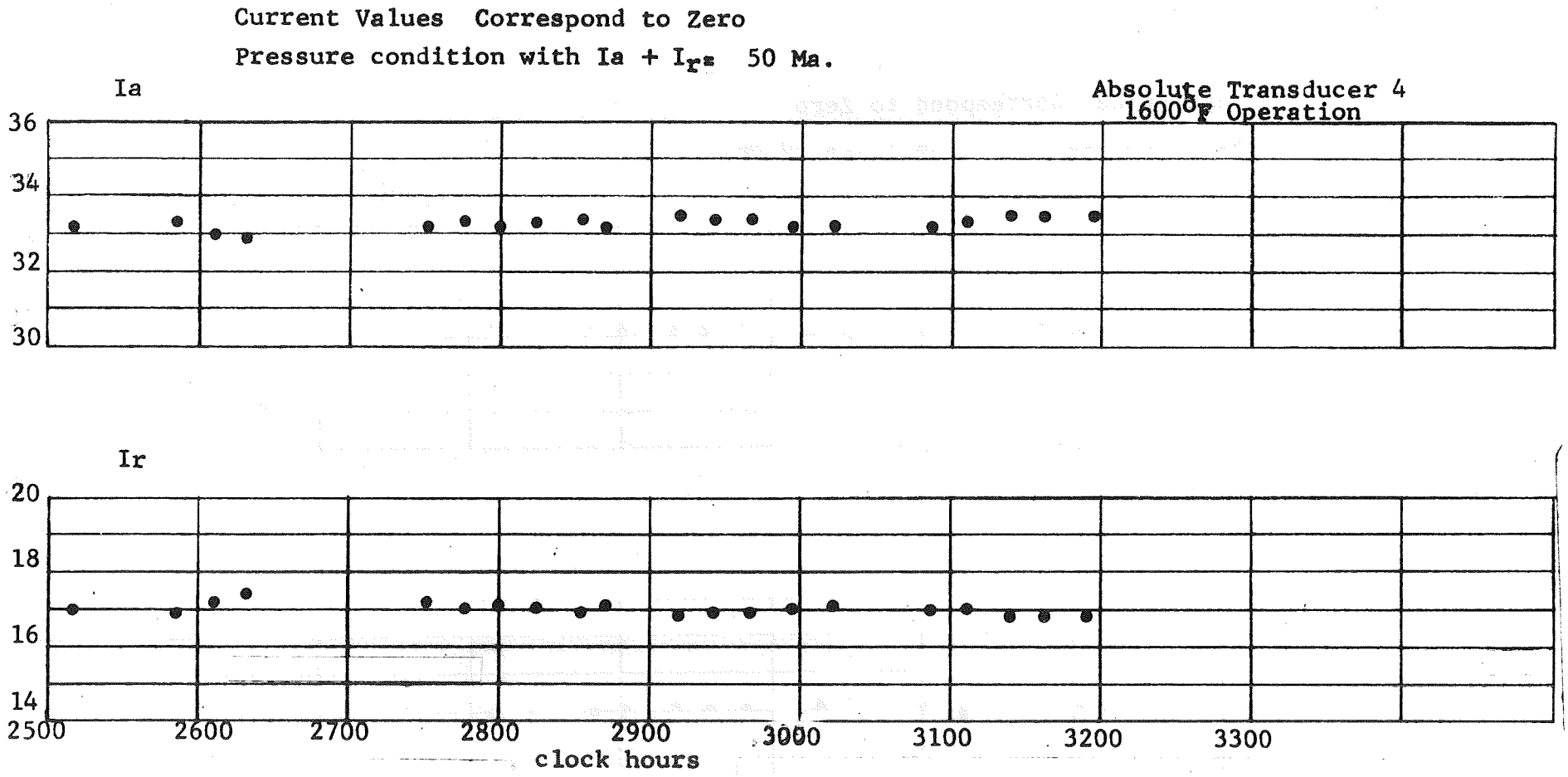


Figure 204

Active and Reference Current Characteristics

Absolute Transducer 4

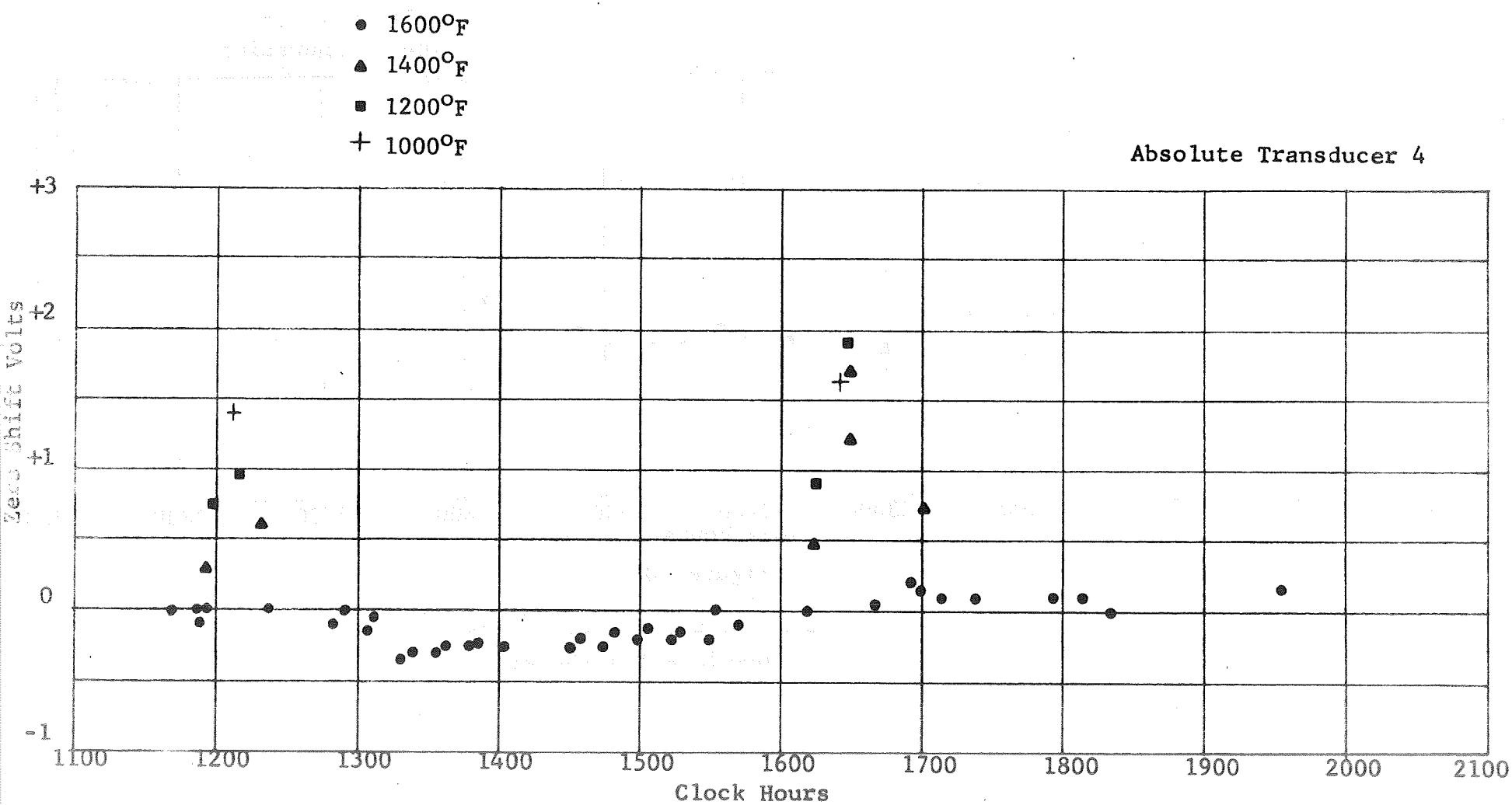


Figure 205

Zero-Shift Characteristics
Absolute Transducer 4

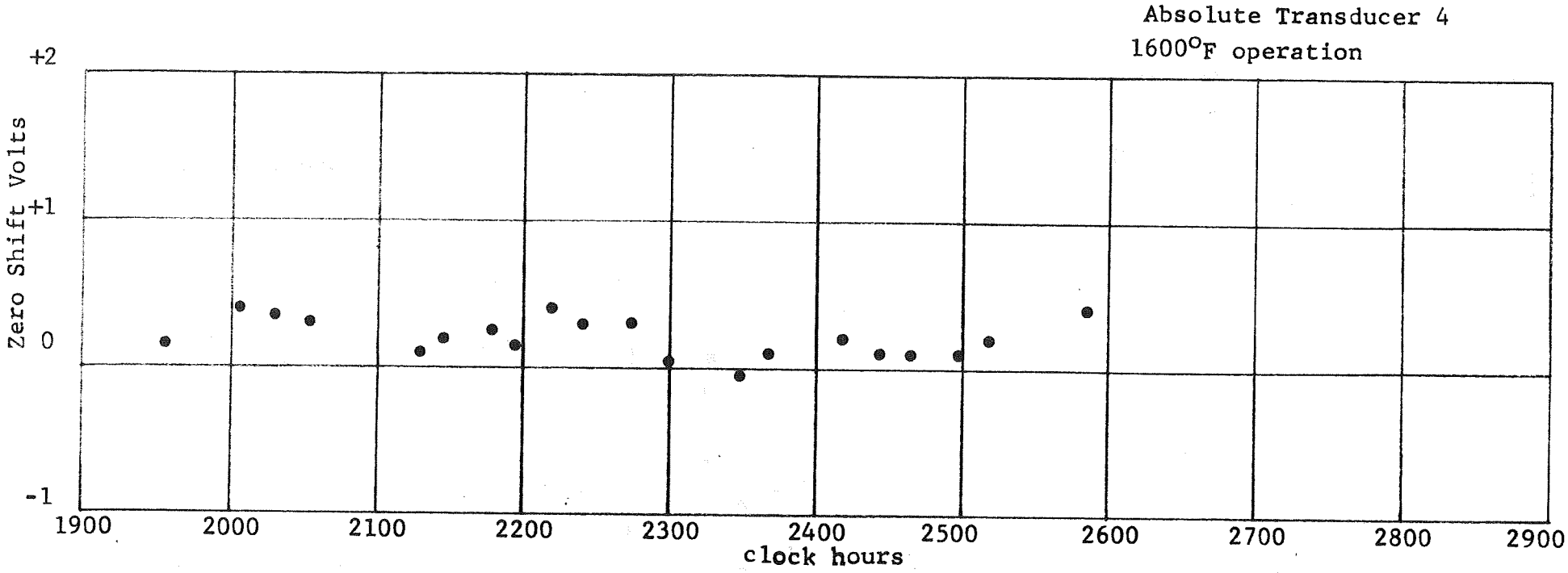


Figure 206

Zero-Shift Characteristics
Absolute Transducer 4

Absolute Transducer 4

1600°F operation

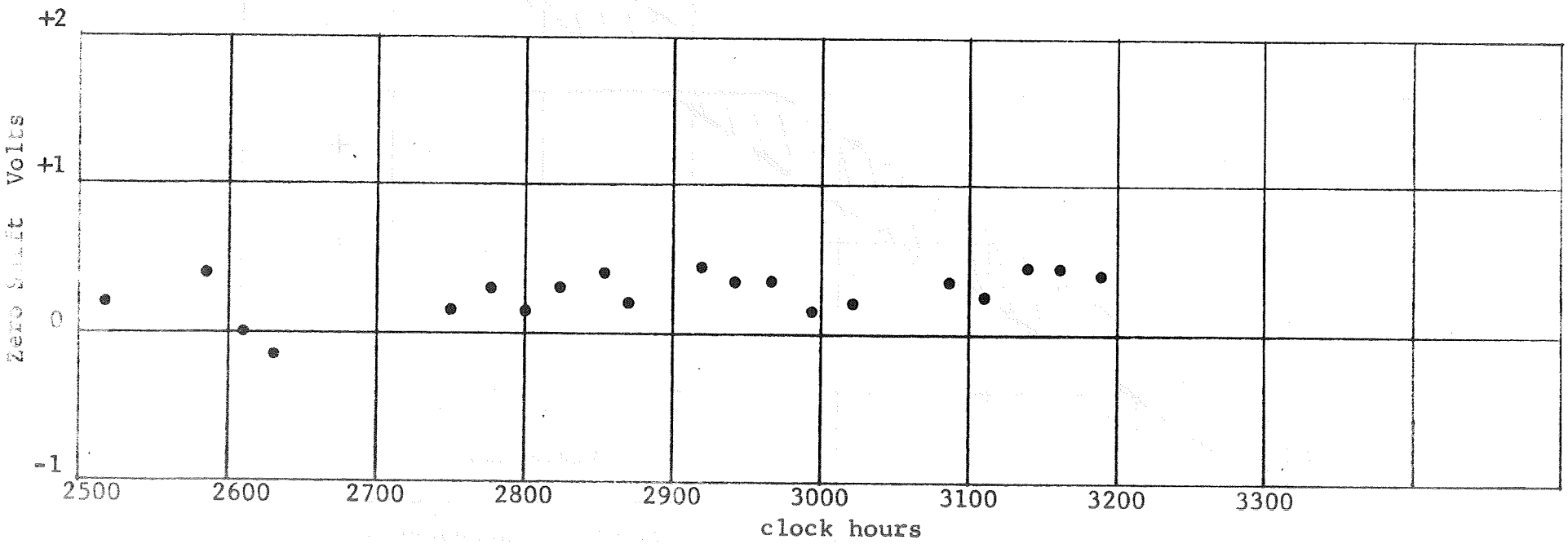


Figure 207

Zero-Shift Characteristics

Absolute Transducer 4

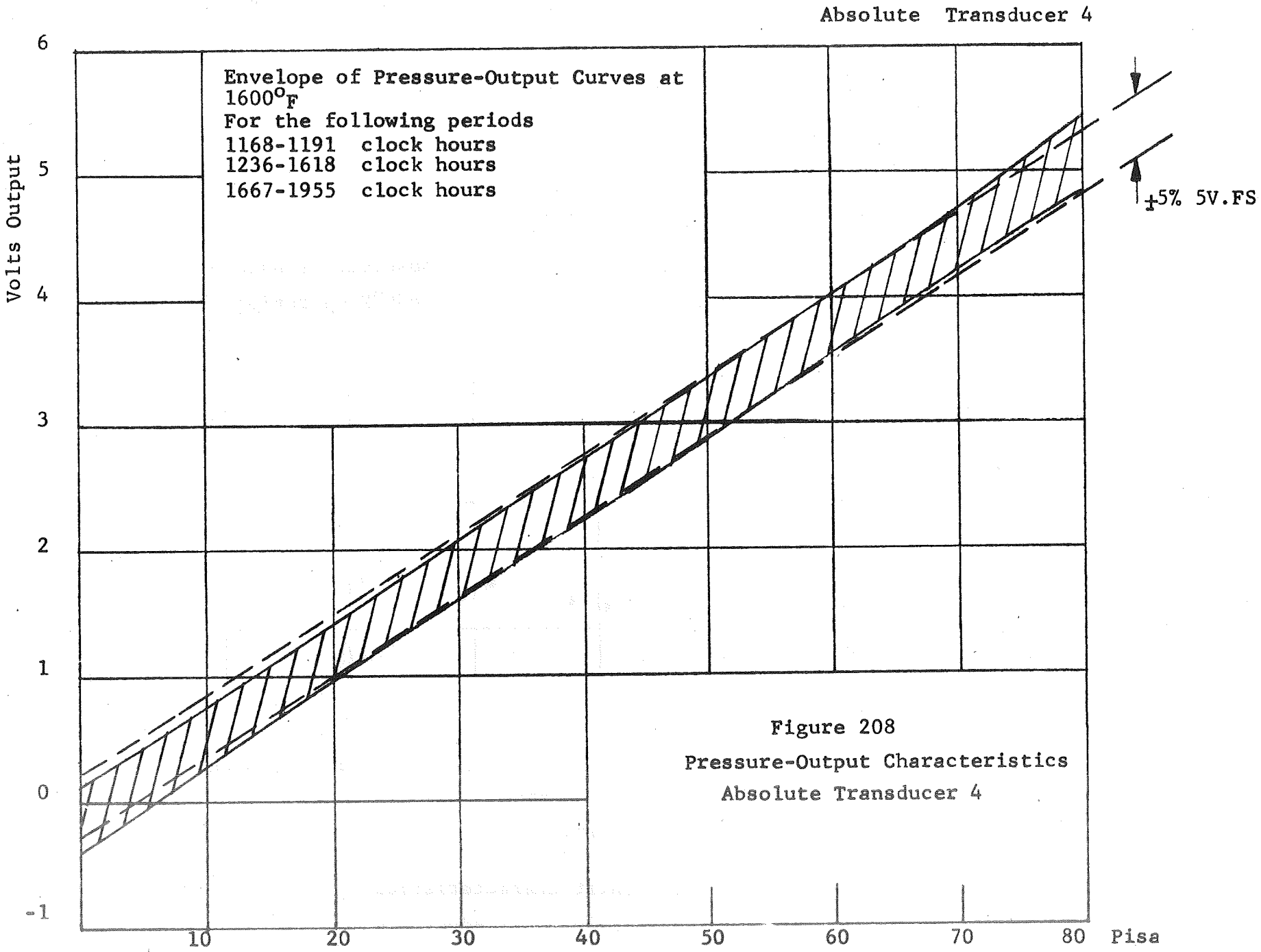


Figure 208
Pressure-Output Characteristics
Absolute Transducer 4

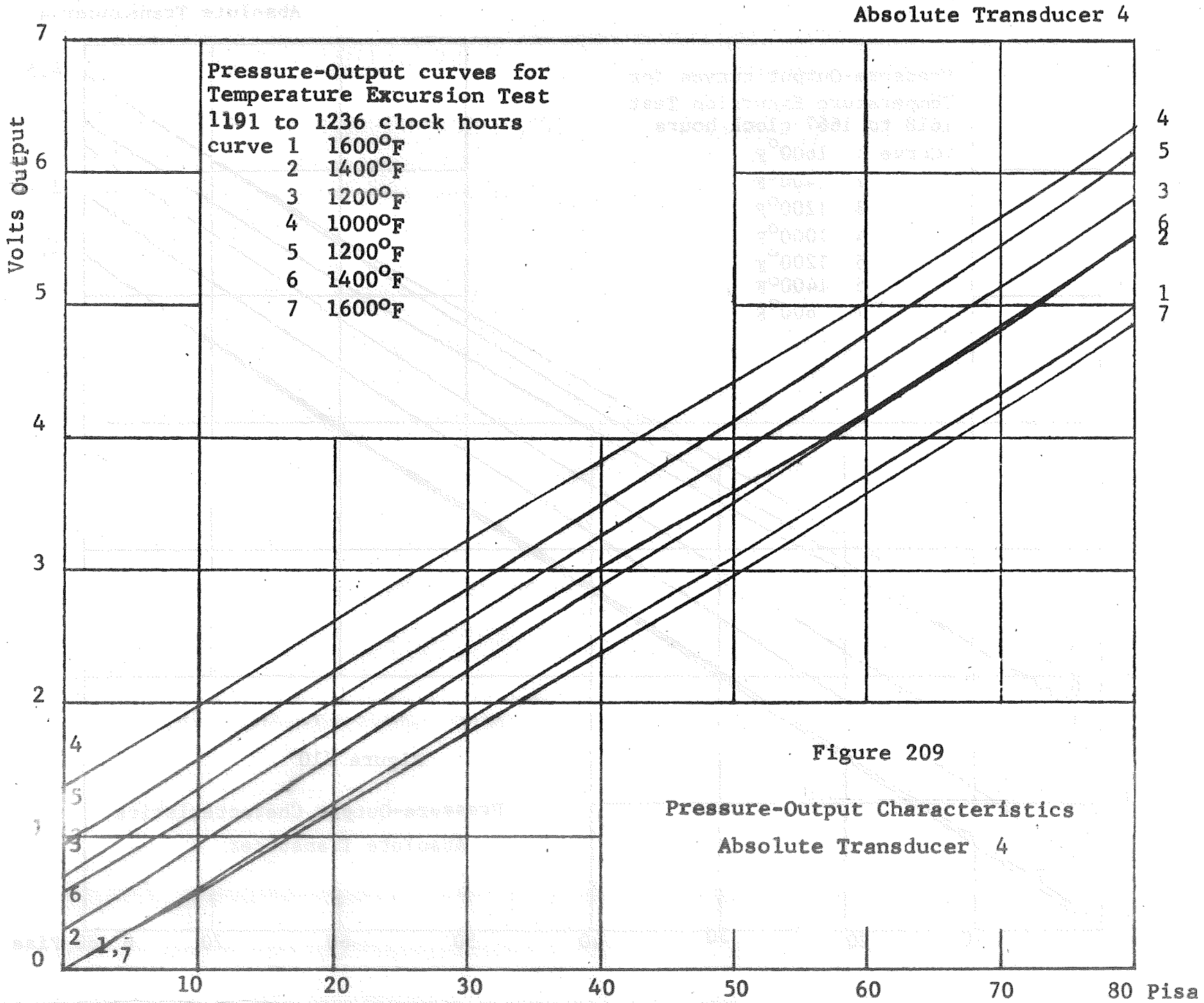


Figure 209

Pressure-Output Characteristics

Absolute Transducer 4

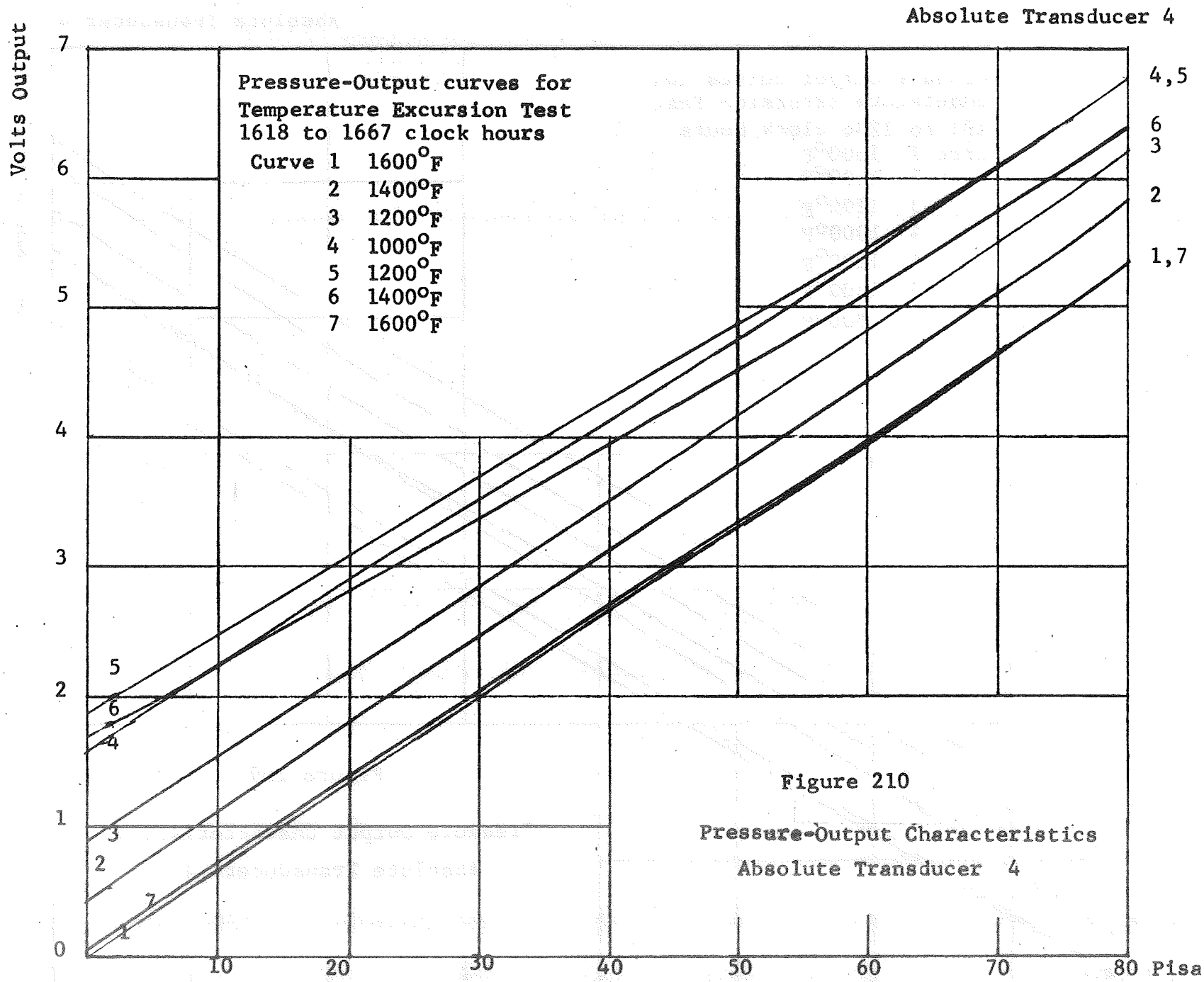


Figure 210

Pressure-Output Characteristics

Absolute Transducer 4

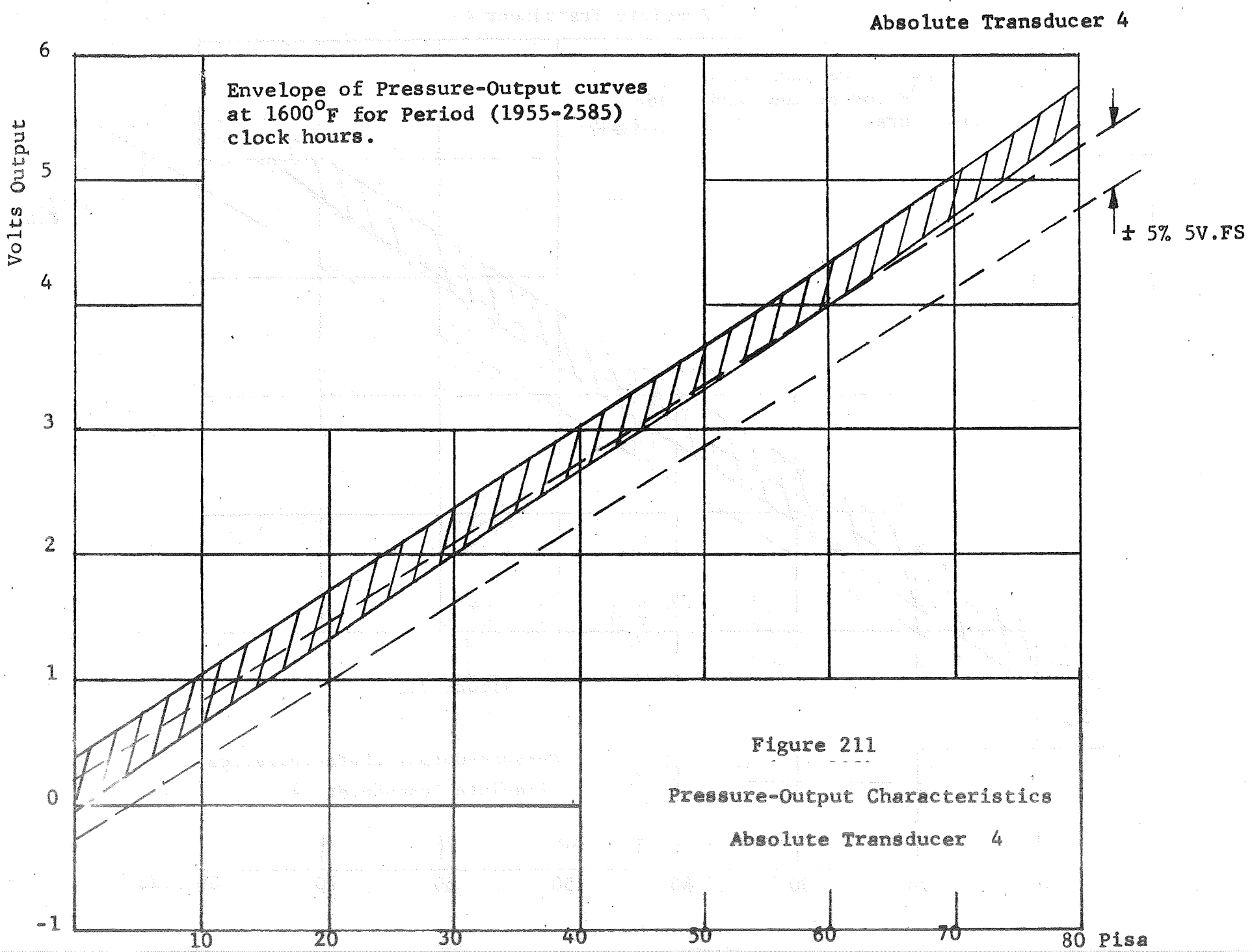


Figure 211

Pressure-Output Characteristics

Absolute Transducer 4

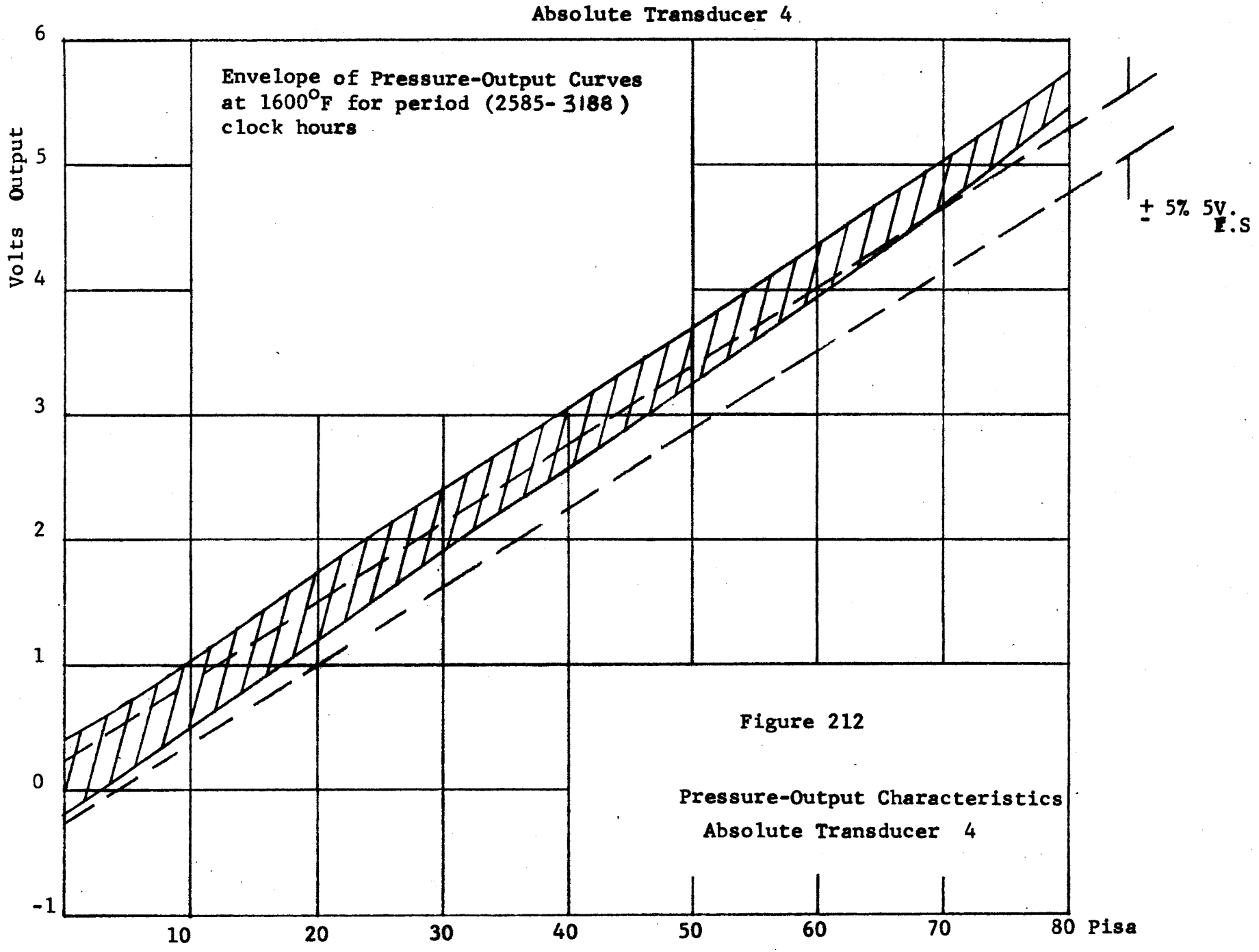


Figure 212

Pressure-Output Characteristics
Absolute Transducer 4

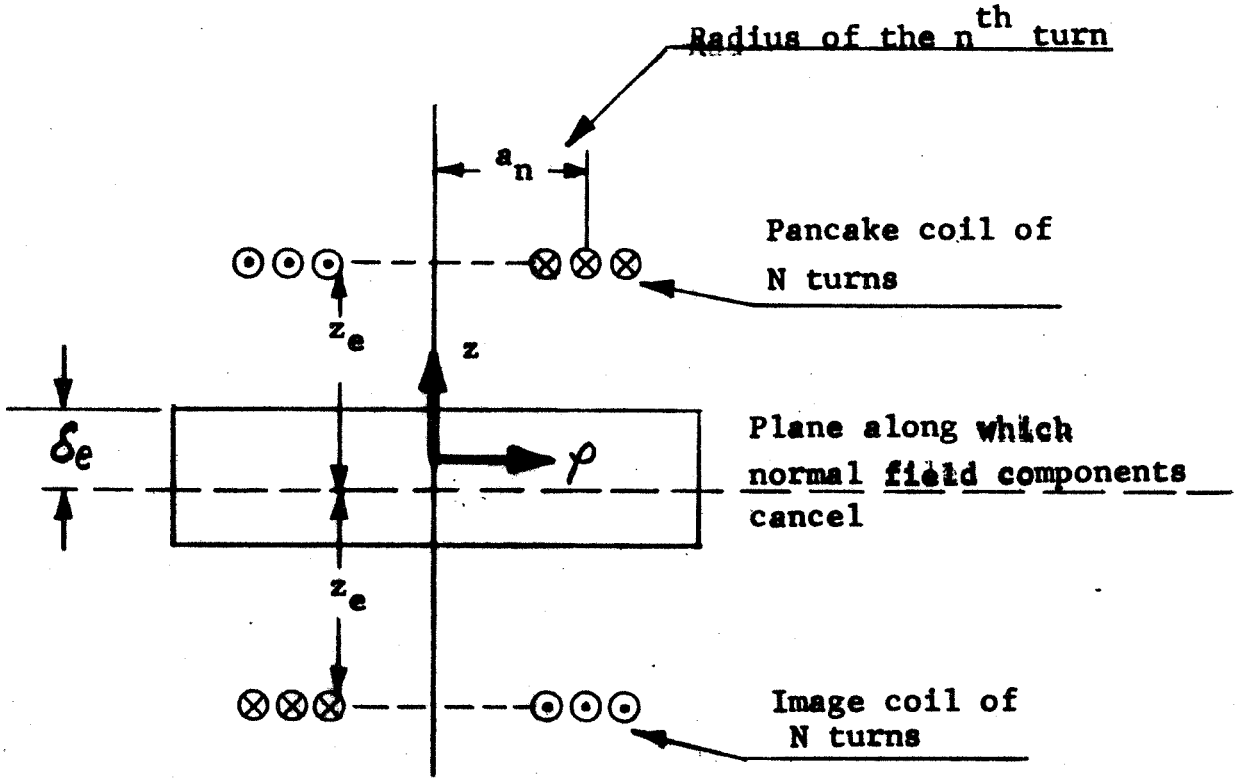


Figure 213

Pancake Coil/Image Coil Geometry

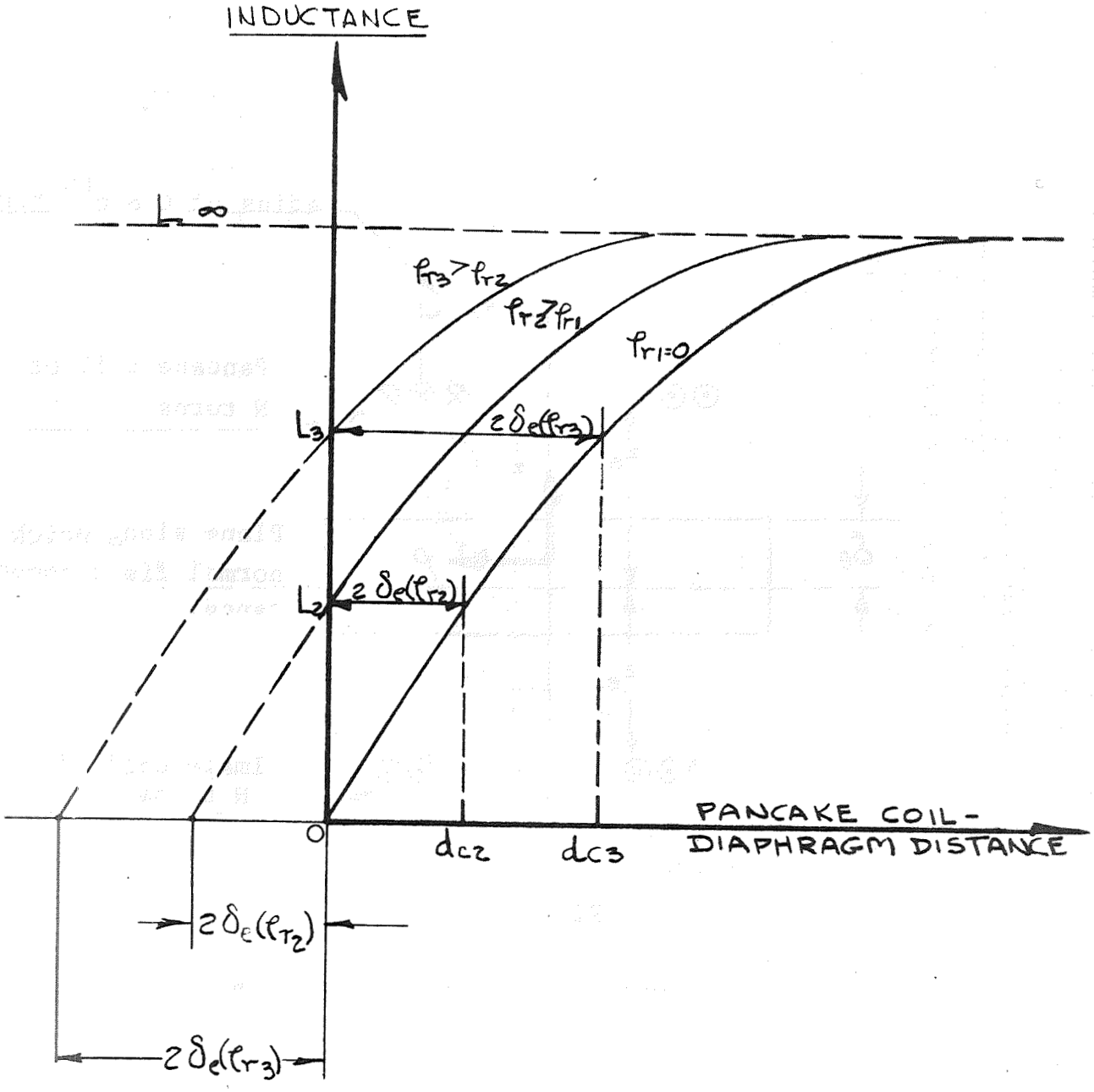


Figure 214

Inductance-Distance Characteristics

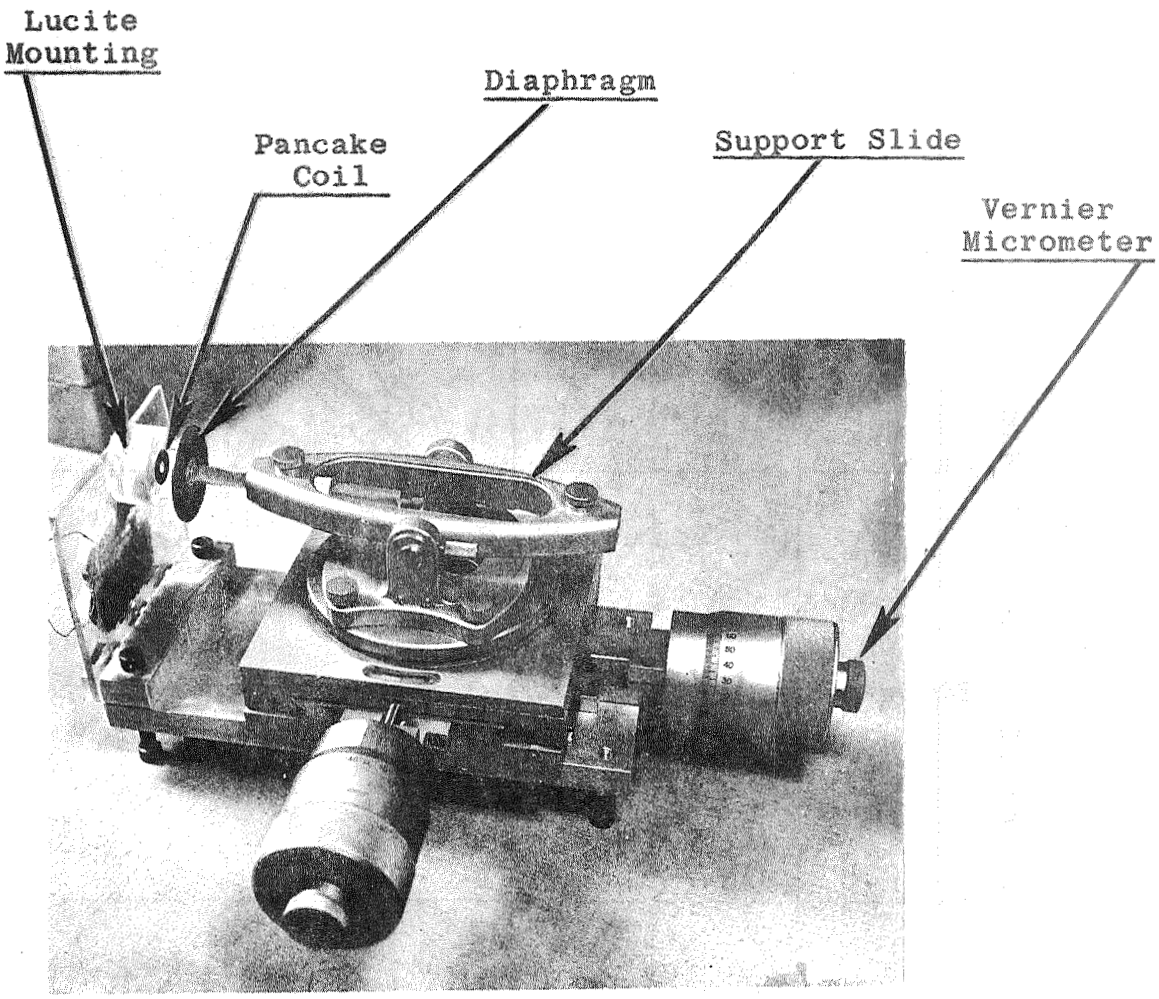


Figure 215

Variable Impedance Test Fixture

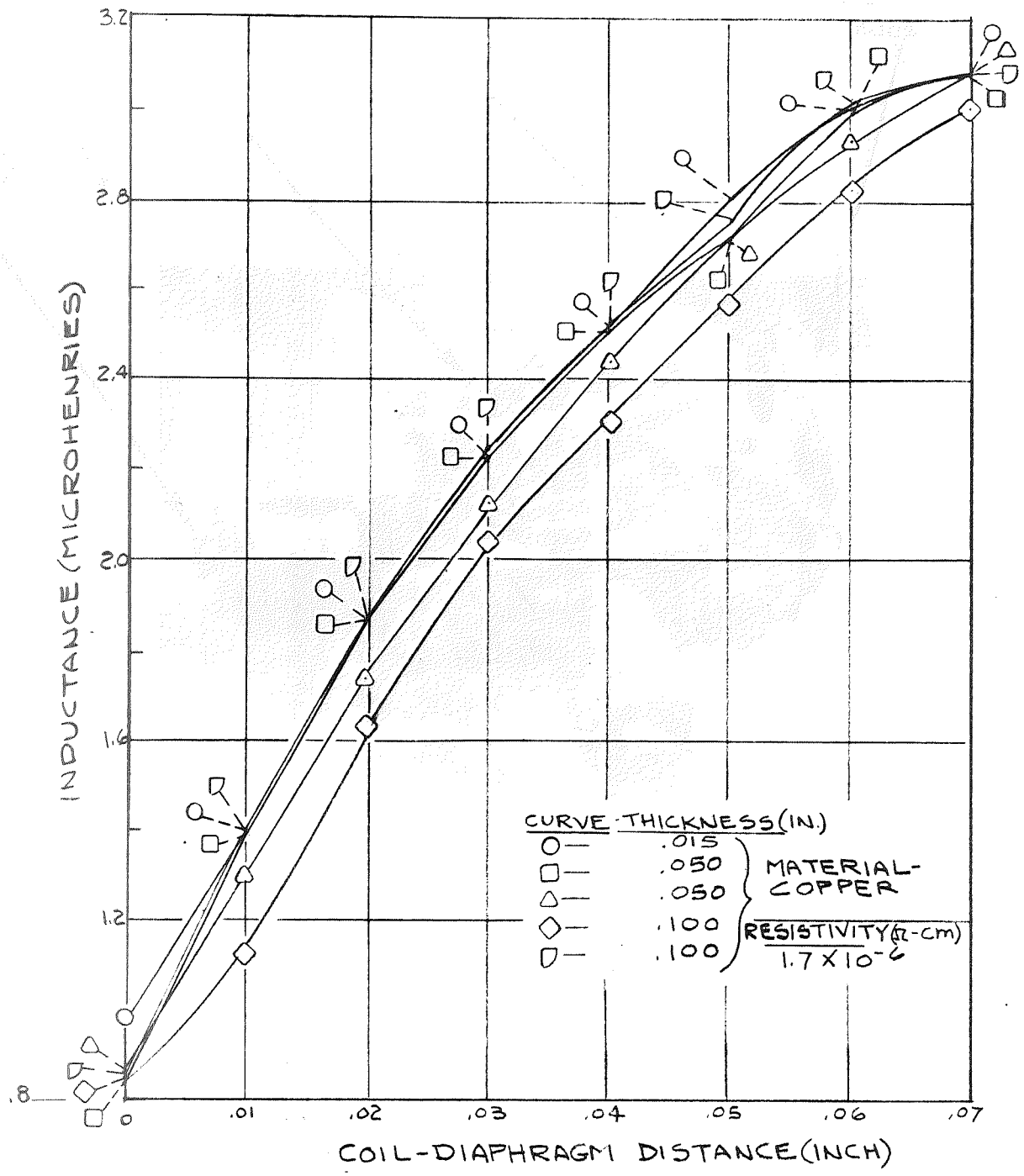


Figure 216

Inductance-Distance Characteristics; Copper Diaphragm

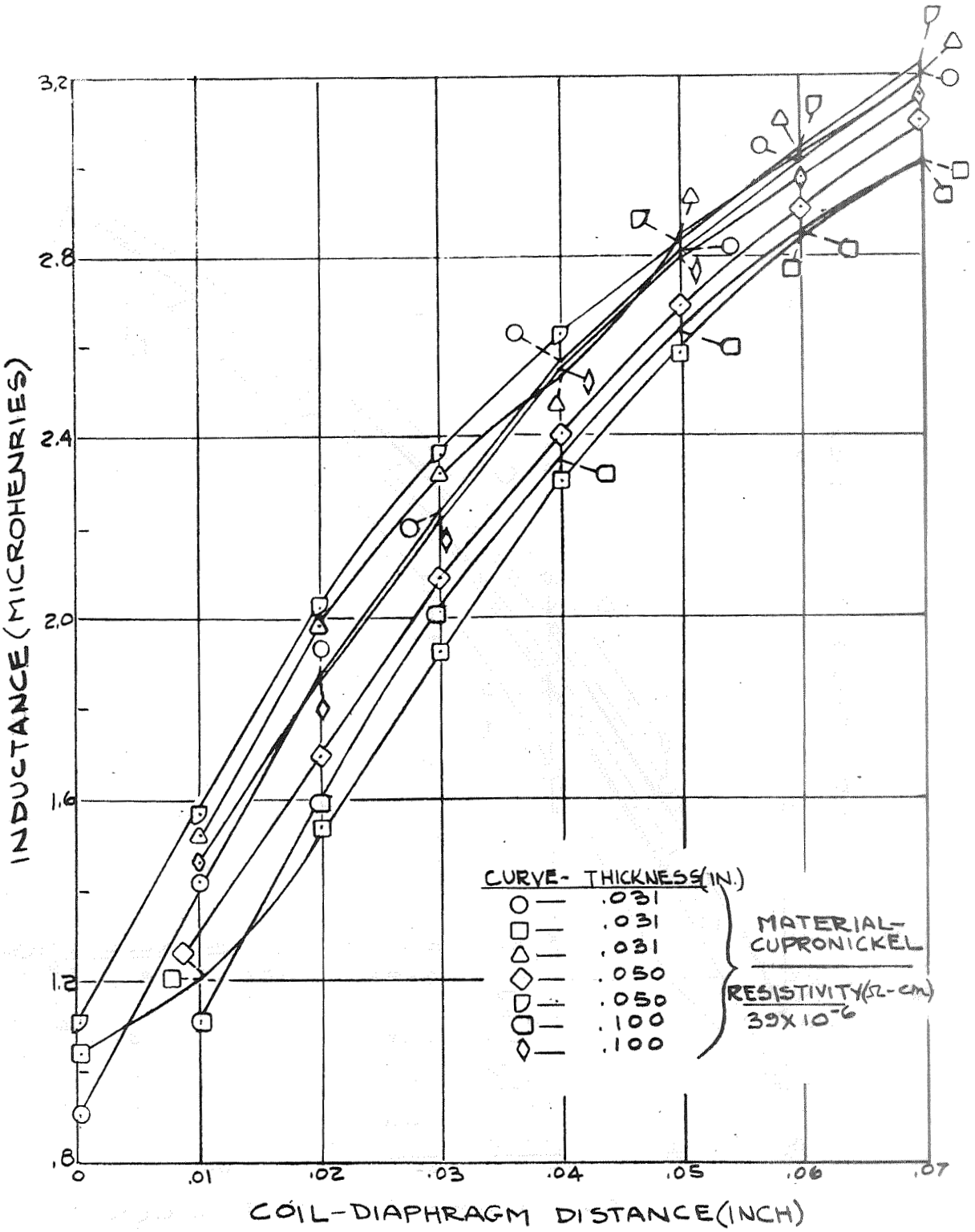


Figure 217

Inductance-Distance Characteristics; Cupronickel Diaphragm

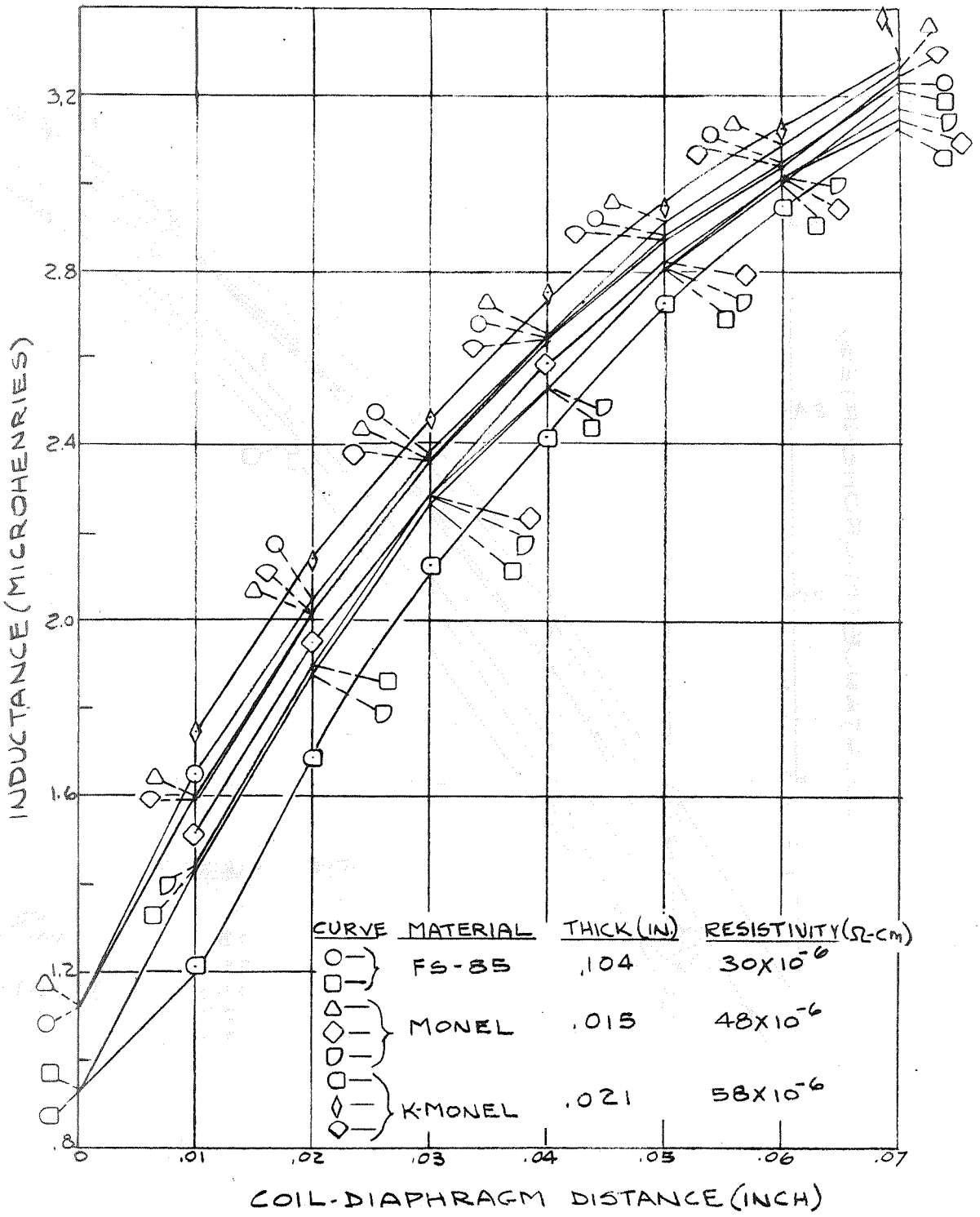


Figure 218

Inductance-Distance Characteristics; FS-85, Monel and K-Monel Diaphragms